Вол. 72, бр. 4

2024

ВОЈНОТЕХНИЧКИ ГЛАСНИК

BTГ

НАУЧНИ ЧАСОПИС МИНИСТАРСТВА ОДБРАНЕ И ВОЈСКЕ СРБИЈЕ

ВОЈНОТЕХНИЧКИ ГЛАСНИК

4 2024

MILITARY TECHNICAL COURIER

4 2024

MTC

MILITARY TECHNICAL COURIER

втг.мо.упр.срб

www.vtg.mod.gov.rs

НАУЧНИ ЧАСОПИС МИНИСТАРСТВА ОДБРАНЕ И ВОЈСКЕ СРБИЈЕ

ВОЈНОТЕХНИЧКИ ГЛАСНИК

ВОЛУМЕН 72•БРОЈ 4• ОКТОБАР – ДЕЦЕМБАР 2024.

NAUČNI ČASOPIS MINISTARSTVA ODBRANE I VOJSKE SRBIJE

VOJNOTEHNIČKI GLASNIK

VOLUMEN 72•BROJ 4•OKTOBAR – DECEMBAR 2024.

НАУЧНЫЙ ЖУРНАЛ МИНИСТЕРСТВА ОБОРОНЫ И ВООРУЖЁННЫХ СИЛ РЕСПУБЛИКИ СЕРБИЯ

ВОЕННО-ТЕХНИЧЕСКИЙ ВЕСТНИК

ТОМ 72•НОМЕР ВЫПУСКА 4•ОКТЯБРЬ – ДЕКАБРЬ 2024.

SCIENTIFIC JOURNAL OF THE MINISTRY OF DEFENCE AND SERBIAN ARMED FORCES

MILITARY TECHNICAL COURIER

VOLUME 72•ISSUE 4•OCTOBER – DECEMBER 2024

С А Д Р Ж А Ј

ОРИГИНАЛНИ НАУЧНИ РАДОВИ

СОДЕРЖАНИЕ

ОРИГИНАЛЬНЫЕ НАУЧНЫЕ СТАТЬИ

C O N T E N T S

ORIGINAL SCIENTIFIC PAPERS

On the KG-Sombor index

Ochirbat Altangoo[a], *Dechinpuntsag* Bolormaa[b],
Badarch Gantuya[c], *Tsend-Ayush* Selenge[d]

[a]Mongolian National University of Education,
  School of Mathematics and Natural Sciences, Ulaanbaatar, Mongolia,
  e-mail: altangoo@msue.edu.mn
  ORCID iD: https://orcid.org/0009-0000-6995-9138

[b]Mongolian National University of Education,
  School of Mathematics and Natural Sciences, Ulaanbaatar, Mongolia,
  e-mail: d.bolormaa@msue.edu.mn,
  ORCID iD: https://orcid.org/0009-0007-2094-9220

[c]Mongolian National University of Education,
  School of Mathematics and Natural Sciences, Ulaanbaatar, Mongolia,
  e-mail: gantuya@msue.edu.mn,
  ORCID iD: https://orcid.org/0000-0001-6323-6510

[d]National University of Mongolia, Department of Mathematics,
  Ulaanbaatar, Mongolia,
  e-mail: selenge@num.edu.mn, **corresponding author**,
  ORCID iD: https://orcid.org/0000-0002-8479-6389

Abstract:

Introduction/purpose: Degree-based graph invariants are a type of molecular descriptor that represent the connectivity of atoms (vertices) in a molecule through bonds (edges). They are used to model structural properties of molecules and provide valuable information for fields such as physical chemistry, pharmacology, environmental science, and material science. Recently, novel degree-based molecular structure descriptors, known as Sombor index-like graph invariants, have been explored from a geometrical perspective. These graph invariants have found applications in network science, where they are used to model dynamic effects in biological, social, and technological complex systems. There is also emerging interest in their potential military applications. Among these descriptors is the KG-Sombor index which is defined using both vertex and edge degrees.

Methods: The study uses combinatorial graph theory to identify and analyze extremal graphs that either maximize or minimize the KG-Sombor index.

Results: The extremal graphs are characterized concerning the KG-Sombor index, with a particular focus on trees, molecular trees, and unicyclic graphs.

Conclusion: This research advances the theoretical understanding of Sombor index-like graph invariants.

Key words: KG-Sombor index, tree, unicyclic graph, molecular tree.

Introduction

Let $G = (V, E)$ be a graph with the vertex set V and the edge set E. For a vertex v, the degree of the vertex v, denoted by d_v, is the number of edges incident with v. The first Zagreb index M_1 and the second Zagreb index M_2 of the graph G are among the most famous and extensively studied vertex-degree-based topological indices (Gutman & Das, 2004; Horoldagva et al., 2021; Selenge & Horoldagva, 2015; Zhang & Zhang, 2006) defined as:

$$M_1(G) = \sum_{uv \in E} (d_u + d_v) \quad \text{and} \quad M_2(G) = \sum_{uv \in E} d_u d_v.$$

For an edge uv, (d_u, d_v) and (d_v, d_u) are referred to as the degree-points of the edge uv. Let O be the origin of the coordinate system, and $M(d_u, d_v)$ and $M^*(d_v, d_u)$ represent the degree-points of an edge. The distance between the points O and M is $\sqrt{d_u^2 + d_v^2}$. Computing this for all edges in a graph and summing them yields the Sombor index (Gutman, 2021), defined as:

$$SO(G) = \sum_{uv \in E} |OM| = \sum_{uv \in E} \sqrt{d_u^2 + d_v^2}. \tag{1}$$

The Sombor-type indices (Dorjsembe & Horoldagva, 2022; Gutman, 2022, 2024; Tang et al., 2023) represent the latest addition to a plethora of topological indices in chemistry. The degree of an edge $e = uv \in E$, denoted by d_e, is the number of edges incident to e. In (Kulli et al., 2022); a novel topological graph invariant named the KG-Sombor index is intro-

duced:

$$KG(G) = \sum_{ue} \sqrt{d_u^2 + d_e^2}, \qquad (2)$$

where $\sum_{ue}$ denotes summation over the vertices $u \in V$ and the edges $e \in E$ incident to u. Some fundamental properties of the KG-Sombor index are established in (Kulli et al., 2022), along with its relationships with other topological indices.

Cruz et al. (Cruz et al., 2021) and Cruz and Rada (Cruz & Rada, 2021) investigated the extremal values of the Sombor index for chemical graphs, unicyclic graphs, and bicyclic graphs. Recent studies on the Sombor index and the KG-Sombor index can be found in (Damnjanović et al., 2023; Das et al., 2021; Horoldagva & Xu, 2021; Kosari et al., 2023; Liu et al., 2022; Rada et al., 2021; Selenge & Horoldagva, 2024) and the references cited therein. In this paper, we aim to determine the extremal graphs concerning the KG-Sombor index for trees, unicyclic graphs, and chemical trees of a given order.

KG-Sombor index of trees and unicyclic graphs

For $e = uv$ of a graph G, let us denote

$$f(d_u, d_v) = \sqrt{d_u^2 + (d_u + d_v - 2)^2} + \sqrt{d_v^2 + (d_u + d_v - 2)^2} \qquad (3)$$

and call it the weight of uv. On the other hand for an edge $e = uv$, there are two terms in the summation $\sum_{ue}$. Hence, we can reformulate the KG-Sombor index as follows.

$$KG(G) = \sum_{uv \in E} f(d_u, d_v). \qquad (4)$$

LEMMA 1. (Gutman & Das, 2004) Let T be a tree of order $n \geq 2$. Then $M_1(T) \geq 4n - 6$ with equality if and only if T is isomorphic to P_n.

Kulli et al. (Kulli et al., 2022) stated the following theorem without proof and mentioned that the proof is analogous to the proof of Theorem 2 in (Gutman, 2021). We now give the proof of it using the well-known result of Lemma 1.

THEOREM 1. *Let T be a tree of order $n \geq 3$. Then*

$$4\sqrt{2}(n-3) + 2\sqrt{2} + 2\sqrt{5} \leq KG(T)$$
$$\leq (n-1)(\sqrt{n^2 - 4n + 5} + \sqrt{2n^2 - 6n + 5}) \quad (5)$$

with equality on the left-hand side if and only if T is isomorphic to P_n, and equality on the right-hand side if and only if T is isomorphic to S_n.

Proof. From (3), one can easily show that

$$f(d_u, d_v) \geq \frac{1}{\sqrt{2}}(d_u + d_u + d_v - 2) + \frac{1}{\sqrt{2}}(d_v + d_u + d_v - 2)$$
$$= \frac{1}{\sqrt{2}}\left(3(d_u + d_v) - 4\right) \quad (6)$$

with equality if and only if $d_u = d_v = 2$.

Since T is the tree, it has at least two pendent edges. Let us denote by $f(1, d_x)$ and $f(1, d_y)$ the weights of two pendent edges e_1 and e_2, respectively. Then $d_x \geq 2$, $d_y \geq 2$ and

$$f(1, d_x) = \sqrt{1 + (d_x - 1)^2} + \sqrt{d_x^2 + (d_x - 1)^2}. \quad (7)$$

First, it is shown that for $d_x \geq 2$,

$$f(1, d_x) \geq \frac{3\sqrt{2}}{2}d_x + \sqrt{5} - 2\sqrt{2} = g(d_x) \quad (8)$$

with equality if and only if $d_x = 2$. If $2 \leq d_x \leq 6$ then from (7) and (8), one obtains $f(1, 2) = \sqrt{5} + \sqrt{2} = g(2)$, $\sqrt{5} + \sqrt{13} = f(1, 3) > g(3) = 2.5\sqrt{2} + \sqrt{5}$, $\sqrt{10} + 5 = f(1, 4) > g(4) = 4\sqrt{2} + \sqrt{5}$, $\sqrt{17} + \sqrt{41} = f(1, 5) > g(5) = 5.5\sqrt{2} + \sqrt{5}$ and $\sqrt{26} + \sqrt{61} = f(1, 6) > g(6) = 7\sqrt{2} + \sqrt{5}$. On the other hand, one gets

$$f(1, d_x) > d_x - 1 + \sqrt{2}(d_x - 1) = (1 + \sqrt{2})(d_x - 1)$$

and from this it can easily be seen that inequality (8) holds for all $d_x \geq 7$.

Similarly as the above there is

$$f(1, d_y) \geq \frac{3\sqrt{2}}{2}d_y + \sqrt{5} - 2\sqrt{2} \quad (9)$$

with equality if and only if $d_y = 2$.

Then by the definition of the KG-Sombor index and (6), one gets

$$KG(T) = \sum_{uv \in E} f(d_u, d_v) = \sum_{uv \in E \setminus \{e_1, e_2\}} f(d_u, d_v) + f(1, d_x) + f(1, d_y)$$

$$\geq \frac{1}{\sqrt{2}} \sum_{uv \in E \setminus \{e_1, e_2\}} [(3(d_u + d_v) - 4)] + f(1, d_x) + f(1, d_y)$$

$$= \frac{3}{\sqrt{2}} \sum_{uv \in E(T)} (d_u + d_v) + f(1, d_x) + f(1, d_y)$$

$$- \frac{3}{\sqrt{2}}(d_x + d_y + 2) - \frac{4}{\sqrt{2}}(n - 3)$$

$$= \frac{3\sqrt{2}}{2} M_1(T) + f(1, d_x) + f(1, d_y) - \frac{3\sqrt{2}}{2}(d_x + d_y + 2) - 2\sqrt{2}(n - 3).$$

Then, using (8), (9) and Lemma 1 in the above inequality gives the lower bound in (5). From (6), (8), (9) and Lemma 1, it can be easily concluded that the left-hand side inequality in (5) holds if and only if T is isomorphic to P_n,

To prove the right-hand side inequality, let us consider the function

$$\phi(x) = \sqrt{x^2 + (n-2)^2} + \sqrt{(n-x)^2 + (n-2)^2}$$

and

$$\phi''(x) = \frac{1}{\sqrt{x^2 + (n-2)^2}} - \frac{x^2}{(x^2 + (n-2)^2)^{3/2}} + \frac{1}{\sqrt{(n-x)^2 + (n-2)^2}}$$

$$- \frac{x^2}{((n-x)^2 + (n-2)^2)^{3/2}}$$

$$= (n-2)^2 \left(\frac{1}{(x^2 + (n-2)^2)^{3/2}} + \frac{1}{((n-x)^2 + (n-2)^2)^{3/2}} \right) > 0.$$

Therefore the function $\phi(x)$ is convex and if $1 \leq x \leq n-1$ then the maximum of ϕ is attained at $x = 1$ or $x = n - 1$.

Let $uv \in E$. Then since T is a tree, one obtains

$$2(n - 1) = 2|E| = \sum_{w \in V} d_w \geq d_u + d_v + n - 2$$

that is, $d_u + d_v \leq n$. Therefore,

$$f(d_u, d_v) \leq \sqrt{d_u^2 + (n-2)^2} + \sqrt{d_v^2 + (n-2)^2} \leq \phi(d_u) \leq \phi(1) = \phi(n-1)$$

from $\phi(x)$ is convex. Then, by the definition of the KG-Sombor index, one gets

$$KG(T) = \sum_{uv \in E} f(d_u, d_v) \leq \sum_{uv \in E} \phi(1) = (n-1)\phi(1)$$

that is our required upper bound. Suppose now that the right-hand side equality holds in (5). Then $d_u = 1$ and $d_v = n - 1$ for all $uv \in E$. Hence T is a star S_n and one can see easily that the right-hand side equality holds in (5) for S_n. This completes the proof. $\qquad\square$

LEMMA 2. (Zhang & Zhang, 2006) Let G be a unicyclic graph of order $n \geq 3$. Then $M_1(G) \geq 4n$ with equality if and only if G is isomorphic to C_n.

THEOREM 2. *Let G be a unicyclic graph of order $n \geq 3$. Then*

$$KG(G) \geq 4n\sqrt{2}$$

with equality if and only if G is isomorphic to C_n.

Proof. Let uv be an edge of G. Then, similarly as in the proof of the previous theorem, one gets

$$f(d_u, d_v) \geq \frac{1}{\sqrt{2}}\left(3(d_u + d_v) - 4\right)$$

with equality if and only if $d_u = d_v = 2$. Therefore, by the above inequality and Lemma 2, one obtains

$$
\begin{aligned}
KG(G) &= \sum_{uv \in E} f(d_u, d_v) \geq \frac{3}{\sqrt{2}} \sum_{uv \in E} (d_u + d_v) - 2n\sqrt{2} \\
&= \frac{3}{\sqrt{2}} M_1(G) - 2n\sqrt{2} \geq 4n\sqrt{2}
\end{aligned}
$$

with equality if and only if G is isomorphic to C_n. $\qquad\square$

KG-Sombor index of molecular trees

By Theorem 1 it is evident that the path P_n has a minimal KG-value among molecular trees of order n. Therefore, this section determines the extremal graphs with the maximal KG-value among molecular trees of order n. For $n = 3k + 2$, $k \geq 1$, we denote by $\mathcal{T}_n$ the set of trees of order

n such that the degree of every vertex is either one or four. For $n = 3k$, $k \geq 3$, we denote by $\mathcal{T}_n$ the set of trees of order n such that only one vertex has degree two, and its neighbors have degree four, while the remaining vertices have degree one or four. For $n = 3k + 1$, $k \geq 4$, we denote by $\mathcal{T}_n$ the set of trees of order n such that only one vertex has degree three, and its neighbors have degree four, while the remaining vertices have degree one or four.

If $n \leq 3$ then there is only one tree of order n. If $n = 4$, then there are two trees that are P_4 and S_4, thus $KG(P_4) < KG(S_4)$. Hence, we assume that $n \geq 5$. For $n = 6$, $n = 7$, $n = 10$, we have determined the graphs with the maximum KG-Sombor index by using SageMath.
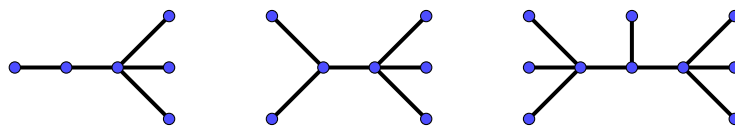
Figure 1 – Graphs with the maximum KG-Sombor index for $n = 6, 7, 10$.

The values of the KG-Sombor index of the above graphs are $3\sqrt{10} + 3\sqrt{5} + 5\sqrt{2} + 15$, $\sqrt{41} + \sqrt{34} + 2\sqrt{13} + 3\sqrt{10} + 2\sqrt{5} + 15$ and $2\sqrt{41} + 2\sqrt{34} + \sqrt{13} + 6\sqrt{10} + \sqrt{5} + 30$, respectively. For the remaining values of n, the following theorem holds.

THEOREM 3. *Let T be a molecular tree of order n.*

(i) *If $n = 3k + 2$, $k \geq 1$ then*

$$KG(T) \leq \frac{10 + 2\sqrt{10}}{3}(n + 1) + \frac{4\sqrt{13}}{3}(n - 5).$$

(ii) *If $n = 3k$, $k \geq 3$ then*

$$KG(T) \leq \frac{(10 + 2\sqrt{10})n}{3} + \frac{4\sqrt{13}n}{3} + 8\sqrt{2} + 4\sqrt{5} - 12\sqrt{13}.$$

(iii) *If $n = 3k + 1$, $k \geq 4$ then*

$$KG(T) \leq \frac{(10 + 2\sqrt{10})n}{3} + \frac{4\sqrt{13}n}{3} + 3\sqrt{34} + 3\sqrt{41} + \frac{5 + \sqrt{10}}{3} - \frac{52\sqrt{13}}{3}.$$

The equalities hold if and only if $T \in \mathcal{T}_n$.

Proof. Let n_i $(i = 1, 2, 3, 4)$ be the number of vertices of the degree i in T. Also let $m_{i,j}$ $(1 \leq i \leq j \leq 4)$ be the number of edges of T connecting the vertices of the degree i and j. Then there is $m_{1,1} = 0$ and

$$n_1 + n_2 + n_3 + n_4 = n$$

$$m_{1,2} + m_{1,3} + m_{1,4} + m_{2,2} + m_{2,3} + m_{2,4} + m_{3,3} + m_{3,4} + m_{4,4} = n - 1$$

$$m_{1,2} + m_{1,3} + m_{1,4} = n_1$$

$$m_{1,2} + 2m_{2,2} + m_{2,3} + m_{2,4} = 2n_2$$

$$m_{1,3} + m_{2,3} + 2m_{3,3} + m_{3,4} = 3n_3$$

$$m_{1,4} + m_{2,4} + m_{3,4} + 2m_{4,4} = 4n_4. \tag{10}$$

From the above, the following equations are easily obtained:

$$n = \frac{3}{2}m_{1,2} + \frac{4}{3}m_{1,3} + \frac{5}{4}m_{1,4} + m_{2,2} + \frac{5}{6}m_{2,3} + \frac{3}{4}m_{2,4}$$
$$+ \frac{2}{3}m_{3,3} + \frac{7}{12}m_{3,4} + \frac{1}{2}m_{4,4},$$

$$m_{1,4} = \frac{2}{3}(n + 1)$$
$$- \frac{2}{3}\left(2m_{1,2} + \frac{5}{3}m_{1,3} + m_{2,2} + \frac{2}{3}m_{2,3} + \frac{1}{2}m_{2,4} + \frac{1}{3}m_{3,3} + \frac{1}{6}m_{3,4}\right),$$

$$m_{4,4} = \frac{1}{3}(n - 5) + \frac{1}{3}m_{1,2} + \frac{1}{9}m_{1,3} - \frac{1}{3}m_{2,2} - \frac{5}{9}m_{2,3} - \frac{2}{3}m_{2,4} - \frac{7}{9}m_{3,3}$$
$$- \frac{8}{9}m_{3,4}. \tag{11}$$

Then, using (11), one obtains

$$KG(T) = \sum_{uv \in E(G)} f(d_u, d_v)$$

$$= \sum_{1 \leq i \leq j \leq 4} \left[\sqrt{i^2 + (i + j - 2)^2} + \sqrt{j^2 + (i + j - 2)^2}\right] \cdot m_{i,j}$$

$$= (\sqrt{2} + \sqrt{5})m_{1,2} + (\sqrt{5} + \sqrt{13})m_{1,3} + (5 + \sqrt{10})m_{1,4} + 4\sqrt{2}m_{2,2}$$
$$+ (3\sqrt{2} + \sqrt{13})m_{2,3} + (4\sqrt{2} + 2\sqrt{5})m_{2,4} + 10m_{3,3}$$
$$+ (\sqrt{34} + \sqrt{41})m_{3,4} + 4\sqrt{13}m_{4,4}$$

$$= \frac{10 + 2\sqrt{10}}{3}(n + 1) + \frac{4\sqrt{13}}{3}(n - 5) + c_{12}m_{1,2} + c_{13}m_{1,3}$$

$$+ c_{22}m_{2,2} + c_{23}m_{2,3} + c_{24}m_{2,4} + c_{33}m_{3,3} + c_{34}m_{3,4}, \qquad (12)$$

where $c_{12} = \sqrt{2} + \sqrt{5} - \frac{4(5+\sqrt{10})}{3} + \frac{4\sqrt{13}}{3} \approx -2.425$, $c_{13} = \sqrt{5} + \sqrt{13} - \frac{10(5+\sqrt{10})}{9} + \frac{4\sqrt{13}}{9} \approx -1.625$, $c_{22} = 4\sqrt{2} - \frac{2(5+\sqrt{10})}{3} - \frac{4\sqrt{13}}{3} \approx -4.592$, $c_{23} = 3\sqrt{2} + \sqrt{13} - \frac{4(5+\sqrt{10})}{9} - \frac{20\sqrt{13}}{9} \approx -3.792$, $c_{24} = 4\sqrt{2} + 2\sqrt{5} - \frac{5+\sqrt{10}}{3} - \frac{8\sqrt{13}}{3} \approx -2.206$, $c_{33} = 10 - \frac{2(5+\sqrt{10})}{9} - \frac{28\sqrt{13}}{9} \approx -3.031$ and $c_{34} = \sqrt{34} + \sqrt{41} - \frac{5+\sqrt{10}}{9} - \frac{32\sqrt{13}}{9} \approx -1.492$. Note that

$$c_{22} < c_{23} < c_{33} < c_{12} < c_{13} < c_{34} < c_{24} < 0. \qquad (13)$$

Now the following three cases are distinguished.

(i) If $n = 3k + 2$, $k \geq 1$ then from (12) and (13), one obtains

$$KG(T) \leq \frac{10 + 2\sqrt{10}}{3}(n + 1) + \frac{4\sqrt{13}}{3}(n - 5)$$

with equality holding if and only if

$$m_{1,2} = m_{1,3} = m_{2,2} = m_{2,3} = m_{2,4} = m_{3,3} = m_{3,4} = 0.$$

Hence one gets $n_1 = m_{1,4} = 2(n + 1)/3$ and $m_{4,4} = (n - 5)/3$. Also, there is $n_2 = n_3 = 0$.

(ii) If $n = 3k$, $k \geq 3$ then one can easily see that $n_2 \neq 0$ or $n_3 \neq 0$. If $n_2 \geq 1$ then

$$m_{1,2} + 2m_{2,2} + m_{2,3} + m_{2,4} = 2n_2 \geq 2$$

from (10). Therefore, one gets

$$\begin{aligned}
KG(T) \leq & \frac{10 + 2\sqrt{10}}{3}(n + 1) + \frac{4\sqrt{13}}{3}(n - 5) \\
& + c_{24}(m_{1,2} + 2m_{2,2} + m_{2,3} + m_{2,4}) \\
\leq & \frac{10 + 2\sqrt{10}}{3}(n + 1) + \frac{4\sqrt{13}}{3}(n - 5) + 2c_{24} \\
= & \frac{(10 + 2\sqrt{10})n}{3} + \frac{4\sqrt{13}n}{3} + 8\sqrt{2} + 4\sqrt{5} - 12\sqrt{13} \qquad (14)
\end{aligned}$$

since $c_{12} < c_{23} < c_{24}$ and $c_{22} < 2c_{24}$.

1501

If $n_3 \geq 1$ then

$$m_{1,3} + m_{2,3} + 2m_{3,3} + m_{3,4} = 3n_3 \geq 3$$

from (10). Hence, one obtains

$$
\begin{aligned}
KG(T) \leq & \frac{10 + 2\sqrt{10}}{3}(n+1) + \frac{4\sqrt{13}}{3}(n-5) \\
& + c_{34}(m_{1,3} + m_{2,3} + 2m_{3,3} + m_{3,4}) \\
\leq & \frac{10 + 2\sqrt{10}}{3}(n+1) + \frac{4\sqrt{13}}{3}(n-5) + 3c_{34} \\
= & \frac{(10 + 2\sqrt{10})n}{3} + \frac{4\sqrt{13}n}{3} + 3\sqrt{34} + 3\sqrt{41} + \frac{5 + \sqrt{10}}{3} \\
& - \frac{52\sqrt{13}}{3}
\end{aligned}
\tag{15}
$$

since $c_{23} < c_{13} < c_{34}$ and $c_{33} < 2c_{34}$. From (14) and (15), one gets the required result because $3c_{34} < 2c_{24}$. Equality holds in (14) if and only if $n_2 = 1$, $n_3 = 0$ and $m_{2,4} = 2$.

(iii) If $n = 3k + 1$, $k \geq 4$ then $n_2 \neq 0$ or $n_3 \neq 0$. If $n_3 \geq 1$, then similarly as in (ii), one gets

$$
\begin{aligned}
KG(T) \leq & \frac{(10 + 2\sqrt{10})n}{3} + \frac{4\sqrt{13}n}{3} + 3\sqrt{34} + 3\sqrt{41} + \frac{5 + \sqrt{10}}{3} \\
& - \frac{52\sqrt{13}}{3}.
\end{aligned}
\tag{16}
$$

Let now $n_3 = 0$. If $n_2 = 1$, then the system of equations $n_1 + n_4 = n - 1$ and $n_1 + 4n_4 = 2(n-2)$ has no integer solution. Thus $n_2 \geq 2$ and, similarly as in (ii), one also gets

$$
\begin{aligned}
KG(T) \leq & \frac{10 + 2\sqrt{10}}{3}(n+1) + \frac{4\sqrt{13}}{3}(n-5) \\
& + c_{24}(m_{1,2} + 2m_{2,2} + m_{2,3} + m_{2,4}) \\
\leq & \frac{10 + 2\sqrt{10}}{3}(n+1) + \frac{4\sqrt{13}}{3}(n-5) + 4c_{24} \\
< & \frac{(10 + 2\sqrt{10})n}{3} + \frac{4\sqrt{13}n}{3} + 3\sqrt{34} + 3\sqrt{41} + \frac{5 + \sqrt{10}}{3} - \frac{52\sqrt{13}}{3}
\end{aligned}
$$

from $4c_{24} < 3c_{34}$. Equality holds in (16) if and only if $n_2 = 0$, $n_3 = 1$ and $m_{3,4} = 3$. On the other hand, in each case it can be easily concluded that the equality holds if and only if $T \in \mathcal{T}_n$. □

Conclusions

Topological indices play a vital role in conducting quantitative structure-activity relationship and quantitative structure-property relationship studies. Numerous topological indices have been defined in the literature and several of them are applied as a means to model physical, chemical, pharmaceutical, and other properties of molecules. Gutman pioneered the introduction of SO-type indices within the field of mathematical chemistry. Our study determined the minimal and the maximal KG-Sombor index for the class of trees and chemical trees. Moreover, we proved that C_n is the unique graph with the minimal KG-Sombor index among all unicyclic graphs of order n. However, the problems of determining the graphs with the maximal KG-Sombor index in the class of unicyclic graphs, and finding the extremal KG-Sombor index in the class of bicyclic graphs remain open.

References

Cruz, R., Gutman, I. & Rada, J. 2021. Sombor index of chemical graphs. *Applied Mathematics and Computation*, 399, art.number:126018. Available at: https://doi.org/10.1016/j.amc.2021.126018.

Cruz, R. & Rada, J. 2021. Extremal values of the Sombor index in unicyclic and bicyclic graphs. *Journal of Mathematical Chemistry*, 59, pp.1098-1116. Available at: https://doi.org/10.1007/s10910-021-01232-8.

Damnjanović, I., Milošević, M. & Stevanović, D. 2023. A Note on Extremal Sombor Indices of Trees with a Given Degree Sequence. *MATCH Communications in Mathematical and in Computer Chemistry*, 90(1), pp.197-202. Available at: https://doi.org/10.46793/match.90-1.197D.

Das, K.C., Cevik, A.S., Cangul, I.N. & Shang, Y. 2021. On Sombor Index. *Symmetry*, 13(1), art.number:140. Available at: https://doi.org/10.3390/sym13010140.

Dorjsembe, Sh. & Horoldagva, B. 2022. Reduced Sombor index of bicyclic graphs. *Asian-European Journal of Mathematics*, 15(07), art.number:2250128. Available at: https://doi.org/10.1142/S1793557122501285.

Gutman, I. 2021. Geometric Approach to Degree–Based Topological Indices: Sombor Indices. *MATCH Communications in Mathematical and in Computer Chemistry*, 86(1), pp.11-16 [online]. Available at: https://match.pmf.kg.ac.rs/electronic_versions/Match86/n1/match86n1_11-16.pdf [Accessed: 14 March 2024].

Gutman, I. 2022. Sombor indices - back to geometry. *Open Journal of Discrete Applied Mathematics*, 5(2), pp.1-5. Available at: https://doi.org/10.30538/psrp-odam2022.0072.

Gutman, I. 2024. Relating Sombor and Euler indices. *Vojnotehnički glasnik/Military Technical Courier*, 72(1), pp.1-12. Available at: https://doi.org/10.5937/vojtehg72-48818.

Gutman, I. & Das, K.Ch. 2004. The first Zagreb index 30 years after. *MATCH Communications in Mathematical and in Computer Chemistry*, 50, pp.83-92 [online]. Available at: https://match.pmf.kg.ac.rs/electronic_versions/Match50/match50_83-92.pdf [Accessed: 14 March 2024].

Horoldagva, B., Selenge, T.-A., Buyantogtokh, L. & Dorjsembe, Sh. 2021. Upper bounds for the reduced second Zagreb index of graphs. *Transactions on Combinatorics*, 10(3), pp.137-148. Available at: https://doi.org/10.22108/toc.2020.125478.1774.

Horoldagva, B. & Xu, C. 2021. On Sombor index of graphs. *MATCH Communications in Mathematical and in Computer Chemistry*, 86(3), pp.703-713 [online]. Available at: https://match.pmf.kg.ac.rs/electronic_versions/Match86/n3/match86n3_703-713.pdf [Accessed: 14 March 2024].

Kosari, S., Dehgardi, N. & Khan, A. 2023. Lower bound on the KG-Sombor index. *Communications in Combinatorics and Optimization*, 8(4), pp.751-757. Available at: https://doi.org/10.22049/cco.2023.28666.1662.

Kulli, V.R., Harish, N., Chaluvaraju, B. & Gutman, I. 2022. Mathematical properties of KG-Sombor index. *Bulletin of International Mathematical Virtual Institute*, 12(2), pp.379-386 [online]. Available at: http://www.imvibl.org/buletin/bulletin_imvi_12_2_22/bulletin_imvi_12_2_22_379_386.pdf [Accessed: 14 March 2024].

Liu, H., Gutman, I., You, H. & Huang, Y. 2022. Sombor index: review of extremal results and bounds. *Journal of Mathematical Chemistry*, 60, pp.771-798. Available at: https://doi.org/10.1007/s10910-022-01333-y.

Rada, J., Rodríguez, J.M. & Sigarreta, J.M. 2021. General properties on Sombor indices. *Discrete Applied Mathematics*, 299, pp.87-97. Available at: https://doi.org/10.1016/j.dam.2021.04.014.

Selenge, T.-A. & Horoldagva, B. 2024. Extremal Kragujevac trees with respect to Sombor indices. *Communications in Combinatorics and Optimization*, 9(1), pp.177-183. Available at: https://doi.org/10.22049/cco.2023.28058.1430.

Selenge, T.-A. & Horoldagva, B. 2015. Maximum Zagreb indices in the class of k-apex trees. *Korean Journal of Mathematics*, 23(3), pp.401-408. Available at: https://doi.org/10.11568/kjm.2015.23.3.401.

Tang, Z., Li, Q. & Deng, H. 2023. Trees with Extremal Values of the Sombor–Index–Like Graph Invariants. *MATCH Communications in Mathematical and in Computer Chemistry*, 90(1), pp.203-222. Available at: https://doi.org/10.46793/match.90-1.203T.

Zhang, H. & Zhang, S. 2006. Uncyclic graphs with the first three smallest and largest first general Zagreb index. *MATCH Communications in Mathematical and in Computer Chemistry*, 55(2), pp.427-438 [online]. Available at: https://match.pmf.kg.ac.rs/electronic_versions/Match55/n2/match55n2_427-438.pdf [Accessed: 14 March 2024].

En el índice KG-Sombor

Ochirbat Altangoo[a], *Dechinpuntsag* Bolormaa[a],
Badarch Gantuya[a], *Tsend-Ayush* Selenge[b]

[a] Universidad Nacional de Educación de Mongolia, Facultad de Matemáticas y Ciencias Naturales, Ulaanbaatar, Mongolia

[b] Universidad Nacional de Mongolia, Departamento de Matemáticas, Ulaanbaatar, Mongolia, **autor de correspondencia**

Resumen:

Introducción/objetivo: Los invariantes de gráficos basados en grados son un tipo de descriptores moleculares que representan la conectividad de los átomos (vértices) en una molécula a través de enlaces (bordes). Se utilizan para modelar propiedades estructurales de moléculas y proporcionar información valiosa para campos como la química física, la farmacología, las ciencias ambientales y las ciencias de materiales. Recientemente, se han explorado desde una perspectiva geométrica nuevos descriptores de estructuras moleculares basados en grados, conocidos como invariantes de gráficos tipo índice de Sombor. Estas invariantes gráficas han encontrado aplicaciones en la ciencia de redes, donde se utilizan para modelar efectos dinámicos en sistemas complejos biológicos, sociales y tecnológicos. También está surgiendo un interés en sus posibles aplicaciones militares. Entre estos descriptores se encuentra el índice KG-Sombor, que se define utilizando grados de vértice y borde.

Métodos: El estudio utiliza la teoría de grafos combinatoria para identificar y analizar gráficos extremos que maximizan o minimizan el índice KG-Sombor.

Resultados: Los gráficos extremos se caracterizan en relación con el índice KG-Sombor, con especial atención a árboles, árboles moleculares y gráficos unicíclicos.

Conclusión: Esta investigación avanza en la comprensión teórica de las invariantes gráficas similares al índice de Sombor.

Palabras claves: índice KG-Sombor, árbol, gráfico unicíclico, árbol molecular.

Индекс КГ-Сомбор

Очирбат Алтангоо[a], *Дичинпунтсаг* Болормаа[a],
Бадарч Гантуя[a], *Тсенд-Аюш* Селенге[б]

[a] Монгольский национальный педагогический университет,
   факультет математики и естественных наук,
   г. Улан-Батор, Монголия

[б] Монгольский национальный университет, математический
   факультет, г. Улан-Батор, Монголия, **корреспондент**

Резюме:

Введение/цель: Недавно с геометрической точки зрения были исследованы новые дискрипторы молекулярной структуры на основе степеней, известные как инварианты графов, подобные Сомборскому индексу. Эти инварианты графа нашли применение в сетевой науке, где они используются для моделирования динамических эффектов в биологических, социальных и сложных технологических системах. Также растет интерес к их потенциальному применению в военных целях. Среди этих дескрипторов и KG-Сомборский индекс, который определяется с использованием степеней как вершины, так и ребра.

Методы: В данном исследовании используется комбинаторная теория графов для выявления и анализа экстремальных графов, которые либо максимизируют, либо минимизируют КГ-Сомборский индекс.

Результаты: Экстремальные графы характеризуются КГ-Сомборским индексом, при этом особое внимание уделяется деревьям, молекулярным деревьям и одноциклическим графам.

Выводы: Данное исследование вносит вклад в расширение теоретического понимания инвариантов графов, подобных Сомборскому индексу.

КГ-Сомборски индекс

Окирбат Алтангу[а], *Дичинпантсаг* Болома[а],
Бадарч Гантуија[а], *Ценд-Ајуш* Селенге[б]

[а] Монголски национални универзитет за образовање,
Факултет математике и природних наука, Улан Батор, Монголија

[б] Национални универзитет Монголије, Одсек за математику,
Улан Батор, Монголија, **аутор за преписку**

Сажетак:

*Увод/циљ: На степенима засноване графовске инваријан-
те тип су молекуларних дескриптора који представљају
повезаност атома (чворова) у молекулу путем веза (гра-
на). Користе се за моделовање структурних својстава мо-
лекула и пружају драгоцене информације у областима по-
пут физичке хемије, фармакологије, науке о животној сре-
дини, као и науке о материјалима. Из геометријске пер-
спективе недавно су проучавани нови дескриптори молеку-
ларне структуре на бази степена, познати као графовске
инваријанте сродне Сомборском индексу. Ове графовске
инваријанте нашле су примену у науци о мрежама где се
користе за моделовање динамичких утицаја у биолошким,
друштвеним и сложеним технолошким системима. Тако-
ђе, постоји и интересовање за потенцијалне примене у вој-
сци. Међу овим дескрипторима налази се КГ-Сомборски ин-
декс који се дефинише коришћењем степенова и чворова и
грана.*

*Методе: У истраживању се користи комбинаторна тео-
рија графова за идентификацију и анализу екстремалних
графова који или максимизују или минимизују КГ-Сомборски
индекс.*

*Резултати: Екстремални графови се карактеришу у од-
носу на КГ-Сомборски индекс, са посебним освртом на ста-
бла, молекуларна стабла и унициклачне графове.*

Fixed point results in controlled revised fuzzy metric spaces with an application to the transformation of solar energy to electric power

Ravichandran Thangathamizh[a], *Abdelhamid* Moussaoui[b],
Tatjana Došenović[c], *Stojan* Radenović[d]

[a] Jeppiaar Institute of Technology (Autonomous), Department of
Mathematics, Kanchipuram, Tamil Nadu, Republic of India,
e-mail: thangathamizhrmaths@krce.ac.in, **corresponding author**,
ORCID ID: https://orcid.org/0000-0002-2449-5103

[b] Sultan Moulay Slimane University, Faculty of Sciences and Technics,
LMACS, Beni Mellal, Kingdom of Morocco,
e-mail: a.moussaoui@usms.ma,
ORCID ID: https://orcid.org/0000-0003-4897-1132

[c] University of Novi Sad, Faculty of Technology,
Novi Sad, Republic of Serbia,
e-mail: tatjanad@tf.uns.ac.rs,
ORCID ID: https://orcid.org/0000-0002-3236-4410

[d] University of Belgrade, Faculty of Mechanical Engineering,
Belgrade, Republic of Serbia,
e-mail: radens@beotel.rs,
ORCID ID: https://orcid.org/0000-0001-8254-6688

Abstract:

Introduction/purpose: This study establishes sufficient conditions for a sequence to be Cauchy within the framework of controlled revised fuzzy metric spaces. It also generalizes the concept of Banach's contraction principle by introducing several new contraction conditions. The aim is to derive various fixed-point results that enhance the understanding of these mathematical structures.

Methods: The researchers employ rigorous mathematical techniques to develop their findings. By defining a set of novel contraction mappings and utilizing properties of controlled revised fuzzy metric spaces, they analyze the implications for sequence convergence. The methodology includes constructing specific examples to illustrate the theoretical results.

Results: The study presents several fixed-point theorems derived from the generalized contraction conditions. Additionally, it provides a number of non-trivial examples that substantiate the claims and demonstrate the applicability of the results in practical scenarios. A significant application is

explored regarding the conversion of solar energy into electric power, utilizing differential equations to highlight this connection.

Conclusion: The findings deepen the understanding of Cauchy sequences in fuzzy metric spaces and offer a broader perspective on the application of the fixed-point theory in real-world scenarios. The results pave the way for further research in both theoretical mathematics and its practical applications, particularly in the field of renewable energy.

Key words: fixed point theorems, revised fuzzy metric space (RFMS), contraction principles(CP), Green's function, differential equation.

Introduction and preliminaries

The existence of a unique fixed point (UFP) for self-mappings under suitable contraction conditions over complete metric spaces(CMS) is guaranteed by Banach's fixed point theory (BSP) (also known as "the contraction mapping theorem"), one of the most significant sources of existence and uniqueness theorems in numerous areas of analysis. New extensions and generalizations of fixed point results are important because they increase our understanding of mathematical systems, enable the solution of specific problems, extend current theorems, and lead to the development of new theories and applications. They are an important aspect of mathematical study and have far-reaching ramifications in a variety of fields.

Fuzzy logic (FL) was established by Zadeh (1965). Unlike the theory of traditional logic, some numbers are not contained within the stand. FL afflation of the numbers in the set defines an element within the interval [0,1]. Zadeh has learned theories of fuzzy sets to be art, the problem of indefinity with the aid of uncertainty, the essential part of genuine difficulty.

The theory is seen as a fixed point (FP) in the fuzzy metric space (FMS) for various processes, one of them utilizing fuzzy logic. Later on, following Zadeh's outcomes, Heilpern (1981) established the fuzzy mapping (FM) notion and a theorem on an FP for fuzzy contraction mapping (FCM) in linear MS, expressing a fuzzy general form of BC-theory. In the definition of FMSs provided by Kaleva & Saikkala (1984), the imprecision is introduced if the distance between the elements is not a precise integer. After the first by Kramosil & Michálek (1975) and further work by George & Veeramani (1994), the notation of an FMS was introduced. After that, Klement et al. (2004) presented some problems on trigonomtric terms and releted operators.

Branga & Olaru (2022) proved several fixed point results for self-mappings by utilizing generalized contractive conditions in the context

of altered MS. Al-Khaleel et al. (2023) used cyclic contractive mappings of Kannan and Chatterjea type in generalized metric spaces. Czerwik (1993) found the solution of the well-known BFPT in the context of b-metric spaces (b-MS). Mlaiki et al. (2018) defined controlled MS as a generalization of b-MS by utilizing a control function $\alpha : \Xi^2 \to [1, \infty)$ of the otherside of the b-triangular inequality. The relation between b-MS and FMS has been discussed by Hassanzadeh & Sedghi (2018). Li et al. (2022) used Kaleva–Seikkala's type FbMSs and proved several fixed point results by using contraction mappings. Furthermore, Sedghi & Shobe (2012) and Sedghi & Shobkolaei (2014) proved various common FPTs for R-weakly commuting maps in the frame work of FbMSs. Sezen (2021) introduced controlled FMS as a generalization of FMS and FbMS by applying a control function $\alpha : \Xi^2 \to [1, \infty)$ in a triangular inequality of the form:

$$M(b, \omega, t + s) \geq M\left(b, z, \frac{t}{\alpha(b, z)}\right) + M\left(z, \omega, \frac{t}{\alpha(z, \omega)}\right), \text{for all } b, \omega, z \in \Xi \text{ and } s, t > 0 \,.$$

If we take $\alpha(b, z) = \alpha(z, \omega) = 1$ then its an FMS and for $\alpha(b, z) = \alpha(z, \omega) \geq s$ with $s \geq 1$ it is then an FbMS.

Ishtiaq et al. (2022, 2023) established the theory of double-controlled intuitionistic fuzzy metric-like spaces by "considering the case where the self-distance is not zero"; if the metric's value is 0, afterwards it must be a self-distance and also an established FP theorem for contraction mappings. See (Schweizer & Sklar, 1960) for triangular conorm (TCN), continuous triangular conorm (CTCN) (Kaleva & Seikkala, 1984), and TN of H-type (Hadžić, 1979; Hassanzadeh & Sedghi, 2018). In (Hussain et al, 2022), the authors worked on CFMSs by utilizing orthogonality and pentagonal CFMSs and proved several FPRs for contraction mappings. Rakić et al. (2020) proved a fuzzy version of BFPT by using Ciric-quasi-contraction in the context of FbMSs. Younis et al. (2022) proved several FPRs in the context of dislocated b-metric spaces and solved the turning circuit problem.

In 2018, Šostak (2018) explored the idea of Revised Fuzzy Metric Spaces (shortly, RFM-Space) as a new idea to express a revised fuzzy set. Then Grigorenko et al. (2020) made several proposals based on RFM-Spaces. Building on the work of Šostak (2018), Muraliraj et al. (2023) defined the notion of retinal-type revised fuzzy contraction and proved a fixed point theorem of RFM spaces. Muraliraj & Thangathamizh (Muraliraj & Thangathamizh, 2021ab) partially came up with the idea of fixed point results for RFM in revised fuzzy contraction (shortly, RFM contractions). The following authors (Adabitabar Firozja & Firouzian, 2015; Kider, 2020,

2021; Moussaoui et al, 2022; Muraliraj & Thangathamizh, 2021a, 2023) provided many concepts of RFMS and they proved to be quite useful in this study. Gregori & Miñana (2021) introduced a new version of contraction principles in the context of fuzzy metric spaces. It is defined by the means of t-conorms. After that Muraliraj & Thangathamizh (2022), Thangathamizh et al. (2024) established new revised fuzzy cone contraction type unique coupled fixed point theorems in revised fuzzy cone metric spaces by using the property of triangular.

In this article,

- we prove that a sequence must be Cauchy in the CRFMS under some conditions;

- we prove a fixed point result by using new Ciric-quasi-contraction and generalize the Banach contraction principle by utilizing several new contraction conditions;

- we provide several non-trivial examples to show the validity of the main results;

- we discuss an application concerning the transformation of solar energy to electric power.

Now, we provide several definitions and results that are helpful to understand the main section.

Definition 1 (Šostak, 2018). A binary operation $\Gamma: [0,1]^2 \to [0,1]$ is a CTCN if it verifies the conditions below:

(C 1) Γ is commutative and associative,

(C 2) Γ is continuous,

(C 3) $\Gamma(\kappa, 0) = \kappa$ for all $\kappa \in [0,1]$,

(C 4) $\Gamma(\kappa, \rho) \leq \Gamma(c, d)$ for $\kappa, \rho, c, d \in [0,1]$ such that $\kappa \leq c$ and $\rho \leq d$.

The examples of CTCN are $\Gamma_p(a, b) = a + b - a \cdot b$, $\Gamma_{max}(a, b) = \max\{a, b\}$, and $\Gamma_L(a, b) = \min\{a + b, 1\}$.

Definition 2 (Hadžić, 1979). Suppose that Γ is a TCN and suppose that $\Gamma_\tau: [0,1] \to [0,1], \tau \in \mathbb{N}$, express the process given below:

$\Gamma_1(b) = \Gamma(b, b), \Gamma_{\tau+1}(b) = \Gamma(\Gamma_\tau(b), b), \ \tau \in \mathbb{N}, b \in [0,1].$

Then, TCN Γ is H-type if the family $\{\Gamma_\tau(b)\}_{\tau \in \mathbb{N}}$ is equi-continuous at $b = 1$.

A TCN of H-type is Γ_{max} and see [9, 18] for examples.

Each t-conorm can be generalized in a different way to an n-ary process via associativity, taking $(b_1, \ldots, b_n) \in [0,1]^n$ for the values

$\Gamma^1_{i=1} b_i = b_1, \Gamma^1_{i=1} b_i = \Gamma(\Gamma^1_{i=1} b_i, b_\tau) = \Gamma(b_1, \ldots, b_\tau).$

Example 1. An n-ary generalization of the TCNΓ_{min}, Γ_L, and Γ_P are:

$\Gamma_{max}(b_1, \ldots, b_\tau) = \max\{b_1, \ldots, b_\tau\}$

$\Gamma_L(b_1, \ldots, b_\tau) = \min\{\sum_{i=1}^\tau b_i - (\tau - 1), 1\}, \ \Gamma_P(b_1, \ldots, b_\tau) = \prod_{i=1}^\tau b_i$

A TCN Γ can be extended to accountable infinite operation, for any sequence $(b_\tau)_{\tau \in \mathbb{N}}$ considering from [0,1] the value $\Gamma_{i=1}^{\infty} = \lim_{\tau \to \infty} \Gamma_{i=1}^{\tau} b_i$

The sequence $\{\Gamma_{i=1}{}^{\tau}(b)\}_{\tau \in \mathbb{N}}$ is non-increasing and bounded below and so the limit $\Gamma_{i=1}{}^{\infty}(b_i)$ exists. In the FP theory (Hadžić & Pap, 2001; Hadžić, 1979), it might be interesting to look at the category of TCNΓ and sequence (b_τ) in the range [0,1] such that $\lim_{\tau \to \infty} b_\tau = 0$ and

$$\lim_{\tau \to \infty} \Gamma_{i=1}{}^{\infty}(b_i) = \lim_{\tau \to \infty} \Gamma_{i=1}{}^{\infty}(b_{\tau+i}) \qquad (1)$$

Proposition 1. Suppose $(b_\tau)_{\tau \in \mathbb{N}}$ is a series of numbers with the range [0,1] such that $\lim_{\tau \to \infty} b_\tau = 0$ and assume Γ to be a TCN of H-type. Then, $\lim_{\tau \to \infty} \Gamma_{i=1}{}^{\infty} b_{\tau+i}$. Throughout this study, we utilize $\Xi^2 : \Xi \times \Xi$.

Definition 3 (Šostak, 2018). A 3-tuple (Ξ, M, Γ) is known as an RFMS if Ξ be a some (nonempty) set, Γ is a CTCN, and M is an RFM on $\Xi^2 \times (0, \infty)$ and satisfies the following conditions, for all $b, \omega, z \in \Xi$, and $t, s > 0$:

(Rfm 1) $M(b, \omega, t) < 1$,
(Rfm 2) $M(b, \omega, t) = 0$ iff $b = \omega$,
(Rfm 3) $M(b, \omega, t) = M(\omega, b, t)$,
(Rfm 4) $\Gamma(M(b, \omega, t), M(\omega, z, s)) \geq M(b, z, t + s)$,
(Rfm 5) $M(b, \omega, .) : (0, \infty) \to [0,1]$ is continuous.

Definition 4. A 3-tuple (Ξ, M, Γ) is called an RFbMS if Ξ is a random (non-empty) set, Γ is a CTCN, and M is an RFM on $\Xi^2 \times (0, \infty)$ and satisfies the following conditions for all $b, \omega, z \in \Xi$, $t, s > 0$, and $\rho \geq 1$ as a real number:

(Rb 1) $M(b, \omega, t) < 1$,
(Rb 2) $M(b, \omega, t) = 0$ iff $b = \omega$,
(Rb 3) $M(b, \omega, t) = M(\omega, b, t)$,
(Rb 4) $\Gamma\big(M(b, \omega, t), M(\omega, z, s)\big) \geq M(b, z, \rho(t + s))$,
(Rb 5) $M(b, \omega, -) : (0, \infty) \to [0,1]$ is continuous.

The following fixed point theorem is using a new Ciric-quasi-contraction in the context of RFbMSs.

Theorem 1. Suppose that $(\Xi, M, \Gamma_{\min})$ is a complete RFbMS, assume that $f : \Xi \to \Xi$. If for some $\aleph \in (0,1)$, such that

$$M_\alpha(fb, f\omega, t) \leq \max \left\{ \begin{matrix} M_\alpha\left(b, \omega, \frac{t}{\aleph}\right), M_\alpha\left(fb, b, \frac{t}{\aleph}\right), M_\alpha\left(f\omega, \omega, \frac{t}{\aleph}\right), \\ M_\alpha\left(fb, \omega, \frac{2t}{\aleph}\right), M_\alpha\left(b, f\omega, \frac{t}{\aleph}\right) \end{matrix} \right\}, \quad b, \omega \in$$

$\Xi, t > 0$. Then, f has a UFP in Ξ.

Lemma 1. Let $M(b, \omega, -)$ be an RFbMS. Then, $M(b, \omega, t)$ is b-non-decreasing with respect to for all $b, \omega \in \Xi$.

Definition 5. Let Ξ be a non-empty set, $\alpha: \Xi^2 \to [1, \infty)$, Γ is a CTCN, and M_α is an RFM on $\Xi^2 \times [0, \infty)$ and satisfies the following conditions for all $b, \omega, z \in \Xi, s$, and $t > 0$:

(ERFMα 1) $M_\alpha(b, \omega, 0) < 1$,

(ERFM$_\alpha$ 2) $M_\alpha(b, \omega, t) = 0$ iff $b = \omega$,

(ERFM$_\alpha$ 3) $M_\alpha(b, \omega, t) = M_\alpha(\omega, b, t)$,

(ERFM$_\alpha$ 4) $M_\alpha\big(b, z, \alpha(b, z)(t + s)\big) \leq \Gamma(M_\alpha(b, \omega, t), M_\alpha(\omega, z, s))$,

(ERFM$_\alpha$ 4) $M(b, \omega, .): (0, \infty) \to [0,1]$ is right continuous.

Then, the triple (Ξ, M_α, Γ) is said to be an extended revised fuzzy b-metric space and M_α is said to be a controlled RFM on Ξ.

Theorem 2. Suppose that (Ξ, M, Γ) is a complete RFMS with $f: \Xi^2 \to [1, \infty)$, assume that $\lim_{t \to \infty} M_\alpha(b, \omega, t) = 0$, for all $b, \omega \in \Xi$. Iff $: \Xi \to \Xi$ satisfies the following for some $\aleph \in (0,1)$, such that

$M_\alpha(fb, f\omega, t) \leq M_\alpha\left(b, \omega, \frac{t}{\aleph}\right)$, for all $b, \omega \in \Xi, t > 0$.

Also suppose that for arbitrary $b_0 \in \Xi$ and $n, q \in N$, there is $\alpha\big(b_n, b_{n+q}\big) \leq \frac{1}{\aleph}$,

where $b_n = f^n b_0$. Then, f has a UFP in Ξ.

Definition 6. Let Ξ be a non-empty set, $\alpha: \Xi^2 \to [1, \infty)$, Γ is a CTCN, and M_α is an RFM on $\Xi^2 \times [0, \infty)$ and satisfies the following conditions for all $b, \omega, z \in \Xi, s$, and $t > 0$:

(RFM$_\alpha$1) $M_\alpha(b, \omega, 0) < 1$,

(RFM$_\alpha$2) $M_\alpha(b, \omega, t) = 0$ iff $b = \omega$,

(RFM$_\alpha$3) $M_\alpha(b, \omega, t) = M_\alpha(\omega, b, t)$,

$(R\text{FM}_\alpha 4) M_\alpha(b, z, t + s) \leq \Gamma\left(M_\alpha\left(b, \omega, \frac{t}{\alpha(b, \omega)}\right), M_\alpha\left(\omega, z, \frac{s}{\alpha(b, \omega)}\right)\right)$,

(RFM$_\alpha$5) $M(b, \omega, .): (0, \infty) \to [0,1]$ is right continuous.

Then, the triple (Ξ, M_α, Γ) is said to be a CRFMS and M_α is said to be a controlled RFM on Ξ.

Muraliraj and Thangathamizh, (2021a) proved the following Banach contraction principle in the context of CRFMS.

Theorem 3. Suppose that (Ξ, M, Γ) is a complete CRFMS with $\alpha: \Xi^2 \to [1, \infty)$, assume that $\lim_{t \to \infty} M_\alpha(b, \omega, t) = 0$, for all $b, \omega \in \Xi$.

If $f: \Xi \to \Xi$ satisfies the following for some $\aleph \in (0, 1)$, such that

$M_\alpha(fb, f\omega, t) \leq M_\alpha\left(b, \omega, \frac{t}{\aleph}\right)$, for all $b, \omega \in \Xi, t > 0$.

Also, suppose that for all $b \in \Xi$, we obtain $\lim_{n \to \infty} M_\alpha(b_n, \omega)$ and $\lim_{n \to \infty} M_\alpha(\omega, b_n)$ which exist and are finite. Then, f has a UFP in Ξ.

Definition 7. Suppose $M(b, \omega, t)$ is a CRFMS. For $t > 0$, the open ball $B(b, l, t)$ with the center $b \in \Xi$ and the radius $0 < l < 1$ is expressed as a sequence $\{b_\tau\}$:

G-Convergent to b if $M(b_\tau, b, t) \to 0$ as $\tau \to \infty$ or for every $t > 0$. We write $\lim_{\tau \to \infty} b_\tau = b$.

is said to be a Cauchy sequence (CS) if for all $0 < \varepsilon < 1$ and $t > 0$ there exist satisfying $\tau_0 \in N$ such that $M(b_\tau, b_m, t) < \varepsilon$ for all $\tau, m \geq \tau_0$.

The CRFMS(Ξ, M, Γ) is a G-complete if every Cauchy sequence is convergent in Ξ.

Main results

In this part, we discuss several new results in the context of CRFMSs.

Lemma 2. Suppose $\{b_\tau\}$ is a sequence in a CRFMS(Ξ, M_α, Γ). Let $\aleph \in (0,1)$ exist such that

$$M_\alpha(b_\tau, b_{\tau+1}, t) \leq M_\alpha\left(b_{\tau-1}, b_\tau, \frac{t}{\aleph}\right) \tag{2}$$

and $b_\tau \in \Xi$, and $v \in (0,1)$ exist such that

$$\lim_{t \to \infty} M(b, \omega, t) = 0, \, t > 0 \tag{3}$$

Then, $\{b_\tau\}$ is a Cauchy sequence.

Proof. Suppose $\kappa \in (\aleph, 1)$ and the total $\sum_{i=1}^\infty \kappa^i$ is convergent, $\tau_0 \in N$ exists such that $\sum_{i=1}^\infty \kappa^i < 1$ for every $\tau > \tau_0$. Let $\tau > m > \tau_0$. Since M_α b-non-decreasing, by (RFM$_\alpha$ 4), for every $t > 0$, one can obtain

$$M_\alpha(b_\tau, b_{\tau+m}, t) \leq M_\alpha\left(b_\tau, b_{\tau+m}, \frac{\sum_{i=\tau}^{\tau+m-1}\kappa^i}{\alpha(b_\tau, b_{\tau+m})}\right)$$

$$\leq$$

$$\Gamma\left(M_\alpha\left(b_\tau, b_{\tau+1}, \frac{t\kappa^\tau}{\alpha(b_\tau, b_{\tau+1})\alpha(b_\tau, b_{\tau+m})}\right), M_\alpha\left(b_{\tau+1}, b_{\tau+m}, \frac{t\sum_{i=\tau+1}^{\tau+m-1}\kappa^i}{\alpha(b_{\tau+1}, b_{\tau+m})\alpha(b_\tau, b_{\tau+m})}\right)\right)$$

$$\leq \Gamma\left(\begin{array}{l} M_\alpha\left(b_\tau, b_{\tau+1}, \frac{t\kappa^\tau}{\alpha(b_\tau, b_{\tau+1})\alpha(b_\tau, b_{\tau+m})}\right), \\ M_\alpha\left(b_{\tau+1}, b_{\tau+2}, \frac{t\kappa^{\tau+1}}{\alpha(b_{\tau+1}, b_{\tau+2})\alpha(b_{\tau+1}, b_{\tau+m})\alpha(b_\tau, b_{\tau+m})}\right), \\ M_\alpha\left(b_{\tau+2}, b_{\tau+m}, \frac{t\sum_{i=\tau+2}^{\tau+m-1}\kappa^i}{\alpha(b_{\tau+2}, b_{\tau+m})\alpha(b_{\tau+1}, b_{\tau+m})\alpha(b_\tau, b_{\tau+m})}\right) \end{array}\right)$$

$$\leq$$

$$\Gamma\left(\begin{array}{c} M_\alpha\left(b_\tau, b_{\tau+1}, \dfrac{t\kappa^\tau}{\alpha(b_\tau,b_{\tau+1})\alpha(b_\tau,b_{\tau+m})}\right), \\[2mm] M_\alpha\left(b_{\tau+1}, b_{\tau+2}, \dfrac{t\kappa^{\tau+1}}{\alpha(b_{\tau+1},b_{\tau+2})\alpha(b_{\tau+1},b_{\tau+m})\alpha(b_\tau,b_{\tau+m})}\right), \\[2mm] M_\alpha\left(b_{\tau+2}, b_{\tau+3}, \dfrac{t\kappa^{\tau+2}}{\alpha(b_{\tau+2},b_{\tau+3})\alpha(b_{\tau+2},b_{\tau+m})\alpha(b_{\tau+1},b_{\tau+m})\alpha(b_\tau,b_{\tau+m})}\right) \\[2mm] M_\alpha\left(b_{\tau+3}, b_{\tau+4}, \dfrac{t\kappa^{\tau+3}}{\alpha(b_{\tau+3},b_{\tau+4})\alpha(b_{\tau+2},b_{\tau+3})\alpha(b_{\tau+2},b_{\tau+m})\alpha(b_{\tau+1},b_{\tau+m})\alpha(b_\tau,b_{\tau+m})}\right) \\ \vdots \\[2mm] M_\alpha\left(b_{\tau+m-2}, b_{\tau+m-1}, \dfrac{t\kappa^{\tau+m-2}}{\alpha(b_{\tau+m-2},b_{\tau+m-1})\prod_{i=\tau}^{\tau+m-2}\alpha(b_i,b_{\tau+m})}\right) \\[2mm] M_\alpha\left(b_{\tau+m-1}, b_{\tau+m}, \dfrac{t\kappa^{\tau+m-1}}{\alpha(b_{\tau+m-2},b_{\tau+m-1})\prod_{i=\tau}^{\tau+m-1}\alpha(b_i,b_{\tau+m})}\right) \end{array}\right)$$

From inequality (2), one deduces $M_\alpha(b_\tau, b_{\tau+1}, t) \leq M_a\left(b_0, b_1, \dfrac{t}{\aleph^\tau}\right)$ and since $\tau > m$ and $\alpha: \Xi^2 \to [1, \infty)$, one can obtain

$$M_\alpha(b_\tau, b_{\tau+m}, t)$$

$$\leq \Gamma\left(\begin{array}{c} M_\alpha\left(b_0, b_1, \dfrac{t\kappa^\tau}{\alpha(b_\tau, b_{\tau+1})\alpha(b_\tau, b_{\tau+m})\aleph^\tau}\right), \\[2mm] M_\alpha\left(b_0, b_1, \dfrac{t\kappa^{\tau+1}}{\alpha(b_{\tau+1}, b_{\tau+2})\alpha(b_{\tau+1}, b_{\tau+m})\alpha(b_\tau, b_{\tau+m})\aleph^{\tau+1}}\right), \\ \vdots \\[2mm] M_\alpha\left(b_0, b_1, \dfrac{t\kappa^{\tau+m-2}}{\alpha(b_{\tau+m-2}, b_{\tau+m-1})\prod_{i=\tau}^{\tau+m-2}\alpha(b_i, b_{\tau+m})\aleph^{\tau+m-1}}\right) \\[2mm] M_\alpha\left(b_0, b_1, \dfrac{t\kappa^{\tau+m-1}}{\prod_{i=\tau}^{\tau+m-1}\alpha(b_i, b_{\tau+m})\aleph^{\tau+m-1}}\right) \end{array}\right)$$

As $\tau \to \infty$ and by utilizing (3), one obtains $M_\alpha(b_\tau, b_{\tau+m}, t) \leq \Gamma(0, 0, \cdots, 0) = 0$. Hence, $\{b_\tau\}$ is a Cauchy sequence in Ξ.

Corollary 1. Suppose $\{b_\tau\}$ is a sequence in CRFMS (Ξ, M_α, Γ) and Γ is H-type. If $\aleph \in (0,1)$ exists such that

$$M_\alpha(b_\tau, b_{\tau+1}, t) \leq M_a\left(b_{\tau-1}, b_\tau, \dfrac{t}{\aleph}\right), \tau \in \mathbb{N}, t > 0. \tag{4}$$

Then, $\{b_\tau\}$ is a continuous Sequence.

Lemma 3. If for $b, \omega \in \Xi$, and some $\aleph \in (0,1)$,

$$M_\alpha(b, \omega, t) \leq M_\alpha\left(b, \omega, \dfrac{t}{\aleph}\right), t > 0. \tag{5}$$

Then, $b = \omega$.

Proof. Inequality (5) implies that

$$M_\alpha(b, \omega, t) \leq M_\alpha\left(b, \omega, \dfrac{t}{\aleph^\tau}\right), \tau \in \mathbb{N}, t > 0.$$

Now,

$$M_\alpha(b, \omega, t) \leq \lim_{\tau \to \infty} M_\alpha\left(b, \omega, \frac{t}{\aleph^\tau}\right) = 0, t > 0.$$

And by $(RFM_\alpha 2)$, it is easy to see that $b = \omega$.

Theorem 4. Suppose that (Ξ, M, Γ) is a complete CRFMS and suppose that $f: \Xi \to \Xi$. Let them exist $\aleph \in (0,1)$ such that

$$M_\alpha(fb, f\omega, t) \leq \min \left\{ \begin{array}{c} M_\alpha\left(b, \omega, \frac{t}{\aleph}\right), M_\alpha\left(b, f\omega, \frac{t}{\aleph}\right), M_\alpha\left(fb, \omega, \frac{t}{\aleph}\right) \\ \frac{M_\alpha\left(b, f\omega, \frac{t}{\aleph}\right) + M_\alpha\left(fb, \omega, \frac{t}{\aleph}\right)}{2} \\ \frac{M_\alpha\left(b, f\omega, \frac{t}{\aleph}\right) + M_\alpha\left(fb, \omega, \frac{t}{\aleph}\right)}{1 + M_\alpha\left(b, \omega, \frac{t}{\aleph}\right)} \end{array} \right\}, b, \omega \in$$

$\Xi, t > 0.$ \hfill (6)

and $b, \omega \in \Xi$ such that

$$\lim_{t \to \infty} M_\alpha(b, \omega, t) = 0, t > 0 \hfill (7)$$

Then, f has a UFP in Ξ.

Proof. Suppose $b_0 \in \Xi$ and $b_{\tau+1} = fb_\tau$, $\tau \in \mathbb{N}$. Consider $b = b_\tau$ and $\omega = b_{\tau-1}$ in (6), then one can obtain

$$M_\alpha(b_\tau, b_{\tau+1}, t) \leq M_a(fb_{\tau-1}, fb_\tau, t),$$
$$\leq$$

$$\min \left\{ \begin{array}{c} M_\alpha\left(b_{\tau-1}, b_\tau, \frac{t}{\aleph}\right), \Gamma\left(M_\alpha\left(b_{\tau-1}, b_\tau, \frac{t}{\aleph}\right)\right), M_\alpha\left(b_\tau, b_{\tau+1}, \frac{t}{\aleph}\right), \\ M_\alpha\left(b_\tau, b_\tau, \frac{t}{\aleph}\right), \frac{M_\alpha\left(b_{\tau-1}, b_{\tau+1}, \frac{t}{\aleph}\right) + M_\alpha\left(b_\tau, b_\tau, \frac{t}{\aleph}\right)}{2} \\ \frac{M_\alpha\left(b_{\tau-1}, b_{\tau+1}, \frac{t}{\aleph}\right) + M_\alpha\left(b_\tau, b_\tau, \frac{t}{\aleph}\right)}{1 + M_\alpha\left(b_{\tau-1}, b_\tau, \frac{t}{\aleph}\right)} \end{array} \right\}$$

$$\leq \min\left\{ M_\alpha\left(b_{\tau-1}, b_\tau, \frac{t}{\aleph}\right), M_\alpha\left(b_\tau, b_{\tau+1}, \frac{t}{\aleph}\right) \right\}$$

If $M_\alpha(b_\tau, b_{\tau+1}, t) \leq M_\alpha\left(b_\tau, b_{\tau+1}, \frac{t}{\aleph}\right), \tau \in \mathbb{N}, t > 0.$

Then by Lemma 3 such that $b_\tau = b_{\tau+1}, \tau \in \mathbb{N}$, there is

$M_\alpha(b_\tau, b_{\tau+1}, t) \leq M_\alpha\left(b_{\tau-1}, b_\tau, \frac{t}{\aleph}\right), \tau \in \mathbb{N}, M_\alpha(b_\tau, b_{\tau+1}, t)$ and by Lemma 2 it follows that $\{b_\tau\}$ is a CS. Since, (Ξ, M, Γ) is complete, $b \in \Xi$ exist such that $\lim_{\tau \to \infty} b_\tau = b$ and

$$\lim_{\tau \to \infty} M_\alpha(b, b_\tau, t) = 0, t > 0. \hfill (8)$$

By utilizing (6) and $(RFM_\alpha 4)$, it is easy to see that b is a FP for f.

Suppose $\kappa_1 \in (\aleph, 1)$ and $\kappa_2 = 1 - \kappa_1$ by (6); one can obtain

$$M_\alpha(fb, b, t) \leq \Gamma\left(M_\alpha\left(fb, b_{\tau-1}, \frac{t\kappa_1}{2\alpha(fb, b_\tau)}\right), M_\alpha\left(b_\tau, b_{\tau-1}, \frac{t\kappa_2}{2\alpha(b_\tau, b)}\right)\right)$$

$$\leq$$

$$\Gamma\left(\min\left\{\begin{array}{c} M_\alpha\left(b,b_{\tau-1},\frac{t\kappa_1}{2\alpha(fb,b_\tau)\aleph}\right), M_\alpha\left(b,b_\tau,\frac{t\kappa_1}{2\alpha(fb,b_\tau)\aleph}\right) \\ \Gamma\left(M_\alpha\left(fb,b,\frac{t\kappa_1}{(2)^2\alpha(fb,b)\alpha(fb,b_\tau)\aleph}\right), M_\alpha\left(b,b_{\tau-1},\frac{t\kappa_1}{(2)^2\alpha(b,b_{\tau-1})\alpha(fb,b_\tau)\aleph}\right)\right), \\ \dfrac{M_\alpha\left(b,b_\tau,\frac{t\kappa_1}{2\alpha(fb,b_\tau)\aleph}\right)+\Gamma\left(\begin{array}{c}M_\alpha\left(fb,b,\frac{t\kappa_1}{(2)^2\alpha(fb,b)\alpha(fb,b_\tau)\aleph}\right),\\ M_\alpha\left(b,b_{\tau-1},\frac{t\kappa_1}{(2)^2\alpha(b,b_{\tau-1})\alpha(fb,b_\tau)\aleph}\right)\end{array}\right)}{2} \\ \dfrac{M_\alpha\left(b,b_\tau,\frac{t\kappa_1}{2\alpha(fb,b_\tau)\aleph}\right).\Gamma\left(\begin{array}{c}M_\alpha\left(fb,b,\frac{t\kappa_1}{(2)^2\alpha(fb,b)\alpha(fb,b_\tau)\aleph}\right),\\ M_\alpha\left(b,b_{\tau-1},\frac{t\kappa_1}{(2)^2\alpha(b,b_{\tau-1})\alpha(fb,b_\tau)\aleph}\right)\end{array}\right)}{1+M_\alpha\left(b,b_{\tau-1},\frac{t}{2\alpha(fb,b_\tau)\aleph}\right)} \\ M_\alpha\left(b_\tau,b,\frac{t}{2\alpha(b_\tau,b)}\right) \end{array}\right\}\right)$$

for all $t > 0$. By (8) and as $\tau \to \infty$, one obtains

$$\leq \Gamma\left(\min\left\{\begin{array}{c} 0,0 \\ \Gamma\left(M_\alpha\left(fb,b,\frac{t\kappa_1}{(2)^2\alpha(fb,b)\alpha(fb,b_\tau)\aleph}\right),0\right), \\ \dfrac{1+\Gamma\left(M_\alpha\left(fb,b,\frac{t\kappa_1}{(2)^2\alpha(fb,b)\alpha(fb,b_\tau)\aleph}\right),\right)}{2} \\ \dfrac{0.\Gamma\left(M_\alpha\left(fb,b,\frac{t\kappa_1}{(2)^2\alpha(fb,b)\alpha(fb,b_\tau)\aleph}\right),\right)}{1+0} \\ 0 \end{array}\right\}\right)$$

Suppose that b and ω are two different FP for f. Then, by applying (6), one can obtain

$$M_a(b,\omega,t) = M_a(fb,f\omega,t)$$

$$\leq \min\left\{\begin{array}{c} M_\alpha\left(b,\omega,\frac{t}{\aleph}\right), M_\alpha\left(b,f\omega,\frac{t}{\aleph}\right), M_\alpha\left(fb,\omega,\frac{t}{\aleph}\right), \\ \dfrac{M_\alpha\left(b,f\omega,\frac{t}{\aleph}\right)+M_\alpha\left(fb,\omega,\frac{t}{\aleph}\right)}{2} \\ \dfrac{M_\alpha\left(b,f\omega,\frac{t}{\aleph}\right).M_\alpha\left(fb,\omega,\frac{t}{\aleph}\right)}{1+M_\alpha\left(b,\omega,\frac{t}{\aleph}\right)} \end{array}\right\}$$

$$= \min \left\{ \begin{array}{c} M_\alpha\left(b, \omega, \frac{t}{\aleph}\right), M_\alpha\left(b, \omega, \frac{t}{\aleph}\right), M_\alpha\left(b, \omega, \frac{t}{\aleph}\right), \\[2mm] \dfrac{M_\alpha\left(b,\omega,\frac{t}{\aleph}\right)+M_\alpha\left(b,\omega,\frac{t}{\aleph}\right)}{2} \\[4mm] \dfrac{M_\alpha\left(b,\omega,\frac{t}{\aleph}\right).M_\alpha\left(b,\omega,\frac{t}{\aleph}\right)}{1+M_\alpha\left(b,\omega,\frac{t}{\aleph}\right)} \end{array} \right\} = M_\alpha\left(b, \omega, \frac{t}{\aleph}\right), t > 0.$$

and by Lemma 3, it is easy to see that $b = \omega$.

Remark 1. If one takes

$$\min \left\{ \begin{array}{c} M_\alpha\left(b, \omega, \frac{t}{\aleph}\right), M_\alpha\left(b, f\omega, \frac{t}{\aleph}\right), M_\alpha\left(fb, \omega, \frac{t}{\aleph}\right), \\[2mm] \dfrac{M_\alpha\left(b, f\omega, \frac{t}{\aleph}\right) + M_\alpha\left(fb, \omega, \frac{t}{\aleph}\right)}{2} \\[4mm] \dfrac{M_\alpha\left(b, f\omega, \frac{t}{\aleph}\right) . M_\alpha\left(fb, \omega, \frac{t}{\aleph}\right)}{1 + M_\alpha\left(b, \omega, \frac{t}{\aleph}\right)} \end{array} \right\} = M_\alpha\left(b, \omega, \frac{t}{\aleph}\right)$$

in the above theorem, one then obtains a revised fuzzy version of the Banach contraction principle.

Example 2. Let $\Xi = \{0,1,3\}$, $M_\alpha(b, \omega, t) = e^{-\frac{(b-\omega)^2}{t}}\left(1 - e^{\frac{(b-\omega)^2}{t}}\right)$, and $\Gamma = \Gamma_p$. Then, (Ξ, M, Γ) is a complete CRFMS with $\alpha(b, \omega) = b + \omega + 1$. Define the function $f: \Xi \to \Xi$ such that $f(0) = f(1) = 1$ and $f(3) = 0$. Observe that if $b = \omega$ or $\omega \in \{0,1\}$, then $M_a(fb, f\omega, t) = 0$ and $t > 0$ and condition (6) is fulfilled. Suppose $b = 1$ and $\omega = 3$. Then, $\aleph \in \left(\frac{1}{9}, \frac{1}{4}\right)$ and one obtains

$$M_\alpha(fb, f\omega, t) = e^{-\frac{1}{t}}\left(1 - e^{\frac{1}{t}}\right) \leq \min\left\{e^{-\frac{4}{\aleph t}}, e^{-\frac{1}{\aleph t}}, e^{-\frac{4}{\aleph t}}, \frac{e^{-\frac{1}{\aleph t}} + e^{-\frac{4}{\aleph t}}}{2}, \frac{e^{-\frac{1}{\aleph t}}.e^{-\frac{4}{\aleph t}}}{1 + e^{-\frac{4}{\aleph t}}}\right\}$$

Now, suppose $b = 1$ and $\omega = 3$, then, choosing $\aleph$ from $\left(\frac{1}{9}, \frac{1}{4}\right)$, one deduces

$$M_\alpha(fb, f\omega, t) = e^{-\frac{1}{t}}\left(1 - e^{\frac{1}{t}}\right) \leq \min\left\{e^{-\frac{4}{\aleph t}}, e^{-\frac{1}{\aleph t}}, e^{-\frac{4}{\aleph t}}, \frac{e^{-\frac{1}{\aleph t}} + e^{-\frac{4}{\aleph t}}}{2}, \frac{e^{-\frac{1}{\aleph t}}.e^{-\frac{4}{\aleph t}}}{1 + e^{-\frac{4}{\aleph t}}}\right\}$$

Similarly, if $b = 3$ and $\omega = 1$ as well as $b = 3$ and $\omega = 1$, one establishes that for $\aleph \in \left(\frac{1}{9}, \frac{1}{4}\right)$ condition (6) is fulfilled for all $b, \omega \in \Xi$, and $t > 0$. Hence, all the conditions of Theorem 4 are satisfied with a UFP $b = 1$.

Corollary 2. Supposing that (Ξ, M, Γ) is a complete CRFMS with $\alpha: \Xi^2 \to [1, \infty)$, assume that $\lim_{t \to \infty} M_\alpha(b, \omega, t) = 0$. For all $b, \omega \in \Xi$. If $f: \Xi \to \Xi$ satisfies the following, for some $\aleph \in (0, 1)$, such that

$M_\alpha(fb, f\omega, t) \le M_\alpha\left(b, \omega, \frac{t}{\aleph}\right)$, for all $b, \omega \in \Xi, t > 0$. Then, f has a UFP in Ξ.

Example 3. $\Xi = A \cup B$, where $A = [0,1], B = \frac{\mathbb{N}}{1}$, and $M_\alpha: \Xi^2 \times (0, \infty) \to [0,1]$, is defined by

$$M_\alpha(b, \omega, t) = \begin{cases} 0 \text{ if } b = \omega \\ \dfrac{t}{t + \dfrac{1}{\omega}} \text{ if } b \in B \text{ and } \omega \in A \\ \dfrac{t}{t + \dfrac{1}{b}} \text{ if } b \in A \text{ and } \omega \in B \\ \dfrac{t}{t + \max\{b, \omega\}} \text{ otherwise} \end{cases}$$

Then, (Ξ, M, Γ) is CRFMS with $\Gamma(b, \omega) = b \cdot \omega$ and a controlled function $\alpha: \Xi^2 \to [0, \infty)$ defined by

$$a(b, \omega) = \begin{cases} 0 \text{ if } b = \omega \\ \min\{b, \omega\} \text{ otherwise} \end{cases}$$

It is easy to see that all the conditions of Corollary 2 are satisfied.

Consider the triangular inequality (RFEM$_\alpha$4) of the revised fuzzy extended b-metric space defined in Definition 5 as

$$M_\alpha(b, z, \alpha(b, z)(t + s)) \le \Gamma(M_\alpha(b, \omega, t), M_\alpha(\omega, z, s))$$

Let $b, z \in A$, and $\omega \in B$, the, $n\alpha(b, z) = 0$. Assume $t = s = 2, b = \frac{1}{2}, z = 1$, and $\omega = 40$. There is

$$\frac{t + s + \dfrac{1}{\min\{b, z\}}}{t + s + \dfrac{1}{\max\{b, z\}}} \le \Gamma\left(\frac{t}{t + \dfrac{1}{\omega}}, \frac{s}{s + \dfrac{1}{\omega}}\right)$$

One obtains $0.8 > 0.975$, which is a contradiction. Hence, M_α is not an extended revised fuzzy b-metric space. Now, consider the triangular inequality (b 4) of $RFbMS$ defined in Definition 4 as

$$M_\alpha(b, z, \rho(t + s)) \le \Gamma(M_\alpha(b, \omega, t), M_\alpha(\omega, z, s)).$$

One obtains

$$\frac{\rho(s + t) + \dfrac{1}{\min\{b, z\}}}{\rho(s + t) + \dfrac{1}{\max\{b, z\}}} \le \Gamma\left(\frac{t}{t + \dfrac{1}{\omega}}, \frac{s}{s + \dfrac{1}{\omega}}\right)$$

1520

For ρ ∈ [1,9], the above inequality is not satisfied.

Theorem 5. Supposing that (Ξ, M_α, Γ) is a complete CRFMS assuming that $f: \Xi \to \Xi$, then $\aleph \in (0,1)$ exists

$$M_\alpha(fb, f\omega, t) \le \max\left\{M_\alpha\left(b, \omega, \frac{t}{\aleph}\right), M_\alpha\left(fb, \omega, \frac{t}{\aleph}\right), M_\alpha\left(b, f\omega, \frac{t}{\aleph}\right)\right\} \qquad (9)$$

For all $b, \omega \in \Xi, t > 0$ such that

$$\lim_{\tau \to \infty} M_\alpha(b, \omega, t) = 0 \qquad (10)$$

For all $t > 0$. Then, f has a UFP in Ξ.

Proof. Suppose $b_0 \in \Xi, b_{\tau+1} = fb_\tau$, and $\tau \in \mathbb{N}$ from (9) with $b = b_\tau$ and $\omega = b_{\tau-1}$, for every $\tau \in \mathbb{N}$ and $t > 0$, one can obtain

$$M_\alpha(b_{\tau+1}, b_\tau, t) \le \max\left\{M_\alpha\left(b_\tau, b_{\tau-1}, \frac{t}{\aleph}\right), M_\alpha\left(b_{\tau+1}, b_\tau, \frac{t}{\aleph}\right), M_\alpha\left(b_\tau, b_{\tau-1}, \frac{t}{\aleph}\right)\right\}$$

$$\le \max\left\{M_\alpha\left(b_\tau, b_{\tau-1}, \frac{t}{\aleph}\right), M_\alpha\left(b_{\tau+1}, b_\tau, \frac{t}{\aleph}\right)\right\}$$

If $M_\alpha(b_{\tau+1}, b_\tau, t) \le M_\alpha\left(b_{\tau+1}, b_\tau, \frac{t}{\aleph}\right)$, $\tau \in \mathbb{N}$, $t > 0$. Then, Lemma 3 implies that $b_\tau, b_{\tau+1}, \tau \in \mathbb{N}$, such that $M_\alpha(b_{\tau+1}, b_\tau, t) \le M_\alpha\left(b_\tau, b_{\tau-1}, \frac{t}{\aleph}\right)$, $\tau \in \mathbb{N}, t > 0$.

Moreover, by Lemma 2 $\{b_\tau\}$ is a Continuous Sequence. Hence, $b \in \Xi$ exists such that $\lim_{\tau \to \infty} b_\tau = b$ and

$$\lim_{\tau \to \infty} M_\alpha(b, b_\tau, t) = 0, t > 0. \qquad (11)$$

Now, it is shown that b is an FP for f. Letting $\kappa_1 \in (\aleph, 1)$ and $\kappa_2 = 1 - \kappa_1$ by (9), one can obtain

$$M_\alpha(fb, b, t) \le \Gamma\left(M_\alpha\left(fb, fb_\tau, \frac{t\kappa_1}{\alpha(fb, fb_\tau)}\right), M_\alpha\left(b_{\tau+1}, fb_\tau, \frac{t\kappa_2}{\alpha(b_{\tau+1}, fb_\tau)}\right)\right)$$

$$\le$$

$$\Gamma\left(\max\left\{\begin{array}{c} M_\alpha\left(b, b_\tau, \frac{t\kappa_1}{\alpha(b, b_\tau)}\right), M_\alpha\left(b, fb, \frac{t\kappa_1}{\alpha(b, fb)}\right) \\ M_\alpha\left(b_\tau, b_{\tau+1}, \frac{t\kappa_1}{\alpha(b_\tau, b_{\tau+1})\aleph}\right) \end{array}\right\}, M_\alpha\left(b_{\tau+1}, b, \frac{t\kappa_2}{\alpha(b_{\tau+1}, b_\tau)}\right)\right)$$

Taking $\tau \to \infty$ and utilizing (11), one deduces

$$M_\alpha(fb, b, t) \le \Gamma\left(\max\left\{0, M_\alpha\left(b, fb, \frac{t\kappa_1}{\alpha(b, fb)\aleph}\right), 0\right\}\right)$$

$$= \Gamma\left(M_\alpha\left(b, fb, \frac{t\kappa_1}{\alpha(b, fb)\aleph}\right), 0\right) = M_\alpha\left(b, fb, \frac{t}{v}\right), \ t > 0.$$

where $v = \frac{\alpha(b, fb)\aleph}{\kappa_1} \in (0,1)$, one has $M_\alpha(fb, b, t) \le M_\alpha\left(fb, b, \frac{t}{v}\right)$ $t > 0$, and by Lemma 3, one has $fb = b$. Suppose that b and ω are to different FP for f, that is, $fb = b$ and $f\omega = \omega$. By (9), one deduces

$$M_\alpha(fb, f\omega, t) \le \max\left\{M_\alpha\left(b, \omega, \frac{t}{\aleph}\right), M_\alpha\left(b, fb, \frac{t}{\aleph}\right), M_\alpha\left(\omega, f\omega, \frac{t}{\aleph}\right)\right\}$$

$$=\max\left\{M_\alpha\left(b,\omega,\frac{t}{\aleph}\right),0,0\right\}=M_\alpha\left(b,\omega,\frac{t}{\aleph}\right)=M_\alpha\left(fb,f\omega,\frac{t}{\aleph}\right)$$

For $t > 0$, and by utilizing the Lemma 3, one has $fb = f\omega$, which gives $b = \omega$.

Remark 2. If one takes

$$\max\left\{M_\alpha\left(b,\omega,\frac{t}{\aleph}\right),M_\alpha\left(fb,b,\frac{t}{\aleph}\right),M_\alpha\left(f\omega,\omega,\frac{t}{\aleph}\right)\right\}=M_\alpha\left(b,\omega,\frac{t}{\aleph}\right)$$

in the above theorem, then one obtains a revised fuzzy version of the Banach contraction principle.

Example 4. Suppose $\Xi = (0,2)$, $M_\alpha(b,\omega,t) = e^{-\frac{(b-\omega)^2}{t}},\left(1 - e^{\frac{(b-\omega)^2}{t}}\right)$, and $\Gamma = \Gamma_p$ Then, (Ξ, M, Γ) is a complete CFMS with $\alpha(b,\omega) = b + \omega + 2$. Let

$$f(b) = \begin{cases} 2 - b, b \in (0,1) \\ 1, b \in [1,2) \end{cases}$$

Part 1: If $b, \omega \in [1,2)$, then $M_\alpha(fb, f\omega, t) = 0, t > 0$ and (9) are trivially verified.

Part 2: If $b \in [1,2)$ and $\omega \in (0,1)$, such that $\aleph \in \left(\frac{1}{4},\frac{1}{2}\right)$, one can obtain

$$M_\alpha(fb, f\omega, t) = e^{-\frac{(1-\omega)^2}{t}}\left(1 - e^{\frac{(1-\omega)^2}{t}}\right) = \left(1 - e^{\frac{4\aleph(1-\omega)^2}{t}}\right) =$$

$M_\alpha\left(f\omega,\omega,\frac{t}{\aleph}\right), t > 0.$

Part 3: As in the preceding section, for $\aleph \in \left(\frac{1}{4},\frac{1}{2}\right)$, one obtains

$$M_\alpha(fb, f\omega, t) \le M_\alpha\left(fb, b,\frac{t}{\aleph}\right), b \in (0,1), \omega \in [1,2), t > 0.$$

Part 4: If $b, \omega \in (0,1)$, then for $\aleph \in \left(\frac{1}{4},\frac{1}{2}\right)$, one has

$$M_\alpha(fb, f\omega, t) = e^{-\frac{(1-\omega)^2}{t}}\left(1 - e^{\frac{(1-\omega)^2}{t}}\right) = e^{-\frac{4\aleph(1-\omega)^2}{t}}\left(1 - e^{\frac{4\aleph(1-\omega)^2}{t}}\right)$$

$$= M_\alpha\left(f\omega,\omega,\frac{t}{\aleph}\right), b > \omega, t > 0 \text{ and } M_\alpha(fb, f\omega, t) \le M_\alpha\left(f\omega,\omega,\frac{t}{\aleph}\right), b > $$
$\omega, t > 0$

So, condition (9) is fulfilled for all $b, \omega \in, t > 0$ and by Theorem 5 it follows that $b = 1$ is a UFP for f. A new Ciric-quasi-contraction is analyzed in the following theorem.

Theorem 6. Supposing that $(\Xi, M, \Gamma_{\max})$ is a complete CRFMS, assume that $f: \Xi \to \Xi$. If for some $\aleph \in (0,1)$, such that

$$M_\alpha(fb, f\omega, t) \le \max\left\{\begin{array}{c} M_\alpha\left(b,\omega,\frac{t}{\aleph}\right), M_\alpha\left(fb, b,\frac{t}{\aleph}\right), \\ M_\alpha\left(f\omega,\omega,\frac{t}{\aleph}\right), M_\alpha\left(fb,\omega,\frac{2t}{\aleph}\right), M_\alpha\left(b, f\omega,\frac{t}{\aleph}\right) \end{array}\right\}, b, \omega \in$$

$\Xi, t > 0.$ \hfill (12)

Then, f has a UFP in Ξ.

Proof. Suppose $b_0 \in \Xi$ and $b_{\tau+1} = fb_\tau, \tau \in \mathbb{N}$. By utilizing condition (12) with $b = b_\tau$, $\omega = b_{\tau-1}$, utilizing $(FM_\alpha 4)$, and the assumption that $\Gamma = \Gamma_{max}$, one can obtain

$$M_\alpha(b_{\tau+1}, b_\tau, t) \leq$$

$$\max \left\{ \begin{array}{c} M_\alpha\left(b_\tau, b_{\tau-1}, \frac{t}{\aleph}\right), M_\alpha\left(b_{\tau+1}, b_\tau, \frac{t}{\aleph}\right), M_\alpha\left(b_\tau, b_{\tau-1}, \frac{t}{\aleph}\right) \\ M_\alpha\left(b_{\tau+1}, b_\tau, \frac{t}{\alpha(b_{\tau+1}, b_\tau)\aleph}\right), M_\alpha\left(b_\tau, b_{\tau-1}, \frac{t}{\alpha(b_\tau, b_{\tau-1})\aleph}\right) \\ M_\alpha\left(b_\tau, b_\tau, \frac{t}{\aleph}\right) \end{array} \right\}$$

$$\leq$$

$$\max \left\{ M_\alpha\left(b_\tau, b_{\tau-1}, \frac{t}{\alpha(b_\tau, b_{\tau-1})\aleph}\right), M_\alpha\left(b_{\tau+1}, b_{\tau-1}, \frac{t}{\alpha(b_{\tau+1}, b_{\tau-1})\aleph}\right) \right\}, \tau \in \mathbb{N}, t > 0.$$

By Lemma 3 and Corollary 2, it is possible to demonstrate Theorem 5 such that

$$M_\alpha(b_{\tau+1}, b_\tau, t) \leq M_\alpha\left(b_\tau, b_{\tau-1}, \frac{t}{\alpha(b_\tau, b_{\tau-1})\aleph}\right), \tau \in \mathbb{N}, t > 0.\text{and } \{b_\tau\} \text{ is a}$$

CS. So, $b \in \Xi$ exists such that $\lim\limits_{\tau \to \infty} b_\tau = b$,

$$\lim\limits_{\tau \to \infty} M_\alpha(b, b_\tau, t) = 0, t > 0 \tag{13}$$

Suppose $\kappa_1 \in (\aleph, 1)$ and $\kappa_2 = 1 - \kappa_1$. By (12) and $(FM_\alpha 4)$, one deduces

$$M_\alpha(fb, b, t) \leq \max\left\{ M_\alpha\left(fb, fb_\tau, \frac{t\kappa_1}{\alpha(fb, fb_\tau)}\right), M_\alpha\left(fb_\tau, fb, \frac{t\kappa_2}{\alpha(fb_\tau, fb)}\right) \right\}$$

$$\leq$$

$$\max \left\{ \begin{array}{c} \max \left\{ \begin{array}{c} M_\alpha\left(b, b_\tau, \frac{t\kappa_1}{\alpha(b, b_\tau)}\right), M_\alpha\left(b, fb, \frac{t\kappa_1}{\alpha(b, fb)\aleph}\right), M_\alpha\left(b_\tau, b_{\tau+1}, \frac{t\kappa_1}{\alpha(b_\tau, b_{\tau+1})\aleph}\right), \\ \max\left\{ M_\alpha\left(fb, b, \frac{t\kappa_1}{\alpha(b, fb)\alpha(fb, b_\tau)}\right), M_\alpha\left(b, b_\tau, \frac{t\kappa_1}{\alpha(b, b_\tau)\alpha(fb, b_\tau)\aleph}\right) \right\} \\ M_\alpha\left(b, b_{\tau+1}, \frac{t\kappa_1}{\alpha(b, b_{\tau+1})\aleph}\right) \end{array} \right\} \\ M_\alpha\left(b_{\tau+1}, b, \frac{t\kappa_2}{\alpha(b_{\tau+1}, b)}\right) \end{array} \right\}$$

For all $\tau \in \mathbb{N}$ and $t > 0$. Taking $\tau \to \infty$ and utilizing (13), one obtains

$$M_\alpha(fb, b, t) \leq \max \left\{ \max \left\{ \begin{array}{c} 0, M_\alpha\left(b, fb, \frac{t\kappa_1}{\alpha(b, fb)\aleph}\right), 0 \\ \max\left\{ M_\alpha\left(fb, b, \frac{t\kappa_1}{\alpha(b, fb)\alpha(fb, b_\tau)\aleph}\right), 0\right\}, 0 \end{array} \right\}, 0 \right\}$$

$$= M_\alpha\left(fb, b, \frac{t\kappa_1}{\alpha(b, fb)\alpha(fb, b_\tau)\aleph}\right), t > 0.$$

and by Lemma 3 with $v = \frac{\alpha(b, fb)\alpha(fb, b_\tau)\aleph}{\kappa_1} \in (0,1)$such that $fb = b$. By condition (12), for two different FPs $b = fb$and $\omega = f\omega$, one can obtain

$$M_\alpha(fb, f\omega, t) \leq$$

$$\max \left\{ \begin{array}{c} M_\alpha\left(b, \omega, \frac{t}{\aleph}\right), M_\alpha\left(fb, b, \frac{t}{\aleph}\right), M_\alpha\left(f\omega, \omega, \frac{t}{\aleph}\right), \\ \max\left\{M_\alpha\left(fb, b, \frac{t}{\alpha(fb,b)\aleph}\right), M_\alpha\left(b, \omega, \frac{t}{\alpha(b,\omega)\aleph}\right)\right\}, M_\alpha\left(b, f\omega, \frac{t}{\aleph}\right) \end{array} \right\}$$

$$= \max \left\{ \begin{array}{c} M_\alpha\left(b, \omega, \frac{t}{\aleph}\right), 1, 1, \\ \max\left\{1, M_\alpha\left(b, \omega, \frac{t}{\alpha(b,\omega)\aleph}\right)\right\}, M_\alpha\left(b, f\omega, \frac{t}{\aleph}\right) \end{array} \right\} =$$

$$M_\alpha\left(b, \omega, \frac{t}{\alpha(b,\omega)\aleph}\right)$$

$$= M_\alpha\left(fb, f\omega, \frac{t}{\alpha(b,\omega)\aleph}\right), t > 0.$$ and by Lemma 3, it follows that $b = \omega$.

The next theorem aims to establish a new contractive condition with the weaker TCN.

Example 5. Suppose $\Xi = A \cup B$ where $A = [0,1], B = \mathbb{N}\backslash 1$ and $M_\alpha: \Xi^2 \times (0, \infty) \to [0,1]$ is a revised fuzzy metric defined by

$$M(b, \omega, t) = \begin{cases} 0 & \text{if } b = \omega \\ e^{-\frac{1}{\omega^t}} & \text{if } b \in B \text{ and } \omega \in A \\ e^{-\frac{1}{bt}} & \text{if } b \in A \text{ and } \omega \in B \\ e^{-\frac{\min\{b,\omega\}}{t}}\left(1 - e^{\frac{\min\{b,\omega\}}{t}}\right) & \text{otherwise} \end{cases}$$

Then, (Ξ, M, Γ) is a CRFMS with $\Gamma(b, \omega) = b.\omega$ and a controlled function $\alpha: \Xi^2 \to [0, \infty)$ defined by

$$\alpha(b, \omega) = \begin{cases} 0 \text{ if } b = \omega \\ \min\{b + \omega, 1\} \text{ otherwise} \end{cases}$$

It is easy to see that all the conditions of Theorem 6 are satisfied.

Let $b = \frac{1}{2}, \omega = 40, z = 1$, and $t = s = 1$. Then, it does not satisfy the triangle inequality $(EM_\alpha 4)$ of Definition 5. Hence, it is not an extended revised fuzzy b-metric space. Now, show that it is not an RFbMS. Considering the triangle inequality (b4) of Definition 4, there is

$$e^{-\frac{\min\{b,\omega\}}{\rho(t+s)}}\left(1 - e^{\frac{\min\{b,\omega\}}{\rho(t+s)}}\right) \leq \Gamma\left(e^{-\frac{1}{\omega^t}}, e^{-\frac{1}{\omega^s}}\right) \Rightarrow e^{-\frac{1}{2\rho}}\left(1 - e^{\frac{1}{2\rho}}\right)$$

$$\leq e^{-\frac{2}{20}}\left(1 - e^{\frac{2}{20}}\right) = e^{-\frac{1}{10}}\left(1 - e^{\frac{1}{10}}\right)$$

It is clear that the above inequality is not satisfied for $\rho = 2$. Hence, it is not RFbMS.

Theorem 7. Supposing that $(\Xi, M, \Gamma), \Gamma \geq \Gamma_p$ is a complete CRFMS, assume that $f: \Xi \to \Xi$. For some $\aleph \in (0,1)$, let

$$M_\alpha(fb, f\omega, t) \leq \max \left\{ \begin{array}{c} M_\alpha\left(b, \omega, \frac{t}{\aleph}\right), M_\alpha\left(fb, b, \frac{t}{\aleph}\right), M_\alpha\left(f\omega, \omega, \frac{t}{\aleph}\right), \\ \sqrt{M_\alpha\left(fb, \omega, \frac{2t}{\aleph}\right)}, M_\alpha\left(b, f\omega, \frac{t}{\aleph}\right) \end{array} \right\}, b, \omega \in$$

$\Xi, t > 0.$ (14)

And $b, \omega \in \Xi$ exists such that $\lim_{\tau \to \infty} M_\alpha(b, \omega, t) = 0, t > 0.$ (15)

Then, f has a UFP in Ξ.

Proof. Let $b_0 \in \Xi$ and $b_{\tau+1} = fb_\tau, \tau \in \mathbb{N}$. Taking $b = b_\tau$ and $\omega = b_{\tau-1}$ in (14), by $(RFM_\alpha 4)$ and $\Gamma \geq \Gamma_p$, one can obtain

$M_\alpha(b_{\tau+1}, b_\tau, t) \leq$

$$\max \left\{ \begin{array}{c} M_\alpha\left(b_\tau, b_{\tau+1}, \frac{t}{\aleph}\right), M_\alpha\left(fb, b, \frac{t}{\aleph}\right), \\ M_\alpha\left(b_{\tau+1}, b_\tau, \frac{t}{\aleph}\right), M_\alpha\left(b_\tau, b_{\tau-1}, \frac{t}{\aleph}\right) \\ \sqrt{M_\alpha\left(fb, \omega, \frac{2t}{\aleph}\right) \cdot M_\alpha\left(b_\tau, b_{\tau-1}, \frac{t}{\alpha(b_\tau, b_{\tau-1})\aleph}\right)}, M_\alpha\left(b_\tau, b_\tau, \frac{t}{\aleph}\right) \end{array} \right\}$$

For all $b, \omega \in \Xi, t > 0$. Since $M_\alpha(b, \omega, t)$ is a b-non-decreasing in t and $\sqrt{\kappa.\rho} = \max\{\kappa, \rho\}$, one deduces

$$M_\alpha(b_{\tau+1}, b_\tau, t) \leq \max \left\{ \begin{array}{c} M_\alpha\left(b_{\tau+1}, b_\tau, \frac{t}{\alpha(b_{\tau+1}, b_\tau)\aleph}\right), \\ M_\alpha\left(b_\tau, b_{\tau-1}, \frac{t}{\alpha(b_\tau, b_{\tau-1})\aleph}\right) \end{array} \right\} \quad \text{Or all } \tau \in \mathbb{N}, \ t > 0.$$

By Lemmas 2 and 3, one can obtain,

$$M_\alpha(b_{\tau+1}, b_\tau, t) \leq M_\alpha\left(b_\tau, b_{\tau-1}, \frac{t}{\alpha(b_\tau, b_{\tau-1})\aleph}\right), \tau \in \mathbb{N}, \ t > 0.$$

Hence, $\{b_\tau\}$ is a CS. Since (Ξ, M, Γ) is complete, $b \in \Xi$ exist such that $\lim_{\tau \to \infty} b_\tau = b$ and $\lim_{\tau \to \infty} M_\alpha(b, b_\tau, t) = 0, t > 0$ (16)

Supposing $\kappa_1 \in (\aleph, 1)$ and $\kappa_2 = 1 - \kappa_1$, by (14) and $(FM_\alpha 4)$ one can obtain

$$M_\alpha(fb, b, t) \leq \Gamma\left(M_\alpha\left(fb, fb_\tau, \frac{t\kappa_1}{\alpha(fb, b_{\tau+1})\aleph}\right), M_\alpha\left(fb_\tau, b, \frac{t\kappa_2}{\alpha(b_{\tau+1}, b)\aleph}\right)\right)$$

$\leq$

$$\Gamma\left(\max \left\{ \begin{array}{c} \left\{ M_\alpha\left(b, b_\tau, \frac{t\kappa_1}{\alpha(b, b_\tau)\aleph}\right), M_\alpha\left(b, fb, \frac{t\kappa_1}{\alpha(b, fb)\aleph}\right), M_\alpha\left(b_\tau, b_{\tau+1}, \frac{t\kappa_1}{\alpha(b_\tau, b_{\tau+1})\aleph}\right) \right\} \\ \sqrt{M_\alpha\left(fb, b, \frac{t\kappa_1}{\alpha(fb, b)\alpha(fb, b_\tau)\aleph}\right) \cdot M_\alpha\left(b, b_\tau, \frac{t\kappa_1}{\alpha(fb, b_\tau)\alpha(b, b_\tau)\aleph}\right)} \\ M_\alpha\left(b, b_{\tau+1}, \frac{t\kappa_1}{\alpha(b, b_{\tau+1})\aleph}\right) \\ M_\alpha\left(b_{\tau+1}, b, \frac{t\kappa_2}{\alpha(b_{\tau+1}, b)}\right) \end{array} \right\} \right)$$

$$\leq \Gamma\left(\max\left\{\begin{array}{c} M_\alpha\left(b, b_\tau, \frac{t\kappa_1}{\alpha(b,b_\tau)\aleph}\right), M_\alpha\left(b, fb, \frac{t\kappa_1}{\alpha(b,fb)\aleph}\right), M_\alpha\left(b_\tau, b_{\tau+1}, \frac{t\kappa_1}{\alpha(b_\tau,b_{\tau+1})\aleph}\right) \\ \max\left\{M_\alpha\left(fb, b, \frac{t\kappa_1}{\alpha(fb,b)\alpha(fb,b_\tau)\aleph}\right), M_\alpha\left(b, b_\tau, \frac{t\kappa_1}{\alpha(fb,b_\tau)\alpha(b,b_\tau)\aleph}\right)\right\} \\ M_\alpha\left(b, b_{\tau+1}, \frac{t\kappa_1}{\alpha(b,b_{\tau+1})\aleph}\right) \\ M_\alpha\left(b_{\tau+1}, b, \frac{t\kappa_2}{\alpha(b_{\tau+1},b)}\right) \end{array}\right\}\right)$$

For all $\tau \in \mathbb{N}$ and $t > 0$. Taking $\tau \to \infty$ and utilizing (16), there is

$$M_\alpha(fb, b, t) \leq \Gamma\left(\max\left\{\begin{array}{c} 0, M_\alpha\left(b, fb, \frac{t\kappa_1}{\alpha(b,fb)\aleph}\right), 0 \\ \max\left\{M_\alpha\left(fb, b, \frac{t\kappa_1}{\alpha(fb,b)\alpha(fb,b_\tau)\aleph}\right), 0\right\}, 0 \end{array}\right\}\right)$$

$$= M_\alpha\left(fb, b, \frac{t\kappa_1}{\alpha(fb,b)\alpha(fb,b_\tau)\aleph}\right), t > 0.$$

And by Lemma 3 with $v = \frac{\alpha(fb,b)\alpha(fb,b_\tau)\aleph}{\kappa_1} \in (0,1)$ such that $fb = b$.

Let b and ω are two different FPs for f. By (2.13), one obtains

$$M_\alpha(fb, f\omega, t) \leq \Gamma\left(\begin{array}{c} M_\alpha\left(b, \omega, \frac{t}{\aleph}\right), M_\alpha\left(fb, b, \frac{t}{\aleph}\right), M_\alpha\left(f\omega, \omega, \frac{t}{\aleph}\right) \\ \sqrt{M_\alpha\left(fb, b, \frac{t}{\alpha(fb,b)\aleph}\right) \cdot M_\alpha\left(b, \omega, \frac{t}{\alpha(b,\omega)\aleph}\right)}, M_\alpha\left(b, \omega, \frac{t}{\aleph}\right) \end{array}\right)$$

$$\leq \Gamma\left(M_\alpha\left(b, \omega, \frac{t}{\aleph}\right), 0, 0, \max\left\{0, M_\alpha\left(b, \omega, \frac{t}{\alpha(b,\omega)\aleph}\right)\right\}, M_\alpha\left(b, \omega, \frac{t}{\aleph}\right)\right)$$

$$= M_\alpha\left(b, \omega, \frac{t}{\alpha(b,\omega)\aleph}\right) = M_\alpha\left(fb, f\omega, \frac{t}{\alpha(fb,f\omega)\aleph}\right), t > 0.$$

And thus, by Lemma 3, one obtains $b = \omega$.

Example 6. Suppose $\Xi = \{0,1,3\}$, $M_\alpha(b, \omega, t) = e^{-\frac{(b-\omega)^2}{t}}\left(1 - e^{\frac{(b-\omega)^2}{t}}\right)$

and $\Gamma = \Gamma_p$. Then, (Ξ, M, Γ) is a complete CRFMS with $\alpha(b, \omega) = b + \omega + 1$. Define the function $f: \Xi \to \Xi$ such that $f0 = f1 = 1$ and $f3 = 0$. Observe that if $b = \omega$ or $\omega \in \{0,1\}$, then, $M_\alpha(fb, f\omega, t) = 0, t > 0$ and (14) is fulfilled. Suppose $b = 1$ and $\omega = 3$. Then, $\aleph \in \left(\frac{1}{9}, \frac{1}{4}\right)$, one obtains

$$M_\alpha(fb, f\omega, t) = e^{-\frac{1}{t}}\left(1 - e^{\frac{1}{t}}\right) \leq \max\left\{e^{-\frac{9\aleph}{t}}, e^{-\frac{\aleph}{t}}, e^{-\frac{9\aleph}{t}}, e^{-\frac{\aleph}{t}}, 0\right\}$$

Suppose $b = 1$ and $\omega = 3$. Then, by choosing $\aleph \in \left(\frac{1}{9}, \frac{1}{4}\right)$, one has

$$M_\alpha(fb, f\omega, t) = e^{-\frac{1}{t}}\left(1 - e^{\frac{1}{t}}\right) \leq \max\left\{e^{-\frac{4\aleph}{t}}, 0, e^{-\frac{9\aleph}{t}}, e^{-\frac{\aleph}{t}}, e^{-\frac{\aleph}{t}}\right\}$$

Similarly, if b = 3 and $\omega = 1$ as well as b = 3 and $\omega = 1$, then for $\aleph \in \left(\frac{1}{9}, \frac{1}{4}\right)$, condition (14) is met for all $b, \omega \in \Xi$, and t > 0. As a result, Theorem 7 is satisfied with a UFP   b = 1.

An application to the transformation of solar energy to electric power

Sun-based boards are currently being distributed and shown widely to reduce people's reliance on petroleum derivatives which are less environmentally friendly. Nearly 19 trillion kilowatts of power were transported internationally in 2007. In comparison, the amount of day light that enters the Earth's surface in a single hour is enough to illuminate the entire planet for a full year. The question is: how do those dazzling and warm beams of light obtain power? A numerical model of the electric flow in an RLC equal circuit, often known as a "tuning" circuit, can be presented with a basic understanding of how light is converted into power. In the fields of radio and communication engineering, this circuit has several uses. The version that is being presented can be used to calculate the production of electric power, provide tools to improve building performance, and can be used as a decision-making tool when designing a hybrid renewable electricity system based on solar power. Every aspect of this system is mathematically expressed as a differential equation in (Younis et al, 2022) using the following equation

$$\begin{cases} \frac{d^2\mathfrak{C}}{d\vartheta^2} = \Omega\big(\vartheta, \mathfrak{C}(\vartheta)\big) - \frac{\mathfrak{R}}{\mathfrak{L}}\frac{d\mathfrak{C}}{d\vartheta} \\ \mathfrak{C}(0) = 0, \mathfrak{C}'(0) = m \end{cases} \tag{17}$$

where $\Omega: [0,1] \times \mathcal{R}^+ \to \mathcal{R}$ is a continuous function that is condition (17) to the integral equation to which it is equivalent.

$$\varrho(\vartheta) = \int_0^\vartheta N(\vartheta, l)\Omega(l, \mathfrak{C}(l))dl, \vartheta \in [0,1] \tag{18}$$

where the Green's function $N(\vartheta, b)$, it follows:

$$N(\vartheta, b) = \begin{cases} (\vartheta - l)e^{\Omega(M(b,\omega)(\vartheta-l))} & 0 \le c \le l \le 1 \\ 0, & 0 \le \vartheta \le l \le 1 \end{cases} \tag{19}$$

where $\Omega(M(b, \omega)) > 0$ is a constant, as determined by the values of $\mathfrak{R}$ and $\mathfrak{L}$, mentioned in (3.1).

Let $\Xi = C([0, \vartheta], \mathcal{R}^+)$ be the set of all real continuous positive functions that are expressed on the set [0,c]. Let Ξ be endowed with the CRFMS given by the following

$$M(b, \omega, t) = \begin{cases} 0 \text{ if } t = 0 \\ \sup_{t \in [0,1]} \frac{\min\{b,\omega\}+t}{\max\{b,\omega\}+t} \text{ otherwise} \end{cases} \text{ for all } b, \omega \in \Xi \tag{20}$$

One can verify that (Ξ, M, Γ) is a complete CRFMS with a controlled function $\alpha\colon \Xi^2 \to [0, \infty)$, defined by $\alpha(b, \omega) = b + \omega + 1$.

It is obvious that b^* is a solution of integral Equation (18), and as a result, a solution of differential equation (17) which governs the system of converting solar energy into electric power if and only if b^* is an FP of f. It is installed as a guarantee of the existence of FP of f.

Theorem 8. Assume the following problem fulfills:

$f\colon [0, \vartheta]^2 \to \mathcal{R}^+$ is a continuous function;

there exists a continuous function $N\colon [0, \vartheta]^2 \to R^+$ such that $\displaystyle\sup_{\alpha\in[0,\vartheta]} \int_0^\vartheta N(\alpha, l) \geq 1$

$\max\{f(\alpha, l, b(l)), f(\alpha, l, \omega(l))\} \geq N(\alpha, b)\max\{D(b(l), \omega(l))\}$ and
$\min\{f(\alpha, l, b(l)), f(\alpha, l, \omega(l))\} \geq N(\alpha, b)\min\{D(b(l), \omega(l))\}$ for all $\alpha, l, \in [0,1]$, $b, \omega \in \mathcal{R}^+$ and $\aleph \in (0,1)$ exists such that

$$\left(b(l), \omega(l)\right)$$

$$= \min \left\{ \begin{array}{c} M_\alpha\left(b(l), \omega(l), \dfrac{t}{\aleph}\right), M_\alpha\left(b(l), f\omega(l), \dfrac{t}{\aleph}\right), M_\alpha\left(fb(l), \omega(l), \dfrac{t}{\aleph}\right) \\[2mm] \dfrac{M_\alpha\left(b(l), f\omega(l), \dfrac{t}{\aleph}\right) + M_\alpha\left(fb(l), \omega(l), \dfrac{t}{\aleph}\right)}{2} \\[2mm] \dfrac{M_\alpha\left(b(l), f\omega(l), \dfrac{t}{\aleph}\right) + M_\alpha\left(fb(l), \omega(l), \dfrac{t}{\aleph}\right)}{1 + M_\alpha\left(b(l), \omega(l), \dfrac{t}{\aleph}\right)} \end{array} \right\}$$

Differential equation (17) that represents the solar energy problem has a solution as a result and integral equation (18) also has a solution.

Proof. For $b, \omega \in \Xi$, by use of assumptions (I) to (III), one has

$$M(fb, f\omega, t) = \sup_{t\in[0,1]} \frac{\min\left\{\int_0^\vartheta N(\vartheta, l)\Omega(l, b(l))dl, \int_0^\vartheta N(\vartheta, l)\Omega(l, \omega(l))dl\right\} + t}{\max\left\{\int_0^\vartheta N(\vartheta, l))\Omega(l, b(l))dl, \int_0^\vartheta N(\vartheta, l)\Omega(l, \omega(l))dl\right\} + t'}$$

$$= \sup_{t\in[0,1]} \frac{\int_0^\vartheta \min\{N(\vartheta, l)\Omega(l, b(l)), \; N(\vartheta, l)\Omega(l, \omega(l))\}\, dl + t}{\int_0^\vartheta \max\{N(\vartheta, l)\,\Omega(l, b(l)), N(\vartheta, l)\Omega(l, \omega(l))\} + t'}$$

$$= \sup_{t\in[0,1]} \frac{\int_0^\vartheta N(\vartheta, l)\min\{\Omega(l, b(l))dl\,\Omega(l, \omega(l))dl\} + t}{\int_0^\vartheta N(\vartheta, l)\max\{\Omega(l, b(l))dl\,\Omega(l, \omega(l))dl\} + t'}$$

$$\leq \sup_{t\in[0,1]} \frac{\int_0^\vartheta N(\vartheta, l)\,\min\{D(b(l), \omega(l))\}\, dl + t}{\int_0^\vartheta N(\vartheta, l)\,\max\{D(b(l), \omega(l))\}\, dl + t'} = M(D(b, \omega, t))$$

Thus, all conditions of Theorem 4 are fulfilled, i.e., the operator f has an FP which is the solution to differential equation (17) regulating the conversion of solar energy to electrical power.

1528

Open Problems 1. The following open problem is provided for further applications of the findings in this article:

Optional appliance renewal is one of the most basic concerns in management science and engineering economics. Corporations periodically purchase new appliances and sell old ones in order to operate the equipment permanently. If $\delta(t,z)$ is the efficiency of the appliance at time period T and $\delta(T)$ is the cost at the purchasing time, then,

$$\mathrm{e}^{-\eta t}\delta(T) = \int_T^{\lambda^{-1}} \mathrm{e}^{-\eta z}[\delta(T,z) - \delta(a(z),z)]\mathrm{d}u\,, -\infty < T < \infty.$$

where z is the usage time of the machine and η is the constant of the industry wide discount rate.

Can the results established in this note or their variants be applied to solve the aforementioned integral equation?

Can the results derived in this article be controlled in graphical revised fuzzy metric spaces? Can one demonstrate the aforementioned findings for multi-valued mappings?

Conclusions

In the perspective of controlled revised fuzzy metric spaces, this manuscript contains a number of fixed point theorems and a sufficient condition for a sequence to be Cauchy. As a result, the well-known contraction requirements with controlled revised fuzzy metric spaces have been combined to simplify the proofs of several fixed point theorems. Furthermore, an application to transform solar energy to electric power has been discussed. In the future, these results will be enhanced in the framework of tripled controlled revised fuzzy metric spaces and pentagonal controlled revised fuzzy metrics spaces.

References

Adabitabar Firozja, A. & Firouzian, S. 2015. Definition of fuzzy metric space with t-conorm. *Annals of Fuzzy Mathematics and Informatics*, 10(4), pp.649-655 [online]. Available at: http://www.afmi.or.kr [Accessed: 02 February 2024].

Al-Khaleel, M., Al-Sharif, S. & AlAhmad, R. 2023. On Cyclic Contractive Mappings of Kannan and Chatterjea Type in Generalized Metric Spaces. *Mathematics*, 11(4), art.number:890. Available at: https://doi.org/10.3390/math11040890.

Branga, A.N. & Olaru, I.M. 2022. Generalized Contractions and Fixed Point Results in Spaces with Altering Metrics. *Mathematics*, 10(21), art.number:4083. Available at: https://doi.org/10.3390/math10214083.

Czerwik, S. 1993. Contraction mappings in b-metricspaces. *Acta Mathematica et Informatica Universitatis Ostraviensis*, 1(1), pp.5-11 [online]. Available at: https://dml.cz/handle/10338.dmlcz/120469 [Accessed: 02 February 2024].

George, A. & Veeramani, P. 1994. On some results in fuzzy metric spaces. *Fuzzy Sets and Systems*, 64(3), pp.395-399. Available at: https://doi.org/10.1016/0165-0114(94)90162-7.

Gregori, V. & Miñana, J.-J. 2021. A Banach contraction principle in fuzzy metric spaces defined by means of t-conorms. *Revista de la Real Academia de Ciencias Exactas, Físicas y Naturales. Serie A. Matemáticas*, 115, art.number:129. Available at: https://doi.org/10.1007/s13398-021-01068-6.

Grigorenko, O., Miñana, J.J., Šostak, A. & Valero, O. 2020. On t-Conorm Based Fuzzy (Pseudo)metrics. *Axioms*, 9(3), art.number:78. Available at: https://doi.org/10.3390/axioms9030078.

Hadžić, O. 1979. A fixed point theorem in Menger spaces. *Publications De L'institute Mathématique, Nouvelle serie*, 20(40), pp.107-112 [online]. Available at: http://elib.mi.sanu.ac.rs/files/journals/publ/46/17.pdf [Accessed: 02 February 2024].

Hadžić, O. & Pap, E. 2001. Probabilistic metric spaces. In: *Fixed Point Theory in Probabilistic Metric Spaces. Mathematics and Its Applications*, 536, pp.47-94. Dordrecht: Springer. Available at: https://doi.org/10.1007/978-94-017-1560-7_2.

Hassanzadeh, Z. & Sedghi, S. 2018. Relation betweenb-metric and fuzzy metric spaces. *Mathematica Moravica*, 22(1), pp.55-63. Available at: https://doi.org/10.5937/MatMor1801055H.

Heilpern, S. 1981. Fuzzy mappings and fixed point theorem. *Journal of Mathematical Analysis and Applications*, 81(2), pp.566-569. Available at: https://doi.org/10.1016/0022-247X(81)90141-4.

Hussain, A., Ishtiaq, U., Ahmed, K. & Al-Sulami, H. 2022. On Pentagonal Controlled Fuzzy Metric Spaces with an Application to Dynamic Market Equilibrium. *Journal of Function Spaces*, 2022(1), art.number: 5301293. Available at: https://doi.org/10.1155/2022/5301293.

Ishtiaq, U., Kattan, D.A., Ahmad, K., Sessa, S. & Ali, F. 2023. Fixed Point Results in Controlled Fuzzy Metric Spaces with an Application to the Transformation of Solar Energy to Electric Power. *Mathematics*, 11(15), art.number:3435. Available at: https://doi.org/10.3390/math11153435.

Ishtiaq, U., Saleem, N., Uddin, F., Sessa, S., Ahmad, K. & di Martino, F. 2022. Graphical Views of Intuitionistic Fuzzy Double-Controlled Metric-Like Spaces and Certain Fixed-Point Results with Application. *Symmetry*, 14(11), art.number:2364. Available at: https://doi.org/10.3390/sym14112364.

Kaleva, O. & Seikkala, S. 1984. On fuzzy metric spaces. *Fuzzy Sets and Systems*, 12(3), pp.215-229. Available at: https://doi.org/10.1016/0165-0114(84)90069-1.

Kider, J.R. 2020. Some Properties of Algebra Fuzzy Metric Space. *Journal of Al-Qadisiyah for Computer Science and Mathematics*, 12(2), pp.43-56. Available at: https://doi.org/10.29304/jqcm.2020.12.2.695.

Kider, J.R. 2021. Application of Fixed Point in Algebra Fuzzy Normed Spaces. *Journal of Physics: Conference Series*, 1879, art.number:022099. Available at: https://doi.org/10.1088/1742-6596/1879/2/022099.

Klement, E.P., Mesiar, R. & Pap, E. 2004. Problems on triangular norms and related operators. *Fuzzy Sets and Systems*, 145(3), pp.471-479. Available at: https://doi.org/10.1016/S0165-0114(03)00303-8.

Kramosil, I. & Michálek, J. 1975. Fuzzy metrics and statistical metric spaces. *Kybernetika*, 11(5), pp.336-344 [online]. Available at: https://www.kybernetika.cz/content/1975/5/336 [Accessed: 19 January 2024].

Li, S.-F., He, F. & Lu, S.-M. 2022. Kaleva-Seikkala'sType Fuzzy b-Metric Spaces and Several Contraction Mappings. *Journal of Function Spaces*, 2022(1), art.number: 2714912. Available at: https://doi.org/10.1155/2022/2714912.

Mlaiki, N., Aydi, H., Souayah, N. & Abdeljawad, T. 2018. Controlled Metric Type Spaces and the Related Contraction Principle. *Mathematics*, 6(10), art.number:194. Available at: https://doi.org/10.3390/math6100194.

Moussaoui, A., Hussain, N., Melliani, S., Nasr, H. & Imdad, M. 2022. Fixed point results via extended FZ-simulation functions in fuzzy metric spaces. *Journal of Inequalities and Applications*, art.number:69. Available at: https://doi.org/10.1186/s13660-022-02806-z.

Muraliraj, A. & Thangathamizh, R. 2021a. Fixed point theorems in revised fuzzy metric space. *Advances in Fuzzy Sets and Systems*, 26(2), pp.103-115. Available at: https://doi.org/10.17654/FS026020103.

Muraliraj, A. & Thangathamizh, R. 2021b. Introduction on Revised fuzzy modular spaces. *Global Journal of Pure and Applied Mathematics*, 17(2), pp.303-317. Available at: https://doi.org/10.37622/GJPAM/17.2.2021.303-317.

Muraliraj, A. & Thangathamizh, R. 2022. Relation-Theoretic Revised Fuzzy Banach Contraction Principle and Revised Fuzzy Eldestein Contraction Theorem. *JMSCM Journal of Mathematical Sciences & Computational Mathematics,* 3(2), pp.197-207. Available at: https://doi.org/10.15864/jmscm.3205.

Muraliraj, A. & Thangathamizh, R. 2023. Some topological properties of revised fuzzy cone metric spaces. *Ratio Mathematica*, 47, pp.42-51. Available at: https://doi.org/10.23755/rm.v47i0.734.

Muraliraj, A., Thangathamizh, R., Popovic, N., Savic, A. & Radenovic, S. 2023. The First Rational Type Revisd Fuzzy-Contractions in Revisd Fuzzy Metric Spaces with an Applications. *Mathematics*, 11(10), art.number:2244. Available at: Available at: https://doi.org/10.3390/math11102244.

Rakić, D., Mukheimer, A., Došenović, T., Mitrović, Z. & Radenović, S. 2020. On some new fixed point results in fuzzy b-metric spaces". *Journal of Inequalities and Applications*, art.number:99. Available at: https://doi.org/10.1186/s13660-020-02371-3.

Sedghi, S. & Shobe, N. 2012. Common fixed point theorem in b-fuzzy metric space. *Nonlinear Functional Analysis and Applications (NFAA),* 17(3), pp.349-

359 [online]. Available at: http://nfaa.kyungnam.ac.kr/journal-nfaa/index.php/NFAA/article/view/38 [Accessed: 02 February 2024].

Sedghi, S. & Shobkolaei, N. 2014. Common fixed point theorem for R-weakly commuting maps in b-fuzzy metric spaces. *Nonlinear Functional Analysis and Applications (NFAA),* 19(2) pp.285-295 [online]. Available at: http://nfaa.kyungnam.ac.kr/journal-nfaa/index.php/NFAA/article/view/238 [Accessed: 02 February 2024].

Sezen, M.S. 2021. Controlled fuzzy metric spaces and some related fixed point results. *Numerical Methods for Partial Differential Equations*, 37(1), pp.583-593. Available at: https://doi.org/10.1002/num.22541.

Schweizer, B. & Sklar, A. 1960. Statistical metric spaces. *Pacific Journal of Mathematics,* 10(1), pp.313-334. Available at: https://doi.org/10.2140/pjm.1960.10.313.

Šostak, A. 2018. George-Veeramani Fuzzy Metrics Revised. *Axioms*, 7(3), art.numner:60. Available at: https://doi.org/10.3390/axioms7030060.

Thangathamizh, R., Muraliraj, A. & Shanmugavel, P. 2024. New approach of Lebesgue integral in revised fuzzy cone metric spaces via unique coupled fixed point theorems. *Vojnotehnički glasnik/Military Technical Courier*, 72(3), pp.1029-1045. Available at: https://doi.org/10.5937/vojtehg72-48816.

Younis, M., Singh, D. & Abdou, A.A.N. 2022. A fixed point approach for tuning circuit problem in dislocated b-metric spaces. *Mathematical Methods in the Applied Science*, 45(4), pp.2234-2253. Available at: https://doi.org/10.1002/mma.7922.

Zadeh, L.A. 1965. Fuzzy Sets. *Information and Control*, 8(3), pp.338-353. Available at: https://doi.org/10.1016/S0019-9958(65)90241-X.

El punto fijo da como resultado espacios métricos difusos revisados y controlados, con una aplicación a la transformación de energía solar en energía eléctrica

Ravichandhiran Thangathamizh[a], *Abdelhamid* Moussaoui[b], *Tatjana* Došenović[c], *Stojan* Radenović[d]

[a] Instituto de Tecnología Jeppiaar (Autónomo), Departamento de Matemáticas, Kanchipuram, Tamil Nadu, República de la India,
autor de correspondencia

[b] Universidad Sultán Moulay Slimane, Facultad de Ciencias y Técnicas, LMACS, Beni Mellal, Reino de Marruecos

[c] Universidad de Novi Sad, Facultad de Tecnología, Novi Sad, República de Serbia

[d] Universidad de Belgrado, Facultad de Ingeniería Mecánica, Belgrado, República de Serbia

CAMPO: matemáticas
TIPO DE ARTÍCULO: artículo científico original

Resumen:

Introducción/objetivo: Este estudio establece condiciones suficientes para que una secuencia sea Cauchy dentro del marco de espacios métricos difusos revisados y controlados. También generaliza el concepto del principio de contracción de Banach al introducir varias condiciones nuevas de nuevas. El objetivo es derivar varios resultados de punto fijo que mejoren la comprensión de estas estructuras matemáticas.

Métodos: Los investigadores emplean técnicas matemáticas rigurosas para desarrollar sus hallazgos. Al definir un conjunto de asignaciones de contracción novedosas y utilizar propiedades de espacios métricos difusos revisados y controlados, analizan las implicaciones para la convergencia de secuencias. La metodología incluye la construcción de ejemplos específicos para ilustrar los resultados teóricos.

Resultados: El estudio presenta varios teoremas de punto fijo derivados de las condiciones de contracción generalizada. Además, proporciona una serie de ejemplos no triviales que fundamentan las afirmaciones y demuestran la aplicabilidad de los resultados en escenarios prácticos. Se explora una aplicación importante con respecto a la conversión de energía solar en energía eléctrica, utilizando ecuaciones diferenciales para resaltar esta conexión.

Conclusión: Los hallazgos profundizan la comprensión de las secuencias de Cauchy en espacios métricos difusos y ofrecen una perspectiva más amplia sobre la aplicación de la teoría del punto fijo en escenarios del mundo real. Los resultados allanaron el camino para futuras investigaciones tanto en matemáticas teóricas como en sus aplicaciones prácticas, particularmente en el campo de las energías renovables.

Palabras claves: teoremas del punto fijo, espacio métrico difuso revisado (RFMS), principios de contracción (CP), función de Green, ecuación diferencial.

Результаты неподвижной точки в управляемых пересмотренных фазовых метрических пространствах, применяемых для преобразования солнечной энергии

Равичандиран Тангатамиж[а], *Абделхамид* Мусауи[б], *Татьяна* Дошенович[в], *Стоян* Раденович[г]

[а] Технологический институт Джеппиара (автономный), математический факультет, Канчипурам, Тамилнад, Республика Индия, **корреспондент**

[б] Университет Султана Мулай Слимана, факультет естественных наук и техники, MACS, Бени-Меллаль, Королевство Марокко

[в] Нови-Садский университет, технологический факультет, г. Нови-Сад, Республика Сербия

[г] Белградский университет, машиностроительный факультет, г. Белград, Республика Сербия

Резюме:

Введение/цель: В данном исследовании установлены условия для того, чтобы последовательность Коши находилась в рамках контролируемых пересмотренных нечетких метрических пространств. В статье также обобщается концепция принципа сжатия Банаха, вводя несколько новых условий сжатия. Цель статьи заключается в получении различных результатов с фиксированной точкой, которые улучшат понимание этих математических структур.

Методы: В исследовании применялись строгие математические методы для представления открытий. Определяя набор новых сокращающихся отображений и используя свойства контролируемых пересмотренных нечетких метрических пространств, были проанализированы импликации для сходимости последовательностей. Методология включает в себя разработку конкретных примеров, иллюстрирующих теоретические результаты.

Результаты: В исследовании представлено несколько теорем о неподвижной точке, полученных из обобщенных условий сжатия. Помимо того, приводится ряд нетривиальных примеров, которые обосновывают утверждения и демонстрируют применимость результатов в практических сценариях. Рассматривается важная сфера применения, связанная с преобразованием солнечной энергии в электрическую с использованием дифференциальных уравнений.

Выводы: Полученные результаты углубляют понимание последовательностей Коши в фазовых метрических пространствах и раскрывают более широкую перспективу для применения теории фиксированной точки в реальных сценариях. Результаты прокладывают путь для дальнейших исследований как в области теоретической математики, так и в области ее практического применения, в частности, в области возобновляемых источников энергии.

Ключевые слова: теоремы о неподвижной точке, пересмотренное нечеткое метрическое пространство (RFMS), принципы сжатия (CP), функция Грина, дифференциальное уравнение.

Резултати непомичне тачке у контролисаним ревидираним фази метричким просторима примењени на претварање соларне енергије у електричну

Равичандиран Тангатамиж[а], *Абделхамид* Мусауи[б],
Татјана Дошеновић[в]*, Стојан* Раденовић[г]

[а] Институт за технологију Џепиар (аутономни), Одељење за математику,
  Канчипурам, Тамил Наду, Република Индија,
  аутор за преписку

[б] Универзитет „Султан Мулај Слимејн“,
  Факултет природних и техничких наука, LMACS,
  Бени Мелал, Краљевина Мароко

[в] Универзитет у Новом Саду, Технолошки факултет,
  Нови Сад, Република Србија

[г] Универзитет у Београду, Машински факултет,
  Београд, Република Србија

ОБЛАСТ: математика
КАТЕГОРИЈА (ТИП) ЧЛАНКА: оригинални научни рад

Сажетак:

Увод/циљ: У студији се успостављају довољни услови да секвенца буде Кошијева у оквиру контролисаних ревидираних фази метричких простора. Такође, генерализује се концепт Банаховог принципа контракције увођењем неколико нових услова контракције. Циљ је да се изведу различити резултати непомичне тачке који доводе до бољег разумевања ове математичке структуре.

Методе: Аутори развијају своја открића коришћењем ригорозних математичких техника. Дефинисањем скупа нових пресликавања контракција и коришћењем својстава контролисаних ревидираних фази метричких простора анализиранесу импликације за конвергенцију секвенце. Методологија укључује конструисање конкретних примера за илустрацију теоријских резултата.

Резултати: Студија представља неколико теорема непомичне тачке изведених из генерализованих услова контракције. Поред тога, наводи бројне нетривијалне примере који поткрепљују тврдње и демонстрирају применљивост резултата у практичним сценаријима. Приказана је важна примена у области претварања соларне енергије у електричну енергију помоћу диференцијалне једначине.

Закључак: Налази продубљују разумевање Кошијевих секвенци у фази метричким просторима и нуде ширу перспективу примене теорије непокретне тачке у сценаријима из реалног живота. Резултати отварају пут за даља истраживања, како у теоријској

математици, тако и у њеним практичним применама, посебно у области обновљиве енергије.

Кључне речи: теореме непокретне тачке, прерађени фази метрички простор (RFMS), принципи контракције (CP), Гринова функција, диференцијална једначина.

Berezin inequalities for sums of operators and classical inequalities concerning the Berezin radius

Mehmet Gürdal[a], *Vuk* N. Stojiljković[b]

[a] Suleyman Demirel University, Department of Mathematics,
Isparta, Republic of Türkiye,
e-mail: gurdalmehmet@sdu.edu.tr,
ORCID iD: https://orcid.org/0000-0003-0866-1869

[b] University of Novi Sad, Faculty of Science, Novi Sad, Republic of Serbia;
Mathematical Grammar School, Belgrade, Republic of Serbia,
e-mail: vuk.stojiljkovic999@gmail.com, **corresponding author**,
ORCID iD: https://orcid.org/0000-0002-4244-4342

Abstract:

Introduction/purpose: In this article, the author's goal is to seek to obtain new inequalities of the Berezin type.

Methods: The methods used are standard for operator theory.

Results: Various inequalities of the type given by Huban et al. and Erkan have been obtained.

Conclusions: In addition to obtaining various inequalities of the form given by Huban et al. and Erkan in particular, the authors sharpened the inequalities related to the Berezin norm.

Key words: Berezin norm, Berezin number, inequalities.

Introduction

The Berezin norm and the Berezin number of an operator have been researched for their many applications in numerical analysis, quantum physics, engineering, and other domains in the literature related to operator theory. In order to explain the Berezin number and norm, the authors first go over several ideas and traits of bounded linear operators on a Hilbert space.

Let $\mathfrak{L}(\mathfrak{H})$ denote the C^*-algebra of all bounded linear operators defined on a complex Hilbert space $\mathfrak{H}$ with the an inner product $\langle .,. \rangle$ and a corresponding norm $\|.\|$. Recall that the functional Hilbert space $\mathfrak{H} = \mathfrak{H}(\Xi)$ is

a Hilbert space of complex-valued functions on a (nonempty) set Ξ such that the evaluation functionals $\varphi_\varrho(f) = f(\varrho)$, $\varrho \in \Xi$, are continuous on $\mathfrak{H}$ and for every $\varrho \in \Xi$ there exists a function $f_\varrho \in \mathfrak{H}$ such that $f_\varrho(\varrho) \neq 0$ or, equivalently, there is no $\varrho_0 \in \Xi$ such that $f(\varrho_0) = 0$ for all $f \in \mathfrak{H}$. The Riesz representation theorem ensures that for each $\varrho \in \Xi$ there is a unique element $\varkappa_\varrho \in \mathfrak{H}$ such that $f(\varrho) = \langle f, \varkappa_\varrho \rangle$ for all $f \in \mathfrak{H}$. The collection $\{\varkappa_\varrho : \varrho \in \Xi\}$ is called the reproducing kernel of $\mathfrak{H}$. For $\varrho \in \Xi$, let $\widehat{\varkappa}_\varrho := \frac{\varkappa_\varrho}{\|\varkappa_\varrho\|}$ be the normalized reproducing kernel of $\mathfrak{H}$. The absolute value of the positive operator is denoted by $|\mathfrak{Z}| = (\mathfrak{Z}^* \mathfrak{Z})^{1/2}$.

For a bounded linear operator $\mathfrak{Z}$ on $\mathfrak{H}$, the function $\widetilde{\mathfrak{Z}}$ defined on Ξ by $\widetilde{\mathfrak{Z}}(\varrho) := \langle \mathfrak{Z} \widehat{\varkappa}_\varrho(z), \widehat{\varkappa}_\varrho(z) \rangle$ is the Berezin symbol of $\mathfrak{Z}$, which firstly have been introduced by Berezin (Berezin, 1972). In other words, the Berezin symbol $\widetilde{\mathfrak{Z}}$ is the function on Ξ defined by restriction of the quadratic form $\langle \mathfrak{Z} x_1, x_1 \rangle$ with $x_1 \in \mathfrak{H}$ to the subset of all normalized reproducing kernels of the unit sphere in $\mathfrak{H}$. It is clear from the Cauchy-Schwarz inequality that $\widetilde{\mathfrak{Z}}$ is the bounded function on Ξ whose values lie in the numerical range of the operator $\widetilde{\mathfrak{Z}}$. The Berezin set (or range) and the Berezin number (or radius) of the operator $\mathfrak{Z}$ are defined by

$$\mathrm{Ber}(\mathfrak{Z}) := \{\widetilde{\mathfrak{Z}}(\varrho) : \varrho \in \Xi\} \text{ and } \mathrm{ber}(\mathfrak{Z}) := \sup_{\varrho \in \Xi} \left| \widetilde{\mathfrak{Z}}(\varrho) \right|,$$

respectively (see (Karaev, 2006)).

A relevant and important concept is a numerical radius which is the supremum of the absolute values of all numbers in $\mathfrak{W}(\mathfrak{Z})$, that is

$$\mathfrak{w}(\mathfrak{Z}) = \sup_{x \in \mathfrak{H}, \|x\|=1} |\langle \mathfrak{Z} x, x \rangle|.$$

It is obvious that $\mathrm{ber}(\mathfrak{Z}) \leq \mathfrak{w}(\mathfrak{Z}) \leq \|\mathfrak{Z}\|$ and $\mathrm{Ber}(\mathfrak{Z}) \subset \mathfrak{W}(\mathfrak{Z})$, where $\mathfrak{w}(\mathfrak{Z})$ denotes the numerical radius and $\mathfrak{W}(\mathfrak{Z})$ is the numerical range of the operator $\mathfrak{Z}$. It is well known that

$$\frac{\|\mathfrak{Z}\|}{2} \leq \mathfrak{w}(\mathfrak{Z}) \leq \|\mathfrak{Z}\|$$

and

$$\mathrm{ber}(\mathfrak{Z}) \leq \mathfrak{w}(\mathfrak{Z}) \leq \|\mathfrak{Z}\|, \tag{1}$$

for any $\mathfrak{Z} \in \mathfrak{L}(\mathfrak{H})$.

In (Huban et al, 2022a), Huban et al. substantially improved the upper bound in (1) by showing that if $\mathfrak{Z} \in \mathfrak{L}(\mathfrak{H})$, then

$$\mathrm{ber}\left(\mathfrak{Z}\right) \leq \frac{1}{2}\left\||\mathfrak{Z}| + |\mathfrak{Z}^*|\right\|_{\mathrm{ber}} \leq \frac{1}{2}\left(\|\mathfrak{Z}\|_{\mathrm{ber}} + \left\|\mathfrak{Z}^2\right\|_{\mathrm{ber}}^{\frac{1}{2}}\right). \qquad (2)$$

Another improvement for inequality (1) was provided by Huban et al. (Huban et al, 2021) as

$$\mathrm{ber}^2\left(\mathfrak{Z}\right) \leq \frac{1}{2}\left\||\mathfrak{Z}|^2 + |\mathfrak{Z}^*|^2\right\|_{\mathrm{ber}}, \qquad (3)$$

which was further improved in (Gürdal & Başaran, 2023) by Başaran and Gürdal as

$$\mathrm{ber}^2\left(\mathfrak{Z}\right) \leq \frac{1}{6}\left\||\mathfrak{Z}|^2 + |\mathfrak{Z}^*|^2\right\|_{\mathrm{ber}} + \frac{1}{3}\mathrm{ber}\left(\mathfrak{Z}\right)\left\||\mathfrak{Z}| + |\mathfrak{Z}^*|\right\|_{\mathrm{ber}}. \qquad (4)$$

The following inequalities for $\mathrm{ber}^2(.)$ have been obtained in (Huban et al, 2021)

$$\frac{1}{4}\left\||\mathfrak{Z}|^2 + |\mathfrak{Z}^*|^2\right\|_{\mathrm{ber}} \leq \mathrm{ber}^2\left(\mathfrak{Z}\right) \leq \frac{1}{2}\left\||\mathfrak{Z}|^2 + |\mathfrak{Z}^*|^2\right\|_{\mathrm{ber}}. \qquad (5)$$

Furthermore, Huban et al. (Huban et al, 2022a) established some refinements of (2) and (5), respectively, that can be presented as

$$\mathrm{ber}^j(\mathfrak{Z}) \leq \frac{1}{2}\left\||\mathfrak{Z}|^{2j\xi} + |\mathfrak{Z}^*|^{2j(1-\xi)}\right\|_{\mathrm{ber}} \qquad (6)$$

and

$$\mathrm{ber}^{2j}(\mathfrak{Z}) \leq \left\|\xi|\mathfrak{Z}|^{2j} + (1-\xi)|\mathfrak{Z}^*|^{2j}\right\|_{\mathrm{ber}}, \qquad (7)$$

where $\mathfrak{Z} \in \mathfrak{L}(\mathfrak{H})$, $0 \leq \xi \leq 1$, and $j \geq 1$.

Another important fact about the Berezin number upper bounds that are of our interest are due to Huban et al. in (Huban et al, 2021): Let $\mathfrak{Z}_1, \mathfrak{Z}_2 \in \mathfrak{L}(\mathfrak{H})$ and $r \geq 1$, then

$$\mathrm{ber}^r(\mathfrak{Z}_2^*\mathfrak{Z}_1) \leq \frac{1}{2}\left\||\mathfrak{Z}_1|^{2r} + |\mathfrak{Z}_2|^{2r}\right\|_{\mathrm{ber}}. \qquad (8)$$

For an in-depth exploration of the intricacies surrounding the Berezin symbol, interested readers are strongly encouraged to refer to (Bakherad & Garayev, 2019; Başaran et al, 2022; Chalendar et al, 2012; Garayev & Alomari, 2021; Garayev et al, 2020; Güntürk & Gürdal, 2024; Garayev

et al, 2021; Stojiljković & Gürdal, 2024a,b; Gürdal et al, 2023; Gürdal & Tapdigoglu, 2023; Tapdigoglu et al, 2021; Yamancı et al, 2020; Gürdal & Stojiljkovic, 2024a; Huban et al, 2022b; Gürdal & Stojiljkovic, 2024b) and the comprehensive references provided therein.

In this paper, motivated by previously reported results (Stojiljković & Dragomir, 2024), this work aims to develop new Berezin number upper bounds for reproducing kernel Hilbert space operators by introducing new improvements to the well-known Cauchy-Schwarz inequality.

Preliminaries

We require a few well-known lemmas in order to demonstrate our extended Berezin number inequalities.

According to the traditional Schwarz inequality for positive operator, for any $x_1, x_2 \in \mathfrak{H}$

$$|\langle \mathfrak{Z}x_1, x_2 \rangle|^2 \leq \langle \mathfrak{Z}x_1, x_1 \rangle \langle \mathfrak{Z}x_2, x_2 \rangle \tag{9}$$

if $\mathfrak{Z} \in \mathfrak{L}(\mathfrak{H})$ is a positive operators. Kato's inequality, sometimes referred to as the combined Cauchy-Schwarz inequality, was initially put out by Kato (Kato, 1952) in 1952 as a companion to the Schwarz inequality (9). It says that

$$|\langle \mathfrak{Z}x_1, x_2 \rangle|^2 \leq \langle |\mathfrak{Z}|^{2\gamma}x_1, x_1 \rangle \langle |\mathfrak{Z}^*|^{2(1-\gamma)}x_2, x_2 \rangle, \ \gamma \in [0, 1] \tag{10}$$

for any operator $\mathfrak{Z} \in \mathfrak{L}(\mathfrak{H})$ and any $x_1, x_2 \in \mathfrak{H}$. In order to generalize this result, in 1994 Furuta (Furuta, 1994) obtained the following result:

$$|\langle \mathfrak{Z}|\mathfrak{Z}|^{\gamma+\eta-1}x_1, x_2 \rangle|^2 \leq \langle |\mathfrak{Z}|^{2\gamma}x_1, x_1 \rangle \langle |\mathfrak{Z}^*|^{2\eta}x_2, x_2 \rangle, \tag{11}$$

for any $x_1, x_2 \in \mathcal{H}$ and $\gamma, \eta \in [0, 1]$ with $\gamma + \eta \geq 1$.

LEMMA 1. *(McCarthy, 1967). Let $\mathfrak{Z} \in \mathfrak{L}(\mathfrak{H})$, $\mathfrak{Z} \geq 0$ and let $x \in \mathfrak{H}$ be any unit vector. Then there is*

$$\langle \mathfrak{Z}x, x \rangle^{\mathfrak{r}} \leq \langle \mathfrak{Z}^{\mathfrak{r}}x, x \rangle \text{ for } \mathfrak{r} \geq 1, \tag{12}$$

$$\langle \mathfrak{Z}^{\mathfrak{r}}x, x \rangle \leq \langle \mathfrak{Z}x, x \rangle^{\mathfrak{r}} \text{ for } 0 < \mathfrak{r} \leq 1. \tag{13}$$

The well-known Buzano's inequality is the following outcome.

LEMMA 2. *Let $x, y, e \in \mathfrak{H}$ with $\|e\| = 1$. Then there is*

$$|\langle x, e \rangle \langle e, y \rangle| \leq \frac{1}{2}(\|x\| \, \|y\| + |\langle x, y \rangle|). \tag{14}$$

The following result is found in ([Singh Aujla & Silva](), 2003) and is related to non-negative convex functions.

LEMMA 3. *Let f be a non-negative convex function on $[0, +\infty)$ and $\mathfrak{Z}_1, \mathfrak{Z}_2 \in \mathfrak{L}(\mathfrak{H})$ be positive operators. Then*

$$\left\| f\left(\frac{\mathfrak{Z}_1 + \mathfrak{Z}_2}{2}\right) \right\| \leq \left\| \frac{f(\mathfrak{Z}_1) + f(\mathfrak{Z}_2)}{2} \right\|. \tag{15}$$

LEMMA 4. *Let $x, y \in \mathfrak{H}$ and $\mathfrak{A} \in \mathfrak{L}(\mathfrak{H})$.*

$$|\langle \mathfrak{A}x, y \rangle|^2 \leq \langle f^2(|\mathfrak{A}|)x, x \rangle \langle g^2(|\mathfrak{A}^*|)y, y \rangle. \tag{16}$$

is the case where f and g are two nonnegative continuous functions on $[0, +\infty)$ that fulfill $f(t)g(t) = t, t \geq 0$.

With regard to the mapping φ, Stojiljković and Gürdal ([Stojiljković & Gürdal](), 2024c) recently acquired the following modification.

LEMMA 5. *Let $u_k, v_k, e \in \mathfrak{H}$, $l, q > 1$, $p \geq 1$, $\frac{1}{l} + \frac{1}{q} = 1$. Let $\mathfrak{J}$ be a set such that $(0,1) \subset \mathfrak{J} \subset \mathbb{R}$. Let φ be a of mapping such that $\varphi : \mathfrak{J} \to \mathbb{R}^+$, such that the following holds $\sum_i^n \varphi(\alpha_i) = 1$. Then the following inequality holds*

$$\left| \sum_{k=1}^{n} \varphi(\alpha_k) \langle u_k, e \rangle \langle e, v_k \rangle \right|^p \leq \frac{\sum_{k=1}^{n} \varphi^{l/2}(\alpha_k)|\langle u_k, e \rangle|^{pl}}{l} +$$
$$+ \frac{\sum_{k=1}^{n} \varphi^{q/2}(\alpha_k)|\langle e, v_k \rangle|^{pq}}{q}. \tag{17}$$

Main results

We give our first result, a consequence of Lemma 5 which is instrumental in the development of the later results.

COROLLARY 1. *Let $l, q > 1$ such that $\frac{1}{l} + \frac{1}{q} = 1$ and $p \geq 1$, $\mathfrak{Z}_i \in \mathfrak{L}(\mathfrak{H})$ and $\varphi : \mathfrak{J} \to \mathbb{R}^+$ with $\sum_{i=1}^{n} \varphi(\alpha_i) = 1$, then the following inequality holds:*

$$\left| \sum_{k=1}^{n} \varphi(\alpha_k) \langle \mathfrak{Z}_k \widehat{\varkappa}_\varrho, \widehat{\varkappa}_\varrho \rangle^2 \right|^p \leq \frac{\sum_{k=1}^{n} \langle |\mathfrak{Z}_k|^{2p\alpha l} \widehat{\varkappa}_\varrho, \widehat{\varkappa}_\varrho \rangle \varphi^{l/2}(\alpha_k)}{2l} +$$
$$+ \frac{\sum_{k=1}^{n} \langle |\mathfrak{Z}_k^*|^{2pl(1-\alpha)} \widehat{\varkappa}_\varrho, \widehat{\varkappa}_\varrho \rangle \varphi^{l/2}(\alpha_k)}{2l} + \frac{\sum_{k=1}^{n} \varphi^{q/2}(\alpha_k)|\langle \mathfrak{Z}_k \widehat{\varkappa}_\varrho, \widehat{\varkappa}_\varrho \rangle|^{pq}}{q}. \tag{18}$$

Proof. If we take $v_k = \mathfrak{Z}_k^* \widehat{\varkappa}_\varrho$, $u_k = \mathfrak{Z}_k \widehat{\varkappa}_\varrho$ and $e = \widehat{\varkappa}_\varrho$ in Lemma 5 above, one obtains

$$
\left| \sum_{k=1}^n \varphi(\alpha_k) \langle \mathfrak{Z}_k \widehat{\varkappa}_\varrho, \widehat{\varkappa}_\varrho \rangle^2 \right|^p
$$

$$
\leq \frac{\sum_{k=1}^n \varphi^{l/2}(\alpha_k) |\langle \mathfrak{Z}_k \widehat{\varkappa}_\varrho, \widehat{\varkappa}_\varrho \rangle|^{pl}}{l} + \frac{\sum_{k=1}^n \varphi^{q/2}(\alpha_k) |\langle \mathfrak{Z}_k \widehat{\varkappa}_\varrho, \widehat{\varkappa}_\varrho \rangle|^{pq}}{q}
$$

$$
\leq \frac{\sum_{k=1}^n \langle |\mathfrak{Z}_k|^{2p\alpha l} \widehat{\varkappa}_\varrho, \widehat{\varkappa}_\varrho \rangle \varphi^{l/2}(\alpha_k)}{2l} + \frac{\sum_{k=1}^n \langle |\mathfrak{Z}_k^*|^{2pl(1-\alpha)} \widehat{\varkappa}_\varrho, \widehat{\varkappa}_\varrho \rangle \varphi^{l/2}(\alpha_k)}{2l} +
$$

$$
+ \frac{\sum_{k=1}^n \varphi^{q/2}(\alpha_k) |\langle \mathfrak{Z}_k \widehat{\varkappa}_\varrho, \widehat{\varkappa}_\varrho \rangle|^{pq}}{q}.
$$

$\square$

REMARK 1. Taking supremum over all $\varrho \in \Xi$, one obtains

$$
\sup_{\varrho \in \Xi} \left| \sum_{k=1}^n \varphi(\alpha_k) \langle \mathfrak{Z}_k \widehat{\varkappa}_\varrho, \widehat{\varkappa}_\varrho \rangle^2 \right|^p
$$

$$
\leq \frac{1}{2l} \sup_{\varrho \in \Xi} \sum_k (\varphi(\alpha_k))^{l/2} \left\langle \left(|\mathfrak{Z}_k|^{2p\alpha l} + |\mathfrak{Z}_k^*|^{2pl(1-\alpha)} \right) \widehat{\varkappa}_\varrho, \widehat{\varkappa}_\varrho \right\rangle +
$$

$$
+ \sup_{\varrho \in \Xi} \frac{\sum_{k=1}^n \varphi^{q/2}(\alpha_k) |\langle \mathfrak{Z}_k \widehat{\varkappa}_\varrho, \widehat{\varkappa}_\varrho \rangle|^{pq}}{q}.
$$

Setting $\mathfrak{Z}_k, \varphi_k = 0$ for $k \in \{2, 3 ..., n\}, q = l = 2$, we obtain the following inequality which sharpens the one given by Huban et al. (Huban et al, 2022a) (7)

$$
\mathrm{ber}^{2p}(\mathfrak{Z}) \leq \frac{\left\| |\mathfrak{Z}|^{4\alpha p} + |\mathfrak{Z}^*|^{4p(1-\alpha)} \right\|_{\mathrm{ber}}}{4} + \frac{\mathrm{ber}^{2p}(\mathfrak{Z})}{2}
$$

$$
\leq \frac{1}{2} \left\| |\mathfrak{Z}|^{4\alpha p} + |\mathfrak{Z}^*|^{4p(1-\alpha)} \right\|_{\mathrm{ber}}.
$$

In particular, we obtain a refinement by setting $\alpha = \frac{1}{2}$ of inequality (7) for $s = \frac{1}{2}$.

Proof. Using (8) on the third term, we obtain the desired inequality. $\square$

THEOREM 1. *Let* $p \geq 1, l, q > 1, \frac{1}{p} + \frac{1}{q} = 1, \alpha \in [0, 1], p \geq \frac{4}{l}, \mathfrak{Z}_i \in \mathfrak{L}(\mathfrak{H})$ *and* H *be such that* $H(l) = f^2(|\mathfrak{Z}_i|^{\alpha pl}) + g^2(|\mathfrak{Z}_i|^{pl\alpha}) + f^2(|\mathfrak{Z}_i^*|^{pl(1-\alpha)}) + g^2(|\mathfrak{Z}_i^*|^{pl(1-\alpha)}),$

then the following inequality holds:

$$\mathrm{ber}^p\left(\sum_i \varphi(\alpha_i)\mathfrak{Z}_i\right) \tag{19}$$

$$\leq \sup_{\varrho\in\Xi}\left\{\frac{\sum_i \varphi^{l/2}(\alpha_i)|\langle\mathfrak{Z}_i\widehat{\varkappa}_\varrho,\widehat{\varkappa}_\varrho\rangle|^{\frac{pl}{2}}}{l} + \frac{\sum_i \varphi^{q/2}(\alpha_i)|\langle\mathfrak{Z}_i\widehat{\varkappa}_\varrho,\widehat{\varkappa}_\varrho\rangle|^{\frac{pq}{2}}}{q}\right\}$$

$$\leq \left\|\sum_i \frac{1}{8}\left(\frac{H(l)}{l}\varphi^{l/2}(\alpha_i) + \frac{H(q)}{q}\varphi^{q/2}(\alpha_i)\right)\right\| + $$

$$\frac{1}{2}\sum_{i=1}^n\left(\varphi^{l/2}(\alpha_i)\frac{\mathrm{ber}^{\frac{pl}{4}}(|\mathfrak{Z}_i^*|^{2(1-\alpha)}|\mathfrak{Z}_i|^{2\alpha})}{l} + \varphi^{q/2}(\alpha_i)\frac{\mathrm{ber}^{\frac{pq}{4}}(|\mathfrak{Z}_i^*|^{2(1-\alpha)}|\mathfrak{Z}_i|^{2\alpha})}{q}\right).$$

Proof. Start from the left-hand side

$$\left|\sum_{i=1}^n \varphi(\alpha_i)\langle\mathfrak{Z}_i\widehat{\varkappa}_\varrho,\widehat{\varkappa}_\varrho\rangle\right|^p$$

$$\leq \sum_{i=1}^n \varphi(\alpha_i)|\langle\mathfrak{Z}_i\widehat{\varkappa}_\varrho,\widehat{\varkappa}_\varrho\rangle|^p$$

$$\leq \left(\sum_{i=1}^n \varphi^{l/2}(\alpha_i)|\langle\mathfrak{Z}_i\widehat{\varkappa}_\varrho,\widehat{\varkappa}_\varrho\rangle|^{\frac{pl}{2}}\right)^{1/l}\left(\sum_{i=1}^n \varphi^{q/2}(\alpha_i)|\langle\mathfrak{Z}_i\widehat{\varkappa}_\varrho,\widehat{\varkappa}_\varrho\rangle|^{\frac{pq}{2}}\right)^{1/q}$$

$$\leq \frac{\sum_{i=1}^n \varphi^{l/2}(\alpha_i)|\langle\mathfrak{Z}_i\widehat{\varkappa}_\varrho,\widehat{\varkappa}_\varrho\rangle|^{\frac{pl}{2}}}{l} + \frac{\sum_{i=1}^n \varphi^{q/2}(\alpha_i)|\langle\mathfrak{Z}_i\widehat{\varkappa}_\varrho,\widehat{\varkappa}_\varrho\rangle|^{\frac{pq}{2}}}{q}.$$

We focus now on the first part, second one is done analogous. First use Kato's inequality

$$|\langle\mathfrak{Z}_i\widehat{\varkappa}_\varrho,\widehat{\varkappa}_\varrho\rangle|^{\frac{pl}{2}}$$

$$\leq \langle|\mathfrak{Z}_i|^{2\alpha}\widehat{\varkappa}_\varrho,\widehat{\varkappa}_\varrho\rangle^{\frac{pl}{4}}\langle\widehat{\varkappa}_\varrho,|\mathfrak{Z}_i^*|^{2(1-\alpha)}\widehat{\varkappa}_\varrho\rangle^{\frac{pl}{4}}$$

$$\leq \frac{1}{2}\left(\left\||\mathfrak{Z}_i|^{2\alpha}\widehat{\varkappa}_\varrho\right\|^{\frac{pl}{4}}\left\||\mathfrak{Z}_i^*|^{2(1-\alpha)}\widehat{\varkappa}_\varrho\right\|^{\frac{pl}{4}} + |\langle|\mathfrak{Z}_i|^{2\alpha}\widehat{\varkappa}_\varrho,|\mathfrak{Z}_i^*|^{2(1-\alpha)}\widehat{\varkappa}_\varrho|^{\frac{pl}{4}}\right)$$

$$\leq \frac{1}{4}\left(\langle|\mathfrak{Z}_i|^{4\alpha}\widehat{\varkappa}_\varrho,\widehat{\varkappa}_\varrho\rangle^{\frac{pl}{4}} + \langle|\mathfrak{Z}_i^*|^{4(1-\alpha)}\widehat{\varkappa}_\varrho,\widehat{\varkappa}_\varrho\rangle^{\frac{pl}{4}}\right) + \frac{1}{2}|\langle|\mathfrak{Z}_i^*|^{2(1-\alpha)}|\mathfrak{Z}_i|^{2\alpha}\widehat{\varkappa}_\varrho,\widehat{\varkappa}_\varrho\rangle|^{\frac{pl}{4}}$$

$$\leq \frac{1}{4}\left(\langle|\mathfrak{Z}_i|^{pl\alpha}\widehat{\varkappa}_\varrho,\widehat{\varkappa}_\varrho\rangle + \langle|\mathfrak{Z}_i^*|^{pl(1-\alpha)}\widehat{\varkappa}_\varrho,\widehat{\varkappa}_\varrho\rangle\right) + \frac{1}{2}|\langle|\mathfrak{Z}_i^*|^{2(1-\alpha)}|\mathfrak{Z}_i|^{2\alpha}\widehat{\varkappa}_\varrho,\widehat{\varkappa}_\varrho\rangle|^{\frac{pl}{4}}$$

$$\leq \frac{1}{8}\left(\langle f^2(|\mathfrak{Z}_i|^{p\alpha l})\widehat{\varkappa}_\varrho, \widehat{\varkappa}_\varrho\rangle + \langle g^2(|\mathfrak{Z}_i|^{pl\alpha})\widehat{\varkappa}_\varrho, \widehat{\varkappa}_\varrho\rangle\right) +$$

$$+ \frac{1}{8}\left(\langle f^2(|\mathfrak{Z}_i^*|^{pl(1-\alpha)})\widehat{\varkappa}_\varrho, \widehat{\varkappa}_\varrho\rangle + \langle g^2(|\mathfrak{Z}_i^*|^{pl(1-\alpha)})\widehat{\varkappa}_\varrho, \widehat{\varkappa}_\varrho\rangle\right) +$$

$$+ \frac{1}{2}|\langle|\mathfrak{Z}_i^*|^{2(1-\alpha)}|\mathfrak{Z}_i|^{2\alpha}\widehat{\varkappa}_\varrho, \widehat{\varkappa}_\varrho\rangle|^{\frac{pl}{4}}.$$

The other part is obtained in an analogous way, adding them and taking a supremum over $\varrho \in \Xi$ we obtain the desired inequality. $\qquad\square$

In particulular, by setting $\mathfrak{Z}_k = 0$, $f(t) = g(t) = \sqrt{t}$, $\varphi_k = 0$ for $k \in \{2, 3..., n\}$, $q = l = 2$, we obtain the refinement of (6), namely

$$\mathrm{ber}^p(\mathfrak{Z}) \leq \frac{1}{4}\left\||\mathfrak{Z}|^{2p\alpha} + |\mathfrak{Z}^*|^{2p(1-\alpha)}\right\|_{\mathrm{ber}} + \frac{1}{2}\mathrm{ber}^{\frac{p}{2}}(|\mathfrak{Z}^*|^{2(1-\alpha)}|\mathfrak{Z}|^{2\alpha})$$

$$\leq \left\|\frac{|\mathfrak{Z}|^{2p\alpha} + |\mathfrak{Z}^*|^{2p(1-\alpha)}}{2}\right\|_{\mathrm{ber}}.$$

In the following we give a variation of the inequality given by Erkan and Gürdal (Erkan & Gürdal, 2024, Theorem 4).

THEOREM 2. *Let* $r \geq 1, \alpha \in [0, 1], \mathfrak{Z}_1, \mathfrak{Z}_2, \mathfrak{Z}_3, \mathfrak{Z}_4 \in \mathfrak{L}(\mathfrak{H})$ *and* $H(\mathfrak{Z}_1) = f^2(|\mathfrak{Z}_1|^{4r\alpha}) + g^2(|\mathfrak{Z}_1|^{4r\alpha}) + f^2(|\mathfrak{Z}_1|^{4r(1-\alpha)}) + g^2(|\mathfrak{Z}_1|^{4r(1-\alpha)})$ *then*

$$\mathrm{ber}^r(\mathfrak{Z}_1^*\mathfrak{Z}_2 + \mathfrak{Z}_3^*\mathfrak{Z}_4) \leq 2^{r-4}\|H(\mathfrak{Z}_2) + H(\mathfrak{Z}_1) + H(\mathfrak{Z}_4) + H(\mathfrak{Z}_3)\|_{\mathrm{ber}}. \quad (20)$$

Proof. We proceed

$$\frac{|\langle(\mathfrak{Z}_1^*\mathfrak{Z}_2 + \mathfrak{Z}_3^*\mathfrak{Z}_4)\widehat{\varkappa}_\varrho, \widehat{\varkappa}_\varrho\rangle|^r}{2^r}$$

$$\leq \left(\frac{|\langle\mathfrak{Z}_1^*\mathfrak{Z}_2\widehat{\varkappa}_\varrho, \widehat{\varkappa}_\varrho\rangle| + |\langle\mathfrak{Z}_3^*\mathfrak{Z}_4\widehat{\varkappa}_\varrho, \widehat{\varkappa}_\varrho\rangle|}{2}\right)^r$$

$$\leq \frac{|\langle\mathfrak{Z}_1^*\mathfrak{Z}_2\widehat{\varkappa}_\varrho, \widehat{\varkappa}_\varrho\rangle|^r + |\langle\mathfrak{Z}_3^*\mathfrak{Z}_4\widehat{\varkappa}_\varrho, \widehat{\varkappa}_\varrho\rangle|^r}{2}$$

$$\leq \frac{1}{8}\langle|\mathfrak{Z}_2|^{4r\alpha}\widehat{\varkappa}_\varrho, \widehat{\varkappa}_\varrho\rangle + \langle|\mathfrak{Z}_2|^{4r(1-\alpha)}\widehat{\varkappa}_\varrho, \widehat{\varkappa}_\varrho + \langle|\mathfrak{Z}_1|^{4\alpha r}\widehat{\varkappa}_\varrho, \widehat{\varkappa}_\varrho\rangle +$$

$$+ \langle|\mathfrak{Z}_1|^{4r(1-\alpha)}\widehat{\varkappa}_\varrho, \widehat{\varkappa}_\varrho\rangle + \langle|\mathfrak{Z}_4|^{4r\alpha}\widehat{\varkappa}_\varrho, \widehat{\varkappa}_\varrho\rangle +$$

$$+ \langle|\mathfrak{Z}_4|^{4r(1-\alpha)}\widehat{\varkappa}_\varrho, \widehat{\varkappa}_\varrho + \langle|\mathfrak{Z}_3|^{4\alpha r}\widehat{\varkappa}_\varrho, \widehat{\varkappa}_\varrho\rangle + \langle|\mathfrak{Z}_3|^{4r(1-\alpha)}\widehat{\varkappa}_\varrho, \widehat{\varkappa}_\varrho\rangle.$$

Proceeding to use (16) and AG inequality, we obtain the desired inequality. $\qquad\square$

COROLLARY 2. *Setting* $f(t) = g(t) = \sqrt{t}$ *and* $\alpha = \frac{1}{2}$ *we obtain a variation of the inequality given by Erkan and Gürdal (Erkan & Gürdal, 2024)*

$$\mathrm{ber}^r(\mathfrak{Z}_1^*\mathfrak{Z}_2 + \mathfrak{Z}_3^*\mathfrak{Z}_4) \leq 2^{r-2} \left\| |\mathfrak{Z}_2|^{2r} + |\mathfrak{Z}_3|^{2r} + |\mathfrak{Z}_4|^{2r} + |\mathfrak{Z}_1|^{2r} \right\|_{\mathrm{ber}}.$$

THEOREM 3. *Let* $r \geq 1, \alpha \in [0,1], \mathfrak{Z}_1, \mathfrak{Z}_2 \in \mathfrak{L}(\mathfrak{H})$ *and* f, g *nonnegative such that* $f(t)g(t) = t$ *also let*

$$H(\mathfrak{Z}_1) = f^2(|\mathfrak{Z}_1|^{2r\alpha}) + g^2(|\mathfrak{Z}_1|^{2r\alpha}) + f^2(|\mathfrak{Z}_1^*|^{2r(1-\alpha)}) + g^2(|\mathfrak{Z}_1^*|^{2r(1-\alpha)})$$

then

$$\mathrm{ber}^r(\mathfrak{Z}_1 + \mathfrak{Z}_2) \leq 2^{r-3} \left\| H(\mathfrak{Z}_1) + H(\mathfrak{Z}_2) \right\|_{\mathrm{ber}}. \tag{21}$$

Proof.

$$\frac{|\langle (\mathfrak{Z}_1 + \mathfrak{Z}_2)\widehat{\varkappa}_\varrho, \widehat{\varkappa}_\varrho \rangle|^r}{2^r}$$

$$\leq \left(\frac{|\langle \mathfrak{Z}_1 \widehat{\varkappa}_\varrho, \widehat{\varkappa}_\varrho \rangle| + |\langle \mathfrak{Z}_2 \widehat{\varkappa}_\varrho, \widehat{\varkappa}_\varrho \rangle|}{2} \right)^r$$

$$\leq \frac{|\langle \mathfrak{Z}_1 \widehat{\varkappa}_\varrho, \widehat{\varkappa}_\varrho \rangle|^r + |\langle \mathfrak{Z}_2 \widehat{\varkappa}_\varrho, \widehat{\varkappa}_\varrho \rangle|^r}{2}$$

$$\leq \frac{\langle |\mathfrak{Z}_1|^{2\alpha}\widehat{\varkappa}_\varrho, \widehat{\varkappa}_\varrho \rangle^{\frac{r}{2}} \langle |\mathfrak{Z}_1^*|^{2(1-\alpha)}\widehat{\varkappa}_\varrho, \widehat{\varkappa}_\varrho \rangle^{\frac{r}{2}}}{2} + \frac{\langle |\mathfrak{Z}_2|^{2\alpha}\widehat{\varkappa}_\varrho, \widehat{\varkappa}_\varrho \rangle^{\frac{r}{2}} \langle |\mathfrak{Z}_2^*|^{2(1-\alpha)}\widehat{\varkappa}_\varrho, \widehat{\varkappa}_\varrho \rangle^{\frac{r}{2}}}{2}$$

$$\leq \frac{\langle |\mathfrak{Z}_1|^{2r\alpha}\widehat{\varkappa}_\varrho, \widehat{\varkappa}_\varrho \rangle + \langle |\mathfrak{Z}_1^*|^{2r(1-\alpha)}\widehat{\varkappa}_\varrho, \widehat{\varkappa}_\varrho \rangle}{4} +$$

$$+ \frac{\langle |\mathfrak{Z}_2|^{2r\alpha}\widehat{\varkappa}_\varrho, \widehat{\varkappa}_\varrho \rangle + \langle |\mathfrak{Z}_2^*|^{2r(1-\alpha)}\widehat{\varkappa}_\varrho, \widehat{\varkappa}_\varrho \rangle}{4}.$$

The proof is finished with using (16) and AG inequality. $\qquad\square$

COROLLARY 3. *Setting* $f(t) = g(t) = \sqrt{t}$ *and replacing the second slot with* y *and proceeding with the proof for the case* $\langle (\mathfrak{Z}_1 + \mathfrak{Z}_2)\widehat{\varkappa}_\varrho, \widehat{\varkappa}_\varrho \rangle$ *the proof still holds and then using triangle inequality we obtain the inequality given by Huban et al. (Huban et al, 2022a, Theorem 3.7)*

$$\|\mathfrak{Z}_1 + \mathfrak{Z}_2\|_{\mathrm{ber}}^r \leq 2^{r-2} \left(\left\| |\mathfrak{Z}_1|^{2\alpha r} + |\mathfrak{Z}_2|^{2\alpha r} \right\|_{\mathrm{ber}} + \left\| |\mathfrak{Z}_1^*|^{2r(1-\alpha)} + |\mathfrak{Z}_2^*|^{2r(1-\alpha)} \right\|_{\mathrm{ber}} \right).$$

We now present a variation of the inequality given by Huban et al. (Huban et al, 2022a).

THEOREM 4. *Let us define* $H(\mathfrak{Z}_1) = f^2(|\mathfrak{Z}_1|^{2\alpha r}) + g^2(|\mathfrak{Z}_1|^{2\alpha r})$, $G(\mathfrak{Z}_1) = f^2(|\mathfrak{Z}^*_1|^{2r(1-\alpha)}) + g^2(|\mathfrak{Z}^*_1|^{2r(1-\alpha)})$ *where* $\mathfrak{Z}_1 = \mathfrak{Z}_2 + i\mathfrak{Z}_3$ $r \geq 2, \alpha \in [0,1], \mathfrak{Z}_1, \mathfrak{Z}_2, \mathfrak{Z}_3 \in \mathfrak{L}(\mathfrak{H})$ *where* $\mathfrak{Z}_2, \mathfrak{Z}_3$ *are the Cartesian decomposition operators of* $\mathfrak{Z}_1$ *where* $\mathfrak{Z}_2, \mathfrak{Z}_3$ *are selfadjoint, then one obtains*

$$\mathrm{ber}^r(\mathfrak{Z}_1) \leq 2^{\frac{r}{2}-3} \|H(\mathfrak{Z}_2) + G(\mathfrak{Z}_2) + H(\mathfrak{Z}_3) + G(\mathfrak{Z}_3)\|_{\mathrm{ber}}.$$

Proof.

$$\frac{|\langle \mathfrak{Z}_1 \widehat{\varkappa}_\varrho, \widehat{\varkappa}_\varrho \rangle|^r}{2^{\frac{r}{2}}}$$

$$= \sqrt[\frac{r}{2}]{\frac{\langle \mathfrak{Z}_2 \widehat{\varkappa}_\varrho, \widehat{\varkappa}_\varrho \rangle^2 + \langle \mathfrak{Z}_3 \widehat{\varkappa}_\varrho, \widehat{\varkappa}_\varrho \rangle^2}{2}}$$

$$\leq \frac{\langle \mathfrak{Z}_2 \widehat{\varkappa}_\varrho, \widehat{\varkappa}_\varrho \rangle^r + \langle \mathfrak{Z}_3 \widehat{\varkappa}_\varrho, \widehat{\varkappa}_\varrho \rangle^r}{2}$$

$$\leq \frac{\langle |\mathfrak{Z}_2|^{2\alpha r} \widehat{\varkappa}_\varrho, \widehat{\varkappa}_\varrho \rangle + \langle |\mathfrak{Z}^*_2|^{2r(1-\alpha)} \widehat{\varkappa}_\varrho, \widehat{\varkappa}_\varrho \rangle}{4} +$$

$$+ \frac{\langle |\mathfrak{Z}_3|^{2\alpha r} \widehat{\varkappa}_\varrho, \widehat{\varkappa}_\varrho \rangle + \langle |\mathfrak{Z}^*_3|^{2r(1-\alpha)} \widehat{\varkappa}_\varrho, \widehat{\varkappa}_\varrho \rangle}{4}$$

following a similar procedure to the one given in (21), we obtain the desired result. ☐

THEOREM 5. *Let* $\mathfrak{Z}_1, \mathfrak{Z}_2 \in \mathfrak{L}(\mathfrak{H})$, $r \geq 2$ *and* $\alpha \in [0,1]$, *then*

$$\mathrm{ber}^r(\mathfrak{Z}_1 + \mathfrak{Z}_2) \leq 2^{r-3} \left\| |\mathfrak{Z}_1|^{2\alpha r} + |\mathfrak{Z}^*_1|^{2r(1-\alpha)} + |\mathfrak{Z}_2|^{2\alpha r} + |\mathfrak{Z}^*_2|^{2r(1-\alpha)} \right\|_{\mathrm{ber}} +$$

$$+ 2^{r-2}(\mathrm{ber}(|\mathfrak{Z}^*_1|^{r(1-\alpha)}|\mathfrak{Z}_1|^{\alpha r}) + \mathrm{ber}(|\mathfrak{Z}^*_2|^{r(1-\alpha)}|\mathfrak{Z}_2|^{\alpha r})). \quad (22)$$

Proof. Following a similar principle to the one given in (21) with an exception of using Buzano's inequality, we obtain the desired inequality; one must only realise that in order to use the Mc-Carthy inequality there must be $r \geq 2$. ☐

COROLLARY 4. *Previously obtained inequality (22) refines the inequality given by Huban et al. in (Huban et al, 2022a), namely Theorem 3.6 (eq. 3.6) for $r \geq 2$; it can be seen by using (6) on both Berezin radius terms, from which we obtain*

$$\mathrm{ber}^r(\mathfrak{Z}_1 + \mathfrak{Z}_2) \leq 2^{r-3} \left\| |\mathfrak{Z}_1|^{2\alpha r} + |\mathfrak{Z}^*_1|^{2r(1-\alpha)} + |\mathfrak{Z}_2|^{2\alpha r} + |\mathfrak{Z}^*_2|^{2r(1-\alpha)} \right\|_{\mathrm{ber}} +$$

$$+ 2^{r-2}(\mathrm{ber}(|\mathfrak{Z^*}_1|^{r(1-\alpha)}|\mathfrak{Z}_1|^{\alpha r}) + \mathrm{ber}(|\mathfrak{Z^*}_2|^{r(1-\alpha)}|\mathfrak{Z}_2|^{\alpha r}))$$

$$\leq 2^{r-3} \left\| |\mathfrak{Z}_1|^{2\alpha r} + |\mathfrak{Z}_1^*|^{2r(1-\alpha)} + |\mathfrak{Z}_2|^{2\alpha r} + |\mathfrak{Z}_2^*|^{2r(1-\alpha)} \right\|_{\mathrm{ber}} +$$

$$+ 2^{r-3} \left(\left\| |\mathfrak{Z}_1|^{2\alpha r} + |\mathfrak{Z}_1^*|^{2r(1-\alpha)} \right\|_{\mathrm{ber}} + \left\| |\mathfrak{Z}_2|^{2\alpha r} + |\mathfrak{Z}_2^*|^{2r(1-\alpha)} \right\|_{\mathrm{ber}} \right)$$

$$\leq 2^{r-2} \left\| |\mathfrak{Z}_1|^{2\alpha r} + |\mathfrak{Z}_1^*|^{2r(1-\alpha)} \right\|_{\mathrm{ber}} + \left\| |\mathfrak{Z}_2|^{2\alpha r} + |\mathfrak{Z}_2^*|^{2r(1-\alpha)} \right\|_{\mathrm{ber}}.$$

If we were to use the triangle inequality on eq. (3.6) (Huban et al, 2022a) we would obtain the right hand side of the above chain of inequalities, which shows that our inequality is sharper than it.

Further, setting $\mathfrak{Z}_1 = \mathfrak{Z}_2$ we obtain (6) on the right-hand side which shows that our inequality (22) is a refinement of (6) for $r \geq 2$.

References

Bakherad, M. & Garayev, M.T. 2019. Berezin number inequalities for operators. *Concrete Operators*, 6(1), pp.33-43. Available at: https://doi.org/10.1515/conop-2019-0003.

Başaran, H., Huban, M.B. & Gürdal, M. 2022. Inequalities related to Berezin norm and Berezin number of operators. *Bulletin of Mathematical Analysis and Applications*, 14(2), pp.1-11 [online]. Available at: https://www.emis.de/journals/BMAA/repository/docs/BMAA14-2-1.pdf [Accessed: 25 June 2024].

Berezin, F.A. 1972. Covariant and contavariant symbols of operators. *Mathematics of the USSR-Izvestiya*, 6(5), pp.1117-1151. Available at: https://doi.org/10.1070/IM1972v006n05ABEH001913.

Chalendar, I., Fricain, E., Gürdal, M. & Karaev, M. 2012. Compactness and Berezin symbols. *Acta Scientiarum Mathematicarum*, 78(1-2), pp.315-329. Available at: https://doi.org/10.1007/BF03651352.

Erkan, G.G. & Gürdal, M. 2024. Operatörlerin Berezin Yarıçap Eşitsizliklerinin İlerletilmesi. In: *3rd International Conference on Engineering, Natural and Social Sciences ICENSOS*, Konya, Turkey, pp.463-470, May 16-17 [online]. Available at: https://www.icensos.com/3rdicensos2024 (in Turkish) [Accessed: 25 June 2024].

Furuta, T. 1994. An extension of the Heinz-Kato theorem. *Proceedings of the American Mathematical Society*, 120(3), pp.785-787. Available at: https://doi.org/10.2307/2160471.

Garayev, M.T. & Alomari, M.W. 2021. Inequalities for the Berezin number of operators and related questions. *Complex Analysis and Operator Theory*, 15, art.number:30. Available at: https://doi.org/10.1007/s11785-021-01078-7.

Garayev, M., Bouzeffour, F., Gürdal, M. & Yangöz, C.M. 2020. Refinements of Kantorovich type, Schwarz and Berezin number inequalitie. *Extracta Mathematicae*, 35(1), pp.1-20. Available at: https://doi.org/10.17398/2605-5686.35.1.1.

Garayev, M.T., Guediri, H., Gürdal, M. & Alsahli, G.M. 2021. On some problems for operators on the reproducing kernel Hilbert space. *Linear and Multilinear Algebra*, 69(11), pp.2059-2077. Available at: https://doi.org/10.1080/03081087.2019.1659220.

Güntürk, B. & Gürdal, M. 2024. On some refining inequalities via Berezin symbols. *Honam Mathematical Journal*, 46(3), pp.473-484. Available at: https://doi.org/10.5831/HMJ.2024.46.3.473.

Gürdal, V. & Başaran, H. 2023. On Berezin radius inequalities via Cauchy-Schwarz type inequalities. *Malaya Journal of Matematik (MJM)*, 11(02), pp.127-141. Available at: https://doi.org/10.26637/mjm1102/002.

Gürdal, V., Başaran, H. & Huban, M.B. 2023. Further Berezin radius inequalities. *Palestine Journal of Mathematics*, 12(1), pp.757-767 [online]. Available at: https://pjm.ppu.edu/paper/1314-further-berezin-radius-inequalities [Accessed: 25 June 2024].

Gürdal, M. & Stojiljkovic, V. 2024a. Berezin radius inequalities for finite sums of functional Hilbert space operators. *Gulf Journal of Mathematics*, 17(1), pp.101-109. Available at: https://doi.org/10.56947/gjom.v17i1.1885.

Gürdal, M. & Stojiljkovic, V. 2024b. Some inequality and Berezin number type inequalities. *Journal of Nonlinear Sciences and Applications*, 17(4), pp.180-190. Available at: https://doi.org/10.22436/jnsa.017.04.02.

Gürdal, M. & Tapdigoglu, R. 2023. New Berezin radius upper bounds. *Proceedings of the Institute of Mathematics and Mechanics*, 49(2), pp.210-218. Available at: https://doi.org/10.30546/2409-4994.2023.49.2.210.

Huban, M.B., Başaran, H. & Gürdal, M. 2021. New upper bounds related to the Berezin number inequalities. *Journal of Inequalities and Special Functions*, 12(3), pp.1-12 [online]. Available at: http://www.ilirias.com/jiasf/repository/docs/JIASF12-3-1.pdf [Accessed: 25 June 2024].

Huban, M.B., Başaran, H. & Gürdal, M. 2022a. Some new inequalities via Berezin numbers. *Turkish Journal of Mathematics and Computer Science*, 14(1), pp.129-137. Available at: https://doi.org/10.47000/tjmcs.1014841.

Huban, M.B., Başaran, H. & Gürdal, M. 2022b. Berezin number inequalities via convex functions. *Filomat*, 36(7), pp.2333-2344. Available at: https://doi.org/10.2298/FIL2207333H.

Karaev, M.T. 2006. Berezin symbol and invertibility of operators on the functional Hilbert spaces. *Journal of Functional Analysis*, 238(1), pp.181-192. Available at: https://doi.org/10.1016/j.jfa.2006.04.030.

Kato, T. 1952. Notes on some inequalities for linear operators. *Mathematische Annalen*, 125, pp.208-212. Available at: https://doi.org/10.1007/BF01343117.

McCarthy, C.A. 1967. Cp. *Israel Journal of Mathematics*, 5, pp.249-271. Available at: https://doi.org/10.1007/BF02771613.

Singh Aujla, J. & Silva, F.C. 2003. Weak majorization inequalities and convex functions. *Linear Algebra and its Applications*, 369, pp.217-233. Available at: https://doi.org/10.1016/S0024-3795(02)00720-6.

Stojiljković, V. & Dragomir, S.S. 2024. Refinement of the Cauchy-Schwartz inequality with refinements and generalizations of the numerical radius type inequalities for operators. *Annals of Mathematics and Computer Science*, 21, pp.33-43. Available at: https://doi.org/10.56947/amcs.v21.246.

Stojiljković, V. & Gürdal, M. 2024a. Generalization of the Buzano's inequality and numerical radius inequalities. *Journal of Applied and Pure Mathematics*, 6(3-4), pp.191-200. Available at https://doi.org/10.23091/japm.2024.191.

Stojiljković, V. & Gürdal, M. 2024b. Berezin radius type inequalities for functional Hilbert space operators. *Electronic Journal of Mathematics*, 7, pp.35-44. Available at: https://doi.org/10.47443/ejm.2024.017.

Stojiljković, V. & Gürdal, M. 2024c. Numerical radius inequalities for two and one operator. Preprint.

Tapdigoglu, R., Gürdal, M., Altwaijry, N. & Sarı, N. 2021. Davis-Wielandt-Berezin radius inequalities via Dragomir inequalities. *Operator and Matrices*, 15(4), pp.1445-1460. Available at: https://doi.org/10.7153/oam-2021-15-90.

Yamancı, U., Tunç, R. & Gürdal, M. 2020. Berezin Number, Grüss-type inequalities and their applications. *Bulletin of the Malaysian Mathematical Sciences Society*, 43, pp.2287-2296. Available at: https://doi.org/10.1007/s40840-019-00804-x.

Desigualdades de Berezin para sumas de operadores y desigualdades clásicas relativas al radio de Berezin

Mehmet Gürdal[a], *Vuk* N. Stojiljković[b], **autor de correspondencia**

[a] Universidad Suleyman Demirel, Departamento de Matemáticas, Isparta, República de Turquía

[b] Universidad de Novi Sad, Facultad de Ciencias, Novi Sad, República de Serbia; Escuela Secundaria de Matemáticas, Belgrado, República de Serbia

CAMPO: matemáticas
TIPO DE ARTÍCULO: artículo científico original

Resumen:

Introducción/objetivo: En este artículo, el objetivo del autor es buscar obtener nuevas desigualdades del tipo Berezin.

Métodos: Los métodos utilizados son estándar para la teoría de operadores.

Resultados: Varias desigualdades del tipo dado por Huban et al. y Erkan han sido obtenidas.

Conclusión: Además de obtener en particular diversas desigualdades de la forma dada por Huban et al. y Erkan, los autores agudizaron las desigualdades relacionadas con la norma Berezin.

Palabras claves: norma de Berezin, número de Berezin, desigualdades.

Неравенства Березина для сумм операторов и классические неравенства относительно радиуса Березина

Мехмет Гурдал[a], *Вук* Н. Соилькович[б], **корреспондент**

[a] Университет имени Сулеймана Демиреля,
   математический факультет, г. Испарта, Турецкая Республика

[б] Нови-Садский университет, факультет науки,
   г. Нови-Сад, Республика Сербия;
   Математическая школа, г. Белград, Республика Сербия

Резюме:

Введение/цель: Целью данной статьи является поиск новых неравенств типа Березина.

Методы: В исследовании использовались стандартные методы для теории операторов.

Результаты: Были получены различные неравенства типа неравенств, приведенных Хубаном и др. и Эрканом.

Выводы: В дополнение к полученным неравенствам типа неравенств, приведенных Хубаном и др. и Эрканом, авторы уточнили неравенства, связанные с нормой Березина.

Березинове неједнакости за збир оператора и класичне неједнакости које се односе на Березинову норму

Мехмет Гурдал[а], *Вук* Н. Стојиљковић[б], **аутор за преписку**

[а] Универзитет „Сулејман Демирел", Катедра за математику, Испарта, Република Турска

[б] Универзитет у Новом Саду, Природно-математички факултет, Катедра за математику, Нови Сад, Република Србија; Математичка гимназија, Београд, Република Србија

Сажетак:

Увод/циљ: Циљ овог рада јесте да се изведу нове неједнакости Березиновог типа.

Методе: Примењене су стандардне методе за теорију оператора.

Резултати: Добијене су разне неједнакости типа које су изнели Хубан и др. и Еркан.

Закључак: Поред добијања разних неједнакости облика које су изнели Хубан и др. и Еркан, аутори су поoштрили неједнакости везане за Березинов радијус.

Кључне речи: Березинова норма, Березинов број, неједнакости.

Models of microeconomic dynamics: bifurcations and complex system behavior algorithms

Lyudmyla Malyarets[a], *Oleksandr* Dorokhov[b],
Anatoly Voronin[c], *Irina* Lebedeva[d], *Stepan* Lebedev[e]

[a] Simon Kuznets Kharkiv National University of Economics,
 Kharkiv, Ukraine,
 e-mail: malyarets@ukr.net,
 ORCID iD: https://orcid.org/0000-0002-1684-9805

[b] University of Tartu, Tartu, Republic of Estonia,
 e-mail: oleksandr.dorokhov@ut.ee, **corresponding author**,
 ORCID iD: https://orcid.org/0000-0002-0737-8714

[c] Simon Kuznets Kharkiv National University of Economics,
 Kharkiv, Ukraine,
 e-mail: voronin61@ukr.net,
 ORCID iD: https://orcid.org/0000-0003-1662-6035

[d] Simon Kuznets Kharkiv National University of Economics,
 Kharkiv, Ukraine,
 e-mail: Irina.lebedeva@hneu.net,
 ORCID iD: https://orcid.org/0000-0002-0381-649X

[e] Simon Kuznets Kharkiv National University of Economics,
 Kharkiv, Ukraine,
 e-mail: Stepan.lebedev1@hneu.net,
 ORCID iD: https://orcid.org/0000-0001-9617-7481

Abstract:

Introduction/purpose: Studying the dynamics of the mutual influence of supply and demand is relevant in connection with the financial losses that arise due to uncertainty in demand and forecast errors. The work aims to build a mathematical model of the dynamics of this interaction for the market of one product.

Methods: The paper proposes a mathematical model of the states of the supply-demand system, within the framework of which the processes occurring in this system are considered from the perspective of the methodology of economic synergetics. The mathematical model of dynamics has the form of a system of two differential equations with quadratic nonlinearity.

Results: The use of the proposed model to reproduce various dynamic states of market self-regulation processes made it possible to identify the

hierarchy of transition from stable dynamic regimes to unstable ones with the appearance of corresponding bifurcations. The main attention was paid to studying the behavior of the system at the boundaries of the stability region.

Conclusion: The existence of a saddle-node bifurcation of limit cycles has been revealed, which suggests the appearance of stable self-oscillations in the case of a "soft" cycle and unstable ones in the case of a "hard" cycle. When studying a bifurcation of codimension two - "double zero" - special dynamic structures were discovered, determined by the properties of global bifurcations. This type of behavior is characterized by self-oscillations with a low frequency, which gives rise to the so-called "ultra-long waves" of the economic state.

Key words: dynamics of the supply-demand system, time lag, limit cycle, bifurcation, chaos.

Introduction

The formation of market equilibrium in the supply-demand system for a particular product in quantitative terms, as well as the equilibrium price for this product, has long attracted the attention of researchers. The problem of constructing a market equilibrium model is currently the focus of research programs of the world's leading scientific centers specialized in microeconomic analysis. The ability to analyze and make informed forecasts regarding the dynamics of the interaction of supply and demand allows decision makers to optimize resource allocation, ensure consumer satisfaction, reduce risks, and improve production efficiency.

Neoclassical economic theory offers two main models to explain the processes leading to the formation of market equilibrium in the supply-demand system. These are the Walras model and the Marshall model (Davar, 2015; Donzelli, 2008; Arena & Caldari, 2024 and etc.). In his model, Leon Walras analyzed the establishment of equilibrium between supply and demand occurring in the short term. According to his model, when the price increases, the quantity demanded will decrease, as a result of which the quantity supplied will exceed the equilibrium value. The market for a particular product is in equilibrium if, at the prices prevailing on the market for all goods, the quantity of the product required to satisfy the demand of potential buyers is equal to the quantity supplied by potential sellers. In contrast to the approach proposed by Walras, Alfred Marshall considered the price of the product as the driving force which is leading the market to a state of equilibrium. If the demand price exceeds the supply price, then, according to the Marshall model, such a price difference stimulates producers to increase supply, and buyers will be able

to expand their demand until the price is established at a new, higher equilibrium level. This is true for a longer period. The last statement from the standpoint of the theory of the firm regarding equilibrium in the supply-demand system is formulated as follows: at the moment of market equilibrium, the price of output must be equal to the marginal cost of the enterprise. The equilibrium price, as well as the equilibrium volume of goods (supply), are determined by the intersection of the supply and demand curves. This is the so-called Marshall Cross Diagram (Figure 1).
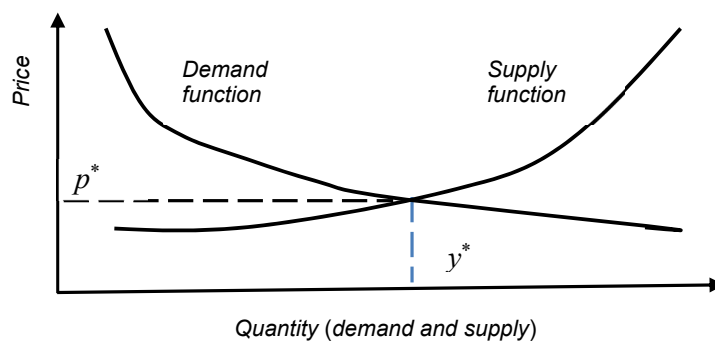
Figure 1 – Market equilibrium as the point of the intersection of the demand curve and the supply curve

It should be noted that both the Walras model and the Marshall model consider market equilibrium as the final result of the interaction of the demand and supply functions, while at the present stage of economic theory development, it is of interest to analyze the dynamics of the processes leading to the establishment of this equilibrium.

Mathematical models of varying complexity are proposed to describe economic dynamics (Li & Ma, 2020; Voronin et al, 2020; Fu et al, 2023; Chen et al, 2024 and etc.), but this problem is still far from being resolved. The founder of the study of economic dynamics is Griffith Conrad Evans, who proposed a mathematical model of monopoly. In his model, Evans used a first-order differential equation with constant coefficients to describe the demand function, which depends on price dynamics. Within the framework of this model, cyclical price fluctuations in the market of one product are considered under the assumption that the price changes smoothly over time. This model has been developed in a number of studies and still continues to attract interest (Nahorski & Ravn, 2000; Pomin, 2018; Dilenko & Tarakanov, 2020 and etc.). But in real conditions, price changes occur abruptly, and it is especially important to take this fact into account

when constructing mathematical models in which the forecast is carried out for a short-term period (He, 2018; He et al, 2021; Zabolotnii & Mogilei, 2023). In addition, the presence of a delay that occurs in the process of establishing the equilibrium price may cause instability of the system and lead to fluctuations. In particular, when analyzing mathematical models of nonlinear systems with delay, which were developed for systems of different nature, such complex phenomena as bifurcations and chaos were discovered (Liao et al, 2007; Wei & Yu, 2011; Le et al, 2012 and etc.).

The study of real economic processes allows us to conclude that changes in the price of goods and production volume have a mutual influence and cannot be considered in isolation from each other. In a number of recent articles (Voronin et al, 2020; He et al, 2021; Zabolotnii & Mogilei, 2023 and etc.), much attention is paid specifically to the dynamics of the processes of interaction between supply and demand. Thus, an increase in operating costs or a shortage of raw materials may cause production delays, as a result of which the supply of goods may not correspond to immediate demand, i.e., there is some delay (Cai, 2005; Hattaf et al, 2017; Davizón et al, 2023). For example, there may be a time lag between the adoption of an investment decision and its implementation. The result of this delay is the emergence of stable fluctuations of price around the market equilibrium, the emergence of large growth cycles and even the possibility of a sudden market collapse (Levi et al, 2018; Chen et al, 2024). This chaotic behavior in the system is the result of the appearance of the Hopf bifurcation, when the delay reaches a critical value (Li et al, 2019; Elkarmouchi et al, 2024).

The purpose of this work is to construct a mathematical model that would allow analyzing the dynamics of the balance between supply and demand. In this work, we will limit ourselves to the simplest situation, when there is only one type of product and its implementation is carried out on one market. Models of such a dimension were studied by both traditional and modern methods of mathematical stability theory with the corresponding conclusions about the behavior of the economic system near the equilibrium position (and no more!), which gives only approximate information about the evolution of the object under consideration. The mathematical model of dynamics proposed in the work also allows us to consider the processes occurring in the market of several goods, but not in a quantitative, but in a qualitative form with the corresponding order parameters. At the same time, changing the system parameters allows us to observe a wide range of market dynamics, namely, the equilibrium state, periodic and chaotic behavior.

Method used and the basic mathematical model

In microeconomic analysis, when constructing mathematical models of the market equilibrium, the following notations are traditionally used: $p = p(t)$ is the price of a unit of goods depending on time t; $y = y(t)$ is the volume of products, which also depends on time; $D = D(p; y)$ is the volume of demand in the market; $S = S(p; y)$ is the volume of supply of goods produced; $P_d = P_d(p; y)$ is the market demand price for a product; and $P_s = P_s(p; y)$ is the market offer price from the manufacturer.

The principles of constructing dynamic models consist of ways to describe time lag factors on both the demand and supply sides. The simplest assumption regarding the delay, if the analysis is carried out in discrete time, is a concentrated delay (lag) of supply from demand for one-time interval (the lag T_1):

$$D(p; y; t) = S(p; y; t - T_1). \qquad (1)$$

Equality (1) occurs when a certain period of time is required to produce a given volume of goods. This period of time is called the production lag. In this case, as a rule, it is assumed that there are no inventories, i.e., to meet demand, all manufactured products are supplied to the market in full. It should also be emphasized that the manufacturer builds his expectations of the future price based on the existing price, i.e., actually focuses on the price of the previous period T_2:

$$P_s(p; y; t) = P_d(p; y; t - T_2). \qquad (2)$$

If we consider the processes of interest to us in continuous time, then we should replace distributed delays with continuously distributed ones. One example of this type of model with a continuously distributed delay is Voltaire's system of integral equations for determining the price $p(t)$ and the volume of a product $y(t)$:

$$\begin{cases} D(p;y;t) = \int\limits_0^t K_1(t;\tau)S(p; y; \tau)d\tau; \\ \\ P_s(p;y;t) = \int\limits_0^t K_2(t;\tau)P_d(p; y; \tau)d\tau. \end{cases} \qquad (3)$$

Functions of two variables $K_1(t;\tau)$ and $K_2(t;\tau)$, called integral equation kernels, determine the shape of the distributed delays.

In this article, which is a further development of the study of one of the authors (Voronin & Chernyshov, 2007), in a qualitatively basic mathematical model we will consider a system of two differential equations

1556

that describe the evolution of the mutual influence of prices and volumes of goods produced:

$$\begin{cases} \alpha\dfrac{dp}{dt} = D(p) - y; \\ \beta\dfrac{dy}{dt} = p - \dfrac{dC(y)}{dy}, \end{cases}$$ (4)

where p – the unit price of the product; y – the volume of production of goods in physical terms; $D(p)$ – the market demand for a manufactured product, depending only on the price at the current moment in time (here and now); $C(y)$ – the production cost; $\dfrac{dC(y)}{dy} = P_s(y)$ – the supply price, which is equal to the marginal cost of production; and α, β – the parameters that have the meaning of the characteristic times for dynamic variables.

The first of the equations of system (4), which is a system of two ordinary differential equations, is essentially a reflection of the classical market pricing scheme in the form of Leon Walras. Its basis is the price formation mechanism which is focused on finding a position of equilibrium between supply and demand. If the volume of demand exceeds the quantity of supply, the price of a unit of goods increases, and in the opposite case, it decreases. The second equation of system (4) describes the process of establishing an equilibrium between the demand price (the actual price of a unit of goods) and the supply price (marginal production costs). The logic of this process provides for the fact of imbalance with the need to regulate the volume of production of goods. Accordingly, if the unit price of a product is greater than the producer's marginal cost, then the firm's profit increases. Conversely, in the opposite case, there is a need to limit production capacity. Significant assumptions were made when constructing the model. The first of these assumptions should be considered the hypothesis about producing only one type of product. The second assumption relates to simplifying the market structure since either the absence of competition is assumed or its impact is considered insignificant. However, despite the above simplifications, system (4) has quite complex behavioral properties, which will be the subject of this study.

Results and discussion

A substantive analysis of the qualitative behavior of system (4) should begin with determining the price of a unit of goods p^* and the value of the

output y^*, corresponding to the equilibrium position. To do this, we solve a system of two algebraic equations with two unknowns:

$$\begin{cases} D(p) = y; \\ p = P_s(y). \end{cases} \qquad (5)$$

Let us assume that the algebraic system (5) has at least one positive solution p^* and y^*. The demand function $D(p)$ will also be assumed to be a nonlinear function of the price and that in a small neighborhood of the equilibrium price value p^* there is an expansion of this function in a Taylor series up to and including cubic terms:

$$D(p) = d_0 + d_1(p - p^*) + \frac{d_2(p - p^*)^2}{2} + \frac{d_3(p - p^*)^3}{6} + 0\left((p - p^*)^3\right). \quad (6)$$

In equation (6), the coefficients d_i $(i = \overline{0,3})$ have the meaning of the corresponding derivatives of the demand function at the point p^*.

The cost function is usually represented as a quadratic function of the variable y:

$$C(y) = \frac{s_1 y^2}{2} + s_0 y + C_0. \qquad (7)$$

In equation (7), the coefficients in each term of the function $C(y)$ are constant values. Having differentiated the cost function by the output volume variable y, one obtains:

$$P_s(y) = s_1 y + s_0. \qquad (8)$$

Then, from (5), one finds the relationship between the equilibrium value of the price p^* and the equilibrium value of the production volume y^*:

$$\begin{cases} s_1 D(p^*) + s_0 - p^* = 0; \\ y^* = \dfrac{p^* - s_0}{s_1}. \end{cases} \qquad (9)$$

At the next stage, it seems advisable to move in system (4) to new variables $\widehat{p} = p - p^*$ and $\widehat{y} = y - y^*$, which have the meaning of the deviation of the original variables p and y from their equilibrium values. To reduce the number of parameters in system (4), the time scale is changed by introducing the coefficient $\gamma = \dfrac{\alpha}{\beta}$. System (4), in this case, takes the form:

1558

$$\begin{cases} \dfrac{d\widehat{p}}{dt} = d_1\widehat{p} + d_2\dfrac{\widehat{p}^2}{2} + d_3\dfrac{\widehat{p}^3}{6} - \widehat{y}; \\[2mm] \dfrac{d\widehat{y}}{dt} = \gamma\left(\widehat{p} - s_1\widehat{y}\right). \end{cases} \quad (10)$$

From system (10), it is easy to obtain the equations for calculating the equilibrium values p^* and y^*:

$$\begin{cases} \widehat{y}^* = \dfrac{\widehat{p}^*}{s_1}; \\[2mm] (s_1 d_1 - 1)\widehat{p}^* + \dfrac{s_1 d_2}{2}\left(\widehat{p}^*\right)^2 + \dfrac{s_1 d_3}{6}\left(\widehat{p}^*\right)^3 = 0. \end{cases} \quad (11)$$

Obviously, one of the solutions of this system is trivial: $\widehat{p}^* = 0$ and $\widehat{y}^* = 0$.

The second equation in system (11) is transformed to the form:

$$\widehat{p}^*\left(s_1 d_3\left(\widehat{p}^*\right)^2 + 3 s_1 d_2 \widehat{p}^* + 6(s_1 d_1 - 1)\right) = 0. \quad (12)$$

It is obvious that equation (12), in addition to the trivial solution $\widehat{p}^* = 0$, can have two more roots:

$$\widehat{p}^*_{1,2} = \dfrac{-3 d_2 \pm \sqrt{9 d_2^2 - 24 d_3 (d_1 - 1/s_1)}}{2 d_3}. \quad (13)$$

For the value p^* to be valid, the following condition must be true:

$$9 d_2^2 - 24 d_3 d_1 + \dfrac{24 d_3}{s_1} \geq 0. \quad (14)$$

If $s_1 d_1 = 1$, then from (13) it follows that $\widehat{p}^*_1 = \widehat{p}^*_0 = 0$ and $\widehat{p}^*_2 = -\dfrac{3 d_2}{d_3}$. This means that there is a double zero root.

To analyze the stability of the trivial equilibrium position $\widehat{p}^*_0$ and $\widehat{y}^*_0$ of system (10), let us construct a characteristic equation to determine the eigenvalues of the linear part:

$$\lambda^2 + (\gamma s_1 - d_1)\lambda + \gamma(1 - d_1 s_1) = 0. \quad (15)$$

Quadratic equation (15) has negative real parts if the conditions for stability of the equilibrium position are met:

$$\begin{cases} \gamma s_1 < d_1; \\ d_1 s_1 < 1. \end{cases} \quad (16)$$

The system of inequalities (16) allows the construction of the stability regions in the parameter space γ, s_1, d_1. An example is the image of the stability region on the plane $\gamma 0 s_1$ (Figure 2).
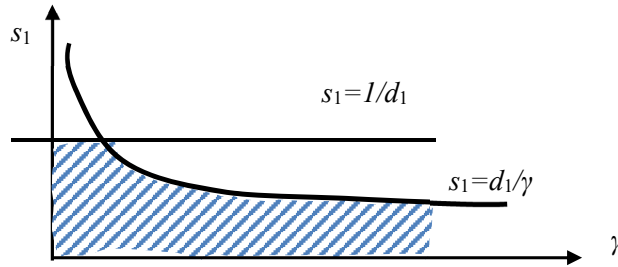
Figure 2 – Stability region at a fixed value d_1 on the plane $\gamma 0 s_1$

It is of significant interest to study the dynamics of system (10) on one of the boundaries of the stability region, namely $\gamma = \dfrac{d_1}{s_1}$. Let us assume that $\gamma s_1 \approx d_1$, and the measure of approximation is determined by the small parameter μ:

$$\mu = d_1 - \gamma s_1. \tag{17}$$

By its nature, the parameter γ is dynamic, i.e., it is associated with the characteristic times of transition processes in price and output. Let us express this parameter through purely static characteristics of the demand and supply price functions, i.e., through d_1 and s_1, respectively:

$$\gamma = \frac{d_1 - \mu}{s_1}. \tag{18}$$

In this case, the characteristic equation (15) takes the form:

$$\lambda^2 - \mu\lambda + \frac{d_1 - \mu}{s_1}(1 - d_1 s_1) = 0. \tag{19}$$

Considering that d_1 and s_1 are positive numbers and the second condition is satisfied, which follows from the stability conditions of system (16), namely $d_1 s_1 < 1$, it makes sense to introduce the following notation:

$$\omega^2 = \frac{d_1}{s_1} - d_1^2 \quad \Rightarrow \quad \frac{1}{s_1} - d_1 = \frac{\omega^2}{d_1}. \tag{20}$$

Then quadratic equation (19) takes the form:

$$\lambda^2 - \mu\lambda + \omega^2\left(1 - \frac{\mu}{d_1}\right) = 0. \qquad (21)$$

Accordingly, one obtains a solution to the quadratic equation (21):

$$\lambda_{1,2} = \frac{\mu}{2} \pm \sqrt{\frac{\mu^2}{4} + \frac{\omega^2\mu}{d_1} - \omega^2}. \qquad (22)$$

Neglecting those powers of the parameter μ that are higher than the first, the following linearization of the roots of the quadratic equation is obtained:

$$\lambda_{1,2} = \frac{\mu}{2} \pm i\omega\left(1 - \frac{\mu}{2d_1}\right). \qquad (23)$$

Since the parameter μ is essentially a small variable quantity, it follows from relation (23) that the trivial equilibrium position of system (10) is the focus. Moreover, if the condition $\mu < 0$ is met, this focus is stable, but otherwise if $\mu > 0$, the focus is unstable. It is obvious that when a small parameter μ passes through zero, one can expect the appearance of a special periodic regime in the dynamic system (10), the implementation of which is due to the Hopf bifurcation. This regime can only be observed in a nonlinear system. It is called a self-oscillatory or limit cycle. Such cycles are characteristic of dissipative systems. In this regard, it is necessary to check an important condition of the Hopf bifurcation theorem concerning the derivative of eigenvalues (23) with respect to the parameter μ.

Having differentiated one of the roots represented by relation (23) with respect to the parameter μ, one obtains:

$$\frac{d\lambda}{d\mu} = \frac{1}{2} - \frac{\omega}{2d_1}. \qquad (24)$$

Obviously, the real part of (24) is not equal to zero: $\mathrm{Re}\dfrac{d\lambda}{d\mu} = \dfrac{1}{2} \neq 0$. For system (10), this means the absence of conservatism conditions with an infinite number of periodic trajectories. In other words, in accordance with the conditions of Hopf's theorem, the appearance of one or several limit cycles near a trivial singular point is possible.

To find the basic characteristics of the limit cycle such as its frequency, amplitude, and direction of stability, the system of differential equations is reduced to a normal form, for which we introduce new phase variables: $\hat{p} = x_1$, $\hat{y} = d_1 x_1 + \omega x_2$, and $t = \omega\tau$. Let us pretend that $\mu = 0$. We obtain the

following system of two differential equations for the variables x_1 and x_2, which is the Poincaré normal form with respect to system (10):

$$\begin{cases} \dfrac{dx_1}{d\tau} = -x_2 + \dfrac{d_2}{\omega} \cdot \dfrac{x_1^2}{2} + \dfrac{d_3}{\omega} \cdot \dfrac{x_1^3}{6}; \\[2mm] \dfrac{dx_2}{d\tau} = x_1 - \dfrac{d_1 d_2}{\omega^2} \cdot \dfrac{x_1^2}{2} - \dfrac{d_1 d_3}{\omega} \cdot \dfrac{x_1^3}{6}. \end{cases} \tag{25}$$

System (25) will store all the information necessary to calculate the so-called first Lyapunov quantity l_1. This quantity determines the direction of stability of the limit cycle. According to fundamental research on the theory of bifurcations (Hassard et al, 1981), the following expression is obtained:

$$l_1(0) = \frac{d_3 \omega^2 + d_2^2 d_1}{16\omega^4}, \tag{26}$$

where ω – the frequency of self-oscillations, which depends on the static parameters d_1 and s_1:

$$\omega = d_1 \sqrt{\frac{1}{s_1 d_1} - 1} > 0. \tag{27}$$

The analysis of expression (26) allows one to draw the following conclusions:

1) if $d_3 \omega^2 + d_2^2 d_1 < 0$, then the limit cycle is stable and a "soft" mode of self-oscillation occurs.

2) if $d_3 \omega^2 + d_2^2 d_1 > 0$, then the so-called "hard" periodic regime is observed, which is accompanied by a catastrophic loss of stability.

For us, the most interesting case is when the first Lyapunov quantity is a sign-alternating parameter close to zero, and accordingly, we introduce the following notation: $l_1 = \nu$. This situation is possible if the following conditions are met: $d_3 \omega^2 + d_2^2 d_1 \approx 0$. From this condition, it follows that $d_3 \approx -\dfrac{d_2^2 d_1}{\omega^2}$. Since there is the inequality $d_1 > 0$, it follows that $d_3 < 0$. In terms of economic theory, this means that the demand function $D(p)$ has a saturation effect, i.e., the demand function cannot increase without limit as price decreases. From a mathematical point of view, the fact that the first Lyapunov value l_1 is close to zero means that stable and unstable limit cycles coexist in the system, which can be transformed into a double cycle by merging.

For a subsequent analysis of the two-parameter bifurcation of the limit cycle, it is necessary to calculate the so-called second Lyapunov quantity $l_2(0)$. Using the corresponding bifurcation formulas given in the work (Golubitsky & Langford, 1981), one obtains:

$$l_2(0) = \frac{d_1^3 d_3}{192\omega^3}\left(\frac{4d_1 d_2^2}{\omega^2} - \frac{3}{2}d_3\right).$$ (28)

Taking into account the fact that there is a relation $d_3 \approx -\dfrac{d_2^2 d_1}{\omega^2}$ formula (28) takes the form:

$$l_2(0) = -\frac{11 d_1^5 d_2^4}{384\omega^7}.$$ (29)

From relation (29) it follows that $l_2(0) < 0$.

In (Kuznetsov, 2023), the corresponding normal form of a bifurcation of codimension two in polar coordinates is given, where r is the magnitude of the amplitude, and φ is the phase of the emerging limit cycles:

$$\begin{cases} \dfrac{dr}{dt} = r(\delta_1 + \delta_2 r^2 - r^4); \\ \dfrac{d\varphi}{dt} = 1. \end{cases}$$ (30)

Moreover, $\delta_1 = \mu$ and $\delta_2 = \nu\sqrt{l_2(0)}$ are small alternating parameters.

The first equation of system (30) has three special solutions. The value $r = 0$ corresponds to the trivial equilibrium, and the remaining solutions must satisfy the biquadratic equation:

$$r^4 - \delta_2 r^2 - \delta_1 = 0.$$ (31)

In order for all solutions of equation (31) to be positive, the following conditions must be met: $\delta_1 < 0,\quad \delta_2 > 0$ and $\delta_2^2 + 4\delta_1 > 0$. There is a Hopf bifurcation on the line $\delta_1 = 0$. For it, the first Lyapunov quantity has the following meaning: $l_1 = \delta_2$. If $\delta_2 < 0$, then this corresponds to birth of the "soft" limit cycle, and if $\delta_2 > 0$, this corresponds to the occurrence of hard self-oscillations. That is, both stable and unstable limit cycles coexist at the same time. On the line $\delta_2^2 + 4\delta_1 = 0$ under the condition $\delta_2 > 0$, both cycles, due to the compaction of trajectories, merge into one double cycle and disappear, i.e., there is a bifurcation of the "fold" type. These results of the bifurcation analysis are similar to those published for the double limit cycle in the work (Dorokhov et al, 2023).

Let us return to equation (12) and use it to determine the equilibrium price $\widehat{p}^*$. First, it is necessary to find out the number of real roots of cubic equation (12) under the conditions of the occurrence of a double cycle. With the equalities $d_3 = -\dfrac{d_2^2 d_1}{\omega^2}$ and $\omega^2 = \dfrac{d_1}{s_1} - d_1^2$, expression (12) is transformed to the form:

$$\widehat{p}\left(\widehat{p}^2 + 3n\widehat{p} + 6n^2\right) = 0, \tag{32}$$

where $n = \dfrac{d_1 s_1 - 1}{d_2 s_1}$.

Equation (32) can be represented in a different form by highlighting the complete square:

$$\widehat{p}\left(\left(\widehat{p} + \frac{3n}{2}\right)^2 + \frac{15n^2}{4}\right) = 0. \tag{33}$$

Obviously, (33) has only one trivial solution $\widehat{p}^* = 0$ if the specified restrictions on the parameters of equation (12) are met. But the bifurcation behavior of system (10) does not end there. Before exploring other bifurcations of codimension two, it is necessary to transform system (10) into another form. Let us reduce system (10), consisting of two differential equations, to one second-order differential equation with respect to the price $\widehat{p}$. After successive identical transformations, one obtains the following differential equation:

$$\frac{d^2\widehat{p}}{dt^2} =$$

$$= \left(d_1 - \gamma s_1\right)\frac{d\widehat{p}}{dt} + \gamma(s_1 d_1 - 1)\widehat{p} + \gamma s_1 d_2 \frac{\widehat{p}^2}{2} + d_2 \widehat{p}\frac{d\widehat{p}}{dt} + \gamma s_1 d_2 \frac{\widehat{p}^3}{6} + \frac{d_3 \widehat{p}^2}{2}\cdot\frac{d\widehat{p}}{dt}. \tag{34}$$

Let us assume that the parameters for the linear terms of differential equation (34) are small, i.e., $d_1 - \gamma s_1 = \mu_2$ and $\gamma(s_1 d_1 - 1) = \mu_1$. We take the following notation: $\widehat{p} = x_1$ and $\dfrac{d\widehat{p}}{dt} = x_2$. Using the new notation, we transform equation (34) into a system of two differential equations:

$$\begin{cases} \dfrac{dx_1}{dt} = x_2; \\ \dfrac{dx_2}{dt} = \mu_1 x_1 + \mu_2 x_2 + d_1 d_2 \dfrac{x_1^2}{2} + d_2 x_1 x_2 + d_1 d_3 \dfrac{x_1^3}{6} + d_3 \dfrac{x_1^2 x_2}{2}. \end{cases} \tag{35}$$

Considering that the parameter μ_2 is small, one can use the coefficient d_1 instead of the product γs_1 for nonlinear terms d_1.

It should be emphasized that system (10), which is represented in the variables $\hat{p}$ (price) and $\hat{y}$ (volume of production), has now been transformed into system (35) with relatively new variables x_1 (price) and x_2 (surplus demand). The linear part of system (35) corresponds to the

matrix $\tilde{A} = \begin{pmatrix} 0 & 1 \\ \mu_1 & \mu_2 \end{pmatrix}$, for which the characteristic polynomial has the form:

$\lambda^2 - \mu_2 \lambda + \mu_1 = 0$. The equality $\mu_1 = \mu_2 = 0$ implies the presence of a Bogdanov–Takens bifurcation, the so-called "double zero" (Guckenheimer & Holmes, 1983). This means that the analysis of the stability of system (35) should be carried out in close proximity to the stability boundaries,

namely $s_1 = \dfrac{1}{d_1}$ and $s_1 = \dfrac{d_1}{\gamma}$ (see Figure 2).

Let us analyze the dynamic properties of system (35). For this purpose, consider two cases. In the first case, assume that $d_3 = 0$. Then system (35) takes the form:

$$\begin{cases} \dfrac{dx_1}{dt} = x_2; \\ \dfrac{dx_2}{dt} = \mu_1 x_1 + \mu_2 x_2 + d_1 d_2 \dfrac{x_1^2}{2} + d_2 x_1 x_2. \end{cases} \quad (36)$$

To pass to the Poincaré normal form for the Bogdanov–Takens bifurcation, one carries out a change of variables: $x_1 = R_1 V_1$, $x_2 = R_2 V_2$ and $t = R_3 \tau$. After substituting new variables into system (35) and performing algebraic transformations, one obtains:

$$\begin{cases} \dfrac{dV_1}{d\tau} = V_2; \\ \dfrac{dV_2}{d\tau} = \dfrac{4\mu_1}{d_1^2} V_1 + \dfrac{2\mu_2}{d_1} V_2 + V_1^2 + V_1 V_2, \end{cases} \quad (37)$$

where $R_1 = \dfrac{8}{d_1^3 d_2}$, $R_2 = \dfrac{16}{d_1^4 d_2}$ and $R_3 = \dfrac{2}{d_1}$.

Using the shift $V_1 = U_1 - \dfrac{2\mu_1}{d_1^2}$ and $V_2 = U_2$, one obtains the final form of

the Poincaré normal form for system (37):

$$\begin{cases} \dfrac{dU_1}{d\tau} = U_2; \\[2mm] \dfrac{dU_2}{d\tau} = \xi_1 + \xi_2 U_2 + U_1^2 + U_1 U_2, \end{cases} \tag{38}$$

where $\xi_1 = -\dfrac{4\mu_1^2}{d_1^4}$ and $\xi_2 = \dfrac{2}{d_1}\left(\mu_2 - \dfrac{\mu_1}{d_1}\right)$.

In the works (Takens, 1974; Kopell & Howard, 1975) for a system similar to system (38), a complete topological analysis of the stability of the equilibrium position was performed when the corresponding bifurcations appeared. Accordingly, system (38) has two equilibrium positions: $U_1^* = \left(-\sqrt{-\xi_1};\ 0\right)$ and $U_2^* = \left(\sqrt{-\xi_1};\ 0\right)$. In this case, the point $\left(\sqrt{-\xi_1};\ 0\right)$ is a point of unstable equilibrium for $\xi_1 < 0$ and for any values of ξ_2. In turn, the equilibrium point $\left(-\sqrt{-\xi_1};\ 0\right)$ is an unstable focus for $\xi_1 < 0$ and $\xi_2 > \sqrt{-\xi_1}$; conversely, it is a stable focus for $\xi_1 < 0$ and $\xi_2 < \sqrt{-\xi_1}$. Thus, it should be assumed that the occurrence of the "saddle - node" bifurcation takes place on the line $\xi_1 = 0,\ \xi_2 \neq 0$, and the occurrence of the Bogdanov - Takens bifurcation takes place on the half-parabola $\xi_2 = \sqrt{-\xi_1},\ \xi_1 < 0$. Moreover, the analysis of the Hopf bifurcation stability indicates that the limit cycle is unstable, i.e., "hard" self-oscillations arise. A similar result was obtained in the work (Elkarmouchi et al, 2024), the authors of which propose a mathematical IS-LM model with two-time delays, which describes many equilibrium positions in the investment-savings markets and the money market. Numerical modeling revealed the presence of a bifurcated periodic solution, which occurs when the time delay exceeds a critical value.

It should also be emphasized that in system (38), there is a global bifurcation, where the limit cycle annihilates inside the separatrix loop of the saddle. Using a special scaling transformation, we convert system (38) into a system close to Hamiltonian (Carr, 1982), and at the same time we obtain an approximate global bifurcation equation:

$$\xi_1 \approx -\frac{49}{25}\xi_2^2,\ \ \xi_2 \geq 0. \tag{39}$$

Returning to the original small parameters μ_1 and μ_2, we can draw the following conclusions:

1) The "saddle-node" bifurcation takes place on the line $\mu_1 = 0$;

2) Hopf bifurcation takes place on the lines $\mu_2 = 0$ and $\mu_2 = \dfrac{2\mu_1}{d_1}$;

3) Global bifurcation exists on the half-lines $\mu_2 = \dfrac{12}{7} \cdot \dfrac{\mu_1}{d_1}$ and

$\mu_2 = \dfrac{2}{7} \cdot \dfrac{\mu_1}{d_1}$ if the constraint is satisfied $\mu_2 > \dfrac{\mu_1}{d_1}$.

In this version, algebraic equation (12), when the condition $d_3 = 0$ is met, takes the form:

$$\frac{d_1 s_1 - 1}{s_1} \cdot \widehat{p}^* + \frac{d_2}{2} \cdot \left(\widehat{p}^*\right)^2 = 0, \tag{40}$$

and when the condition $\mu_1 = 0$, i.e., $d_1 s_1 = 1$, there is a twofold trivial equilibrium $\widehat{p}^* = 0,\ \widehat{y}^* = 0$.

   Let us consider a different configuration of system (35), assuming, accordingly, in this case, there is no quadratic nonlinearity. Now let us rewrite system (35) as follows:

$$\begin{cases} \dfrac{dx_1}{dt} = x_2; \\[2mm] \dfrac{dx_2}{dt} = \mu_1 x_1 + \mu_2 x_2 + d_1 d_3 \dfrac{x_1^3}{6} + d_3 \dfrac{x_1^2 x_2}{2}. \end{cases} \tag{41}$$

It is easy to see that system (41) has central symmetry, or symmetry with respect to rotation through an angle of 180^0. Let us transform system (41) to the Poincaré normal form for the "double zero" bifurcation with cubic

nonlinearities. Using the new variables: $x_1 = \sqrt{\dfrac{-2d_1}{3d_3}}\, y_1$, $x_2 = \dfrac{d_1}{3}\sqrt{\dfrac{-2d_1}{3d_3}}\, y_2$ and

$t = \dfrac{3}{d_1}\tau$, let us reduce system (41) to the form:

$$\begin{cases} \dfrac{dy_1}{d\tau} = y_2; \\[2mm] \dfrac{dy_2}{d\tau} = \dfrac{9}{d_1^2}\mu_1 y_1 + \dfrac{3}{d_1}\mu_2 y_2 - y_1^3 - y_1^2 y_2. \end{cases} \tag{42}$$

   The main results of the study of this system based on its mathematical model can be presented in the form of comments to the bifurcation diagram shown in Figure 3.

1567
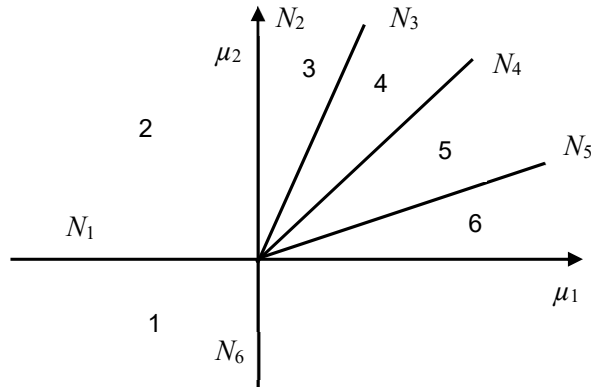
Figure 3 – Bifurcation diagram of "double zero"

System (42) has three equilibrium positions, one of which is trivial $E_0 = (0;0)$, and if $\mu_1 > 0$ there are two nontrivial solutions: $E_{1,2} = \left(\pm\sqrt{\mu_1};0\right)$. In region 1 (see Figure 3), where $\mu_1 < 0$, there is a single trivial equilibrium E_0, which is a stable node that smoothly passes into the focus. On the left side of the straight line N_1, where $N_1 = \{(\mu_1;\mu_2): \mu_1 < 0; \mu_2 = 0\}$, there is the Andronov–Hopf bifurcation with the appearance of a stable limit cycle. Two stable nodes E_1 and E_2 are separated from the trivial equilibrium position E_0 when the half-line $N_2 = \{(\mu_1;\mu_2): \mu_1 = 0; \mu_2 > 0\}$ is crossing those on the border between regions 2 and 3 as a result of the "pitchfork" bifurcation. In region 3, all three equilibrium positions E_0, E_1 and E_2, are inside the "large" limit cycle. On the half-line

$$N_3 = \left\{(\mu_1;\mu_2): \mu_2 = \frac{3}{d_1}\mu_1; \ \mu_1 > 0\right\}$$ the foci E_1 and E_2 pass through the

Andronov–Hopf bifurcation. This effect leads to the appearance of two small unstable limit cycles around the equilibrium positions E_1 and E_2. In other words, three limit cycles coexist in region 4. On the half-line

$$N_4 = \left\{(\mu_1;\mu_2): \mu_2 = \frac{12}{5d_1}\mu_1; \ \mu_1 > 0\right\}$$ as a result of the homoclinic

bifurcation, "small" cycles are contracted to the trivial equilibrium position E_0 and form a symmetrical curve that has an external resemblance to

Bernoulli's lemniscate. On the half-line N_4 the saddle point E_0 has two closed homoclinic orbits. When passing through the half-line N_4, which is the boundary between regions 4 and 5, the destruction of "small" cycles occurs with the simultaneous appearance of a "large" cycle. In area 5, two "large" cycles with different types of stability simultaneously coexist: the outer one is stable, and the inner one is unstable. Both of these cycles merge and disappear along the half-line $N_5 = \left(\mu_2 = \frac{3k_0}{d_1} \mu_1; \ \mu_1 > 0 \right)$, where $k_0 = 0.752...$ is a transcendental number. The disappearance of these two cycles is explained by the presence of a saddle-node bifurcation of the limit cycle. With this, the cyclic behavior of system (41) is completely exhausted. All three equilibrium positions, E_0, E_1 and E_2, in area 6, merge on the half-line $N_6 = \{(\mu_1; \mu_2): \mu_1 = 0; \mu_2 < 0\}$ as a result of the "pitchfork" bifurcation, and a return to area 1 occurs.

Regarding algebraic equation (12), it should be noted that in the context of the above assumptions, the three equilibrium positions merge to form a threefold equilibrium value.

In further research, while constructing a mathematical model, it is advisable to introduce a cyclic component into the demand function, which corresponds to seasonal fluctuations. In this case, one can expect the occurrence of resonance in the system, which can cause complex chaotic behavior of the system.

Conclusion

The mathematical model of a dynamic system proposed in the work describes the state of the market for one product as a result of the interaction of supply and demand functions with a time lag. The model is a system of two differential equations with quadratic nonlinearity, which made it possible, using qualitative analysis (along trajectories), to study the basic properties of this economic system. It was discovered that the nonlinear demand function ensures the presence of non-unique market equilibrium positions, which is a fact that is far from trivial. From the authors' point of view, the main problem for this dynamic system is to study the stability of equilibrium positions, taking into account the nonlinear interaction of its main variables which are the price of a product and the volume of its supply. Modeling of the behavioral properties of multi-product markets, which was carried out by Sir John Richard Hicks, Vasily Leontiev, and Oskar Ryszard Lange, is a much more complex task, the solution of which is complicated by the high dimensionality of the economic system,

and the presence of nonlinearity of connections does not allow the use of analytical methods. However, the existing approximate methods of reducing multidimensional dynamic systems allow such systems to be reduced to a system with one or two degrees of freedom, but this problem requires independent study and was not considered in this work.

As a result of the research, the area of stability of the economic system was identified and the parameters of this area were determined, as well as an analysis of the behavior of the system at the boundaries of the area of stability was carried out and a bifurcation diagram was constructed for the characterization of the processes occurring at these boundaries. A number of types of changes in the stability of the equilibrium regimes with the appearance of characteristic bifurcations have been identified. This includes the saddle-node bifurcation, as well as the bifurcation of the birth or death of a limit cycle. In addition, there is a symbiosis of the above-mentioned bifurcations in the form of a bifurcation of codimension two, i.e., the so-called Bogdanov–Takens bifurcation arises. This is accompanied by a global restructuring of the phase portrait with the appearance of ultra-low frequency cycles. Such trends in the production and economic system evolution are a unique phenomenon manifested in the presence of so-called turning points, at which a change in the increasing phase of long waves to a decreasing one and vice versa occurs. All these factors should be taken into account when developing strategic plans for managing under conditions of a constantly changing market environment. The ability to anticipate the existence of such phenomena and eliminate their occurrence allows decision makers to optimize the allocation of resources thus increasing production efficiency and fully satisfying customer needs.

References

Arena, R. & Caldari, K. 2024. Léon Walras and Alfred Marshall: microeconomic rational choice or human and social nature? *Cambridge Journal of Economics*, 48(3), pp.369-396. Available at: https://doi.org/10.1093/cje/beae005.

Cai, J. P. 2005. Hopf bifurcation in the IS-LM business cycle model with time delay. *Electronic Journal of Differential Equations*. 2005(15), pp.1-6. Available at: https://ejde.math.txstate.edu/Volumes/2005/15/cai.pdf.

Carr, J. 1982. *Applications of Centre Manifold Theory*. New York: Springer. Available at: https://doi.org/10.1007/978-1-4612-5929-9.

Chen, Q., Kumar, P. & Baskonus, H.M. 2024. Modeling and analysis of demand-supply dynamics with a collectability factor using delay differential equations in economic growth via the Caputo operator. *AIMS Mathematics*, 9(3), pp.7471-7491. Available at: https://doi.org/10.3934/math.2024362.

Davar, E. 2015. Is Walras's Theory So Different From Marshall's? *Journal of Social Science Studies*, 2(1), pp.64-86. Available at: https://doi.org/10.5296/jsss.v2i1.6234.

Davizón, Y.A., Amillano-Cisneros, J.M., Leyva-Morales, J.B., Smith, E.D., Sanchez-Leal, J. & Smith, N.R. 2023. Mathematical Modeling of Dynamic Supply Chains Subject to Demand Fluctuations. *Engineering, Technology & Applied Science Research*, 13(6), pp.12360-12365. Available at: https://doi.org/10.48084/etasr.6491.

Dilenko, V.O. & Tarakanov, N.L. 2020. Mathematical Modeling of the Equilibrium Price Formation Taking into Account the Logistic Factor. *Business Inform,* 7, pp.125-130. Available at: https://doi.org/10.32983/2222-4459-2020-7-125-130.

Donzelli, F. 2008. Marshall vs. Walras on Equilibrium and Disequilibrium. *History of Economics Review*, 48(1), pp.1-38. Available at: https://doi.org/10.1080/18386318.2008.11682129.

Dorokhov, A., Lebedeva, I., Malyarets, L. & Voronin, A. 2023. Non-linear model of the macroeconomic system dynamics: multiplier-accelerator. *Bulletin of the Transilvania University of Brasov. Series III: Mathematics and Computer Science*, 3(65), pp.181-200. Available at: https://doi.org/10.31926/but.mif.2023.3.65.2.16.

Elkarmouchi, M., Lasfar, S., Hattaf, K. & Yousfi, N. 2024. Mathematical analysis of a spatiotemporal dynamics of a delayed IS-LM model in economics. *Mathematical Modeling and Computing*, 11(1), pp.189-202. Available at: https://doi.org/10.23939/mmc2024.01.189.

Fu, N., Geng, L., Ma, J. & Ding, X. 2023. Price, Complexity, and Mathematical Model. *Mathematics,* 11(13), art.number:2883. Available at: https://doi.org/10.3390/math11132883.

Golubitsky, M. & Langford, W.F. 1981. Classification and unfoldings of degenerate Hopf bifurcation. *Journal of Differential Equations*, 41(3), pp.375-415. Available at: https://doi.org/10.1016/0022-0396(81)90045-0.

Guckenheimer, J. & Holmes, P. 1983. *Nonlinear Oscillations, Dynamical Systems, and Bifurcations of Vector Fields*, New York: Springer. Available at: https://doi.org/10.1007/978-1-4612-1140-2.

Hassard, B.D., Kazarinoff, N.D., & Wan, Y.-H. 1981. *Theory and Applications of Hopf Bifurcation*. Chembridge: Chembridge University Press. ISBN: 9780521231589

Hattaf, K., Riad, D. & Yousfi, N.A. 2017. Generalized business cycle model with delays in gross product and capital stock. *Chaos, Solitons & Fractals*. 98, pp.31-37. Available at: https://doi.org/10.1016/j.chaos.2017.03.001.

He, J.-H. 2018. Fractal calculus and its geometrical explanation. *Results in Physics*, 10, pp.272-276. Available at: https://doi.org/10.1016/j.rinp.2018.06.011.

He, J.-H., He, C.-H. & Sedighi, H.M. 2021. Evans model for dynamic economics revised. *AIMS Mathematics,* 6(9), pp.9194-9206. Available at: https://doi.org/10.3934/math.2021534.

Kopell, N. & Howard, L.N. 1975. Bifurcations and trajectories joining critical points. *Advances in Mathematics*, 18(3), pp.306-358. Available at: http://doi.org/10.1016/0001-8708(75)90048-1.

Kuznetsov, Y.A. 2023. *Elements of Applied Bifurcation Theory.* Cham: Springer. Available at: https://doi.org/10.1007/978-3-031-22007-4.

Le, L.B., Konishi, K. & Hara, N. 2012. Design and experimental verification of multiple delay feedback control for time delay nonlinear oscillators. *Nonlinear Dynamics,* 67, pp.1407-1418. Available at: https://doi.org/10.1007/s11071-011-0077-4.

Levi, A., Sabuco, J. & Sanjuán, M.A.F. 2018. Supply based on demand dynamical model. *Communications in Nonlinear Science and Numerical Simulation*, 57, pp.402-414. Available at: https://doi.org/10.1016/j.cnsns.2017.10.008.

Li, C. & Ma, Z. 2020. Dynamics Analysis of a Mathematical Model for New Product Innovation Diffusion. *Discrete Dynamics in Nature and Society,* 2020(1), art.number:4716064. Available at: https://doi.org/10.1155/2020/4716064.

Li, T., Wang, Y. & Zhou, X. 2019. Bifurcation analysis of a first time-delay chaotic system. *Advances in Continuous and Discrete Models,* 2019, art.number:78. Available at: https://doi.org/10.1186/s13662-019-2010-y.

Liao, X., Guo, S. & Li, C. 2007. Stability and bifurcation analysis in tri-neuron model with time delay. *Nonlinear Dynamics,* 49, pp.319-345. Available at: https://doi.org/10.1007/s11071-006-9137-6.

Nahorski, Z. & Ravn, H.F. 2000. A review of mathematical models in economic environmental problems. *Annals of Operations Research,* 97, pp.165-201. Available at: https://doi.org/10.1023/A:1018913316076.

Pomin, M. 2018. Economic dynamics and the calculus of variations in the interwar period. *Journal of the History of Economic Thought*, 40(1), pp.57-79. Available at: https://doi.org/10.1017/S1053837217000116.

Takens, F. 1974. Singularities of vector fields. *Publications Mathématiques de l'IHÉS*, 43, pp.47-100 [online]. Available at: http://eudml.org/doc/103931 [Accessed: 14. July 2024].

Voronin, A.V. & Chernyshov, S.I. 2007. Cycles in Nonlinear Macroeconomics. *arXiv:0706.1013*, 7 June. Available at: https://doi.org/10.48550/arXiv.0706.1013.

Voronin, A., Lebedeva, I. & Lebedev, S. 2020. Dynamics of formation of transitional prices on the chain of sequential markets: analytical model. *Economics of Development*, 21(1), pp.25-36. Available at: https://doi.org/10.57111/econ.21(1).2022.25-35.

Wei, J. & Yu, C. 2011. Stability and bifurcation analysis in the cross-coupled laser model with delay. *Nonlinear Dynamics,* 66, pp.29-38. Available at: https://doi.org/10.1007/s11071-010-9908-y.

Zabolotnii, S. & Mogilei, S. 2023. Modifications of Evans Price Equilibrium Model. *IAPGOŚ Informatyka, Automatyka, Pomiary W Gospodarce I Ochronie Środowiska*, 13(1), pp.58-63. Available at: https://doi.org/10.35784/iapgos.3507.

Modelos de dinámica microeconómica: bifurcaciones y algoritmos de comportamiento de sistemas complejos

Lyudmyla Malyarets[a], *Oleksandr* Dorokhov[b], **autor de correspondencia**, *Anatoly* Voronin[a], *Irina* Lebedeva[a], Stepan Lebedev[a]

[a] Universidad Nacional de Economía Simon Kuznets Kharkiv, Kharkiv, Ucrania
[b] Universidad de Tartu, Tartu, República de Estonia

CAMPO: matemáticas
TIPO DE ARTÍCULO: artículo científico original

Resumen:

Introducción/objetivo: El estudio de la dinámica de la influencia mutua de la oferta y la demanda es relevante en relación con las pérdidas financieras que surgen debido a la incertidumbre en la demanda y los errores de pronóstico. El trabajo tiene como objetivo construir un modelo matemático de la dinámica de esta interacción para el mercado de un producto.

Métodos: En el presente trabajo se propone un modelo matemático de los estados del sistema oferta-demanda, en cuyo marco se consideran los procesos que ocurren en dicho sistema desde la perspectiva de la metodología de la sinergética económica. El modelo matemático de la dinámica tiene la forma de un sistema de dos ecuaciones diferenciales con no linealidad cuadrática.

Resultados: La utilización del modelo propuesto para reproducir diversos estados dinámicos de los procesos de autorregulación del mercado permitió identificar la jerarquía de transición de regímenes dinámicos estables a inestables con la aparición de las correspondientes bifurcaciones. Se prestó especial atención al estudio del comportamiento del sistema en los límites de la región de estabilidad.

Conclusión: Se ha revelado la existencia de una bifurcación de los nodos de silla de los ciclos límite, lo que sugiere la aparición de autooscilaciones estables en el caso de un ciclo "suave" e inestables en el caso de un ciclo "duro". Al estudiar una bifurcación de codimensión dos – "doble cero" – se descubrieron estructuras dinámicas especiales, determinadas por las propiedades de las bifurcaciones globales. Este tipo de comportamiento se caracteriza por autooscilaciones de baja frecuencia, lo que da lugar a las llamadas "ondas ultralargas" del estado económico.

Palabras claves: dinámica del sistema de oferta y demanda, desfase temporal, ciclo límite, bifurcación, caos.

Модели микроэкономической динамики: бифуркационные алгоритмы поведения сложных систем

Людмила Малярец[a], *Олександр* Дорохов[б], **корреспондент**, *Анатолий* Воронин[a], *Ирина* Лебедева[a], *Степан* Лебедев[a]

ᵃ Харьковский национальный экономический университет
  имени Семёна Кузнеца, Харьков, Украина

ᵇ Тартуский университет, Тарту, Эстонская Республика

Резюме:

Введение/цель: Изучение динамики взаимного влияния спроса и предложения актуально в связи с финансовыми потерями, возникающими из-за неопределенности спроса и ошибок прогнозов. Целью работы является построение математической модели динамики этого взаимодействия для рынка одного товара.

Методы: В статье предложена математическая модель состояний системы спроса и предложения, в рамках которой процессы, происходящие в этой системе, рассматриваются с позиций методологии экономической синергетики. Математическая модель динамики имеет вид системы двух дифференциальных уравнений с квадратичной нелинейностью.

Результаты: Использование предложенной модели для воспроизведения различных динамических состояний процессов рыночного саморегулирования позволило выявить иерархию перехода от устойчивых динамических режимов к неустойчивым с возникновением соответствующих бифуркаций. Основное внимание уделено изучению поведения системы на границах области устойчивости.

Выводы: Выявлено существование узловой бифуркации предельных циклов, что означает возникновение устойчивых автоколебаний в случае «мягкого» цикла и неустойчивых в случае «жесткого» цикла. Также обнаружены особые динамические структуры, определяемые свойствами глобальных бифуркаций. Для этого типа поведения системы характерны автоколебания с низкой частотой, что приводит к возникновению так называемых «сверхдлинных волн» экономического состояния.

Ключевые слова: динамика систем спроса и предложения, временной лаг, предельный цикл, бифуркация, хаос.

Модели микроекономске динамике: алгоритми бифуркације и понашања сложених система

Људмила Маљарецᵃ, *Олександр* Дороховᵇ, **аутор за преписку**, *Анатолиј* Воронинᵃ, *Ирина* Лебедеваᵃ, *Степан* Лебедевᵃ

ᵃ Харковски национални економски универзитет „Семјон Кузњец",
  Харков, Украјина

ᵇ Универзитет у Тартуу, Тарту, Република Естонија

ОБЛАСТ: математика
КАТЕГОРИЈА (ТИП) ЧЛАНКА: оригинални научни рад

Сажетак:

Увод/циљ: Проучавање динамике узајамног утицаја понуде и потражње важно је када је реч о финансијским губицима услед неизвесне потражње и грешака у предвиђању. Циљ рада јесте да креира математички модел динамике ове интеракције за тржиште једног производа.

Методе: У раду се предлаже математички модел стања система понуде и потражње унутар оквира у којем се разматрају процеси који делују у овом систему са аспекта методологије економске синергије. Математички модел динамике има облик система две диференцијалне једначине са квадратном нелинеарношћу.

Резултати:Коришћење предложеног модела за репродукцију различитих динамичких стања процеса тржишне саморегулације омогућило је идентификацију хијерархије преласка из стабилних динамичких режима у нестабилне са појавом одговарајућих бифуркација. Највише пажње посвећено је проучавању понашања система на границама области стабилности.

Закључак: Откривено је постојање бифуркације седло-чвор граничних циклуса што указује на појаву аутоосцилација које су стабилне у случају „меког" циклуса, а нестабилне у случају „тврдог" циклуса. Приликом проучавања бифуркације кодимензије 2 – „двострука нула" откривене су специјалне динамичке структуре, одређене својствима општих бифуркација. Ова врста понашања карактерише се аутоосцилацијама ниске фреквенције што доводи до такозваних „ултрадугих" таласа економског стања.

Кључне речи: динамика система понуде и потражње, временско кашњење, гранични циклус, бифуркација, хаос.

A model for evaluating menu performance in collective nutrition organizations based on the DEA method

Slaviša N. Arsić[a], *Dragan* S. Pamučar[b], *Marjan* A. Milenkov[c], *Vlada* S. Sokolović[d], *Miljojko* M. Janošević[e]

[a] University of Defence in Belgrade, Military Academy,
    Section for Logistics, Belgrade, Republic of Serbia,
    e-mail: arsic.slavisa@gmail.com, **corresponding author,**
    ORCID iD: https://orcid.org/0000-0001-7431-7308

[b] University of Belgrade, Faculty of Organizational Sciences,
    Department of Operations Research and Statistics,
    Belgrade, Republic of Serbia,
    e-mail: dpamucar@gmail.com,
    ORCID iD: https://orcid.org/0000-0001-8522-1942

[c] University of Defence in Belgrade, Military Academy,
    Department of Logistics, Belgrade, Republic of Serbia,
    e-mail: marjan.milenkov@va.mod.gov.rs,
    ORCID iD: https://orcid.org/0000-0003-2054-0525

[d] University of Defence in Belgrade, Military Academy,
    Department of Logistics, Belgrade, Republic of Serbia,
    e-mail: vlada.sokolovic@va.mod.gov.rs,
    ORCID iD: https://orcid.org/0000-0003-0782-0506

[e] "Union - Nikola Tesla" University, Faculty of Business Studies
    and Law, Belgrade, Republic of Serbia,
    e-mail: miljojko.janosevic@fpsp.edu.rs,
    ORCID iD: https://orcid.org/0000-0001-9202-8649

FIELD: operations research, logistics, engineering management
ARTICLE TYPE: original scientific paper

Abstract:

Introduction/purpose: In the paper, a model for evaluating menu performance in collective nutrition organizations is presented, enabling quantification of the efficiency of each individual dish.

Methods: The Data Envelopment Analysis (DEA) method has been applied to evaluate the efficiency of dishes.

Results: The model has been successfully tested on the menu of the collective nutrition restaurant for cadets at the Military Academy in Belgrade (MAB). The evaluation included 20 existing dishes and 11 substitute dishes formed using the Food Replacement Table (FRT), allowing insight into the efficiency of each individual dish. In line with the specified criteria, 10 out of a total of 31 dishes have been evaluated as efficient (7 existing and 3 replacement dishes). By replacing inefficient existing dishes with new efficient dishes, the overall efficiency of the menu will increase, implying greater satisfaction of food users and reduction of the waste of prepared and uneaten meals.

Conclusion: A proposed model can be applied in practice because it provides objective and measurable values for assessing the performance of dishes, aiming to optimize the menu assortment in collective nutrition organizations and reduce the shortcomings of subjective decision making in selecting substitute meals. This model can be further improved by the use of other different methods for determining the weights of the criteria and ranking.

Key words: menu evaluation, restaurant management, DEA method, collective nutrition.

Introduction

Planning and implementing efficient nutrition for personnel pose highly complex challenges in collective nutrition organizations, such as the military, police, healthcare institutions, educational establishments, and others. Nutrition for personnel represents the most critical task within the logistics support function of the Serbian Armed Forces (SAF).

Research indicates that military logisticians, even in the most powerful armed forces globally, encounter numerous issues in logistics planning. These challenges include difficulties in forecasting, lengthy processes, mismatched demands, and limited visibility of logistical resources. Quartermaster services responsible for food supply tasks are not exempt from these problems and difficulties.

In the U.S. regulation 'The Army Food Program' (AR 30–22, 2019), necessary policies are outlined to ensure that soldiers are provided with safe, nutritionally balanced, sufficiently diverse, and appealing meals, appropriately timed. Meanwhile, according to the Rulebook on quartermastership in the Ministry of Defense (MD) and the SAF, nutrition for personnel is to be provided in a prescribed, regular, and health-approved manner. This nutrition should be based on scientific knowledge, technical and technological capabilities, acquired experience, scientific principles, and dietary traditions that align with the psychophysical

demands and coordinated requirements of command and management. The goal is to ensure the quality and complete satisfaction of the energy and biological needs of the members of the SAF.

The most valuable resource of the military is the soldier (the individual), capable of executing assigned tasks. As such, they deserve the best available support for life and work. Proper human nutrition allows for a balanced intake of nutrients and protective materials necessary for proper functioning, recovery, development, and defense of the human body against external influences.

Food influences biochemical processes at the cellular level, stimulates willpower and positive thinking, reduces tension, and enhances mood. Deviations from this balance can lead to overnutrition or inadequate nutrition, negatively impacting health, psychophysical fitness, work capacity, and overall lifespan.

Numerous epidemiological studies have shown that food is, in most cases, a factor that either causes or exacerbates civilization-related diseases (Bleich et al, 2015; De Ridder et al, 2017; Schulze et al, 2018). In this context, the responsibility of logisticians is to learn from the past, analyze the present, and predict the future in order to provide the best support to military personnel. Proper planning and organization of collective nutrition for military members enable the development of capabilities to achieve the proclaimed short-term, medium-term, and long-term goals of the military organization. These goals stem from the broader interests of society and impact the stability and overall development of the state.

Menus for younger populations, such as students and cadets in military schools, receive special attention (Budowle et al, 2023; Schinkel et al, 2023). Furthermore, the ongoing research at the MAB focuses on improving the nutrition of cadets at the MAB restaurant, primarily through research projects VA-DH-4/17-19 and VA-TT-1/20-25.

To achieve complete, diverse, consistent, and high-quality nutrition, dietary plans are developed. These plans define norms for food allocation, the structure of food items, and recipes based on scientific, medical, nutritional, and culinary foundations.

On the basis of the conducted research and regular monitoring of food service implementation at the MAB by experts, it has been observed that a portion of prepared meals, according to the approved menu and the reported number of cadets, was not utilized for consumption. The main reason is the mismatch between the type of food products and the sensory properties of meal components with user preferences.

This phenomenon has negative effects in terms of resource utilization and engagement for preparing meals that go unused. Additionally, it results in deficits of programmed nutrients and protective substances that users either did not intake or replaced inadequately through surrogate meals. Such imbalances can lead to the degradation of psychophysical abilities (including cognitive and motivational aspects) and, over an extended period, contribute to the development of chronic illnesses. Treating these illnesses requires further resource allocation.

To rationalize resource usage and enhance user satisfaction, two approaches are commonly applied.

The first approach involves logistical experts of Quartermaster Service (QMS) partially minimizing the number of prepared meals that are unpopular among users based on experiential assessment. While this reduces costs, it does not fully achieve the goal of collective nutrition, as some users may still remain dissatisfied.

The second approach is normatively regulated. It involves developing a monthly menu by considering all factors affecting nutrition implementation. This menu allows for the substitution of meals specified in the Meal Application Cycle (MAC)[1] to create a realistically achievable and functional monthly menu. When certain meals cannot be implemented, logistical experts of QMS, considering available ingredients, technical-technological conditions, and personnel resources, subjectively choose the most suitable replacements, either for entire meals or for components with similar energy and biological value.

The mentioned approaches are quite experiential and subjective, and in current practice, there is no adequate model that would provide logistical experts with support in making objective decisions regarding the optimal selection of substitute meals from the group of existing meals in the NP or meals modified by replacing some of the components according to the FRT, which is an integral part of it. The verification of the proposed model was conducted at the MAB.The overview of the applied methodology is given in Figure 1.

Generally, menu planning is a multi-criteria problem that requires consideration of a wide range of quantitative and qualitative criteria, often accompanied by various forms of uncertainty, insecurity, imprecision, and subjectivity on the part of decision makers. This can make the decision-making process quite complex, challenging, and time-consuming.

---

[1] The MAC cycle is prescribed by the Nutrition Plan (NP) in the SAF. By adhering to the meal application cycle, the average planned energy and biological value of meals are ensured, along with the consumption of the planned food products.

Therefore, the application of specific multi-criteria optimization methods and linear programming techniques serves as a useful tool for comprehensively identifying relevant criteria for evaluating meal performance and creating a model for optimizing menus in collective nutrition organizations, all while aligning with established norms to enhance user satisfaction.
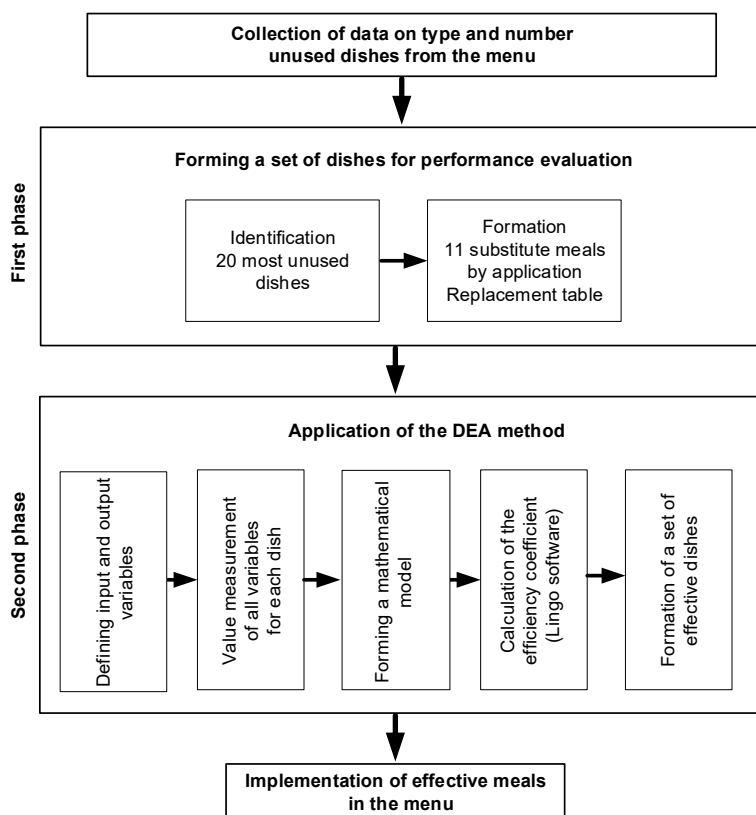
Figure 1 – Phases and steps for the application of the proposed model

To mitigate the shortcomings of subjective decision making and obtain more objective and measurable assessments of meal performance and menu optimization, this study proposes a model based on the DEA method which relies on mathematical programming to assess the relationships between relevant input and output parameters, quantifying their efficiency. As a result, it provides real-time insights into the performance of each individual dish from the observed set of dishes.

Background

In this chapter, we provide an overview of previous research (literature), describe the menu, and present the necessary theoretical foundation for the DEA method. This method is used to develop a model for evaluating the performance of dishes in the menu of collective nutrition organizations.

Review of the previous research and literature

Researchers have always worked on creating menu optimization models to enhance efficiency, guest satisfaction, and profits (Taylor et al, 2009).

Menu engineering models allow for systematic evaluation by comparing individual dishes based on pre-defined criteria. Earlier approaches to menu evaluation focused on the cost contribution of food items and the popularity of the 'product mix'.

Miller conducted the first menu analysis using a four-quadrant matrix, where he tracked the value defined as the sales velocity via vectors related to dish popularity and sales levels (Miller, 1996). Kasawana and Smith applied the 'Boston Consulting Group Portfolio Analysis' as the basis for the 'Menu Engineering Matrix approach', incorporating profitability (measured by contribution margin) but excluding the possibility of mutual influence between low food costs and high gross profit (Kasavana & Smith, 1982).

Pavesic recognized the connection between low food costs and high gross profit, replacing gross profit with the weighted ratio of gross profit to contribution margin. Pavesic also treated 'dish popularity' as an indirect third variable (Pavesic, 1983). Hayes and Huffman attempted to allocate all costs, including labor and fixed costs, to individual menu items in their profit and loss analysis (Hayes & Huffman, 1985). Later, Miller developed a matrix model for analyzing menu profitability based on food costs and the product mix, without considering production costs (Miller, 1996).

Bayou and Bennett constructed a model for profitability analysis and attempted to allocate variable costs, such as labor, to assess the financial strength of each dish (Bayou & Bennett, 1992). Le Bruto, Quain, and Ashley modified the 'Kasawana and Smith model' (KSM) by allocating labor costs separately as fixed and variable components for each menu item (LeBruto et al, 1995).

The limitation of all matrix models lies in the assumption that indirect costs are equally allocated to all menu items (Morrison, 1996). To overcome this limitation, Cohen included five factors (food costs, price,

labor costs, popularity, and contribution margin) and normalized input values into scalar variables on a scale of 1-10 (Cohen et al.,1998). This approach did not consider other production factors and did not explain how labor costs were measured. Horton modified KSM by incorporating the value of 'estimated labor' into the contribution margin (gross profit) (Horton, 2001). Taylor, Raynolds and Brown introduced a non-parametric statistical approach that addressed the shortcomings of the previous models related to labor measurement and data analysis. Tom and Annaraud applied fuzzy techniques within KSM to handle uncertainties in menu alternative evaluation through linguistic variables, providing relevant information for decision makers in multi-criteria decision making (Tom & Annaraud, 2017).

For food to fulfill its nutritional mission, it needs to provide both short-term (subconscious sensory perception during and immediately before and after a meal, motivating repeated consumption of the chosen meal) and long-term satisfaction (conscious feelings of health, vitality, capability, and enthusiasm for life and work). Previous studies and works have not sufficiently leveraged feedback obtained from food consumers, which is a necessary parameter in the architecture of a nutrition system that is relevant and up-to-date in the context of new knowledge in the science of nutrition and comprehensive user needs.

The common characteristic of the previous research works is that they inadequately exploited the advantages of objective methods that allow measuring the relative efficiency of individual dishes from the set of existing menu items and selected substitute dishes formed in accordance with FRT. These methods consider a broader spectrum of relevant criteria (economic, organizational, technical, nutritional, gastronomic, etc.) including those reflecting user satisfaction.

The first application of the DEA method in practice was carried out for military purposes, by the authors themselves, to evaluate the efficiency of equipment maintenance and recruitment processes (Charnes et al, 1984), followed by subsequent applications by other authors for measuring financial efficiency (Bowlin, 1987, 1989), combat unit capabilities (Crino, 1996) and other defense-related aspects (Bowlin, 2004; Hanson, 2016).

DEA has also been successfully used in the restaurant industry in restaurant ranking (Hadad et al, 2007). An extended the CRS-DEA model from the work of (Taylor et al, 2009) to a variable returns-to-scale (VRS) DEA model was used under a metafrontier framework and simultaneously determined which items should be retained on a menu based on efficiency as determined by VRS-DEA in order to increase financial performance (Fang & Hsu, 2014). The DEA method has been successfully applied in

the integration of menu analysis and revenue management approaches in order to improve strategy formulation (Lai et al, 2019), then for the formation of the CDMA model for menu analysis as a tool to support management in making strategic decisions (Nemeschansky et al, 2020), and for developing an innovative SBM-DEA model to evaluate the menu item efficiency with a better discrimination power and determine the input targets for each menu item by comparing the efficiency frontier.

The new approach presented in this study enables the evaluation of dish performance using the DEA method based on nine relevant input/output variables. These variables include organoleptic and digestive characteristics of dishes, which have not been previously used in combination with organizational, nutritional, and technical-technological variables. The goal is to enhance the existing menu assortment by replacing inefficient dishes with more suitable ones, thereby increasing user satisfaction with the food and improving the efficiency of food-related tasks within the organization.

The description of a menu

A menu represents the list of dishes offered by a restaurant and results from synthesizing the needs of the target user group on one hand, and the restaurant's ability to prepare food in an affordable manner according to defined standards on the other. The menu is structured based on the restaurant's production capabilities (technical, technological, and organizational) and available resources, as well as user preferences for restaurant services.

Menus can be categorized as follows: Fixed menus - characteristic of à la carte restaurants; Daily menus - for breakfast, lunch, and dinner; Weekly menus - spanning a week; Ten-Day menus - common for pension-style consumption; Monthly menus - used in student cafeterias, preschools, hospitals, etc; Cyclical menus - repeated in specific time intervals and Seasonal menus - designed for tourist seasons or specific times of the year. In military and related organizational systems where collective nutrition occurs, an annual menu specifies the types of dishes, their monthly cycles, and criteria for creating monthly menus.

User food needs arise from their daily activities (psychophysical engagement) and dietary habits. These needs represent the energy-biological value of daily nutrition and the expected sensory perception during and after meals. If a nutritionally balanced menu does not align with users' expectations regarding sensory properties (taste, texture, digestibility), meal components, and preparation methods, satisfaction may be lacking. This can discourage subsequent meal consumption,

disrupting the user's health equilibrium. Additionally, inefficient menus can lead to wasted resources and potential health risks due to inadequate nutrient intake or harmful substitutes.

Optimizing menus ensures a balanced compensation for energy-biological expenditures, avoiding excesses or deficiencies. It also provides subjective satisfaction during meals and maintains overall well-being. An optimized menu allows efficient utilization of restaurant capacities and resources, satisfying both user expectations and restaurant management. Measurement of efficiency of units of similar type, not only help in identifying the shortcomings of the unit, but also helps in the development of the unit by eradicating or minimizing those shortcomings.

DEA method

In 1978, DEA methodology was introduced to calculate the relative efficiency of units based on multiple outputs and multiple inputs (Charnes et al, 1978).

DEA is a mathematical programming approach based on numerical data. It is successfully used for evaluating heterogeneous entities (such as organizational or production units). Some notable advantages of DEA are that it can accommodate multiple input and output variables, even when they have different units, it can work with both qualitative and quantitative data, and it acts as an effective decision-making tool in directing the attention of management to the area that can be improved (Xie et al, 2021).

Notably, the first paper titled "Evaluating Program and Managerial Efficiency: An Application of Data Envelopment Analysis to Program Follow Through" (Charnes et al, 1981) marked the beginning of its application. The increasing number of published scientific papers attests to the significance of the method and its practical value.

DEA was considered an excellent mathematical programming and a powerful management tool that can be used to measure, evaluate, and analyze the efficiency of the state, government, and military units (Okromtchedlishvili, 2022).

As of 2021, there have been a total of 17,164 papers using DEA methodology (in its original or improved form) listed in the Web of Science database.There has been a substantial growth in published works (Figure 2).

The application of the method is particularly suitable for assessing efficiency in cases where the complex nature of the relationship between multiple inputs and multiple outputs makes it impossible to apply other approaches for efficiency evaluation (Cooper et al, 2007).

1584
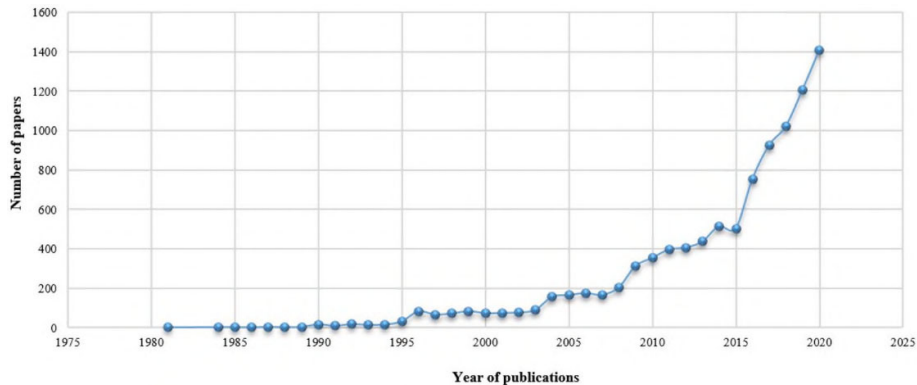
Figure 2 – DEA publications since 1980

The concept of the DEA method

The main advantage of the DEA method is that it does not require assumptions about the functional form of the production function, which excludes the estimation of parameter values (non-parametric method). In relation to other methods, the efficiency of input and output weights should not be known "a priori", because entities are grouped into efficient or inefficient depending on their relative geometric location in relation to an empirically set efficiency limit that is based on best practice, and not on averaging.

There are several methods similar to Data Envelopment Analysis (DEA) for measuring efficiency. A few notable ones are: Stochastic Frontier Analysis (SFA)[2], Free Disposal Hull (FDH)[3], Multiple-Criteria Decision Analysis (MCDA)[4], Ratio Analysis[5] and Tobit and OLS Regression Models[6].

The name "DEA" stems from the way the method identifies the "frontier" used to assess the performance of all subjects under evaluation.

---

[2] This method uses statistical techniques to estimate the efficiency of decision-making units (DMUs) by separating random errors from inefficiency effects.

[3] FDH is a non-parametric method like DEA but does not assume convexity of the production possibility set, making it more flexible in certain applications.

[4] MCDA evaluates efficiency by considering multiple criteria and often involves stakeholder preferences to weigh different factors.

[5] This method involves calculating ratios of outputs to inputs to assess efficiency, which is simpler but less comprehensive than DEA.

[6] These models can be used in conjunction with DEA to analyze the determinants of efficiency, providing additional insights into the factors influencing performance.

The authors of DEA propose a solution that overcomes subjectively imposed preferences of decision makers. They suggest that each Decision Making Unit (DMU) should have the freedom to determine the weight coefficients to maximize its own efficiency and present itself in the best light. All weight coefficients must be greater than 0 and the efficiency score for any DMU cannot exceed 1. DEA simplifies the scaling problem, expressing efficiency as a number between 0 and 1. Units achieving a score of 1 are considered efficient and lie on the efficiency boundary. Deviations from 1 indicate excess inputs or insufficient outputs. A DMU is efficient if it does not satisfy two conditions (Charnes et al, 1978): a) it is possible to increase any output without increasing any input or decreasing any other output; and b) it is possible to decrease any input without decreasing any output or increasing any other input.

DEA analyzes each DMU to determine whether its inputs can be achieved from below (i.e., achieving a given output with fewer inputs) and whether its outputs can be achieved from above (i.e., producing a larger output with a given input) based on the values of other units' inputs and outputs. If a unit can be achieved, it is relatively inefficient; otherwise, it contributes to forming the efficiency boundary, which represents the equivalent of the production frontier. For each inefficient DMU, DEA identifies the content and level of inefficiency for each input and output. The level of inefficiency is determined by comparing it to either a single reference DMU or a convex combination of other reference DMUs that lie on the efficiency boundary.

These reference DMUs use proportionally the same input levels and produce proportionally the same or greater output levels. In simpler terms, DEA helps to understand how much an inefficient DMU deviates from the best-performing units. It is like finding the optimal balance between inputs and outputs to achieve efficiency.

Efficiency can be achieved by projecting onto the efficient frontier, as shown in Figure 3.
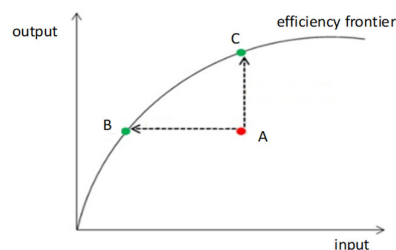
Figure 3 – Approximate representation of the limit of efficiency

This representation is approximate because it assumes only one input and output, one inefficient unit, and no change in the efficiency boundary. The Figure depicts the efficiency boundary where the efficient units B and C lie, while the inefficient unit A can approach the efficiency boundary by reducing its input or increasing its output.

There ara two fundamental models used in measuring efficiency: CCR (Charnes, Cooper, and Rhodes) and BCC (Banker, Charnes, and Cooper). The CCR model assumes that DMUs operate with constant return to scale, meaning that increasing inputs must result in a proportional increase in outputs. This efficiency includes both pure technical efficiency (how well inputs are transformed into outputs) and scale efficiency (how efficiently the DMU operates at its chosen scale).The efficiency frontier provided by CCR models takes the shape of a convex cone). The BCC model also known as the DEA model with variable returns to scale focuses on pure technical efficiency, ignoring the impact of the scale. In the BCC model, a specific DMU is compared only to other units with similar scales of operation. It provides a measure of efficiency that considers the impact of inputs and outputs without assuming constant returns to the scale. In the mentioned context, the CCR model was used in this paper.

DEA CCR model

DEA models can generally have two forms: input or output oriented (Figure 4).
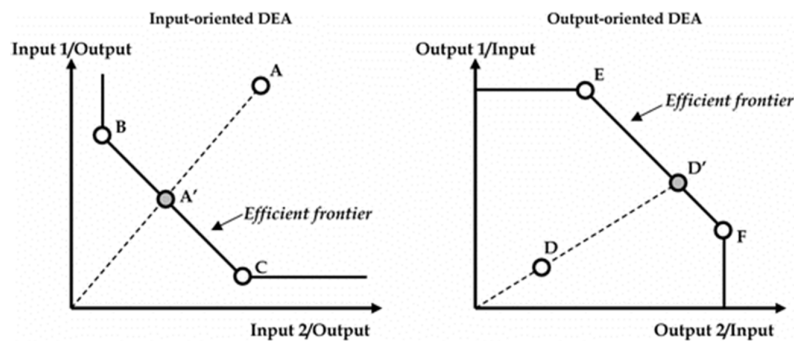
Figure 4 – Input and output-oriented CCR models

The efficiency frontier or envelope consists of the efficient units C, B, D, and E. The difference lies only in the way inefficient units are enveloped.

Input-oriented approach (input minimization or contraction) focuses on achieving the desired output while using the least amount of input

resources. The output-oriented approach (output maximization or expansion) aims to maximize the outputs while maintaining a specified level of input resources.

The input-oriented CCR model is obtained by converting a non-linear to a linear problem, which is then solved by the method of linear programming, by applying a system of linear equations (1):

$$DEA_{input} = \min \sum_{i=1}^{m} w_i x_i - input$$

$$st:$$

$$\sum_{i=1}^{m} w_i x_{ij} - \sum_{i=m+1}^{m+s} w_i y_{ij} \geq 0, \ j = 1,...,n$$

$$\sum_{i=m+1}^{m+s} w_i y_{i-output} = 1$$

$$w_i \geq 0, \ i = 1,...,m+s \tag{1}$$

The DMU consists of *m* input parameters for each alternative *xij*, *s* represents the output parameters for each alternative *yij*, taking into account the weights of the parameters denoted by *wi*, and *n* represents the total number of DMUs.

The output-oriented CCR model, where the optimization criterion is the maximization of the value of the objective function (efficiency), is solved by applying a systems of linear equations (2):

$$DEA_{output} = \max \sum_{i=m+1}^{m+s} w_i x_i - output$$

$$st:$$

$$-\left(\sum_{i=1}^{m} w_i x_{ij}\right) + \sum_{i=m+1}^{m+s} w_i y_{ij} \leq 0, \ j = 1,...,n$$

$$\sum_{i=1}^{m} w_i y_{i-intput} = 1$$

$$w_i \geq 0, \ i = 1,...,m+s \tag{2}$$

To obtain the efficiency index for each DMU, it is necessary to apply expression (3):

$$Efficiency = \frac{\max OUTPUT}{\min INPUT} \tag{3}$$

Although input- and output-oriented models have different optimization criteria, the problem is unique and the following expression applies:

$$FX^0 = \max_{x \in D} FX$$
$$FX^0 = \min_{x \in D} \left[-F(X) \right] \qquad (4)$$

where *D* is the domain of admissible solutions.

Application of the model

During the observed period in the 2023 calendar year, based on the indicators tracking lunch meals, according to the 'Record of Prepared and Unused Meals', 20 dishes in the menu were identified as not being frequently chosen by users. These dishes are numbered from 1 to 20 in order from the least desirable to more desirable. In collaboration with a nutritionist, a group of 11 new dishes was formed by replacing certain components of the meals numbered from 21 to 31.

For effective interpretation, acceptance, and utilization of the results obtained from the DEA analysis, a final group of relevant criteria reflecting the performance of each individual dish in the menu was identified based on questionnaires and expert surveys. The collected data were selected according to the following categories: food price (Official prices from the Serbian Armed Forces and the Ministry of Defense during the observed period, based on valid contracts with suppliers and market scans for fresh seasonal fruits and vegetables); technological preparation requirements (represents the number and complexity of work operations needed to prepare the dish - e.g., sorting, peeling, slicing, breading, frying, etc. Values were obtained through surveys with the restaurant staff involved in food preparation and are presented on a scale from 1 to 100); technical equipment requirements for dish preparation (Represents the number and complexity of devices used in dish preparation - e.g., peeling machines, cutting machines, sautéing equipment, cooking kettles, convection ovens, etc. Values were obtained through surveys with the restaurant staff involved in food preparation and are presented on a scale from 1 to 100); preparation time (represented on a scale from 1 to 100 based on the experience of restaurant chefs); technical-technological requirements for food storage (includes the use of storage capacities and equipment for preserving food until consumption); nutritional quality index of dishes (a comprehensive indicator considering the nutritional contribution of proteins, carbohydrates, and fats in the total calories intake during dish consumption.

Unlike the purely energy-focused calorific value, this index synthesizes the structural, protective, and energy contributions of the dish to the body. The Nutritional Quality Index of Dishes was calculated based on the methodology for calculation the Nutrient Rich Food Index (Drewnowski, 2009) and it relies on data regarding the nutritional composition of dishes including proteins, fats, and carbohydrates, from the NP.); sensory properties of dishes[7]; digestibility of dishes[8], and post-meal feeling[9].

Based on formulas (1) and (2), systems of linear equations were formed for 31 dishes[10]. By solving these linear equations using the Lingo 20.0 software package[11], the values for the minimum Input and maximum Output are obtained for the first dish 'Potato Moussaka' (Figure 5).

The efficiency index for the first dish 'Potato Moussaka' is E= 0.7637242/1,309373= 0.583275. In the same manner, the values were obtained for the remaining dishes.

By applying formula (3), the efficiency coefficients were calculated for each dish (Figure 6).

After calculating the efficiency coefficient and conducting the analysis, it can be observed that, in line with the specified criteria, 10 out of a total of 31 dishes have been evaluated as efficient (*E=1*).

---

[7] Includes texture, aroma, taste, and appearance of the dish. Ratings for criteria 7, 8, and 9 were obtained through surveys with a representative sample of cadets from all classes and genders.

[8] Subjective perception of digestion and satiety after consuming the meal by food users.

[9] Common implications include post-lunch energy levels, heavier-to-digest dishes may reduce post-meal energy and agility.

[10] The mathematically posed task can be described as follows: determine the values of the weights of (independently variable) inputs and outputs so that the DMU has the highest relative efficiency (dependently variable) in the output orientation or inefficiency in the input orientation, and that the weighted sum of the inputs of the observed DMU is equal to one and other DMUs greater than or equal to zero.

[11] The first specialized software for DEA was developed at the University of Massachusetts in 1989 under the name IDEAS.Today, numerous software programs are widely known and applied.
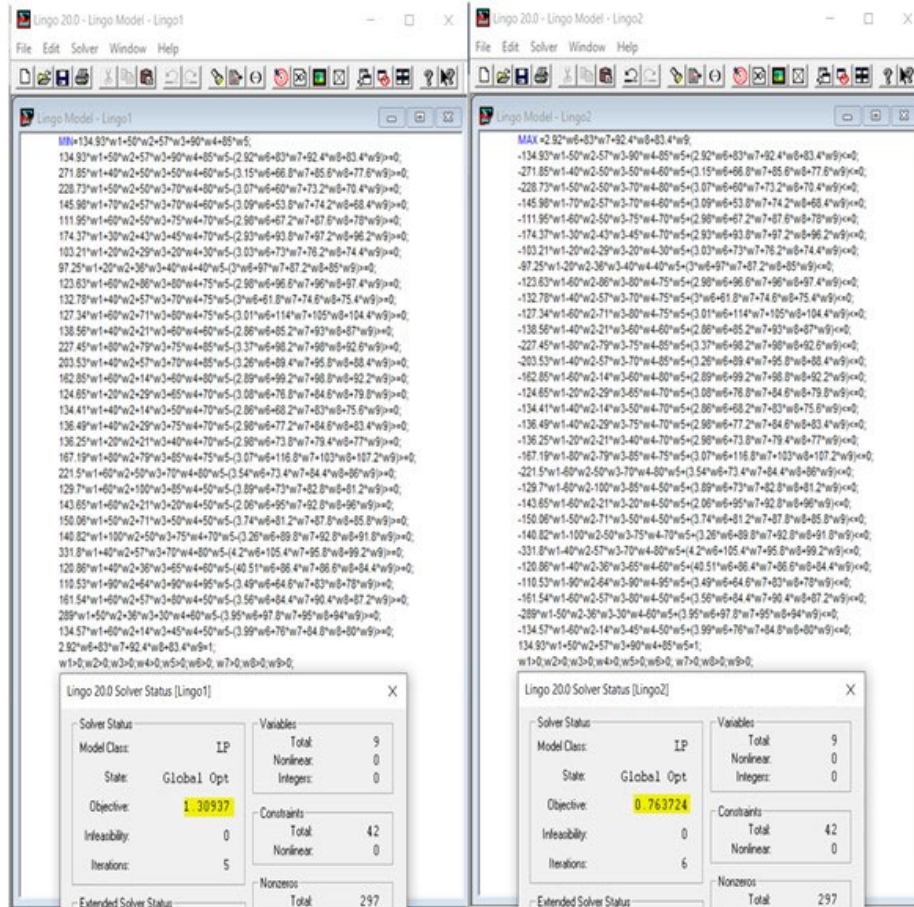
Figure 5 – A system of linear equations of the input and output-oriented CCR model

Ord. no.	Name of the dish on the menu/ Criterion	Price of food products	Technological requirements for preparation	Technical requirements for dish preparation	Cooking time	Technical and technological requirements for food storage	Nutritional quality index	Sensory properties	Digestibility	Feeling after lunch (zeal for work)	min INPUT	max OUTPUT	E = max OUTPUT/min INPUT
		I	II	III	IV	V	VI	VII	VIII	IX			
1.	Potato Moussaka	134,93	50	57	90	85	2,92	83	92,40	83,40	1,309373	0,763724	0,583275
2.	Trout and salted potatoes	217,85	40	50	50	60	3,15	66,8	85,60	77,60	1,630336	0,613371	0,376223
3.	Roast lamb, stewed peas, and roasted potatoes	228,73	50	50	70	80	3,07	60	73,20	70,40	2,126991	0,470148	0,221039
4.	Mackerel and salted potatoes	145,98	70	57	70	60	3,09	53,8	74,20	68,40	1,751512	0,570935	0,325967
5.	Fried fish, stewed carrots, and stewed rice	111,95	60	50	75	70	2,98	67,2	87,60	78,00	1,145900	0,872676	0,761564
6.	Turkey fillet, stewed rice, and stewed sweet cabba	174,37	30	43	45	70	2,93	93,8	97,20	96,20	1,210845	0,825869	0,682060
7.	Military bean stew with canned pork goulash	103,21	20	29	20	30	3,03	73	76,20	74,40	1,000000	1,000000	1,000000
8.	Bean soup with smoked bacon	97,25	20	36	40	40	3,00	97	87,20	85,00	1,000000	1,000000	1,000000
9.	Parisian schnitzel, stewed green beans, and salted potatoes	123,63	60	86	80	75	2,98	96,6	96,00	97,40	1,109415	0,901376	0,812478
10.	Greek meatballs	134,78	40	57	70	75	3,00	61,8	74,60	75,40	1,535281	0,651347	0,424252
11.	Viennese schnitzel, stewed peas, and mashed potatoes	127,34	60	71	80	75	3,01	114	105,00	104,40	1,066089	0,938008	0,879859
12.	Hunter's potatoes with meat	138,56	40	21	60	60	2,86	85,2	93,00	87,00	1,000000	1,000000	1,000000
13.	Breaded fish, mashed spinach, and fried potatoes	227,45	80	79	75	85	3,37	98,2	98,00	92,60	1,943255	0,514601	0,264814
14.	Breaded fish and fried potatoes	203,53	40	57	70	85	3,26	89,4	95,80	88,40	1,633740	0,612074	0,374634
15.	Stuffed peppers and mashed potatoes	162,85	60	14	60	80	2,89	99,2	98,80	92,20	1,000000	1,000000	1,000000
16.	Roast pork, sauerkraut, and mashed potatoes	124,65	20	29	65	70	3,08	76,8	84,60	79,80	1,000000	1,000000	1,000000
17.	Potato stew with beef	134,41	40	14	50	70	2,86	68,2	83,00	75,60	1,000000	1,000000	1,000000
18.	Roast pork, stewed peas, and roasted potatoes	136,49	40	29	75	70	2,98	77,2	84,60	83,40	1,154228	0,866380	0,750614
19.	Beef with vegetables	136,25	20	21	40	70	2,98	73,8	79,40	77,00	1,000000	1,000000	1,000000
20.	Karađorđe's schnitzel, stewed green beans, and roasted potatoes	167,19	80	79	85	75	3,07	116,8	103,00	107,20	1,363154	0,733593	0,538159
21.	Lamb in milk with mashed potatoes and stewed carrots	221,50	60	50	70	80	3,54	73,4	84,40	86,00	1,802074	0,554916	0,307932
22.	Larded beef and lentils with potatoes	129,70	60	100	85	50	3,89	73	82,80	81,20	1,329773	0,752008	0,565516
23.	Baker's potatoes with sausage	143,65	60	21	20	50	2,06	95	92,80	96,00	1,000000	1,000000	1,000000
24.	Grilled mackerel fillet and risotto with eggplant	150,06	50	71	50	50	3,74	81,2	87,80	85,80	1,349072	0,741251	0,549452
25.	Pork chop and grilled vegetables	140,82	100	50	75	70	3,26	89,8	92,80	91,80	1,319026	0,758135	0,574769
26.	Turkey fillet in cream with gnocchi	331,80	40	57	70	80	4,20	105,4	95,80	99,20	1,510142	0,662189	0,438495
27.	Beef stew with mashed potatoes	120,86	40	36	65	60	4,51	86,4	86,60	84,40	1,000000	1,000000	1,000000
28.	Cauliflower and eggplant moussaka	110,53	90	64	90	95	3,49	64,6	83,00	78,00	1,188796	0,841187	0,707596
29.	Minced beef roll and risi e bisi	161,54	60	57	80	50	3,56	64,4	90,40	87,20	1,362762	0,733804	0,538468
30.	Baked broccoli with chicken	289,00	50	36	30	60	3,95	97,8	95,00	94,00	1,168148	0,856056	0,732832
31.	Sautéed beef liver and mashed potatoes	134,57	60	14	45	50	3,99	76	84,80	80,00	1,000000	1,000000	1,000000

Figure 6 – Criterion and coefficient values

Conclusion

In the process of planning logistics support, logistics units must continuously observe, study, and analyze user requirements from various angles. They generally make numerous decisions based on subjective perception and experientially chosen criteria to respond rationally to user

demands within the available resource capacities of the logistics system (Milenkov et al, 2020).

To reduce the shortcomings of subjective decision making and obtain a more objective and measurable assessment of dish performance, as well as to optimize menu assortments in collective nutrition organizations, this study proposes a model for evaluating dish efficiency using the DEA method which relies on mathematical programming to assess the relationship between relevant input and output parameters, quantifying their efficiency.

The application of the proposed model identified 10 efficient dishes (7 existing and 3 replacement dishes) out of 31 considered. The replacement dishes assessed as efficient can be incorporated into the menu, replacing some of the lowest-ranked 13 inefficient existing dishes. By doing so, the overall efficiency of the menu will increase, implying greater satisfaction of food users. Ranking can be based on the obtained efficiency coefficient values (from the lowest to the highest ones) or by creating a more precise model for multi-criteria optimization using rough numbers or fuzzy logic (Bozanic et al, 2023; Badi et al, 2024). This approach could serve as a basis for further research and enhancement of the model presented in this study.

Considering that the model's output criteria focus on user satisfaction after meals, while the input criteria relate to technical-technological and material requirements for dish preparation, and recognizing that user dietary habits and perceptions continually evolve from scientific, technical-technological, and sociological perspectives, this model can effectively be used for periodic, objective dish evaluation. It serves as a tool for logistics support personnel (QMS) to adjust menus based on user dietary habits, staff expertise, facility equipment, market conditions, and the material capabilities of the SAF.

Also, the presented model can be very effectively applied when it is necessary to create a menu according to the defined effects it should have on the target group of users (by favoring certain criteria, such as nutritional composition, digestibility, energy for physical work after a meal, possibility of preparation in extraordinary circumstances, necessity to bring the organism to a state of optimal psychophysical performance for the realization of planned activities and enable adequate recovery afterwards) in collective nutrition facilities for public sector (evaluating meal programs in public institutions like prisons and police facilities to ensure they are both nutritious and cost-effective), as well as school catering (assessing the efficiency of school meal programs to provide balanced nutrition within budget constraints), corporate catering (analyzing the efficiency of meal

services in corporate settings to optimize costs and employee satisfaction), healthcare (evaluating the efficiency of meal plans in hospitals and nursing homes to ensure nutritional needs are met cost-effectively) and hospitality industry (assessing the efficiency of restaurant menus to balance cost, customer satisfaction, and nutritional value).

By minimizing the negative effects of menu misalignment with user needs (on the one hand) and resource constraints (on the other), this approach can enhance user satisfaction and reduce material waste resulting from unused prepared meals.

References

Badi, I., Bouraima, M.B., Stević, Ž., Oloketuyi, E.A. & Makinde, O.O. 2024. View of Optimizing Vendor-Managed Inventory in Multi-Tier Distribution Systems. *Spectrum of Operational Research*, 1(1), pp.33-43. Available at: https://doi.org/10.31181/sor1120243.

Bayou, M.E. & Bennett, L.B. 1992. Profitability Analysis for Table-Service Restaurants. *Cornell Hotel and Restaurant Administration Quarterly*, 33(2), pp.49-55. Available at: https://doi.org/10.1177/001088049203300220.

Bleich, S.N., Jones-Smith, J., Wolfson, J.A., Zhu, X. & Story, M. 2015. The Complex Relationship Between Diet And Health. *Health Affairs*, 34(11), pp.1813–1820. Available at: https://doi.org/10.1377/hlthaff.2015.0606.

Bowlin, W.F. 1987. Evaluating the Efficiency of US Air Force Real-Property Maintenance Activities. *Journal of the Operational Research Society*, 38(2), pp.127-135. Available at: https://doi.org/10.1057/jors.1987.25.

Bowlin, W.F. 1989. An intertemporal assessment of the efficiency of air force accounting and finance offices. *Research in Government and Nonprofit Accounting*, 5, pp.293-310.

Bowlin, W.F. 2004. Financial analysis of civil reserve air fleet participants using data envelopment analysis. *European Journal of Operational Research*, 154(3), pp.691-709. Available at: https://doi.org/10.1016/S0377-2217(02)00814-7.

Bozanic, D., Tešić, D., Komazec, N., Marinković, D. & Puška, A. 2023. Interval fuzzy AHP method in risk assessment. *Reports in Mechanical Engineering*, 4(1), pp.131-140. Available at: https://doi.org/10.31181/rme040122082023b.

Budowle, R., Porter, C.M. & McLennan, C. 2023. Justice and equity approaches to college and university student food (in)security. *Journal of Agriculture, Food Systems, and Community Development*, 12(2), pp.3-9. Available at: https://doi.org/10.5304/jafscd.2023.122.013.

Charnes, A., Clark, C.T., Cooper, W.W. & Golany, B. 1984. A developmental study of data envelopment analysis in measuring the efficiency of maintenance

units in the U.S. air forces. *Annals of Operations Research*, 2, pp.95-112. Available at: https://doi.org/10.1007/BF01874734.

Charnes, A., Cooper, W.W. & Rhodes, E. 1978. Measuring the efficiency of decision making units. *European Journal of Operational Research*, 2(6), pp.429-444. Available at: https://doi.org/10.1016/0377-2217(78)90138-8.

Charnes, A., Cooper, W.W. & Rhodes, E. 1981. Evaluating Program and Managerial Efficiency: An Application of Data Envelopment Analysis to Program Follow Through. *Management Science*, 27(6), pp.668-697. Available at: https://doi.org/10.1287/mnsc.27.6.668.

Cohen, E., Mesika, R. & Schwartz, Z. 1998. A multidimensional approach to menu sales mix analysis. *Praxis*, 2(1), pp.130-144.

Cooper, W.W., Seiford, L.M., Tone, K. & Zhu, J. 2007. Some models and measures for evaluating performances with DEA: past accomplishments and future prospects. *Journal of Productivity Analysis*, 28, pp.151-163. Available at: https://doi.org/10.1007/s11123-007-0056-4.

Crino, J.R. 1996. Measuring the efficiency of U.S. Army combat units: an application of data envelopment analysis. *MINES Repository* [online]. Available at: http://hdl.handle.net/11124/14792 [Accessed: 05 August 2024].

De Ridder, D., Kroese, F., Evers, C., Adriaanse, M. & Gillebaart, M. 2017. Healthy diet: Health impact, prevalence, correlates, and interventions. *Psychology and Health*, 32(8), pp.907-941. Available at: https://doi.org/10.1080/08870446.2017.1316849.

Drewnowski, A. 2009. Defining Nutrient Density: Development and Validation of the Nutrient Rich Foods Index. *Journal of the American College of Nutrition*, 28(4), pp.421S-426S. Available at. https://doi.org/10.1080/07315724.2009.10718106.

Fang, C.Y. & Hsu, F.S. 2014. An Efficiency-Based Metafrontier Approach To Menu Analysis. *Journal of Hospitality and Tourism Research*, 38(2), pp.199-221. Available at: https://doi.org/10.1177/1096348012451461.

Hadad, Y., Friedman, L., Hanani, M.Z. 2007. Measuring efficiency of restaurants using the data envelopment analysis methodology. *Computer Modelling and New Technologies*, 11(4), pp.25-35 [online]. Available at: http://cmnt.lv/upload-files/ns_3911_4_cmnt2007.pdf#page=26 [Accessed: 05 August 2024].

Hanson, T. 2016. Efficiency and productivity in the operational units of the armed forces: A Norwegian example. *International Journal of Production Economics*, 179, pp.12-23. Available at: https://doi.org/10.1016/j.ijpe.2016.05.016.

Hayes, D.K. & Huffman, L. 1985. Menu Analysis: A Better Way. *Cornell Hotel and Restaurant Administration Quarterly*, 25(4), pp.64-70. Available at: https://doi.org/10.1177/001088048502500412.

Horton, B.W. 2001. Labor and Menu Category: Effects on Analysis. *Hospitality Review*, 19(2), art.number:4 [online]. Available at: https://digitalcommons.fiu.edu/hospitalityreview/vol19/iss2/4 [Accessed: 05 August 2024].

Kasavana, M.L. & Smith, D.I. 1982. *Menu Engineering: A Practical Guide to Menu Analysis*. Lansing, MI, USA: Hospitality Publications. ISBN: 9780932235015.

Lai, H.B.J., Karim, S., Krauss, S.E. & Ishak, F.A.C. 2019. Can restaurant revenue management work with menu analysis? *Journal of Revenue and Pricing Management*, 18, pp.204-212. Available at: https://doi.org/10.1057/s41272-019-00194-6.

LeBruto, S.M., Quain, W.J. & Ashley, R.A. 1995. Menu Engineering: A Model Including Labor. *Hospitality Review*, 13(1), art.number:5 [online]. Available at: https://digitalcommons.fiu.edu/hospitalityreview/vol13/iss1/5/ [Accessed: 05 August 2024].

Milenkov, M.A., Sokolović V.S., Milovanović V.R. & Milić, M.D. 2020. Logistics: Its role, significance and approaches. *Vojnotehnički glasnik/Military Technical Courier*, 68(1), pp.79-106. Available at: https://doi.org/10.5937/vojtehg68-24805.

Miller, J.E. 1996. *Menu Pricing & Strategy, 4th Edition*. Wiley. ISBN: 978-0471287476.

Morrison, P. 1996. Menu engineering in upscale restaurants. *International Journal of Contemporary Hospitality Management*, 8(4), pp.17-24. Available at: https://doi.org/10.1108/09596119610119949.

Nemeschansky, B., von der Heiden, T. & Kim, P.B. 2020. Customer-driven menu analysis (CDMA): Capturing customer voice in menu management. *International Journal of Hospitality Management*, 91, art.number:102417. Available at: https://doi.org/10.1016/j.ijhm.2019.102417.

Okromtchedlishvili, I. 2022. Using Data Envelopment Analysis (DEA) for measuring efficiency in the defense sector. *Defense and Security Studies*, 3, pp.83-100. Available at: https://doi.org/10.37868/dss.v3.id199.

Pavesic, D.V. 1983. Cost/margin analysis: a third approach to menu pricing and design. *International Journal of Hospitality Management*, 2(3), pp.127-134. Available at: https://doi.org/10.1016/0278-4319(83)90033-6.

Schinkel, K.R., Budowle, R., Porter, C.M., Dai, B., Gifford, C. & Keith, J.F. 2023. Service, Scholarship, and Sacrifice: A Qualitative Analysis of Food Security Barriers and Strategies among Military-Connected Students. *Journal of the Academy of Nutrition and Dietetics*, 123(3), pp.454-465. Available at: https://doi.org/10.1016/J.JAND.2022.07.002.

Schulze, M.B., Martínez-González, M.A., Fung, T.T., Lichtenstein, A.H. & Forouhi, N.G. 2018. Food based dietary patterns and chronic disease prevention. *BMJ*, 361, k2396. Available at: https://doi.org/10.1136/BMJ.K2396.

Taylor, J., Reynolds, D. & Brown, D.M. 2009. Multi-factor menu analysis using data envelopment analysis. *International Journal of Contemporary Hospitality Management*, 21(2), pp.213-225. Available at: https://doi.org/10.1108/09596110910935705.

Tom, M. & Annaraud, K. 2017. A fuzzy multi-criteria decision making model for menu engineering. In: *2017 IEEE International Conference on Fuzzy Systems*

(FUZZ-IEEE), Naples, Italy, pp.1-6, July 09-12. Available at: https://doi.org/10.1109/FUZZ-IEEE.2017.8015612.

Xie, Q., Zhu, Y., Shang, H. & Li, Y. 2021. Variations on the theme of slacks-based measure of efficiency: Convex hull-based algorithms. *Computers & Industrial Engineering*, 159, art.number:107474. Available at: https://doi.org/10.1016/j.cie.2021.107474.

Un modelo para evaluar el desempeño del menú en organizaciones de nutrición colectiva basado en el método DEA

Slaviša N. Arsić[a], **autor de correspondencia**, *Dragan* S. Pamučar[b], *Marjan* A. Milenkov[c], *Vlada* S. Sokolović[c], *Miljojko* M. Janošević[d]

[a] Universidad de Defensa en Belgrado, Academia Militar, Sección de Logística, Belgrado, República de Serbia

[b] Universidad de Belgrado, Facultad de Ciencias Organizacionales, Departamento de Investigación de Operaciones y Estadística, Belgrado, República de Serbia

[c] Universidad de Defensa de Belgrado, Academia Militar, Departamento de Logística, Belgrado, República de Serbia

[d] Unión - Universidad Nikola Tesla, Facultad de Estudios Empresariales y Derecho, Belgrado, República de Serbia

CAMPO: investigación de operaciones, logística, gestión de ingeniería
TIPO DE ARTÍCULO: artículo científico original

Resumen:

Introducción/objetivo: En el artículo se presenta un modelo para evaluar el desempeño del menú en organizaciones de nutrición colectiva, que permite cuantificar la eficiencia de cada plato individual.

Métodos: Se ha aplicado el método de Análisis Envolvente de Datos (DEA) para evaluar la eficiencia de los platillos.

Resultados: El modelo ha sido probado con éxito en el menú del restaurante de nutrición colectiva para cadetes de la Academia Militar de Belgrado (MAB). La evaluación incluyó 20 platillos existentes y 11 platillos sustitutos formados utilizando la Tabla de Reemplazo de Alimentos (FRT), lo que permite conocer la eficiencia de cada platillo individual. De acuerdo con los criterios especificados, 10 de un total de 31 platillos han sido evaluados como eficientes (7 platillos existentes y 3 de sustitución). Al reemplazar los platillos existentes ineficientes por platillos nuevos y eficientes, la eficiencia general del menú aumentará, lo que implicará una mayor satisfacción de los usuarios de los alimentos y una reducción del desperdicio de comidas preparadas y no consumidas.

Conclusión: El modelo propuesto puede aplicarse en la práctica porque proporciona valores objetivos y medibles para evaluar el desempeño de los

platillos, con el objetivo de optimizar la variedad del menú en organizaciones de nutrición colectiva y reducir las deficiencias de la toma de decisiones subjetiva en la selección de comidas sustitutivas. Este modelo se puede mejorar aún más mediante el uso de otros métodos diferentes para determinar las ponderaciones de los criterios y la clasificación.

Palabras claves: evaluación de menús, gestión de restaurantes, método DEA, nutrición colectiva.

Модель оценки эффективности меню на предприятиях общественного питания, основанная на методе DEA

Славиша Н. Арсич[а], **корреспондент**, *Драган* С. Памучар[б],
Марьян А. Миленков[в], *Влада* С. Соколович[в], *Милойко* М. Яношевич[г]

[а] Университет обороны в г. Белград, Военная академия,
   отделение логистики, г. Белград, Республика Сербия

[б] Белградский университет, факультет организационных наук,
   кафедра исследований операций и статистики,
   г. Белград, Республика Сербия

[в] Университет обороны в г. Белград, Военная академия,
   кафедра логистики, г. Белград, Республика Сербия

[г] Университет «Юнион - Никола Тесла»,
   Факультет бизнес-исследований и права, г. Белград, Республика Сербия

Резюме:

Введение/цель: В статье представлена модель оценки эффективности меню на предприятиях общественного питания, позволяющая количественно оценить эффективность каждого отдельного блюда.

Методы: Для оценки эффективности блюд был применен анализ свертки данных (DEA).

Результаты: Модель была успешно протестирована на меню столовой для кадетов Военной академии в Белграде. Оценка включала 20 существующих блюд и 11 заменяемых блюд, составленных с использованием Таблицы замены продуктов, что позволило получить представление об эффективности каждого отдельного блюда. В соответствии с указанными критериями 10 из 31 блюда были оценены как эффективные (7 существующих и 3 заменяемых блюда). Заменив неэффективные существующие блюда новыми эффективными блюдами, общая эффективность меню увеличится, что приведет к большему удовлетворению

пользователей питания и сокращению отходов приготовленных, но не съеденных блюд.

Вывод: Предложенная модель может быть применена на практике, так как она предоставляет объективные и измеримые значения для оценки эффективности блюд, направленные на оптимизацию ассортимента меню на предприятиях общественного питания. Также такая модель уменьшит недостатки, связанные с субъективным принятием решений при выборе заменяемых блюд. Эта модель может быть дополнительно улучшена за счет использования и других методов для определения весовых коэффициентов и ранжирования.

Ключевые слова: оценка меню, управление предприятием общественного питания, метод DEA, общественное питание.

Модел за евалуацију перформанси јеловника у организацијама колективне исхране заснован на методи DEA

Славиша Н. Арсић[a], **аутор за преписку**, *Драган* С. Памучар[б], *Марјан* А. Миленков[в], *Влада* С. Соколовић[в], *Миљојко* М. Јаношевић[г]

[a] Универзитет одбране у Београду, Војна академија, Одељење за логистику, Београд, Република Србија

[б] Универзитет у Београду, Факултет организационих наука, Катедра за операциона истраживања и статистику, Београд, Република Србија

[в] Универзитет одбране у Београду, Војна академија, Катедра логистике, Београд, Република Србија

[г] Универзитет „Унион – Никола Тесла", Факултет за пословне студије и право, Београд, Република Србија

ОБЛАСТ: операциона истраживања, логистика, инжењерски менаџмент
ВРСТА ЧЛАНКА: оригинални научни рад

Сажетак:

Увод/циљ: У раду је приказан модел за евалуацију перформанси јеловника у организацијама колективне исхране, који омогућава квантификацију ефикасности сваког појединачног јела.

Методе: За оцену ефикасности јела примењена је метода DEA.

Резултати: Модел је успешно тестиран на менију ресторана колективне исхране кадета Војне академије у Београду. Евалуација је обухватила 20 постојећих јела и 11 заменских јела формираних коришћењем Таблица замене, омогућавајући увид у ефикасност сваког појединачног јела. У складу са наведеним критеријумима, 10 од укупно 31 јела оцењено је као ефикасно (7 постојећих и 3 заменска). Заменом неефикасних постојећих јела новим ефикасним јелима повећаће се укупна ефикасност јеловника, чиме ће се

повећати задовољство корисника хране и смањити расипање припремљених а непоједених јела.

Закључак: Предложени модел може се применити у пракси, јер даје објективне и мерљиве вредности за процену перформанси оброка ради оптимизације асортимана менија у организацијама колективне исхране и смањења недостатака субјективног одлучивања у избору заменског оброка. Овај модел се може додатно унапредити употребом других различитих метода за одређивање тежине критеријума и рангирања.

Кључне речи: евалуација менија, ресторански менаџмент, метода DEA, колективна исхрана.

Analytical and numerical methods for estimating the probability of interlaminar fracture in Mode I of composite structures under the peel test

Nadia Benchaib[a], *Belaïd* Mechab[b],
Malika Medjahdi[c], *Aicha* Metehri[d],
Mokadem Salem[e], *Bel Abbes* Bachir Bouiadjra[f]

University of Sidi Bel Abbes,
Sidi Bel Abbès, People's Democratic Republic of Algeria

[a] Faculty of Technology, Mechanical Engineering Department,
   Laboratory of Physical Mechanics of Materials,
   e-mail: benchaibnadia95@gmail.com,
   ORCID iD: https://orcid.org/0009-0005-8797-2279

[b] Faculty of Technology, Mechanical Engineering Department,
   Laboratory of Physical Mechanics of Materials,
   e-mail: bmechab@yahoo.fr,
   ORCID iD: https://orcid.org/0009-0000-7483-5527

[c] Laboratory of Applications of Plasmas, Electrostatics and
   Electromagnetic Compatibility,
   e-mail: mmedjahdi@yahoo.fr,
   ORCID iD: https://orcid.org/0000-0003-2940-4538

[d] Faculty of Technology, Mechanical Engineering Department,
   Laboratory of Physical Mechanics of Materials,
   e-mail: ametehri@yahoo.com, **corresponding author**,
   ORCID iD: https://orcid.org/0009-0002-2221-6833

[e] Faculty of Technology, Mechanical Engineering Department,
   Laboratory of Physical Mechanics of Materials,
   e-mail: moka_salem@yahoo.fr,
   ORCID iD: https://orcid.org/0000-0001-7558-714X

[f] Faculty of Technology, Mechanical Engineering Department,
   Laboratory of Physical Mechanics of Materials,
   e-mail: bachirbou@yahoo.fr,
   ORCID iD: https://orcid.org/0000-0002-1925-7194

Abstract:

Introduction/purpose: The present work utilizes a numerical and analytical approach to predict the likelihood of interlaminar fracture in Mode I of a composite structure under the peel test.

1601

Methods:The finite element approach, which incorporates the Virtual Crack Closure (VCCT) method, is utilized to examine the delamination of the composite structure. The research investigated the effects of many aspects, including dimension, fiber alignment, and composite properties.

Results: The numerical results significantly concur with the analytical solution recorded in the current body of literature. The Monte Carlo technique predicts the distribution function of composite damage. As previously stated, the probability of structural failure is assessed by considering both the model's uncertainty and the statistical uncertainty linked to the essential variables.

Conclusion: The probability density function (pdf) is derived by fitting specific theoretical models to the histogram. The durability of composite structures is primarily dependent on their mechanical properties.

Keywords: composite, delamination, peel test, VCCT method, durability.

Introduction

Composite structures are frequently employed in the aerospace, construction, and automotive sectors to enhance the stiffness of various elements. The degradation process of composite laminates leads to their collapse over time. Load redistribution resulting from local failure leads to the accumulation of different failure modes, hence compromising the stiffness of the composite material, diminishing its load-bearing capacity, and ultimately resulting in overall failure (Kishore et al, 2021; Hatti et al, 2022). The primary constraint in advancing composite materials for aeronautical applications has consistently been the challenges associated with accurately forecasting damage events and understanding their interactions (Ibrahim et al, 2018; Mechab et al, 2016; Serier et al, 2016). The capacity of a design to mitigate damage and prevent severe structural failure during flight or ground loads is frequently constrained by the tendency for delamination in traditional laminated fiber-reinforced polymer (FRP) constructions (Das et al, 2021).

Delamination arises from elevated interlaminar stresses, typically caused by impact (De Carvalho et al, 2015), deviations in material and structure (Fotouhi et al, 2020), or the propagation of further types of harm. Within the aerospace industry, using design features like stiffener terminations and ply-drops to modify thickness can result in multiple regions of an aircraft that are subjected to elevated interlaminar stresses. (Jokinen & Kanerva, 2019; Krueger, 2015). Hence, delamination is frequently identified as the primary failure mode in composite airframe design (Rybicki & Kanninen, 1977). The load capacity of a structure is typically negatively impacted by delamination damage, especially when

exposed to compressive stress circumstances. Delaminations result in reduced buckling loads (Madukauwa-David & Drissi-Habti, 2016). The visible detection of delaminations is frequently challenging, and in the majority of instances, internal delamination can only be identified by non-destructive inspection (NDI) techniques like ultrasound (Kaźmierczyk et al, 2022; Gliszczyński & Kubiak, 2017).

Several different approaches are used to predict and analyze composite delamination. Among these methods is the Virtual Crack Closure Technique (VCCT), which allows for the prediction of the delamination growth from the first crack and includes both the delamination initiation and growth (Rozylo, 2021; Yu et al, 2021). The VCCT technique requires mesh size improvements and measuring the critical strain energy release rate. Many authors have used the VCCT method to evaluate the delamination spread in composite structures subjected to different loading scenarios or impacts at low velocities (Rozylo, 2022; Debski et al, 2021). However, the limitations resulting from the discretization of the numerical model continue to impede the application of the VCCT-based computational methodologies for damage prediction and aircraft structure design (Aveiga & Ribeiro, 2018; Rozylo et al, 2021; Cepero et al, 2019; Turon et al, 2010). This work aims to predict when delamination will occur in Composite Structure Mode I under shear stress circumstances. This study aimed to analyse the mode I interlaminar fracture tests on unidirectional laminates under the peel test. The Virtual Crack Closure Technique (VCCT) uses the finite element method to assess a structure's delamination. The impact of fiber orientation, thickness, and properties of the composite beam is investigated in this work. The Monte Carlo method is used to predict the distribution function of the composite damage.

Material and geometric model

This study presents interlaminar fracture in Mode I of the composite structure under the peel test. The thickness of the composite beam ranges from 1 mm to 3 mm, and the length is L=120 mm. The pre-crack a=25 mm and Widthb=20mm.The diagram illustrates the geometric characteristics and the applied load on the composite beam. A single load cell was used for the test with displacement control at a 0.5 mm/min speed. The developed composite structure exhibited a symmetrical stacking sequence of laminate layers. [0/30/-30/0] s, [0/90/0/90] s, [0/45/-45/0] s, [90/0/90/0] s.
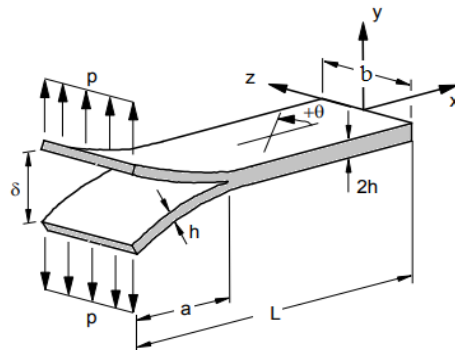
Figure 1 – Geometrical model

Tables 1 and 2 show the mechanical properties of the material used in this study.

Table 1 – Mechanical properties of different materials (Salem et al, 2015)

	E_1 (GPa)	E_2 (GPa)	E_3 (GPa)	v_{12}	v_{13}	v_{23}	G_{12} (GPa)	G_{13} (GPa)	G_{23} (GPa)
Carbon/epoxy	120.0	10.5	10.5	0.3	0.3	0.5	5.25	5.25	3.48
Glass/epoxy	45.6	16.2	16.2	0.278	0.278	0.4	5.83	5.83	4.5

Table 2 – Mechanical interface properties of different composites (Turon et al, 2010)

	G_{Ic} (kj/m^2)	G_{IIc} (kj/m^2)	η
Carbon/epoxy	0,260	1.002	2
Glass/epoxy	0.118	2.905	Two .6

FE Model

The numerical model using the VCCT was generated using ABAQUS (Dassault Systems, The 3D EXPERIENCE platform, 2014) in this investigation. The schematic depicted in Figure 2 illustrates the numerical model subjected to mechanical load. The study employed solid finite elements (C3D8R) with a regular hexagonal mesh. Every element consists of eight nodes, each having three degrees of freedom. The shape function is linear, and the integration is lowered. The discrete model consisted of 16.250 elements, specifically linear hexahedral elements of type C3D8R, and 35.620 nodes. The boundary conditions were applied to the upper (point A) item, allowing for movement only in the direction of the composite

beam with respect to the Y-axis, and at (point B) given embedded. Figure 2 represents the boundary conditions and the discrete model.
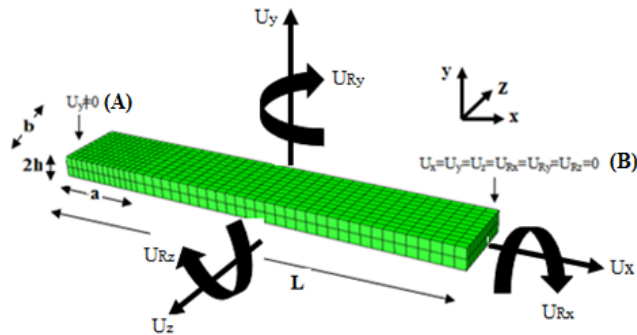
Figure 2 – Mesh and boundary conditions of the structure

Analytical formulation

The VCCT formulation

The VCCT employs an LEFM (Linear Elastic Fracture Mechanics) based method for forecasting the propagation of cracks in epoxy fiber-reinforced composites commonly used to construct aircraft structural elements. The VCCT, as introduced by Rybicki and Kanninen (1977) offers a notable reduction in the computational cost of the analysis compared to the previous method.

For sufficiently small values of (Δa), implying a finely meshed scenario where fracture propagation is anticipated, the extension of delamination from (a+Δa) (node l) to (a+2Δa) (node i) in the three-dimensional problem illustrated in Figure 3 (Rybicki & Kanninen, 1977) does not significantly impact the state at the crack tip. Consequently, the displacements behind the extended crack tip at node (i) are approximately equal to those behind the original crack tip at node (l). The strain energy release rate predictions will utilize equations (1, 2, and 3).

The components of Mode-I, Mode-II, and Mode-III strain energy release rates, denoted as GI, GII, and GIII, are determined as follows:

$$G_I = \frac{1}{2\Delta A} Y_{Li} \left(v_{Ll} - v_{Ll*} \right) \tag{1}$$

$$G_{II} = \frac{1}{2\Delta A} X_{Li} \left(u_{Ll} - u_{Ll*} \right) \tag{2}$$

$$G_{III} = \frac{1}{2\Delta A} Z_{Li}\left(w_{Ll} - w_{Ll*}\right)$$ (3)

where ($\Delta A = b.\Delta a$) represents the virtually closed area, with s being the width of the elements at the delamination front. In Figure 3, the columns are designated by capital letters, and the rows are identified by small letters. Thus, (X_{Li}), (Y_{Li}), and (Z_{Li}) denote the forces at the delamination front in the column L, row i.

The corresponding displacements behind the delamination at the top face in row l are denoted (u_{Ll}, v_{Ll}, and w_{Ll}), while at the lower face in row l*, they are denoted (u_{Ll*}), (v_{Ll*}), and (w_{Ll*})
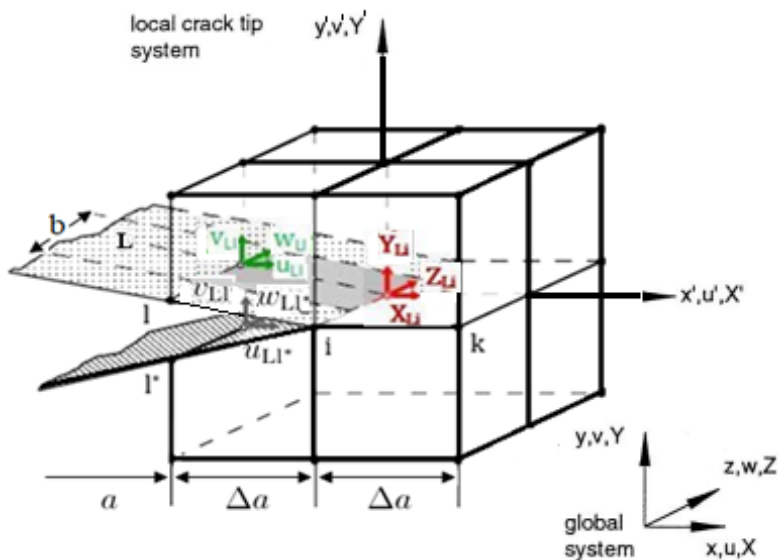
Figure 3 – The virtual crack closure technique (VCCT) for 3D solid elements (Rybicki & Kanninen, 1977)

Griffith's (1921) fracture theory obtained the fracture toughness values, KC, for a wide range of materials. Under the assumption of the plane stresses condition, the stress intensity factor K is related to the strain energy release rates G by the following expressions:

$$K_I = \sqrt{G_I E}$$ (4)

$$K_{II} = \sqrt{G_{II} E}$$ (5)

1606

while the assumption of a plane strain condition yields

$$K_{\mathrm{I}} = \sqrt{\frac{G_{\mathrm{I}} E}{1 - \upsilon^2}} \qquad (6)$$

$$K_{II} = \sqrt{\frac{G_{\mathrm{II}} E}{1 - \upsilon^2}} \qquad (7)$$

$$K_{\mathrm{III}} = \sqrt{\frac{G_{\mathrm{III}} E}{1 - \upsilon^2}} \qquad (8)$$

The total energy release rate (G_T), assessed at a specific point along the delamination front, attains a critical value denoted as (G_C), representing the material's mixed-mode fracture toughness.

$G_T \geq G_C \Rightarrow$ Delamination propagation

Various criteria are accessible for establishing a precise estimation of (G_C). Concerning (G_T), it can be computed as the summation of the nodal energy release rates for pure Mode I (opening), Mode II (sliding), and Mode III (scissoring).

$$f = \frac{G_T}{G_{I_C} + \left(G_{II_C} - G_{I_C} \right) * \left(\dfrac{G_{II} + G_{III}}{G_T} \right)^{\eta}} \geq 1.0 \qquad (9)$$

$$G_T = G_{\mathrm{I}} + G_{\mathrm{II}} + G_{\mathrm{III}} \qquad (10)$$

where: G_{I}, G_{II}, and G_{III} are respectively the Mode I, II, and III energy release rates, respectively.
  f: the effective energy release rate ratio
  η: the material constant

Analytical solution for the mode I DCB test

The analytical solution for the end-notched flexure specimens (ENF) test can be split into the three stages of the load-displacement curve. The load and displacement can be calculated with the following equations:

The necessary force P for crack propagation is given by

$$P = \sqrt{\frac{G_{IC}b^3h^3E_{11}}{12(a + \chi h)^2}} \tag{11}$$

χ can be calculated as

$$\chi = \sqrt{\frac{E_{11}}{11G_{13}}\left\{3 - 2\left(\frac{\Gamma}{1+\Gamma}\right)^2\right\}} \tag{12}$$

where Γ is the transverse modulus correction parameter and can be obtained using

$$\Gamma = 1.18\sqrt{\frac{E_{11}E_{22}}{G_{13}}} \tag{13}$$

The corresponding displacement δ is given by

$$\delta = P\frac{8(a + \chi h)^3}{bh^3E_{11}} \tag{14}$$

where (G_{IC}) is the critical mode I strain energy release rate, (B) is the width of the test sample, (h) is the half of the thickness of the sample, (E1) is the longitudinal Young's modulus, (P) is the applied force, (a) is the crack length, and (L) is the half of the span.

Results and discussion

Validation of the model

Figure 5 demonstrates that the force-displacement curve of the FEM findings closely aligns with the analytical solution for all two types of materials. We note that the numerical results are in good agreement compared with the analytical solution found in the literature (equation (14)). The force exhibits a linear relationship with the applied displacement in the first loading phase. Upon achieving the maximum load, a sudden decrease in force suggests unstable delamination crack growth.
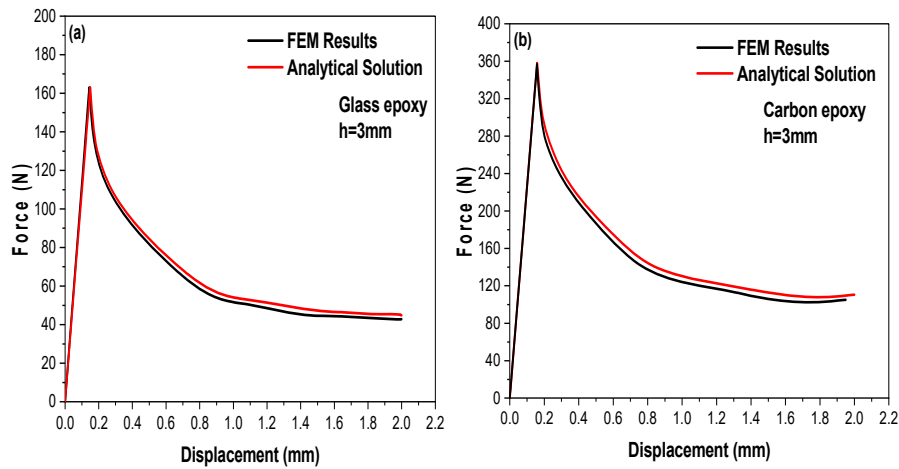
Figure 4 – Curve force displacement in Mode I of the FEM results compared with the analytical solution

Effect of the properties of the composite

The force-displacement curves for different materials, such as carbon/epoxy and glass/epoxy, are depicted in Figure 5. The force demonstrates a linear augmentation of the applied displacement during the initial loading period. After attaining the maximum load, a rapid decrease occurs, suggesting an unstable expansion of the delamination fracture.

The carbon/epoxy beam provides good fracture resistance compared to glass/epoxy beams and this composite increases the service life of the composite beam. Upon analyzing the energy distribution inside the delamination zone depicted in Figure 6, it is worth mentioning that the carbon/epoxy material demonstrates a lower energy value for (G_I) than the glass/epoxy. This characteristic contributes to an increased ability of the composite structure to withstand failure.
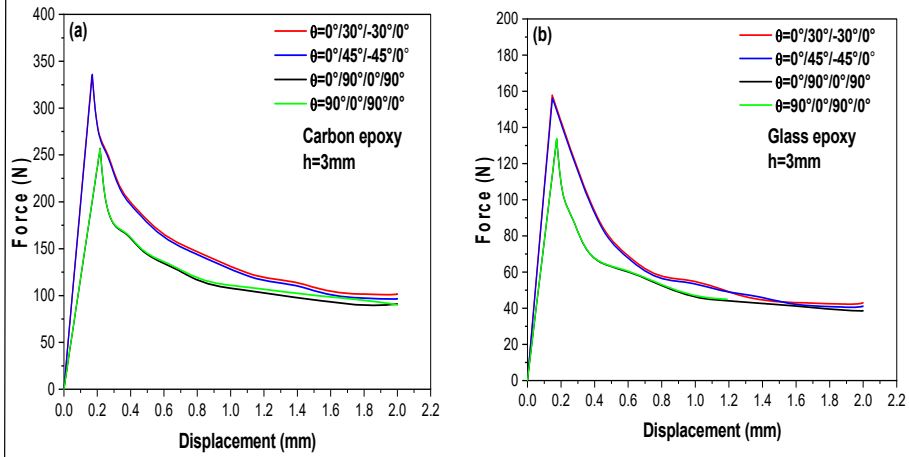
Figure 5 – Curve force-displacement in Mode I for different properties of the composite
.
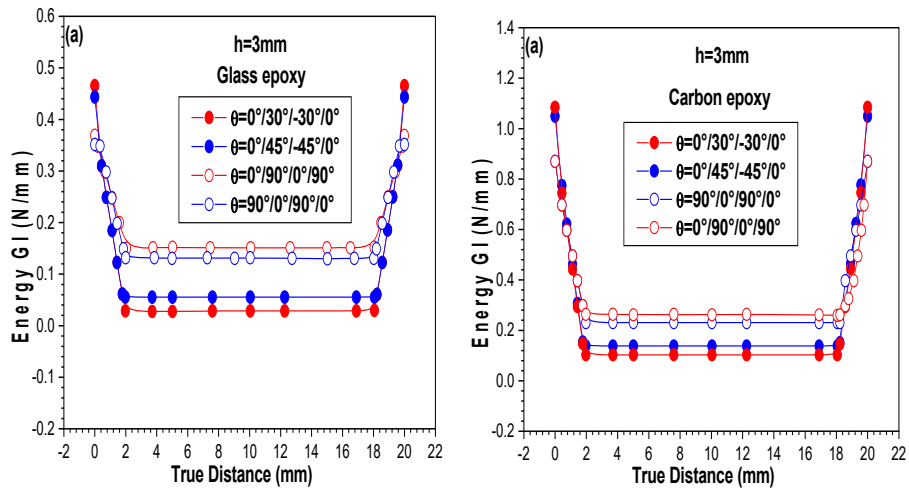
Figure 6 – Curve Energy (G_I) according to the true distance different properties of the composite

1610

Effect of fiber orientation

This section of the study investigates the impact of fiber orientation in laminates as a determining factor that can enhance structural resistance against damage. The load transfer inside the delamination zone is facilitated by its rigidity, which is achieved through the alignment of the fibers. Consequently, the aim is to assess the amount of the braking force by adjusting the stiffness of the composite material.

Figure 7 illustrates the curve force-displacement for four different fiber orientations, namely [0/30/-30/0]s, [0/45/-45/0]s, [90/0/90/0]s, and [0/90/0/90]s, to evaluate the performance of the fiber orientation. The results indicate that the orientation [0/30/-30/0] exhibits superior performance in comparison to the other three orientations, namely [0/45/-45/0]s, [90/0/90/0]s, and [0/90/0/90]s, respectively.

The energy distribution along the delamination zone, as depicted in Figure 8, reveals that the energy value of (GI) is comparatively smaller for [0/30/30/0]s than in the other three samples. This observation confirms the plate's resistance to failure for [0/30/30/0]s.
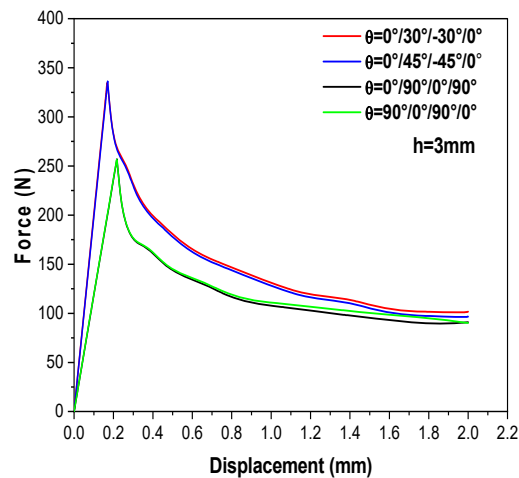
Figure 7 – Curve force-displacement in Mode I for different fiber orientations of carbon epoxy
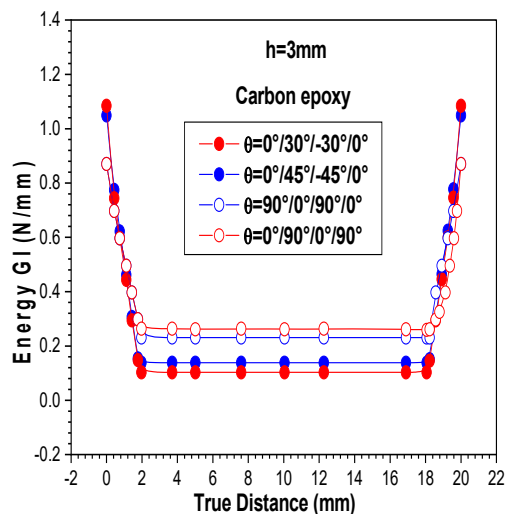
Figure 8 – Curve Energy (GI)according to the true distance for different fiber orientations for a thickness, h=3mm

Effect of the thickness of the composite

The force-displacement curves of the specimens at various thicknesses, specifically 1, 2, and 3mm, are depicted in Figure 9. In the initial loading phase, the force exhibits a linear relationship with the increment in applied displacement. The load experiences a sudden decrease following the peak load, suggesting the presence of unstable delamination crack propagation. The beam with a thickness equal to 3 mm gives excellent performance superior to those of beams with a thickness of 1 mm and 2 mm, respectively, because to reach the beam fracture for a thickness equal to 3 mm, it is necessary to apply a force higher than 300N compared to that applied to the beams of thickness 1 mm and 2 mm which are significantly lower.

Figure 10 illustrates the energy distribution along the delamination zone. It is evident that at a thickness of h=3mm, the energy value of (G_l) is lower than that for other thicknesses. This decrease in energy value enhances the composite structure's resistance to failure.
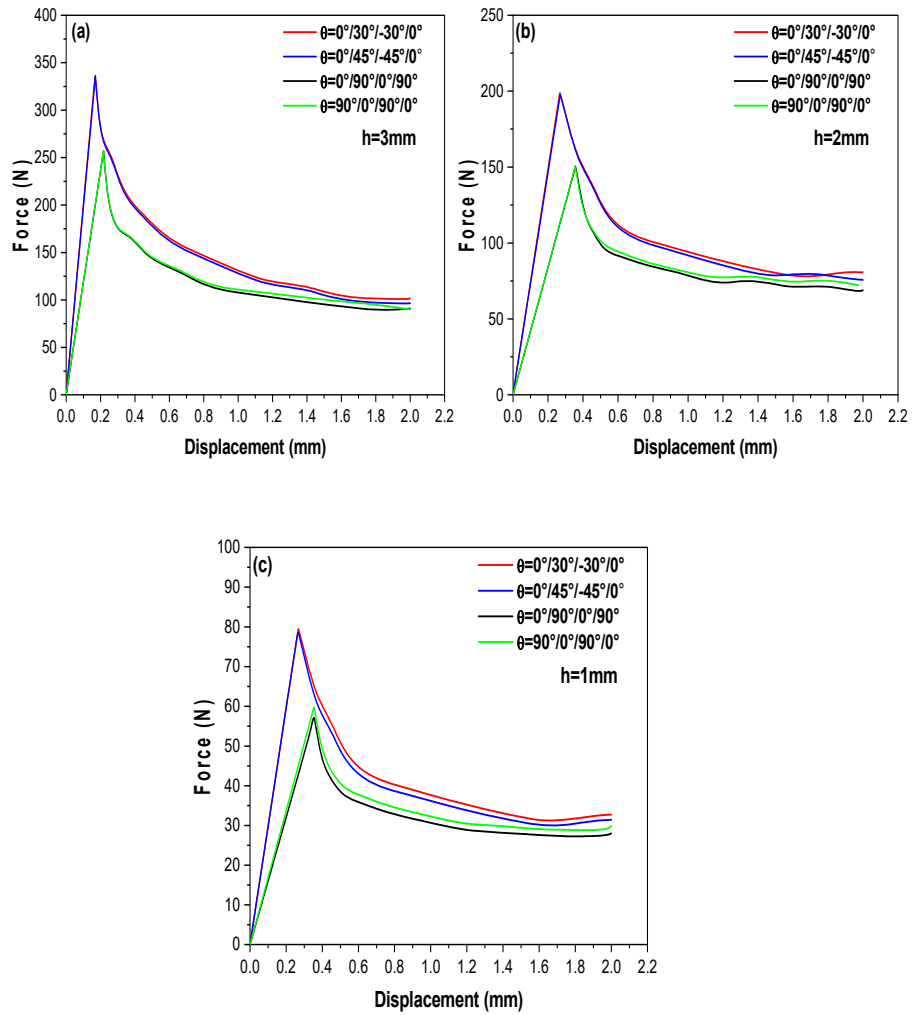
Figure 9 – Curve force displacement in Mode I for three different thicknesses of carbon epoxy
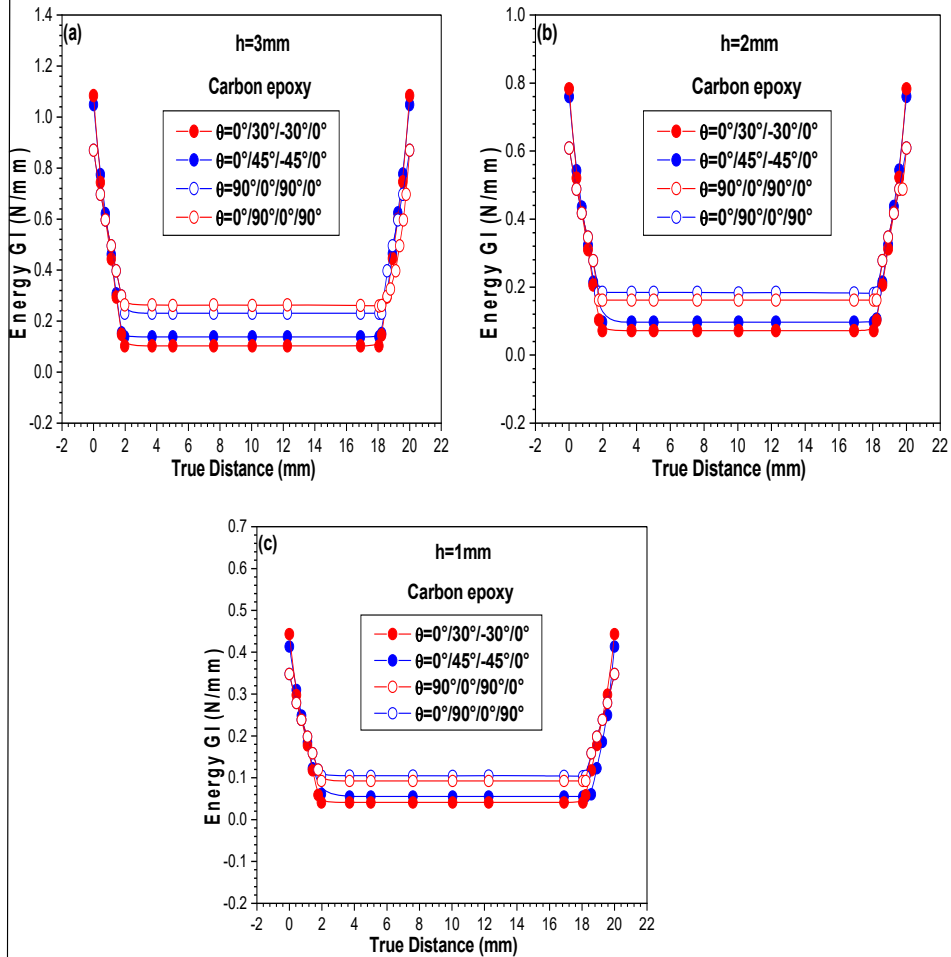
Figure 10 – Curve Energy GI according to the true distance for different thicknesses of carbon epoxy

Analytical solution of the prediction of delamination

To comprehend the significance of the random variables, it is imperative to initially examine the sensitivity of the displacement $\delta(x)$ concerning the uncertainties associated with the input parameters (refer to

Table 2). By calculating the dispersion of the mechanical reaction about the scatter of the input parameters, it is possible to derive sensitivity measurements. The authors have integrated two FORTRAN programs to analyze the multi-layered composite pipe. The first program computes the mechanical response by determining the stress distribution, while the second program employs Monte Carlo simulations to calculate the probabilistic response. To ensure a high level of accuracy in the obtained results, a total of 105 simulations were conducted.

The abovementioned factors are denoted as stochastic variables that exhibit distinct distribution classes and parameters. Effectively handling the uncertainties present in the system is crucial to guarantee safety in the design process, thus averting hazardous circumstances. Plate uncertainties connected with geometry (Length (L) and thickness (h)) and material properties (Young's modulus (E) and fiber orientation (θ)) are modeled using eight random variables.

Table 1 – Random variables and the corresponding parameters

Variable	Mean	Coefficient of variation (COV)
E (MPa)	120. 10^3	1%
L (mm)	120mm	2%
B (mm)	20mm	2%
h (mm)	3mm	2%
θ(°)	0°/30°/-30°/0°	2%

The histogram plot of the displacement $\delta(x)$ obtained from the Monte Carlo simulations is depicted in Figure 11. The calculation of the probability density function (pdf) involves the process of fitting a theoretical model to the histogram. The Gaussian distribution is a reliable approximation of the displacement $\delta(x)$ probability density function, accurately estimating the average, as seen in Figure 11.

Figure 12 displays the failure probability for the displacement $\delta(x)$ in different materials, specifically glass/epoxy and carbon/epoxy. It is worth mentioning that the carbon/epoxy composite has a decreased likelihood of failure compared to the glass/epoxy composite, as shown in Figure 12. The presence of uncertainties related to the type of material and the orientation of fibers significantly contributes to a notable augmentation in the margin of failure. The likelihood of failure ultimately depends on the selected materials and the orientation of the fibers.
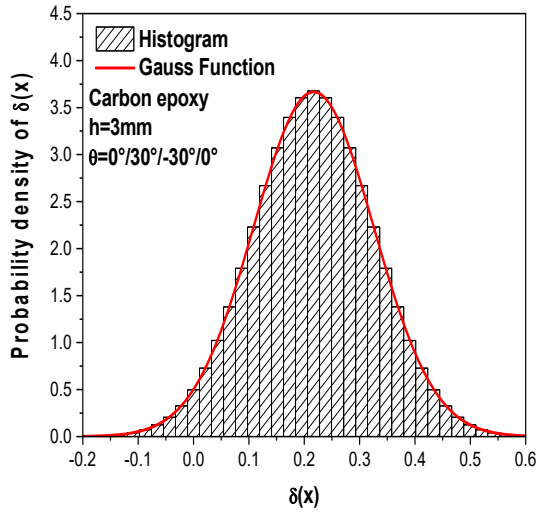
*Figure 11 – Histogram and the probability density of the displacement δ(x)
(Carbon epoxy, h=3mm, θ=0/30/-30/0)*
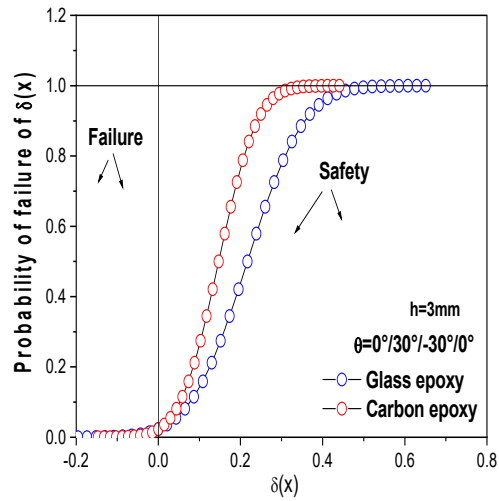
*Figure 12 – Probability of displacement failure δ(x) for different properties of the
composite*

Conclusions

Because of their exceptional stiffness and strength, composite materials are widely used in various industries, including aircraft, transportation, automotive engineering, building infrastructure, and more. The current work investigates the mechanical response of composite structures subjected to peel loading through the development of analytical and numerical methods. Our parametric analysis is more detailed and more deepened than those found in the literature.

A methodology for predicting delamination propagation of interlaminar fracture in Mode I of composite structures under the peel test with the Virtual Crack Closure Technique (VCCT) approach is proposed in this study using a three-dimensional finite element analysis of a composite beam. The effects of the properties of the composite, the fiber orientation, and the thickness are presented. The numerical results are in good agreement with those of the analytical solution found in the literature (equation 14).

The Monte Carlo method was used to predict the damage of the composite. The structure failure probability is computed, considering the statistical uncertainty associated with the fundamental variables and the model uncertainty. The probability density function, or the pdf, is obtained by fitting the histogram using theoretical models. It is important to note that the mechanical properties parameter is vital in determining the degree to which the composite structure offers increased durability.

References

Aveiga, D. & Ribeiro, M.L. 2018. A Delamination Propagation Model for Fiber Reinforced Laminated Composite Materials. *Mathematical Problems in Engineering,* 2018(1), art.number :1861268. Available at: https://doi.org/10.1155/2018/1861268.

Cepero, F, García, I.G., Justo, J., Mantič, V. & París, F. 2019. An experimental study of the translaminar fracture toughnesses in composites for different crack growth directions, parallel and transverse to the fiber direction. *Composites Science and Technology* 181, art.number:107679. Available at: https://doi.org/10.1016/j.compscitech.2019.107679.

Das, M., Sahu, S. & Parhi, D.R. 2021. Composite materials and their damage detection using AI techniques for aerospace application: A brief review. *Materials Today: Proceedings,* 44(1), pp.955-960. Available at: https://doi.org/10.1016/j.matpr.2020.11.005.

-Dassault Systems, The 3D EXPERIENCE platform. 2014. *Simulia: AbaqusFinite Element Analysis for Mechanical Engineering and Civil Engineering* [online]. Available at: https://www.3ds.com/products/simulia/abaqus [Accessed: 25 March 2024].

De Carvalho, N.V., Chen, B.Y., Pinho, S.T., Ratcliffe, J.G., Baiz, P.M. & Tay, T.E. 2015. Modeling delamination migration in cross-ply tape laminates. *Composites Part A: Applied Science and Manufacturing*, 71, pp.192-203. Available at: https://doi.org/10.1016/j.compositesa.2015.01.021.

Debski, H., Rozylo, P., Wysmulski, P., Falkowicz, K. & Ferdynus, M. 2021. Experimental study on the effect of eccentric compressive load on the stability and load-carrying capacity of thin-walled composite profiles. *Composites Part B: Engineering,* 226, art.number:109346. Available at: https://doi.org/10.1016/J.Compositesb.2021.109346.

Fotouhi, M., Damghani, M., Leong, M.C., Fotouhi, S., Jalalvand, M. & Wisnom, M.R. 2020. A comparative study on glass and carbon fiber reinforced laminated composites in scaled quasi-static indentation tests. *Composite Structures*, 245, art.number:112327. Available at: https://doi.org/10.1016/j.compstruct.2020.112327.

Gliszczyński, A. & Kubiak, T. 2017. Load-carrying capacity of thin-walled composite beams subject to pure bending. *Thin-Walled Structures*, 115, pp.76-85. Available at: https://doi.org/10.1016/j.tws.2017.02.009.

Griffith, A.A. 1921. VI. The phenomena of rupture and flow in solids. *Philosophical Transactions of the Royal Society of London. Series A, Containing Papers of a Mathematical or Physical Character*, 221, pp.163-198. Available at: https://doi.org/10.1098/rsta.1921.0006.

Hatti, P.S., Sampath Kumar, L., Somanakatti, A.B. & Rakshith, M.N. 2022. Investigation on tensile behavior of glass-fiber reinforced polymer matrix composite with varying orientations of fibers. *Materials Today: Proceedings*, 54(2), pp.137-140. Available at: https://doi.org/10.1016/j.matpr.2021.08.196.

Ibrahim, N.C., Boualem, S. & Belaïd, M. 2018. Analysis of the crack-crack interaction effect initiated in aeronautical structures and repaired by composite patch. *Frattura Ed Integrità Strutturale*, 12(46), pp.140-149. Available at: https://doi.org/10.3221/IGF-ESIS.46.14.

Jokinen, J. & Kanerva, M. 2019. Simulation of Delamination Growth at CFRP-TungstenAerospace Laminates Using VCCT and CZM Modelling Techniques. *Applied Composite Materials,* 26, pp.709-721. Available at: https://doi.org/10.1007/s10443-018-9746-5.

Kaźmierczyk, F., Urbaniak, M., Świniarski, J. & Kubiak, T. 2022. Influence of boundary conditions on the behavior of composite channel section subjected to pure bending – Experimental study. *Composite Structures*, 279, art.number:114727. Available at: https://doi.org/10.1016/j.compstruct.2021.114727.

Kishore, C., Jaiswal, R., Bhatt, V., Jugran, S., Rawat, D. & Verma, D. 2021. Analysis of glass fiber reinforced with epoxy resin using FEM. *Materials Today: Proceedings*, 46(20), pp.11120-11128. Available at: https://doi.org/10.1016/j.matpr.2021.02.273.

Krueger, R. 2015. 1 - The virtual crack closure technique for modeling interlaminar failure and delamination in advanced composite materials. In: *Woodhead Publishing Series in Composites Science and Engineering, Numerical Modelling of Failure in Advanced Composite Materials,* pp.3-53. Woodhead Publishing. Available at: https://doi.org/10.1016/B978-0-08-100332-9.00001-3.

Madukauwa-David, I. & Drissi-Habti, M. 2016. Numerical simulation of the mechanical behavior of a large, intelligent composite platform under static loads. *Composites Part B: Engineering,* 88, pp.19-25. Available at: https://doi.org/10.1016/J.Compositesb.2015.10.041.

Mechab, B., Chama, M., Kaddouri, K.& Slimani, D. 2016. Probabilistic elastic-plastic analysis of repaired cracks with bonded composite patch. *Steel and Composite Structures*, 20(6), pp.1173-1182. Available at: https://doi.org/10.12989/scs.2016.20.6.1173.

Rozylo, P. 2022. Comparison of Failure for Thin-Walled Composite Columns. *Materials*, 15(1), art.number:167. Available at: https://doi.org/10.3390/Ma15010167.

Rozylo, P. 2021. Failure analysis of thin-walled composite structures using independent advanced damage models. *Composite Structures*, 262, art.number:113598. Available at: https://doi.org/10.1016/j.compstruct.2021.113598.

Rozylo, P., Debski, H., Falkowicz, K., Wysmulski, P., Pasnik, J. & Kral, J. 2021. Experimental-Numerical Failure Analysis of Thin-Walled Composite Columns Using Advanced Damage Models. *Materials*, 14(6), art.number:1506. Available at: https://doi.org/10.3390/ma14061506.

Rybicki, E.F. & Kanninen, M.F. 1977. A finite element calculation of stress intensity factors by a modified crack closure integral. *Engineering Fracture Mechanics,* 9(4), pp.931-938. Available at: https://doi.org/10.1016/0013-7944(77)90013-3.

Salem, M., Bachir Bouiadjra, B.A., Mechab, B. & Kaddouri, K. 2015. Elastic-plastic analysis of the J integral for repaired cracks in plates". *Advances in materials Research,* 4(2), pp.87-96. Available at: https://doi.org/10.12989/AMR.2015.4.2.087.

Serier, N., Mechab, B., Mhamdia, R. & Serier, B. 2016. A new formulation of the J integral of bonded composite repair in aircraft structures. *Structural Engineering and Mechanics*, 58(5), pp.745-755. Available at: https://doi.org/10.12989/sem.2016.58.5.745.

Turon, A., Camanho, P.P., Costa, J. & Renart, J. 2010. Accurate simulation of delamination growth under mixed-mode loading using cohesive elements: Definition of interlaminar strengths and elastic stiffness. *Composite Structures*, 92(8), pp.1857-1864. Available at: https://doi.org/10.1016/J.Compstruct.2010.01.012.

Yu, Z., Zhang, J., Shen, J. & Chen, H. 2021. Simulation of crack propagation behavior of nuclear graphite by using XFEM, VCCT and CZM methods. *Nuclear Materials and Energy*, 29, art.number:101063. Available at: https://doi.org/10.1016/J.Nme.2021.101063.

Métodos analíticos y numéricos para estimar la probabilidad de fractura interlaminar en Modo I de estructuras compuestas bajo el ensayo de pelado

Nadia Benchaib[a], *Belaïd* Mechab[a],
Malika Medjahdi[b], *Aicha* Metehri[a], **autor de correspondencia**,
Mokadem Salem[a], *Bel Abbes* Bachir Bouiadjra[a]

Universidad de Sidi Bel Abbes,
Sidi Bel Abbès, República Argelina Democrática y Popular

[a] Facultad de Tecnología, Departamento de Ingeniería Mecánica,
  Laboratorio de Mecánica Física de Materiales

[b] Laboratorio de Aplicaciones de Plasmas, Electrostática y Compatibilidad
  Electromagnética

CAMPO: mecánica
TIPO DE ARTÍCULO: artículo científico original

Resumen:

Introducción/objetivo: El presente trabajo utiliza un enfoque numérico y analítico para predecir la probabilidad de fractura interlaminar en el Modo I de una estructura compuesta bajo la prueba de pelado.

Métodos: El método de elementos finitos, que incorpora el método de cierre virtual de fisuras (VCCT), se utiliza para examinar la delaminación de la estructura compuesta. La investigación exploró los efectos de muchos aspectos, incluida la dimensión, la alineación de las fibras y las propiedades del compuesto.

Resultados: Los resultados numéricos coinciden significativamente con la solución analítica registrada en el cúmulo de literatura actual. La técnica de Monte Carlo predice la función de distribución del daño compuesto. Como se indicó anteriormente, la probabilidad de falla estructural se evalúa considerando tanto la incertidumbre del modelo como la incertidumbre estadística vinculada a las variables esenciales.

Conclusión: La función de densidad de probabilidad (pdf) se obtiene ajustando modelos teóricos específicos al histograma. La durabilidad de las estructuras compuestas depende principalmente de sus propiedades mecánicas.

Palabras claves: compuesto, delaminación, prueba de pelado, método VCCT, durabilidad.

Аналитические и численные методы оценки вероятности межслойного разрушения в первом режиме композитных структур при испытании на отслаивание

Надя Бенчейб[а], *Белаид* Мехаб[а],
Малика Меджахди[б], *Айша Метери*[а], **корреспондент**,
Мокадем Салем[а], *Бел Аббас* Башир Буяжра[а]

Университет Сиди-Бель-Аббес,
Сиди-Бель-Аббес, Алжирская Народная Демократическая Республика

[а] технологический факультет, кафедра машиностроения,
 Лаборатория физической механики материалов

[б] Лаборатория применения плазмы, электростатики и электромагнитной
 совместимости

Резюме:

Введение/цель: В данной статье используется численный и аналитический подход для прогнозирования вероятности межслойного разрушения в первом режиме композитной структуре при испытании на отслаивание.

Методы: Метод конечных элементов, включающий в себя метод виртуального закрытия трещин (VCC), используется в изучении расслаивания композитной структуры. В ходе исследования были изучены многие аспекты, включая размеры, выравнивание волокон и свойства композита.

Результаты: Численные результаты в значительной степени согласуются с аналитическим решением, описанным в современной литературе. Методом Монте-Карло прогнозируется функция распределения повреждений композитных материалов. Как указывалось ранее, вероятность разрушения конструкции оценивается с учетом неопределенности модели и статистической неопределенности, связанной с основными переменными.

Вывод: Функция плотности вероятности получена путем подгонки конкретных теоретических моделей к гистограмме. Долгосрочность композитных структур в первую очередь зависит от их механических свойств.

Ключевые слова: композитные материалы, расслаивание, испытание на отслаивание, метод VCC, долговечность.

Аналитичке и нумеричке методе за процену вероватноће интерламинарног лома у Моду 1 композитних структура путем теста љуштења

Надја Бенчеј[а], *Белаид* Мехаб[а], *Малика* Меџахди[б], *Ајша* Метери[а], **аутор за преписку**, *Мукејдам* Салем[а], *Бел Аббас* Башир Бујажра[а]

Универзитет Сиди Бел Абес,
Сиди Бел Абес, Народна Демократска Република Алжир

[а] Технолошки факултет, Одсек машинства,
  Лабораторија за физичку механику материјала

[б] Лабораторија за примену плазме, електростатике и електромагнетне
  компатибилности

ОБЛАСТ: механика
КАТЕГОРИЈА (ТИП) ЧЛАНКА: оригинални научни рад

Сажетак:

Увод/циљ: У раду је коришћен нумерички и аналитички приступ за предвиђање вероватноће интерламинарног лома у Моду 1 композитне структуре током теста љуштења.

Методе: Метода коначних елемената, која укључује методу виртуелног затварања прслине (Virtual Crack Closure – VCC), користи се за испитивање деламинације композитне структуре. Истражују се ефекти многих аспеката као што су димензије, правци пружања влакана и својства композита.

Резултати: Нумерички резултати се у великој мери слажу са аналитичким решењем из актуелне литературе. Техника Монте Карло предвиђа функцију дистрибуције оштећења композита. Вероватноћа структурног лома процењује се узимањем у обзир и несигурности модела и статистичке несигурности повезане са основним варијаблама.

Закључак: Функција густине вероватноће изведена је уклапањем специфичних теоријских модела у хистограм. Трајност композитних структура зависи, пре свега, од њихових механичких својстава.

Кључне речи: композит, деламинација, тест љуштења, метода VCC, трајност.

Numerical investigation on the impact of particle density and flow velocity on particle transport and deposition in a randomly oriented fracture

Kheira Bouragaa[a], *Lyacine* Bennacer[b], *Mustapha* Akacem[c]

Adrar University, Faculty of Science and Technology, Civil Engineering Department, Adrar, People's Democratic Republic of Algeria

[a] Laboratory of Sustainable Development and IT (LDDI),
   e-mail: bourag.kheira@univ-adrar.edu.dz, **corresponding author**,
   ORCID iD: https://orcid.org/0009-0002-4908-9037

[b] Laboratory of Energy, Environment and Information Systems (LEESI),
   e-mail: lyacine.bennacer@univ-adrar.edu.dz,
   ORCID iD: https://orcid.org/0000-0002-8547-6811

[c] Laboratory of Sustainable Development and IT (LDDI),
   e-mail: akacem@univ-adrar.edu.dz,
   ORCID iD: https://orcid.org/0000-0003-4126-5788

Abstract:

Introduction/purpose: Fractured formations recently gained significant interest as a landscape for securing both energy and groundwater demands, However, the dual role of fracture in transporting fluids and contaminants underscores the need for further investigations to mitigate the impact on human health. This study aims to numerically investigate the combined effect of particle density and flow velocity on their transport and deposition in different fracture orientations.

Methods: A 2D particle tracing simulation was implemented accounting for drag and gravity forces on a smooth fracture. The derived particle numbers under the studied scenario e.g., fracture orientation, particle density, and flow velocity, were fitted to a 1D advection-dispersion equation with a deposition term.

Results: The model elucidated that both particle densities yielded an increase in the normalized concentration in non-horizontal scenarios as the fracture orientation angle increased. The overall increment led to an observed decrease in the deposition coefficients and was associated with an increase in the dispersion coefficients. Hence the effect was more pronounced for denser particles where gravitational settling dominated, particularly in horizontal fractures. Less dense particles (1.05 g/cm³) were more strongly influenced by hydrodynamic forces, exhibiting lower overall

1623

deposition and dispersion across all fracture orientations. Additionally, increased flow velocity enhanced mechanical mixing and amplified dispersion and deposition coefficients.

Conclusion: The findings demonstrated a clear dependency on the combined effect of fracture orientation, particle density, and flow velocity. These valuable insights into particle transport mechanisms in fractured media have applications in subsurface flow, contaminant migration, and reservoir engineering.

Keywords: fractured media, particle density, inclination angle, flow velocity, dispersion, deposition.

Introduction

The evolving global landscape is increasingly characterized by escalating energy and water requirements, which have led to the depletion of hydrocarbon reserves and the deterioration of groundwater quality. Recently, porous fractured formations have emerged as crucial resources to meet future water demands and ensure sustainable long-term energy supply (Qu et al, 2021). The development of fractured rock reservoirs necessitates a balanced approach, as it has the potential to significantly impact surrounding groundwater systems and, by extension, human health. Groundwater contamination, particularly in areas dependent on fractured aquifers, poses a serious threat. Studies reveal that approximately 5% of annual deaths, among 820,000 individuals are attributed to compromised groundwater quality, particularly affecting children under the age of 5 (Lin et al, 2022). Such alarming statistics highlight the urgent need to improve our understanding of groundwater flow and contaminant migration in fractured media.

The term fracture is a general description of geological discontinuities including joints, faults, and cracks (Chrysikopoulos & Syngouna, 2014), that results when mechanical shear or normal stress reaches a certain extent. Naturel fractures occupy a small portion with respect to the entire volume of the hosting rock and encounter a variety of surfaces and expanding directions based on their origin formation. For example, tectonic fractures are characterized by complex rough wall surfaces and random orientation associated with the local tectonic events (Baiyu et al, 2021), while regional fractures exhibit fewer orientation changes along their length (Tiab & Donaldson, 2016). Meanwhile, local apertures of the natural fracture tend to vary spatially following a normal or lognormal distribution (Chrysikopoulos & James, 2003; Stoll et al, 2019), adding more complexities to fluids and particle transport phenomena. However, the fluid velocity across these apertures remains orders of magnitude higher than

that in the matrix (Zvikelsky & Weisbrod, 2006) serving fractures as primary channels and contributing to increasing the permeability of the rock (James & Chrysikopoulos, 2003).

In association with mechanical rupture processes or as a result of internal micro-erosion, solid particles can filtrate from the vadose zone towards the fractured reservoirs with a size distribution that could reach 10 µm (Zhang et al, 2012) and their origin can significantly define their charge and density. The cumulative studies have also justified that larger particles are inhibited from diffusing into the matrix and travel faster compared to solutes in single fractures due to charge, size exclusion, or the combined effect (Stoll et al, 2019; Spanik et al, 2021). Dense large particles are subject to gravity settling and demonstrated as a major mechanism accounting for particle deposition and retention in horizontally oriented fracture (Ding et al, 2021).

Numerical and experimental studies have been dedicated to examining the physical factors influencing the behavior of particles and solutes during their transport in fractured media such as dense particles in a uniform aperture (Bagalkot & Kumar, 2018; James & Chrysikopoulos, 1999), flow velocity variation effect (Medici et al, 2019; Mondal & Sleep, 2012), aperture distribution (Stoll et al, 2019; Ding et al, 2021) and the consideration of fracture surface roughness (Baiyu et al, 2021; Wang et al, 2020). Hence, the aforementioned body of literature treats the settling effect perpendicularly to the flow direction as fractures are oriented horizontally. Theoretically considering, the gravity effect is dependent on the inclination angles of the sample, which could promote or retard the transport mechanism. In porous media, the dispersion coefficient is highly susceptible to the inclination angle of the packed column as discussed by Chrysikopoulos & Syngouna (2014); hence the orientation of the fractures affected the recovered dense polydisperse particles where vertically oriented fractures which exhibited faster transport compared to diagonals and horizontals (Ding et al, 2021). Despite these valuable insights, a critical research gap remains in understanding the specific effects of particle density on transport and retention in non-horizontal fractures. While the behavior of dense particles in vertical fractures has been explored to some extent, there is a limited understanding of how varying particle densities influence transport in fractures that are not horizontally aligned. Non-horizontal fractures, including those with diagonal or complex inclinations, introduce additional complexities to particle transport, such as altered flow velocities, shear forces, and gravitational impacts that may interact differently with particles of varying densities.

The current study aims to numerically investigate the effect of fracture orientation on the transport and retention of solid particles and tends to compare the impact of particle density and flow velocity on the overall implemented scenarios. First, a 2D particle tracing simulation is constructed on a rough matched wall fracture using COMSOL Multiphysics software.

The simulation accounts for upward and downward flow on different fracture inclination angles, and the injected particles at the fracture inlet were characterized with 2.6 g/cm^3 and 1.05 g/cm^3 densities. Moreover, the breakthrough curves, representing the recovered particles at the outlet, were analyzed and fitted using a one-dimensional advection-dispersion equation that incorporates a deposition term to derive the transport parameters.

This approach enables a more comprehensive understanding of particle transport dynamics under varying the aforementioned physical conditions.

Methodology

The current study employed a numerical simulation approach following the combination of finite elements methods (FEMs) and the Lagrangian particle tracking (LPT) method on a two-dimensional confined single fracture using COMSOL Multiphysics. The following constructed model aims to investigate the interactions between fluid flow and solid particles considering realistic conditions of particles motion within different fracture orientations. The following sections provide a detailed breakdown of the simulation setup, the governing equations, the boundary conditions, and the solver configuration.

Physical system

To examine the particle transport behavior in fractured media while considering the effect of fracture surface roughness, fracture orientation, particle density, and flow velocity, a sinusoidal fracture is constructed in this study (Natarajan & Kumar, 2010) and the elevation points (y_i) along the length of the fracture are obtained as follows:

$$y_i = sin(x_i) - sin\left(\frac{x_i}{4}\right) \times sin(3x_i) \qquad (1)$$

where x_i is the coordinates of points (100 points with a separation distance of 1 mm) along the x direction as depicted in Figure1.
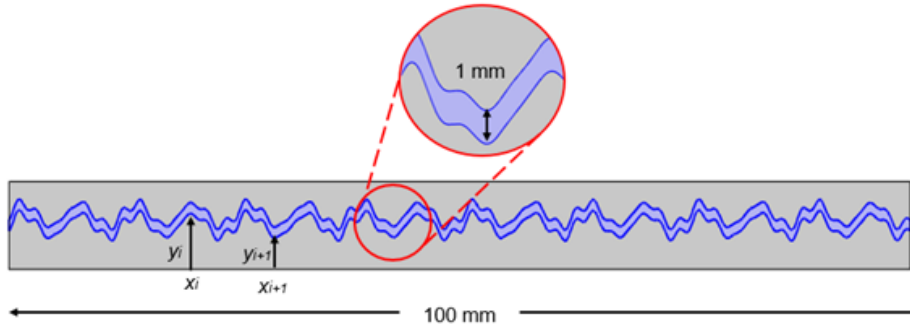
Figure 1 – Geometrical configuration of the sinusoidal fracture

A fine mesh with non-uniform size was constructed to optimize the accuracy in the areas where the particle-wall interactions and the flow gradient were significant. Ten layers of a finer mesh near the fracture walls were constructed to capture the parabolic flow velocity and particle positions. The mesh element size ranged from 0.0125 and 0.0286 mm. A mesh independence study was conducted to ensure that further refinement had a negligible impact on the results, with the final mesh containing 22865 domain elements and 2425 boundary elements.

Governing equations

Particle transport in a 2D saturated fracture with different inclinations was modeled using a particle tracing module implemented in COMSOL Multiphysics. (COMSOL Inc., Stockholm, Sweden). The fracture is 100 mm in length with 1 mm of aperture (Figure1). Particle transport occurs following the local parabolic velocity profile along the x direction at different fracture orientations. A simplified scheme of the general system model in this study is illustrated in Figure 2.

This study considers that particles are transported under a laminar regime. The fluid motion is governed using Navier's-Stokes equation (Baiyu et al, 2021) as follows:

$$\rho \frac{\partial U}{\partial t} + \rho (U.\nabla)U = \nabla.(-pI + K) + F_{ex} \tag{2}$$

$$\rho \nabla. U = 0 \tag{3}$$

where ρ and U are the fluid density (M.L-3) and velocity (L.T-1), ∇ p is the pressure gradient and F_{ex} denotes the volume external force term (M.L.T-2), K the liquid stress tensor (ML-1T-2), and I is the identity matrix.

Diagonal downward flow	Vertical downward flow	Horizontal flow	Diagonal upward flow	Vertical upward flow
$\theta = -45°$	$\theta = -90°$	$\theta = 0$	$\theta = 45°$	$\theta = 90°$
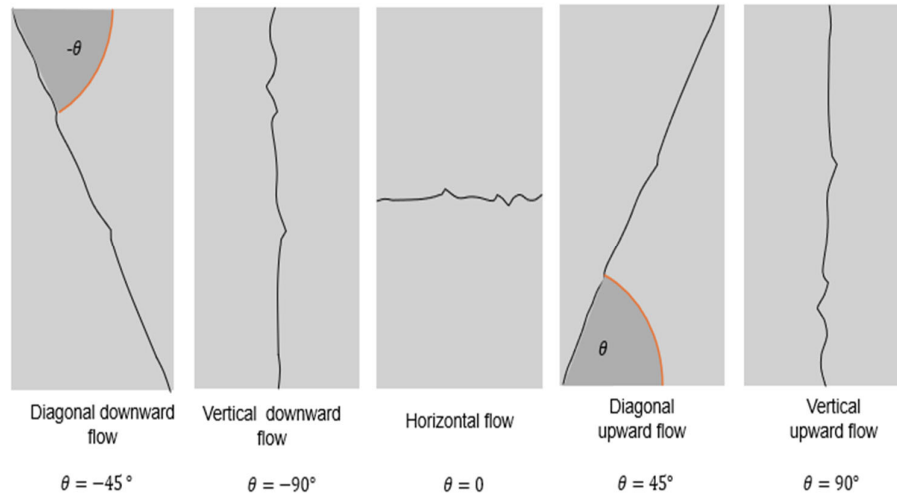
Figure 2 – Different fracture inclinations scenarios

The particle tracing method employed in this study models particles as discrete entities that move through a fluid, interacting with their environment under the influence of various external forces. This approach allows for a detailed examination of particle behavior within the flow field. This study assumes particle transport is governed primarily by advection, without considering other transport mechanisms such as diffusion. As a result of this assumption, the forces acting on the particles are simplified to include only drag and gravity.

Gravitational force exerts an influence on the particle and acts perpendicular to the flow direction. According to Bennacer et al. (2017) and Bennacer et al. (2023), the gravity force is expressed as:

$$F_g = \frac{4}{3}\pi\, d_p^3\left(\rho_p - \rho\right).g \tag{4}$$

The drag force on a spherical particle is determined by Stokes' law (Guha Roy & Singh, 2016):

$$F_d = \frac{1}{\tau_p}m_p\left(U - U_p\right) \tag{5}$$

Here m_p and U_p are the particle mass (M), and velocity (L.T^{-1}) respectively, d_p is the particle diameter (L) ρ_p is the particle density (M.L^{-3}), g is the acceleration of gravity, and τ_p Is the relaxation time (T) given by Stokes drag law (Kim & Zydney, 2004) as:

$$\tau_p = \frac{\rho_p\, d_p^2}{18} \tag{6}$$

The particle trajectories and positions as a function of time are determined by Newton's second law and force balance acting on particles (Belfort & Nagata, 1985):

$$m_p \frac{d\, U_p}{dt} = F_g + F_d \tag{7}$$

Particle generation and boundary condition

During this simulation, in order to explore the effect of gravity, the particles are assumed to be spherical and monodisperse with a uniform size of 1 μm and a density of 2.6 g/cm^3 and 1.05 g/cm^3. An N_0 number consisting of 100,000 particles is released as a short pulse for 30 seconds with a random distribution at the inlet of the fracture. Moreover, the interaction of particles with the walls of the domain was governed by freeze boundary conditions as follows:

$$v = v_c \tag{8}$$

where v is the vertical component of the particle velocity, and v_c is the particle velocity when striking the wall.

Freeze condition was used to mimic favorable conditions for particle attachment with the fracture surface. The particle's vertical position no longer changes after establishing contact with the fracture wall.

This study assumes no flow between the fracture and the matrix (no matrix diffusion). A no-slip condition was implemented for the boundaries, and the laminar flow is controlled from the inlet at two average flow velocities of 0.02 and 0.03 cm/s while the outlet boundary condition was set to a constant pressure p_0 of 0 Pa, allowing for continuous fluid flow through the domain.

$$[-pI + K]n = p_0 n \tag{9}$$

1629

An implicit time-stepping scheme was used to solve time-dependent studies of the governing equation regarding particle trajectory and fluid flow through the confined geometry. This approach allows suitable transient dynamics capturing and ensuring numerical stability. A sensitivity analysis was conducted to ensure further reduction of time step did not affect simulation results. Furthermore, 0.001s was set as a fixed time step throughout the simulation.

The governing equations of the studied system were solved according to the Multifrontal Massively Parallel Sparse Direct (MUMPS) Solver. The solver is well-suited for 2D systems and all scale problems with complex boundary conditions. To maintain the model accuracy, 1E-6 was set as a strict convergence tolerance. The solver's strict tolerance ensured that residuals in the governing equations were minimized, leading to reliable convergence.

Advection dispersion equation

The relationship describing the one-dimensional transport of particles in a saturated fracture with no matrix diffusion considering advection, dispersion, and deposition term (Abdel-Salam & Chrysikopoulos, 1994) is:

$$\frac{\partial C}{\partial t} + K_{dep}C = D_L \frac{\partial^2 C}{\partial x^2} - U_p \frac{\partial C}{\partial x} \tag{10}$$

where C is the effluent concentration of particles (M/L^3), x is the distance along the fracture from the inlet (L), t is the time, U_p is the particle velocity (L/T), D_L is the hydrodynamic longitudinal dispersion coefficient (L.T^{-2}) and K_{dep} is the kinetic deposition coefficient (T^{-1}).

A short pulse is mathematically considered as an instantaneous injection (Bennacer et al, 2022). The following initial and boundary conditions are applied:

$$C(x,0) = 0 \tag{11}$$

$$C_{(x=0,t)} = \begin{cases} C_0 , 0 \le t \le t_{inj} \\ 0 , \qquad t > t_{inj} \end{cases} \tag{12}$$

$$\frac{\partial C}{\partial x}_{(x=L,t)} = 0 \tag{13}$$

An analytical solution for Eq.(7), at the fracture outlet ($x = L$), for an instantaneous injection at the fracture inlet is given in Eq.(9) (Bodin et al, 2003; Yosri et al, 2021):

$$C(L,t) = \frac{M_0 L}{Q\sqrt{4\pi D_L t^3}} \exp\left[-\frac{(L - U_p t)^2}{4\,D_L t}\right] \exp[K_{dep} t] \tag{14}$$

In order to fit the obtained result from the particle tracing module to the analytic solution, the cumulative particle number at the outlet for each scenario is expressed as concentrations with the initial particle concentration obtained as follows (Zvikelsky et al, 2008):

$$C = \frac{\rho_p\, N_0\, \pi d^3}{6\, V_{inj}} \tag{15}$$

where N_0 is the initial particle number released at the inlet and V_{inj} is the injected particle suspension volume. In this study, the V_{inj} is considered as 3 fracture volumes ($3FV$) where $FV = L.W.b$

Table 1 – Simulation parameters

	Value	Unit
Injected particle number	1000 000	
Particle diameter (monodisperse)	1	μm
Particle density	2600 1050	kg/m^3
Water density	1000	kg/m^3
Water viscosity	0.001	Pa.s
Water inlet velocity	0.02 0.03	cm/s

Results and discussion

Particle transport behavior under the effect of fracture orientation

Based on the particle tracing methodology outlined earlier, this study has expanded to simulate distinct scenarios, each characterized by variations in fracture orientation. The scenarios explore different combinations of flow velocity and particle density. The transport

parameters are determined by fitting the obtained result from the particle tracing simulation breakthrough curves (BTCs) to the analytical solution of Eq. (9). Figure 3 shows the BTCs at different fracture orientations under the tested flow velocities and particle densities.
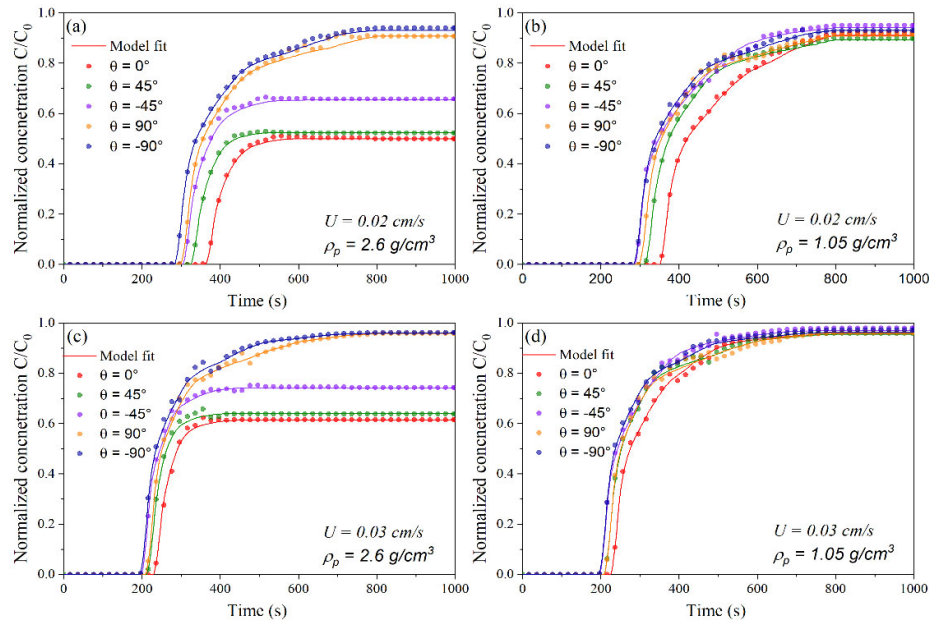
Figure 3 – BTCs of the injected particles (a), (b) $U = 0.02\ cm/s$ (c), (d) $U = 0.03\ cm/s$ for $\rho_p = 2.6\ g/cm^3$ and $\rho_p = 1.05\ g/cm^3$

The observation from Figure 3 demonstrates a strong correlation between the analytic solution and the derived results of particle tracing simulations, which underscores the reliability of the developed model in accurately depicting particle transport mechanisms. Across the tested flow velocities and particle densities, the earliest breakthrough occurs when the inclination angle θ = ±90°, indicating the least retardation of particles in both upward and downward flow conditions. The slight reduction in the normalized concentration observed at +90° is attributed primarily to the influence of gravity, as particles moving upward experience greater gravitational resistance unlike those moving downward. Similar results were found by Ding et al. (2021).

In non-vertical configurations, the transport of dense particles exhibited distinct behaviors. At a flow velocity of U = 0.02 cm/s, the

normalized concentration reached 0.65 for an inclination of -45° and 0.52 for +45° (Figure 3 (a),(c)). When the flow velocity increased to U = 0.03 cm/s, the normalized concentration at these angles increased to approximately 0.74 and 0.63, respectively, as depicted in Figure 3 (b),(d). Notably, these inclined conditions exhibited higher concentration plateaus compared to the horizontal fractures, indicating greater particle retention within the fracture under horizontal flow conditions, Figure 4(a).
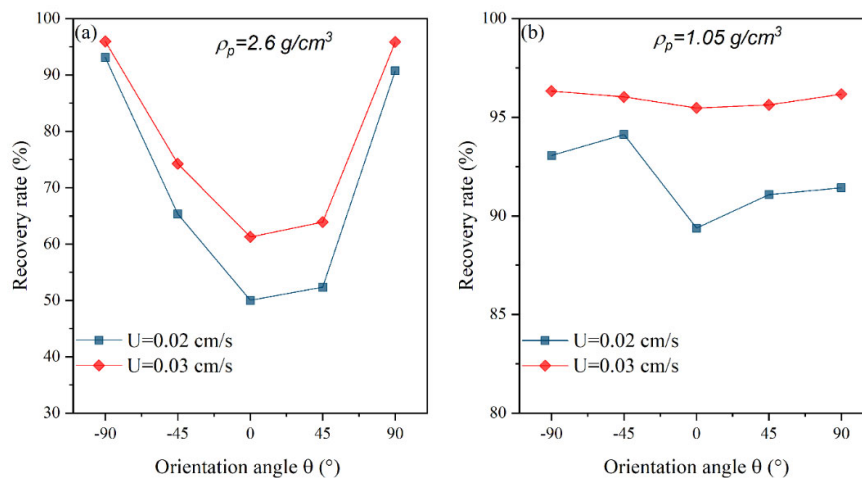
Figure 4 – Recovery rates for (a) $\rho_p = 2.6 \ g/cm^3$ and (b) $\rho_p = 1.05 \ g/cm^3$.

For particles with a density of 1.05 g/cm³, the effect of orientation on transport dynamics was less pronounced. In both upward and downward non-horizontal flow scenarios, these particles experienced similar breakthrough curves, characterized by an increased relative concentration and the establishment of a plateau after 800 seconds at U = 0.02 cm/s and 650 seconds at U = 0.03 cm/s (Figure 3). Unlike the behavior of dense particles, where gravity plays a substantial role, the transport of these lighter particles is governed primarily by buoyancy forces maintaining the particles within the central streamlines, resulting in rapid transport through the fracture and higher recovery rates as depicted in Figure 4(b).

Additionally, the flow velocity was found to have a significant influence on particle transport across all scenarios. Higher flow velocities consistently led to faster breakthroughs and higher recovery rates. The enhanced advective forces reduce the residence time of a particle and help to overcome the retardation caused by gravitational settling or

particle-wall interactions, allowing for faster movement through the fracture.

Hydrodynamic dispersion coefficient

The effect of fracture orientation, particle density, and flow velocity on the dispersion coefficient is illustrated in Figure 5. As it is clear, the orientation had a significant effect on the dispersion process and was more pronounced for dense particles. At 0° all particles have the minimum dispersion coefficient, hence as the fracture orientation deviates from horizontal, the dispersion increases to reach the highest values for downward flow conditions. The modeled fracture in the current study is rough to a certain extent due to sinusoidal undulation and at nonhorizontal fracture orientation, the flow and the settling effect led to a more lateral spread of particles and increased the likelihood of wall-particle interaction compared to 0° fracture orientation. This behavior leads to an increase in the dispersion coefficient. Hence at downward flow, the gravitational force acts as a positive driver that amplifies particle velocity which yields the highest dispersion coefficient.
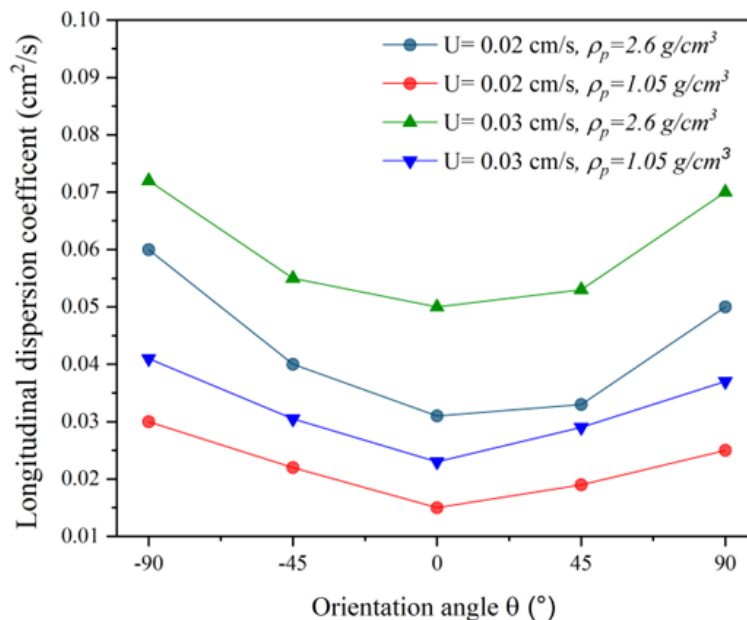
Figure 5 – Hydrodynamic longitudinal dispersion coefficient as a function of the fracture inclination angle

The effect of orientation was significant; however, the density also played a major role. Dense particles exhibited higher dispersion coefficients compared to those with 1.05 g/cm3. This can be attributed to the settling effect wherein denser particles experience a greater degree of gravitational pull. As these particles settle, their vertical movement is impeded, leading to a lateral shift towards the lower surface of the fracture which in turn increases particle-wall interactions, thereby enhancing dispersion. In contrast, less dense particles tend to remain within the streamline, where the flow velocity is at its maximum. These particles experience less residence time in the system, resulting in fewer particle-surface collisions and, consequently, lower dispersion coefficients.

Higher flow velocities lead to an increase in dispersion coefficient under all the fracture orientations and particle densities. Similar results were reported by Mondal & Sleep (2012) and Hawi et al. (2023). The behavior has been attributed to the mechanical mixing and the formation of vortices near the rough fracture walls. These vortices promote more chaotic particle motion, increasing the likelihood of particles interacting with the fracture surfaces, which further amplifies particle dispersion, particularly in fractures with non-horizontal orientations.

Deposition coefficient

Figure 6 illustrates the variation in the kinetic deposition coefficient K_{dep} as a function of fracture orientation angles under given flow velocities and particle densities. The results demonstrate a clear dependency of deposition kinetics on the fracture inclination angle, with horizontal fractures (0°) exhibiting the highest deposition coefficient across all tested scenarios, and it is significant for denser particles. The observation is consistent with the low particle recovery rates observed in the horizontal fracture, as previously shown in Figure 4(a). As the fracture orientation increases from horizontal to more inclined positions, the deposition coefficient decreases for all conditions, indicating that fracture geometry significantly influences particle settling and deposition dynamics.

Dense particles encounter a pronounced deposition process where the horizontal fracture seems an ideal configuration for particle settling. At horizontal inclination gravity acts perpendicularly to the flow direction and causes a significant reduction in the vertical component of particle velocity, delaying the particle's overall migration through the fracture. This deceleration increases the likelihood of particle-wall interactions, as particles are pulled toward the stagnation zones located near the fracture surfaces where the flow velocity approaches zero.
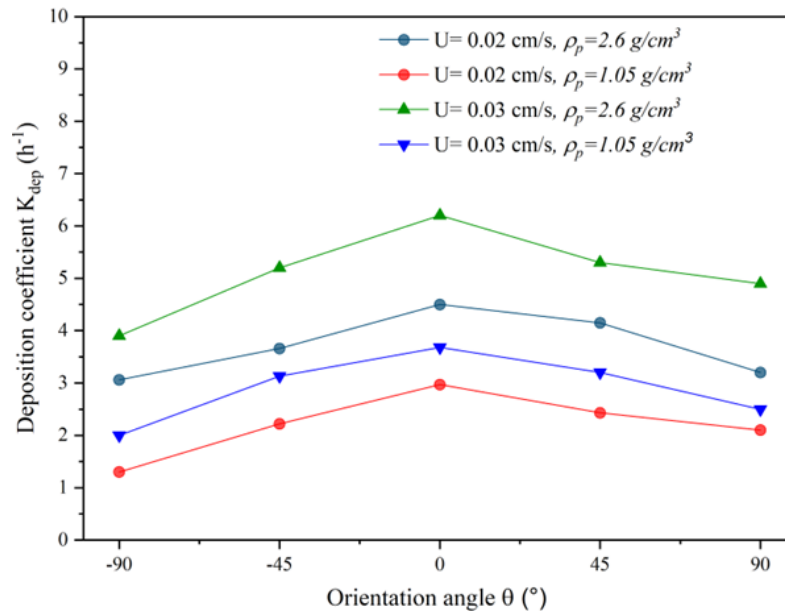
Figure 6 – Deposition coefficient versus the fracture inclination angle

The role of gravity becomes even more complex when considering inclined fractures; hence it plays a positive role in downward flow accelerating particle velocity and is characterized by a lower deposition coefficient compared to upward flow conditions. Less dense particles, though following a similar trend, exhibit lower deposition coefficients compared to their denser counterparts. In this case, the primary mechanism driving deposition is not gravitational settling but rather the interaction of particles with trapping zones within the fracture geometry. These trapping zones of low flow velocity are caused by the undulations in the modeled fracture surface. The trapped particles in these regions experience minimum transport forces but significant shear stress leading to re-entrainment towards the centerline where the velocity is maximal and exhibits a lower deposition coefficient than that of dense particles under similar conditions.

As the flow velocity increases, the deposition coefficient rises across all tested fracture inclination angles and particle densities. Similar trends of increased deposition with rising flow velocity have been observed in porous media studies, as discussed by Bennacer et al. (2013) and in the

recent work (Bennacer et al, 2022). The author attributed the behavior to the increased mechanical mixing generated at higher flow velocities where particles are more likely to establish enhanced particle-wall interactions.

Conclusion

A numerical approach has been developed and applied to simulate the impact of particle density and flow velocity of monodispersed particles transported in a randomly orientated rough fracture. A particle tracing simulation is implemented to track particle movement in a laminar flow determined by Navier's Stocks equation within a sinusoidal 2D fracture. Moreover, a 1D advection-dispersion equation is employed to quantify and analyze the transport parameters. The study revealed that fracture orientation plays a critical role in governing particle transport, dispersion, and deposition. As the orientation angle increases, the normalized concentration increases and is higher in downflow scenarios, e.g. -45 and -90.

Moreover, there is a marked decrease in the deposition coefficient and a corresponding increase in the dispersion coefficient for particles of both densities. However, this effect is notably more pronounced for denser particles (2.6 g/cm^3) due to sedimentation emerging as the primary deposition mechanism, particularly in horizontal fractures. In this configuration, gravity acts perpendicularly to the flow, decelerating particle velocity and promoting deposition by increasing particle-wall interactions and trapping particles in stagnation zones. This gravitational deceleration leads to enhanced retention of denser particles in horizontal fractures.

In contrast, less dense particles (1.05 g/cm³) are more strongly governed by hydrodynamic forces rather than gravitational settling. This results in reduced overall deposition and dispersion for these particles across all fracture orientations, with their behavior being more influenced by flow dynamics than by orientation-specific effects.

Irrespective of the studied density, particles experience greater drag force as flow velocity increases, which in turn enhances their contact with the fracture surface. This results in an increase in both the dispersion and deposition coefficients. The improved mechanical mixing disrupts the flow streamlines, promoting particle interactions with the rough fracture walls and amplifying particle spreading and retention within the fracture. This effect is more significant for denser particles due to their greater susceptibility to gravitational settling. Still, less dense particles also exhibit increased dispersion and deposition at higher flow velocities, driven by enhanced drag force.

References

Abdel-Salam, A. & Chrysikopoulos, C.V. 1994. Analytical solutions for one-dimensional colloid transport in saturated fractures. *Advances in Water Resources* 17(5), pp.283-296. Available at: https://doi.org/10.1016/0309-1708(94)90032-9.

Bagalkot, N. & Kumar, G.S. 2018. Colloid Transport in a Single Fracture–Matrix System: Gravity Effects, Influence of Colloid Size and Density. *Water,* 10(11), art.number:1531. Available at: https://doi.org/10.3390/w10111531.

Baiyu, Z., Hongming, T., Senlin, Y., Gongyang, C., Feng, Z. & Shiyu, X. 2021. Effect of fracture roughness on transport of suspended particles in fracture during drilling. *Journal of Petroleum Science and Engineering*, 207, art.number:109080. Available at: https://doi.org/10.1016/j.petrol.2021.109080.

Belfort, G. & Nagata, N. 1985. Fluid mechanics and cross-flow filtration: some thoughts. *Desalination* 53(1-3), pp.57-79. Available at: https://doi.org/10.1016/0011-9164(85)85052-9.

Bennacer, L., Ahfir, N.-D., Alem, A. & Huaqing, W. 2022. Influence of Particles Sizes and Flow Velocity on the Transport of Polydisperse Fine Particles in Saturated Porous Media: Laboratory Experiments. *Water, Air, & Soil Pollution,* 233, art.number:249. Available at: https://doi.org/10.1007/s11270-022-05732-4.

Bennacer, L., Ahfir, N.-D., Alem, A. & Wang, H. 2017. Coupled Effects of Ionic Strength, Particle Size, and Flow Velocity on Transport and Deposition of Suspended Particles in Saturated Porous Media. *Transport in Porous Media,* 118, pp.251-269. Available at: https://doi.org/10.1007/s11242-017-0856-6.

Bennacer, L., Ahfir, N.-D., Bouanani, A., Alem, A. & Wang, H. 2013. Suspended Particles Transport and Deposition in Saturated Granular Porous Medium: Particle Size Effects. *Transport in Porous Media,* 100, pp.377-392. Available at: https://doi.org/10.1007/s11242-013-0220-4.

Bennacer, L., Nassim, K. & Djilali, B. 2023. Laboratory Studies on the Influence of Ionic Strength on Particle Transport Behavior in a Saturated Porous Medium. *AEF - Advanced Engineering Forum*, 49, pp.91-102. Available at: https://doi.org/10.4028/p-xm3w08.

Bodin, J., Porel, G. & Delay, F. 2003. Simulation of solute transport in discrete fracture networks using the time domain random walk method. *Earth and Planetary Science Letters*, 208(3-4), pp.297-304. Available at: https://doi.org/10.1016/S0012-821X(03)00052-9.

Chrysikopoulos, C.V. & James, S.C. 2003. Transport of Neutrally Buoyant and Dense Variably Sized Colloids in a Two-Dimensional Fracture with Anisotropic Aperture. *Transport in Porous Media*, 51, pp.191-210. Available at: https://doi.org/10.1023/A:1021952226861.

Chrysikopoulos, C.V. & Syngouna, V.I. 2014. Effect of Gravity on Colloid Transport through Water-Saturated Columns Packed with Glass Beads: Modeling and Experiments. *Environmental Science & Technology*, 48(12), pp.6805-6813. Available at: https://doi.org/10.1021/es501295n.

Ding, Y., Meng, X. & Yang, D. 2021. Numerical simulation of polydisperse dense particles transport in a random-orientated fracture with spatially variable apertures. *Colloids and Surfaces A: Physicochemical and Engineering Aspects*, 610, art.number:125729. Available at: https://doi.org/10.1016/j.colsurfa.2020.125729.

Guha Roy, D. & Singh, T.N. 2016. Fluid Flow through Rough Rock Fractures: Parametric Study. *International Journal of* Geomechanics, 16(3). Available at: https://doi.org/10.1061/(ASCE)GM.1943-5622.0000522.

Hawi, H., Ahfir, N.-D., Ouahbi, T., Alem, A. & Wang, H. 2023. Particle Transport in Saturated Fractured Media: Effect of Flow Velocity and Fracture Aperture. *ACS ES&T Water*, 3(9), pp.3132-3140. Available at: https://doi.org/10.1021/acsestwater.3c00284.

James, S.C. & Chrysikopoulos, C.V. 2003. Effective velocity and effective dispersion coefficient for finite-sized particles flowing in a uniform fracture. *Journal of Colloid and Interface Science*, 263(1), pp.288-295. Available at: https://doi.org/10.1016/S0021-9797(03)00254-6.

James, S.C. & Chrysikopoulos, C.V. 1999. Transport of polydisperse colloid suspensions in a single fracture. W*ater Resources Research*, 35(3), pp.707-718. Available at: https://doi.org/10.1029/1998WR900059.

Kim, M.-m. & Zydney, A.L. 2004. Effect of electrostatic, hydrodynamic, and Brownian forces on particle trajectories and sieving in normal flow filtration. *Journal of Colloid and Interface Science*, 269(2), pp.425-431. Available at: https://doi.org/10.1016/j.jcis.2003.08.004.

Lin, L., Yang, H. & Xu, X. 2022. Effects of Water Pollution on Human Health and Disease Heterogeneity: A Review. *Frontiers in Environmental Science*, 10, art.number:880246. Available at: https://doi.org/10.3389/fenvs.2022.880246.

Medici, G., West, L.J. & Banwart, S.A. 2019. Groundwater flow velocities in a fractured carbonate aquifer-type: Implications for contaminant transport. *Journal of Contaminant Hydrology*, 222, pp.1-16. Available at: https://doi.org/10.1016/j.jconhyd.2019.02.001.

Mondal, P.K. & Sleep, B.E. 2012. Colloid Transport in Dolomite Rock Fractures: Effects of Fracture Characteristics, Specific Discharge, and Ionic Strength. *Environmental Science & Technology*, 46(18), pp.9987-9994. Available at: https://doi.org/10.1021/es301721f.

Natarajan, N. & Kumar, G.S. 2010. Thermal transport in a coupled sinusoidal fracture-matrix system. *International journal of engineering science and technology*, 2(7), pp.2645-2650 [online]. Available at: https://api.semanticscholar.org/CorpusID:136055037 [Accessed: 05 September 2024].

Qu, H., Wang, R., Ao, X., Liu, Z., Lin, H. & Xiao, Q. 2021. Experimental investigation of particle transport and distribution in a vertical nonplanar fracture. *Powder Technology*, 394, pp.935-950. Available at: https://doi.org/10.1016/j.powtec.2021.09.028.

Spanik, S., Rrokaj, E., Mondal, P.K. & Sleep, B.E. 2021. Favorable and unfavorable attachment of colloids in a discrete sandstone fracture. *Journal of*

Contaminant Hydrology, 243, art.number:103919. Available at: https://doi.org/10.1016/j.jconhyd.2021.103919.

Stoll, M., Huber, F.M., Trumm, M., Enzmann, F., Meinel, D., Wenka, A., Schill, E. & Schäfer, T. 2019. Experimental and numerical investigations on the effect of fracture geometry and fracture aperture distribution on flow and solute transport in natural fractures. *Journal of Contaminant Hydrology*, 221, pp.82-97. Available at: https://doi.org/10.1016/j.jconhyd.2018.11.008.

Tiab, D. & Donaldson, E.C. 2016. Chapter 8 - Naturally Fractured Reservoirs. In: Tiab, D. & Donaldson, E.C. (Eds.) *Petrophysics, Fourth Edition,* pp.415-481. Boston: Gulf Professional Publishing. Available at: https://doi.org/10.1016/B978-0-12-803188-9.00008-5.

Wang, X., Yao, J., Gong, L., Sun, H., Yang, Y., Liu, W. & Li, Y. 2020. Numerical study on particle transport and deposition in rough fractures. *Oil & Gas Science and Technology - Rev. IFP Energies nouvelles*, 75, art.number:23. Available at: https://doi.org/10.2516/ogst/2020015.

Yosri, A., Dickson-Anderson, S., Siam, A. & El-Dakhakhni, W. 2021. Analytical description of colloid behavior in single fractures under irreversible deposition. *Journal of Colloid and Interface Science*, 589, pp.597-604. Available at: https://doi.org/10.1016/j.jcis.2020.12.089.

Zhang, W., Tang, X., Weisbrod, N. & Guan, Z. 2012. A review of colloid transport in fractured rocks. *Journal of Mountain Science*, 9, pp.770-787. Available at: https://doi.org/10.1007/s11629-012-2443-1.

Zvikelsky, O. & Weisbrod, N. 2006. Impact of particle size on colloid transport in discrete fractures. *Water Resources Research*, 42(12), art.number:W12S08. Available at: https://doi.org/10.1029/2006WR004873.

Zvikelsky, O., Weisbrod, N. & Dody, A. 2008. A comparison of clay colloid and artificial microsphere transport in natural discrete fractures. *Journal of Colloid and Interface Science*, 323(2), pp.286-292. Available at: https://doi.org/10.1016/j.jcis.2008.04.035.

Investigación numérica sobre el impacto de la densidad de partículas y la velocidad del flujo en el transporte y deposición de partículas en una fractura orientada aleatoriamente

Kheira Bouragaa[a]*, **autor de correspondencia**,
Lyacine Bennacer[b]*, Mustapha* Akacem[a]

Universidad de Adrar, Facultad de Ciencia y Tecnología, Departamento de Ingeniería Civil, Adrar, República Argelina Democrática y Popular

[a] Laboratorio de Desarrollo Sostenible y IT (LDDI),

[b] Laboratorio de Energía, Medio Ambiente y Sistemas de Información (LEESI)

CAMPO: ciencias de computación, mecánica
TIPO DE ARTÍCULO: artículo científico original

Resumen:

Introducción/propósito: Las formaciones fracturadas ganaron recientemente un interés significativo como paisaje para asegurar las demandas de energía y agua subterránea. Sin embargo, el doble papel de la fractura en el transporte de fluidos y contaminantes subraya la necesidad de realizar más investigaciones para mitigar el impacto en la salud humana. Este estudio tiene como objetivo investigar numéricamente el efecto combinado de la densidad de las partículas y la velocidad del flujo en su transporte y deposición en diferentes orientaciones de fractura.

Métodos: Se implementó una simulación de seguimiento de partículas en 2D que tiene en cuenta las fuerzas de arrastre y gravedad en una fractura lisa. Los números de partículas derivados en el escenario estudiado, por ejemplo, orientación de fractura, densidad de partículas y velocidad de flujo, se ajustaron a una ecuación de advección-dispersión 1D con un término de deposición.

Resultados: El modelo aclaró que ambas densidades de partículas produjeron un aumento en la concentración normalizada en escenarios no horizontales a medida que aumentaba el ángulo de orientación de la fractura. El incremento general condujo a una disminución observada en los coeficientes de deposición y se asoció con un aumento en los coeficientes de dispersión. Por lo tanto, el efecto fue más pronunciado para las partículas más densas donde dominaba la sedimentación gravitacional, particularmente en las fracturas horizontales. Las partículas menos densas (1,05 g/cm³) se vieron más influenciadas por las fuerzas hidrodinámicas, exhibiendo una menor deposición y dispersión general en todas las orientaciones de fractura. Además, el aumento de la velocidad del flujo mejoró la mezcla mecánica y amplificó los coeficientes de dispersión y deposición.

Conclusión: Los hallazgos demostraron una clara dependencia del efecto combinado de la orientación de la fractura, la densidad de las partículas y la velocidad del flujo. Estos valiosos conocimientos sobre los mecanismos de transporte de partículas en medios fracturados tienen aplicaciones en el flujo subterráneo, la migración de contaminantes y la ingeniería de yacimientos.

Palabras clave: medios fracturados, densidad de partículas, ángulo de inclinación, velocidad de flujo, dispersión, deposición.

Численное исследование влияния плотности частиц и скорости потока на перенос частиц и осаждение в случайно ориентированной трещине

Кеира Бурага[а]*,* **корреспондент**, *Лейсин* Бенасер[б], *Мустафа* Акасем[а]

Адрарский университет, факультет науки и технологий,
кафедра гражданского строительства,
г. Адрар, Алжирская Народная Демократическая Республика

[а] Лаборатория устойчивого развития и
  информационных технологий (LDDI)

[б] Лаборатория энергетики, охраны окружающей среды и
  информационных системых (LEESI)

Резюме:

Введение/цель: В последнее время значительно возрастает интерес к трещиноватым пластам в силу потребности в энергии и подземных водах. Однако двойная роль, которую трещины играют в распределении жидкостей и загрязнений, указывает на необходимость в дальнейших исследованиях для минимизации воздействия на здоровье человека. Целью данной статьи является численное исследование совместного влияния плотности частиц и скорости потока на их перенос и осаждение в трещинах различной пространственной ориентации.

Методы: Применено 2D-моделирование движения частиц с учетом сил сопротивления и притяжения к гладкой трещине. Затем численные результаты частиц, полученные в этом сценарии, т.е. ориентация трещины, плотность частиц и скорость потока, были введены в одномерное уравнение адвекции и дисперсии с выражением осаждения.

Результаты: Модель показала, что обе плотности частиц приводят к увеличению нормализованной концентрации в негоризонтальных сценариях с увеличением угла ориентации трещины. Общее увеличение привело к наблюдаемому снижению коэффициентов осаждения, что связано с увеличением коэффициентов дисперсии. Вследствие чего эффект был более выраженным у более плотных частиц, у которых преобладало гравитационное осаждение, особенно в горизонтальных трещинах. Выявлено, что частицы с меньшей плотностью (1,05 г/см³) в большей степени подвержены влиянию гидродинамических сил, что приводит к снижению общего осаждения и дисперсии во всех направлениях трещин. Кроме

того, увеличение скорости потока улучшает механическое перемешивание и увеличивает коэффициенты дисперсии и осаждения.

Вывод: Полученные данные показали прямую зависимость от совместного влияния ориентации трещины, плотности частиц и скорости потока. Эти ценные сведения о механизмах переноса частиц в трещиноватых средах находят применение в подземном течении, миграции загрязняющих веществ и разработке коллекторов.

Ключевые слова: трещиноватая среда, плотность частиц, угол наклона, скорость потока, диспергирование, осаждение.

Нумеричко истраживање утицаја густине честица и брзине струјања на транспорт и депозицију честица у присуству произвољно оријентисаног лома

Кеира Бурага[a]*,* **аутор за преписку**, *Лејсин* Бенасер[б]*, Мустафа* Акасем[a]

Универзитет Адрар, Факултет науке и технологије, Одељење за грађевинарство, Адрар, Народна Демократска Република Алжир

[a] Лабораторија за одрживи развој и ИТ (ЛДДИ)

[б] Лабораторија за енергетику, животну средину и информационе системе (ЛЕЕСИ)

ОБЛАСТ: рачунарске науке, механика
КАТЕГОРИЈА (ТИП) ЧЛАНКА: оригинални научни рад

Сажетак:

Увод/циљ: Однедавно је знатно повећан интерес за формације са ломом у оквиру задовољавања потреба за енергијом и подземним водама. Међутим, двострука улога коју има лом у транспорту течности и контаминаната скреће пажњу на неопходност даљих истраживања како би се умањио утицај на здравље људи. Циљ ове студије јесте да нумеричким путем испита комбиновани утицај густине честица и брзине струјања на њихов транспорт и депоновање у присуству ломова различитих оријентација.

Методе: Примењена је 2Д симулација кретања честица при чему су узете у обзир сила отпора и гравитације на глатком лому. Затим су нумерички резултати честица добијени у том сценарију, тј. оријентација лома, густина честица и брзина струјања, унети у 1Д једначину адвекције и дисперзије са изразом за депозицију.

Резултати: Модел је показао да су, како се угао оријентације лома повећавао, обе густине честица довеле до повећања нормализоване концентрације у нехоризонталним случајевима. Укупан прираст је довео до уоченог смањивања коефицијената депозиције и повезан је са повећањем коефицијената дисперзије.

Стога је ефекат био израженији у случају гушћих честица где је доминирало гравитационо окружење, нарочито код хоризонталних ломова. Честице мање густине (1,05 g/cm³) биле су под јачим утицајем хидродинамичких сила, па су показале слабију укупну депозицију и дисперзију код свих оријентација лома. При томе је повећана брзина струјања побољшала механичко мешање и повећала коефицијенте дисперзије и депозиције.

Закључак: Налази показују јасну зависност од комбинованих ефеката оријентације лома, густине честица и брзине струјања. Ови значајни увиди у механизам транспорта честица у срединама с присуством лома имају примену у подземним токовима, редукцији контаминације и конструисању резервоара.

Кључне речи: средине са ломом, густина честица, угао нагиба, брзина струјања, дисперзија, депозиција.

A computer vision approach with OpenCV and deep learning for determining inductance in planar coils

Younes Benazzouz[a]*, Djilalia* Guendouz[b]

University of Oran 2 Mohamed Ben Ahmed, Industrial Maintenance and Safety Institute (IMSI), Department of instrumentation maintenance, Laboratory of Production Engineering and Industrial Maintenance (LGPMI), Oran, People's Democratic Republic of of Algeria

[a] e-mail: benazzouzyounes14@gmail.com, **corresponding author**,
 ORCID iD: https://orcid.org/0009-0004-8736-7610

[b] e-mail: lila.guen@yahoo.fr,
 ORCID iD: https://orcid.org/0009-0006-7129-5960

Abstract:

Introduction/purpose: In the realm of development and use of computer vision and AI methodologies, this research introduces a combination and advanced method using YOLOv9, a deep learning concept of whole image processing in one pass through a convolutional neural network (CNN) and the OpenCV Python image processing library to determine the geometry of planar coils. These geometric parameters are the main parameters used to calculate the inductance value using Mohan's formula, which exclusively utilizes only geometric data to estimate inductance values. This method significantly speeds up the verification and calculation processes, while also playing a role in improving quality control after manufacturing.

Methods: The methodology is divided into two main phases. Initially, a YOLOv9 model was trained for object recognition using a generated synthetic dataset of coil shapes created with Python's Turtle graphics library. Then, after the detection phase, OpenCV was used to identify the geometric parameters of the images. The pixels were converted into millimeters using a ratio method to calculate the inductance value accurately.

Results: The YOLOv9 model successfully identified various planar coil shapes, and the geometric parameters were identified through OpenCV. Subsequently, the inductance was successfully calculated.

Conclusion: The results show that the proposed method is a novel and effective way of calculating inductance.

Key words: Convolutional Neural Networks (CNN), OpenCV, planar coil, inductance, YOLOv9, image processing.

Introduction

Planar coils are crucial components in electronic systems and can be found in the architecture of wireless power transfer (WPT) systems, ensuring energy management and transmission. They are useful in applications such as electric vehicle charging. Their operation is based on electromagnetic induction between two parallel coils; without physical contact, electrical energy is transferred when electrical current is passed through one of them (Luo & Wei, 2017). Additionally, they can be used for position sensing in permanent magnet synchronous motors, offering a resilient design compared with traditional sensors like Hall sensors. They are easy to produce without occupying a lot of space and function as converters of magnetic flux in the air gap of the motor into an electrical signal (Im & Hur, 2021). Moreover, planar coils are used as monolithic integrated circuits on chips to minimize planar surface area and are subsequently integrated into DC-DC Forward converters for both high and low frequency uses, allowing perfect miniaturization for modern electronic devices (Derkaoui et al, 2021). In the implementation of biomedical devices, they play a principal role, offering an ideal solution for wireless recharging of pacemakers' batteries using square-shaped printed spiral designs (Ahire et al, 2022). In NFC-enabled devices, planar coils play a crucial role, with those in the PICC (Proximity Integrated Circuit Card) harvesting energy from the magnetic field created by the PCD (Proximity Coupling Device). Thus, they perform a dual role: facilitating data transfer between the reader and the receiver, and serving as power supply for the NFC system (Couraud et al, 2020).

The inductance is the main parameter related to coils in the field of electromagnetics. Various estimation methods and calculations are used to calculate or estimate it with an objective of a low level of error. The formula of Mohan (Mohan et al, 1999) is one of them. What makes it different is that it is based solely on the geometrical parameters of the planar coil. Knowing these parameters will give an inductance value with a 3% error margin compared to field solver predictions. Researchers have successfully employed Mohan's formula to optimize the performance of planar inductors on Kapton (Kharbouch et al, 2017). It is not complex to estimate the inductance value using this method, and because the parameters used are purely geometrical and some constants, it facilitates the integration of computer vision technologies to capture these values and automate the inductance calculation.

Building upon the idea of capturing geometrical parameters, an image treatment process was employed. It can be divided into two main sections:

the first is coil shape recognition using a YOLOv9 deep learning object detection model (Wang et al, 2024), and the second is geometrical parameter capturing and calculating inductance using the OpenCV image treatment Python library.

A number of studies have started using YOLOv9 for different objectives. For example, YOLOv9 has been applied for fracture detection in pediatric wrist X-ray images (Chien et al, 2024). It has also been used for the objective of detecting small-scale (<20km) ocean eddies to monitor changes in the Earth's oceans and climate (Mostafa et al, 2024). To train the YOLOv9 coil shapes detection model, a synthetic dataset was created using the Python Turtle library. This allowed the generation of a varied dataset with multiple spiral configurations (square, hexagonal, octagonal, and circular). After the creation of the data, augmentation was applied using the Roboflow platform. Then, OpenCV was used to detect the contours with perfect accuracy, leading to precise distance measurements of the geometry. All values were in pixels, so we made a ratio based on the known diameter of a coin to convert all values to millimeters for inductance calculation. Figure 1 presents our work in the form of a chart flow visualization to summarize the entire process.
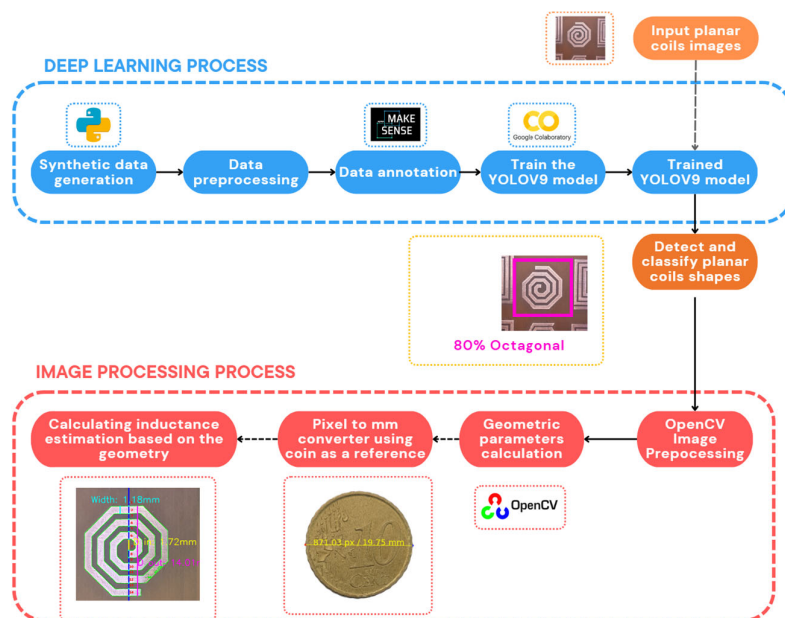
Figure 1 – Flowchart: Process for coil shape detection and inductance calculation using YOLOv9 and OpenCV

Overview of Mohan's formula

Mohan developed a simple and accurate expression for calculating the inductance of single-layer spiral shapes, including square, circular, hexagonal, and octagonal (Mohan et al, 1999). Since this expression relies directly on geometric parameters, the integration of computer vision is applied to automate inductance measurements.

The expression of the inductance is given in equation (1)

$$L = \frac{\mu_0 n^2 d_{avg} c_1}{2} \left(ln(c_2/\rho) + c_3 \rho + c_4 \rho^2 \right) \tag{1}$$

The average diameter d_{avg} and the form factor ρ are generally defined as follows:

$$d_{avg} = \frac{d_{out} + d_{in}}{2} \tag{2}$$

$$\rho = \frac{d_{out} - d_{in}}{d_{out} + d_{in}} \tag{3}$$

where d_{in} is the inner diameter, d_{out} is the outer diameter, μ_0 is the vacuum permeability, and n is the number of turns. The coefficients from C_1 to C_4 vary based on the coil geometry and are listed in Table 1.

Table 1 – Coefficients for the analytical calculation of inductance

Form	C_1	C_2	C_3	C_4
square	1.27	2.07	0.18	0.13
hexagonal	1.09	2.23	0	0.17
Octagonal	1.07	2.29	0	0.19
Circular	1	2.46	0	0.2

Figure 2 illustrates the single-layer coil spiral shapes in various geometries, including square, circular, hexagonal, and octagonal forms.
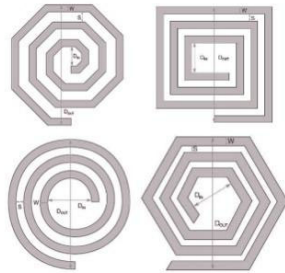
Figure 2 – Single-layer coil spiral shapes (Square, Circular, Hexagonal, And octagonal)

Dataset creation and pre-processing

Synthetic planar coil image dataset generation

Machine learning and deep learning fields latest research is highly focused on data generation to train models. The geographic information system (GIS) framework generates realistic pictures using deep neural networks and adversarial training for instance segmentation (Abu Alhaija et al, 2019; Paulin & Ivasic-Kos, 2023). Others render 3D geometric models using the ShapeNet dataset as a method for 3D object reconstruction (Richardson et al, 2016). A Python library called Turtle was utilized to generate the coils dataset. Different scripts were programmed to generate realistic pictures of planar spiral coils in hexagonal, octagonal, circular, and square geometries. This library was chosen for its capability and feature to design spiral shapes using coding. The code for each shape controlled the geometric parameters. Figure 3 is an example of how the Turtle library scripting plots the generation of spiral shapes. Each shape represents a distinct algorithmic approach to drawing patterns (Anderson, 2018).
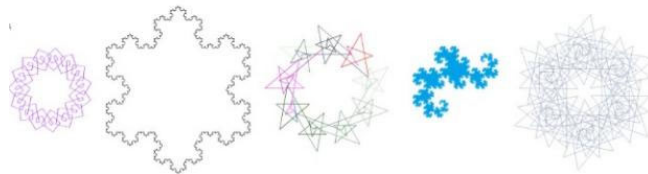
Figure 3 – Different patterned shapes plotted using the Turtle library (Anderson, 2018)

Four distinct scripts were developed to generate the dataset. The specific variable parameters included the number of spiral turns, the width

range, and the side lengths range, including inner and outer diameters. Using nested loops, each script iterates through a combination of these parameters, resulting in multiple outputs. The resulting pictures were created with the dimensions of 640 x 640 pixels, saved as EPS files, and then converted to JPEG. This automated approach ensures a perfect method to generate a comprehensive dataset. The focus was on creating a high-quality set of synthetic images to represent various geometries of planar spiral coils. The entire dataset consisted of binary color images, with each class designed to follow a clear and distinct pattern, with each single image represented in a simple 2D format with a single top-view angle. The key variations within each class were limited to the turn number and width as primary distinguishing features. This careful and clear diversity in class design ensured that even with a smaller dataset, the model had sufficient information to learn and differentiate between the four shape classes. The clear distinction between the classes made it easy for the model to recognize and learn the differences between them. Figure 4 shows a sample of generated spiral shapes using the Turtle library scripts.
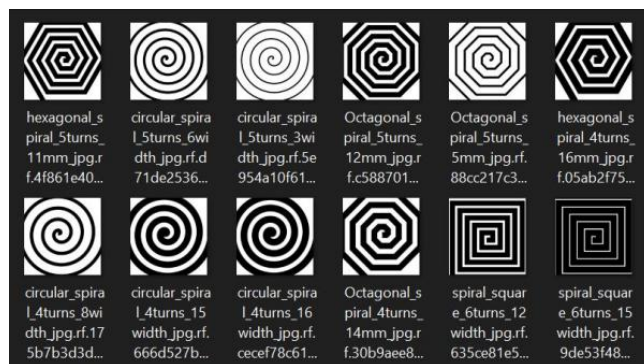
Figure 4 – Generated spiral shapes using the Turtle library scripts

Data labeling and annotation

Data labeling is an important step in dataset preparation tasks. After creating 230 different images, the annotation and labeling process was conducted using Makesense.ai, a manual online platform for annotation. Each spiral coil was labeled and annotated to categorize them into four classes. This involved perfect identification of shapes, leading to the division into specified classes, as illustrated in Figure 5, which shows the labeled classes: Hexagonal, Octagonal, Square, and Circular.
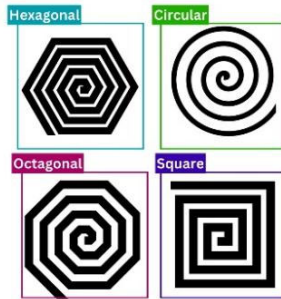
Figure 5 – Labeled classes (Hexagonal, Octagonal, Square, Circular)

Data augmentation and splitting

After the manual annotation, Roboflow, an open-source platform for data augmentation, was used to enlarge and diversify the dataset. This process expanded the dataset to a total of 547 different pictures. The techniques that were applied include blurring, rotation, flipping, and zooming. Specifically, horizontal and vertical flips, as well as 90° rotations in clockwise, counter-clockwise, and upside-down directions, were used. Preprocessing steps included auto-orientation and resizing with a center crop to 640x640 pixels. In the end, the augmented dataset was split into 87.4% for training (478 images), 8.4% for validation (46 images), and 4.2% for testing (23 images). This step is important to achieve a balanced and representative distribution of data, making it a perfect input for the AI model, as shown in Figure 6, which displays a screenshot from Roboflow showing the data split numbers with rounded percentages to 87%, 8%, and 4% for simplicity.
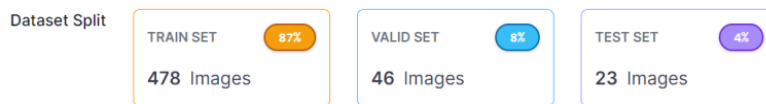
Figure 6 – Screenshot from Robotflow

YOLOv9 classification model implementation

Choice of a model

Deep learning model training requires high-performance computers to handle the training process. Google Colab found a solution for that by providing an online notebook environment that serves as an integrated

development environment (IDE) to execute the Python code directly from a browser. Colab is integrated directly with Google Drive, allowing for online file management, and comes with many machine learning libraries. The key point of the performance is the Tesla GPU acceleration, which is a suitable configuration for intensive deep learning training tasks. Figure 7 shows the specifications of the Tesla T6 GPU used.

```
▶  !nvidia-smi

⊡  Sun Mar 10 13:49:11 2024
    +-----------------------------------------------------------------------------+
    | NVIDIA-SMI 535.104.05      Driver Version: 535.104.05      CUDA Version: 12.2 |
    |-------------------------------+----------------------+----------------------+
    | GPU  Name        Persistence-M | Bus-Id        Disp.A | Volatile Uncorr. ECC |
    | Fan  Temp   Perf   Pwr:Usage/Cap |         Memory-Usage | GPU-Util  Compute M. |
    |                                 |                      |               MIG M. |
    |===============================+======================+======================|
    |   0  Tesla T4          Off | 00000000:00:04.0 Off |                    0 |
    | N/A  49C    P8     10W /  70W |      0MiB / 15360MiB |      0%      Default |
    |                                 |                      |                  N/A |
    +-------------------------------+----------------------+----------------------+

    +-----------------------------------------------------------------------------+
    | Processes:                                                                  |
    |  GPU   GI   CI        PID   Type   Process name                  GPU Memory |
    |        ID   ID                                                    Usage      |
    |=============================================================================|
    |  No running processes found                                                 |
    +-----------------------------------------------------------------------------+
```

Figure 7 – Tesla T6 GPU specifications

The YOLOv9 model was implemented and programmed as a novel deep learning classification method for real-time object detection, released in February 2024. YOLOv9 came with Programmable Gradient Information (PGI), which addresses the issue of information loss through deep network layers. The new framework, PGI, generates reliable gradients using an auxiliary reversible branch, ensuring that deep features retain essential characteristics for accurate predictions. Another key improvement of this model compared to older models is the Generalized Efficient Layer Aggregation Network (GELAN), which optimizes parameter utilization and computational efficiency without affecting accuracy. It maintains lightweight and fast inference capabilities (Wang et al, 2024).

The decision to utilize YOLOv9 was made because of its status as the most recent version in the YOLO series, so it offers improved performance in terms of speed and accuracy compared to earlier versions and effectively handles complex patterned image data in classification and object detection, aligning perfectly with the needs of this study.

Training setup and hyperparameters

The model was trained with a configuration of a batch size $N_{batch\_size}=4$, indicating that 4 data samples were processed simultaneously during each training iteration. After processing these 4 data samples, the model parameters were updated. This batch size was applied uniformly throughout each epoch, with a training duration of 50 epochs. The hyperparameters for Stochastic Gradient Descent (SGD) were as follows: momentum of 0.937 and weight decay of 0.0005. Other augmentation techniques include blur, median blur, gray conversion, and CLAHE (Contrast Limited Adaptive Histogram Equalization). This augmentation introduces further specified variations and it helps the model to better generalize new, unseen data by exposing it to a wider range of data distortions. It aims to reduce overfitting and it fine-tunes the model's ability to be adapted with different data conditions while this augmentation is often applied automatically as part of the data preprocessing pipeline of the YOLOV9 model. The model architecture comprised 930 layers with 60,804,152 parameters, and TensorBoard was used for process logging and visualization. The model has a perfect focus on the recognition of geometrical patterns over color. Even though the dataset consisted of black and white synthetic images, the model learned the spatial arrangements of pixels that form pattern shapes during training. Thus, it is capable of detecting shapes without color differences and can identify high-level features such as shapes, edges, and patterns.

Model evaluation indicators

To observe and evaluate the model's performance in detecting various classes of shapes, different evaluation indicators are used. The primary key metric is the Mean Average Precision (mAP), which yields a total value by averaging the aggregation of the precision-recall curves from each class. Precision is the measurement of positive predictions. Accuracy and recall detect all relevant instances of the coil shapes by measuring them. The F1 Score is also used, which is the harmonic mean of precision and recall, indicating how reliable the model is. It ranges between 0 and 1. mAP was used for the evaluation, computing the AP of each class and the average over several classes. These metrics are good indicators of the YOLOv9 model's ability to detect and classify objects, and they are represented mathematically as:

$$Precision = \frac{True\ Positive}{True\ Positive + False\ Positive} \qquad (4)$$

$$Recall = \frac{True\ Positive}{True\ Positive + False\ Negatives} \qquad (5)$$

$$F1\ Score = \frac{2 \times Precision \times Recall}{Precision + Recall} \qquad (6)$$

$$mAP = \frac{1}{N}\sum_{i=1}^{N} AP_i \qquad (7)$$

where N is the number of classes and AP_i represents the average precision for the class i.

Geometric parameter extraction using OpenCV

Overview of OpenCV

After using the deep learning model to detect the classes of different spiral coils, the next step is processing each image of the detected shape separately using OpenCV (Open-Source Computer Vision Library), a widely-used computer vision library (Xie & Lu, 2013). It provides a set of tools and functions for processing image and motion data (Mishra et al, 2022) at the pixel scale. OpenCV supports multiple techniques such as filtering, edge detection (Xie & Lu, 2013), and contour detection (Ni et al, 2016), leading to efficient extraction of geometric parameters. Images of the spiral coils were captured using a phone camera from the top view. The following image shows the setup with the phone camera capturing the spiral coils from above. These images were then processed using OpenCV. Figure 8 shows the setup with a fixed phone capturing the spiral coils, which were then processed using OpenCV to experiment with geometry extraction and calculation.
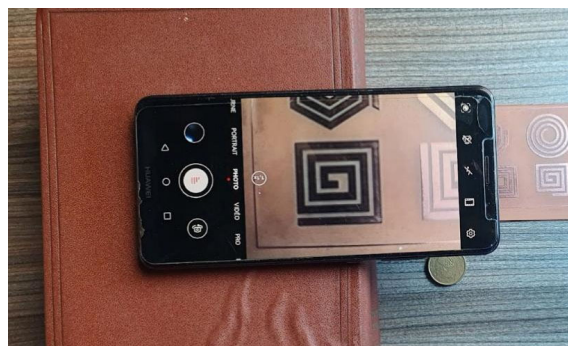
Figure 8 – Fixed phone capturing a spiral coil from above

Planar coils images preprocessing

OpenCV has a large collection of functions, with over 500 functions in computer vision that can be applied in different fields for various purposes (Mohamad et al, 2015). Specific functions are used in our research to calculate different distances and geometric parameters. These functions are described in the following steps:

Grayscale conversion and noise reduction with Gaussian blur

After capturing the image using a camera phone, the image will be loaded for processing. The first treatment involves converting this colored RGB image to a grayscale image by eliminating color information. This reduces unnecessary information from the image and decreases complexity, using the function cv2.cvtColor(). Once the image is converted to grayscale, Gaussian blur is applied to enhance the accuracy of the subsequent thresholding operation and minimize the impact of noise by smoothing the image. This is achieved using the function cv2.GaussianBlur(), which performs a convolution operation with a gaussian kernel of parameter size (9, 9) and a standard deviation (σ) of 10 to control the amount of blur. This value of kernel size was selected to achieve an optimal balance between noise reduction and detail preservation so it reduces high-frequency noise and prevents essential structural details, particularly important for the intricate patterns of planar coils. The standard deviation was set to 10 to ensure extensive smoothing for broader impact, minimizing digital noise distortions.

Figure 9 shows a grayscale image of the planar coil after the application of this process.
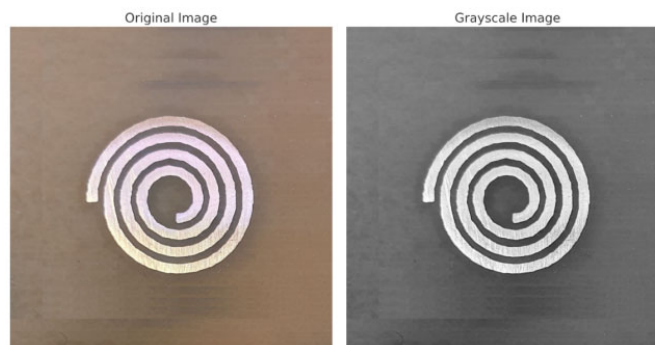
Figure 9 – Color image and its grayscale version

Binarization using Otsu's thresholding

The blurred grayscale image is then converted to a binary image using Otsu's thresholding method (Otsu, 1979). This adaptive thresholding technique calculates an optimal threshold value to separate the foreground coil image from the background, ensuring effective binarization. The function cv2.threshold() is used for this purpose, with the parameters including the blurred grayscale image an initial threshold value of 128 that serves as a starting point that typically works well for images with fair contrast and provides a balanced approach for separating the foreground from the background, and a maximum value of 255 for the binary thresholding type. Binary thresholding is applied to the grayscale image to produce a binary image where pixel values are set to either 0 or 255 based on the determined threshold. Otsu's method works by maximizing the between-class variance $\sigma_b^2(t)$, which is expressed as:

$$\sigma_b^2(t) = w_0(t)w_1(t)[\mu_0(t) - \mu_1(t)]^2 \tag{8}$$

where $w_0(t)$ and $w_1(t)$ are the class probabilities, and $\mu_0(t)$ and $\mu_1(t)$ are the means of the two classes. This method ensures the best separation between the background and the foreground in an image by maximizing the variance between these two classes.
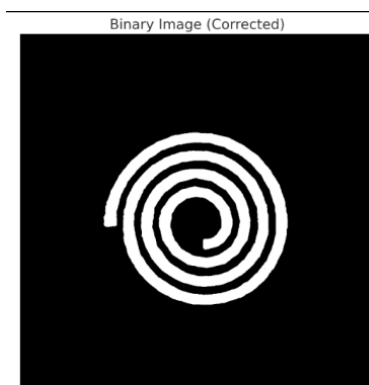
Figure 10 – Circular coil image after binarization

Contour detection and drawing

After obtaining a binary image with only white and black pixels, it is now easy to draw and detect contours. This helps identify the boundaries

of the spiral coil. The function cv2.findContours() is applied to the binary image, and then the contours are drawn and plotted on the original image using the cv2.drawContours() function, which highlights a green contour of the detected shape.

Figure 11 illustrates the circular coil image after the process of contour detection and drawing.

Figure 11 – Circular coil image after contour detection and drawing

Intersection points and parameters calculation

The measurement of specific geometries and extracting distances requires a logic to be implemented as an algorithm. For this purpose, guiding lines were designed to aid in calculating specific geometries by utilizing the cv2.line() drawing function. These lines make the intersection points with the contour. A custom-developed function detects these intersections between the guide line and the contour of the spiral coils, and these points are recorded and enumerated.

The first parameter is the width of the coil, which is calculated by the distance between the first and second intersection points along the guiding line. d_{out} represents the outer diameter of the spiral coil, which is calculated by the distance between the leftmost and rightmost intersection points. d_{in} is the inner diameter, and the logic to calculate it involves finding the first right point and the first left point near the middle of the guiding line. The number of turns n is calculated since each set of four intersection points makes one turn, so it is calculated by dividing the total number of points by four.

Figure 12 displays the measurements annotated in pixels.
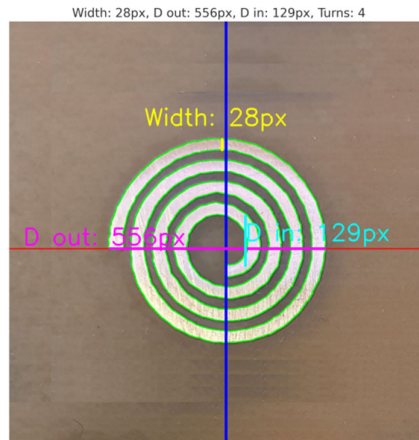
Figure 12 – Circular planar coil with pixel-extracted geometry

These geometric calculations serve as a conceptual framework for analyzing spiral coils:

$$Width = distance(i_1, i_2) \tag{9}$$

$$d_{in} = distance(i_{\text{ first left near middle}}, i_{\text{ first right near middle}}) \tag{10}$$

$$d_{out} = distance(i_{\text{ leftmost}}, i_{\text{ rightmost}}) \tag{11}$$

$$n = \left| \frac{number\ of\ intersection\ points}{4} \right| \tag{12}$$

where i_1 and i_2 represent the first and second intersection points along the guiding line, $i_{\text{ leftmost}}$ and $i_{\text{ rightmost}}$ are the extremal points on the left and right sides, $i_{\text{ first left near middle}}$ and $i_{\text{ first right near middle}}$ refer to the closest intersection points to the center of the object on each side.

Pixel-to-millimeter conversion

After extracting the required geometrical parameters of the spiral coil shapes in pixels, they should be converted to real-world units, which are millimeters. This conversion is done using a pixel-to-millimeter ratio. To calculate this ratio, a reference object with a known size is used. For this, a 10 euro cent coin was used; the diameter of the coin is 19.75 mm, so it serves as the basis for conversion. An important point to ensure the

consistency and reliability of the measurement taking is that both the reference object and the spiral coil should be captured in the same condition of the camera angle from the top and at the same distance too. The coin image processing begins by converting it to grayscale, then applying Gaussian Blur. This step reduces image noise and smooths the edges with a kernel size of (5, 5). This kernel size was selected based on preliminary tests that indicated it minimized edge distortion while adequately preserving the necessary details for accurate edge detection. Next, the Canny edge detector is applied to identify the strong edges while ignoring weaker ones with the parameters Lower Threshold: 50 and Upper Threshold: 150. These thresholds were empirically determined to provide the best balance between sensitivity to true edges and immunity to noise-induced false edges, as validated by repeated trials under varying imaging conditions. Then, the diameter can be calculated based on the last result of this image processing using a script that can detect the extreme left and right edges of the coin image. Measure the distance between these points using the Euclidean distance formula and finally, using the actual diameter of the coin and the measured diameter in pixels, calculate the conversion ratio from pixels to millimeters.

$$distance(pixels) = \sqrt{(x_{right-}x_{left})^2 + (y_{right-}y_{left})^2} \qquad (13)$$

$$Ratio(px/mm) = \frac{distance(pixels)}{Actual\ Diameter\ (mm)} \qquad (14)$$

where x_{right} and y_{right} are the coordinates of the rightmost point, and x_{left} and y_{left} are the coordinates of the leftmost point, measuring the maximum span across their widest points to get the diameter. Figure 13 demonstrates the coin image processing used for converting pixels to millimeters.

Figure 13 – Coin image processing for pixel-to-millimeter conversion

The obtained pixel-to-mm ratio is utilized to convert various parameter values of the spiral coil for all captured shapes. In Table 2, these values are presented with the conversions, allowing them to be used as inputs in Mohan's Law to compute the inductance.

Table 2 – Geometric values of different shapes: measurements in millimeters and pixels

Shape	Number of turns (n)	Width (mm)	Width (px)	d_{out} (mm)	d_{out} (px)	d_{in} (mm)	d_{in} (px)
Circular	4	0.63	28	12.61	556	2.92	129
Hexagonal	3	0.77	34	10.34	456	3.43	151
Octagonal	3	1.18	52	14.01	618	1.72	76
Square	3	1.09	48	11.95	527	2.86	126

Results

The results section is divided into two parts: the first evaluates the YOLOv9 classification model performance, and the second is about geometric parameter and inductance value calculation validation.

Model performance

The model indicates an improvement in the accuracy of bounding box coordinates and object class detection. This indication is proven by the consistent decrease in box loss, classification loss, and focal loss, across 50 epochs. In Table 3, the results demonstrate that the model is effectively learning, with performance improvement evident. The mAP values at an intersection over Union (IOU) 0.5 and other thresholds from 0.5 to 0.95 remain high and stable. The maximum recorded values for precision, recall, and F1 score are 0.989, 1.000, and 0.995, respectively.

Table 3 – Performance variability of the YOLOv9 model during training

Metric	25th Percentile	Median	75th Percentile	Max
Precision	0.579	0.881	0.982	0.989
Recall	0.541	0.973	1	1
F1 Score	0.532	0.882	0.991	0.995
mAP (IoU=0.5)	0.496	0.988	0.995	0.995
mAP (IoU=0.5:0.95)	0.264	0.83	0.89	0.913

The F1-Confidence curve reflects that the model has strong predictive capabilities for different shape classes. This curve is a graphical representation that illustrates the relationship between the confidence level of predictions and the corresponding F1 score, and it combines the precision level and the recall into a single metric, achieving an optimal macro-average F1 score of 0.98 at a confidence threshold of 0.501 with a balanced precision and recall. The Octagonal and Circular classes show a well-balanced trade-off between precision and recall. The Hexagonal class also performs impressively well, with high F1 scores at lower levels of confidence. The class of Square, on the other hand, has a bit of fluctuation at high confidence but gives good F1 scores. Figure 14 illustrates the F1-Confidence curves for various coil shapes.
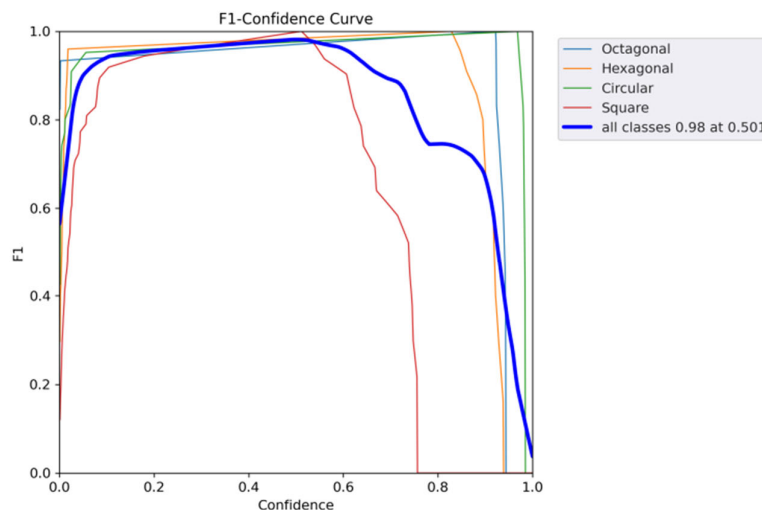
Figure 14 – F1-Confidence curves for different coil shapes

After experimental testing, the model demonstrated that a Square coil was detected with a confidence level of 0.91, a Circular coil with a confidence level of 0.80, a Hexagonal coil with a confidence level of 0.60, and an Octagonal coil with a confidence level of 0.65. In this context, the confidence level represents the model's degree of certainty in correctly identifying and classifying the detected object as belonging to a specific geometric shape class as a final prediction level. These confidence levels, which are directly related to the model's classification task in the image, indicate how certain the model is that the identified shape corresponds to

its labeled class, such as Square, Circular, Hexagonal, or Octagonal. These results confirm the robustness and reliability of the model in categorizing different geometric shapes. Figure 15 presents the detection confidence levels for various coil shapes.
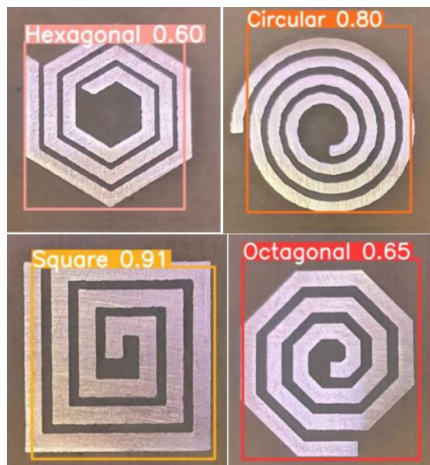
Figure 15 – Detection confidence scores for coil shapes

Geometric parameter and inductance value validation

A comparison is made between the extracted inductance values calculated based on the design geometry created with the computer aided design (CAD) software, and the values computed from the results of OpenCV. Table 4 shows the difference between the value sets of different shapes.

Table 4 – Inductance measurement comparison across different geometric shapes based on CAD and computer vision (CV) data

Shape	d_{out}		d_{in}		Inductance CV (nH)	Inductance CAD (nH)
	CAD (mm)	CV (mm)	CAD (mm)	CV (mm)		
Circular	12.5	12.61	3	2.92	113.24	114.13
Square	11.8	11.95	2.8	2.86	73.09	72.80
Octagonal	14.07	14.01	1.73	1.72	56.73	55.20
Hexagonal	10.3	10.34	3.3	3.43	65.08	63.12

The accuracy of the geometric parameters extracted by OpenCV is remarkably high, leading to good accuracy in the estimated inductance value. These results underline the effectiveness of our high-resolution measurement techniques, which are essential for in-depth assessments in precision engineering contexts and quality control during construction. Figure 16 shows the inductance value for a circular coil geometry, where the CV system measured 113.24 nH, closely matching the CAD value of 114.13 nH. At the same time, Figure 17 presents the hexagonal coil geometry, with an inductance of 65.08 nH measured by CV, aligning well with the CAD value of 63.12 nH. Figures 18 and 19 display the octagonal and square geometries, with inductance values of 56.73 nH and 73.09 nH, respectively, both showing good agreement with their CAD values.

The difference with the values of the computer vision method and the inductance value of design geometry may be explained by the fact that, in realistic coil manufacturing, physical dimensions and software design values may not be exactly identical to each other. Deviations from the manufacturing process and small deviations in physical dimensions can result in theoretical design parameters that differ from actual measured values. Overall, the results show good agreement between the inductance values. Minor inconsistencies, as indicated, may be expected with the granularity of the pixel-based measurements too and have little or no impact on the overall inductance calculations while working with nanohenries. This means that the computer vision method can be relied upon to establish inductance values accurately. Figures 16 to 19 present the results of the analysis and inductance calculations for various planar coil geometries using OpenCV.
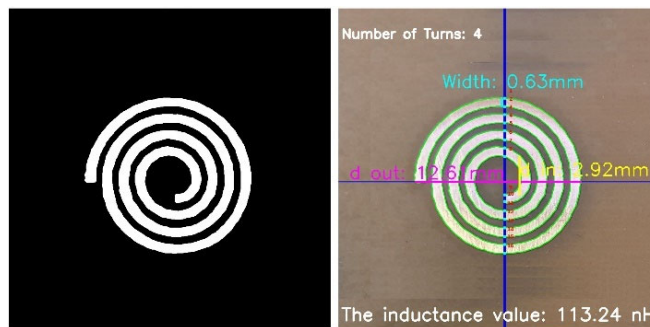
Figure 16 – Analysis of circular planar coil geometry and inductance calculation with OpenCV
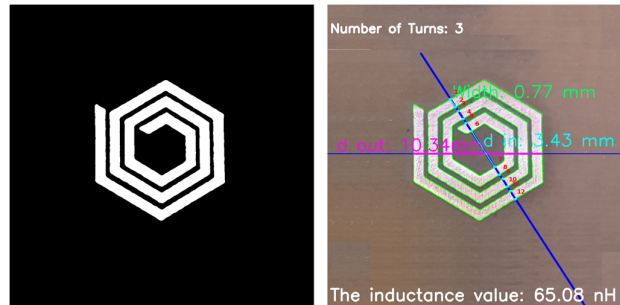
Figure 17 – Analysis of hexagonal planar coil geometry and inductance calculation with OpenCV
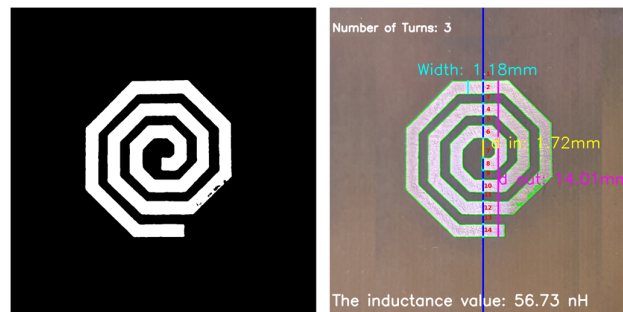
Figure 18 – Analysis of octagonal planar coil geometry and inductance calculation with OpenCV
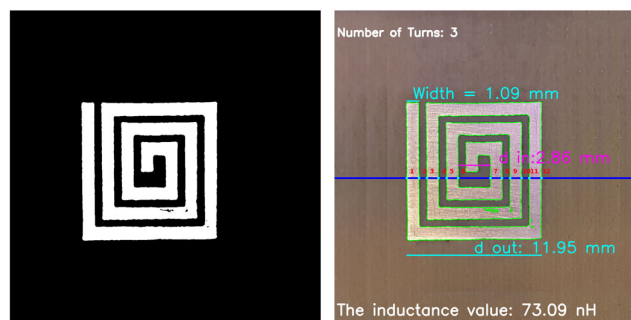
Figure 19 – Analysis of square planar coil geometry and inductance calculation with OpenCV

Conclusion

The work demonstrates how computer vision and deep learning techniques can be useful in assisting the calculation of inductance in the case of planar coils. Utilizing YOLOv9 for shape recognition and OpenCV to extract geometric parameters, the proposed methodology resulted in a way such that it performs with a high accuracy rating. This, in a way, makes the method reliable for industrial purposes where more precision in the manufacturing of a component is required. In further work, this model can be designed to work with more coil shapes, hence reducing the discrepancy in the measurements in the process. An extension of this work could be in integrating this computer vision with real-time monitoring systems for further advancement in automated manufacturing systems.

References

Abu Alhaija, H., Mustikovela, S.K., Geiger, A. & Rother, C. 2019. Geometric image synthesis. In: Jawahar, C., Li, H., Mori, G. & Schindler, K. (Eds.) *Computer Vision – ACCV 2018. ACCV 2018. Lecture Notes in Computer Science*, 11366, pp.85-100. Cham: Springer. Available at: https://doi.org/10.1007/978-3-030-20876-9_6.

Ahire, D.B., Gond, V.J. & Chopade, J.J. 2022. Geometrical parameter optimization of planner square-shaped printed spiral coil for efficient wireless power transfer system to biomedical implant application. *e-Prime-Advances in Electrical Engineering, Electronics and Energy*, 2, art.number:100045. Available at: https://doi.org/10.1016/j.prime.2022.100045.

Anderson, E.F. 2018. Turtle Fractals and Spirolaterals: Effective Assignments for Novice Graphics Programmers. In: *Eurographics 2018*, Delft, The Netherlands, pp.39-42, April 20 [online]. Available at: https://eprints.bournemouth.ac.uk/30590/ [Accessed: 05.06.2024].

Chien, C.-T., Ju, R.-Y., Chou, K.-Y. & Chiang, J.-S. 2024. YOLOv9 for fracture detection in pediatric wrist trauma X-ray images. *Electronics Letters*, 60(11), e13248. Available at: https://doi.org/10.1049/ell2.13248.

Couraud, B., Deleruyelle, T., Vauche, R., Flynn, D. & Daskalakis, S.N. 2020. A low complexity design framework for nfc-rfid inductive coupled antennas. *IEEE Access*, 8, pp.111074-111088. Available at: https://doi.org/10.1109/ACCESS.2020.3001610.

Derkaoui, M., Benhadda, Y., Hamid, A. & Temmar, A. 2021. Design and Modeling of Octagonal Planar Inductor and Transformer in Monolithic Technology for RF Systems. *Journal of Electrical Engineering & Technology*, 16(3), pp.1481-1493. Available at: https://doi.org/10.1007/s42835-021-00692-x.

Im, J.-H. & Hur, J. 2021. Proposing new planar-type search coil for permanent magnet synchronous motor: Design and application for position estimation. *IEEE Access*, 9, pp.129078-129087. Available at: https://doi.org/10.1109/ACCESS.2021.3113384.

Kharbouch, H., Hamid, A., Lebey, T., Bley, V., Havez, L. & Combette, C. 2017. Using the variable width in a planar inductor on Kapton for optimizing its performance. *Turkish Journal of Electrical Engineering and Computer Sciences*, 25(5), pp.3798-3810. Available at: https://doi.org/10.3906/elk-1606-343.

Luo, Z. & Wei, X. 2017. Analysis of Square and Circular Planar Spiral Coils in Wireless Power Transfer System for Electric Vehicles. *IEEE Transactions on Industrial Electronics*, 65(1), pp.331-341. Available at: https://doi.org/10.1109/TIE.2017.2723867.

Mishra, S., Verma, V., Akhtar, N., Chaturvedi, S. & Perwej, Y. 2022. An Intelligent Motion Detection Using OpenCV. *International Journal of Scientific Research in Science, Engineering and Technology*, 9(2), pp.51-63. Available at: https://doi.org//10.32628/IJSRSET22925.

Mohamad, M., Saman, M.Y.M. & Hitam, M.S. 2015. A Review on OpenCV. *ResearchGate*, August Available at: https://doi.org/10.13140/RG.2.1.2269.8721.

Mohan, S.S., del Mar Hershenson, M., Boyd, S.P. & Lee, T.H. 1999. Simple accurate expressions for planar spiral inductances. *IEEE Journal of Solid-State Circuits*, 34(10), pp.1419-1424. Available at: https://doi.org/10.1109/4.792620.

Mostafa, S.A.M., Wang, J., Holt, B. & Wang, J. 2024. YOLO based Ocean Eddy Localization with AWS SageMaker. *arXiv:2404.06744v1*, 10 April. Available at: https://doi.org/10.48550/arXiv.2404.06744.

Ni, J., Khan, Z., Wang, S., Wang, K. & Haider, S.K. 2016. Automatic detection and counting of circular shaped overlapped objects using circular hough transform and contour detection. In: *2016 12th World Congress on Intelligent Control and Automation (WCICA)*, Guilin, China, pp.2902-2906, June 12-15. Available at: https://doi.org/10.1109/WCICA.2016.7578268.

Otsu, N. 1979. A Threshold Selection Method from Gray-Level Histograms. *IEEE Transactions on Systems, Man, and Cybernetics*, 9(1), pp.62-66. Available at: https://www.doi.org/10.1109/TSMC.1979.4310076.

Paulin, G. & Ivasic-Kos, M. 2023. Review and analysis of synthetic dataset generation methods and techniques for application in computer vision. *Artificial Intelligence Review*, 56(9), pp.9221-9265. Available at: https://doi.org/10.1007/s10462-022-10358-3.

Richardson, E., Sela, M. & Kimmel, R. 2016. 3D Face Reconstruction by Learning from Synthetic Data. In: *2016 Fourth International Conference on 3D Vision (3DV)*, Stanford, CA, USA, pp.460-469, October 25-28. Available at: https://doi.org/10.1109/3DV.2016.56.

Wang, C.-Y., Yeh, I.-H. & Liao, H.-Y.M. 2024. YOLOv9: Learning What You Want to Learn Using Programmable Gradient Information. *arXiv:2402.13616v2*, 29 February. Available at: https://doi.org/10.48550/arXiv.2402.13616.

Xie, G. & Lu, W. 2013. Image Edge Detection Based On Opencv. *International Journal of Electronics and Electrical Engineering*, 1(2), pp.104-106. Available at: https://doi.org/10.12720/ijeee.1.2.104-106.

Un enfoque de visión por computadora con OpenCV y aprendizaje profundo para determinar la inductancia en bobinas planas

Younes Benazzouz, **autor de correspondencia***, Djilalia* Guendouz

Universidad de Orán 2 Mohamed Ben Ahmed, Instituto de Seguridad y Mantenimiento Industrial (IMSI), Departamento de mantenimiento de instrumentación, Laboratorio de Ingeniería de Producción y Mantenimiento Industrial (LGPMI), Orán, República Argelina Democrática y Popular

CAMPO: ciencias de la computación, electrónica
TIPO DE ARTÍCULO: artículo científico original

Resumen:

Introducción/propósito: En el ámbito del desarrollo y uso de metodologías de visión por computadora e inteligencia artificial, esta investigación presenta una combinación y un método avanzado que utiliza YOLOv9, un concepto de aprendizaje profundo de procesamiento de imágenes completas en un solo paso a través de una red neuronal convolucional (CNN) y la Biblioteca de procesamiento de imágenes OpenCV Python para determinar la geometría de bobinas planas. Estos parámetros geométricos son los principales parámetros utilizados para calcular el valor de inductancia utilizando la fórmula de Mohan, que utiliza exclusivamente datos geométricos para calcular los valores de inductancia. Este método acelera significativamente los procesos de verificación y cálculo, al mismo tiempo que contribuye a mejorar el control de calidad después de la fabricación.

Métodos: La metodología se divide en dos fases principales. Inicialmente, se entrenó un modelo YOLOv9 para el reconocimiento de objetos utilizando un conjunto de datos sintéticos generados de formas de bobinas creadas con la biblioteca de gráficos Turtle de Python. Luego, después de la fase de detección, se utilizó OpenCV para identificar los parámetros geométricos de las imágenes. Los píxeles se convirtieron a milímetros utilizando un método de relación para calcular el valor de inductancia con precisión.

Resultados: El modelo YOLOv9 identificó con éxito varias formas de bobinas planas y los parámetros geométricos se identificaron mediante OpenCV. Posteriormente, se calculó con éxito la inductancia.

Conclusión: Los resultados muestran que el método propuesto es una forma novedosa y eficaz de calcular la inductancia.

Palabras claves: redes neuronales convolucionales (CNN), OpenCV, bobina plana, inductancia, YOLOv9, procesamiento de imágenes.

Применение компьютерного зрения с использованием OpenCV и глубокого обучения для определения индуктивности плоских катушек

Юнез Беназзоуз, **корреспондент**, Джилалия Гуендоуз

Университет Орана 2 Мохамед Бен Ахмед, Институт технического обслуживания и промышленной безопасности (IMSI), кафедра технического обслуживания контрольно-измерительных приборов, Лаборатория производственного инжиниринга и промышленного обслуживания (LGPMI),
г. Оран, Алжирская Народная Демократическая Республика

Резюме:

Введение/цель: В свете развития и использования методологий компьютерного зрения и искусственного интеллекта данное исследование представляет собой комбинированный и продвинутый метод, использующий YOLOv9, концепцию глубокого обучения для обработки полного изображения за один проход через свёрточную нейронную сеть (CNN) и библиотеку обработки изображений OpenCV Python для определения геометрии плоских катушек. Данные геометрические параметры являются главными в расчёте значений индуктивности с использованием формулы Мохана, которая использует геометрические данные исключительно для оценки значений индуктивности. Этот метод значительно ускоряет процессы верификации и расчёта, а также способствует повышению качества контроля производства.

Методы: Методология исследования распределена на два основных этапа. Сначала была обучена модель YOLOv9 для распознавания объектов, используя сгенерированный синтетический набор данных форм катушек, созданный с помощью библиотеки Turtle Graphics в Python. Затем, после этапа обнаружения, с помощью OpenCV были идентифицированы геометрические параметры изображений. Пиксели были преобразованы в миллиметры, используя метод соотношения для точного расчета значения индуктивности.

Результаты: Модель YOLOv9 успешно идентифицировала различные формы плоских катушек, а геометрические параметры были определены с помощью OpenCV. Индуктивность также была успешно рассчитана.

Выводы: Результаты показывают, что предложенный метод является инновационным и эффективным способом расчета индуктивности.

Ключевые слова: сверточные нейронные сети (CNN), OpenCV, плоская катушка, индуктивность, YOLOv9, обработка изображений.

Примена рачунарског вида помоћу OpenCV и дубоког учења за одређивање индуктивности у пљоснатим намотајима

Јунез Беназуз, **аутор за преписку**, *Дајлија* Гундуз

Универзитет Оран 2 Мохамед Бен Ахмед, Институт за индустријско одржавање и безбедност (IMSI), Одељење за одржавање инструментације, Лабораторија за производно машинство и индустријско одржавање (LGPMI), Оран, Народна Демократска Република Алжир

Сажетак:

Увод/циљ: У области развоја и примене методологија рачунарског вида и вештачке интелигенције, ово истраживање представља комбинацију и напредну методу која користи YOLOv9 – концепт дубоког учења за обраду целокупне слике у једном пролазу кроз конволуциону неуронску мрежу (CNN) и библиотеку за обраду слика OpenCV на Pythonu за одређивање геометрије пљоснатих намотаја. Ови основни геометријски параметри користе се за израчунавање вредности индуктивности помоћу Моханове формуле, која искључиво употребљава геометријске податке за процену вредности индуктивности. Ова метода знатно убрзава процесе верификације и израчунавања, а побољшава и контролу квалитета после производње.

Методе: Методологија је подељена на две главне фазе. У почетку је модел YOLOv9 био конструисан за препознавање објеката коришћењем генерисаног синтетичког скупа података облика намотаја створеног помоћу Pythonove библиотеке Turtle Graphics. Затим, након фазе детекције, OpenCV је коришћен за идентификацију геометријских параметара слика. Пиксели су претворени у милиметре применомметоде пропорција за тачно израчунавање вредности индуктивности.

Резултати: Модел YOLOv9 је успешно идентификовао различите облике пљоснатих намотаја, а геометријски параметри су идентификовани путем OpenCV. Након тога, индуктивност је успешно израчуната.

Закључак: Резултати показују да је предложена метода нов и ефикасан начин за израчунавање индуктивности.

Кључне речи: конволуционе неуронске мреже (CNN), OpenCV, пљоснати намотај, индуктивност, YOLOv9, обрада слика.

Flexible Variable Weight Zero Cross-Correlation (FVWZCC) investigations for multimedia applications

Abdellah Bensaad[a], *Abbes* Beloufa[b], *Ahmed* Garadi[c]

[a] Dr. Moulay Tahar University, Department of Electronics,
 Saida, People's Democratic Republic of Algeria*,*
 e-mail: abdellah.bensaad@univ-saida.dz, **corresponding author,**
 ORCID iD: https://orcid.org/0000-0001-9305-2421

[b] Mustapha Stambouli University, Faculty of Sciences and Technology,
 Mascara, People's Democratic Republic of Algeria,
 e-mail: abbes.beloufa@univ-mascara.dz,
 ORCID iD: https://orcid.org/0000-0002-3776-9097

[c] Djillali Liabes University, Applied Materials Laboratory,
 Sidi Bel Abbes, People's Democratic Republic of Algeria*,*
 e-mail: garadi20@yahoo.fr,
 ORCID iD: https://orcid.org/0000-0003-1822-0936

Abstract:

Introduction/purpose: In this paper, we propose a novel code construction method with the zero cross-correlation property, the Flexible Variable Weight Zero Cross-Correlation (FVWZCC). This method is simple and flexible, using different code weights to support different classes of users according to their transmission distance and the quality of services they require (data, audio, and video) in OCDMA systems. The use of higher code weights enables the support of higher-priority application networks, such as long-haul reach networks. The ZCC code structure does not have overlapping of bit '1' and can efficiently eliminates the MAI interference between users and PIIN noise, thus enhancing the system overall performance.

Methods: The shifting element position and the concatenation matrix process of the three basic matrices denoted as the Right vector, the basic matrix, and the Left vector were used for the construction of the proposed FVWZCC code. The mathematical analysis and simulations with Matlab and Optisystem software were used to evaluate the performance of the proposed FVWZCC method in SAC-OCDMA systems using the direct detection.

Results: The results show a significant improvement in the presented code compared to other existing codes in terms of simplicity, flexibility, and cost implementation. The method uses either constant or variable weight with

the Zero cross-correlation property. For a maximum acceptable BER of 10^{-9}, the simulation results of the SAC-OCDMA system using direct detection under OptiSystem software show better performance of the proposed code with four users of weight 6 at $10\,Gb/s$. Moreover, it can support up to 60 users simultaneously and reach a fibre distance of about 67 km. Consequently, the proposed FVWZCC code can be applied to support different Quality of Service (QOS) requirements with low cost and low complexity with a direct detection receiver.

Conclusion: The findings of this study highlight the need for the FVWZCC code to support end-user QoS requirements. The new approach to code construction offers low-cost implementation, simplicity, and flexibility.

Key words: FVWZCC code, OCDMA, ZCC, Bit Error Rate BER.

Introduction

The unprecedented exponential growth in global mobile traffic and the huge development of smart devices such as the Internet of Things (IoT) expected for the future 5G/6G communication networks has increased the demand for a wide range of applications with substantial improvements to the data transfer rates, a huge amount of bandwidth and enhanced Quality of Services (QoS) requirements (Dat et al, 2018; Teli et al, 2018; Hakeem et al, 2022). Several multiple access techniques have been proposed for future applications with high bandwidth and high performance such as wavelength division multiple access (WDMA) (Dixit et al, 2013), time division multiple access (TDMA) (Osadola et al, 2011), and optical code division multiple access (OCDMA) (Mostafa et al, 2015). The optical OCDMA technique can be considered prominent and more suitable technology in the field of optical communication and computer networks due its high spectral efficiency, inherent security, low interference characteristics, scalability, multiplexing capability, and seamless integration with existing networks (Kaur & Sing, 2018; Lu et al, 2021; Pendeza Martinez et al, 2021). Furthermore, OCDMA is used in various optical network applications such as optical fiber sensors (Rahimian et al, 2019), metro networks (Zhang et al, 2019; Troia et al, 2020), passive optical networks (PONs) (Farghal, 2016; Zhang et al, 2019; Pendeza Martinez et al, 2021; Ahmed et al, 2022), and radio-of-fiber (RoF) (Ji & Chang, 2013; Kbashi et al, 2021).

In the spectral amplitude coding SAC-OCDMA system, asynchronous multiple users access the same channel medium simultaneously with a high level of security and flexibility. Each user is allocated a unique coding sequence which distinguishes the desired information from the other receiving sequences. However, it suffers from multiple access interference

(MAI) and phase-induced intensity noise (PIIN) phenomena at the receiver which reduces the maximum number of allowed optical codes (Huang et al, 2008; Kaur & Sing, 2018; Bensaad et al, 2019). A proper choice of codes with maximum auto-correlation and minimum cross-correlation known as Zero Cross-Correlation (ZCC) codes or using more sophisticated detection techniques can eliminate the MAI and the PIIN effects (Ahmed et al, 2022; El-Mottaleb et al, 2020; Abd et al, 2011).

In the literature, various codes with zero-cross correlation have been proposed for SAC-OCDMA such as random diagonal code (RD) (Fadhil et al, 2009a), multi-diagonal code (MD) (Imtiaz et al, 2020), and zero cross-correlation code (ZCC) (Bensaad et al, 2023; Anuar et al, 2009; Nisar et al, 2019). Other codes have been proposed that deal with the presence of PIIN effects at the receiver using suitable detection processes such as modified double weight code (MDW) (Upadhyay et al, 2020), Flexible Cross-Correlation code (FCC) (Rashidi et al, 2014), and diagonal Eigen Unity Code (DEU) (Ahmed & Nisar, 2013).

The above-reported codes were designed with constant code weight (CW) while variable code weight (VW) is used to support multimedia services such as voice, video, and image transmission at the physical layer with different bit rates (Nasaruddin & Tsujioka, 2008; Li et al, 2023). Physical layer QoS was made possible for the OCDMA system by varying the weight of the code, the length, or both the weight and the length. Higher quality services have been assigned more weights or more wavelengths corresponding to higher transmitted power sent by each code. A higher code length transports data information at a lower transmission rate (Li et al, 2020; Kumawatn & Maddila, 2017).

Variable code weights have been proposed by several researchers to provide different quality of service (QoS) requirements for the SAC-OCDMA network, among them: variable weight OOC codes for multimedia SAC-OCDMA systems (Nasaruddin & Tsujioka, 2008), Variable Weight Zero Cross-Correlation Code (VW-ZCCC) (Kumawat & Maddila, 2017), service differentiation using Khazani-Syed (KS) code (Anas et al, 2009), Variable Weight code for Multimedia Service (VW-MS) (Kumawat & Ravi Kumar, 2018), Variable code weight using Random Diagonal Code (RD) for Spectral Amplitude Coding OCDMA Systems (Fadhil et al, 2009b), Zero Cross-Correlation Magic Square Variable Weight Optical Orthogonal Code (ZMS-VWOOC) (Lu et al, 2021), Variable Weight Quadratic Congruence Code (VWQCC) (Feng et al, 2015), and variable weight Zero Cross-Correlation Code (VZCC) (Nisar et al, 2021).

In this paper, we proposed a new code construction design method for SAC-OCDMA systems which has the following properties:

- Zero Cross-Correlation ZCC property, which reduces significantly the MAI and PIIN noise effects, thus improving the performance of the system,
- The method offers a good flexibility in the choice of any number of users or code weight,
- It can be used with constant or variable code weight, and
- The mapping procedure of this method is simple and based on shifting a three elementary matrices which can reduce the cost and the system complexity.

The remainder of the manuscript is organized as follows: first, we present the need for the proposed FVWZCC code for multimedia applications and describe mathematically the code design construction. Then, the performance analysis of the code using Direct Detection (DD) is introduced followed by a theoretical analysis and performance comparison with other codes from the references to prove the efficiency of the proposed code. Next, the performance of the proposed FVWZCC code is validated by using simulations under Optisystem software Version 7.0. Finally, a conclusion is given to summarize the work.

FVWZCC code for multimedia applications

The proposed FVWZCC code can support the diversity of multimedia services where a higher transmission rate is assigned to video applications, since a high video transmission rate provides high video quality, the medium data rate is assigned to audio transmission whereas data transmission such as image supports low data rate transmission. The FVWZCC code is characterized by the code weight W_i, the code length L_i, and the number of users K_i, where $i \in \{1, 2, 3\}$ denotes one of the three services: audio, video and data. For different quality of services, W_i represents the low-level weight dictated for data transmission with low quality of services, W_{i+1} represents the medium-level weight dictated for audio transmission with medium quality of services, and W_{i+2} represents the high-level weight dictated for video transmission with high quality of services. Let k_i^d, k_i^a, and k_i^v be constants for the ith data, audio, and video services, respectively. The code length for each service can be expressed as:

$$L_d = k_i^d W_i \qquad \text{for data transmission} \qquad (1)$$
$$L_a = k_i^a W_{i+1} \qquad \text{for audio transmission} \qquad (2)$$
$$L_v = k_i^v W_{i+2} \qquad \text{for video transmission} \qquad (3)$$

For the code weight W_i, $i \in \{1, 2, 3\}$ denotes one of the three services: audio (W_1), video (W_2), and data (W_3). The subscript $(i + 1)$ or $(i + 2)$ denotes the code weight increment by one for video and data services, respectively.

$$\text{For } i = 1, W_i = W_1 = W \Rightarrow L_1 = L_d = k_i^d \, W_i = k_i^d \, W$$
$$i = 2, W_2 = W_{i+1} = W_i + 1 \Rightarrow L_2 = L_d = k_i^a \, W_{i+1} = k_i^a \, (W + 1)$$
$$i = 3, W_3 = W_{i+2} = W_i + 2 \Rightarrow L_3 = L_d = k_i^v \, W_{i+2} = k_i^v \, (W + 2)$$

The resulting matrix of the FVWZCC code can support two classes of users according to their transmission distance with different quality of services (data, audio, and video). The first class is the long-haul reach network of hundreds or thousands of kilometers and the second is the short-haul reach network with several tens of kilometers. Note that the weight assigned to each class of users or quality of services obeys some conditions such as:

$$W_{i+2} > W_{i+1} > W_i \tag{4}$$
$$W_{i,C_1} > W_{i+2,C_2} \tag{5}$$

where W_{i,C_1} and W_{i,C_2} denotes the code weight of the ith transmission service (audio, data or video) used for the corresponding long-haul reach network class of the application zone and the short-haul reach network class of the application zone in the descending order of distance ($C_1 > C_2$), respectively. Figure 1 gives an example for two classes of networks length with a code weight of $W_i = 5$ and three transmission services.
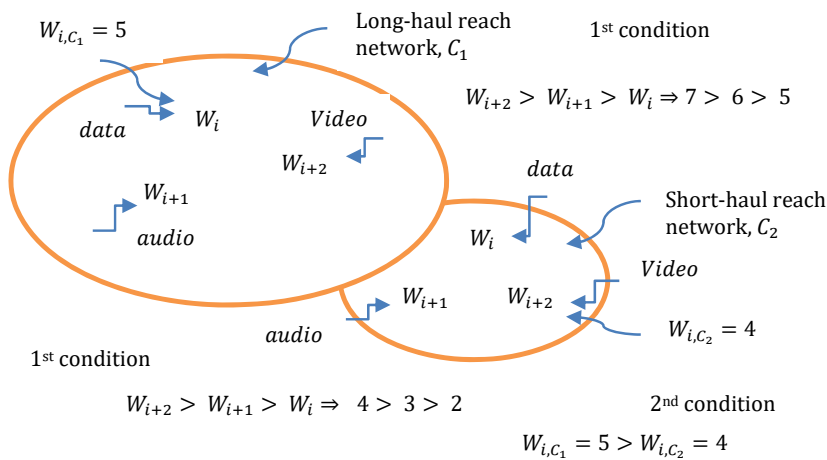
Figure 1 – Example of two classes: the long-haul reach network and the short-haul reach network

Construction method of the FVWZCC code

The process design construction of the proposed Flexible Variable Weight Zero Cross-Correlation matrix code FVWZCC is described by the following steps.

Step 1
Consider a basic matrix denoted by H_b of size $(K \times L)$ given by:

$$H_{b=1} = \begin{bmatrix} 1 & 0 & 1 & 0 \\ 0 & 1 & 0 & 1 \end{bmatrix}_{(K \times L)}.$$

(6)

where $K = 2$ rows represent the number of users, $L = 4$ columns represent the minimum code length, and the number of one element values $W = 2$ represents the code weight. Clearly, the cross-correlation of the proposed basic matrix is zero.

The basic matrix H_b is formed by the concatenation of three elementary basic compounds as:
the elementary matrix M_b of the size (2×2) denoted by: $M_b = \begin{bmatrix} 0 & 1 \\ 1 & 0 \end{bmatrix}_{(2 \times 2)}$,
the right vector $V_R = [1\ 0\ ]^T$ inserted in the right of the elementary matrix M_b, and
the left vector $V_L = [0\ 1\ ]^T$ inserted in the left of the elementary matrix M_b.

Step 2
Case 1: Consider a fixed number of users $K = 2$
To increase the code weight while maintaining the number of users fixed, the two elementary vectors V_R and V_L are inserted alternatively in the left and the right of the basic matrix H_b leading to a new matrix code characterized by:

a code weight: $\quad W_N = W + W_v\ = 2 + W_v$ (7)
a code length: $\quad L_N = L + 2W_v\ = 4 + 2W_v$ (8)

where W_v denotes the number of vectors inserted into the left or the right of the basic matrix H_b.

1676

The resulting new matrix code of weight W_N is shown as:

$$H_N = [V_R \, V_L \, ... \, V_R \, V_L \, H_b \, V_R \, V_L \, ... \, V_R \, V_L] \tag{9}$$

For instance, the resulting new matrix of the code weight $W_N = 3$ is obtained as:

$$H_{N,W_N=4} = \begin{bmatrix} 0 \\ 1 \end{bmatrix} \begin{bmatrix} 1 & 0 & 1 & 0 \\ 0 & 1 & 0 & 1 \end{bmatrix} \begin{bmatrix} 1 \\ 0 \end{bmatrix}_{(K \times (L + 2W_v)) = (2 \times 6)} \tag{10}$$

Case 2: Consider a fixed code weight W of the basic matrix H_b

In this phase, the number of users can be further increased using a particular shifted process for the three elementary compounds of the basic matrix H_b. The right vector V_R is shifted to the right by some positions (or columns) equal to: $\left[0 : \left(\frac{K}{2} - 1\right)\right]$, where K denotes the number of users. The elementary matrix M_b is shifted to the right by some positions (or columns) equal to: $\left[\left(\frac{K}{2} - 1\right) : (K - 2)\right]$, and the left vector V_L is shifted to the left by some positions equal to: $\left[(K - 2) : \left(\frac{K}{2} - 1\right)\right]$, The number of shifted positions to the right side is filled with the same number of zeros. In the results, the total number of inserted zeros for the three elementary matrix and vector compounds is given below:

$$V_R \to \left[0 : \left(\frac{K}{2} - 1\right)\right]$$

$$M_b \to \left[\left(\frac{K}{2} - 1\right) : (K - 2)\right] \cup \{V_R \text{ total number of zeros shifted positions}\}$$

$$\Rightarrow M_b \to \left[\left(\frac{K}{2} - 1\right) : (K - 2)\right] \cup \left[0 : \left(\frac{K}{2} - 1\right)\right]$$

$$V_L \to \left[(K - 2) : \left(\frac{K}{2} - 1\right)\right] \cup \{M_b \text{ total number of zeros shifted positions}\}$$

$$\Rightarrow V_L \to \left[(K - 2) : \left(\frac{K}{2} - 1\right)\right] \cup \left[\left(\frac{K}{2} - 1\right) : (K - 2)\right] \cup \left[0 : \left(\frac{K}{2} - 1\right)\right]$$

For example, let the number of users $K = 4$, the weight $W = 2$, and the length code $L = 4$.

Following the above strategy, the resulting matrix code is given by:

Basic Matrix M_b

The Right vector V_R

Left Vector V_L

No shifting position

$\begin{bmatrix}1\\0\end{bmatrix}$ is the Right Vector V $\begin{bmatrix}1\\0\end{bmatrix}, \begin{bmatrix}0 & 1\\1 & 0\end{bmatrix}, \begin{bmatrix}0\\1\end{bmatrix}$

⓪

$$V_R \rightarrow \left[0 : \left(\frac{K}{2} - 1\right)\right] = \left[0 : \frac{4}{2} - 1\right] = [0 : 1] \Rightarrow \begin{bmatrix}1\\0\end{bmatrix}, \begin{bmatrix}\begin{bmatrix}1\\0\end{bmatrix} & [\square]\\ [\square] & \begin{bmatrix}1\\0\end{bmatrix}\end{bmatrix}$$

There are two shifting positions possibilities to the right, one with zero shifting position, the second with one shifting position (0,1).

One shifting position of the right Vector V_R

①

One shifting position of the right Vector V_R

$$\Rightarrow \begin{bmatrix}\begin{bmatrix}1\\0\end{bmatrix} & \begin{bmatrix}0\\0\end{bmatrix}\\ \begin{bmatrix}0\\0\end{bmatrix} & \begin{bmatrix}1\\0\end{bmatrix}\end{bmatrix}$$

The resulting matrix after shifting positions using the Right Vector V_R.

One zero shifting position

Three zero shifting positions

$$M_b \rightarrow \left[\left(\frac{K}{2} - 1\right) : (K - 2)\right] \cup \left[0 : \left(\frac{K}{2} - 1\right)\right] =$$

$$= [1 : 2] \cup [0 : 1] = [1 : 3]$$

One shifting positions for the matrix M_b

Two shifting positions for the matrix M_b

One zero shifting position

① →

One shifting position for the matrix M_b

$$\Rightarrow \begin{bmatrix}0 & 1\\1 & 0\end{bmatrix} \begin{bmatrix}\begin{bmatrix}0 & \square\\1 & \square\end{bmatrix} & \begin{bmatrix}0 & 1\\1 & 0\end{bmatrix} & \begin{bmatrix}\square & \square\\\square & \square\end{bmatrix}\\ \begin{bmatrix}\square & 1\\\square & 0\end{bmatrix} & \begin{bmatrix}\square & \square\\\square & \square\end{bmatrix} & \begin{bmatrix}0 & 1\\1 & 0\end{bmatrix}\end{bmatrix}$$

There are two shifting positions possibilities for the matrix M_b to the right, one with one shifting position, the second with two shifting positions (1,2).

Matrix M_b

②

Three zero shifting positions

Two shifting positions for the matrix M_b

$$V_L \to \left[(K-2) : \left(\frac{K}{2}-1\right)\right] \cup \left[\left(\frac{K}{2}-1\right) : (K-2)\right] \cup \left[0 : \left(\frac{K}{2}-1\right)\right]$$
$$= [2 : 1] \cup [1 : 2] \cup [0 : 1] = [3 : 4]$$

Three zero shifting positions.

② Two shifting positions for the Left vector V_L.

Left vector V_L

$$\Rightarrow \begin{bmatrix} 0 \\ 1 \end{bmatrix} \quad \begin{bmatrix} 1 & \square & 0 & 1 & \square & \square & 0 & \square \\ 0 & \square & 1 & 0 & \square & \square & 1 & \square \\ \square & 1 & \square & \square & 0 & 1 & \square & 0 \\ \square & 0 & \square & \square & 1 & 0 & \square & 1 \end{bmatrix}$$

Four zero shifting positions.

①
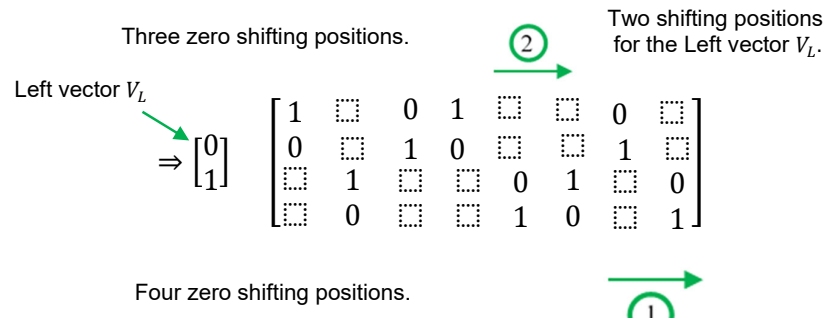
There are two shifting positions possibilities for the Left vector V_L to the right, one with two shifting positions, the second with one shifting position (2,1).

One shifting position for the Left vector V_L.

$$H = \begin{bmatrix} 1 & & 0 & 1 & \square & & 0 & \square \\ 0 & \square & 1 & 0 & \square & \square & 1 & \square \\ & 1 & \square & & 0 & 1 & & 0 \\ & 0 & \square & \square & 1 & 0 & & 1 \end{bmatrix}$$

$$\Rightarrow H = \begin{bmatrix} 1 & 0 & 0 & 1 & 0 & 0 & 0 & 0 \\ 0 & 0 & 1 & 0 & 0 & 0 & 1 & 0 \\ 0 & 1 & 0 & 0 & 0 & 1 & 0 & 0 \\ 0 & 0 & 0 & 0 & 1 & 0 & 0 & 1 \end{bmatrix}. \tag{11}$$

where the shifted positions of each elementary matrix are: (0,1), (1,2) and (2,1), respectively.

Case 3: Consider a fixed number of users $K > 2$.
The code weight of the matrix code is increased using the following strategy:

Odd Code weight: The code weight of the basic matrix H_b is equal to $(W = 2)$. The code weight can be increased by using the elementary

matrix compound M_b alternatively with the basic matrix H_b to get an odd code weight value W_o.

$$H_o = [H_b][M_b][H_b] \quad [H_b][H_b].\tag{12}$$

Even Code weight: For an even code weight value, we choose one of the three possible configurations:

The basic matrix H_b is used in concatenation one with the other,

$$H_o = [H_b][H_b][H_b] \quad [H_b][H_b].\tag{13}$$

We use the concatenation of the resulting odd code weight matrix codes H_o obtained from the precedent step.

$$H_o = [H_0][M_b][H_0][M_b] \quad [H_0].\tag{14}$$

We can also use the concatenation of elementary matrix compounds M_b.

$$H_o = [M_b][M_b][M_b] \quad [M_b].\tag{15}$$

Then, the size of the resulting matrix is $(K \times L)$, where $L = K * W$ represents the matrix code length. For two kinds of services with $K = 6, W = 4$ and $K = 3, W = 3$, the code matrix is given by:

$$H = \begin{bmatrix} \begin{bmatrix} 1\,0\,0\,0\,1\,0\,0\,0\,0\,0\,0\,1\,0\,0\,0\,1\,0\,0\,0\,0\,0\,0\,0 \\ 0\,0\,0\,1\,0\,0\,0\,0\,1\,0\,0\,0\,0\,0\,1\,0\,0\,0\,0\,0\,1\,0\,0 \\ 0\,1\,0\,0\,0\,0\,1\,0\,0\,0\,0\,0\,1\,0\,0\,0\,0\,1\,0\,0\,0\,0\,0 \\ 0\,0\,0\,0\,0\,1\,0\,0\,0\,0\,1\,0\,0\,0\,0\,0\,0\,1\,0\,0\,0\,0\,1\,0 \\ 0\,0\,1\,0\,0\,0\,0\,0\,1\,0\,0\,0\,0\,0\,1\,0\,0\,0\,0\,0\,1\,0\,0\,0 \\ 0\,0\,0\,0\,0\,0\,0\,1\,0\,0\,0\,1\,0\,0\,0\,0\,0\,0\,0\,1\,0\,0\,0\,1 \end{bmatrix} & [0] \\ [0] & \begin{bmatrix} 1\,1\,0\,0\,1\,0\,0\,0 \\ 0\,0\,1\,0\,0\,1\,0\,0 \\ 0\,0\,0\,1\,0\,0\,1\,1 \end{bmatrix} \end{bmatrix}$$

The total length of the matrix code is: $L = 6 \times 4 + 3 \times 3 = 33$.

Performance analysis using Direct Detection (DD)

In direct decoding (DD), a single input only is used at the receiver compared to other techniques which reduce the number of filters required

for implementation. For a given user at the receiver using direct detection (DD), the number of FBGs that have bandwidths centered at the used wavelength is equal to the number of non-overlapping spectra $C_f(j)$ incident on the photodetector. The code correlation function using the DD technique of the FVWZCC can be written as:

$$\sum_{j=1}^{L_{Tot}} C_f(j)C_g(j) =$$
$$\begin{cases} W_i & f = g, \quad \text{same user with similar weight} \\ 0 & f \neq g, \quad \text{other users with similar weight} \\ 0 & f \neq g, \quad \text{other users with distinct weight} \end{cases} \quad (16)$$

where $C_f(j)$ represent the jth component of the Cth proposed code sequence.

The variance of photocurrent due to the detection of an ideally unpolarized thermal light, which is generated by spontaneous emission, can be written as the sum of the Phase Induced Intensity Noise $\langle I_{piin}^2 \rangle$, the shot noise $\langle I_{shot}^2 \rangle$, and the thermal noise $\langle I_{thermal}^2 \rangle$ (Ahmed et al, 2012; Shi & Gafouri-Shiraz, 2016; Kumawat & Maddila, 2017):

$$\langle i_{noise}^2 \rangle = \langle I_{piin}^2 \rangle + \langle I_{shot}^2 \rangle + \langle I_{thermal}^2 \rangle \quad (17)$$

The thermal noise $\langle I_{thermal}^2 \rangle$ is defined as (Ahmed et al, 2012):

$$\langle I_{thermal}^2 \rangle = \frac{4k_b T_n B}{R_L} \quad (18)$$

The shot noise $\langle I_{shot}^2 \rangle$ is defined as (Ahmed et al, 2012):

$$\langle I_{shot}^2 \rangle = 2eBI \quad (19)$$

where e represents the electron charge, B the electrical bandwidth, I the average photocurrent, k_b the Constant Boltzmann, T_n the receiver noise temperature, R_L the receiver load, and the Phase Induced Intensity Noise $\langle I_{piin}^2 \rangle$ is given as (Ahmed et al, 2012, 2019):

$$\langle I_{piin}^2 \rangle = BI^2 \tau_c \quad (20)$$

The coherence time τ_c of the source can be expressed as (Ahmed & Nisar, 2013; Wei & Ghafouri-Shiraz, 2002):

$$\tau_c = \frac{\int_0^\infty G^2(v)dv}{[\int_0^\infty G(v)dv]^2} \qquad (21)$$

where $G(v)$ denotes the single sideband power spectral density (PSD) of the source incident at the input of the photodiode.

For mathematical simplicity, the Gaussian approximation is used for all the noise distributions to analyze the system performance. Furthermore, the assumptions below are adopted for the transmitter and the receiver as follows:
- The light source is ideally unpolarized and its spectrum is flat for a given bandwidth $[v_0 - \Delta v/2, v_0 + \Delta v/2\,]$, where v_0 is the central optical frequency and Δv is the optical source bandwidth,
- The spectral width is the same for each frequency component,
- For each user, the bit stream is synchronized, and
- The same power is received by each user.

The power spectral density (PSD) of the received optical signals can be written as (Osadola et al, 2011; Mostafa et al, 2015):

$$r(v) = \frac{P_{sr}}{\Delta v} \sum_{f=1}^{K_{Tot}} d_f \sum_{i=1}^{L_{Tot}} c_f(i).rect(i) \qquad (22)$$

where P_{sr} denotes the effective power, d_f the fth user data bit, K_{Tot} is the total number of users and L_{Tot} is the total code length. The function $rect(.)$ is expressed as (Ahmed et al, 2012; Kumawat & Maddila, 2017):

$$rect(i) = u\left[v - v_0 - \frac{\Delta v}{2L_{Tot}}(-L_{Tot} + 2i - 2)\right] - u\left[v - v_0 - \frac{\Delta v}{2L_{Tot}}(-L_{Tot} + 2i)\right] = u\left[\frac{\Delta v}{L_{Tot}}\right] \qquad (23)$$

where $u(v)$ is a step unit function defined as:

$$u(v) = \begin{cases} 1, & v \geq 0 \\ 0, & v < 0 \end{cases}$$

The total power at the fth receiver of the proposed flexible variable weight

for one period is obtained based on Eq. 22, Eq. 23, and using the code correlation property of Eq. 16 as:

$$\int_0^{+\infty} G(v)\, dv = \int_0^{+\infty} \left[\frac{P_{sr}}{\Delta v} \sum_{f=1}^{K_{Tot}} d_f \sum_{i=1}^{L_{Tot}} c_f(i) c_g(i)\, rect(i)\right] dv$$

$$\Rightarrow \int_0^{+\infty} G(v)\, dv =$$

$$\left[\frac{P_{sr}}{\Delta v} \sum_{f=1}^{K_{Tot}} d_f \sum_{i=1}^{L_{Tot}} c_f(i) c_g(i)\right] \int_{v-v_0-\frac{\Delta v}{2L_{Tot}}(-L_{Tot}+2i-2)}^{v-v_0-\frac{\Delta v}{2L_{Tot}}(-L_{Tot}+2i)} rect(i)\, dv$$

$$\Rightarrow \int_0^{+\infty} G(v)\, dv = \frac{P_{sr}}{\Delta v} \frac{\Delta v}{L_{Tot}} \sum_{f=1}^{K_{Tot}} d_f \sum_{i=1}^{L_{Tot}} c_f(i) c_g(i)$$

$$\Rightarrow \int_0^{+\infty} G(v)\, dv =$$

$$\frac{P_{sr}}{L_{Tot}} \left[\sum_{f=1}^{K_{Tot}} d_f \sum_{i=1}^{L_{Tot}} c_f(i) c_g(i) + \sum_{f \neq 1}^{K_{Tot}} d_f \sum_{i=1}^{L_{Tot}} c_f(i) c_g(i)\right]$$

$$\Rightarrow \int_0^{+\infty} G(v)\, dv = \frac{P_{sr}}{L_{Tot}} \left[\sum_{f=1}^{K_{Tot}} d_f\, W_i + \sum_{f \neq 1}^{K_{Tot}} d_f \times 0\right]$$

Based on $\sum_{f=1}^{K_{Tot}} d_f = 1$, the total power at the fth receiver is given by:

$$\Rightarrow \int_0^{+\infty} G(v)\, dv = \frac{P_{sr}\, W_i}{L_{Tot}} \tag{24}$$

Then, the resulting photocurrent due to the incident optical power I_{FVWZCC} is defined as (Kumawat & Maddila, 2017):

$$I_{FVWZCC} = \Re \int_0^{+\infty} G(v)\, dv = \Re\, \frac{P_{sr}\, W_i}{L_{Tot}} \tag{25}$$

where $\Re = \frac{\eta.e}{h.v_0}$ is the responsivity of the photodetectors, η denotes the quantum efficiency, e is the electron charge, and $h.v_0$ is the photon energy.

Substituting Eq. 25 in Eq. 19, the shot noise power is deduced as (Imtiaz et al, 2016; Kumawat & Maddila, 2017):

$$\langle I_{shot}^2 \rangle = 2eB\Re\left[\int_0^{+\infty} G(v)\, dv\right] = 2eB\Re\left[\frac{P_{sr}\, W_i}{L_{Tot}}\right] \tag{26}$$

1683

and the PIIN noise power is given by (Ahmed et al, 2012; Kumawat & Maddila, 2017):

$$\langle I_{piin}^2 \rangle = B\,I^2\,\tau_c = B\mathfrak{R}^2 \Big[\int_0^\infty G^2(v)\,dv \Big] \qquad (27)$$

When all active users are transmitting bit '1', and using the average approximation, the code sequence C_k is given by:

$$\sum_{k=1}^{K_{Tot}} C_k(j) = \frac{1}{L_{Tot}} \sum_{i=1}^{W_{Tot}} K_{W_i}\,W_i \qquad (28)$$

where $K_{Tot} = \sum_{i=1}^{W_{Tot}} K_{W_i}$ denotes the total number of active users with different weights, K_{W_i} is the number of users corresponding to the weight W_i, and W_{Tot} is the total number of weights.

Using Eq. 27, the variance of PIIN noise is determined as follows:

$$\langle I_{piin}^2 \rangle = B\mathfrak{R}^2 \Big[\int_0^\infty G^2(v)\,dv \Big]$$

$$\Rightarrow \langle I_{piin}^2 \rangle = B\mathfrak{R}^2 \int_0^\infty \Big[\frac{P_{sr}}{\Delta v} \sum_{f=1}^{K_{Tot}} d_f \sum_{i=1}^{L_{Tot}} c_f(i)c_g(i)\,rect(i) \Big]^2 dv$$

$$\Rightarrow \langle I_{piin}^2 \rangle = B\mathfrak{R}^2 \Big[\frac{P_{sr}}{\Delta v} \Big]^2 \Big[\frac{\Delta v}{L_{Tot}} \Big] \Big[\sum_{f=1}^{K_{Tot}} d_f \sum_{i=1}^{L_{Tot}} c_f(i)c_g(i) \Big]^2$$

$$\Rightarrow \langle I_{piin}^2 \rangle = B\mathfrak{R}^2 \frac{P_{sr}^2}{L_{Tot}\,\Delta v} \Big[\sum_{f=1}^{K_{Tot}} d_f \sum_{i=1}^{L_{Tot}} c_f(i)c_g(i) \Big]^2$$

$$\Rightarrow \langle I_{piin}^2 \rangle = B\mathfrak{R}^2 \frac{P_{sr}^2}{L_{Tot}\,\Delta v} \sum_{i=1}^{L_{Tot}} \Big\{ c_g(i) \Big[\sum_{f=1}^{K_{Tot}} d_f\,c_f(i) \Big] \Big[\sum_{m=1}^{K_{Tot}} d_m\,c_m(i) \Big] \Big\}$$

Substituting Eq. 28, one obtains:

$$\langle I_{piin}^2 \rangle = B\mathfrak{R}^2 \frac{P_{sr}^2}{L_{Tot}\,\Delta v} [W_i] \Big[\frac{1}{L_{Tot}} \sum_{i=1}^{W_{Tot}} K_{W_i}\,W_i \Big] \qquad (29)$$

As a result, the variance of PIIN noise is given by:

$$\langle I_{piin}^2 \rangle = \frac{B\mathfrak{R}^2\,P_{sr}^2}{L_{Tot}^2\,\Delta v} \Big[\sum_{i=1}^{W_{Tot}} K_{W_i}\,W_i \Big] W_i \qquad (30)$$

1684

For each user, the probability of transmitting bit '1' and '0' is the same at any time; then the photocurrent noise can be written as:

$$\langle i_{noise}^2 \rangle = \frac{B\Re^2 P_{sr}^2}{2L_{Tot}^2 \Delta v} \left[\sum_{i=1}^{W_{Tot}} K_{W_i} W_i \right] W_i + eB\Re \left[\frac{P_{sr} W_i}{L_{Tot}} \right] + \frac{4k_b T_n B}{R_L} \qquad (31)$$

Since the probability of transmitting bit '1' at any time for each user is half, then the average Signal to Noise Ratio SNR for a particular weight W_i used for evaluating the FVWZCC code in the SAC-OCDMA system can be expressed as (Shi & Ghafouri-Shiraz, 2016):

$$SNR = \frac{(I_{FVWZCC})^2}{\langle i_{noise}^2 \rangle} \qquad (32)$$

Substituting Eq. 25 and Eq 30 in Eq. 31, the average SNR is deduced as:

$$SNR = \frac{\left(\Re \frac{P_{sr} W_i}{L_{Tot}} \right)^2}{\frac{B\Re^2 P_{sr}^2}{2L_{Tot}^2 \Delta v} \left[\sum_{i=1}^{W_{Tot}} K_{W_i} W_i \right] W_i + eB\Re \frac{P_{sr} W_i}{L_{Tot}} + \frac{4 \, k_b T_n B}{R_L}} \qquad (33)$$

Based on the Gaussian approximation, the Bit Error Rate BER or the probability of error $P_{e,i}$ of a particular weight W_i is calculated from the SNR as (Kaur & Singh, 2018; Wei et al, 2001):

$$\text{BER} = P_{e,i} = \frac{1}{2} \, \text{erfc} \left(\sqrt{\frac{SNR}{8}} \right) \qquad (34)$$

Code comparison and discussions

In this section, simulations with the Matlab program were achieved for analysis and performance comparison between the proposed code and other reported codes.

The main parameters shown in Table I were fairly selected to provide a reasonable results comparison.

Table 1 – Table of parameters

Symbol	Parameters	Values
$\mathcal{R}$	Responsivity of the photodiode	1
B	Electrical equivalent noise bandwidth of the receiver	$311\ MHz$
K_b	Boltzmann constant	$1.38 \times 10^{-23}\ J/K$
R_L	Resistance load	$1030\ \Omega$
T_b	Temperature of noise at the receiver	$300\ K$
P_{rc}	Effective power at the receiver	$-10\ dBm$
e	Charge of electron	$1.6 \times 10^{-19} C$

The BER curve variation as a function of the number of active users for each code weight service taking into account the PIIN effects is shown in Figure 2.
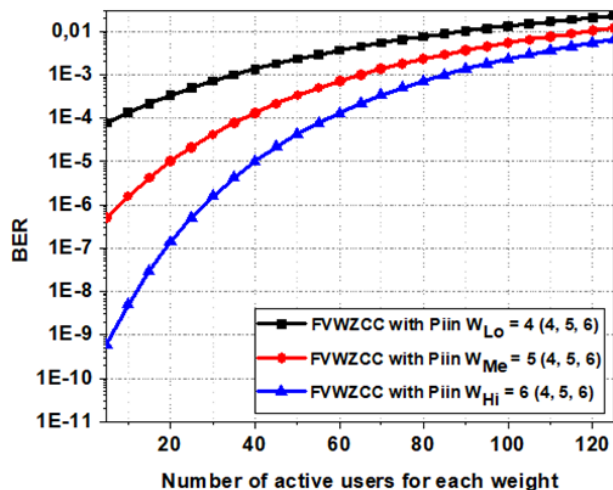
Figure 2 – BER as a function of the number of users for the three code weighs services
($W_{Lo} = 4, W_{Me} = 5$ and, $W_{Hi} = 6$)

The number of users is varied for each of the three code weights $W_{Lo} = 4\ (4, 5, 6), W_{Me} = 5\ (4, 5, 6)$ and, $W_{Hi} = 6\ (4, 5, 6)$ assigned to video, audio and data services, respectively. The BER curve is plotted by varying the number of users for one code weight service while the other weights are kept constant to 40 users. The BER performance of the three code weights decreases as the total number of simultaneous users increases

1686

which can be referred to as the amount of noise level collected from an additional number of users leading to the degradation of the system performance. Moreover, up to the threshold value of 60 users, the total number of active users has fewer and low effects on the system performance for all weight codes. The BER performance of the system is better from high to low weight for some users fewer than 60 users and moderate up of this number of users which gives a good way for the choice of the range of the number of users with an appropriate quality of service in terms of the minimum desired bit error rate BER.

Figure 3 illustrates the BER performance comparison of the proposed FVWZCC code with and without PIIN consideration for the high-weight service $W_{Hi} = 6$ $(4, 5, 6)$. The number of users of the high weight is set to $K_{Hi} = 15, 25,$ and 30 while it is kept constant to 40 users for low and medium weights services $(K_{Lo} = K_{Me} = 40)$. As it can be concluded, the BER performance of the system is better with neglecting the term of PIIN effects and increases as the number of users for the high-weight service decreases which decreases the code length. Meanwhile, taking as reference the number of accommodated users with and without the PIIN term effects at the maximum acceptable BER (10^{-9}), the difference is large enough $(13 \, users)$ to consider the hypothesis of neglecting the PIIN term effects may be worst. For example, with $K_{Hi} = 15$, the number of accommodated users is 50 users without the PIIN term effects while it is only 37 with them.

Consequently, the performance comparison of the codes in the case presented in this work will be done by taking into account the PIIN term effects. Moreover, the BER performance of the system experiences the same behavior when the number of users of the low and medium weights exceeds approximately 80 users with a high BER value.

The performance comparison between the proposed flexible constant weight FCWZCC code and other reported codes with PIIN consideration such as MQC, MFH, Hadamard, CWZCCC, and RD versus the number of active users is plotted in Figure 4. The proposed FCWZCC code gives the best and the same BER performance as the reported CWZCCC code while it outperforms all the other reported codes. The BER performance is better although with a lower code weight value $(W = 4)$ compared to others codes with code weight values $(W = 7, 12)$ taking into account the PIIN effects. Given two code sequences $X = (x_1, x_2, ..., x_N)$ and $Y = (y_1, y_2, ..., y_N)$, the cross-correlation is defined as $\lambda = \sum_{i=1}^{N} x_i y_i$. When $\lambda = 0$, the code is said to the have zero cross-correlation property. It is obvious that since the FCWZCC code has the property of zero cross-correlation $(\lambda = 0)$, the MAI and PIIN interference effects, which are the major sources

of performance degradation, can be eliminated effectively. For a maximum acceptable BER of 10^{-9}, the number of accommodated users for the proposed FCWZCC is 71 users which is the same number of users as the reported CWZCCC code, 53 for the RD code, 40 for the MQC code, 27 for the MFH code and 19 for the Hadamard code, respectively.
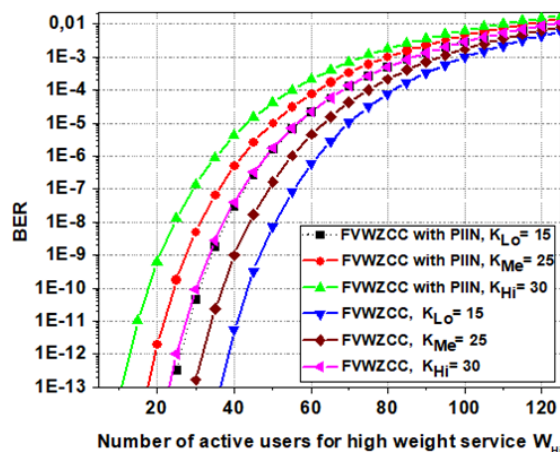
Figure 3 – BER performance comparison of the proposed FVWZCC code with and without PIIN consideration as a function of the number of active users of the high-weight service
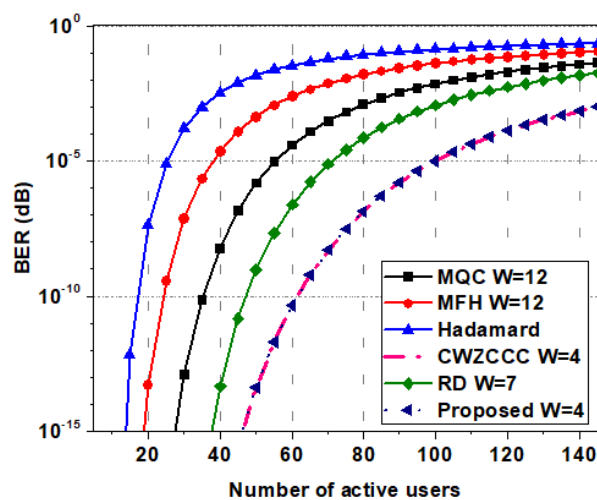
Figure 4 – BER as a function of the number of users for different codes in the SAC-OCDMA system

Figure 4 shows the BER performance system comparison of the proposed FVWZCC code with other published variable weight codes such as VWQCC, VWZCCC, and VWKS. The BER curve is plotted as a function of the number of users for medium and high weights ($W = 4, 6$) while varying the high-weight users from 0 to 100. The number of users for the medium weight is set to 30 users. The proposed code's BER performance is better than that of the reported VWZCCC code and outperforms all the remainder reported codes.

The improvement in the system performed of the proposed code derives from the good correlation property and a shorter code length which is the same as the reported VWZCCC code while it is large compared to other codes. The VWKS code experiences the same system performance as the code proposed in this work when the total number of users exceeds 60 users corresponding to a bit error rate of approximately $\approx 10^{-7}$.
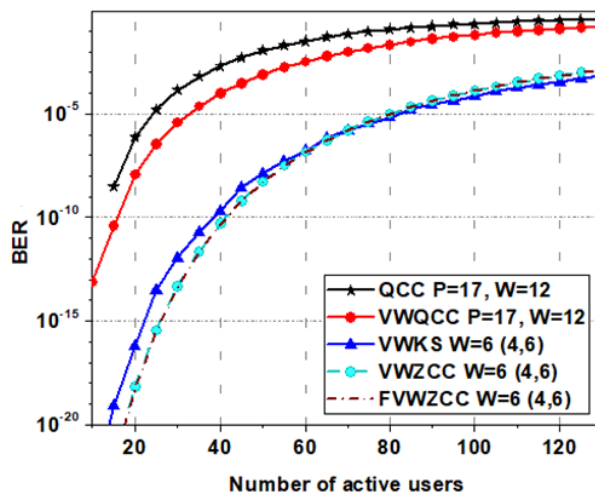
Figure 5 – BER as a function of the number of users for different variable weight codes in the SAC-OCDMA system

System description and the simulation results

The simulation of the proposed FVWZCC code design was carried out using Optisystem version 7.0. The block diagram with 5 users and the code weight value $W = 6$ is shown in Figure 6. In the transmission part, a series of W number of laser light sources were used each of them with a power of $0.417 \ mW$. Multiplexers and Demultiplexers for encoding optical

signals, a pseudo-random bit sequence (PRBS) generator, and a non-return-zero (NRZ) pulse generator are used to generate the data signal. Then, the electric data of each user is modulated by the external intensity modulator Mach–Zehnder. The bit rate of $10\ Gbps$ was adopted for simulations over a fiber optic distance varying in the range of $20\ km$ to $90\ km$. The ITU-T G.652 standard single mode optical fiber with all the non-linearity effects was considered, attenuation of $0.2\ dB/km$, dispersion of $16.75ps/nm/km$ and a spectral width of 0.8 nm for each chip were also adopted.

At the receiver part, Fiber Bragg grating FBGs corresponding to a unique wavelength from a specified code sequence followed by photo-detectors PDs were used to decode the signal. Finally, the detected signal is passed through a low-pass filter to remove the remaining noise. The performance of the system was analyzed using the BER and the eye patterns.
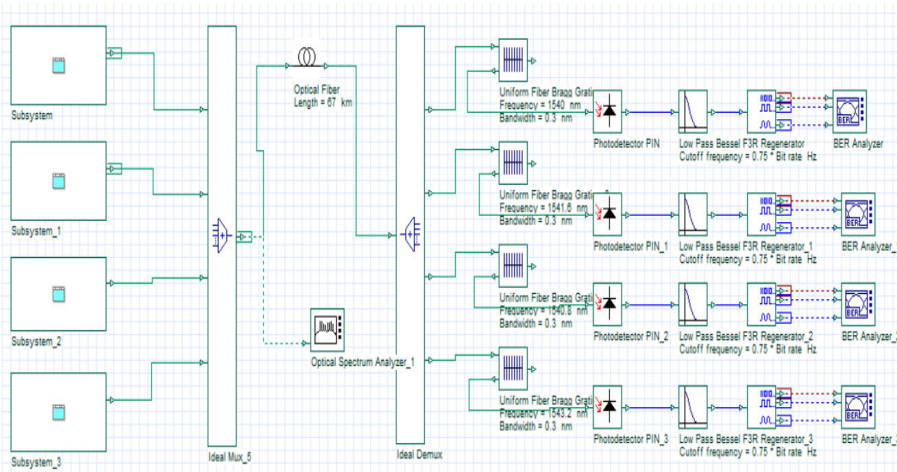
Figure 6 – Simulation design of the proposed VFWZCC scheme for 4 users of code weight 6

Figures 7 a) and 7 b) show the eye diagram and the BER values of the proposed FVWZCC code in the OCDMA system at $10\ GBps$ data rates through two different optical fiber distance lengths $(30\ km,\text{and }67\ km)$, respectively. As it can be seen, the eye diagram clearly illustrates that the proposed code gives better performance for fiber distance length shorter than $67\ km$ corresponding to the basic required bit error rate value for

acceptable system performance (10^{-9}). A shorter fiber distance provides low attenuation and dispersion which decreases the bit error rate and thus improve the performance of the system. The more the eye closes, the more difficult it is to distinguish between ones and zeros in the signal which can be deduced from Figures 6 a) and 6 b). The height of the eye-opening at the specified sampling time shows the noise margin or immunity to noise. The BER value of 1.62×10^{-9} was obtained for a fiber distance of $67 \ km$ while it is about 7×10^{-42} for $30 \ km$ which is much better and prove the feasibility of the code for optical applications with a data rate of $10 \ GBps$.
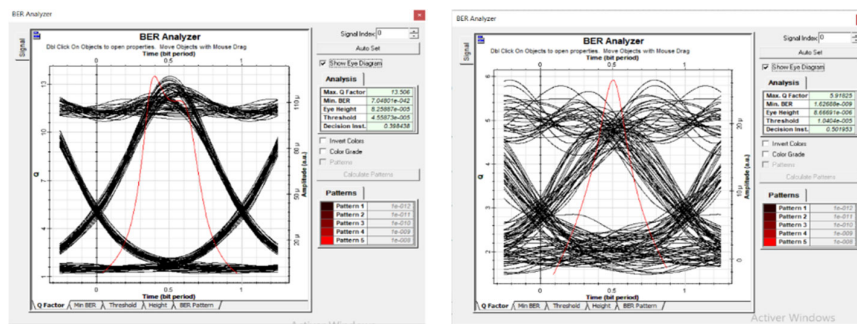
Figure 7 – Eye diagram for the proposed FVWZCC code at $10 \ GBps$ for two optical fiber distances a) $30 \ km$, and b) $50 \ km$, respectively

Conclusion

A new FVWZCC code design is proposed for multimedia applications in SAC-OCDMA systems. The design procedure is flexible and can be used for any constant or variable code weight number with any number of users based on an appropriate shifting manner of three elementary matrices. The cross-correlation property of value zero between any pairs of users reduces the PIIN interference effects leading to the improvement of the system performance. The performance comparison shows that the proposed code with a good correlation property and a shorter code length which is the same as the reported VWZCCC gives better performance over other constant or variable reported weight codes. Moreover, the good simulation results obtained in terms of the BER and eye diagram of the proposed code design for OCDMA systems at $10 \ Gb/s$ with direct detection clearly depict a strong possibility to be used for multimedia applications diversity. The proposed code gives better performance until

the fiber distance length value of $67\ km$ corresponds to the basic required bit error rate for the acceptable system performance (10^{-9}). On the other hand, changing code weights (CW or VW) provides better BER from high to low weight for several users fewer than 60 users and moderate up of this amount of users which gives a good way for the choice of the range of number of users with an appropriate quality of service in terms of the minimum desired bit error rate BER. The low complexity and the low-cost design of the receiver using direct detection is another important factor for the implementation of the proposed FVWZCC code.

References

Abd, T.H., Aljunid, S.A. & Fadhil, H.A. 2011. A New Technique for Reduction the Phase Induced Intensity Noise in SAC-OCDMA Systems. *Journal of Optical Communications*, 32(4), pp.263-267. Available at: https://doi.org/10.1515/joc.2011.054.

Ahmed, N., Aljunid, S.A., Ahmad, R.B., Fadil, H.A. & Rashid, M.A. 2012. Novel OCDMA Detection Technique based on Modified Double Weight Code for Optical Access Network. *Elektronika Ir Elektrotechnika*, 18(8), pp.117-121. Available at: https://doi.org/10.5755/j01.eee.18.8.2638.

Ahmed, H.Y. & Nisar, K.S. 2013. Diagonal Eigenvalue Unity (DEU) code for spectral amplitude coding-optical code division multiple access. *Optical Fiber Technology*, 19(4), pp.335-347. Available at: https://doi.org/10.1016/j.yofte.2013.04.001.

Ahmed, H.Y., Zeghid, M., Imtiaz, W.A. & Sghaier, A. 2019. Two dimensional Fixed Right Shift (FRS) code for SAC-OCDMA systems. *Optical Fiber Technology*, 47, pp.73-87. Available at: https://doi.org/10.1016/j.yofte.2018.11.021.

Ahmed, H.Y., Zeghid, M., Sharma, T., Imtiaz, W.A. & El-Mottaleb, S.A.A. 2022. An efficient algorithm to provide triple play services in passive optical network (PON)-OCDMA network. *Optical and Quantum Electronics*, 54, art.number:351. Available at: https://doi.org/10.1007/s11082-022-03714-8.

Anas, S.B.A., Abdullah, M. K., Mokhtar, M., Aljunid, S. A. & Walker, S. D. 2009. Optical domain service differentiation using spectral amplitude-coding. Optical Fiber Technology, 15(1), pp.26-32. Available at: https://doi.org/10.1016/j.yofte.2008.04.001.

Anuar, M.S., Aljunid, S.A., Saad, N.M. & Hamzah, S.M. 2009. New design of spectral amplitude coding in OCDMA with zero cross-correlation. *Optics communications*, 282(14), pp.2659-2664. Available at: https://doi.org/10.1016/j.optcom.2009.03.079.

Bensaad, A., Bensaad, Z., Garadi, A. & Beloufa, A. 2019. An efficient zero cross-correlation codes for OCDMA networks. In: *2019: International Conference on Advanced Electrical Engineering (ICAEE),* Algiers, Algeria, pp.1-4, November 19-21. Available at: https://doi.org/10.1109/icaee47123.2019.9014798.

Bensaad, A., Garadi, A., Beloufa, A. & Bensaad, Z. 2023. New Zero Cross-Correlation Codes Based on Zech Method's for OCDMA Systems. *Gazi University Journal of Science*, 36(1), pp.238-247. Available at: https://doi.org/10.35378/gujs.994461.

Dat, P.T., Kanno, A., Yamamoto, N. & Kawanishi, T. 2018. Seamless convergence of fiber and wireless systems for 5G and beyond networks. *Journal of Lightwave Technology*, 37(2), pp.592-605. Available at: https://doi.org/10.1109/jlt.2018.2883337.

Dixit, A., Lannoo, B., Das, G., Colle, D., Pickavet, M. & Demeester, P. 2013. Flexible TDMA/WDMA passive optical network: Energy efficient next-generation optical access solution. *Optical Switching and Networking*, 10(4), pp.491-506. Available at: https://doi.org/10.1016/j.osn.2013.03.001.

El-Mottaleb, S.A.A., Fayed, H.A., Ismail, N.E., Aly, M.H. & Rizk, M.R.M. 2020. MDW and EDW/DDW codes with AND subtraction/single photodiode detection for high performance hybrid SAC-OCDMA/OFDM system. *Optical and Quantum Electronics*, 52, art.number:239. Available at: https://doi.org/10.1007/s11082-020-02357-x.

Fadhil, H.A., Aljunid, S.A. & Ahmad, R.B. 2009a. Performance of random diagonal code for OCDMA systems using new spectral direct detection technique. *Optical Fiber Technology*, 15(3), pp.283-289. Available at: https://doi.org/10.1016/j.yofte.2008.12.005.

Fadhil, H.A., Aljunid, S.A. & Badlisha, R. 2009b. Triple-play Services using Random Diagonal Code for Spectral Amplitude Coding OCDMA Systems. *Journal of Optical Communications*, 30(3), pp.155-159. Available at: https://doi.org/10.1515/joc.2009.30.3.155.

Farghal, A.E.A. 2016. Performance Analysis of Core-Multiplexed Spectral Amplitude Coded OCDMA PON. *Journal of Optical Communications and Networking*, 8(9), pp.666-675. Available at: https://doi.org/10.1364%2Fjocn.8.000666.

Feng, G., Cheng, W.-Q. & Chen, F.-J. 2015. Design of variable-weight quadratic congruence code for optical CDMA. *Infrared Physics & Technology*, 72, pp.281-285. Available at: https://doi.org/10.1016/j.infrared.2015.08.008.

Hakeem, S.A.A., Hussein, H.H. & Kim, H. 2022. Vision and research directions of 6G technologies and applications. *Journal of King Saud University-Computer and Information Sciences*, 34(6), Part A, pp.2419-2442. Available at: https://doi.org/10.1016/j.jksuci.2022.03.019.

Huang, J.-F., Yen, C.-T. & Li, T.-Y. 2008. Nonlinearity effect of electro-optical modulator response in double spread CDMA radio-over-fiber transmissions. *Optical Fiber Technology*, 14(3), pp.247-258. Available at: https://doi.org/10.1016/j.yofte.2007.12.007.

Imtiaz, W.A., Ahmed, H.Y., Zeghid, M. & Sharief, Y. 2020. Two-dimensional optimized enhanced multi-diagonal code for OCDMA passive optical networks. *Optical and Quantum Electronics*, 52, art.number:33. Available at: https://doi.org/10.1007/s11082-019-2145-9.

Imtiaz, W.A., Ilyas, M. & Khan, Y. 2016. Performance optimization of spectral amplitude coding OCDMA system using new enhanced multi-diagonal code. *Infrared Physics & Technology*, 79, pp.36-44. Available at: https://doi.org/10.1016/j.infrared.2016.09.006.

Ji, W. & Chang, J. 2013. The radio-on-fiber-wavelength-division-multiplexed-passive-optical network (WDM-RoF-PON) for wireless and wire layout with linearly-polarized dual-wavelength fiber laser and carrier reusing. *Optics & Laser Technology*, 49, pp.301-306. Available at: https://doi.org/10.1016/j.osn.2019.100551.

Kaur, S. & Singh, S. 2018. Review on developments in all-optical spectral amplitude coding techniques. *Optical engineering*, 57(11), art.number:116102. Available at: https://doi.org/10.1117/1.oe.57.11.116102.

Kbashi, H.J., Sharma, V. & Sergeyev, S. 2021. Dual-wavelength fiber-laser-based transmission of millimeter waves for 5G-supported Radio-over-Fiber (RoF) links. *Optical Fiber Technology*, 65, art.number:102588. Available at: https://doi.org/10.1016/j.yofte.2021.102588.

Kumawat, S. & Maddila, R.K. 2017. Development of ZCCC for multimedia service using SAC-OCDMA systems. *Optical Fiber Technology*, 39, pp.12-20. Available at: https://doi.org/10.1016/j.yofte.2017.09.015.

Kumawat, S. & Ravi Kumar, M. 2018. Design of variable weight code for multimedia service in SAC--OCDMA systems. *IET Optoelectronics*, 12(2), pp.56-64. Available at: https://doi.org/10.1049/iet-opt.2017.0046.

Li, X., Ding, Q.A., Nie, B., Liu, C., Wang, X., Song, J. & Zhang, L. 2023. Development and performance improvement of a novel zero cross-correlation code for SAC-OCDMA systems. *Journal of Optical Communications*, 44(s1), pp.s1327-s1339. Available at: https://doi.org/10.1515/joc-2020-0086.

Lu, Z., Lu, Y. & Li, C. 2021. Design of zero cross-correlation variable weight codes for multimedia services based on magic square in SAC-OCDMA systems. *Optoelectronics Letters*, 17(9), pp.539-545. Available at: https://doi.org/10.1007/s11801-021-0198-z.

Mostafa, S., Mohamed, A.E.-N.A., El-Samie, F.E.A. & Rashed, A.N Z. 2015. Eradication of Multiple Access Interference Using a Modified Multi-service Code for SAC–OCDMA. *Wireless Personal Communications*, 83, pp.855-872. Available at: https://doi.org/10.1007/s11277-015-2430-2.

Nasaruddin, N. & Tsujioka, T. 2008. Design of strict variable-weight optical orthogonal codes for differentiated quality of service in optical CDMA networks. *Computer Networks*, 52(10), pp.2077-2086. Available at: https://doi.org/10.1016/j.comnet.2008.02.014.

Nisar, K.S., Ahmed, H.Y., Zeghid, M., Imtiaz, W.A., Sarangal, H. & Thapar, S.S. 2021. The multi-service schemes for SAC-OCDMA systems with variable code weight. *Optical and Quantum Electronics*, 53, art.number:293. Available at: https://doi.org/10.1007/s11082-021-02932-w.

Nisar, K.S., Sarangal, H. & Thapar, S.S. 2019. Performance evaluation of newly constructed NZCC for SAC-OCDMA using direct detection technique.

Photonic Network Communications, 37(1), pp.75-82. Available at: https://doi.org/10.1007/s11107-018-0794-4.

Osadola, T.B., Idris, S.K., Glesk, I. & Kwong, W.C. 2011. Network Scaling Using OCDMA Over OTDM. *IEEE Photonics Technology Letters*, 24(5), pp.395-397. Available at: https://doi.org/10.1109/lpt.2011.2179924.

Pendeza Martinez, C.A., Abrao, T. & Martinez, A.L.M. 2021. Energy and spectral efficiency trade-off in OCDMA-PON assisted by non-linear programming methods. *Computer Networks*, 189, art.number:107920. Available at: https://doi.org/10.1016/j.comnet.2021.107920.

Rahimian, F.P., Seyedzadeh, S. & Glesk, I. 2019. OCDMA-based sensor network for monitoring construction sites affected by vibrations. *Journal of Information Technology in Construction*, 24, pp.299-317 [online]. Available at: http://www.itcon.org/2019/16 [Accessed: 15 April 2024].

Rashidi, C.B.M., Aljunid, S.A., Ghani, F., Fadhil, H.A., Anuar, M.S. & Arief, A.R. 2014. Cardinality enrichment of flexible cross correlation (FCC) code for SAC-OCDMA system by alleviation interference scheme (AIS). *Optik*, 125(17), pp.4889-4894. Available at: https://doi.org/10.1016/j.ijleo.2014.04.035.

Shi, F. & Ghafouri-Shiraz, H. 2016. Performance Analysis of Two New Code Families for Spectral-Amplitude-Coding Optical CDMA Systems. *Journal of Lightwave Technology*, 34(17), pp.4005-4014. Available at: https://doi.org/10.1109/JLT.2016.2586527.

Teli, S.R., Zvanovec, S. & Ghassemlooy, Z. 2018. Optical internet of things within 5G: Applications and challenges. In: *2018 IEEE International Conference on Internet of Things and Intelligence System (IOTAIS)*, Bali, Indonesia, pp.40-45, November 01-03. Available at: https://doi.org/10.1109/iotais.2018.8600894.

Troia, S., Cibari, A., Alvizu, R. & Maier, G. 2020. Dynamic programming of network slices in software-defined metro-core optical networks. *Optical Switching and Networking*, 36, art.number:100551. Available at: https://doi.org/10.1016/j.osn.2019.100551.

Upadhyay, K.K., Shukla, N.K. & Chaudhary, S. 2020. A high speed 100 Gbps MDM-SAC-OCDMA multimode transmission system for short haul communication. *Optik*, 202, art.number:163665. Available at: https://doi.org/10.1016/j.ijleo.2019.163665.

Wei, Z., Ghafouri-Shiraz, H. & Shalaby, H.M.H. 2001. Performance analysis of optical spectral-amplitude-coding CDMA systems using a super-fluorescent fiber source. *IEEE Photonics Technology Letters*, 13(8), pp.88-889. Available at: https://doi.org/10.1109/68.935837.

Wei, Z. & Ghafouri-Shiraz, H. 2002. Codes for spectral-amplitude-coding optical CDMA systems. *Journal of Lightwave Technology*, 20(8), pp. 1284-1291. Available at: https://doi.org/10.1109/jlt.2002.800301.

Zhang, Y., Gan, C., Gou, K. & Hua, J. 2017. GPON-and-EPON transmission based on multi-standard OLT management structure for VPON in metro-access optical network. *Optical Switching and Networking*, 25, pp.24-32. Available at: https://doi.org/10.1016/j.osn.2017.01.001.

Investigaciones de correlación flexible cruzada cero de peso variable (FVWZCC) para aplicaciones multimedia

Abdellah Bensaad[a], *Abbes* Beloufa[b], *Ahmed* Garadi[c]

[a] Universidad Dr. Moulay Tahar, Departamento de Electrónica, Saida, República Argelina Democrática y Popular, **autor de correspondencia**

[b] Universidad Mustapha Stambouli, Facultad de Ciencias y Tecnología, Mascara, República Argelina Democrática y Popular

[c] Universidad Djillali Liabes, Laboratorio de Materiales Aplicados, Sidi Bel Abbes, República Argelina Democrática y Popular

Resumen:

Introducción/objetivo: En este artículo, proponemos un método novedoso de construcción de código con la propiedad de correlación cruzada cero, la correlación cruzada cero de peso variable flexible (FVWZCC). Este método es simple y flexible, utiliza diferentes pesos de código para soportar diferentes clases de usuarios según su distancia de transmisión y la calidad de los servicios que requieren (datos, audio y video) en sistemas OCDMA. El uso de pesos de código más altos permite el soporte de redes de aplicaciones de mayor prioridad, como redes de largo alcance. La estructura del código ZCC no tiene superposición del bit '1' y puede eliminar eficientemente la interferencia MAI entre usuarios y el ruido PIIN, mejorando así el rendimiento general del sistema.

Métodos: Para la construcción del código FVWZCC propuesto se utilizó la posición cambiante del elemento y el proceso de matriz de concatenación de las tres matrices básicas denominadas vector derecho, matriz básica y vector izquierdo. El análisis matemático y las simulaciones con los software Matlab y Optisystem se utilizaron para evaluar el desempeño del método FVWZCC propuesto en sistemas SAC-OCDMA utilizando la detección directa.

Resultados: Los resultados muestran una mejora significativa en el código presentado en comparación con otros códigos existentes en términos de simplicidad, flexibilidad y costo de implementación. El método utiliza un peso constante o variable con la propiedad de correlación cruzada cero. Para una BER máxima aceptable de 10^{-9} , los resultados de la simulación del sistema SAC-OCDMA que utiliza detección directa bajo el software OptiSystem muestran un mejor rendimiento del código propuesto con cuatro usuarios de peso 6 a 10 Gb/s. Además, puede admitir hasta 60 usuarios simultáneamente y alcanzar una distancia de fibra de unos 67 km. En consecuencia, el código FVWZCC propuesto se puede aplicar para soportar diferentes requisitos de Calidad de Servicio (QOS) con bajo costo y baja complejidad con un receptor de detección directa.

Conclusión: Los hallazgos de este estudio resaltan la necesidad de que el código FVWZCC admita los requisitos de QoS del usuario final. El nuevo enfoque para la construcción de código ofrece implementación de bajo costo, simplicidad y flexibilidad.

Palabras claves: código FVWZCC, OCDMA, ZCC, tasa de error de bits BER.

Исследование нулевой взаимной корреляции с гибкими переменными весами (FVWZCC) для мультимедийных приложений

Абдуллах Бенсаад[а], *Аббес* Белуфа[б], *Ахмад* Гаради[в]

[а] Университет Саиды „Доктор Мулай Тахар", факультет электроники,
  г. Саида, Алжирская Народная Демократическая Республика,
  корреспондент

[б] Университет Мустафы Стамбули, факультет науки и технологий,
  г. Маскара, Алжирская Народная Демократическая Республика

[в] Университет Джиллали Лиабес - Сиди-Бель-Аббес,
  Лаборатория прикладных материалов,
  г. Сиди-Бель-Аббес, Алжирская Народная Демократическая Республика

Резюме:

Введение/цель: В данной статье представлен новый метод разработки кода со свойством нулевой взаимной корреляции (Flexible Variable Weight Zero Cross-Correlation - FVWZCC). Это простой и гибкий метод, использующий различные веса кода для поддержки разных классов пользователей в зависимости от расстояния передачи и качества требуемых им услуг (передачи данных, аудио и видео) в системах OCDMA. Использование более высокого веса кода обеспечивает поддержку сетей приложений с более высоким приоритетом, таких как сети дальней связи. Структура кода ZCC не перекрывает бит "1" и может эффективно устранять помехи MAI между пользователями и шум PIIN, тем самым повышая общую производительность системы.

Методы: Для разработки предлагаемого кода FVWZCC были использованы сдвиг положения элемента и матричный процесс конкатенации трех базовых матриц, обозначенных как правый вектор, базовая матрица и левый вектор. Математический анализ и моделирование с помощью программного обеспечения Matlab и Optisystem были использованы для оценки

1697

эффективности предложенного метода FVWZCC в системах SAC-OCDMA, использующих прямую детекцию.

Результаты: Результаты показывают значительное улучшение представленного кода по сравнению с другими существующими кодами с точки зрения простоты, гибкости и стоимости внедрения. В методе используется постоянные или переменные веса со свойством нулевой взаимной корреляции. При удельном значении BER, равном 10-9, результаты моделирования системы SAC-OCDMA с использованием прямого обнаружения в программном обеспечении OptiSystem показывают лучшую производительность предложенного кода с четырьмя пользователями весом 6 со скоростью 10 Гбит/с. Помимо того, он может поддерживать до 60 пользователей одновременно и обеспечивать волоконно-оптическую связь на расстоянии до 67 км. Следовательно, предлагаемый код FVWZCC можно применять для поддержки различных требований к качеству обслуживания (QoS) при низкой стоимости и низкой сложности в использовании детекторного приемника.

Вывод: Результаты данного исследования подчеркивают необходимость в коде FVWZCC для поддержки требований QoS конечного пользователя. Новый подход к разработке кода обеспечивает низкую стоимость внедрения, простоту и гибкость.

Ключевые слова: FVWZCC-код, OCDMA, ZCC, частота ошибок в битах BER.

Испитивање нулте унакрсне корелације флексибилне променљиве тежине (FVWZCC) за примену у различитим медијима

Абдулах Бенсад[а], *Абас* Белуфа[б], *Ахмед* Јаради[в]

[а] Универзитет „Др Моулаи Тахар”, Одсек за електронику,
 Саида, Народна Демократска Република Алжир, **аутор за преписку**

[б] Универзитет „Мустафа Стамболи”, Факултет наука и технологије,
 Маскара, Народна Демократска Република Алжир

[в] Универзитет „Ђилали Лиабес”, Лабораторија за примењене материјале,
 Сиди Бел Абес, Народна Демократска Република Алжир

ОБЛАСТ: телекомуникације, оптички преноси
КАТЕГОРИЈА (ТИП) ЧЛАНКА: оригинални научни рад

Сажетак:

Увод/циљ: У раду се предлаже нова метода за конструисање кода са својством нулте унакрсне корелације (Flexible Variable Weight Zero Cross-Correlation – FVWZCC). Метода је једноставна, флексибилна и користи различите тежине кода да подржи различите класе

корисника зависно од њихове даљине преноса и квалитета услуга које су им потребне (подаци, аудио или видео) у системима OCDMA. Коришћењем тежина вишег кода омогућава се подршка мрежним апликацијама вишег приоритета као што су мреже великог домета. Структура кода ZCC се не преклапа са битом '1' и може ефикасно да елиминише интерференцију MAI међу корисницима, као и PIIN шум, повећавајући тако укупне перформансе система.

Методе: За конструкцију предложеног кода FVWZCC коришћени су позиција елемента померања и процес конкатенације матрице три основне матрице означен као десни вектор, основна матрица, као и леви вектор. Математичка анализа и симулације помоћу софтверских програма Matlab и OptiSystem коришћене су за евалуацију перформансе предложене методе FVWZCC у системима SAC-OCDMA директном детекцијом.

Резултати: Резултати показују значајан напредак у представљеном коду у поређењу са осталим постојећим кодовима, што се огледа у једноставности, флексибилности и цени имплементације. Метода користи или константну или променљиву тежину са својством нулте унакрсне корелације. За максимално прихватљив BER од 10^{-9}, резултати симулације система SAC-OCDMA коришћењем директне детекције у софтверу OptiSystem показују боље перформансе од предложеног кода са четири корисника тежине 6 при $10\,Gb/s$. Штавише, може да подржава до 60 корисника истовремено и да достигне дужину влакна од око 67 km. Зато предложени код FVWZCC може да подржава захтеве за различит квалитет услуге (QoS), уз ниску цену и једноставну примену са пријемником директне детекције.

Закључак: Налази ове студије наглашавају потребу за кодом FVWZCC ради подршке захтевима QoS крајњих корисника. Нови приступ конструкцији кода обезбеђује ниску цену имплементације, једноставност и флексибилност.

Кључне речи: код FVWZCC, OCDMA, ZCC, BER (Bit Error Rate).

Systematic design of ADRC-based unmanned tracked vehicle trajectory tracking with FPGA-in-the-loop validation

Momir R. Stanković[a], *Rafal* Madonski[b],
Stojadin M. Manojlović[c]

[a] University of Defence in Belgrade, Military Academy,
  Belgrade, Republic of Serbia,
  e-mail: momir_stankovic@yahoo.com, **corresponding author**,
  ORCID iD: https://orcid.org/0000-0001-8371-9341

[b] Silesian University of Technology,
  Faculty of Automatic Control, Electronics and Computer Science,
  Gliwice, Republic of Poland,
  e-mail: madonski@polsl.pl,
  ORCID iD: https://orcid.org/0000-0002-1798-0717

[c] University of Defence in Belgrade, Military Academy,
  Belgrade, Republic of Serbia,
  e-mail: stojadin.manojlovic@va.mod.gov.rs,
  ORCID iD: https://orcid.org/0000-0003-1268-5310

Abstract:

Introduction/purpose: The trajectory tracking control problem in an unmanned tracked vehicle (UTV) represents a challenging task, due to unknown and unmeasurable slippage dynamics which inevitably exists during movement. Therefore, the application of standard industrial control schemes is often limited.

Methods: In this paper, an active disturbance rejection control (ADRC) scheme is proposed for the longitudinal (vehicle longitudinal velocity control) and lateral (vehicle course angle control) control channels of the UTV to collectively handle all the plant modeling uncertainties and acting slippage disturbances.

Results: A step-by-step procedure for applying the ADRC algorithm for the specific case of UTV trajectory tracking is presented. It includes systematic design, discretization as well as performance analysis and validation utilizing FPGA-in-the-loop (FIL) simulations.

Conclusions: The proposed FIL-based validation method reduces the gap between pure simulation design (which may be too idealized) and implementation on the real vehicle (which may be time-consuming). The obtained experimental results show the advantages of the proposed control structure over standard industrial PI/PID controllers in different working conditions.

Key words: unmanned tracked vehicles, trajectory tracking, active disturbance rejection control, velocity control, PID controller, FPGA-in-the-loop, hardware validation.

Introduction

In recent years, unmanned tracked vehicles (UTVs) have received considerable attention in both civilian and military applications, mostly due to their high mobility and performance in different terrain (Nonami et al., 2013).

The control algorithms for UTVs often take into account the dynamic behavior and construction limits of the vehicle to ensure high movement performance along with sufficient robustness against external disturbances. UTVs are commonly designed without a steering mechanism and the direction of motion is changed by adjusting the angular velocities of the right and left track drive wheels. This provides a fast vehicle response to control signals with a minimum turning radius. However, complex dynamics of the interaction between the tracks and ground causes significant slippage during maneuvering (Janarthanan et al., 2012), leading to the UTV's motion being largely dependent on the terrain properties (Wong, 2022). The UTV slip models based on the tracks instantaneous centers of rotation were analyzed, for example, in (Pentzer et al., 2014) and (Lu et al., 2016), where it was shown that, besides the terrain characteristics, the important factors which significantly affect slippage dynamics are path curvature and the absolute value of the UTV lateral acceleration.

The most common tasks for unmanned vehicles are point-to-point motion, path following, and trajectory tracking (De Luca et al., 1998). The first is a stabilization problem, where the vehicle, starting from a given initial point, has to reach the desired point in space, regardless of the motion profile. Path following and trajectory tracking require motion along the defined geometric path/trajectory, where the trajectory is additionally constrained by time.

To ensure the realization of appropriate motion tasks for UTVs, different control strategies can be used. The usual choice is the time-tested PI/PID

controllers. In (Hu et al., 2019), for example, a torque-speed control strategy was proposed based on low-complexity PID controllers. The authors of (Zou et al., 2018) suggested relying on precise vehicle kinematics and dynamics models and applying control structures with back-stepping PID. Finally, in (Huang et al., 2018b), look-ahead lateral errors were used to design a PI-based path-tracking control system. The main advantages of using the PID-family controllers are their simple design, intuitive procedures for parameter settings, and straightforward implementation. However, their applications to UTVs are often limited in practice by the level of modeling uncertainties and the influence of large, unmodeled slippage dynamics. Therefore, the solutions to the problems of UTV path following and trajectory tracking on uneven terrains often have to rely in real life on using more sophisticated control techniques.

Analyzing the literature on advanced control for UTVs, one can notice three main types of governing algorithms, namely intelligent control, so-called modern control, and observer-based control, with some notable, representative works recalled below.

- The first type is usually based on fuzzy logic and neural networks (Li et al., 2020; Dai et al., 2018) or their combination with classical controllers, like those seen in (Huang et al., 2018a; Al-Jarrah et al., 2019). Although these advanced control structures can provide high trajectory tracking performance even in challenging terrains, their hardware implementation is often limited due to algorithmic complexity and resultant increased computational requirements.

- The so-called modern control approaches are mostly based on model predictive control (Mitsuhashi et al., 2019; Tao et al., 2021; Burke, 2012), adaptive control (Tang et al., 2021; Gonzalez et al., 2010; Hiramatsu et al., 2019), nonlinear control (Hong et al., 2009), or sliding mode control (Sabiha et al., 2022). Those methods, even though effective, rely either on precise modeling of UTV motion and slippage disturbance (Hong et al., 2009; Mitsuhashi et al., 2019) or utilizing a dedicated, separate function block for model parameters identification and/or slippage dynamics estimation.

- The third type of advanced control scheme for UTVs is observed-based control. In this category, an example extended Kalman filter was applied in (Tao et al., 2021) to estimate the coefficients of road resistance, thus strengthening the model predictive control's adapt-

ability to uncertain road conditions. Another example can be (Burke, 2012), where the compensation of slip disturbance was addressed using an adaptive least squares slippage estimator. In (Hiramatsu et al., 2019), a structure composed of an adaptive controller and disturbance observer was proposed for UTV angular and linear velocity estimation, where the observer was responsible for estimating the effects of slippage which in return improved the tracking performance without making the model unbearably complex.

Having analyzed the literature on UTV control, it seems that the current method landscape is missing an approach that would be a compromise between effectiveness, overall complexity as well as knowledge about the controlled system and the environment affecting it. Therefore, in this work, we propose the use of an active disturbance rejection control (ADRC) scheme (Gao, 2006), which is a general methodology known to provide robust performance, straightforward tuning and implementation, and operation not being overly dependent on the plant's mathematical model. The ADRC's recent successful industrial applications (discussed in the overview paper (Zhang et al., 2021)) are the main motivation for using it in this work for the UTV trajectory tracking control system. In fact, this is not the first time ADRC has been considered for UTVs. In (Chen et al., 2019), the authors have introduced back-stepping ADRC as their lateral control for the path-following problem, which featured an extended state observer (ESO) for jointly estimating internal model uncertainties and slippage disturbances.

The contribution of our work is the extensions provided to (Chen et al., 2019). Firstly, our research deals with the UTV trajectory tracking task, where the trajectory is additionally constrained with time. Secondly, this paper extends the scope to designing both controllers: lateral and longitudinal. Finally, in contrast to (Chen et al., 2019), we go beyond just a simulation study and perform FPGA-in-the-loop (FIL) verification. Such a methodology reduces the gap between a pure simulation design (which may be too idealized) and implementation on the real vehicle (which may be resource-consuming). With this paper, we want to show a comprehensive application of ADRC to UTVs (with all its unique characteristics and intricacies), including systematic design, performance analysis, and validation.

The paper is organized as follows. The UTV model is briefly recalled in the UTV motion model section. Then, the design of lateral and longitudinal controllers is shown in the Lateral controller design and Longitudinal controller design sections. The verification of the proposed control system is described in the Control system verification. The section entitled Conclusion summarizes the work.

UTV motion model

The kinematic model of the considered UTV can be described as:

$$\begin{pmatrix} \dot{x}(t) \\ \dot{y}(t) \\ \dot{\theta}(t) \end{pmatrix} = \begin{pmatrix} \cos\theta(t) & 0 \\ \sin\theta(t) & 0 \\ 0 & 1 \end{pmatrix} \cdot \begin{pmatrix} v(t) + v_{\mathrm{d}}(t) \\ \omega(t) + \omega_{\mathrm{d}}(t) \end{pmatrix}, \tag{1}$$

where $x(t)$ and $y(t)$ denote vehicle coordinates in the inertial coordinate system, $\theta(t)$ is the course angle of UTV, $v(t)$ and $\omega(t)$ are the UTV longitudinal and angular velocity, respectively, both considered to be the UTV control inputs. The uncertainties in the longitudinal and angular velocity, caused by unknown track friction, i.e. track slippage, are represented with $v_{\mathrm{d}}(t)$ and $\omega_{\mathrm{d}}(t)$, respectively.

Including the dynamic model of the UTV, the relation between the control inputs $v(t)$ and $\omega(t)$ and the angular velocities of the right and left track drive wheel $\Omega_{\mathrm{R}}(t)$ and $\Omega_{\mathrm{L}}(t)$, are given respectively as:

$$v(t) = \frac{r}{2}\left(\Omega_{\mathrm{R}}(t) + \Omega_{\mathrm{L}}(t)\right), \tag{2}$$

$$\omega(t) = \frac{r}{B}\left(\Omega_{\mathrm{R}}(t) - \Omega_{\mathrm{L}}(t)\right), \tag{3}$$

where r is the drive wheel radius and B is the normal distance between the right and left track.

In the presence of the track slippage, (2) and (3) can be modified respectively as:

$$v(t) + v_{\mathrm{d}}(t) = \frac{r}{2}\left(\Omega_{\mathrm{R}}(t)\cdot a_{\mathrm{R}}(t) + \Omega_{\mathrm{L}}(t)\cdot a_{\mathrm{L}}(t)\right), \tag{4}$$

$$\omega(t) + \omega_{\mathrm{d}}(t) = \frac{r}{B}\left(\Omega_{\mathrm{R}}(t)\cdot a_{\mathrm{R}}(t) - \Omega_{\mathrm{L}}(t)\cdot a_{\mathrm{L}}(t)\right), \tag{5}$$

where $a_{\mathrm{R}}(t)$ and $a_{\mathrm{L}}(t)$ are the unknown friction coefficients of the right and left track, which are in the range $[0,1]$.

One can notice that the UTV motion control involves designing two control subsystems. The first one is for angular velocity control and involves a so-called lateral controller. The second subsystem is for longitudinal velocity control and deals with constructing a longitudinal controller.

Lateral controller design

To define the lateral control model, let us consider the UTV reference trajectory tracking problem shown in Figure 1, where the reference trajectory is defined by the kinematic model of a virtual target:

$$\begin{pmatrix} \dot{x}_{\mathrm{r}}(t) \\ \dot{y}_{\mathrm{r}}(t) \end{pmatrix} = \begin{pmatrix} \cos\theta_{\mathrm{r}}(t) \\ \sin\theta_{\mathrm{r}}(t) \end{pmatrix} \cdot \bar{v}_{\mathrm{r}}. \tag{6}$$

where $x_{\mathrm{r}}(t)$ and $y_{\mathrm{r}}(t)$ are the coordinates of the virtual target in the inertial coordinate system (X,Y), $\bar{v}_{\mathrm{r}} > 0$ is the virtual target longitudinal velocity and $\theta_{\mathrm{r}}(t)$ is the virtual target course angle. The path along track error $e_{\mathrm{s}}(t)$ and the cross-track error $e_{\mathrm{d}}(t)$ are defined in the vehicle coordinate system (X_{v}, Y_{v}) as:

$$\begin{pmatrix} e_{\mathrm{s}}(t) \\ e_{\mathrm{d}}(t) \end{pmatrix} = \begin{pmatrix} \cos\theta(t) & \sin\theta(t) \\ -\sin\theta(t) & \cos\theta(t) \end{pmatrix} \cdot \begin{pmatrix} x_{\mathrm{r}}(t) - x(t) \\ y_{\mathrm{r}}(t) - y(t) \end{pmatrix}. \tag{7}$$

By denoting the course angle error as:

$$\theta_{\mathrm{e}}(t) = \theta(t) - \theta_{\mathrm{r}}(t), \tag{8}$$

and substituting (1) and (6) in the derivative of (7), one can obtain trajectory tracking and course angle errors dynamics as:

$$\begin{aligned} \dot{e}_{\mathrm{s}}(t) &= \dot{\theta}(t) \cdot e_{\mathrm{d}}(t) - v(t) - v_{\mathrm{d}}(t) + \bar{v}_{\mathrm{r}} \cos\theta_{\mathrm{e}}(t), \\ \dot{e}_{\mathrm{d}}(t) &= \bar{v}_{\mathrm{r}} \sin\theta_{\mathrm{e}}(t) - \dot{\theta}(t) \cdot e_{\mathrm{s}}(t), \\ \dot{\theta}_{\mathrm{e}}(t) &= \omega(t) + \omega_{\mathrm{d}}(t) - \dot{\theta}_{\mathrm{r}}(t). \end{aligned} \tag{9}$$

As in practice, the cross-track error is the main concern (Chen et al., 2019). To facilitate that, the lateral control subsystem can be formulated from (9) as:

$$\dot{e}_{\mathrm{d}}(t) = \bar{v}_{\mathrm{r}} \sin\theta_{\mathrm{e}}(t) + d_1(t), \tag{10}$$

$$\dot{\theta}_{\mathrm{e}}(t) = \omega(t) + d_2(t), \tag{11}$$
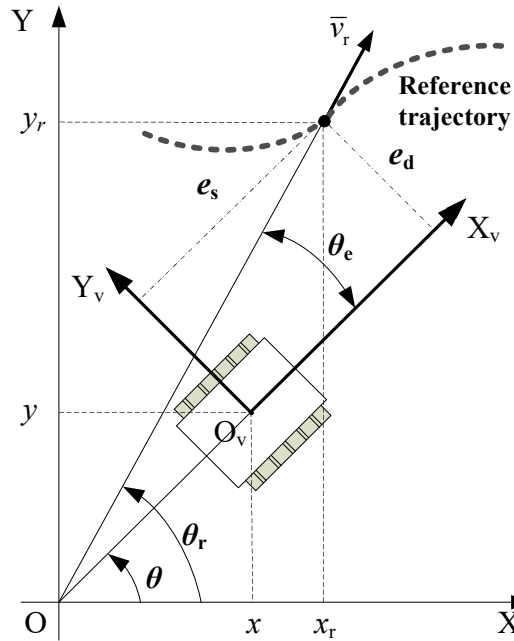
Figure 1 – Considered UTV trajectory tracking problem

with $d_1(t) = \dot{\theta}(t) \cdot e_{\mathrm{s}}(t)$ and $d_2(t) = \omega_{\mathrm{d}}(t) + \dot{\theta}_{\mathrm{r}}(t)$, which represents collectively the disturbances caused by slippage, reference trajectory dynamics, and longitudinal channel coupling (reflected in the influence of the $v(t)$ on the lateral controller).

By substituting (11) in the derivative of (10), the cross-track error dynamics can be presented in a compact ADRC form as:

$$\ddot{e}_{\mathrm{d}}(t) = b_0 \cdot \omega(t) + f_1(t), \tag{12}$$

where $b_0 = \bar{v}_{\mathrm{r}}$ is the known part of the lateral model and $f_1(t) = \bar{v}_{\mathrm{r}}(\cos \theta_{\mathrm{e}}(t) - 1) \cdot \omega(t) + \bar{v}_{\mathrm{r}} \cos \theta_{\mathrm{e}}(t) \cdot d_2(t) + \dot{d}_1(t)$ is denoted as the total disturbance of the lateral control subsystem. One can see that the lateral control is formulated as a regulation problem, where the error signal $e_{\mathrm{d}}(t)$ has to be minimized by manipulating the control input $\omega(t)$, all in the presence of perturbing effects like slippage disturbances, coupling dynamics with the longitudinal channel, and the reference trajectory dynamics.

To design the ADRC controller, model ([12](#)) is expressed as a following extended state-space model:

$$
\begin{pmatrix} \dot{e}_{\mathrm{d}}(t) \\ \ddot{e}_{\mathrm{d}}(t) \\ \dot{f}_{\mathrm{l}}(t) \end{pmatrix} = \begin{pmatrix} 0 & 1 & 0 \\ 0 & 0 & 1 \\ 0 & 0 & 0 \end{pmatrix} \cdot \begin{pmatrix} e_{\mathrm{d}}(t) \\ \dot{e}_{\mathrm{d}}(t) \\ f_{\mathrm{l}}(t) \end{pmatrix} + \begin{pmatrix} 0 \\ b_0 \\ 0 \end{pmatrix} \cdot \omega(t) + \begin{pmatrix} 0 \\ 0 \\ 1 \end{pmatrix} \cdot \dot{f}_{\mathrm{l}}(t), \quad (13)
$$

and the states can be estimated by an appropriate observer, for example, a linear ESO shown in ([Łakomy et al., 2020](#)):

$$
\begin{pmatrix} \dot{\hat{e}}_{\mathrm{d}}(t) \\ \dot{\hat{e}}_{\mathrm{d}}(t) \\ \dot{\hat{f}}_{\mathrm{l}}(t) \end{pmatrix} = \begin{pmatrix} 0 & 1 & 0 \\ 0 & 0 & 1 \\ 0 & 0 & 0 \end{pmatrix} \cdot \begin{pmatrix} \hat{e}_{\mathrm{d}}(t) \\ \dot{\hat{e}}_{\mathrm{d}}(t) \\ \hat{f}_{\mathrm{l}}(t) \end{pmatrix} + \begin{pmatrix} 0 \\ b_0 \\ 0 \end{pmatrix} \cdot \omega(t)
$$

$$
+ \begin{pmatrix} l_{\mathrm{l}1} \\ l_{\mathrm{l}2} \\ l_{\mathrm{l}3} \end{pmatrix} \cdot (e_{\mathrm{d}}(t) - \hat{e}_{\mathrm{d}}(t)), \quad (14)
$$

where $l_{\mathrm{l}1}$, $l_{\mathrm{l}2}$, and $l_{\mathrm{l}3}$ are the observer gains, which can be relatively simply tuned by the *bandwidth parameterization* from ([Gao, 2003](#)) by placing observer poles at the same location $\lambda = -\omega_{\mathrm{ESO_l}}$:

$$
(\lambda + \omega_{\mathrm{ESO_l}})^3 \overset{!}{=} \lambda^3 + l_{\mathrm{l}1} \cdot \lambda^2 + l_{\mathrm{l}2} \cdot \lambda + l_{\mathrm{l}3}, \quad (15)
$$

where $\omega_{\mathrm{ESO_l}}$ is the desired observer bandwidth.

By assuming $\theta_{\mathrm{e}}(t) \in \{-\pi, \pi\}$, the saturated lateral control law can be proposed as:

$$
\omega(t) = \begin{cases} \omega_{\max} \cdot \mathrm{sat}\left(u_{\mathrm{l}}(t)/\omega_{\max}\right), & \text{when} \quad |\theta_{\mathrm{e}}(t)| < \frac{\pi}{2} \\ \omega_{\max}, & \text{when} \quad \frac{\pi}{2} \leq \theta_{\mathrm{e}}(t) < \pi \\ -\omega_{\max}, & \text{when} \quad -\pi < \theta_{\mathrm{e}}(t) \leq -\frac{\pi}{2} \end{cases} \quad (16)
$$

where $\mathrm{sat}(a) = \min\left(1, |a|\right) \cdot \mathrm{sign}(a)$ is a saturation function, $\omega_{\max} > 0$ is saturation level of the lateral ADRC signal, denoted as:

$$
u_{\mathrm{l}}(t) = \frac{1}{b_0} \left(-k_{\mathrm{pl}} \cdot \hat{e}_{\mathrm{d}}(t) - k_{\mathrm{dl}} \cdot \dot{\hat{e}}_{\mathrm{d}}(t) - \hat{f}_{\mathrm{l}}(t) \right), \quad (17)
$$

with the controller design parameters k_{pl} and k_{dl}. The saturation $\omega_{\max}$ is introduced to reduce slippage caused by the large centrifugal force, i.e. the high value of the UTV angular acceleration, as discussed in ([Lu et al.,

2016). It should be also noted that control law (16) is designed to enable quick reduction of the course angle error in the range $\theta_{\mathrm{e}}(t) \in \{-\pi/2, \pi/2\}$ and to avoid the control signal (17) saturation.

Now, by assuming $f_{\mathrm{l}}(t) \approx \hat{f}_{\mathrm{l}}(t)$, $\dot{e}_{\mathrm{d}}(t) \approx \hat{\dot{e}}_{\mathrm{d}}(t)$, $e_{\mathrm{d}}(t) \approx \hat{e}_{\mathrm{d}}(t)$ and substituting (16) in (12), the following relation can take place:

$$\ddot{e}_{\mathrm{d}}(t) + k_{\mathrm{dl}} \cdot \dot{e}_{\mathrm{d}}(t) + k_{\mathrm{pl}} \cdot e_{\mathrm{d}}(t) \approx 0. \tag{18}$$

From (18) one can see that the lateral control performances can be adjusted by appropriately selecting the parameters k_{pl} and k_{dl}. Applying the already mentioned *bandwidth parameterization*, the controller parameters can be tuned by placing closed-loop controller poles at the common location $\lambda = -\omega_{\mathrm{CL}_{\mathrm{l}}}$:

$$(\lambda + \omega_{\mathrm{CL}_{\mathrm{l}}})^2 \overset{!}{=} \lambda^2 + k_{\mathrm{dl}} \cdot \lambda + k_{\mathrm{pl}}, \tag{19}$$

where $\omega_{\mathrm{CL}_{\mathrm{l}}}$ is the desired closed-loop lateral control system bandwidth.

Longitudinal controller design

Let us denote the UTV longitudinal velocity in the presence of slippage disturbance as $v_{\mathrm{v}}(t) = v(t) + v_{\mathrm{d}}(t)$. Thus, the longitudinal velocity control model can be formulated as:

$$\dot{v}_{\mathrm{v}}(t) = u_{\mathrm{v}}(t) + \dot{v}_{\mathrm{d}}(t), \tag{20}$$

where $u_{\mathrm{v}}(t) = \dot{v}(t)$ represents the control signal which should be designed to make $v_{\mathrm{v}}(t)$ track the reference target longitudinal velocity $\bar{v}_{\mathrm{r}}$ even in the presence of the disturbance $v_{\mathrm{d}}(t)$. To apply the ADRC concept to the considered problem, system (20) can be rewritten in the extended state-space form as:

$$\begin{pmatrix} \dot{v}_{\mathrm{v}}(t) \\ \dot{f}_{\mathrm{v}}(t) \end{pmatrix} = \begin{pmatrix} 0 & 1 \\ 0 & 0 \end{pmatrix} \cdot \begin{pmatrix} v_{\mathrm{v}}(t) \\ f_{\mathrm{v}}(t) \end{pmatrix} + \begin{pmatrix} 1 \\ 0 \end{pmatrix} \cdot u_{\mathrm{v}}(t) + \begin{pmatrix} 0 \\ 1 \end{pmatrix} \cdot \dot{f}_{\mathrm{v}}(t), \tag{21}$$

where $f_{\mathrm{v}}(t) = \dot{v}_{\mathrm{d}}(t)$ is the longitudinal channel total disturbance, which can be estimated by an appropriately constructed ESO:

$$\begin{pmatrix} \dot{\hat{v}}_{\mathrm{v}}(t) \\ \dot{\hat{f}}_{\mathrm{v}}(t) \end{pmatrix} = \begin{pmatrix} 0 & 1 \\ 0 & 0 \end{pmatrix} \cdot \begin{pmatrix} \hat{v}_{\mathrm{v}}(t) \\ \hat{f}_{\mathrm{v}}(t) \end{pmatrix} + \begin{pmatrix} 1 \\ 0 \end{pmatrix} \cdot u_{\mathrm{v}}(t) + \begin{pmatrix} l_{\mathrm{v1}} \\ l_{\mathrm{v2}} \end{pmatrix} \cdot (v_{\mathrm{v}}(t) - \hat{v}_{\mathrm{v}}(t)), \tag{22}$$

where l_{v1} and l_{v2} are the observer gains. As in the previously shown lateral control channel, the active rejection of the total disturbance $f_v(t)$ can be realized using its estimation $\hat{f}_v(t)$ by applying the following ADRC governing law:

$$u_v(t) = k_{pv}\left(\bar{v}_r - v_v(t)\right) - \hat{f}_v(t), \tag{23}$$

where k_{pv} is an adjustable controller parameter. Assuming $f_v(t) \approx \hat{f}_v(t)$ and substituting (23) into (20) results in:

$$\dot{v}_v(t) + k_{pv} \cdot v_v(t) \approx k_{pv} \cdot \bar{v}_r, \tag{24}$$

where one can see that the desired control performances can be obtained by an appropriate selection of the parameter k_{pv}.

In the same manner, as in the lateral control subsystem, the longitudinal ESO and controller gains can be tuned by utilizing the *bandwidth parameterization* methodology, i.e.:

$$\left(\lambda + \omega_{ESO_v}\right)^2 \overset{!}{=} \lambda^2 + l_{v1} \cdot \lambda + l_{v2}, \tag{25}$$

$$\lambda + \omega_{CL_v} \overset{!}{=} \lambda + k_{pv}, \tag{26}$$

where ω_{ESO_v} and ω_{CL_v} are the desired longitudinal ESO bandwidth and the longitudinal closed-loop control system bandwidth, respectively.

A schematic representation of the UTV control architecture, based on the proposed ADRC lateral and longitudinal controllers, is shown in Figure 2.
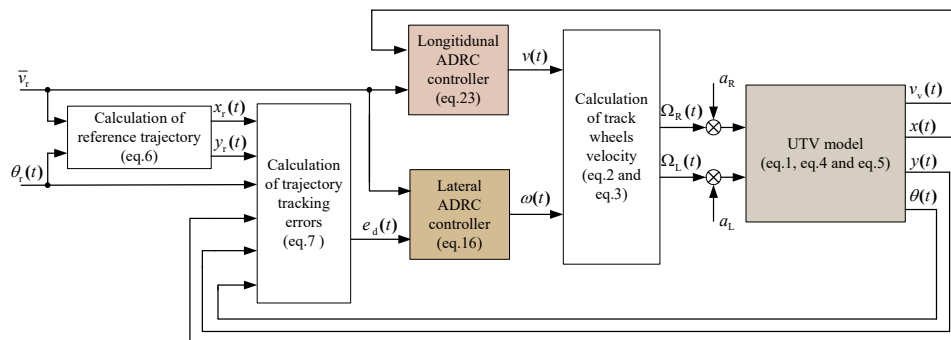
Figure 2 – The proposed UTV control architecture

Control system verification

Since the hardware implementation of the control algorithm requires its discrete form, simulation experiments are carried out with a discrete-time version of the proposed UTV controllers. Therefore, the discretization of the lateral and longitudinal controllers is presented first, followed by simulation results.

Simulation validation

Since the lateral and the longitudinal ADRC control laws (17) and (23) are in linear forms, only the observer need to be discretized. To enhance the closed-loop system stability for a low sampling rate T_s, the current discrete models from (Miklosovic et al., 2006; Herbst & Madonski, 2023) are used. Therefore, for the lateral ESO (14), its discrete form is defined as:

$$
\begin{pmatrix} \hat{\dot{e}}_{\mathrm{d}}(k) \\ \hat{\dot{e}}_{\mathrm{d}}(k) \\ \hat{f}_{\mathrm{l}}(k) \end{pmatrix} = \left(A_{\mathrm{dl}} - L_{\mathrm{cl}} \cdot C_{\mathrm{dl}} \cdot A_{\mathrm{dl}} \right) \cdot \begin{pmatrix} \hat{e}_{\mathrm{d}}(k-1) \\ \hat{\dot{e}}_{\mathrm{d}}(k-1) \\ \hat{f}_{\mathrm{l}}(k-1) \end{pmatrix}
$$
$$
+ \left(B_{\mathrm{dl}} - L_{\mathrm{cl}} \cdot C_{\mathrm{dl}} \cdot B_{\mathrm{dl}} \right) \cdot \omega(k-1) + L_{\mathrm{cl}} \cdot e_{\mathrm{d}}(k), \qquad (27)
$$

where:

$$
A_{\mathrm{dl}} = \begin{pmatrix} 1 & T_s & T_s^2/2 \\ 0 & 1 & T_s \\ 0 & 0 & 1 \end{pmatrix}, B_{\mathrm{dl}} = \begin{pmatrix} b_0 \cdot T_s^2/2 \\ b_0 \cdot T_s \\ 0 \end{pmatrix}, C_{\mathrm{dl}} = \begin{pmatrix} 1 & 0 & 0 \end{pmatrix},
$$

are the discrete observer matrices obtained by applying the zero-order hold (ZOH) discretization method from (Miklosovic et al., 2006). The discrete ESO gains vector L_{cl} is computed by placing the discrete observer poles in one location $\beta = e^{-\omega_{\mathrm{ESO_l}} T_s}$, i.e.:

$$
|zI - (A_{\mathrm{dl}} - A_{\mathrm{dl}} \cdot L_{\mathrm{cl}} \cdot C_{\mathrm{dl}})| \overset{!}{=} (z - \beta)^3.
$$

In the same manner, the discrete-time model of the longitudinal controller ESO (22) is obtained as:

$$
\begin{pmatrix} \hat{v}_{\mathrm{v}}(k) \\ \hat{\dot{f}}_{\mathrm{v}}(k) \end{pmatrix} = \left(A_{\mathrm{dv}} - L_{\mathrm{cv}} \cdot C_{\mathrm{dv}} \cdot A_{\mathrm{dv}} \right) \cdot \begin{pmatrix} \hat{v}_{\mathrm{v}}(k-1) \\ \hat{f}_{\mathrm{v}}(k-1) \end{pmatrix}
$$

$$+ \left(B_{\text{dv}} - L_{\text{cv}} \cdot C_{\text{dv}} \cdot B_{dv} \right) \cdot u_{\text{v}}(k-1) + L_{\text{cv}} \cdot v_{\text{v}}(k), \qquad (28)$$

where:

$$A_{\text{dv}} = \begin{pmatrix} 1 & T_s \\ 0 & 1 \end{pmatrix}, B_{\text{dv}} = \begin{pmatrix} b_0 \cdot T_s \\ 0 \end{pmatrix}, C_{\text{dv}} = \begin{pmatrix} 1 & 0 \end{pmatrix},$$

are the matrices determined by the ZOH discretization. The longitudinal discrete ESO gains vector L_{cv} is computed by placing discrete observer poles in the location $\beta = e^{-\omega_{\text{ESO}_{\text{v}}} T_s}$, i.e.:

$$|zI - (A_{\text{dv}} - A_{\text{dv}} \cdot L_{\text{cv}} \cdot C_{\text{dv}})| \stackrel{!}{=} (z - \beta)^2.$$

The simulation experiments are conducted in MATLAB/Simulink using the model of the laboratory skid-steer UTV, with dimensions $r = 0.3\,\text{m}$ and $B = 0.7\,\text{m}$. To demonstrate the effectiveness of the proposed ADRC algorithm, its performance is compared with the UTV control architecture realized by the standard industrial discrete PID controller with a noise filter in the lateral control subsystem and the PI controller in the longitudinal control subsystem. To make the test more realistic, the maximal UTV angular velocity is limited to $\omega_{\text{max}} = 2 \cdot \pi\,\text{rad/s}$. The reference trajectory is defined using the kinematic model (6), with $\bar{v}_{\text{r}} = 2\,\text{m/s}$ and:

$$\theta_{\text{r}}(k \cdot T_s) = \begin{cases} 0.05 \cdot k \cdot T_s, & \text{when} \quad 0\,\text{s} < k \cdot T_s \leq 8\,\text{s}; \\ -0.1 \cdot k \cdot T_s, & \text{when} \quad 8\,\text{s} < k \cdot T_s \leq 16\,\text{s}; \\ -0.05 \cdot k \cdot T_s, & \text{when} \quad 16\,\text{s} < k \cdot T_s \leq 22\,\text{s}; \\ 0.15 \cdot k \cdot T_s, & \text{when} \quad 22\,\text{s} < k \cdot T_s \leq 35\,\text{s}. \end{cases} \qquad (29)$$

The simulations are realized through the following two cases.

Simulation case #1

In this case, it is assumed that the UTV is not affected by the slippage disturbances ($a_{\text{R}} = 1$ and $a_{\text{L}} = 1$). Both of the considered control approaches (the proposed ADRC and the standard PI/PID) were tuned empirically with the goal to enable similar control performances in terms of minimization of the cross-track error e_{d}. Therefore, in the lateral PID controller, four parameters: proportional, integral, and derivative gains, as well as the noise filter coefficient, are set as $k_{\text{P}_1} = 4.5$, $k_{\text{I}_1} = 1$, $k_{\text{D}_1} = 0.5$ and $N = 85$, and the proportional and integral gains of the longitudinal PI controller are set as $k_{\text{P}_{\text{v}}} = 1.5$, $k_{\text{I}_{\text{v}}} = 0.1$. The ADRC control structure is tuned

$$\boxed{1711}$$

by choosing $\omega_{\mathrm{CL_l}} = 1\,\text{rad/s}$ and $\omega_{\mathrm{ESO_l}} = 10\,\text{rad/s}$ for the lateral controller, and $\omega_{\mathrm{CL_v}} = 1.4\,\text{rad/s}$ and $\omega_{\mathrm{ESO_v}} = 16\,\text{rad/s}$ for the longitudinal controller. Both systems are discretized with the same sampling time $T_s = 20\,\text{ms}$. The obtained results of the reference trajectory tracking performances, including cross-track errors, longitudinal velocities, and drive wheels velocities are depicted in Figure 3.
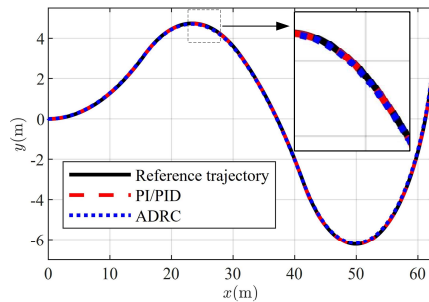
(a) Reference trajectory tracking
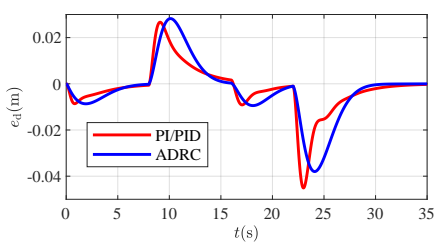
(b) Cross-track errors
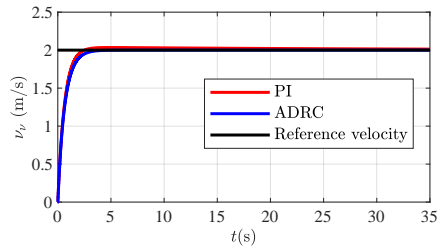
(c) Longitudinal velocity control
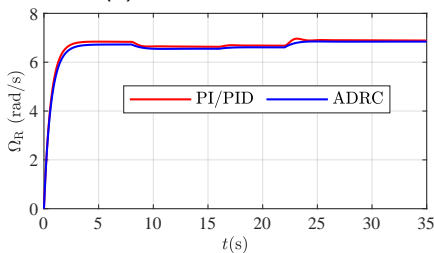
(d) Right wheel velocity
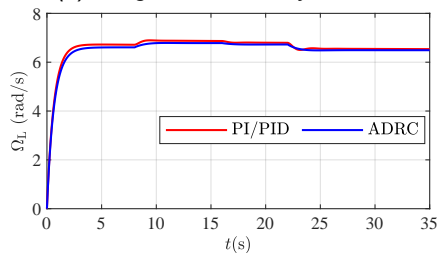
(e) Left wheel velocity

Figure 3 – Simulation results for simulation case #1

In accordance with the set goal of this simulation case, one can see that both control approaches provide effective tracking of the reference trajectory, with similar values of the cross-track errors peaks that occur when $\theta_{\mathrm{r}}(t)$ changes the value (see (29)). The drive wheels velocities are bounded

1712

and smooth for both systems, and it can be seen that the PI/PID algorithms generate slightly larger values.

Simulation case #2

In this case, the controllers have kept the settings from the previous one. The slippage disturbances with dynamics $a_{\mathrm{R}} = 0.7 + 0.3\sin(2 \cdot k \cdot T_s)$ and $a_{\mathrm{L}} = 0.7 + 0.3\sin(4 \cdot k \cdot T_s)$, which simulate vehicle motion over uneven dirt terrains, are included from $t = 10\,\mathrm{s}$.
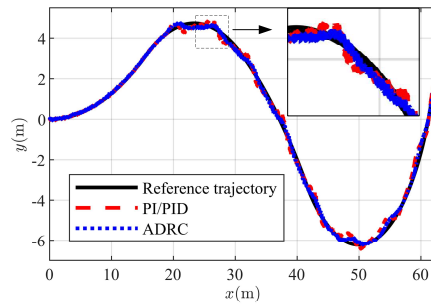
(a) Reference trajectory tracking
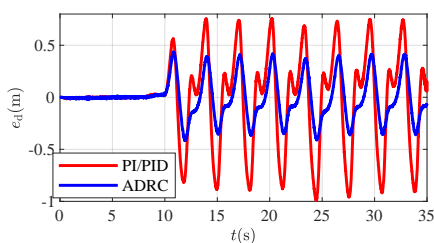
(b) Cross-track errors
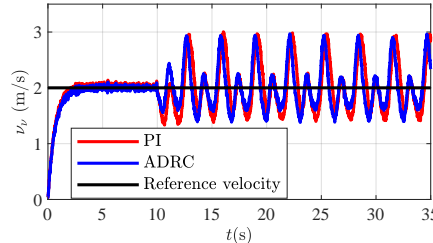
(c) Longitudinal velocity control
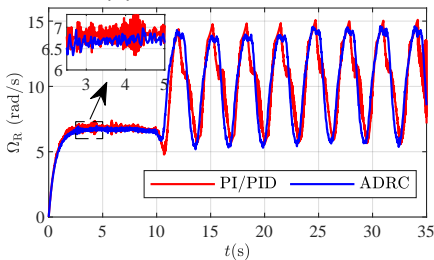
(d) Right wheel velocity
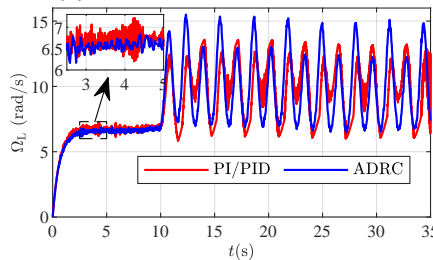
(e) Left wheel velocity

Figure 4 – Simulation results for simulation case #2

Also, the measurement errors of the UTV position (x, y), the angle orientation (θ), and the longitudinal velocity (v_v) are modeled as Gaussian noises with zero means and standard deviations [0.1 m, 0.1 m, 0.01 rad, 0.1 m/s], respectively. It corresponds with the errors of the GPS and inertial sensors in the real vehicle. The reference trajectory tracking performances and drive wheel velocities comparisons of PI/PID and ADRC are shown in Figure 4. It is noticeable that in the presence of the slippage dynamics, ADRC enables better tracking performances, with significantly lower values of the cross-track error peaks. In addition, it can be noted that the added measurement errors caused ruggedness in drive wheel velocities. However, from the zoomed part of Figure 4d and Figure 4e, it is evident that ADRC generates more smooth drive wheels velocities than the PI/PID algorithm, which is important for practical implementation.

FPGA-in-the-loop simulation validation

In order to analyze the challenges of the practical implementation, the FIL (FPGA-in-the-loop) simulation with the proposed ADRC-based UTV control is carried out. Such a validation method reduces the gap between pure simulation design (which may be too idealized) and implementation on the real vehicle (which may be time-consuming). To this end, a hardware description language code of the discrete lateral and longitudinal controllers is generated in the fixed-point word-length (WL) format, for the signals and coefficients representations, and implemented in FPGA board Basys 3 with Xilinx chip XC7A35T. By connecting JTAG port of the FPGA board and the personal computer USB port, the FIL simulations are executed by exchanging signals between the UTV model, defined in MATLAB/Simulink, and the controllers, implemented in the FPGA chip. The graphical structure of the FIL simulation methodology is demonstrated in Figure 5.
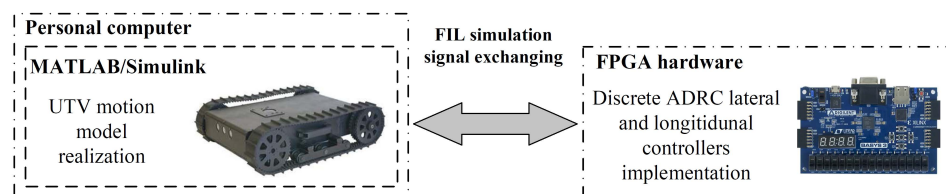
Figure 5 – FIL validation methodology

The FIL simulations are performed with the setup as in simulation case #2. The reference trajectory and longitudinal velocity tracking performances, for the ADRC algorithm implemented in the fixed-point format with WLs of 24, 22, and 20 bits, are compared with the pure MATLAB/Simulink simulation results (shown in simulation case #2) and gathered in Figure 6.

(a) Reference trajectory tracking

(b) Longitudinal velocity control
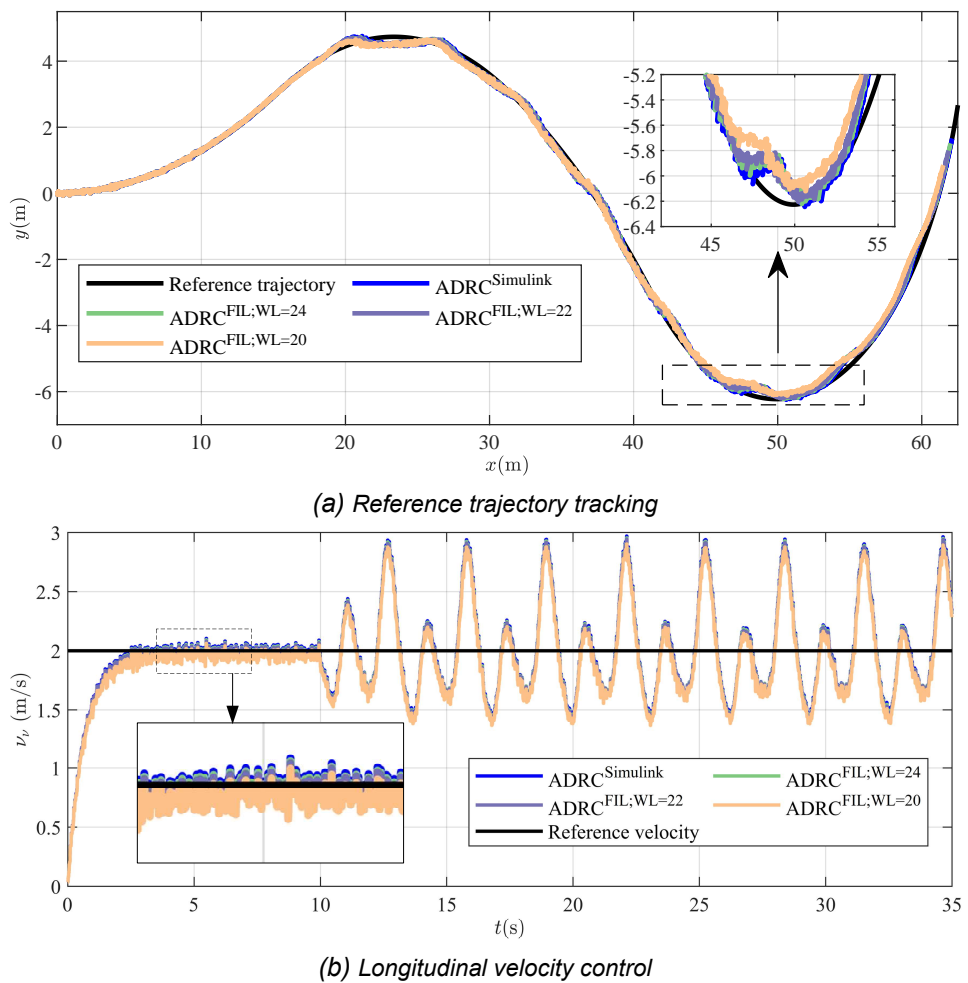
Figure 6 – FIL simulation reference trajectory tracking results

In order to make the impact of the fixed-point format quantization error (QE) more visible, the differences in cross-track errors, between the pure MATLAB/Simulink simulation and the appropriate FIL simulations, denoted

as $e_{\mathrm{d}}^{\mathrm{QE}}$, are shown in Figure 7. The obtained drive wheels velocities are shown in Figure 8. In addition, the appropriate FPGA resource occupancy values, for different values of WLs, are shown in Table 1.
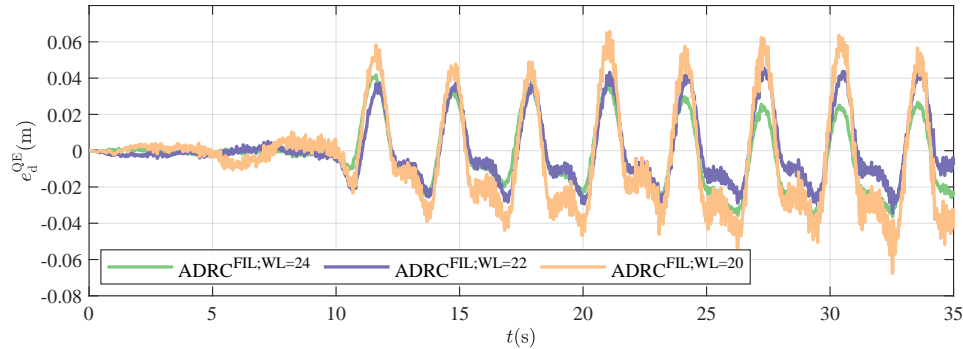
Figure 7 – The difference in the cross-track error between the Simulink simulation and the FIL simulations with the appropriate WL of the fixed-point format

Table 1 – Resource occupancy of FPGA chip XC7A35T for the fixed-point ADRC controllers implementation with different WLs

FPGA resource	WL $= 24$	WL $= 22$	WL $= 20$	Available
LUTs	5433 (26.2%)	4821 (23.2%)	4441(21.3%)	20800 (100%)
FF blocks	545 (1.3%)	525 (1.2%)	499(1.2%)	41600 (100%)
DSP blocks	82 (91%)	81 (90%)	78 (87%)	90 (100%)

As it can be seen, the FIL simulation results are close to the simulation results, which confirms the high performances of the FPGA-based implementation of the lateral and longitudinal ADRC controllers. As expected, the slight performance degradation occurs with the decrease of WL, i.e. with lower precision of the signals and coefficients in the implemented controllers. Although increasing WL requires more FPGA resource occupancy, from Table 1 one can see that it is not a significant increase that enables the realization of a high-precision fixed-point ADRC implementation on low-cost FPGA chip, such as XC7A35T.
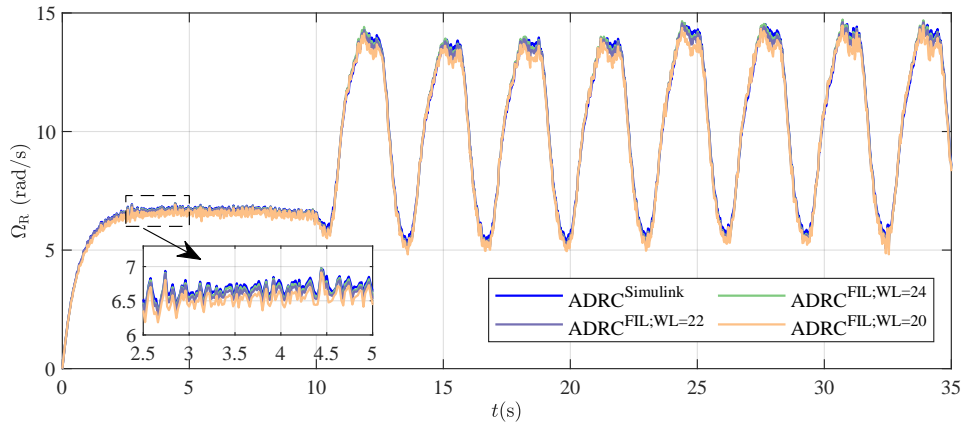
(a) Right wheel velocity
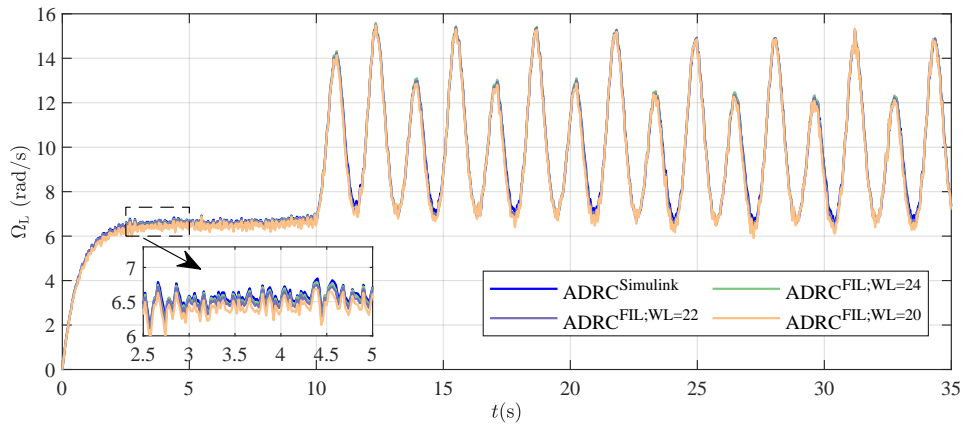
(b) Left wheel velocity

Figure 8 – FIL simulation drive wheel velocities

Conclusion

To improve the UTV trajectory tracking performances, the systematic use of an ADRC-based control structure was suggested in this research. The slippage disturbances and the internal UTV model uncertainties were treated collectively as lumped (total) disturbances in the lateral and longitudinal control channels. The efficiency of the proposed ADRC approach was illustrated in comparison with the classical PI/PID control, through the typical UTV trajectory tracking simulation scenarios.

Additionally, the FIL simulation was used to experimentally validate the fixed-point FPGA implementation of the proposed lateral and longitudinal ADRC controllers. The conducted applied research has validated the efficacy of the proposed systematic procedure of applying the ADRC methodology for the specific UTV trajectory tracking problem, which includes its design, tuning, FPGA implementation, and performance verification.

References

Al-Jarrah, A., Salah, M. & Almomani, F. 2019. Controlling a Skid-Steered Tracked Mobile Robot with Slippage Using Various Control Schemes. In: *2019 20th International Conference on Research and Education in Mechatronics (REM)*. Wels, Austria, pp.1-7, May 23-24. Available at: https://doi.org/10.1109/REM.2019.8744123.

Burke, M. 2012. Path-following control of a velocity constrained tracked vehicle incorporating adaptive slip estimation. In: *2012 IEEE International Conference on Robotics and Automation*. Saint Paul, MN, USA, pp.97-102, May 14-18. Available at: https://doi.org/10.1109/ICRA.2012.6224684.

Chen, S., Xue, W., Lin, Z. & Huang, Y. 2019. On Active Disturbance Rejection Control for Path Following of Automated Guided Vehicle with Uncertain Velocities. In: *2019 American Control Conference (ACC)*. Philadelphia, PA, USA, pp.2446-2451, July 10-12. Available at: https://doi.org/10.23919/ACC.2019.8815348.

Dai, Y., Zhu, X., Zhou, H., Mao, Z. & Wu, W. 2018. Trajectory Tracking Control for Seafloor Tracked Vehicle By Adaptive Neural-Fuzzy Inference System Algorithm. *International Journal of Computers Communications & Control*, 13(4), pp. 465–476 [online]. Available at: https://www.univagora.ro/jour/index.php/ijccc/article/view/3267 [Accessed: 20 March 2024].

De Luca, A., Oriolo, G. & Samson, C. 1998. Feedback control of a nonholonomic car-like robot. In: *Laumond, J.P. (Ed.) Robot Motion Planning and Control. Lecture Notes in Control and Information Sciences*. 229, pp.171-253. Berlin, Heidelberg: Springer. Available at: https://doi.org/10.1007/BFb0036073.

Gao, Z. 2003. Scaling and bandwidth-parameterization based controller tuning. In: *Proceedings of the 2003 American Control Conference*. Denver, CO, USA, pp.4989-4996, June 04-06. Available at: https://doi.org/10.1109/ACC.2003.1242516.

Gao, Z. 2006. Active disturbance rejection control: a paradigm shift in feedback control system design. In: *2006 American Control Conference*. Minneapolis, MN, USA, p.7, June 14-16. Available at: https://doi.org/10.1109/ACC.2006.1656579.

Gonzalez, R., Fiacchini, M., Alamo, T., Guzman, J.L. & Rodriguez, F. 2010. Adaptive Control for a Mobile Robot Under Slip Conditions Using an LMI-Based Approach. *European Journal of Control*, 16(2), pp. 144–155. Available at: https://doi.org/10.3166/ejc.16.144-155.

Herbst, G. & Madonski, R. 2023. Tuning and implementation variants of discrete-time ADRC. *Control Theory and Technology*, 21, pp. 72–88. Available at: https://doi.org/10.1007/s11768-023-00127-0.

Hiramatsu, T., Morita, S., Pencelli, M., Niccolini, M., Ragaglia, M. & Argiolas, A. 2019. Path-Tracking Controller for Tracked Mobile Robot on Rough Terrain. *International Journal of Electrical and Computer Engineering*, 13(2), pp. 59–64. Available at: https://doi.org/10.5281/zenodo.2571922.

Hong, S., Choi, J.S., Kim, H.W., Won, M.C., Shin, S.C., Rhee, J.S. & Park, H.u. 2009. A path tracking control algorithm for underwater mining vehicles. *Journal of Mechanical Science and Technology*, 23(8), pp. 2030–2037.

Hu, J., Tao, J., Zhao, W. & Han, Y. 2019. Modeling and simulation of steering control strategy for dual-motor coupling drive tracked vehicle. *Journal of the Brazilian Society of Mechanical Sciences and Engineering*, 41, art.number:190. Available at: https://doi.org/10.1007/s40430-019-1692-0.

Huang, H., Zhai, L. & Wang, Z. 2018a. A Power Coupling System for Electric Tracked Vehicles during High-Speed Steering with Optimization-Based Torque Distribution Control. *Energies*, 11(6), art.number:1538. Available at: https://doi.org/10.3390/en11061538.

Huang, P., Zhang, Z., Luo, X., Zhang, J. & Huang, P. 2018b. Path Tracking Control of a Differential-Drive Tracked Robot Based on Look-ahead Distance. *IFAC-PapersOnLine*, 51(17), pp. 112–117. Available at: https://doi.org/10.1016/j.ifacol.2018.08.072.

Janarthanan, B., Padmanabhan, C. & Sujatha, C. 2012. Longitudinal dynamics of a tracked vehicle: Simulation and experiment. *Journal of Terramechanics*, 49(2), pp. 63–72. Available at: https://doi.org/10.1016/j.jterra.2011.11.001.

Łakomy, K., Patelski, R. & Pazderski, D. 2020. ESO Architectures in the Trajectory Tracking ADR Controller for a Mechanical System: A Comparison. In: *Bartoszewicz, A., Kabziński, J. & Kacprzyk, J. (Eds.) Advanced, Contemporary Control*. 1196, pp.1323–1335. Cham: Springer. Available at: https://doi.org/10.1007/978-3-030-50936-1_110.

Li, Y., Yu, J., Guo, X. & Sun, J. 2020. Path Tracking Method Of Unmanned Agricultural Vehicle Based On Compound Fuzzy Control. In: *IEEE 9th Joint International Information Technology and Artificial Intelligence Conference (ITAIC)*. Chongqing, China, pp.1301-1305, December 11-13. Available at: https://doi.org/10.1109/ITAIC49862.2020.9338981.

Lu, H., Xiong, G. & Guo, K. 2016. Motion Predicting of Autonomous Tracked Vehicles with Online Slip Model Identification. *Mathematical Problems in Engineering*, 2016(1), art.number:6375652. Available at: https://doi.org/10.1155/2016/6375652.

Miklosovic, R., Radke, A. & Gao, Z. 2006. Discrete implementation and generalization of the extended state observer. In: *2006 American Control Conference*. Minneapolis, MN, USA, p.6, June 14-16. Available at: https://doi.org/10.1109/ACC.2006.1656547.

Mitsuhashi, T., Chida, Y. & Tanemura, M. 2019. Autonomous Travel of Lettuce Harvester using Model Predictive Control. *IFAC-PapersOnLine*, 52(30), pp. 155–160. Available at: https://doi.org/10.1016/j.ifacol.2019.12.514.

Nonami, K., Kartidjo, M., Yoon, K.J. & Budiyono, A. 2013. *Autonomous Control Systems and Vehicles, Intelligent Unmanned Systems*. Tokyo: Springer. Available at: https://doi.org/10.1007/978-4-431-54276-6.

Pentzer, J., Brennan, S. & Reichard, K. 2014. Model-based Prediction of Skidsteer Robot Kinematics Using Online Estimation of Track Instantaneous Centers of Rotation. *Journal of Field Robotics*, 31(3), pp. 455–476. Available at: https://doi.org/10.1002/rob.21509.

Sabiha, A.D., Kamel, M.A., Said, E. & Hussein, W.M. 2022. ROS-based trajectory tracking control for autonomous tracked vehicle using optimized backstepping and sliding mode control. *Robotics and Autonomous Systems*, 152, art.number:104058. Available at: https://doi.org/10.1016/j.robot.2022.104058.

Tang, Z., Liu, H., Zhao, Z., Lu, J., Guan, H. & Chen, H. 2021. Trajectory tracking of unmanned tracked vehicle based on model-free algorithm for off-road driving conditions. In: *2021 IEEE International Conference on Unmanned Systems (ICUS)*. Beijing, China, pp.870-877, October 15-17. Available at: https://doi.org/10.1109/ICUS52573.2021.9641176.

Tao, J., Liu, H., Li, Y., Guan, H., Liu, J. & Chen, H. 2021. Design of Trajectory Tracking Controller of Unmanned Tracked Vehicles Based on Torque Control. In: *2021 IEEE International Conference on Unmanned Systems (ICUS)*. Beijing, China, pp.85-92, October 15-17. Available at: https://doi.org/10.1109/ICUS52573.2021.9641159.

Wong, J.Y. 2022. *Theory of Ground Vehicles, 5th Edition*. Hoboken, NJ, USA: John Wiley & Sons. ISBN: 978-1-119-71970-0.

Zhang, X., Zhang, X., Xue, W. & Xin, B. 2021. An overview on recent progress of extended state observers for uncertain systems: Methods, theory, and applications. *Advanced Control for Applications: Engineering and Industrial Systems*, 3(2), e89. Available at: https://doi.org/10.1002/adc2.89.

Zou, T., Angeles, J. & Hassani, F. 2018. Dynamic modeling and trajectory tracking control of unmanned tracked vehicles. *Robotics and Autonomous Systems*, 110, pp. 102–111. Available at: https://doi.org/10.1016/j.robot.2018.09.008.

Diseño sistemático de la trayectoria de un vehículo de orugas no tripulado basado en ADRC seguimiento con validación FPGA-en-el-bucle

Momir R. Stanković[a], **autor de correspondencia**,
Rafal Madonski[b], *Stojadin* M. Manojlović[a]

[a] Universidad de Defensa de Belgrado, Academia Militar,
 Belgrado, República de Serbia

[b] Universidad Tecnológica de Silesia, Facultad de Control Automático,
 Electrónica e Informática, Gliwice, República de Polonia

CAMPO: control automático, ingeniería de control,
 robótica móvil

TIPO DE ARTÍCULO: artículo científico original

Resumen:

Introducción/objetivo: El problema del control de seguimiento de trayectoria en un vehículo de orugas no tripulado (UTV) representa una tarea desafiante, debido a la dinámica de deslizamiento desconocida e inmensurable que inevitablemente existe durante el movimiento. Por lo tanto, la aplicación de esquemas de control industrial estándar suele ser limitada.

Métodos: En este artículo, se propone un esquema de control activo de rechazo de perturbaciones (ADRC) para los canales de control longitudinal (control de velocidad longitudinal del vehículo) y canales de control lateral (control del ángulo de trayectoria del vehículo) del UTV para manejar colectivamente todas las incertidumbres del modelado de la planta y las perturbaciones de deslizamiento actuantes.

Resultados: Se presenta un procedimiento paso a paso para aplicar el algoritmo ADRC para el caso específico de seguimiento de trayectoria de UTV. Incluye diseño sistemático, discretización, así como análisis y validación del rendimiento utilizando simulaciones FPGA-en-el-bucle (FIL).

Conclusión: El método de validación basado en FIL propuesto reduce la brecha entre el diseño de simulación pura (que puede estar demasiado idealizado) y la implementación en el vehículo real (que puede llevar mucho tiempo). Los resultados experimentales obtenidos muestran las ventajas de la estructura de control propuesta sobre los controladores PI/PID industriales.

Проектирование движения беспилотной гусеничной машины по заданной траектории на основе контроллера ADRC и моделирования

Момир Р. Станкович[a], **корресподент**,
Рафал Мадонски[б], *Стоядин* М. Манойлович[a]

[a] Универстет обороны в Белграде, Военная академя,
 г. Белград, Республика Сербия

[б] Силезский технологический университет, Факультет
 автоматического управления, электроники и вычислительной
 техники, г. Гливице, Республика Польша

РУБРИКА ГРНТИ: 50.43.00 Системы автоматического
                        управления, регулирования и
                        контроля
ВИД СТАТЬИ: оригинальная научная статья

Резюме:

Введение/цель: Разработка системы автономного слежения за заданной траекторией беспилотной гусеничной машины является сложной задачей из-за неизвестной и неизмеримой динамики скольжения. Поэтому применение стандартных алгоритмов промышленного управления зачастую ограничено.

Методы: В данной статье представлена схема активного управления подавлением помех (ADRC) для продольного (управление продольной скоростью транспортного средства) и бокового (управление углом наклона транспортного средства) каналов управления UTV, позволяющая в совокупности справляться со всеми неопределенностями, связанными с моделированием установки и действующими возмущениями при скольжении.

Результаты: В статье представлена пошаговая процедура применения алгоритма ADRC для конкретного случая отслеживания траектории беспилотной гусеничной машины.

Процедура включает: систематическое проектирование, дискретизацию, а также анализ производительности и валидацию с использованием моделирования FPGA-in-the-loop (FIL).

Выводы: Предлагаемый метод проверки на основе встроенного моделирования FIL сокращает разрыв между имитационным проектированием (которое может быть слишком идеализированным) и реализацией на реальном транспортном средстве (что может занять много времени). Полученные экспериментальные результаты демонстрируют преимущества предложенной системы управления по сравнению со стандартными промышленными контроллерами в различных условиях эксплуатации беспилотной гусеничной машины.

Ключевые слова: беспилотные гусеничные машины, отслеживание траектории, активное управление подавлением помех, регулирование скорости, PID-контроллер, моделирование FIL, валидация аппаратного обеспечения.

Пројектовање кретања беспосадног гусеничног возила по задатој путањи на основу ADRC регулатора и FIL симулација

Момир Р. Станковић[а], **аутор за преписку**,
Рафал Мадонски[б], *Стојадин* М. Манојловић[в]

[а] Универзитет одбране у Београду, Војна академија,
   Београд, Република Србија

[б] Шлески технолошки универзитет,
   Факултет за аутоматско управљање, електронику и рачунарство,
   Гливице, Република Пољска

ОБЛАСТ: аутоматско управљање, рачунарске науке, роботика
КАТЕГОРИЈА (ТИП) ЧЛАНКА: оригинални научни рад

Сажетак:

Увод/циљ: Пројектовање система аутономног праћења задате трајекторије беспосадног гусеничног возила представља сложен задатак због постојања непознате и немерљиве динамике проклизавања. Стога је примена стандардних индустријских управљачких алгоритама често ограничена.

Методе: Предложена је примена регулатора на осно-ву управљања са активним потискивањем поремећаја (ADRC), посебно пројектованих за лонгитудинални и ла-терални канал управљања возила. Примена наведеног ал-горитма омогућила је високе перформансе управљања у условима постојања нестационарности модела објекта управљања и утицаја поремећаја проклизавања.

Резултати: Представљена је детаљна процедура приме-не ADRC алгоритма за праћење задате путање беспосад-ног гусеничног возила, која је обухватила пројектовање, дискретизацију, симулациону анализу перформанси и екс-периманталну верификацију на основу симулација са FP-GA хардвером у петљи управљања (FIL симулације).

Закључак: Предложена методологија валидације пројекто-ваног система управљања на основу FIL симулација омо-гућила је смањење пројектантског времена између чисто рачунарских симулација (које су најчешће сувише идеализо-ване) и експерименталних верификација на реалном систе-му. Добијени резултати су показали предности предложе-ног решења у односу на стандардне индустријске регула-торе у различитим условима употребе беспосадног гусе-ничног возила.

Кључне речи: беспосадно гусенично возило, праћење пу-тање, управљање са активним потискивањем поремећаја (ADRC), управљање брзином, PID регулатор, FIL симулаци-ја, хардверска валидација.

1724

Paper received on: 22.03.2024.
Manuscript corrections submitted on: 16.11.2024.
Paper accepted for publishing on: 18.11.2024.

1725

Effect of some parameters on the separation process of a saboted bullet

Xuan Son Bui[a], *Quang Tuan* Nguyen[b], *Hai Minh* Nguyen[c]

Le Quy Don Technical University, Faculty of Special Equipment, Hanoi, Socialist Republic of Vietnam

[a] e-mail: buixuanson.mta@gmail.com,
 ORCID iD: https://orcid.org/0000-0003-4520-5168

[b] e-mail: tuannguyenmta28@gmail.com, **corresponding author**,
 ORCID iD: https://orcid.org/0000-0002-7741-8232

[c] e-mail: nguyenhaiminhtb2013@gmail.com,
 ORCID iD: https://orcid.org/0000-0002-5170-6228

Abstract:

Introduction/purpose: In this paper, the influence of muzzle velocity and the initial friction between the sabot and the penetrator of a sub-caliber bullet on the separation process was investigated. A special armor-piercing bullet was chosen as a research object.

Methods: A hybrid approach was applied in the study to solve the set tasks. In the first place, the equation system describing the motion of the sabot and the penetrator was established analytically. The aerodynamic drags acting on the sabot and the penetrator were then obtained numerically using CFD methods. Eventually, the equations of motion of the sabot and the penetrator were solved using the Runge-Kutta method to analyze the effect of the bullet muzzle velocity and the initial friction of the sabot and the penetrator on the separation process.

Results: The research results have shown the significant influence of the bullet muzzle velocity and the initial friction on the parameters of the sabot and the penetrator at the very moment they completely separate from each other. Based on the obtained data, weapon designers can appropriately select the ballistic and structural parameters for the bullet.

Conclusion: The hybrid approach presented in this paper is effective in studying the separation process of armor-piercing saboted bullets. The research results are useful contributions to the field of sub-caliber ammunition. The presented method can be applied in the design process of armor-piercing saboted projectiles of different calibers.

Key words: sabot separation, sub-caliber bullets, Ansys Fluent, CFD, numerical simulation.

Introduction

In the ongoing armed conflicts around the world today, soldiers are better protected on the battlefield. Ballistic vests are constantly improved to resist different types of bullets and projectiles. For instance, the Russian army has equipped its soldiers with RATNIK-3 smart suits (Dada et al, 2022). The Interceptor Body Armor (IBA) is widely used by soldiers in the US armed forces (Lestari et al, 2022). The increasing effectiveness of modern body armor poses an urgent need for weapon designers to find solutions to improve the penetration performance of bullets and projectiles. There are several solutions proposed to achieve this goal, such as increasing the muzzle kinetic energy of bullets, using bullets with cores made of heavy materials like tungsten carbide, depleted uranium, using discarding sabot, etc. Among them, the spin-stabilized sabot structure is a very promising direction. The most notable bullets which use this principle include Singaporean 12.7mm SLAP (Starek & Stepniak, 2021) and Swedish 6.5x25mm CBJ (CBJ Tech, 2024). Unlike standard bullets, this type of bullets has a number of different operating characteristics. The bullet is composed of a penetrator made of tungsten carbide or depleted uranium, a polymer sabot and an aluminum support. After exiting the barrel, under the effect of centrifugal force, the sabot deforms, its petals open to increase the area surface exposed to the air. The aerodynamic drag acting on the sabot is very large compared to the aerodynamic drag acting on the penetrator. As a result, the penetrator moves faster than the sabot and gradually separates from the sabot and continues to move towards the target alone as illustrated in Figure 1.
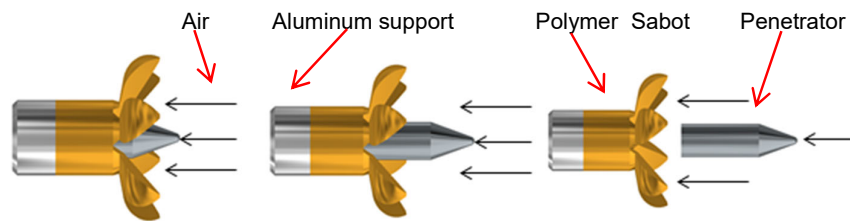
Figure 1 – Sabot separation process

Currently, although there is a large number of studies dedicated to the separation process of armour-piercing fin-stabilized discarding sabots (Lesage & Girard, 1996; Lin & Lai, 1997; Huang et al, 2014; Mohanan & Rajesh, 2020), there are very few studies on the sabot separation process of spin-stabilized sub-caliber projectiles. In a recent paper (Bui et al, 2024), the authors studied the separation process of a sub-caliber bullet with an

aluminum sabot. Research results show that, for this structure, the difference between the aerodynamic drag acting on the sabot and the aerodynamic drag acting on the penetrator is not large; consequently, the range of the maximum allowable initial friction between the sabot and the penetrator is limited in a narrow interval. In this regard, the bullets with polymer sabots, like Swedish 6.5x25mm CBJ, have advantage over the bullets with aluminum sabots, as the aerodynamic drag acting on the deformed polymer sabot is much larger than the aerodynamic drag acting on the aluminum sabot. In our previous work (Nguyen et al, 2024), we investigated the supersonic flow around this kind of bullets. As a logical continuation of the recently mentioned studies, the main purpose of this paper is to investigate the influence of some parameters such as the initial friction between the sabot and the penetrator, as well as the influence of the bullet muzzle velocity on the separation process, namely, on the penetrator velocity at the separation moment and on the separation distance (distance from the gun muzzle to the position where the penetrator completely separates from the sabot) for this sub-caliber bullet. The method and research results presented in this study can be effectively adopted in the process of designing saboted bullets, particularly those with the structure like the structure of the Swedish 6.5x25mm CBJ bullet.

Materials and methods

Equations of motion for the sabot and the penetrator

The equations of motion for the sabot and the penetrator will be established based on the following assumptions: the gravity is negligible; the bullet moves with a zero angle of attack; the bullet rotational and translational motions are independent of each other; the opening angle of the sabot petals remain constant during the separation process. Consequently, the forces acting on the sabot and the penetrator are aerodynamic drags and friction.

The motion of the sabot and the penetrator is considered as the motion of two material points O_s and O_p respectively; here, O_s is the center of the cross section of the sabot bottom surface, and O_p is the center of the cross section of the penetrator aft surface, as shown in Figure 2.

The origin O of the coordinate system is the centre of the cross section of the penetrator aft surface at the very moment when the bullet exits the barrel. One can easily notice that, when the bullet leaves the gun muzzle, three points O, O_s and O_p are at the same position. The positive direction of the coordinate axis is the same as of the bullet muzzle velocity vector as illustrated in Figure 3.

1728

It is easy to derive the equations of motion for the sabot and the penetrator as follows (Bui et al, 2024):

$$\dot{v}_s = \frac{-F_{ds} + F_{fr}}{m_s},$$ (1)

$$\dot{x}_s = v_s,$$ (2)

$$\dot{v}_p = \frac{-F_{dp} - F_{fr}}{m_p},$$ (3)

$$\dot{x}_p = v_p,$$ (4)

Here, v_s is the sabot velocity; x_s is the sabot coordinate; m_s is the sabot mass; v_p is the penetrator velocity; x_p is the penetrator coordinate; m_p is the penetrator mass; F_{ds} is the aerodynamic drag acting on the sabot; F_{dp} is the aerodynamic drag acting on the penetrator; and F_{fr} is the friction force between the sabot and the penetrator.
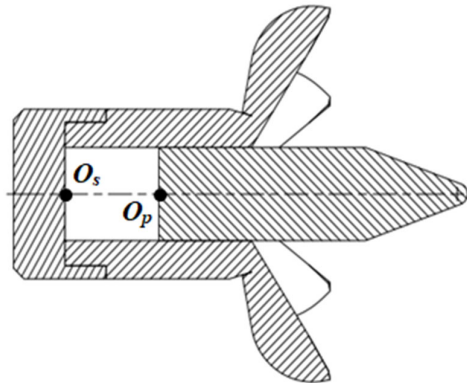
Figure 2 – Material points **O_s** and **O_p**
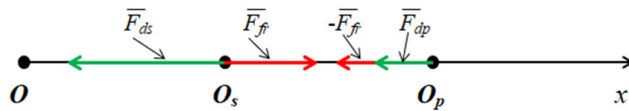
Figure 3 – Forces acting on the sabot (**O_s**) and the penetrator (**O_p**)

The initial conditions are as follows:

$$v_{s0} = v_{p0} = v_0; \, x_{s0} = x_{p0} = 0. \tag{5}$$

Here, v_{s0} is the sabot initial velocity; v_{p0} is the penetrator initial velocity; v_0 is the bullet muzzle velocity; x_{s0} is the sabot initial coordinate; and x_{p0} is the penetrator initial coordinate.

The friction force between the sabot and the penetrator can be determined as follows:

$$F_{fr} = f_{fr} \, p S \,. \tag{6}$$

Here f_{fr} is the friction coefficient between the sabot and the penetrator; p is the specific pressure acting on the contact surface between the sabot and the penetrator, and S is the contact surface area between the sabot and the penetrator. The parameter S can be determined through the following formula:

$$S = \pi d_p l \,, \tag{7}$$

where d_p is the penetrator diameter and l is the length of the longitudinal contact between the sabot and the penetrator as shown in Figure 4.
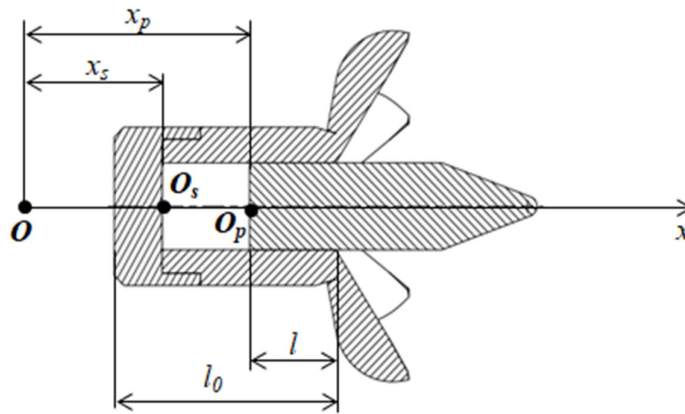
Figure 4 – Length of the longitudinal contact between the sabot and the penetrator

The parameter l can be defined through the following expression:

$$l = l_0 - (x_p - x_s) \,, \tag{8}$$

where l_0 is the initial length of longitudinal contact between the penetrator and the sabot. The penetrator is considered completely separated from the sabot when there is no mechanical contact between them, which means $l = 0$.

Substituting (7) into (6) gives:

$$F_{fr} = f_{fr} \, p \pi d_p l = f_{fr} \, p \pi d_p l_0 \times \frac{l}{l_0}.$$ (9)

Naming $F_{fr0} = f_{fr} \, p \pi d_p l_0$, it is obvious that F_{fr0} is the initial friction between the sabot and the penetrator when the bullet just exits the muzzle. As a result, formula (6) can be rewritten in the following way:

$$F_{fr} = f_{fr} \, p \pi d_p l = F_{fr0} \times \frac{l}{l_0}.$$ (10)

It is easy to notice that the friction between the sabot and the penetrator at that moment linearly depends on their initial friction.

Solution method

The system of equations (1), (2), (3), (4), (8), (10) in conjunction with the initial condition (5) can be integrated if the aerodynamic drags F_{ds} and F_{dp} are known at any time step. The following method is proposed to determine these drags. First step - the aerodynamic drags will be obtained numerically at certain discrete points using CFD methods. Next, F_{ds} and F_{dp} will be approximated using the numerical method. With the sabot and the penetrator of fixed dimensions, the aerodynamic drags acting on the sabot and the penetrator are only dependent on their velocities and relative positions, which means they can be presented as follows:

$$F_{ds} = F_{ds}(v_s, l), \quad F_{dp} = F_{dp}(v_p, l).$$ (11)

Hence, using the CFD method, for instance, performing simulation on the Ansys Fluent software package, one can obtain F_{ds} and F_{dp} at certain discrete points. Then the bilinear interpolation method can be applied to approximate the value of aerodynamic drags at any given point of velocity and relative position (v, l). Finally, the equation system will be solved using, for instance, the fourth order Runge-Kutta method.

Determination of the aerodynamic drags

In order to obtain the aerodynamic drags acting on the sabot and the penetrator, Ansys Fluent software was utilized in this research. The simulation procedure has been introduced in numerous works (Jerković et al, 2016; Matsson, 2023; Ferfouri et al, 2023). The 3D models of the bullet were created in Inventor CAD software. For the purpose of simplification, the aluminum support and the polymer sabot were modeled as a unified object as shown in Figure 5. It is acceptable as they are connected together for the entire separation process. A simulation air domain was initiated with the size of 40L x 10L x 10L as presented in Figure 6; here *L* is the bullet length. A grid sensitivity study has indicated that, in our case,

for a 3D RANS simulation, the grid of about 4.45 million elements could provide sufficiently accurate results. The mesh around the bullet is presented in Figure 7. In our case, the aerodynamic drags acting on both the sabot and the penetrator are needed, so the exposed to the air surfaces of the penetrator and the sabot are named individually as shown in Figure 8. The turbulence model k-ε was used. The density-based solver was applied. The air was considered the ideal gas. The air viscosity model was the Sutherland model. Velocity, static pressure, and static temperature were set for the inlet flow. Static pressure was defined for the outlet flow. The Coupled algorithm was utilized in this study to ensure the simulation accuracy. The convergence criterion was set to 10-5.
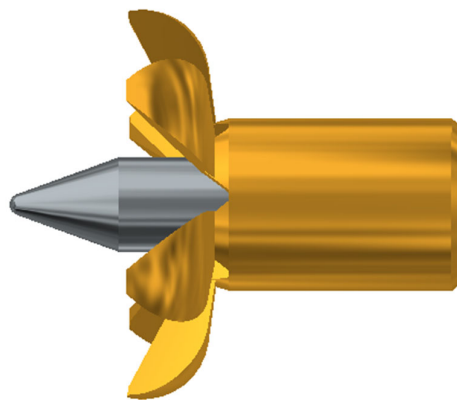
Figure 5 – 3D model of the bullet
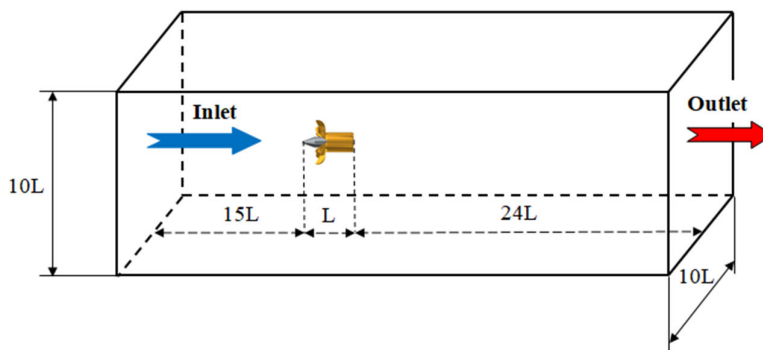
Figure 6 – Simulation air domain
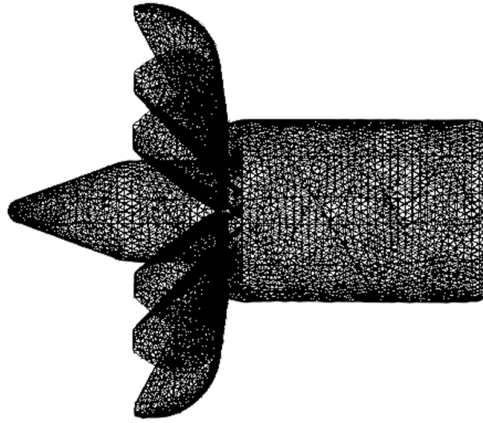
Figure 7 – Mesh around the bullet

a) Named section for the penetrator

b) Named section for the sabot
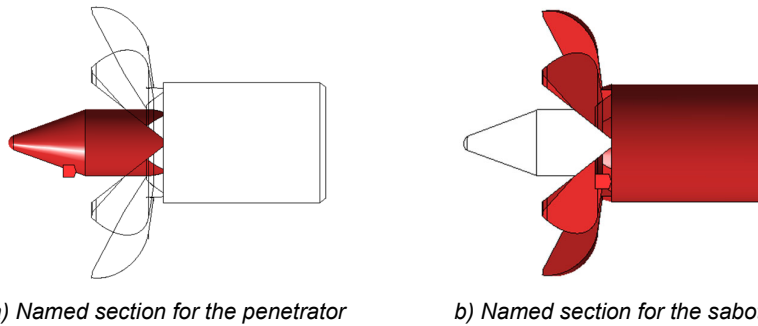
Figure 8 – Named sections for the penetrator (a) and the sabot (b)

Approximation of the aerodynamic drags

After the determination of the aerodynamic drags acting on the penetrator and the sabot at certain discrete points of velocity and their relative positions, the next step is to approximate them at any given time step based on their current velocity and relative position. To achieve this goal, the bilinear interpolation method was implemented. Assume that, using Ansys Fluent, the aerodynamic drag F has been determined at four given points $F_{11}(v_1, l_1)$, $F_{12}(v_1, l_2)$, $F_{21}(v_2, l_1)$, $F_{22}(v_2, l_2)$. According to the bilinear interpolation method (Kang, 2006), the value of drag $F(v, l)$, where $v_1 < v < v_2$ and $l_1 < l < l_2$, could be approximated as follows:

$$F(v,l) = F_{11} + (F_{21} - F_{11})\frac{v - v_1}{v_2 - v_1} + (F_{12} - F_{11})\frac{l - l_1}{l_2 - l_1} + (F_{22} - F_{12} - F_{21} + F_{11})\frac{(v - v_1)(l - l_1)}{(v_2 - v_1)(l_2 - l_1)}.$$

In general, after the approximation of the aerodynamic drags acting on the penetrator and the sabot, the equations of motion of the penetrator and the sabot can be integrated to analyze the separation process.

Results and discussion

Although sub-caliber bullets have some significant advantages over standard bullets in terms of impact velocity and ballistic performance, they require a proper separation process to ensure that the penetrator will function correctly during the next flight stage to the target. The sabot separation process of sub-caliber bullets is affected by multiple factors such as the bullet velocity, aerodynamics, the bullet structure and materials, etc. In this study, the influence of the bullet muzzle velocity and the initial friction between the sabot and the penetrator on the separation process, specifically, on the penetrator velocity at the separation moment and on the separation distance (the distance from the gun muzzle to the point where the penetrator loses mechanical contact with the sabot) will be investigated. The configuration of the penetrator, the aluminum support and the polymer sabot are presented in Figure 9, Figure 10 and Figure 11, respectively.
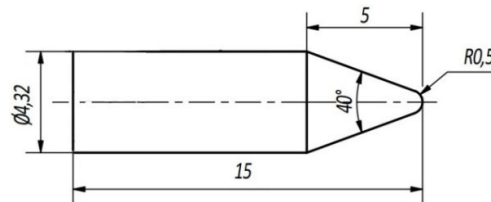
Figure 9 – Penetrator configuration (in mm)
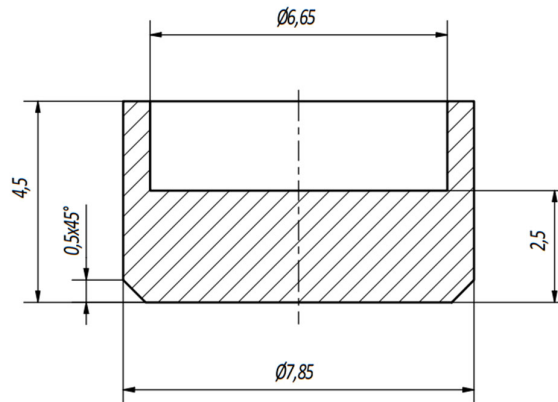
Figure 10 – Aluminum support configuration (in mm)
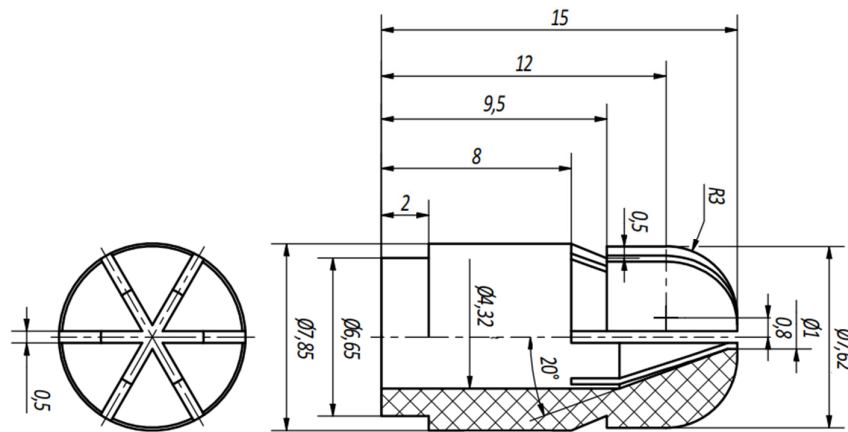
Figure 11 – Polymer sabot configuration (in mm)

In addition, the main parameters of the sabot and the penetrator are presented in Table 1.

Table 1 – Main parameters of the bullet

Parameter	Units	Notation	Value
Mass of the support and the sabot	kg	m_s	0.00079
Mass of the tungsten penetrator	kg	m_p	0.00274
Initial length of the longitudinal contact	m	l	0.008

Estimation of the maximum allowable initial friction

The bullet consists of three components: aluminum support, polymer sabot and tungsten carbide penetrator. To ensure the integrity of the bullet, there must be sufficient friction between the sabot and the penetrator. However, if the friction is too large, it can negatively affect the separation process. For instance, the penetrator may take too long to completely separate from the sabot, or in the worst-case scenario, the penetrator could not leave the sabot at all. Hence, an appropriate initial friction between the penetrator and the sabot must be selected to ensure a proper sabot separation.

For the penetrator to leave the sabot reliably, it has to maintain a velocity greater than the sabot velocity during the separation process, which means:

$$v_p > v_s .$$ (12)

Combining with (1) and (3), one obtains:

$$\int_0^t \frac{-F_{dp} - F_{fr}}{m_p} dt + v_{p0} > \int_0^t \frac{-F_{ds} + F_{fr}}{m_s} dt + v_{s0} \qquad (13)$$

Since $v_{p0} = v_{s0}$, expression (13) becoms:

$$\int_0^t \frac{-F_{dp} - F_{fr}}{m_p} dt > \int_0^t \frac{-F_{ds} + F_{fr}}{m_s} dt \qquad (14)$$

During the first small period of time immediately after the bullet exits the gun muzzle, the friction between the sabot and the penetrator as well as the aerodynamic drags acting on the sabot and the penetrator change very little and can be considered constant. Then (14) becomes:

$$\frac{-F_{dp0} - F_{fr0}}{m_p} > \frac{-F_{ds0} + F_{fr0}}{m_s} \qquad (15)$$

where F_{dp0}, F_{ds0}, respectively, are the initial aerodynamic drags acting on the penetrator and the sabot when the bullet just leaves the gun barrel. After performing some simple algebraic transformations to (15), one obtained the following relationship:

$$F_{fr0} < \frac{m_p F_{ds0} - m_s F_{dp0}}{m_p + m_s} \qquad (16)$$

Formula (16) is the necessary condition for the initial friction between the sabot and the penetrator to ensure that the penetrator can separate from the sabot. It is easy to see that the maximum allowable friction is greater if the mass of the penetrator and the initial aerodynamic drag acting on the sabot are greater, and vice versa, when the mass of the sabot and the aerodynamic drag acting on the penetrator are smaller. Relationship (16) helps designers determine the maximum allowable initial friction between the sabot and the penetrator to ensure that the sabot separation process can occur.

Based on formula (16), the maximum allowable initial friction between the sabot and the penetrator was determined for the bullet muzzle velocity ranging from 600 m/s to 700 m/s with the increments of 20 m/s. The effect of the bullet muzzle velocity on the maximum allowable initial friction is shown in Figure 12.
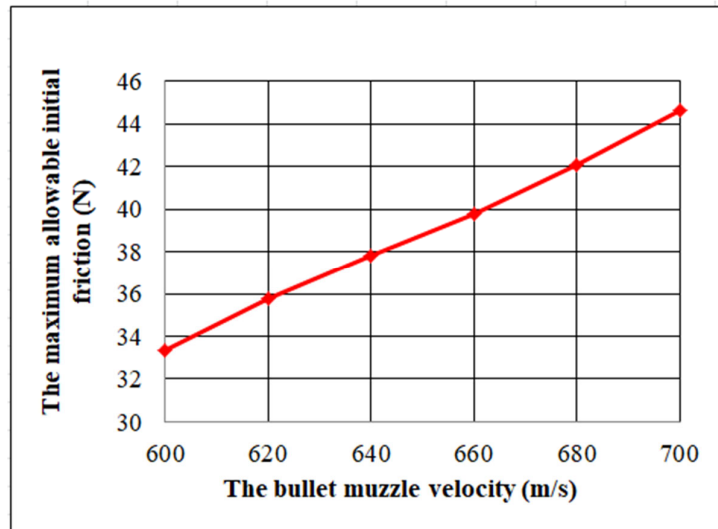
Figure 12 – Effect of the bullet muzzle velocity on the maximum allowable initial friction between the sabot and the penetrator

Clearly, the greater bullet muzzle velocity, the greater maximum allowable initial friction. The dependence of the maximum allowable initial friction on the bullet muzzle velocity is almost linear.The maximum allowable initial friction increases from 33.3 N to 44.6 N when the bullet muzzle velocity changes from 600 m/s to 700 m/s.

Influence of the initial friction

As mentioned before, the initial friction between the sabot and the penetrator is an important parameter, effecting not only the functinality but also the separation process of sub-caliber bullets. Based on the presented hybrid approach, the influence of the initial friction on the separation process was carried out for the bullet muzzle velocity of 640 m/s, 660 m/s, 680 m/s and 700 m/s. The initial friction varied from 5 N to 37 N with the increments of 5 N. The effect of the initial friction on the separation distance is presented in Figure 13.

Obviousy, the greater the initial friction, the greater the separation distance. Moreover, the dependence of the separation distance on the initial friction has a similar trend for all values of the bullet muzzle velocity. The separation distance increases quickly when the initial friction

increases, especially for lower bullet muzzle velocity. At small initial friction, the separation distance is almost the same for every muzzle velocity, but at greater initial friction, the separation distance greatly differs with different muzzle velocities.
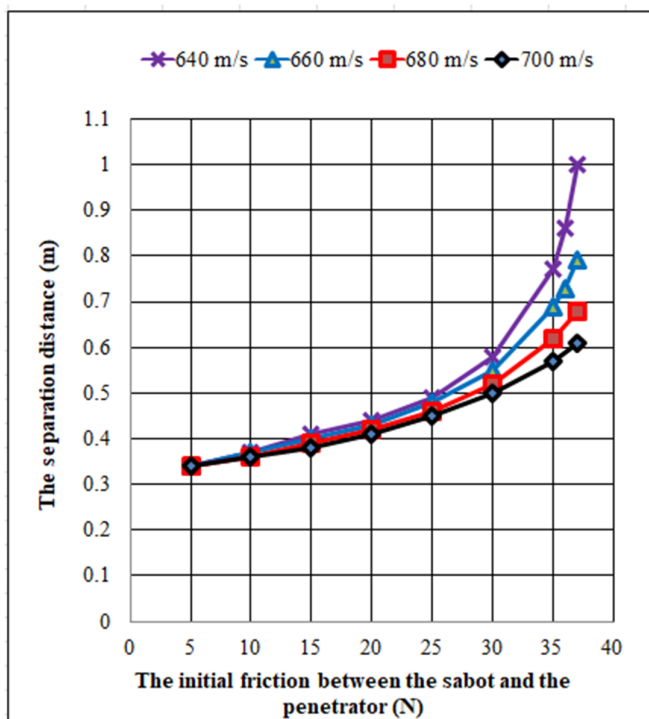
Figure 13 – Effect of the initial friction between the sabot and the penetrator on the separation distance

The dependence of the penetrator velocity at the separation moment on the initial friction is shown in Figure 14. Clearly, if the initial friction increases, the penetrator velocity at the separation moment decreases due to aerodynamic loss. For a given muzzle velocity, the greater initial friction, the higher penetrator velocity loss at the separation moment.

The influence of the initial friction on the penetrator velocity at the separation moment is practically identical for different muzzle velocities.
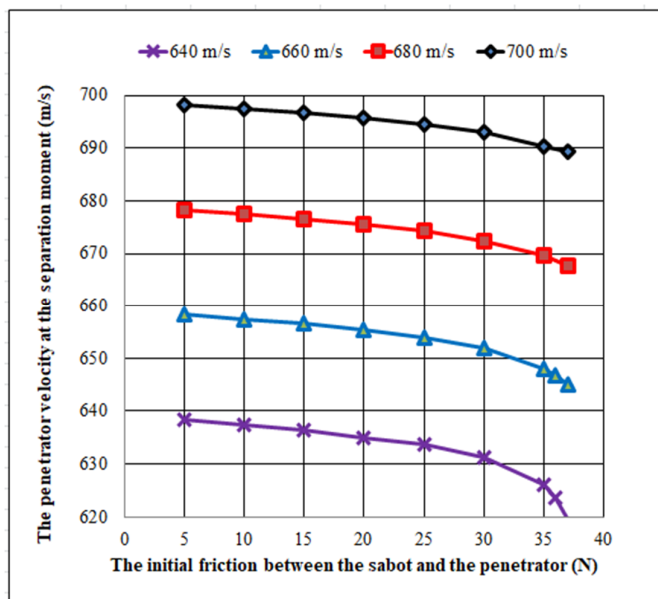
Figure 14 – Effect of the initial friction on the penetrator velocity at the separation moment

Influence of the bullet muzzle velocity

The bullet muzzle velocity plays a crucial role in ammunition design practice. It affects the trajectory, flight stability and ballistic performance of the bullet. A consistent muzzle velocity leads to more predictable flight paths, which is very important for accuracy, especially over longer distances. Changes in the bullet muzzle velocity can result in differing points of impact, affecting precision. Higher muzzle velocities generally lead to greater kinetic energy and better penetration. Higher muzzle velocities also help keep the bullet's stability and speed over longer distances, lowering the effects of gravity and wind drift. However, besides these advantages, higher muzzle velocities also could result in several negative effects. First of all, high velocities can accelerate wear on the gun barrel, due to increased heat and pressure. This can reduce the longevity of the weapon and potentially lead to more frequent maintenance or even structural damage over time. Higher muzzle velocities generally lead to increased recoil. This recoil can be uncomfortable for soilders, affecting their ability to maintain accuracy and control during firing. Consequently, it is necessary to select appropriate muzzle velocities to solve a concrete given task.

In this paper, the equations of motion of the sabot and the penetrator were solved for the bullet muzzle velocity of 640 m/s, 660 m/s, 680 m/s and 700 m/s at various values of initial friction ranging from 20 N to 37 N with icrements of 5 N. The influence of the bullet muzzle velocity on the separation distance and the penetrator velocity at the separation moment is presented in Figure 15 and Figure 16.
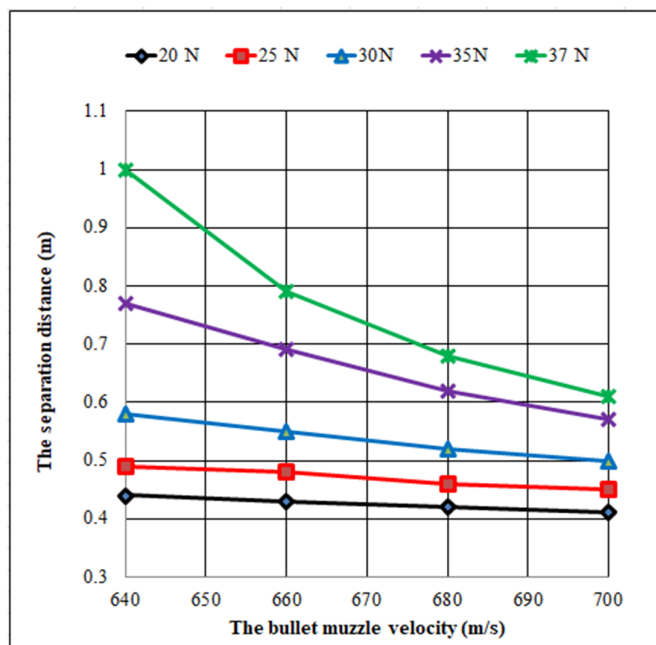
Figure 15 – Effect of the bullet muzzle velocity on the separation distance

It is apparent that the separation distance decreases with the increase of muzzle velocity. Moreover, a clear trend can be observed that, the greater initial friction, the more significant influence the muzzle velocity has on the separation distance. At the initial friction of 20 N, the separation distance only changes slightly when the muzzle velocity increases from 640 m/s to 700 ms. But at the initial friction of 37 N, the separation distance changes significantly with the change of muzzle velocity.

The effect of the muzzle velocity on the penetrator velocity at the separation moment has nearly identical and linear characteristics for different values of initial friction.
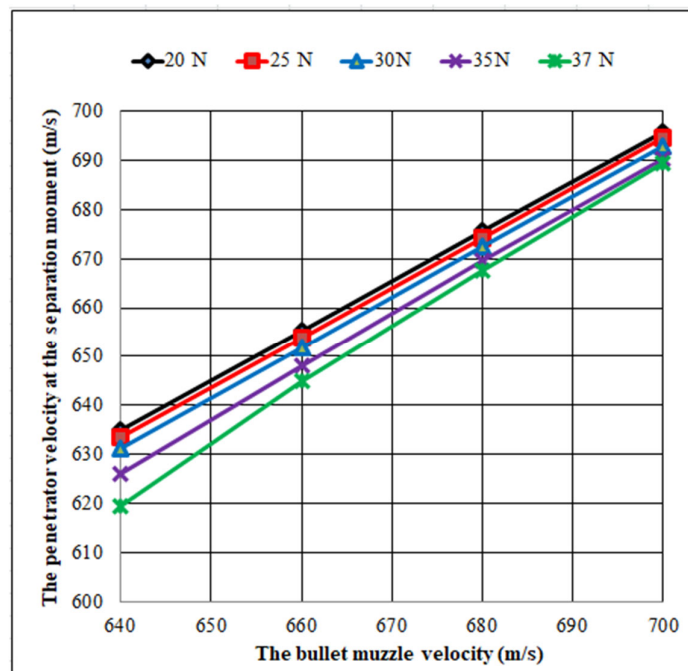
Figure 16 – Effect of the muzzle velocity on the penetrator velocity at the separation moment

Conclusion

In this study, the effect of the muzzle velocity and the initial friction between the sabot and the penetrator of a special armor-piercing sub-caliber bullet on its separation process was investigated using a hybrid approach of analytical and numerical methods. The following conclusions can be deduced from the research:

The bullet muzzle velocity significantly affects the separation process. Namely, the greater muzzle velocity, the higher maximum allowable initial friction between the sabot and the penetrator. Additionally, when the muzzle velocity increases, the separation distance decreases significantly.

The initial friction between the sabot and the penetrator has a significant impact on the separation process. Specifically, when the initial friction increases, the separation distance also quickly increases and the penetrator velocity at the separation moment drops notably. This trending influence especially becomes more apparent as the initial friction gradually approaches its maximum allowable value.

The results obtained in this work can be used for selecting suitable values of muzzle velocity and initial friction between the sabot and the penetrator in the process of designing sub-caliber bullets of the studied or similar structures.

References

Bui, X.S., Nguyen, Q.T., Nguyen, H.M. & Doan, V.D. 2024. Theoretical study on the sabot separation process of a sub-caliber projectile fired from rifled guns. *Defense and Security Studies*, 5, pp.29-45. Available at: https://doi.org/10.37868/dss.v5.id264.

-CBJ Tech. 2024. *6.5x25 CBJ APDS Tungsten core inside a discarding sabot. Cbjtech.com* [online]. Available at: https://www.cbjtech.com/ammunition/6-5x25-cbj/6-5x25-cbj-apds/ [Accessed: 10 July 2024].

Dada, K.S., Akila, J., Suleiman, U.O. & Akinbinu, A. 2022. Adoption and deployment of 21st century technologies in armed forces operations. *Journal of Advances in Military Studies*, 5(1), pp.95-107. Available at: https://doi.org/10.37944/jams.v5i1.135.

Ferfouri, A., Allouche, T., Jerković, D.D., Hristov, N., Vučković, M. & Benmeddah, A. 2023. Prediction of drag aerodynamic coefficient of the 155 mm projectile under axisymmetric flow using different approaches. *Journal of the Serbian Society for Computational Mechanics*, 17(2), pp.69-86. Available at: https://doi.org/10.24874/jsscm.2023.17.02.06.

Huang, Z.-g., Wessam, M.E. & Chen, Z.-h. 2014. Numerical investigation of the three-dimensional dynamic process of sabot discard. *Journal of Mechanical Science and Technology*, 28, pp.2637-2649. Available at: https://doi.org/10.1007/s12206-014-0620-6.

Jerković, D., Kari, A., Hristov, N., Ilić, S. & Savić, S. 2016. Numerical and experimental investigation of aerodynamic characteristics of spin stabilized projectile. In: *7th International Scientific Conference on Defensive Technologies OTEH 2016*, Belgrade, Serbia, October 06-07 [online]. Available at: http://www.vti.mod.gov.rs/oteh16/elementi/rad/065.html [Accessed: 12 July 2024].

Kang, H.R. 2006. *Computational Color Tec*hnology. Society of Photo Optical. Available at: https://doi.org/10.1117/3.660835.

Lesage, F. & Girard, B. 1996. Wind tunnel and CFD investigation of aerodynamic interactions during sabot separation. In: *34th Aerospace Sciences Meeting and Exhibit*, Reno, NV, USA, January 15-18. Available at: https://doi.org/10.2514/6.1996-193.

Lestari, A., Melati, L.T., Kasim, K., Jupriyanto, J. & Deksino, G.R. 2022. Ceramic Armor as Protective Material in Defense Industry Product: A Literature Review. *Journal of Mechanical, Electrical and Industrial Engineering*, 5(1), pp.101-112. Available at: https://doi.org/10.46574/motivection.v5i1.175.

Lin, H. & Lai, C.-L. 1997. Systematic study and numerical simulation of sabot projectile aerodynamics. *Journal of the Chinese Institute of Engineers*, 20(3), pp.275-284. Available at: https://doi.org/10.1080/02533839.1997.9741831.

Matsson, J.E. 2023. *An Introduction to Ansys Fluent 2023*. Mission, KS, USA: SDC Publications. ISBN: 978-1-63057-648-6.

Mohanan, S. & Rajesh, G. 2020. Trajectory predictions of new lift separation sabots. *Defence Technology*, 17(4), pp.1361-1373. Available at: https://doi.org/10.1016/j.dt.2020.07.005.

Nguyen, Q.T., Nguyen, H.M. & Son, B.X. 2024. Numerical investigation on the supersonic flow around a saboted bullet. *Vojnotehnički glasnik/Military Technical Courier*, 72(2), pp.676-694. Available at: https://doi.org/10.5937/vojtehg72-48837.

Starek, W. & Stepniak, W. 2021. Analysis and evaluation of small arms and ammunition with the reference to known foreign developments. *Problemy Techniki Uzbrojenia/Issues of Armament Technology,* R.35, z.99 pp.65-89 [online]. Available at: https://yadda.icm.edu.pl/baztech/element/bwmeta1.element.baztech-article-PWAA-0025-0007 (in Polish) [Accessed: 10 July 2024].

El efecto de algunos parámetros en el proceso de separación de una bala sabot

Xuan Son Bui, *Quang Tuan* Nguyen*,* **autor de correspondencia**, *Hai Minh* Nguyen

Universidad Técnica Le Quy Don,
Facultad de Equipos Especiales,
Hanói, República Socialista de Vietnam

CAMPO: ingeniería mecánica, dinámica de fluidos, balística exterior.
TIPO DE ARTÍCULO: artículo científico original

Resumen:

Introducción/objetivo: En este artículo, se investigó la influencia de la velocidad de salida y la fricción inicial entre el sabot y el penetrador de una bala de sub-calibre en el proceso de separación. Como objeto de investigación se eligió una bala especial perforadora de armaduras.

Métodos: En el estudio se aplicó un enfoque híbrido para resolver las tareas planteadas. En primer lugar, se estableció analíticamente el sistema de ecuaciones que describe el movimiento del sabot y del penetrador. Las resistencias aerodinámicas que actúan sobre el sabot y el penetrador se obtuvieron numéricamente utilizando métodos CFD. Finalmente, las ecuaciones de movimiento del sabot y del penetrador se resolvieron utilizando el método de Runge-Kutta para analizar el efecto de la velocidad de salida de la bala y la fricción inicialdel sabot y el penetrador en el proceso de separación.

Resultados: Los resultados de la investigación han demostrado la influencia significativa de la velocidad de salida de la bala y la fricción inicial sobre los parámetros del sabot y del penetrador en el momento en que se separan completamente uno del otro. A partir de los datos obtenidos, los diseñadores de armas pueden seleccionar adecuadamente los parámetros balísticos y estructurales de la bala.

Conclusión: El enfoque híbrido presentado en este artículo es eficaz para estudiar el proceso de separación de balas sabot perforantes. Los resultados de la investigación son contribuciones significativas al campo de las municiones de subcalibre. El método presentado se puede aplicar en el proceso de diseño de proyectiles sabot perforantes de diferentes calibres.

Palabras claves: separación de sabot, balas de subcalibre, Ansys Fluent, CFD, simulación numérica.

Влияние некоторых параметров на процесс отделения сердечника от поддона подкалиберной пули

Суан Шон Буй, *Куанг Туан* Нгуен, **корреспондент**, *Хай Минь* Нгуен
Государственный технический университет им. Ле Куй Дона,
факультет специального машиностроения,
г. Ханой, Социалистическая Республика Вьетнам

Резюме:

Введение/цель: В данной работе исследовано влияние начальной скорости и начального трения между поддоном и сердечником подкалиберной пули на процесс их отделения. Предметом исследования была специальная бронебойная пуля.

Методы: Для решения поставленных задач был применен гибридный подход. Прежде всего аналитически была установлена система уравнений, описывающая движение поддона и сердечника. Аэродинамическое сопротивление, действующие на поддон и сердечник было получены численно с использованием методов CFD. В конечном итоге уравнения движения поддона и сердечника были решены с использованием метода Рунге-Кутты для анализа влияния начальной скорости пули и начального трения на процесс отделения.

Результаты: Результаты исследований показали существенное влияние начальной скорости пули и начального трения на параметры поддона и сердечника в момент их полного отделения друг от друга. На основе полученных данных

конструкторы оружия могут соответствующим образом подобрать баллистические и конструктивные параметры пули.

Выводы: Представленный в статье гибридный подход эффективен в изучении процесса отделения сердечника от поддона подкалиберной пули. Результаты исследований являются полезным вкладом в область подкалиберных боеприпасов. Представленный метод может быть применен в процессе проектирования бронебойных подкалиберных снарядов различного калибра.

Ключевые слова: отделение подкалибра, подкалиберные пули, Ansys Fluent, CFD, численное моделирование.

Утицај неких параметара на процес одвајања поткалибарног пројектила са одвојивим носачем (саботом)

Суан Сон Буи, *Кван Туан* Нуиен, **аутор за преписку,** *Хаи Мин* Нуиен

Државни технички универзитет „Ле Куи Дон",
Факултет специјалног машинства,
Ханој, Социјалистичка Република Вијетнам

Сажетак:

Увод/циљ: У овом раду истражен је утицај брзине пројектила на устима цеви и почетног трења између носача (сабота) и пенетратора поткалибарног пројектила на процес раздвајања. За објекат истраживања изабран је специјални панцирни пројектил.

Методе: За решавање постављених задатака у студији је примењен хибридни приступ. На почетку, аналитички је успостављен систем једначина који описује кретање сабота и пенетратора. Затим је аеродинамички отпор који делује на носач (сабот) и пенетратор добијен нумеричким путем коришћењем CFD методе. На крају су једначине кретања сабота и пенетратора решене применом методе Рунге-Кута да би се анализирао ефекат брзине пројектила на устима цеви и почетног трења сабота и пенетратора на процес раздвајања.

Резултати: Резултати истраживања су показали значајан утицај брзине на устима цеви и почетног трења на параметре сабота и пенетратора у тренутку потпуног одвајања. На основу добијених података, пројектанти оружја могу да одаберу, на одговарајући начин, балистичке и структурне параметре за пројектил.

Закључак: Представљен хибридни приступ ефикасан је у проучавању процеса одвајања панцирних поткалибарних

пројектила са одвојивим носачем. Резултати истраживања представљају значајан допринос у области поткалибарне муниције. Приказани метод може се применити у процесу пројектовања панцирних поткалибарних пројектила са одвојивим носачем различитих калибара.

Кључне речи: одвајање носача (сабота), поткалибарни пројектили, Ansys Fluent, CFD, нумеричка симулација.

A new investigation used to predict the burst pressure in straight corroded pipes under internal pressure

Aicha Metehri[a], *Belaïd* Mechab[b], *Bel Abbes* Bachir Bouiadjra[c]

University of Sidi Bel Abbes, Faculty of Technology,
Mechanical Engineering Department,
Laboratory of Physical Mechanics of Materials,
Sidi Bel Abbès, People's Democratic Republic of Algeria

[a] e-mail: ametehri@yahoo.com, **corresponding author**,
ORCID iD: https://orcid.org/0009-0002-2221-6833

[b] e-mail: bmechab@yahoo.fr,
ORCID iD: https://orcid.org/0009-0000-7483-5527

[c] e-mail: bachirbou@yahoo.fr,
ORCID iD: https://orcid.org/0000-0002-1925-7194

Abstract:

Introduction/purpose: There is a growing interest in pipeline integrity and its effects on economic and safety aspects. This study examines the process of corrosion evaluation in order to identify the remaining structural integrity of thin-walled pipelines with corrosion problems.

Methods: This work aims to create a corrosion evaluation model that can analyse the deterioration of steel pipes caused by internal pressure. A study utilised the finite element approach to build models for predicting the burst pressure of defect-free straight pipes. The study involved analytical and numerical analysis and used the mathematical extrapolation method.

Results: This paper discusses the impact of several factors on the integrity of a pipe, including the depth of defects, the thickness of the pipe, the shape, the size, and the position of faults, as well as the interaction between internal and external defects. Additionally, the influence of external defects on the overall integrity is discussed.

Conclusion: It is concluded that the pipeline corrosion failure criterion (PCORRC) model and the presented model align with the analytical solution documented in the literature. This holds immense importance in the field of structural design and safety evaluation.

Keywords: corrosion defect, steel pipe, internal pressure, failure, stress, modelling.

Introduction

Pipelines are pivotal components of the energy infrastructure, facilitating the cost-effective transportation of gas, oil, and various hydrocarbons across extensive distances to fulfil the requirements of the petrochemical sector (Mechab et al, 2011, 2014).

Pipeline integrity management adopts a performance-oriented strategy aimed at guaranteeing the operational reliability of pipelines and averting potential failures, with careful consideration given to the hazardous properties of the transported substances (Mechab et al, 2018, 2020; Fezazi et al, 2021; Salem et al, 2019). This comprehensive process comprises pipeline inspection, integrity evaluation, and maintenance tasks, with inspections to detect anomalies like corrosion defects and cracks (Guidara et al, 2018; Amaya-Gómez et al, 2019; Muthanna et al, 2021). Corrosion emerges as a leading cause of deterioration in pipelines, marked by the gradual erosion of metal over time, often detected through in-line Inspections (Deng et al, 2021; Jiang & Zhao, 2022). The corrosion observed on pipelines displays a range of shapes. Categorised by these shapes, corroded pipelines can be grouped into three main types: single-point corrosion defects, multi-point corrosion defects, and complex corrosion defects (Zhao et al, 2022; Teohet al, 2022; Yeomet al, 2015; Yi et al, 2022; Zelmati et al, 2020).

Over time, predictive models targeting the estimation of burst pressure in cylindrical vessels and pipes have evolved. They seek to quantify the maximum failure pressure by considering material properties, diameter, and wall thickness (Wang et al, 2020; Zhuwu et al, 2020). Numerous prediction models have been developed for determining burst pressure in pipes with isolated surface defects, mainly focusing on materials exhibiting elastic/ideally plastic behaviour (Abyani et al, 2022; Zhou et al, 2021).

Present models used to forecast the burst pressure of pipes with surface corrosion defects, utilising finite element analysis (FEA), generally presuppose defects to be axially oriented and either elliptical or rectangular (Kiefner et al, 1973) as per (DNV, 2021); elliptical shapes are assumed for shorter defects, whereas longer ones are deemed rectangular. Conversely, an alternative reference (ASME, 2012) posts an arbitrary defect profile aligned with the axis. Rectangular defect geometry

is uniformly employed in all other current FEA-based models for predicting burst pressure in such pipes.

This study aims to develop a corrosion assessment model to analyse damage in pipes under internal pressure. The finite element method is used to diagnose a corrosion defect in a steel pipe. The effect of the depth of the defect, the thickness of the pipe, the shape, the size, the position, the interaction between internal and external defects, and the external defect associated with a higher risk is discussed in this work. The new model presented in this paper predicts the burst pressure of a defect-free straight pipe, which is of great significance to structural design and safety assessment.

Numerical modeling and FE

In this case, the primary structure analysed is a three-dimensional structure. The ABAQUS calculation software (Hibbitt, Karlsson & Sorensen, 2014) was used in the present work to obtain the equivalent circumferential, radial, and longitudinal stress fields generated in a pipeline bearing a centred square external defect.

Geometrical and materials models

In this study, the defect is located in the central square outer wall of the pipe, and the dimensions of the defect length, width, and depth are a=40mm, b=40mm, and c=4 mm, respectively. Figure 1 shows the geometrical characteristics of the corroded pipe and different paths of study. It is worth noting that the external diameter is R_{ext}, R_{int} is the inner diameter, L is the longitudinal length, and ''t'' is the thickness of the pipe, as shown in Table 1. The tube material is API 5L X65 steel. This pipe was subjected to internal pressure.

Table 1 – Geometrical structure dimensions

t(mm)	L(mm)	R_{ext} (mm)	R_{int} (mm)	P (MPa)
5mm	500mm	50	45	10-15-20
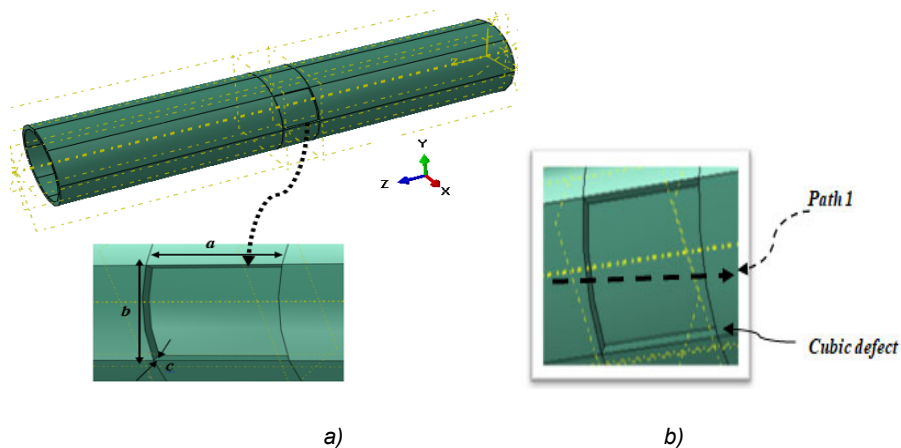
Figure 1 – a) Geometrical characteristics of the corrosion defect, b) Path of study

Table 2 presents the mechanical properties of the material used in this study (Olusegun & Akid, 2014).

Table 2 – API 5L X65 steel mechanical properties

Material	5L X65
Young's modulus E (GPa)	211
Poisson ratio ν	0.3
n (work hardening coefficient)	0.127
σ_{uits} [MPa]	500
σ_e [MPa]	380

Initial conditions and limitation

Boundary conditions are necessary for any finite element calculation. A section of steel pipe was cut in the circumferential direction, so we fixed it at both ends of the pipe ($U_1=U_2=U_3=0$, $UR_1=UR_2=UR_3=0$: displacement and rotation are blocked).

A load applied to the structure studied is represented by a pressure defined on the pipe's inner surface. The boundary conditions are presented in Figure 2.
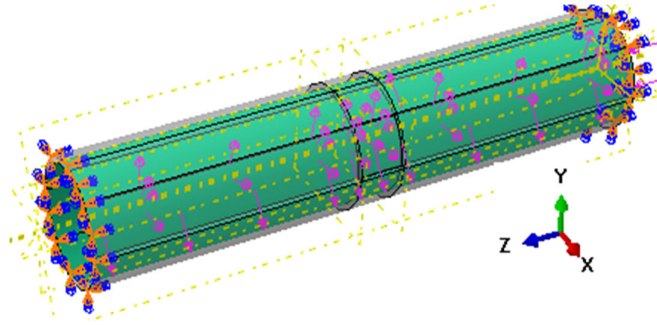
Figure 2 – Boundary conditions of the corroded pipe

Mesh model

The overall structure is based on a regular mesh for all calculations in this study. The mesh remains unchanged throughout the calculation to prevent any impact on the results, as shown in Figure 3. For the type of mesh elements, one was satisfied with the C3D8R elements, widely used in the modelling of these structures. The total number of nodes is 7660. The total number of the pipe elements is about 5010.
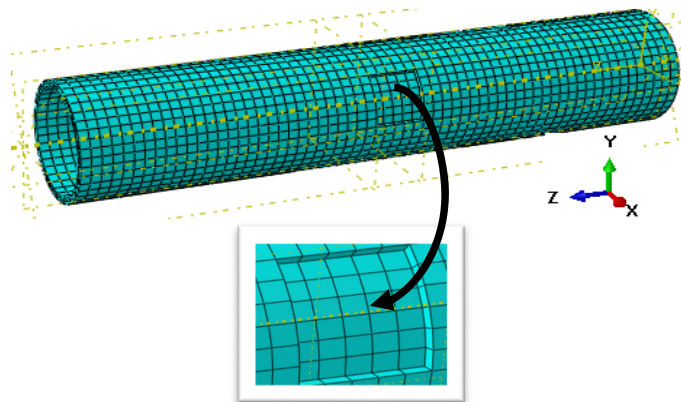
Figure 3 – Detailed mesh used for a numerical model of the corroded pipe

Convergence of the results

In finite element simulations, it is generally observed that using a more detailed mesh leads to more accurate results. Conducting mesh convergence research of this kind can provide a precise answer.

Furthermore, this paper aims to enhance the mesh density through a convergence study of the structure's density to strike a balance between computation time and desired accuracy.

Figure 4 illustrates the impact of changing the density of the mesh on the highest value of the von Mises constraint in the assembly. Based on Figure 4, a refined mesh leads to a higher value of the von Mises constraint. However, the von Mises value remains relatively constant if the mesh is adjusted to have a higher density across the structure.

The pipe dimensions were set as shown in Table 1 and the type of hexagonal linear meshing chosen. The number of finite elements was increased in order to refine the structure mesh from 1601 (less refined) to 33886 elements (very refined mesh) by using this technique in the Abaqus software, thanks to the options such as seed part instance, where the number of elements can be modified until achieving stability in the value of the von Mises stress.
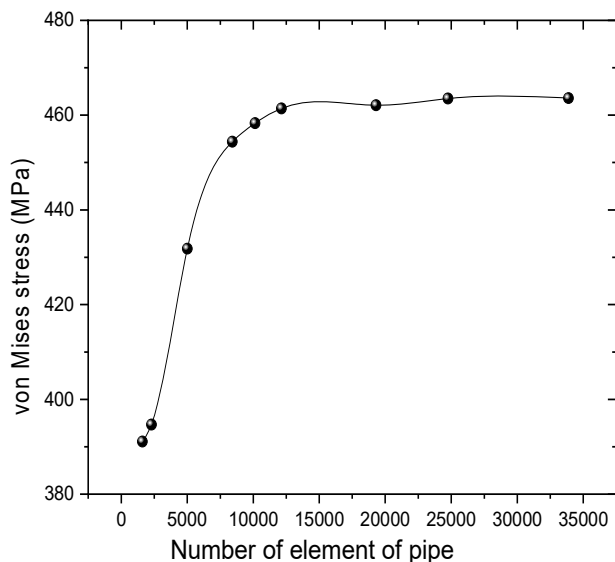
Figure 4 – Variation of von Mises stress as a function of the mesh density in the pipe for P=20MPa

Results and discussion

Model of burst pressure without defect

Burst pressure for intact pipelines

Some available approaches estimate burst pressure for free-defect pipes or with grooves with an infinite longitude. The approach of the von Mises is expressed as follows: (Amaya-Gómez et al, 2019)

$$P_b = \frac{4t\sigma_{uts}}{D}\left(\frac{k}{2}\right)^{n+1} \tag{1}$$

and

$$k = \frac{2}{\sqrt{3}}$$

where

P_b is the burst pressure,
σ_{uts} is the ultimate stress,
t is the pipe thickness, and
D is the Internal diameter.

Based on our finite element model, we have developed an analytical model for calculating burst pressure for an undamaged pipe; that is to say, the present model (equation 2) is obtained by the interpolation of the numerical results (FEM results), see Table 3, written as follows:

$$P_b = \frac{\sigma_{uts}}{n}\left(\frac{R_{ext}}{R_{int}}\right)\left(3{,}74325.10^{-5} + 0{,}00297\,t - 1{,}03764.10^{-4}\,t^2\right) \tag{2}$$

n: The hardening coefficient is equal to 0.127 for the used steel,

where

R_{ext} is the external radius of the pipe, and
R_{int} is the internal radius of the pipe.
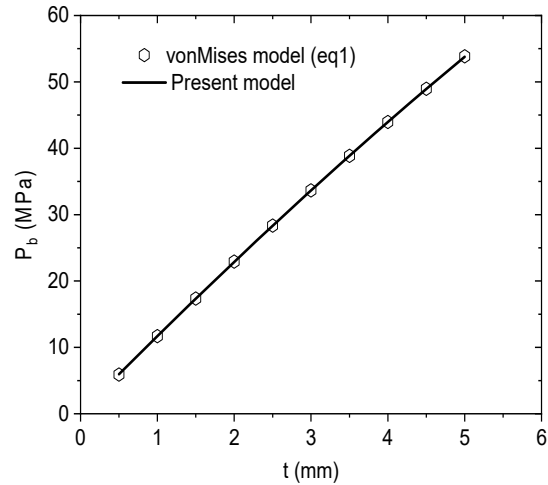
Figure 5 – von Mises results compared with the present model

Figure 5 presents the von Mises results compared with the present model. The maximum and minimum variations are 0.6789% and 0.00043%, respectively (See Table 3). The analytical solution gives a good agreement of the burst pressure for intact pipelines compared with the von Mises results.

$$e(\%) = \left| \frac{P_b^{\text{von Mises}} - P_b^{\text{present model}}}{P_b^{\text{von Mises}}} \right| \times 100 \qquad (3)$$

Table 3 – von Mises results are compared to the current model

P_b (von Mises)	P_b (Present model)	e (%)
5.91698926	5.95716214	0.6789413
11.7053483	11.685805	0.16696062
17.3692265	17.3264919	0.24603626
22.9125967	22.8724143	0.17537247
28.3392643	28.3167635	0.07939824
33.6528764	33.6527307	0.00043289
38.8569294	38.8735074	0.04266414
43.9547773	43.9722849	0.0398309
48.9496384	48.9422545	0.0150846
53.8446022	53.7766076	0.12627935

Effect of internal pressure

This part of the work numerically analysed the effect of internal pressure applied to a pipeline bearing an external square defect centred on the level and distribution of stresses induced in this structure using the finite element method. The results obtained are illustrated in Figure 6. It shows the distribution and variation of equivalent von Mises stresses as a function of internal pressure. The stresses were computed along path one, as shown schematically in Figure 1b.

Evaluation of stresses along path 1

This study evaluated the equivalent and the internal stresses along path 1; the obtained results are shown in Figure 6. The stresses were computed along path 1.

The effect of internal pressure on the intensity of equivalent and normal stresses is illustrated in Figure 6. Increasing internal pressure increases the amplitude of this stress, which reaches its maximum at the centre of the defect. The von Mises stress reaches its maximum level ($\sigma\sim280$MPa) at the defect located at the centre of the pipe with a pressure of 20MPa (Figure 6a).

The damage rate is equal to 60%. Even for internal normal stresses, radial stresses (Figure 6b) are almost half as high as von Mises stresses ($\sigma\sim50$MPa) for an applied internal pressure of 20 MPa.

The distribution of circumferential stress (Figure 6c) is identical to that of von Mises stresses and at the same level, which is the highest. Longitudinal stresses increase with each applied pressure and reach the lowest level at the ends relative to the centre of the defect, as shown in Figure 6d.

Comparative analysis

This part of the work, a comparative study between a flawless pipe and a pipe with an external-centred cubic defect (a =40mm, b=40mm, and c=4mm), presents the von Mises stress induced in the two pipes studied, subjected to internal stresses (10-15-20MPa), to see the effect of the defect and internal pressure on the increase in stress intensities demanded in this no-defect pipe, see Figure 7.

The first point to note from this Figure is that these equivalent stress levels lead us to conclude that the pipeline with a defect, subjected to very high internal pressures, particularly at the defect centre (over 452 MPa 20MPa internal pressures), can lead to ruin and put these pipes out of service. On the other hand, the equivalent von Mises stresses of a defect-free pipeline are much lower (over 188 MPa at 20 MPa internal pressures). These observations conclude that the pipe bearing the external defect should be repaired with a composite casing to reduce and absorb these high stresses. The damage rate is equal to 46%.
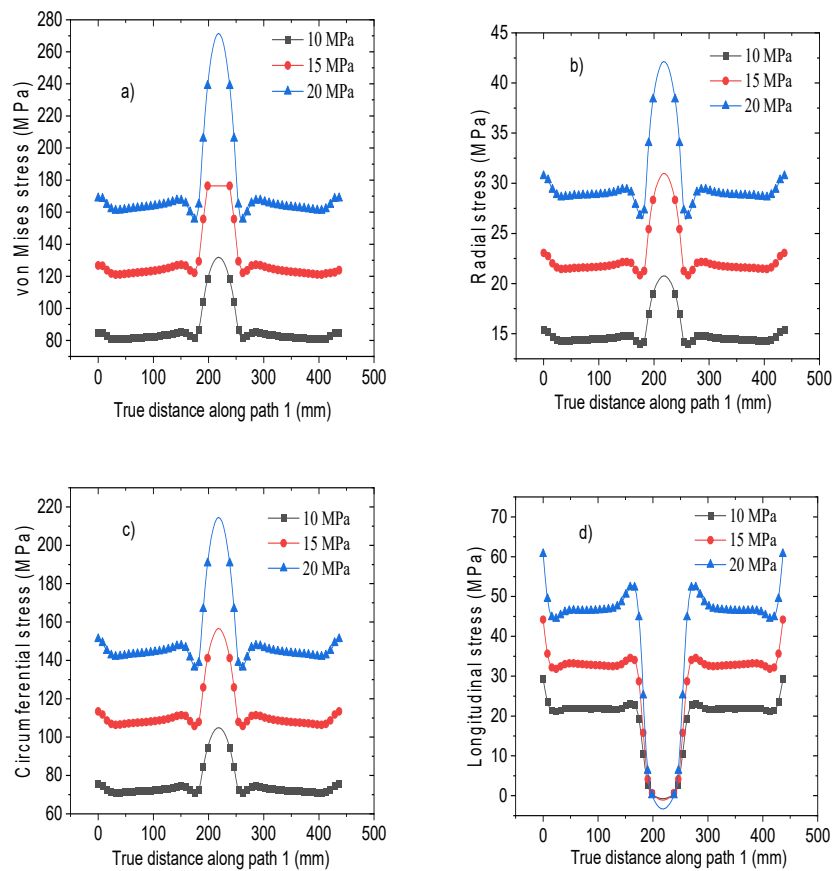
Figure 6 – von Mises and normal stress variation as a function of internal pressure along path 1

a) **10MPa**   **15 MPa**   **20MPa**

S, Mises
(Avg: 75%)
+9.420e+01
+8.924e+01
+8.427e+01
+7.931e+01
+7.434e+01
+6.938e+01
+6.441e+01
+5.945e+01
+5.448e+01
+4.952e+01
+4.455e+01
+3.959e+01
+3.462e+01

S, Mises
(Avg: 75%)
+1.413e+02
+1.339e+02
+1.264e+02
+1.190e+02
+1.115e+02
+1.041e+02
+9.663e+01
+8.918e+01
+8.173e+01
+7.428e+01
+6.683e+01
+5.939e+01
+5.194e+01

S, Mises
(Avg: 75%)
+1.884e+02
+1.785e+02
+1.686e+02
+1.586e+02
+1.487e+02
+1.388e+02
+1.288e+02
+1.189e+02
+1.090e+02
+9.905e+01
+8.912e+01
+7.918e+01
+6.925e+01

b) **10MPa**   **15 MPa**   **20MPa**

S, Mises
(Avg: 75%)
+3.818e+02
+3.523e+02
+3.228e+02
+2.933e+02
+2.638e+02
+2.342e+02
+2.047e+02
+1.752e+02
+1.457e+02
+1.162e+02
+8.665e+01
+5.713e+01
+2.761e+01

S, Mises
(Avg: 75%)
+4.028e+02
+3.711e+02
+3.395e+02
+3.078e+02
+2.761e+02
+2.445e+02
+2.128e+02
+1.811e+02
+1.495e+02
+1.178e+02
+8.612e+01
+5.446e+01
+2.279e+01

S, Mises
(Avg: 75%)
+4.522e+02
+4.194e+02
+3.865e+02
+3.536e+02
+3.207e+02
+2.879e+02
+2.550e+02
+2.221e+02
+1.893e+02
+1.564e+02
+1.235e+02
+9.063e+01
+5.776e+01

Figure 7 – von Mises equivalent stress level as a function of internal pressure: a) Pipe without defect, b) Pipe with defect

Depth and spacing effect

This part of the work will present the effect of the interaction of two centred cubic corrosion defects located outside the pipe on the level and distribution of equivalent stress generated in the pipeline as a function of defect depth and imposed internal pressure. Metehri et al. (2018) conducted almost the same study which determined the effect of two interactions on the stress intensity factors in S_iC particles reinforced Al composite.

It can be seen in Figure 8 that high stress occurs at the centre of the corrosion defect. The von Mises stress was calculated over a range of defect distances d=5-10-20-40-60 and 80mm and with varying defect depths c=1-2-3 and 4mm. The analysis by the finite element method of this Figure illustrates that the equivalent stress induced in the pipe, specifically in the defects, increases progressively as the distance between the two corrosion defects decreases (d=5mm). In other words, a decrease in the distance between square defects leads to an increase in the equivalent

1757

stress, and this value is accentuated if the defect depth (c= 4mm) is too great about the thickness of the steel pipe itself. This behaviour constitutes a risk of the pipe bursting since it has exceeded the ultimate stress (σ_{uts}=500MPa) at internal pressure P=20MPa. The damage rate is equal to 50%. On the contrary, these stresses generally decrease if the distance between defects increases.
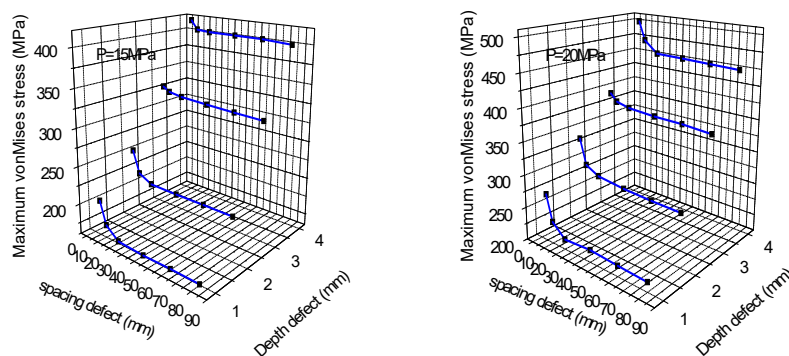
Figure 8 – Maximum von Mises stress variation in the pipe in correlation to the spacing and depth defect

Size effect

In the present study, the finite element method has been inserted to analyse the equivalent von stresses in three models of different sizes, but the same defect shape and the same depth defect (c=4mm). The first defect has the dimensions a=40mm, b=40mm; the second defect has the dimensions: a=50mm, b=50mm; the third defect has the dimensions: a=60mm, b=60mm, and, depending on the application, the internal pressure is from 15 to 20 MPa. The results were obtained by plotting the curves along path 1 (Figure 1b).

From these curves (Figure 9), the defect size considerably determines the level of equivalent stresses. As the defect size increases, the stress level automatically increases; always remember the effect of internal pressure. Equivalent stress values at internal pressure P=20MPa, whether path one and with large defect sizes, reach very high values, leading to catastrophic failure.
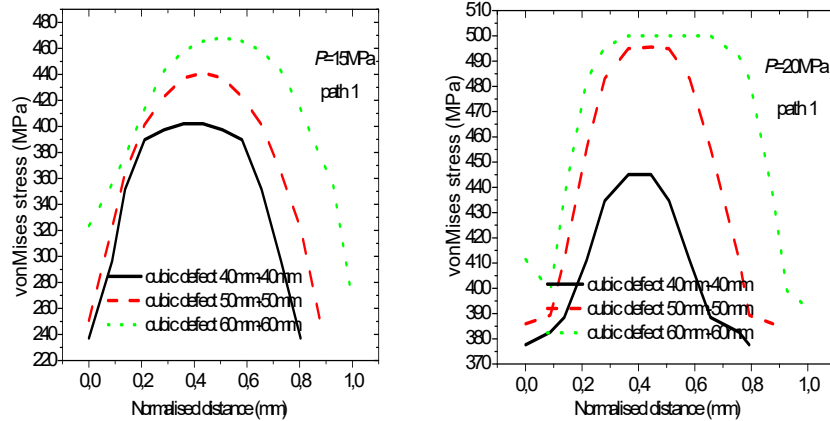
Figure 9 – von Mises stress variation in the pipe related to the size defect

Thickness and depth effect

Gas pipelines are constantly exposed to high internal pressure due to the transport of hydrocarbons. For this reason, it is strictly essential that special attention must be paid to a three-dimensional numerical study to analyse the geometric parameters of the cylindrical structure, including the effect of the pipeline radius and, therefore, its thickness, plus the fundamental parameter (defect depth) when the pipe carries defect to the outside. Two curves are plotted for this study for two values of internal pressure. The results are shown in Figure 10. This later shows the variation of the maximum von Mises stress related to the pipe thickness and defect depth, respectively. The analysis of this Figure shows that even if the pipe thickness is optimised (t=8mm), the equivalent stress value increases with increasing the defect depth value, exceeding the elastic limit, even the ultimate strength, especially at high pressure.

On the contrary, if the defect depth is minimal (c=1mm) and the pipe thickness is maximised (t=24mm), the equivalent stress values present no risk of damage. High internal pressures (P=20MPa) inducing high von Mises stress values should be avoided. As mentioned above, thick gas pipelines have good strength and resistance, firstly to high pressures and secondly to bursting, and guarantee good performance for this type of transport. However, it must be stressed that this geometric parameter

1759

(thickness pipe) determines the rigidity of cylindrical structures. It is, therefore, advisable to use thick-walled pipelines with a minimum depth defect.
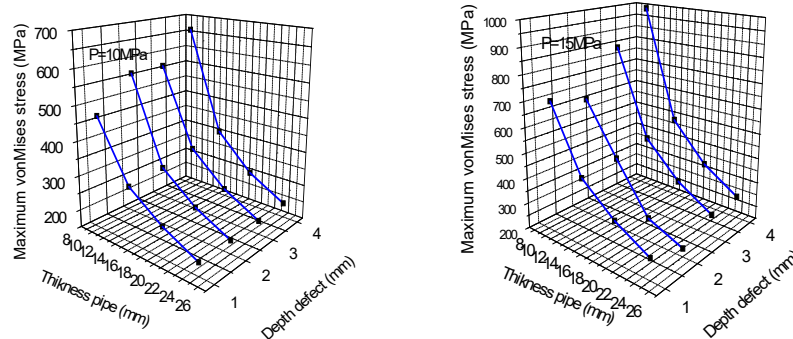
Figure 10 – Maximum von Mises stress variation in the pipe as a function of the thickness defect

Location effect

Cubic defect

This part of the work deals with the shape of a square corrosion defect of the dimensions a=40mm, b=40mm, and c=4mm. In the first case, this defect is located inside the centre of the cylindrical pipe, and in the second case, it is outside at the edges. This study aims to show the effect of the defect location on the variation and level of von Mises stress along path 1.

The analysis of Figure 11 by the finite element method shows that the equivalent stresses generated in a pipe by a square defect are generally of a higher level, mainly when the defect is located outside the edge, where these stresses reach ~440MPa if 20MPa of internal pressure is applied and a value that exceeds the elastic limit of steel. These stresses may present a high probability of pipe bursting. As a result, the equivalent stress values of a pipe with a square corrosion defect in the centre of the interior are correspondingly higher. Based on the results presented below, it is clear that pipelines with square defects, whether on the inside, inside edge, or in the centre, are at risk of ductile damage to the corroded pipe.
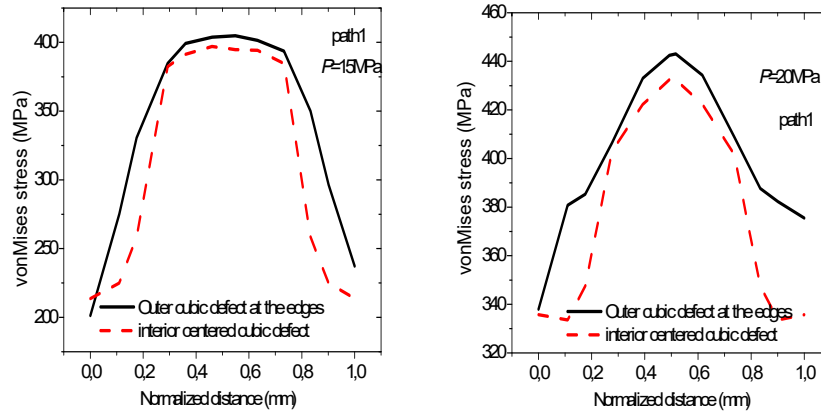
Figure 11 – von Mises stress variation in pipe as a function of the location of the cubic defect

Rectangular parallelepiped defect

In this study, it is also important to note that the rectangular parallelepiped corrosion defect of the dimensions a=40mm, b=60mm, and c=4mm generally located outside at the edges of the structure and inside at the centre, was chosen. This study by FEM analysis aims to determine the effect of the defect position on the variation and level of von Mises stresses along path 1.

The analysis of Figure 12 illustrates that the von Mises stresses generated by the rectangular parallelepiped defect are intensive and very high when positioned outside the pipe edge. They reach ~430MPa in case of the application of 15MPa of internal pressure, they reach more than 480 MPa, and in case of the application of 20MPa, this value exceeds the elastic limit of steel material and is close to the ultimate strength; the damage rate is equal to 50%. The higher these stresses, the greater the risk of pipe bursting. On the other hand, the equivalent stress values for a pipe with a rectangular parallelepiped corrosion defect in the centre of the interior present no risk of bursting. Based on the results presented below, it is clear that pipelines with rectangular defects in the centre and interior of the pipe are most often at risk of damage and reliability.
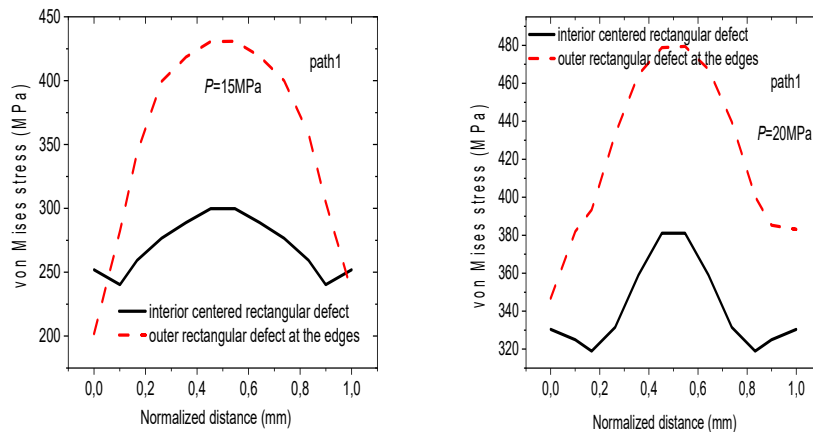
Figure 12 – von Mises stress variation in pipe as a function of the location of the rectangular defect

Shape effect

In this study, we wanted to numerically demonstrate the effect of the defect shape on the distribution and level of von Mises stresses. For this reason, we took samples of different defect shapes, provided the defect is located in the centre of the pipeline, with a maximum depth of 4mm. The dimensions for the cube-shaped defect were chosen to be a=40mm and b=40mm, for circular-shaped defects 2a= 8mm and 2b= 8mm, and for the elliptical-shaped defect 2a=40mm and 2b=8mm. The parallelepiped rectangle-shaped defects for the last sample were of the dimensions a=40 and b=70mm.

The results are shown in Figure 13. The latter shows the von Mises stress distribution according to path one at an internal pressure of 10 MPa, with different defect shapes and sizes. In the case of the circular defect, the maximum value of the equivalent stress, which is evenly distributed, remains at a low level of 200 MPa. When the defect becomes elliptical, there is a concentration of stress in the corners of the defect. In this case, the maximum equivalent stress exists at the pointed corner. It can reach 450 MPa, a value almost equal to the ultimate stress of steel (see Table 2), which is a higher level corresponding to just 10 MPa internal pressures and which can lead to damage to gas transport; the damage rate is equal to ~ 45%. As a comparison between circular and elliptical defects, we can

see a difference of more than half in the very high level of the circular defect, which presents no risk of pipe bursting. The level of the cubic defect is 370 MPa, while the level of the rectangular parallelepiped defect is 384 MPa, which exceeds the material's elastic limit. The distribution and value of the equivalent stress in the flaw vary depending on the flaw shape and internal pressure. If the pressure is increased, the level of equivalent stress increases. The maximum equivalent plastic strain in steel bearing an elliptical-shaped defect is much higher than that in a pipe bearing a circular defect, where the strain is distributed uniformly around the defect.
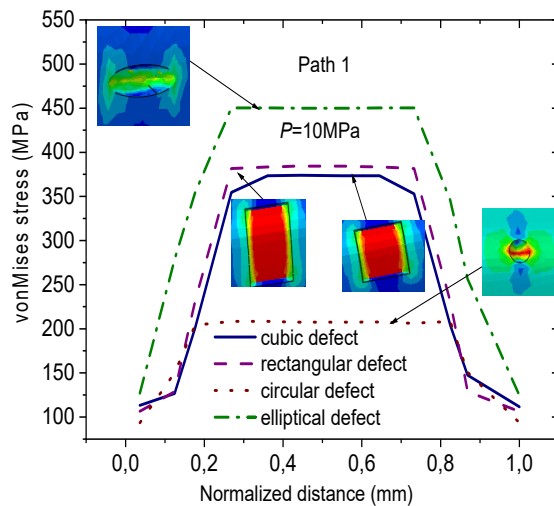
Figure 13 – von Mises stress variation in the pipe depending on the shape effect for P = 10MPa

Analytical model with the elliptical defect

From the above results (Figure 13), where the elliptical defect was found to have a very high level of von Mises stresses compared to other defects, we opted to perform an analytical validation in the case of a pipe with an elliptical defect. Therefore, an analytical model was developed to determine the bursting pressure for a pipe with an elliptical corrosion defect. The results of this model will be compared with those of the recalibrated PCORRC model. (Teoh et al, 2022).

Recalibrated PCORRC Model

Yeom et al. (2015) recalibrated the PCORRC model for X65 corroded pipes using full-scale test data and 3D FEA computations.

$$P_b = \frac{2t(0.9\sigma_{uts})}{D}\left(1-\frac{d}{t}\left(1-\exp\left(-0.224\frac{L}{\sqrt{D(t-d)/2}}\right)\right)\right). \qquad (4)$$

for $0.1\le$

$\frac{L}{\sqrt{Dt}} \le 12, 0.1 \le d \le 0.875$

where
D/t is the ratio of the defect, and
L is the length of the defect.

Lacking a defect, equation (4) reduces to Pb = $0.9\sigma_{uts}$ × (2t/D) for defect-free pipes. This model may also be conservative.

Present model

From the finite element results, the following model was extracted

$$P_b = \frac{2t(0.9\sigma_{uts})}{D}\left(A_0+A_1\exp\left(A_2\left(\frac{L}{\sqrt{Dt}}\right)\right)\right). \qquad (5)$$

for $0.1 \le \frac{L}{\sqrt{Dt}} \le 12,\ 0.1 \le d \le 0.875$

$$A_0 = -8,8817.10^{-16}\left(\frac{d}{t}\right)^2 -\left(\frac{d}{t}\right)+1$$

$$A_1 = 8,88178.10^{-16}\left(\frac{d}{t}\right)^2 +\left(\frac{d}{t}\right)+1.66533.10^{-16} \qquad (6)$$

$$A_2 = -1,17376\left(\frac{d}{t}\right)^2 +0,41926\left(\frac{d}{t}\right)-0,36419$$

where
t is the pipe thickness (mm),
d is the depth defect (mm), and
A_0, A_1, and A_2 are the Integration functions.

This model determines the variation of the burst pressure as a function of the geometrical parameters of the defect and the pipe. In the comparison between our model and the PCORRC model one (Figure 14), we can see an excellent agreement; the results of the two models are practically equal. This allows us to validate our model. The results

presented in Table 4 consolidate this validation, as the maximum error between the two models does not exceed 0.3%.

Table 4 – Burst pressure results of the PCORRC model compared with the present model for the defect ratios defect (d/t=, and 0.8)

0≤L/(Dt)^0.5≤12								
	d/t=0.1			d/t=0.5			d/t=0.8		
L/(Dt)^0.5	Pb/Pbi (Present)	Pb/Pbi (PCORRC)	e (%)	Pb/Pbi (Present)	Pb/Pbi (PCORRC)	e (%)	Pb/Pbi (Present)	Pb/Pbi (PCORRC)	e (%)
0	1	1	$2,21.10^{-14}$	1	1	$2,22.10^{-14}$	1	1	$2,22.10^{-14}$
0,0365	0,9987	0,9987	$-2,037.10^{-4}$	0,9918	0,9918	$-1,73.10^{-4}$	0,9718	0,9718	$-6,59E^{-6}$
0,3651	0,9885	0,9885	$-1,702.10^{-4}$	0,9245	0,9245	$-4,08.10^{-4}$	0,7558	0,7558	$-1,55E^{-4}$
0,5477	0,9832	0,9832	$-8,272.10^{-4}$	0,8912	0,8912	$4,653.10^{-4}$	0,6606	0,6606	$4,73E^{-4}$
0,9128	0,9737	0,9737	$-0,00106$	0,8321	0,8321	$-1,81.10^{-4}$	0,5111	0,5111	$-6,75E^{-4}$
1,0954	0,9693	0,9693	$-1,588.10^{-4}$	0,8060	0,8060	$-2,76.10^{-4}$	0,4529	0,4529	$-3,81E^{-4}$
1,8257	0,9543	0,9543	$-4,243.10^{-4}$	0,7206	0,7206	$2,512.10^{-4}$	0,2954	0,2954	$-0,00103$
2,1908	0,9481	0,9481	$-4,091.10^{-4}$	0,6873	0,6873	$1,119.10^{-4}$	0,2478	0,2478	$-8,10E^{-4}$
3,2863	0,9333	0,9333	$-4,644.10^{-4}$	0,6147	0,6147	$1,4469E^{4}$	0,1711	0,1711	$-0,0015$
4,5643	0,9217	0,9217	$-7,610.10^{-4}$	0,5647	0,5647	$2,0734E^{-4}$	0,1396	0,1396	$0,0014$
5,4772	0,9160	0,9160	$-9,904.10^{-4}$	0,5429	0,5429	$5,8709E^{-4}$	0,1314	0,1314	$-0,0026$
7,3029	0,9087	0,9087	$-7,671.10^{-4}$	0,5189	0,5189	$6,8554E^{-6}$	0,1262	0,1262	$-3,299E^{-4}$
9,1287	0,9047	0,9047	$6,774.10^{-4}$	0,5083	0,5083	$4,8104E^{-4}$	0,1252	0,1252	$-0,0037$
10,9541	0,9025	0,9025	$-4,064.10^{-4}$	0,5037	0,503	$-9,677E^{-4}$	0,1250	0,1250	$-0,0018$
	0,90182	0,90181	$7,6899.10^{-4}$	0,50231	0,5023	$0,0026$	0,12502	0,12502	$-0,00102$
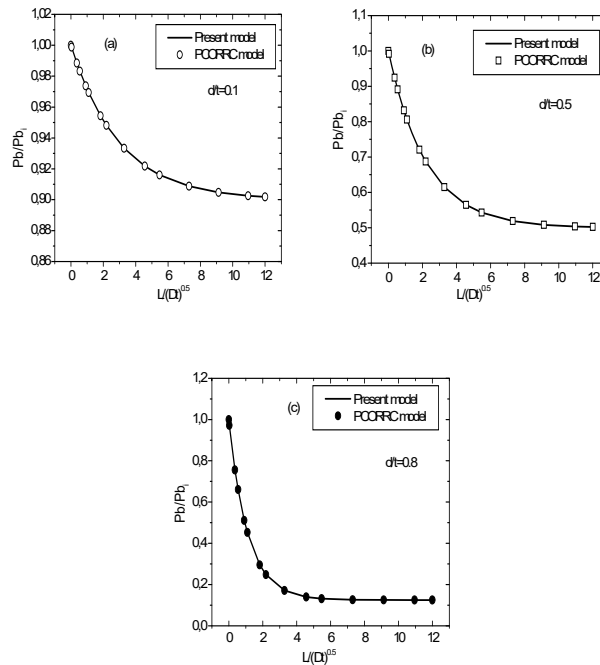
Figure 14 – Comparison of the burst pressure of the present model with the PCORRC model

Conclusions

This study examines the process of corrosion evaluation in order to identify the remaining structural integrity of thin-walled pipelines with corrosion problems. The objective is to develop a corrosion assessment model specifically tailored to analyse the effects of damage on pipes under internal pressure. This study employed the finite element approach to conduct an analytical and numerical investigation of a pipe. The objective was to construct models that can accurately estimate the burst pressure of defect-free straight pipes using mathematical extrapolation. This paper discusses the impact of several factors on the integrity of pipes, including the depth of flaws, the pipe thickness, the form, the size, the position, the distance between corrosion defects, the interaction between internal and exterior defects, and the influence of external defects on the overall integrity. This study enables assessing the damage rates of all flaws more accurately, considering other parameters such as internal pressure. The research introduces a novel model that accurately forecasts the burst pressure of a flawed straight pipe. This prediction holds immense importance for structural design and safety evaluation. The obtained results are compared with those of the PCORRC model, and the presented model aligns with the analytical solution found in the literature. Future research will focus on analysing the fluctuation of burst pressure in corroded pipes that have been repaired using bonded composite wrap.

References

Abyani, M., Bahaari, M.R., Zarrin, M. & Nasseri, M. 2022. Predicting failure pressure of corroded offshore pipelines using an efficient finite element-based algorithm and machine learning techniques. *Ocean Engineering*, 254, art.number:111382. Available at: https://doi.org/10.1016/j.oceaneng.2022.111382.

Amaya-Gómez, Sánchez-Silva, M., Bastidas-Arteaga, E., Schoefs, F. & Muñoz, F. 2019. Reliability assessments of corroded pipelines based on internal pressure – A review. *Engineering Failure Analysis*. 98, pp.190-214. Available at: https://doi.org/10.1016/j.engfailanal.2019.01.064.

-ASME. 2012. *B31 - Manual for Determining the Remaining Strength of Corroded Pipelines* [online]. Available at: https://www.asme.org/codes-standards/find-codes-standards/b31g-manual-determining-remaining-strength-corroded-pipelines/2012/pdf [Accessed: 09 April 2024]. ISBN: 978079183448.

Deng, K., Yang, P., Bing, L., Lin, Y. & Jiandong, W. 2021. Through-wall yield ductile burst pressure of high-grade steel tube and casing with and without corroded defect. *Marine Structures*, 76, art.number:102902. Available at: https://doi.org/10.1016/J.Marstruc.2020.102902.

-DNV. 2021. *DNV-RP-F101 Corroded pipelines, Recommended practice, Edition 2019-09 - Amended 2021-09*. *dnv.com* [online]. Available at: https://www.dnv.com/oilgas/download/dnv-rp-f101-corroded-pipelines/
[Accessed: 09 April 2024].

Fezazi, A.I., Mechab, B., Salem, M. & Serier, B. 2021. Numerical prediction of the ductile damage for axial cracks in pipe under internal pressure. *Frattura ed Integrità Strutturale*, 15(58), pp.231-241. Available at: https://doi.org/10.3221/IGF-ESIS.58.17.

Guidara, M.A., Bouaziz, M.A., Dallali, M., Schmitt. C., Haj Taieb, E. & Azari, Z. 2018. HDPE Pipe Failure Analysis Under Over pressure in Presence of Defect. In: Haddar, M., Chaari, F., Benamara, A., Chouchane, M., Karra, C. & Aifaoui, N. (Eds.) *Design and Modeling of Mechanical Systems—III. CMSM 2017. Lecture Notes in Mechanical Engineering,* pp.1027-1038. Cham: Springer. Available at: https://doi.org/10.1007/978-3-319-66697-6_101.

-Hibbitt, Karlsson & Sorensen, Inc. 2014. *ABAQUS/CAE, User's Manual, Ver 6.14*. Hibbitt, Karlsson & Sorensen, Inc.

Jiang, F. & Zhao, E. 2022. An integrated risk analysis model for corroded pipelines subjected to internal pressures: Considering the interacting effects. *Ocean Engineering*, 247, art.number:110683. Available at: https://doi.org/10.1016/j.oceaneng.2022.110683.

Mechab, Be,. Chioukh, N., Mechab, Bo. & Serier, B. 2018. Probabilistic Fracture Mechanics for Analysis of Longitudinal Cracks in Pipes under Internal Pressure. *Journal of Failure Analysis and Prevention*, 18, pp.1643-1651. Available at: https://doi.org/10.1007/S11668-018-0564-8.

Mechab, B., Salem, M., Medjahdi, M. & Serier, B. 2020. Probabilistic Elastic-plastic Fracture Mechanics Analysis of Propagation of Cracks in Pipes under Internal Pressure. *Frattura ed Integrità Strutturale*,14(54), pp.202-210. Available at: https://doi.org/10.3221/IGF-ESIS.54.15.

Mechab, B., Serier, B., Bachir Bouiadjra, B.A., Kaddouri, K. & Feaugas, X. 2011. Linear and non-linear analyses for semi-elliptical surface cracks in pipes under bending. *International Journal of Pressure Vessels and Piping*, 88(1), pp.57-63. Available at: https://doi.org/10.1016/J.Ijpvp.2010.11.001.

Mechab, B., Serier, B., Kaddouri, K., Bachir Bouiadjra, B.A. 2014. Probabilistic elastic plastic analysis of cracked pipes subjected to internal pressure loads. *Nuclear Engineering and Design*, 275, pp.281-286. Available at: https://doi.org/10.1016/j.nucengdes.2014.05.008.

Metehri, A., Madani, K. & Lousdad, A. 2018. Effect of crack position and size of particle on SIF in SiC particles reinforced Al composite. *Frattura ed Integrità Strutturale*, 13(48), pp.152-160. Available at: https://doi.org/10.3221/IGF-ESIS.48.18.

Muthanna, B.G.N., Bouledroua, O., Meriem-Benziane, M., Razavi Setvati, M. & Djukic, M.B. 2021. Assessment of corroded API 5L X52 pipe elbow using a modified failure assessment diagram. *International Journal of Pressure Vessels and Piping*, 190, art.number:104291. Available at: https://doi.org/10.1016/J.Ijpvp.2020.104291.

Salem, M., Mechab, B., Berrahou, M., Bachir Bouiadjra, B.A. & Serier, B. 2019. Failure Analyses of Propagation of Cracks Repaired Pipe Under Internal Pressure. *Journal of Failure Analysis and Prevention,* 19, pp.212-218. Available at: https://doi.org/10.1007/s11668-019-00592-3.

Teoh, C.Y., Pang, J.S., Abdul Hamid, M.N, Ooi, L.E. & Tan, W.H. 2022. Ultrasonic guided wave testing on pipeline corrosion detection using torsional T(0,1) guided waves. *Journal of Mechanical Engineering and Sciences (JMES)*, 16(4), pp.9157-9166. Available at: https://doi.org/10.15282/jmes.16.4.2022.01.0725.

Wang, Z., Zhou, Z., Xu, W., Yang, L., Zhang, B. & Li, Y. 2020. Study on inner corrosion behavior of high strength product oil pipelines. *Engineering Failure Analysis*, 115, art.number:104659. Available at: https://doi.org/10.1016/J.Engfailanal.2020.104659.

Yeom, K.J., Lee. Y.-K., Oh, K.H. & Kim, W.S. 2015. Integrity assessment of a corroded API X70 pipe with a single defect by burst pressure analysis. *Engineering Failure Analysis*, 57, pp.553-561. Available at: https://doi.org/10.1016/J.Engfailanal.2015.07.024.

Yi, S., Xiao, Z., Can, F., Junyan, H. & Cheng, Y.F. 2022. A novel model for prediction of burst capacity of corroded pipelines subjected to combined loads of bending moment and axial compression. *International Journal of Pressure Vessels and Piping*, 196, art.number:104621. Available at: https://doi.org/10.1016/J.Ijpvp.2022.104621.

Zelmati, D., Bouledroua, O., Hafsi, Z. & Djukic, M.B. 2020. Probabilistic analysis of corroded pipeline under localised corrosion defects based on the intelligent inspection tool. *Engineering Failure Analysis*, 115, art.number:104683. Available at: https://doi.org/10.1016/j.engfailanal.2020.104683.

Zhao, J., Lv, Y. & Cheng, Y.F. 2022. A new method for assessment of burst pressure capacity of corroded X80 steel pipelines containing a dent. *International Journal of Pressure Vessels and Piping*, 199, art.number:104742. Available at: https://doi.org/10.1016/j.ijpvp.2022.104742.

Zhou, W., Bao, J., Cui, X.Z. & Hong, H.P. 2021. Modeling and simulating non homogeneous non-Gaussian corrosion fields on buried pipelines and its use in predicting burst capacities of corroded pipelines. *Engineering Structures*, 245, art.number:112957. Available at: https://doi.org/10.1016/j.engstruct.2021.112957.

Zhuwu, Z., Liping, G. & Cheng, Y.F. 2020. Interaction betweeninternal and externaldefects on pipelines and its effect on failure pressure. *Thin-Walled Structures*, 159, art.number:107230. Available at: https://doi.org/10.1016/J.Tws.2020.107230.

Una nueva investigación utilizada para predecir la presión de la explosión en tuberías rectas corroídas bajo presión interna

Aicha Metehri*, **autor de correspondencia**,*
Belaïd Mechab*, Bel Abbes* Bachir Bouiadjra

Universidad de Sidi Bel Abbes, Facultad de Tecnología, Departamento de Ingeniería Mecánica, Laboratorio de Mecánica Física de Materiales, Sidi Bel Abbès, República Argelina Democrática y Popular

Resumen:

Introducción/objetivo: Existe un interés creciente en la integridad de las tuberías y sus efectos en los aspectos económicos y de seguridad. Este estudio examina el proceso de evaluación de la corrosión para identificar la integridad estructural restante de tuberías de paredes delgadas con problemas de corrosión.

Métodos: Este trabajo tiene como objetivo crear un modelo de evaluación de la corrosión que pueda analizar el deterioro de tuberías de acero causado por la presión interna. Un estudio utilizó el enfoque de elementos finitos para construir modelos para predecir la presión de rotura de tuberías rectas sin defectos. El estudio involucró análisis analítico y numérico y utilizó el método de extrapolación matemática.

Resultados: Este artículo discute el impacto de varios factores en la integridad de una tubería, incluida la profundidad de los defectos, el espesor de la tubería, la forma, el tamaño y la posición de las fallas, así como la interacción entre los defectos internos y externos. Adicionalmente, se discute la influencia de los defectos externos en la integridad general.

Conclusión: Se concluye que el modelo del criterio de falla por corrosión de tuberías (PCORRC) y el modelo presentado se alinean con la solución analítica documentada en la bibliografía. Esto tiene una inmensa importancia en el campo del diseño estructural y la evaluación de la seguridad.

Palabras claves: defecto de corrosión, tubería de acero, presión interna, falla, tensión, modelado.

Новейшие испытания, используемые для прогнозирования давления разрыва в прямых корродированных трубах под внутренним давлением

Айша Метехри, **корреспондент**,
Белаид Мехаб*, Бел Аббас* Башир Буяжра
Университет Сиди Бель-Аббес, технологический факультет,
Кафедра машиностроения,
Лаборатория физической механики материалов,
г. Сиди Бель-Аббес, Народная Демократическря Республика Алжир

РУБРИКА ГРНТИ: 55.09.43 Композиционные материалы
ВИД СТАТЬИ: оригинальная научная статья

Резюме:

Введение/цель: С каждым днем возрастает интерес к целостности трубопроводов и ее влиянию на экономические аспекты и безопасность. В данном исследовании рассматривается процесс оценки коррозии с целью выявления остаточной структурной целостности тонкостенных корродирующих трубопроводов.

Методы: Целью данной статьи является создание модели оценки коррозии, анализирующей износ стальных труб, вызванный внутренним давлением. В данном исследовании использовался метод конечных элементов в разработке моделей для прогнозирования давления разрыва неповрежденных прямых труб. В исследовании также применялись аналитический и численный анализы и метод математической экстраполяции.

Результаты: В статье рассматривается влияние нескольких факторов на целостность трубы, включая глубину повреждений, толщину трубы, форму, размер и расположение дефектов, а также взаимодействие между внутренними и внешними повреждениями. Кроме того, обсуждается влияние внешних повреждений на общую целостность трубопровода.

Вывод: В заключении сделан вывод о том, что модель критерия разрушения трубопровода вследствие коррозии (PCORRC) и представленная модель соответствуют аналитическому решению, описанному в существующей литературе. Результаты исследования представляют огромную значимость в области проектирования конструкций и оценки безопасности.

Ключевые слова: коррозионный дефект, стальная труба, внутреннее давление, разрушение, напряжение, моделирование.

Ново испитивање коришћено за предвиђање притиска прскања праве кородиране цеви под унутрашњим притиском

Ајша Метери, **аутор за преписку**,
Белаид Мехаб, *Бел Абас* Башир Бујажра

Универзитет Сиди Бел Абес, Технолошки факултет,
Одсек машинства, Лабораторија за физичку механику материјала,
Сиди Бел Абес, Народна Демократска Република Алжир

ОБЛАСТ: механика
КАТЕГОРИЈА (ТИП) ЧЛАНКА: оригинални научни рад

Сажетак:

Увод/циљ: Све је веће интересовање за интегритет цевовода као и за његов ефекат на економске и сигурносне аспекте. У овој студији испитује се процес процене корозије ради идентификације преосталог структурног интегритета кородираних танкозидних цевовода.

Методе: Креиран је модел евалуације корозије који може да анализира детериорацију челичних цеви услед унутрашњег притиска. Коришћен је приступ коначних елемената ради израде модела за предвиђање притиска прскања правих цеви без дефеката. Примењена је аналитичка и нумеричка анализа, као и математички метод екстраполације.

Резултати: Рад приказује утицај неколико фактора на интегритет цеви као што су дубина дефекта, дебљина цеви, облик, величина и позиција дефекта, као и међусобни утицај унутрашњих и спољашњих дефеката. Приказан је и утицај спољашњих дефеката на свеукупни интегритет.

Закључак: Закључује се да се модел критеријума лома цеви услед корозије (PCORRC) и модел представљен у овој студији подударају са аналитичким решењем из литературе. То има огроман значај у области пројектовања конструкција и процене сигурности.

Кључне речи: дефекат корозије, челична цев, унутрашњи притисак, лом, напон, моделовање.

Resonance heat transfer during the forced convection of the Al_2O_3 nanofluid in a horizontal channel with a heat sink

Abdelouahab Bouttout

National Center of Building Integrated Studies and Research (CNERIB),
Algiers, People's Democratic Republic of Algeria,
e-mail: bouttout@gmail.com,
ORCID iD: https://orcid.org/0000-0003-3907-0471

Abstract:

Introduction/purpose: The continuous advancements in electronic device technologies have led to increased power densities, resulting in substantial heat generation during their operation. Efficient thermal management is essential to maintain optimal performance, prolong device lifespan, and prevent thermal-induced failures. Traditional cooling methods, such as air and liquid cooling, have reached their limitations in meeting the escalating cooling demands. Consequently, the implementation of nanofluids as a novel cooling medium has gained significant attention in recent years.

Methods: The current study aims to determine the wide band of the frequencies for which the heat transfer is maximal during the cooling of nine electronic components mounted on a horizontal channel using the Al_2O_3 nanofluid. This phenomenon is called resonance heat transfer, and it occurs when the frequency of external forcing (pulsation or oscillation) matches the natural frequency of the convective flow of the nanofluid. The finite volume method has been used to solve the governing equation. Two cases are considered in this work: uniform and pulsed inlet flow. The electronic components have been considered as heated blocks with the same space between them.

Results: The results show that the flow is unstable for the critical Reynolds number $Re \approx 2000$ Al_2O_3 nanofluid with frequency as the Strouhal number St=1.2 and a fraction concentration of 0.10. It corresponds to a flow velocity of 0.211 m/s and a dominant frequency of fr=34 Hz.

Conclusions: The enhanced heat transfer is calculated as the rate of Nusselt number of pulsation flow with the Nusselt number of uniform flow. An enhanced heat transfer rate can be achieved 30-170 % within a band of the Strouhal number St=[0.2-1.2] corresponding to a band of frequency fr =[12-34] Hz.

Key words: nanofluid, resonance, heat transfer, heat sink, convection, Strouhal number.

Introduction

In many industrial applications, heat flux is amplified due to the complexity of manufacturing processes. In such instances, various equipment and components exhibit sensitivity to variations in temperature during their operation. In order to keep the functionality of components in their temperature level, it is important to transport calories away from hot spot locations. In electronic components, the heat flux dissipation of CPU can achieve 110-140 W; it increases significantly with input voltage and frequency (Putra et al, 2011). Bar-Cohen, A. (1987) showed that durability can be improved significantly by operating a device with reasonable temperature below 85 °C. In addition, the reliability of silicon chips can decrease by 50 % for every 10 °C temperature rise. In addition to change in the architectural configuration of heat exchangers such as chaps and roughness of surfaces in order to increase heat transfer rate, it is important to modify the physical characteristics of the fluid (Bar-Cohen et al, 2007). Nanofluid particles dispersed in the base fluid demonstrate a good heat transfer transport phenomena (Choi & Eastman, 1995). Nanofluids are engineered suspensions of nanometer-sized solid particles or nanoparticles in a base fluid, exhibiting extraordinary thermophysical properties compared to conventional cooling fluids. The combination of nanoparticles and base fluids results in an enhanced heat transfer coefficient and improved thermal conductivity, making nanofluids promising candidates for efficient cooling. Abchouyeh et al. (2019) studied the heat transfer and nanofluid flow around four sinusoidal side obstacles in a horizontal channel using the Lattice Boltzman Method LBM. The effects of the Reynolds number and the nanoparticles volume fraction at different nondimensional amplitudes of the wavy wall of sinusoidal obstacles are studied. An increase of the Reynolds number leads to a rise of the temperature gradient on the channel walls. An increment of nanoparticles concentration results in the heat transfer enhancement. Mohammed et al. (2015) present the laminar mixed convection flow of Al_2O_3/water nanofluids through two hot obstacles mounted on the bottom wall of a horizontal channel. The effect on heat transfer of different parameters such as the Richardson number, the Rayleigh number, the nanoparticles volume fraction and the aspect ratios of obstacles are examined. Their results show that the difference between the average Nusselt numbers obtained from the three sets of thermophysical models does not exceed 3%. In addition, the increase of the nanofluid concentration from 0% to 5% leads to an increase lower than 10% of the average Nusselt number over the obstacles.

Mohammed et al. (2015) present a summary of experimental and numerical works of heat transfer enhancement through facing step and corrugated channels using conventional fluids and nanofluids. Laminar and turbulent flows regimes through facing step and corrugated channels are presented. Their previous works show good agreement between numerical and experimental studies to enhance heat transfer. The corrugated facing step channel is a new design proposed to enhance heat transfer rate. The heat transfer enhancement was evaluated up to 60% when using nanofluid in the facing step channel configurations. Regression equations can correlate relationships between the Nusselt number and the flow parameters. The friction factor is an important parameter to calculate the pressure drop through the inlet and the outlet of the corrugated channel and keep optimum heat transfer enhancement.

Pishkar & Ghasemi (2012) present a numerical study of laminar mixed convection in a horizontal channel using pure water and Cu-water nanofluid over two blocks mounted on the bottom wall heated at a constant temperature. Different parameters are studied: the Reynolds and the Richardson numbers, the solid volume fraction, and the distance and the thermal conductivity of the blocks. The distance and the thermal conductivity of the blocks have a significant effect on the heat transfer rate. The influence of the solid volume fraction on the increase of heat transfer is clearer at a higher Reynolds number.

Bouttout et al. (2014) studied numerically hydrodynamic amplification and thermal instabilities by imposing pulsation during forced convection of air cooling of nine identical heated blocks mounted on a horizontal channel. The new feature of this work is that a narrowband of frequencies where the enhancement of heat transfer of all electronic components is in the range of 25%-55% compared with steady non-pulsation flow is obtained. Good agreement between numerical simulations and experimental results available from literature is obtained. Recently, Bouttout, A. (2023) investigated the forced convection flow of air through a power supply box with a piezoelectric fan of nine identical electrical devices. The efficiency of the piezoelectric fan is expressed by the maximum temperature of the ninth electrical device which does not exceed 80 °C for a time-averaged velocity of 0.556 m/s and a vibration frequency of 34.75 Hz of the piezoelectric fan. The pressure drop and the power pumping of the piezoelectric fan are obtained for different Reynolds numbers. The power loss was 4.6 times higher than that of the piezoelectric fan at re=500.

The present work examines the combination of the two methods such as an active method (pulsation of the fluid at the entrance of the channel) with a passive method (the addition of Al_2O_3 nanoparticles in the base fluid). We numerically simulated the existence of a large band of frequencies for which the heat transfer is maximal and proved the existence of resonance heat transfer using nanofluid. The resonance heat transfer occurs when the frequency of external forcing (pulsation or oscillation) matches the natural frequency of the nanofluid or the system. When this resonance condition is met, the nanofluid experiences significant energy transfer, leading to enhanced heat dissipation capabilities. It is crucial to note that employing acoustic waves with higher frequencies in an axial flow can promote the occurrence of resonant heat transfer within electronic systems.

Electronic cooling system and a physical model

The miniaturization in electronic chips has contributed to heavy pressure on the heat transfer process, in which huge heat must be effectively removed to protect the components from dangerous peak temperatures, and kept lower than 85 °C (Bar-Cohen, 1987).

The electronic components can be considered as small chips or protruding blocks which dissipate the heat during electrical current circulation.

In most practical situations, electronic components are mounted on a horizontal channel or embedded inside packaging and enclosures. Electronic components are made with ceramic, silver, nickel and copper; generally, components are mounted on a Printed Circuit Board, PCB, with copper materials (Young & Vafai, 1998). The solders fusible metal alloys are used to attach electronic components to the printed circuit board. During any peak of current, this junction has the potential to deteriorate, and protective measures should be implemented to safeguard the component. The most commonly used solders are tin-silver-copper (SAC) alloys.

The general outline of the steps and configurations involved in the transition from a real electronic cooling heat sink model to physical models integrated into a Fortran program using the finite volume method is:

- Real Electronic Cooling Heat Sink Model: The process begins with the real electronic cooling heat sink which is a physical prototype or system used for cooling electronic components to dissipate heat.

This model is based on the actual geometry and material properties of the heat sink (Figure 1 (a), (b)). The various configurations of microchannels MCHSs with heat sink and pin fins are accurately represented as real models, as depicted in Figure 2(a) and Figure 2(b).

- Geometric Representation: The geometry of the real heat sink is represented using appropriate mathematical models. This representation may include 2D or 3D geometric elements, such as polygons or meshes, depending on the complexity of the heat sink (Figure 3).
- Material Properties: The material properties of the heat sink, such as thermal conductivity and specific heat capacity, are considered to model the heat transfer within the system.
- Finite Volume Method (FVM): The finite volume method is chosen as the numerical technique for solving the heat transfer equations within the heat sink. The FVM divides the domain into control volumes and discretizes the governing equations to solve for temperature distribution and heat transfer rates.
- Numerical Solver: A Fortran program is developed to implement the finite volume method and solve the discretized heat transfer equations iteratively. The solver calculates temperature profiles and heat transfer rates for heat sink.
- Model Validation: The results obtained from the Fortran program are compared with experimental data or analytical solutions from simplified cases to validate the accuracy of the model.
- Optimization: The physical models may be further optimized based on the simulation results to improve the heat sink's design and performance (maximum temperature of heat sink, power pumping of the nanofluid and pressure loss).

By integrating the real electronic cooling heat sink model into a Fortran program using the finite volume method, engineers can efficiently analyze and optimize the thermal behavior of electronic components to design more effective cooling solutions.
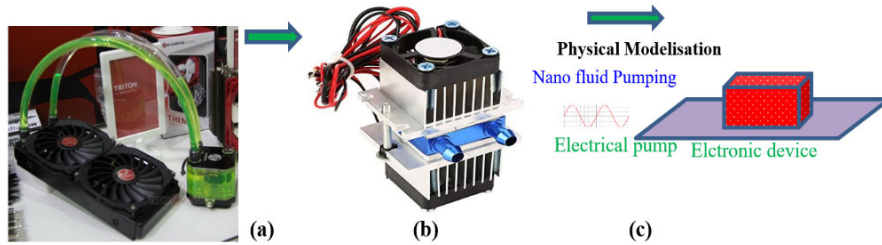
Figure 1 – Water cooling kit (a), DIY semiconductor water cooling systems (b), and modeling of electronic devices with a nanofluid pumping flow (c). The water-cooling system is used when the heat generated by the CPU is high, and classical cooling techniques with air are not sufficient.
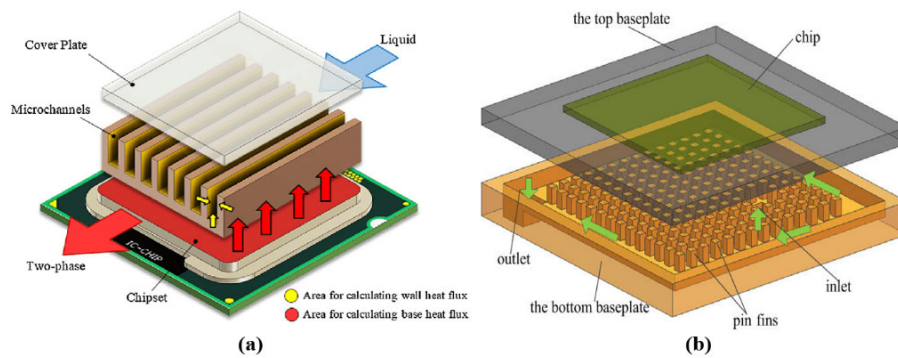
Figure 2 – Various configurations of microchannel heat sinks, MCHSs (a) straightforward channel, (b) pin fins. MCHSs combine the advantageous features of efficient electronic device operation, increased surface area per unit volume, enhanced heat transfer, and economically viable fabrication processes.
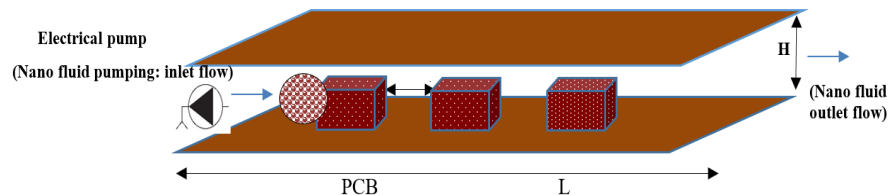
Figure 3 – General sketch of the physical model: electrical pump, electrical devices mounted on the printed circuit board (PCB) packaging. The Al_2O_3 nanofluid is used as coolant fluid. Heat in the electrical components is produced through the Joule effect occurring when electrical current passes through them. H=0.0074 m.

1777

Mathematical formulation

The heat sink system is considered as heat convection in channels and enclosures with different configurations of heated blocks. The effects of the important parameters such as the Reynolds numbers, the Grashof number, thermal conductivity, the aspect ratio of the channel, the pitch ratio of the blocks and the method of heating on heat transfer have been examined in many works.

The following characteristics for the cooling process using nanofluids are considered:

1. No agglomeration during flow: The assumption of no agglomeration of nanoparticles ensures that they remain uniformly dispersed in the base fluid throughout the cooling system. This uniform distribution is crucial for achieving consistent and enhanced heat transfer performance.

2. The same temperature of the fluid and the particles: By assuming that the nanofluid reaches thermal equilibrium, we can consider the fluid and nanoparticles to have the same temperature. This assumption simplifies the analysis and allows us to treat the nanofluid as a single-phase medium with enhanced thermophysical properties.

3. Neglecting viscous dissipation: Viscous dissipation refers to the conversion of mechanical energy into heat due to fluid friction. Neglecting this effect implies that the energy losses due to viscous effects are insignificant, simplifying the heat transfer analysis further.

The flow through the channel is assumed to be two-dimensional, unsteady and laminar. The dimensionless variables are defined:

$$X = \frac{x}{H}, \quad Y = \frac{y}{H} \ , \quad U = \frac{u}{u_0}, \quad V = \frac{v}{u_0}$$

$$\tau = \frac{t.u_0}{H}, P = \frac{p - p_0}{\rho_0 u_0^2}, \quad \theta = \frac{T - T_0}{Ts - T_0} \ , \quad v^* = \frac{v}{v_a} \tag{1}$$

The Nusselt number of each heated block (electronic component) is expressed in terms of the given heat flux, the measured surface temperature and the inlet temperature. It is defined as follows:

$$Nu = \frac{h.H}{k} \tag{2}$$

$$Nu = \frac{q.(H/k)}{(T_S - T_a)} \tag{3}$$

where u and v are the velocity components in the x and y directions, respectively. H is the height of the channel and t is the time.

With neglect of viscous dissipation and buoyancy force, the governing differential equations in the dimensionless form can be expressed as:

$$\frac{\partial U}{\partial X} + \frac{\partial V}{\partial Y} = 0 \tag{4}$$

$$\frac{\partial U}{\partial \tau} + \frac{\partial}{\partial X}(UU) + \frac{\partial}{\partial Y}(UV) = -\frac{\partial P}{\partial X} + \frac{1}{(1-\phi+\phi\frac{\rho_s}{\rho_f})(1-\phi)^{2.5}\,\mathrm{Re}}\left\{\frac{\partial^2 U}{\partial X^2} + \frac{\partial U^2}{\partial Y^2}\right\} \tag{5}$$

$$\frac{\partial V}{\partial \tau} + \frac{\partial}{\partial X}(UV) + \frac{\partial}{\partial Y}(VV) = -\frac{\partial P}{\partial Y} + \frac{1}{(1-\phi+\phi\frac{\rho_s}{\rho_f})(1-\phi)^{2.5}\,\mathrm{Re}}\left\{\frac{\partial^2 V}{\partial X^2} + \frac{\partial V^2}{\partial Y^2}\right\} \tag{6}$$

$$\frac{\partial \theta}{\partial \tau} + \frac{\partial}{\partial X}(U\theta) + \frac{\partial}{\partial Y}(V\theta) = \frac{1}{(1-\phi+\phi\frac{\rho Cp_s}{\rho Cp_f})} \times \frac{2-2\phi+(1+\phi)(\frac{ks}{kf})}{2+\phi+(1-\phi)(\frac{ks}{kf})}\frac{1}{\mathrm{Re}.\mathrm{Pr}}\left\{\frac{\partial^2 \theta}{\partial X^2} + \frac{\partial^2 \theta}{\partial Y^2}\right\} \tag{7}$$

where $Re=U_0H/u= \rho U_0H/\mu$, $Pr=v/\alpha$ are the Reynolds and Prandl numbers, respectively.

In the computational treatment of momentum equations (3) and (4), v^* for the block can be set to an infinitely large value such as 10^{20} to simulate solid blocks.

The density, the heat capacity and the thermal expansion coefficient of the nanofluid are defined as follows:

$$\rho_{nf} = (1-\phi)\rho_f + \phi\rho_s \tag{8}$$

$$(\rho Cp)_{nf} = (1-\phi)(\rho Cp)_f + \phi(\rho Cp)_s \tag{9}$$

$$(\rho\beta)_{nf} = (1-\phi)(\rho\beta)_f + \phi(\rho\beta)_s \tag{10}$$

The thermal conductivity of the nanofluid is defined using (Maxwell, 2010):

$$\frac{k_{nf}}{k_f} = \frac{(k_s + 2k_f) - 2\phi(k_f - k_s)}{(k_s + 2k_f) + \phi(k_f - k_s)} \tag{11}$$

The mathematical relation between the dynamic viscosity μnf of the conventional base fluid and solid nano-size particles is given by Brinkman, (1952):

$$\mu nf = \frac{1}{(1-\phi)^{2.5}} \mu f \tag{12}$$

μf is the dynamic viscosity of the base fluid (water).
ϕ is the volume fraction.

The initial conditions of the flow are:
$$U = V = \theta = 0 \tag{13}$$
The boundary conditions are:
$$X = 0, \quad 0 \le Y \le 1, \quad U = 1 + A\sin(2\pi St\tau), V = 0, \quad \theta = 0 \tag{14}$$
$$X = L, \quad 0 \le Y \le 1, \quad \frac{\partial U}{\partial X} = \frac{\partial V}{\partial X} = \frac{\partial \theta}{\partial X} = 0 \tag{15}$$
$$Y = 0, \quad 0 \le X \le 40, \quad \frac{\partial \theta}{\partial Y} = 0 \tag{16}$$
$$Y = 1, \quad 0 \le X \le 40, \quad \frac{\partial \theta}{\partial Y} = 0 \tag{17}$$

St: the Strouhal number (Flow pulsation frequency: dimensionless frequency) is related to frequency, the height of the heat sink system (H with m) and inlet velocity U_0 (with m/s) and pulsation frequency f (with Hz). The Strouhal number is used by many researchers in the literature (Moon et al, 2005, 2002; Greiner, 1991) especially to control the flow pulsation, as given by the following equation:

$$St = \frac{f.H}{U0} \tag{18}$$

Numerical approach

The governing equations are discretized using the finite volume method while the coupling between velocity and pressure fields is done

using the SIMPLER algorithm (Patankar, 1980). The components of velocity (U and V) were stored at the staggered locations, and the scalar quantities (P and θ) were stored in the centers of these volumes.

The diffusion and the convective terms in equations (5), (6) and (7) are discretized by a second order central difference scheme. Finally, the discretized algebraic equations are solved by the line-by-line tri-diagonal matrix algorithm (TDMA).

```
                    ┌──────────┐
                    │  Start   │
                    └────┬─────┘
                         ▼
   ┌──────────────────────────────────────────────────┐
   │ Geometric data and physical properties of the nanofluid │
   └──────────────────────┬───────────────────────────┘
                         ▼
       ┌──────────────────────────────────────┐
       │ Variables Initialisation (U, V, P et θ) │
       └──────────────────┬───────────────────┘
                         ▼
           ┌──────────────────────────┐
           │  Mesh calculation (2D)    │
           └──────────────┬───────────┘
                         ▼
              ┌────────────────────┐
              │ Increment over time │
              └─────────┬──────────┘
                         ▼
   ┌──────────────────────────────────────────────────┐
   │ Calculation of the coefficients of the momentum equations X and Y │
   └──────────────────────┬───────────────────────────┘
                         │
   ┌──────────────────────────────────────────────────┐
   │ Calculation of pseudo-velocities                  │
   └──────────────────────┬───────────────────────────┘
                         │
   ┌──────────────────────────────────────────────────┐
   │ Calculation of the coefficients of the pressure equation │
   └──────────────────────┬───────────────────────────┘
                         │
   ┌──────────────────────────────────────────────────┐
   │ Solving the pressure equation                     │
   └──────────────────────┬───────────────────────────┘
                         │
   ┌──────────────────────────────────────────────────┐
   │ Solving Algebraic Momentum Equations              │
   └──────────────────────┬───────────────────────────┘
                         │
   ┌──────────────────────────────────────────────────┐
   │ Calculation of the coefficients of the algebraic pressure correction equation │
   └──────────────────────┬───────────────────────────┘
                         │
   ┌──────────────────────────────────────────────────┐
   │ Solving the pressure correction equation P'       │
   └──────────────────────┬───────────────────────────┘
                         │
   ┌──────────────────────────────────────────────────┐
   │ Correction of velocity fields U and V             │
   └──────────────────────┬───────────────────────────┘
                         │
   ┌──────────────────────────────────────────────────┐
   │ Calculation of the coefficients of the energy equation │
   └──────────────────────┬───────────────────────────┘
                         │
   ┌──────────────────────────────────────────────────┐
   │ Solving the Energy Equation                       │
   └──────────────────────┬───────────────────────────┘
                         ▼
              ┌────────────────────┐
              │  Convergence test   │
              └─────────┬──────────┘
                         ▼
   ┌──────────────────────────────────────────────────┐
   │ Results (Velocity field, stream lines, temperature, Nusselt number) │
   └──────────────────────────────────────────────────┘
```

Figure 4 – Flowchart of the numerical solution using the SIMPLER Algorithm (Patankar, 1980). This flowchart presents the main steeps used to solve the coupled governing equations of the problem and to obtain the velocity field, the stream lines, the isotherms and the Nusselt number of the blocks. A Fortran program employing the finite volume method has been utilized.

A fully implicit time marching method was realized with a fixed dimensionless time step ($\Delta\tau=10^{-3}$). Convergence at a given time step is declared when the maximum change between two consecutive iteration levels falls below 10^{-4}, for U, V and θ. At this stage, the steady state solution or oscillatory regime is obtained.

This work introduces the unsteady forced convection model of nanofluid through the horizontal channel in the FORTRAN program (Afrid & Zebib,1990).

It is important to highlight that the results obtained at a specific Reynolds number were utilized as the initial conditions for computing the solutions at subsequent Reynolds numbers. For instance, the solutions obtained for Re=100 were considered as the starting point to calculate the solution for Re=200.

The Simpson rule has been used to calculate the averaged Nusselt numbers of the heated blocks by the integration over the front, top and rear surfaces of the blocks.

Figure 4 illustrates the flowchart depicting the numerical solution process utilizing the SIMPLER algorithm (Patankar, 1980).

Results and discussions

Code validation

Figure 5 shows the quantitative and qualitative validation of the code with the previous experimental and numerical works available in the literature – the experimental work of Farhanieh et al. (1993), the numerical work of Furukawa & Yang (2003) and the experimental work of Moon et al. (2005).

The different dimensional values of the configuration C2 (horizontal channel containing heated blocks) are listed in the Table 1. It is noted that (Moon et al, 2005) studied experimentally several configurations with similar dimensions of (Greiner, 1991).

The code is executed, in order to define the values of the Nusselt number of each block for different configurations and different Reynolds numbers.

It is noted that the values obtained by our numerical simulations are in good agreement compared to the results of the authors, with some differences between the geometries examined and the Reynolds number interval (cooling rate).

1782
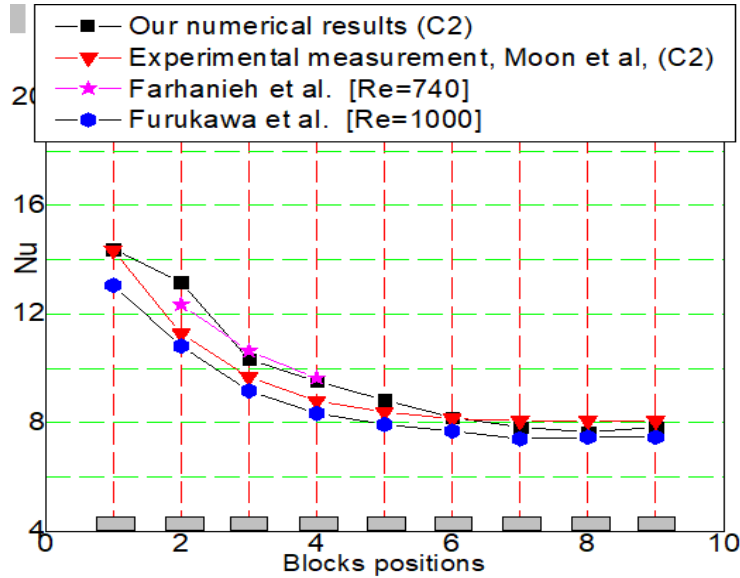
Figure 5 – Distribution of the Nusselt number along the blocks. Qualitative and quantitative comparison of our results with the previous works. The Simpson's rule has been employed to determine the average Nusselt numbers for the heated blocks by integrating across the front, top, and rear surfaces of the blocks.

Table 1 – Geometric details of the configuration. It refers to the dimensions of the geometrical block in the channel of the heat sink system

Configuration	l/L	L/H	D/h	h/H
C2	0.50	2.00	2.00	0.5

Grid and time step sensitivities

In numerical computations, conducting a grid independence study is crucial. In this study, the grid independence is examined by employing three different grid sizes for the same computational domain (502×11, 602×22, and 702×32) for Re=500 (Figure 6).

Figure 7 shows the averaged Nusselt number of the block. The number of nodes was chosen to be 602×22 after a grid-dependency test was carried out. The time step, $\Delta\tau$, was varied from 5×10^{-4} to 4×10^{-3} ($\Delta\tau$ =2.5×10^{-4}, $\Delta\tau$=5×10^{-4}, $\Delta\tau$=1×10^{-3}, $\Delta\tau$=2×10^{-3} and $\Delta\tau$ =4×10^{-3}); for Re=500 using a grid size of 602×22. There is the variation of the averaged Nusselt

number Nu1 of the first block with time for five various accuracies for computations.
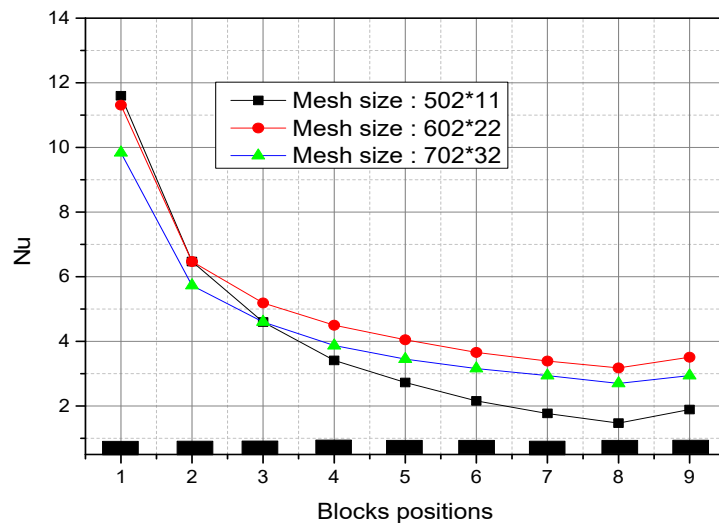
Figure 6 – Grid sensitivity for Re= 100. Φ=0.10. Grid sensitivity refers to the dependence of the solution on the size and distribution of the computational grid or mesh.
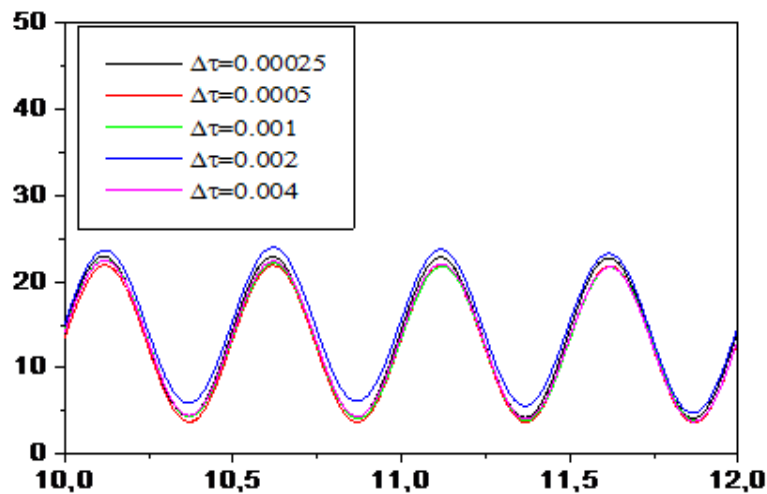
Figure 7 – Time step sensitivity for Re= 100. Φ=0.10. Convergence at a specific time step is confirmed when the maximum change between two consecutive iteration levels drops below 10^{-4} for the variables U, V, and θ. At this stage, the steady state solution or oscillatory regime is obtained.

Discussions

Steady state flow

Brownian motion exerts a significant influence on the rheological properties of nanoparticles and the thermal behavior of nanofluids. Brownian motion refers to the unpredictable stochastic movement of suspended nanoparticles, sustained by thermal diffusion; it notably intensifies at higher temperatures, smaller nanoparticle sizes, and lower viscosity. The random collision of nanoparticles in Brownian fluid environments is a fundamental factor contributing to the increased thermal conductivity of nanofluids. Additionally, a high surface-to-volume ratio of the channel with heat sinks due to reduced length scales plays a crucial role. Consequently, this phenomenon is largely confined to the interaction zone between the fluid and the surface of the channel and the heat sink, making it highly relevant.

In a steady-state flow, the fluid moves steadily and continuously without any change in velocity over time (Figure 8).
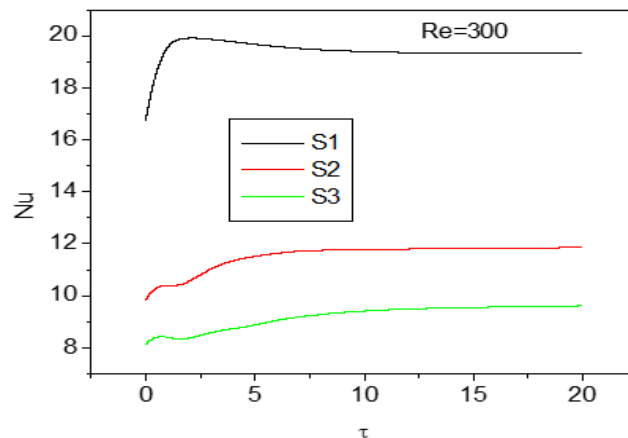
Figure 8 – Time evolution of the Nusselt number of S1, S2 and S3 for Re=300 and Φ=0.10. Steady state over time for the Nusselt number is obtained. S1, S2, and S3 denote the heat source numbers.

Stream lines flow and isotherms in the heat sink system

The streamlines and isotherms inside the system are depicted in Figure 9 for Re=500, revealing the emergence of vortices in the interlock regions of the channel. The streamlines exhibit distinct motion patterns, indicating that the flow in this area is separated from the main flow.

Notably, vortex formation is observed, suggesting specialized fluid dynamics in these regions. Additionally, the isotherm lines cluster near the blocks, and the temperature modulation induced by the voltage input frequency can disturb the thermal layer in close proximity to the blocks.

Previous studies indicate that, with an increase in the Reynolds number, the streamlines reveal a corresponding augmentation in both the size and strength of the vortices formed behind the blocks. At elevated Reynolds numbers, a robust vortex emerges, amplifying heat transfer from the surfaces of the blocks. Nevertheless, when employing the Al_2O_3 nanofluid, a distinct observation is a larger vortex formed behind the blocks. This occurrence can be attributed to the higher density and dynamic viscosity of the nanofluid. The heightened shear stress between the layers of the nanofluid contributes to the creation of a larger vortex. The velocity difference between the nanofluid and pure water is insignificant at low Reynolds numbers. However, as the Reynolds number increases, this disparity becomes more pronounced, as demonstrated in prior research (Pishkar & Ghasemi, 2012).

At low Reynolds numbers, heat transfer is primarily governed by conduction, resulting in the isotherms extending above the blocks and occupying a substantial area within the channel. As the Reynolds number increases, convection becomes the predominant heat transfer mechanism. The intensified cold inlet flow at higher Reynolds numbers pushes the isotherms closer to the bottom wall. The isotherms of the nanofluid indicate that at every point in the channel, the temperature of the nanofluid is higher. This phenomenon is attributed to the higher thermal conductivity of the nanofluid, as documented in the previous research (Pishkar & Ghasemi, 2012).

Pressures losses and power pumping
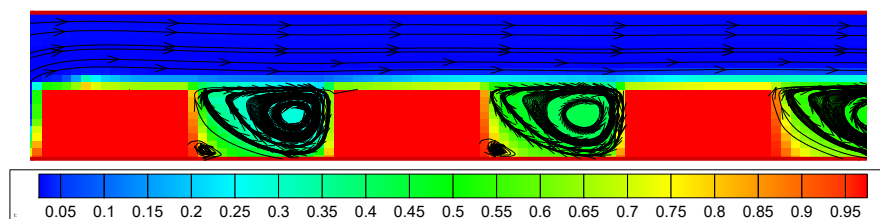
Figure 9 – Streamlines and isotherms in the section between 1st, 2nd and 3rd block. Re=500, volume fraction of Al_2O_3 nanoparticles, Φ=0.15. The streamlines exhibit distinct motion patterns, indicating that the flow in this area is separated from the main flow. The isotherm lines cluster near the blocks.

When nanofluids flow through a channel with blockages (obstacles or structures that disrupt the flow), they experience pressure losses due to fluid friction and changes in flow direction. Nanofluids typically have different rheological properties compared to conventional fluids, such as higher viscosity or different thermal conductivity. These properties affect the pressure drop across the channel. The presence of nanoparticles can alter the momentum transfer and energy dissipation in the flow, resulting in different pressure loss characteristics compared to pure base fluids.

The concentration of nanoparticles in the nanofluid plays a significant role in determining pressure loss. Higher nanoparticle concentrations can lead to increased viscosity and enhanced resistance to flow, resulting in higher pressure losses. On the other hand, lower nanoparticle concentrations may have minimal impact on pressure drop compared to the base fluid.

The geometry of blockages in the channel can influence pressure losses. Different blockage shapes, sizes, and arrangements will create varying flow patterns and turbulence, impacting pressure drop in the nanofluid.

Pumping power is the amount of energy required to overcome pressure losses and maintain fluid flow through the channel. In the case of nanofluids in a channel with blockages, pumping power will be influenced by the nanofluid viscosity and thermal conductivity, as well as the blockage geometry and the flow rate. Higher viscosity nanofluids may demand more pumping power compared to low viscosity fluids. Additionally, higher thermal conductivity nanofluids may help dissipate heat generated due to pressure losses, affecting the overall pumping power.

Heat transfer

The heat transfer gradually decreases and eventually reaches an asymptotic limit, indicating that the flow regime periodically develops along the solid blocks and then stabilizes into a steady state starting from the fifth block. Notably, the reduction rate of the average Nusselt number between the first and ninth blocks is approximately 50% for air cooling and 38% for nanofluid cooling (using Al_2O_3-water with a particle volume fraction Φ of 8%). Moreover, the analysis reveals that both cooling methods exhibit an overall heat transfer gain, with approximately 44% improvement observed for the upstream blocks and around 20% for the downstream blocks when using nanofluid cooling compared to air cooling. In practical scenarios, where heat-generating components are involved, the nanofluid cooling system activates and efficiently ensures temperature reduction,

indicating its potential for effective thermal management in such applications (Figure 10 and Figure 11).
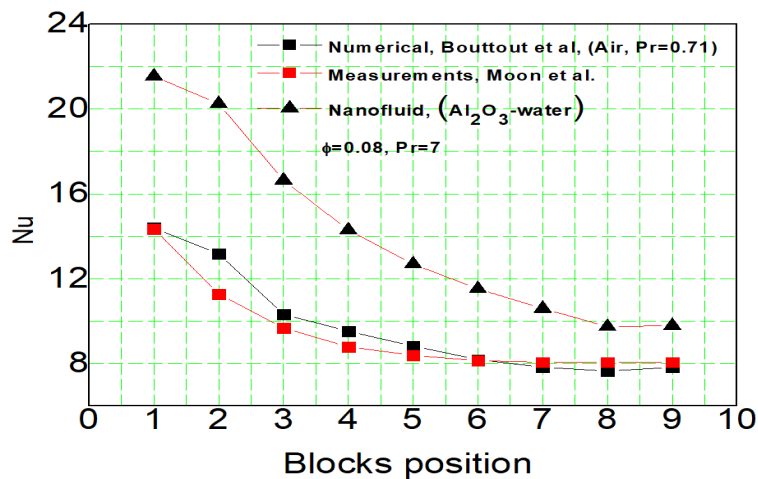
Figure 10 – Distribution of the Nusselt number along the blocks. A=0.0, Re=700 (air cooling, Pr=0.71) and cooling using a nanofluid (Al₂O₃/water - Pr=7.0, Φ=8%). Heat transfer is higher for the nanofluid in the heated sink compared to both water and air cooling methods.
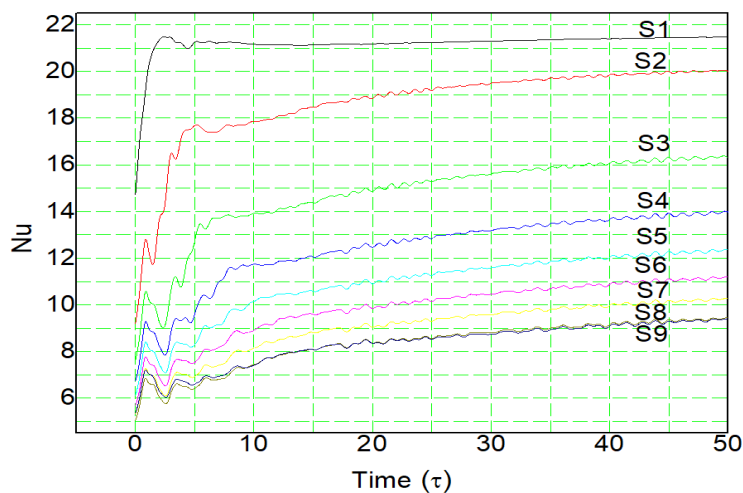
Figure 11 – Distribution of the Nusselt number along the blocks, for Re=300 and Φ=0.10. Configuration C2. The heat transfer from the heat sinks gradually decreases and eventually reaches an asymptotic limit. S1, S2, S3, S4, S5, S6, S7, S8 and S9 denote the heat source numbers.

Pulsation state flow

The numerical simulation involves employing an electrical pumping model to simulate pulsating nanofluid flow at the channel inlet. The heat sink is regarded as a heated block that receives the coolant flow to achieve functional safety temperature.

As the velocity of the nanofluid increases, the Brownian motion of the particles also intensifies, leading to a consequent enhancement in the nanofluid thermal transport capabilities. Consequently, at higher Reynolds numbers, there is a decrease in thermal resistance. Figure 12 illustrates the resonance heat transfer of the heat sink, showcasing the maximum heat transfer occurring at various positions of the heat sinks.

The maximum heat transfer factor E is determined by comparing the Nusselt number in both steady-state and unsteady pulsating conditions during the Al_2O_3 nanofluid cooling process (Figure 12). The maximum heat transfer factor, E, is expressed by the following equation:

$$E = \frac{max(Nu(St))}{\max(Nu(St=0))} \tag{19}$$
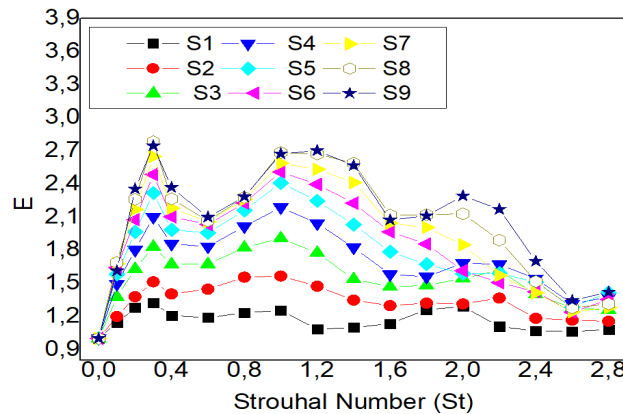
Figure 12 – Distribution of the enhancement factor of the Nusselt number E along the blocks for Re=500 and Φ=0.10. Configuration C2. It is observed that the enhancement factor of the heat sinks achieves the maximum values within a certain frequency range. This phenomenon is referred to as resonance heat transfer enhancement. S1, S2, S3, S4, S5, S6, S7, S8 and S9 denote the heat source numbers.

The results reveal the flow instability at the critical Reynolds number (Re ≈ 2000) in the Al_2O_3 nanofluid, with frequencies corresponding to the Strouhal number (St) of 1.2 and a fractional concentration of 0.10. This observation is associated with a flow velocity of 0.211 m/s and a dominant

frequency of fr = 34 Hz. Figure 13 illustrates the temporal evolution of the dimensionless vertical velocity of the nanofluid inside the heat sink system. This figure shows that the flow exhibits instability at Re ≈ 2000. In this regime, the flow transitions from a stable to an unstable regime due to the concentration of nanoparticles, heat generation by electronic components, and disrupted boundary layer through the channel. These findings provide valuable insights into the thermodynamic behavior of the system under consideration, considering variations in different parameters such as the nanoparticle concentration, the Reynolds number and the geometric configuration of different blocks within the system.

Figure 14 illustrates the Fast Fourier Transform (FFT) analysis of the vertical velocity within a heat sink system. The FFT analysis is a powerful tool for analyzing the frequency components of a signal, in this case, the temporal vertical velocity of nanofluid. It helps to identify dominant frequencies and understand the dynamics of the nanofluid flow within the heat sink. The peaks in the FFT plot indicate a dominant frequency of 34 Hz (St=1.2) at which the vertical velocity oscillates, revealing periodic oscillations due to flow instabilities. The same analysis using the FFT is employed by other authors (Afrid & Zebib,1990).

Figure 15 illustrates the temporal variation of the Nusselt number of the heat sinks blocks for Re=500 and Φ=0.10. As time increases, the influence of the velocity pulsation component of the nanofluid on the heat transfer rate for each heat sink gradually becomes more pronounced. Ultimately, the variation of the heat transfer approaches a periodic state with time $\tau \geq 10$.
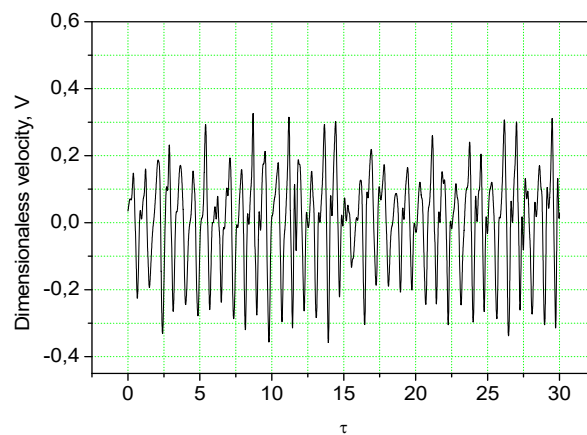
Figure 13 – Temporal evolution of the dimensionless vertical velocity of the nanofluid inside the heat sink system. Re= 2000, ϕ=0.10.
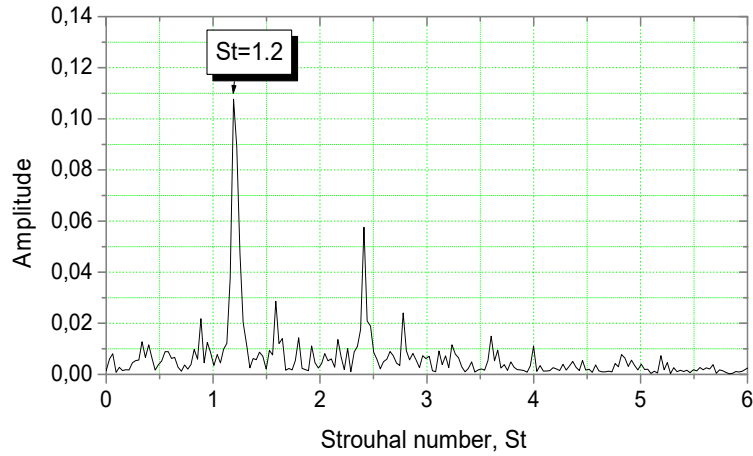
Figure 14 – Fast Fourier Transform of the dimensionless vertical velocity of the nanofluid inside the heat sink system. Re= 2000, φ=0.10. St=1.2, H=0.0074m, U0=0.211 m/s, (f=34 Hz).
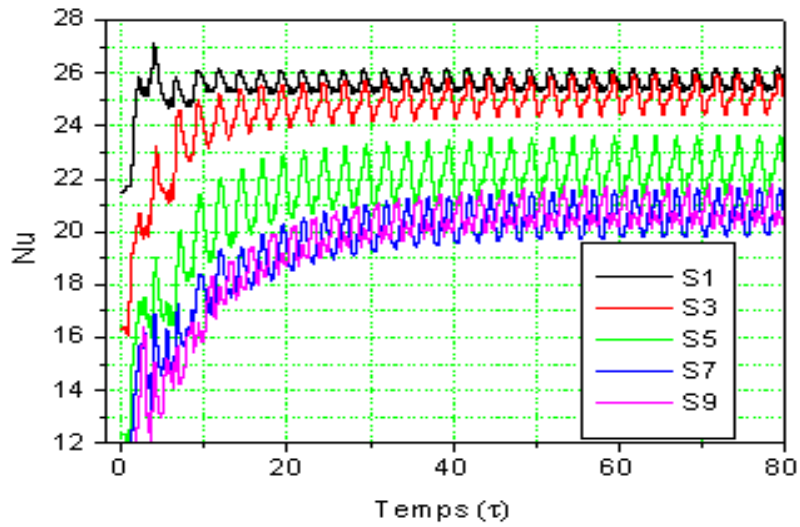
Figure 15 – Distribution of the Nusselt number along the blocks. St=1.2. Re=500 and Φ=0.10. The oscillatory convection inside the channel has been obtained. S1, S3, S5, S7 and S9 denote the heat source numbers.

Calculation of the dimensional temperatures of the heated blocks

The miniaturization in electronic chips has contributed to heavy pressure on heat transfer process, in which huge heat must be effectively removed to protect the components from the dangerous peak temperatures, and kept lower than 85 °C (Bar-Cohen, 1987).

In addition, the reliability of silicon chips can decrease by 50 % for every 10 °C temperature rise.

In the present configuration, the temperature of each electronic component has been calculated by the following formula:

$$T_S = \frac{q.(h/k)}{Nu} + T_a \qquad (20)$$

where
T_s is the temperature of the heated block in °C,
q is the heat flux in W/ m^2,
h is the height of the heated block in m,
Nu is the averaged Nusselt number,
T_a is air temperature in °C (25 °C), and
k is the thermal conductivity of air W/ m.K.

In numerical simulation, we considered that conduction losses across the plate and radiation are neglected. In the practice of cooling electronic components, it is more convenient to estimate the percent dissipation of each mode to properly quantify the average Nusselt number. We consider that the heat flux per area is in the range of 110 and 140 W. The heat dissipation resulting from a processor increases significantly with the voltage and the frequency (Pishkar & Ghasemi, 2012).

It is worth noting that the majority of measurements in the literature are conducted on solid blocks heated by the Joule effect and exposed to high temperatures as in the case of aluminum blocks in the studies by (Moon et al, 2005). However, diodes and transistors mounted on electronic circuit boards typically withstand temperatures ranging from 80 to 90°C. These values depend on the nature of the electronic components and their constituent materials.

Figure 16 illustrates the temperature by varying the Reynolds number at fixed volume fractions of Al_2O_3/water nanoparticles (0.10). It has been observed that for both Al_2O_3/water nanofluids and distilled water, the Nusselt number increases with higher Reynolds numbers, indicating that the temperature of the heat block is sensitive to the Reynolds number.

Figure 17 illustrates that the temperature of the blocks of Al_2O_3/water nanofluids at the volume concentrations of 0.05, 0.10, and 0.15 experiences a significant decrease temperature of 66 °C, 61°C, and 56°C, respectively for the 8th block. This decrease in the temperature is attributed to the greater participation of nanoparticles in the nanofluids, leading to a notable enhancement of thermal conductivity. In essence, the higher the concentration of nanoparticles in nanofluids, the greater the improvement in thermal conductivity, resulting in elevated Nusselt numbers.

The study conducted by (Putra et al, 2011) concluded that the most favorable outcomes were achieved when employing Al_2O_3-water nanofluids. Under an inlet temperature of 30 °C, the average CPU temperature, utilizing water as a coolant in the heat pipe liquid block, was recorded at 39.7 °C. In contrast, temperatures for Al_2O_3-water were measured at 38.5 °C and 37.8 °C for the volume fractions of 0.5% and 1.0%, respectively (Putra et al, 2011).

The pulsation of nanofluids within electronic systems leads to a substantial improvement in heat and mass transfer. This enhancement is attributed to mechanical agitation and micro-convection, particularly facilitated by the Brownian motion of alumina nanoparticles suspended in the base fluid. The pulsation promotes micro-convection along the boundary layer over the surfaces of electronic components at different frequencies, further optimizing heat and mass transfer in the system.

The increase in the volume fraction of nanoparticles (Al_2O_3) in the base fluid (water) leads to an enhancement in the Nusselt number. Additionally, the increase in nanoparticles results in an improvement in the conductive heat transfer coefficient, while the augmentation of mass motion of the fluid contributes to enhanced heat transfer. The same results are obtained by other authors using the Al_2O_3 nanofluid as a cooling fluid inside a rectangular ribbed channel (Parsaiemehr et al, 2018).
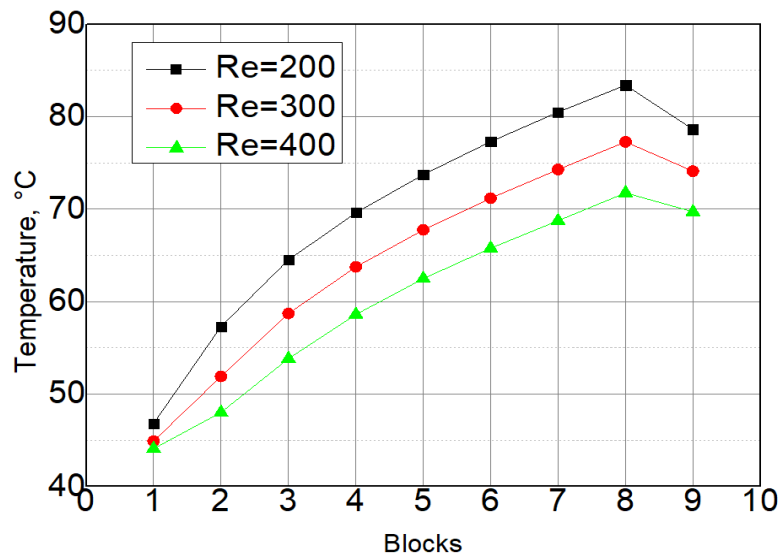
*Figure 16 – Distribution of temperature along the blocks for different Reynolds numbers.
φ=0.15. The increase in Reynolds numbers leads to a decrease in the temperature of
heat sinks, resulting in better cooling performance for thermal systems.*
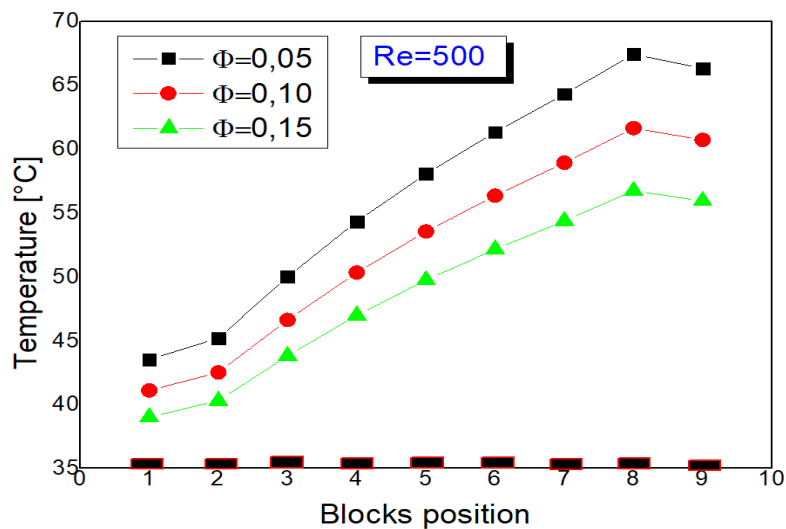
*Figure 17 – Distribution of temperature along the blocks for different nanofluid
concentrations. The increase in nanofluid concentration leads to a decrease in the
temperature of heat sinks, resulting in better cooling performance for thermal systems.*

Conclusion

The growing performance capabilities of electronic devices have led to a corresponding increase in generated heat, necessitating effective thermal management systems for maintaining optimal operating temperatures. Nanofluid cooling presents a compelling and innovative solution for tackling thermal challenges faced by modern electronic devices. Continued research and development in this area have the potential to revolutionize thermal management and significantly improve the performance and reliability of electronic systems across various industries.

The findings of the paper can be summarized as follows:

- The forced convection flow of a nanofluid with and without pulsation at the entrance of a channel equipped with electronic components has been studied numerically. The nanofluid models are introduced into the Navier-Stokes equations coupled with the energy equation.
- The results show that the pulsation of the nanofluid (10% by volume of Al_2O_3 particles), with 50% of the mean flow and with the Strouhal number range of [0.2-1.2], leads to an increase in heat transfer of approximately 30% to 170%. As a result, there is improved cooling of electronic components.
- Nanofluids, which include Al_2O_3 in water, and which are subjected to a pulsation frequency range of [12-34] Hz, exhibit significant temperature reductions at volume concentrations of 0.05, 0.10, and 0.15. On average, a notable decrease of 60 °C is observed across the blocks.
- During nanofluids flow inside an electronic system, the heat and mass transfer can be improved remarkably as a result of mechanical agitation and micro-convection created principally by the Brownian motion of alumina nanoparticles in the base fluid.
- The results of this study can be used to optimize the pumping power of the nanofluid and precisely size the cooling pumps for electronic systems, as well as to control their operating temperatures effectively.
- In the perspective of this study, it is recommended to investigate the impact of acoustic excitation on enhancing the cooling performance of a heat sink using a nanofluid. The analysis should focus on studying the frequency of acoustic excitation and its effects on nanoparticle dispersion within the nanofluid, as well as the resulting Brownian motion, contributing to enhanced heat transfer.

References

Abchouyeh, M.A., Fard, O.S., Mohebbi, R. & Sheremet, M.A. 2019. Enhancement of heat transfer of nanofluids in the presence of sinusoidal side obstacles between two parallel plates through the lattice Boltzmann method. *International Journal of Mechanical Sciences*, 156, pp.159-169. Available at: https://doi.org/10.1016/j.ijmecsci.2019.03.035.

Afrid, M. & Zebib, A. 1990. Oscillatory three-dimensional convection in rectangular cavities and enclosures. *Physics of Fluids A: Fluid Dynamics*, 2(8), pp.1318-1327. Available at: https://doi.org/10.1063/1.857582.

Bar-Cohen, A., Wang, P. & Rahim, E. 2007. Thermal management of high heat flux nanoelectronic chips. *Microgravity Science and Technology*, 19, pp.48-52. Available at: https://doi.org/10.1007/BF02915748.

Bar-Cohen, A. 1983. Thermal Frontiers in the Design and Packaging of Microelectronic. *Equipment Mechanical Engineering*, 150, art.number:53 [online]. Available at: https://cir.nii.ac.jp/crid/1570572699153144192 [Accessed: 02 January 2024].

Bouttout, A. 2023. Forced Convection during Cooling of Power Supply Box using Pulsation Flow with Piezoelectric Fan. *IEEJ Transactions on Electrical and Electronic Engineering*, 18(6), pp.865-875. Available at: https://doi.org/10.1002/tee.23800.

Bouttout, A., Benissaad, S. & Bessaïh, R. 2014. Numerical Study of Forced Convection in a Horizontal Channel with Heated Blocks Due to Oscillation of Incoming Flow. *Numerical Heat Transfer, Part A: Applications*, 65(6), pp.584-600. Available at: https://doi.org/10.1080/10407782.2013.836013.

Brinkman, H.C. 1952. The Viscosity of Concentrated Suspensions and Solutions. *The Journal of Chemical Physics*, 20(4), art.number:571. Available at: https://doi.org/10.1063/1.1700493.

Choi, S.U.S. & Eastman, J.A. 1995. Enhancing thermal conductivity of fluids with nanoparticles. In: *International mechanical engineering congress and exhibition*, San Francisco, CA, USA, November 12-17 [online]. Available at: https://www.osti.gov/biblio/196525 [Accessed: 02 January 2024].

Farhanieh, B., Herman, Č. & Sundén, B. 1993. Numerical and experimental analysis of laminar fluid flow and forced convection heat transfer in a grooved duct. *International Journal of Heat and Mass Transfer*, 36(6), pp.1609-1617. Available at: https://doi.org/10.1016/S0017-9310(05)80070-5.

Furukawa, T. & Yang, W.-J. 2003. Thermal-fluid flow in parallel boards with heat generating blocks. *International Journal of Heat and Mass Transfer*, 46(26), pp.5005-5015. Available at: https://doi.org/10.1016/S0017-9310(03)00357-0.

Greiner, M. 1991. An experimental investigation of resonant heat transfer enhancement in grooved channels. *International Journal of Heat and Mass Transfer*, 34(6), pp.1383-1391. Available at: https://doi.org/10.1016/0017-9310(91)90282-J.

Maxwell, J.C. 2010. *A Treatise on Electricity and Magnetism, Volume 1*. Cambridge University Press. Available at: https://doi.org/10.1017/CBO9780511709333.

Mohammed, H.A., Alawi, O.A. & Wahid, M.A. 2015. Mixed convective nanofluid flow in a channel having backward-facing step with a baffle. *Powder Technology*, 275, pp.329-343. Available at: https://doi.org/10.1016/j.powtec.2014.09.046.

Moon, J.W., Kim, S.Y. & Cho, H.H. 2005. Frequency-dependent heat transfer enhancement from rectangular heated block array in a pulsating channel flow. *International Journal of Heat and Mass Transfer*, 48(23-24), pp.4904-4913. Available at: https://doi.org/10.1016/j.ijheatmasstransfer.2005.06.006.

Moon, J.W., Kim, S.Y. & Cho, H.H. 2002, January. An Experimental Study on Forced Convection From a Rectangular Heated Block by Acoustic Excitation in a Channel Flow. In: *ASME International Mechanical Engineering Congress and Exposition,* New Orleans, Louisiana, USA, paper no:IMECE2002-33721, pp.81-88, November 17-22. Available at: https://doi.org/10.1115/IMECE2002-33721.

Parsaiemehr, M., Pourfattah, F., Akbari, O.A., Toghraie, D. & Sheikhzadeh, G. 2018. Turbulent flow and heat transfer of Water/Al_2O_3 nanofluid inside a rectangular ribbed channel. *Physica E: Low-Dimensional Systems and Nanostructures*, 96, pp.73-84. Available at: https://doi.org/10.1016/j.physe.2017.10.012.

Patankar, S. 1980. *Numerical Heat Transfer and Fluid Flow, 1st Edition*. Boca Raton: CRC press. Available at: doi.org/10.1201/9781482234213.

Pishkar, I. & Ghasemi, B. 2012. Cooling enhancement of two fins in a horizontal channel by nanofluid mixed convection. *International Journal of Thermal Sciences*, 59, pp.141-151. Available at: https://doi.org/10.1016/j.ijthermalsci.2012.04.015.

Putra, N., Yanuar,nd & Iskandar, F.N. 2011. Application of nanofluids to a heat pipe liquid-block and the thermoelectric cooling of electronic equipment. *Experimental Thermal and Fluid Science*, 35(7), pp.1274-1281. Available at: https://doi.org/10.1016/j.expthermflusci.2011.04.015.

Young, T.J. & Vafai, K. 1998. Convective flow and heat transfer in a channel containing multiple heated obstacles. *International Journal of Heat and Mass Transfer*, 41(21), pp.3279-3298. Available at: https://doi.org/10.1016/S0017-9310(98)00014-3.

Transferencia de calor por resonancia durante la convección forzada del nanofluido Al_2O_3 en un canal horizontal con disipador de calor

Abdelouahab Bouttout

Centro Nacional de Estudios e Investigaciones Integradas de la Construcción (CNERIB), Argel, República Argelina Democrática y Popular

CAMPO: ingeniería mecánica
TIPO DE ARTÍCULO: artículo científico original

Resumen:

Introducción/objetivo: Los continuos avances en las tecnologías de dispositivos electrónicos han llevado a mayores densidades de energía, lo que resulta en una generación sustancial de calor durante su funcionamiento. La gestión térmica eficiente es esencial para mantener un rendimiento óptimo, prolongar la vida útil del dispositivo y prevenir fallas inducidas térmicamente. Los métodos de enfriamiento tradicionales, como el enfriamiento por aire y por líquido, han alcanzado sus limitaciones a la hora de satisfacer las crecientes demandas de enfriamiento. En consecuencia, la implementación de nanofluidos como un nuevo medio de enfriamiento ha ganado mucha atención en los últimos años.

Métodos: El presente estudio tiene como objetivo determinar la banda ancha de frecuencias para las cuales la transferencia de calor es máxima durante el enfriamiento de nueve componentes electrónicos montados en un canal horizontal utilizando el nanofluido Al_2O_3. Este fenómeno se llama transferencia de calor por resonancia y ocurre cuando la frecuencia del forzamiento externo (pulsación u oscilación) coincide con la frecuencia natural del flujo convectivo del nanofluido. Se ha utilizado el método del volumen finito para resolver la ecuación gobernante. En este trabajo se consideran dos casos: flujo de entrada uniforme y pulsado. Los componentes electrónicos se han considerado como bloques calentados con el mismo espacio entre ellos.

Resultados: Los resultados muestran que el flujo es inestable para el nanofluido crítico con número de Reynolds Re≈2000 Al_2O_3 con una frecuencia como el número de Strouhal St = 1.2 y una concentración de fracción de 0.10. Corresponde a una velocidad de flujo de 0.211 m/s y una frecuencia dominante de fr=34 Hz.

Conclusión: La transferencia de calor mejorada se calcula como la relación del número de Nusselt de flujo pulsante con el número de Nusselt de flujo uniforme. Se puede lograr una tasa de transferencia de calor mejorada del 30 al 170 % dentro de una banda del número de Strouhal St = [0.2-1.2] correspondiente a una banda de frecuencia fr = [12-34] Hz.

Palabras claves: nanofluido, resonancia, transferencia de calor, disipador de calor, convección, número de Strouhal.

Резонансный теплообмен при принудительной конвекции наножидкости Al_2O_3 в горизонтальном канале с системой охлаждения

Абделуахаб Буттаут

Национальный центр комплексных исследований в области строительства (CRIB),
г. Алжир, Алжирская Народная Демократическая Республика

Резюме:

Введение/цель: Постоянный технологический прогресс электронных устройств привел к повышению плотности электрической энергии, которая, в свою очередь, выделяет значительное количество тепла во время эксплуатации. Эффективное управление температурным режимом необходимо для поддержания оптимальной производительности, продления срока службы устройства и предотвращения поломок, вызванных перегревом. Традиционные методы охлаждения с помощью воздуха и жидкости не отвечают возросшим потребностям в охлаждении. Вследствие чего применение наножидкостей в качестве нового охлаждающего средства в последнее время приобретает большую значимость.

Методы: Целью данного исследования является определение широкого диапазона частот в условиях максимального теплообмена при охлаждении девяти электронных компонентов, установленных на горизонтальном канале, с помощью наножидкости Al_2O_3. Это явление называется резонансной теплопередачей и возникает, когда частота внешнего воздействия (пульсации или колебания) совпадает с собственной частотой конвективного течения наножидкости. Для решения основного уравнения использовался метод конечных объемов. В данной статье рассматриваются два случая: равномерный и пульсирующий входной поток. Электронные компоненты представляют собой блоки, которые нагреваются и расположены на равном расстоянии друг от друга.

Результаты: Результаты исследования показали, что течение неустойчиво при критическом числе Рейнольдса $Re \approx 2000$ для наножидкости Al_2O_3 с частотой, равной числу Струхаля $St = 1,2$, и концентрацией фракции 0,10. Это соответствует скорости потока 0,211 м/с и преобладающей частоте $fr = 34$ Гц.

Вывод: Улучшенная теплопередача рассчитывается как соотношение числа Нуссельта для пульсирующего потока и числа Нуссельта для равномерного потока. Повышенная скорость теплопередачи может быть достигнута на 30-170% в диапазоне чисел Струхаля $St = [0,2-1,2]$, соответствующем диапазону частот $fr = [12-34]$ Гц.

Ключевые слова: наножидкость, резонанс, теплопередача, система охлаждения, конвекция, число Струхаля.

Резонантни пренос топлоте током форсиране конвекције нанофлуида Al_2O_3 у хоризонталном каналу са хладњаком

Абделуахаб Бутаут

Национални центар за изградњу интегрисаних студија и истраживања (CNERIB), Алжир, Народна Демократска Република Алжир

Сажетак:

Увод/циљ: Стални напредак у технологијама електронских уређаја довео је до повећаних густина електричне енергије што производи знатне количине топлоте током њиховог рада. Ефикасно управљање топлотом је суштинско за одржавање оптималних перформанси, продужавање века трајања уређаја, као и за спречавање кварова узрокованих топлотом. Традиционалне методе хлађења, на пример ваздухом и течношћу, нису више у стању да прате повећане потребе за хлађењем. Зато примена нанофлуида, као новог расхладног средства, у последње време добија на значају.

Методе: Циљ ове студије јесте да одреди широки опсег фреквенција за које је пренос топлоте максималан током хлађења девет електронских компоненти постављених на хоризонтални канал помоћу нанофлуида Al_2O_3. Ова појава се назива резонантни пренос топлоте и до ње долази када се фреквенција спољашње принуде (пулсирања или осцилације) поклапа са природном фреквенцијом конвективног тока нанофлуида. Метода коначних запремина коришћена је у решавању водеће једначине. Разматрана су два случаја: униформни и пулсни улазни проток. Електронске компоненте представљају блокове који се греју и налазе се на подједнаком растојању једни од других.

Резултати: Показано је да је проток нестабилан за критични Рејнолдсов број $Re≈2000$ нанофлуида Al_2O_3 са фреквенцијом као Строхаловим бројем $St=1,2$ и концентрацијом фракција од 0,10, што одговара брзини протока од 0,211 m/s и доминантној фреквенцији од $fr=34$ Hz.

Закључак: Повећани пренос топлоте израчунава се као брзина Нуселтовог броја пулсног протока са Нуселтовим бројем равномерног протока. Повећана брзина преноса топлоте може се постићи 30–70% унутар опсега Строхаловог броја $St=[0,2–1,2]$, што одговара опсегу фреквенције $fr =[12–34]$ Hz.

Кључне речи: нанофлуид, резонанција, пренос топлоте, хладњак, конвекција, Строхалов број.

Paper received on: 02.01.2024.
Manuscript corrections submitted on: 16.11.2024.
Paper accepted for publishing on: 18.11.2024.

Design and performance of a manual extruder for recycled plastic-brick composite pavers

Abdelkader Daikh[a]*, Youcef* Moulai Arbi[b],
Mohammed Bentahar[c], *Noureddine* Mahmoudi[d]

[a] University of Mustapha Stambouli, Faculty of Technology,
   Department of hydraulics,
   Mascara, People's Democratic Republic of Algeria,
   e-mail: daikhaek@gmail.com,
   ORCID ID: https://orcid.org/0009-0006-4090-4516

[b] University of Mustapha Stambouli, Laboratory of Quantum Physics of
   Matter and Mathematical Modeling (LPQ3M),
   Mascara, People's Democratic Republic of Algeria,
   e-mail: youcef.moulaiarbi@univ-mascara.dz, **corresponding author**,
   ORCID ID: https://orcid.org/0000-0002-6534-8820

[c] Universiy of Saida Dr. Moulay Tahar, Faculty of Technology,
   Department of Civil Engineering and Hydraulics,
   Saida, People's Democratic Republic of Algeria,
   e-mail: bentahae@yahoo.fr,
   ORCID ID: https://orcid.org/0000-0002-2166-678X

[d] Universiy of Saida Dr. Moulay Tahar, Faculty of Technology,
   Department of Civil Engineering and Hydraulics,
   Saida, People's Democratic Republic of Algeria,
   e-mail: mahmoudi.noureddine@yahoo.fr,
   ORCID ID: https://orcid.org/0000-0002-9740-0857

FIELD: mechanical engineering, civil engineering
ARTICLE TYPE: original scientific paper

Abstract:

Introduction/purpose: This study aimed to develop a cost-effective manual plastic brick extruder for manufacturing composite bricks from recycled polypropylene and brick powder. The goal was to address housing challenges in developing countries while promoting sustainable waste management.

Methods: A single screw extruder with a 60 mm die was fabricated, featuring a manual crank, a heating system, and a hopper. Composite specimens with varying polypropylene (30-80 weight percentages) and brick powder (20-70 weight percentages) ratios were produced. Mechanical testing was conducted, including compressive strength, flexural strength, impact resistance, and density measurements.

Results: The 40:60 polypropylene:brick powder mixture exhibited optimal compressive strength, ranging from 23.76-24.90 MPa. Flexural strength

peaked at the 50:50 ratio (11.86-12.5 MPa). Impact resistance decreased with increasing brick powder content. Density increased linearly with brick powder content, ranging from 1.48-1.77 g/cm³. The extruder successfully produced uniform composite specimens across all mixtures.

Conclusions: The study demonstrated the feasibility of producing composite bricks using a low-cost, manually operated extruder. Two optimal mixture compositions were identified: 40:60 polypropylene:brick powder for maximum compressive strength and 50:50 for optimal flexural strength. This approach offers a promising solution for affordable housing construction while addressing plastic waste management in developing regions. Future research should focus on optimizing the extrusion process, exploring additional waste materials, and conducting long-term durability studies of composite bricks.

Key words: manual extruder, polypropylene, brick powder, composite, pavers.

Introduction

Composite materials, integral to modern materials science and engineering, combine distinct phases to achieve superior properties. Comprising a matrix and reinforcing elements, these materials offer tailored characteristics that surpass individual components.

The synthesis of polymer-ceramic composites represents a significant frontier in materials science, combining the flexibility and low density of polymers with the high strength, hardness, and thermal stability of ceramics. The melting method emerges as a key technique in this field, wherein the polymer matrix is transformed into a molten state to facilitate the integration of ceramic reinforcements. This approach allows for the creation of materials that synergistically blend the advantageous properties of both constituents (Ali et al, 2023). The meticulous control of temperature during the melting phase ensures the homogenous dispersion of ceramic particles within the molten polymer. Subsequent cooling solidifies the composite, leading to a final material with a synergistic blend of properties. The melting method offers precision in tailoring the composite's microstructure, resulting in enhanced mechanical, thermal, and functional characteristics.

Polymer-ceramic composites, produced via cost-effective methods like melting, offer an innovative solution for plastic brick manufacturing in developing countries. These composites combine polymer flexibility with ceramic strength, creating affordable, durable bricks ideal for refugee housing or earthquake-prone areas (Moulai Arbi, 2024). This approach offers dual benefits: providing affordable construction materials and

reducing waste through plastic recycling. It presents a sustainable solution for resource-constrained regions while advancing eco-friendly, economical building materials globally. (Thatheyus et al, 2020)

In their study, Patil et al. (2020) conducted an experimental study on manufacturing plastic sand bricks using waste polypropylene (PP) and polyethylene (PET). They processed post-consumer plastic waste, melting PP and PET at 160°C and 180°C, respectively, and mixed them with sand in ratios from 1:2 to 2:5. Six brick samples were produced and tested according to standard methods. Notably, the brick with a 2:1 plastic-to-sand ratio achieved a compressive strength of 12.43 N/mm², exceeding that of traditional clay bricks. The samples also exhibited excellent durability, with zero efflorescence and low water absorption rates (0-2.82%). This study demonstrates the potential of converting plastic waste into high-quality construction materials.

Moulai Arbi et al. (2023) investigated the enhancement of thermal and mechanical properties of waste polyethylene terephthalate (PET) composites by incorporating brick sand reinforcement. The study evaluated the effects of varying sand filler content (30% to 45%) on the degradation temperature, glass transition, crystallization temperatures, tensile strength, Young's modulus, and Charpy impact strength. The addition of 45 wt% sand significantly improved the thermal degradation temperature from 220°C in neat PET to over 314°C. Optimal tensile strength (26.26 MPa) and Young's modulus (2771 MPa) were achieved at 30 wt% sand, but further increases in the filler content led to a decrease in Charpy impact strength due to poor interfacial adhesion.

Hamzah & Alkhafaj (2022) developed an innovative method for producing lightweight, eco-friendly bricks using low-density polyethylene (LDPE) plastic waste, such as medical syringes, combined with natural fillers like sawdust and sand. The study evaluated the mechanical and physical properties of these bricks. Bricks with 20% sawdust filler showed superior compressive strength (66 MPa) compared to those with higher sand content (61 MPa at 60% filler). Sand-filled bricks had low water absorption rates (under 1%), while sawdust variants absorbed up to 21%. The bricks' density varied, with 0.7 g/cm³ for 50% sawdust, and hardness peaked at 70D with 60% sand content.

Lamba et al. (2022) reviewed researchers using the hand rod mixing method to create plastic brick composites. This artisanal technique involves manually blending polymer and ceramic materials, highlighting a handcrafted approach, but it has significant scalability limitations. The hand rod mixing method, though meticulous, is inefficient for large-scale plastic brick production. Its manual nature limits rapid manufacturing and

1804

consistent quality, making it impractical for mass production despite its craftsmanship appeal.

Plastic extruders provide an efficient, automated solution for producing uniform filaments from recycled plastic, enhancing sustainability in material repurposing (Abeykoon et al, 2016).

Qin et al. (2024) analyzed extruder screw design and plastic wire diameter control, emphasizing the importance of die design and heater temperature for optimal efficiency. The study also highlighted extrusion technology's adaptability in recycling thermoplastic materials.

Hanifah et al. (2023) examined the impact of screw-barrel clearance and cooling fans on non-wheat noodle extruders. They found that reducing clearance and using cooling fans improved the extruder performance by preventing backflow, maintaining temperature, and enhancing the noodle quality and energy efficiency.

Reichel & Krause (2016) investigated waste heat during the extrusion of tubular profiles, focusing on energy efficiency and heat reuse. Their study identified opportunities for utilizing waste heat in single grooved barrel extruders. However, current extruder applications are mainly limited to thin plastic filaments for testing or 3D printing, with challenges in processing thicker materials, limiting broader industrial use.

Plastic extruders face limitations in producing polymer-ceramic composites due to their thin exit holes, hindering large-scale manufacturing of composite bricks. To address this, a dedicated plastic brick extruder has been proposed, designed to handle the unique requirements of polymer-ceramic composites. This specialized extruder, available in both manual and automated versions, aims to overcome the exit hole constraint and facilitate the production of larger structures. It features a large spiral screw and a dual-mode turning mechanism for enhanced efficiency and cost-effectiveness, particularly suited for developing countries. This innovation promises to advance composite material production and offer sustainable solutions for housing and infrastructure challenges.

Plastic brick extruder

The fabricated extruder is a single screw extruder. Single screw extruders are extruders which have only one screw in the system. They are commonly used for simple and general materials. In recent years, a lot of research has been done for more constant and stable extrusion. In extruders, a material is mixed inside the barrel until the length of the extrusion machine.

Extruders typically consist of mechanical parts and electrical parts.

Mechanical parts

Manual crank

The crank handle, an essential component of manual extruders, serves as a manual actuation mechanism for rotating the extruder screw within the barrel. This hand-operated device is characterized by its ergonomic design, facilitating the user's application of rotational force to the screw (Figure 1a)). Integral to its functionality is the presence of a notch (Figure 1b)) strategically positioned along its circumference. This notch serves a pivotal role by engaging with a complementary feature on the screw shaft, ensuring precise alignment and secure attachment. Through this engagement, the crank handle effectively translates the rotational motion exerted by the user into the corresponding movement of the extruder screw, thereby facilitating the controlled extrusion process essential for plastic processing applications.
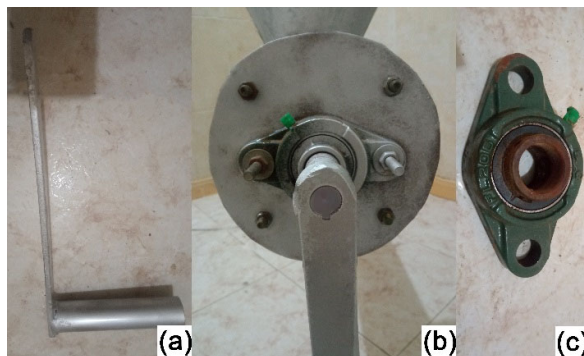
Figure 1 – (a) Crank handle, (b) notch for the crank handle, (c) Self-aligning bearing housings

The self-aligning bearing housings are pivotal components within manual extruder assemblies, instrumental in securing and positioning the extruder screw within the barrel (Figure 1c)). Crafted from durable cast iron, these housings provide robust support to the screw shaft, effectively enduring the mechanical stresses inherent to extrusion operations. Their inherent self-aligning capability enables them to adapt to minor misalignments, thereby enhancing operational efficiency and prolonging the extruder's lifespan. By ensuring the secure and precise fixation of the screw shaft, these bearing housings play a vital role in facilitating consistent and accurate plastic extrusion, meeting stringent quality requirements across diverse industrial applications.

Hopper

The hopper in Figure 2 serves as a pivotal component in the plastic extrusion process, acting as the entry point for raw materials into the extruder barrel. Typically situated atop the extruder assembly, the hopper provides a reservoir for the plastic pellets or granules, ensuring a continuous supply of material for the extrusion process. Its design often incorporates features to facilitate efficient material feeding, such as a wide opening for easy loading and a sloped interior to promote material flow towards the extruder screw.

The larger diameter opening at the top of the hopper, where materials are loaded, is a "filling port." In addition, it has a diameter of 20 mm. The smaller diameter opening, situated at the bottom of the hopper and connecting to the extruder barrel, is a "feeding inlet" and its diameter is 10 mm.

Figure 2 – Hopper

The feet of the extruder, integral to its stability and support, are constructed from stainless steel. These feet are engineered to withstand the mechanical forces exerted during extrusion operations while ensuring the extruder remains securely anchored to the operating surface. Additionally, the incorporation of small holes within these feet enhances

their functionality by providing convenient attachment points for securing the extruder to auxiliary surfaces, such as wooden platforms or workbenches. Through these strategically positioned holes, users can employ screws or bolts to firmly affix the extruder, thereby optimizing its operational stability and minimizing the risk of movement or displacement during use.

Screw

Fabrication of a screw involves precise and methodical processes to ensure optimal performance and durability. The initial step in fabrication is the cutting and shaping of the screw flights as seen in Figure 3, which are typically made from flat metal sheets of stainless steel. These sheets are cut into the desired flight shapes, then formed into helical structures using metal forming tools. Once shaped, the flights are meticulously welded onto a central shaft, ensuring strong and smooth welds to prevent material buildup and ensure structural integrity.
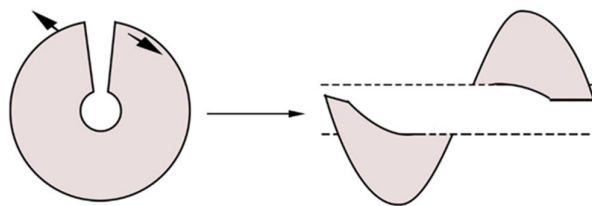
Figure 3 – Screw fabrication method

The screw conveyor under consideration features a pitch of 140 mm, a critical dimension influencing the material flow rate and conveying efficiency (Figure 4). The screw has a unique design, with a small diameter of 50 mm and a larger diameter of 160 mm, indicating a tapered or variable diameter design that can accommodate varying material characteristics and flow requirements. This design ensures efficient handling of materials by gradually increasing the conveyor's capacity along its length, thereby optimizing the load distribution and reducing the risk of blockages. The total length of the screw conveyor is 1000 mm, providing a substantial conveying distance suitable for various industrial applications. The combination of these dimensions—specifically, the 140 mm pitch with a tapered screw design—facilitates smooth and efficient material transport.
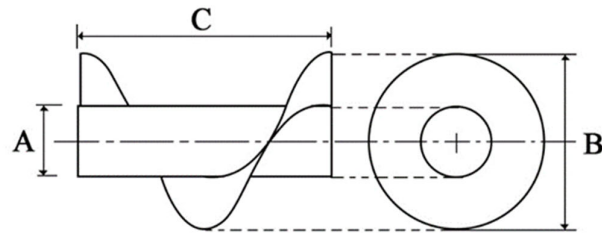
Figure 4 – screw conveyor dimensions

A= 50 mm
B= 160 mm
C= 140 mm

Figure 5 shows the manufactured screw. Typical plastic extruder screws have three zones of heating (feed zone, compression zone, and metering zone); however, our work does not include these zones because it works with big quantity of plastic and brick and the temperature is uniform all over the tube in order to avoid difficulty in moving the mixture.
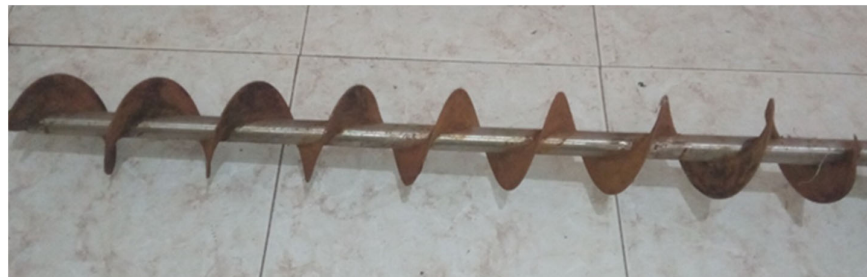
Figure 5 – Manufactured screw conveyor

Electrical parts

Electrical heaters are widely used nowadays because they are very efficient and cost reducing. They are not expensive to maintain in comparison to other heating systems.

A certain amount of current passes through the conductor with a certain resistance which works as a barrier in the flow and generate heat. The heat thus obtained is given below in the equation of Joule's Law:

$$Q = I^2Rt = VIt = V^2/Rt \tag{1}$$

where:

Q=charge flow, R = resistance , I= current, V= voltage, and t= time .

Resistors as shown in Figure 6 are connected in parallel; they are subjected to the same voltage. Each resistor will have the same voltage across it, resulting in the same current flowing through each one. This ensures that they all generate the same amount of heat and thus maintain the same temperature.

Heating bands

The heating bands are manually fabricated by forming a cylindrical shape using ceramic paste (Figure 6a)), followed by creating four holes to allow electrical wires to pass through. Subsequently (Figure 6b)), the bands are cut in half to facilitate their installation in the extruder. The four heating bands in the extruder serve to prevent the transmission of electricity to the external body, ensuring safety.
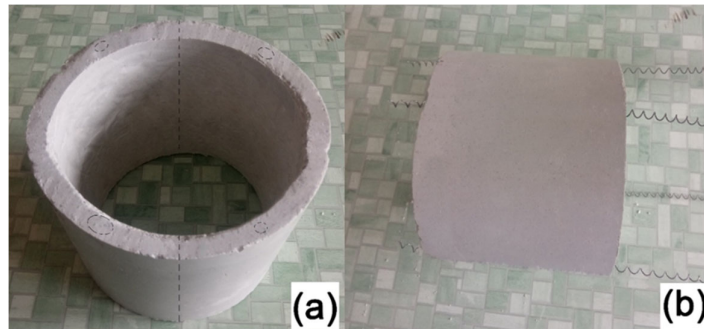
Figure 6 – (a) Heating bands, (b) Heating bands with resistance wires

PID controller

A PID (Proportional-Integral-Derivative) controller is a device which provides the Information to SSR (Solid State Relay) when to turn on and when to turn off. A PID reads the temperature of any system with the help of a thermostat. It functions as the input panel to the system (Figure 7a)).

General-purpose temperature controllers are used to control most typical processes in industry. Typically, they come in a range of DIN sizes and have multiple outputs and programmable output functions. These controllers can also perform PID control for excellent general control

situations. They are traditionally placed in the front panel with the display for easy operator accessibility. These controllers have a pre-tune function to initially calculate the PID temperature for a process, and a continuous tune function to constantly refine the PID temperature. This allows for quick setup, saving time and reducing waste.

A sensor which is used to measure the temperature is known as a thermocouple. It consists of two wires made of different metals. When the two materials are subjected to the heat, it produces some electric voltage, which determines the reading of the temperature in the system. Thermocouples are used for their low cost, durability, and a high temperature range.

Thermocouple

The thermocouple (Figure 7b)), was connected to the input port. This port was the place where the heat sensor was connected. It was able to read temperature of the tube after connecting.

This enabled switching the heater on and off after obtaining required temperature. The power supply for the heater was also supplied thus completing the electrical wiring of the heat control mechanism.
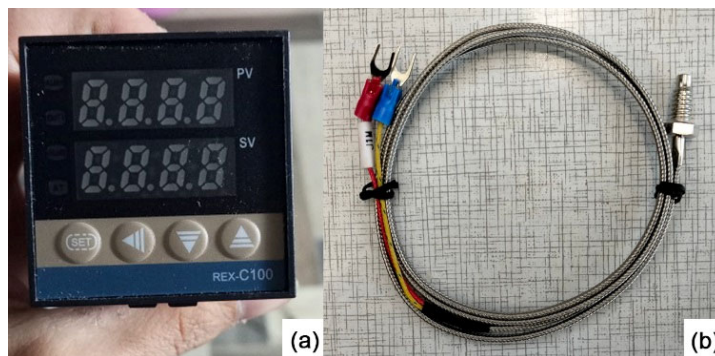
Figure 7 – (a) PID controler, (b) Thermocouple

Full body

Figure 8 illustrates the complete structure of the extruder, highlighting its essential components for its operation. The extruder features a tubular trough with a total length of 1400 mm, providing an extended path for the material to be processed. At the end of the trough, there is an exit hole, also known as the nozzle, which has a diameter of 60 mm. This exit hole

is crucial for shaping the extruded material as it exits the conveyor. Additionally, the extruder includes a cylinder that encapsulates the resistance section, designed to maintain the necessary temperature for efficient extrusion. This cylinder, often referred to as a heating barrel, ensures that the material within the extruder remains at a consistent and optimal temperature, preventing cooling and solidification before it reaches the exit hole.

Figure 8 – Manuel plastic brick extruder

Preparation of plastic bricks

After the assembly of the extruder parts was completed, the machine was left 30 min with turning on the heat of 160 C°. After acquiring the stable temperature, the crank handle was turned on. The pellets and brick powder were then poured into the hopper. The handle turns at a speed of 5 rpm.

The composite was driven by the screw along the barrel. When the composite reached the heating section, it started melting and the pressure was created inside the tube. Due to heating from the heater, the temperature rises and completely melts the plastic. The paste was extruded through the die hole with a diameter of 60 mm.

Sand brick

Brick waste was collected from a brick factory. As shown in Figure 9, brick waste passed through a crushing process in order to obtain brick powder. The sieve pass used is 80μm. The brick powder was analyzed in the LAFARGE Company.

Figure 9 – Crushing presses for brick powder

Table 1 lists the chemical compositions and the physical characteristics of brick powder.

X ray diffraction analysis (XRD) is a technique used to analyze the crystalline structure of materials, while X-ray Fluorescence (XRF), is a technique used to determine the elemental composition of materials. The utilized machines are the Bruker S8 for XRF and the Bruker D4 for XRD.

The results show that the sum of the components [Al2 O3 + Fe2 O3 + SiO2] for brick powder is 83.37%, which meets the requirements of ASTM C618. PAF (Particulate Airborne Fraction) is a column that contains a value representing the particulate airborne fraction, which is often a measure of the proportion of airborne particles emitted during a particular process or activity. It is reported as 0.74 (R_wp) and contains a value representing the weighted profile R-factor, which is a measure of the agreement between the observed and calculated X-ray diffraction patterns.

Table 1 – Properties of brick powder

Chemical composition (%)										
Compon ents	SiO2	Al2O3	Fe2 O3	CaO	MgO	K2O	Na 2O	SO3	Loss	PA F
Quantity (%)	62.45	14	6.92	8.54	2	2.07	0.2 2	0.59	3.21	0.7 4
Mineral phases (W %)										
R_wp	calc ite	dolo mite	quar tz	illite	kaoli nite	chlor ite	albi te	microl ine	diasp ore	top az
7.54	0.95	3.97	47.48	17.17	0.75	0.43	11.81	13.71	0.27	3.96
Physical characteristics										
Density (g/cm3)	2.43									
Blaine-specific surface (cm2/g)	3140									

Abdelkader, D. et al, Design and performance of a manual extruder for recycled plastic-brick composite pavers, pp.1802-1831

Polypropylene

PP is a strong lightweight plastic from the polymer family, known as a nonbiodegradable thermoplastic with a strong moisture barrier. PP, like all thermoplastics, becomes liquid at its melting point (160°C) and can be cooled without significant degradation of its properties. The excellent properties of PP made it commonly used in everyday items.

PP is used in this work as a matrix. PP waste was collected and cleaned with tap water to remove all forms of contaminants and harmful materials before sun drying for at least 3 days. The dried waste was then ground and pulverized into pellets ranging in size from 1 mm to 8 mm. Figure 10 shows the ground material.

Figure 10 – Polypropylene particles.

Preparation of test specimens

PP and brick powder were dried at 50° in the oven and then passed into the fabricated plastic brick extruder at a temperature of 160°. After that, the melted mixture was recovered at the outlet and then put into molds. The utilized molds are for mechanical tests, compressive strength, flexural strength, Charpy test and cylindrical compressive test. The molds were oiled in order to facilitate specimen's removal.

The dimensions of the compressive strength specimens are cubic: 50mmX50mmX50mm in accordance with ASTM C109 (ASTM, 2020).

The dimensions of the flexural strength specimens are prismatic: 40mmX40mmX160mm in accordance with ASTM C78 (ASTM, 2022).

The dimensions of the Charpy test specimens are prismatic with a V notch of angle 45° in the middle: 40mmX40mmX160mm in accordance with ASTM D6110 (ASTM, 2018).

The dimensions of the cylindrical test specimens are 160mmX320mm (diameter x height) in accordance with ASTM C39 (ASTM, 2023).

Figure 11 displays the prismatic specimens with varying weight percentages of polypropylene (PP) in the mixture, ranging from 30 w% to 80 w%. The specimens with less than 30 w% PP could not form correctly because the low PP content was insufficient to properly bind the reinforcement. Conversely, the specimens with more than 80 w% PP exhibited poor distribution of brick powder, leading to clusters of PP and brick powder that made the specimens prone to cracking. Consequently, these specimens were excluded from the testing.

Figure 11 – Plastic brick specimens (prismatic).

Table 2 presents the mixtures with different PP W% and brick powder W%. Six samples were obtained for every mixture. Only for the cylindrical test specimens there were three samples. The mixture utilized for the cylindrical test specimen is based on the high results of the compressive strength test.

Table 2 – Mixtures with different weight percentages

Mixtures n°	M_1	M_2	M_3	M_4	M_5	M_6
PP weight%	80	70	60	50	40	30
Brick powder weight%	20	30	40	50	60	70

Mechanical tests

Mechanical tests were conducted on the specimens to investigate their performance under various conditions.

Bending test

Figure 12 presents the utilization of the three-point bending methodology employing an ELE International machine where the maximum applied load is quantified in kilonewtons (kN). This approach determines flexural strength by dividing the maximum load by the specimen's cross-sectional area, yielding a measurement expressed in newton's per square millimeter (N/mm²), commonly referred to as megapascals (MPa). Prismatic specimens are subjected to bending forces, necessitating pre- and post-testing observations to discern any structural alterations. This experimental procedure offers indispensable insights into a material's capacity to endure bending stresses, furnishing invaluable empirical evidence for engineering and material science inquiries.
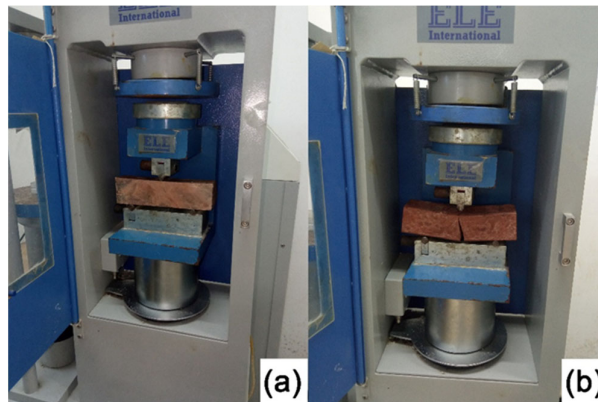
Figure 12 – Three-point bending test (a) before the test, (b) after the test

Compressive strength test

Figure 13 illustrates the compression testing process before (fFgure 13a)) and after the test (Figure 13b)), conducted utilizing an ELE International machine, with the cubic specimens employed for evaluation. The compressive strength of the material is assessed through this method. Similarly to the bending test, the specimens undergo observation both before and after compression to identify any structural changes. This experimental approach, facilitated by the ELE International apparatus,

provides crucial insights into the material's ability to withstand compressive forces by comparing the conditions of the specimens before and after the testing.
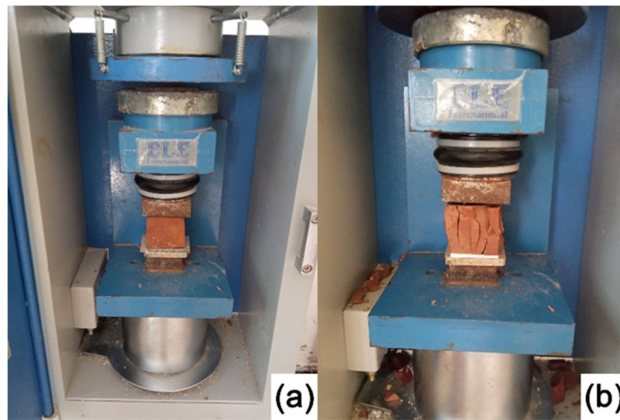
Figure 13 – Compressive test, (a) before the test, (b) after the test

Charpy test

Figure 14 displays the prismatic specimen featuring a notch (Figure 14a) , 14b)), alongside the JB-300B machine utilized for Charpy impact testing (Figure 14c)). This test, conducted to assess a material's resistance to sudden impact, yields results in terms of impact energy, measured in joules (J). The specimen is subjected to a swinging pendulum, which strikes the notched area, causing fracture. The amount of energy absorbed by the specimen before fracture provides crucial information about its toughness and resilience.
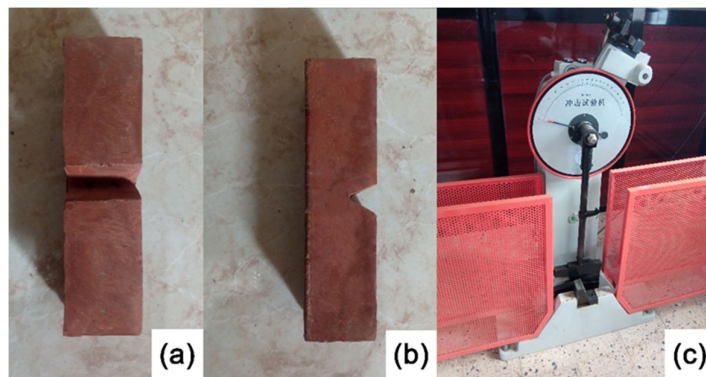
Figure 14 – Charpy test, (a,b) notched specimen, (c) test machine

Compressive strength (160X320 cylinder)

Figure 15 presents the cylindrical specimen used for compressive strength testing (Figure 15a)), alongside the RP 3000 XP machine employed for the procedure (Figure 15b)). This test, conducted on a 160x320mm cylindrical specimen, aims to determine the material's compressive strength. The RP 3000 XP machine applies a gradually increasing load to the specimen until failure occurs, allowing for the measurement of the maximum compressive force endured by the material.
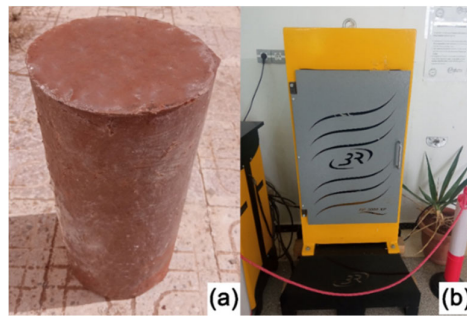
Figure 15 – Compression test of cylindrical specimens (a), using a test machine (b).

Density test

The cubic specimens were weighed using an electronic scale in Figure 16 to determine their mass in grams (g), then their volume in cubic centimeters (cm^3), which allowed us to use the equation below to determine their density.

$$\rho = \frac{m}{v} \qquad (2)$$
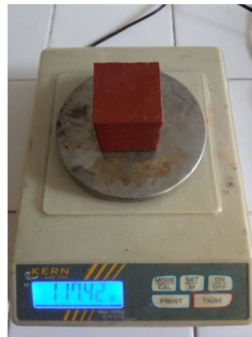
Figure 16 – Density test

Results and discussion

The experimental results obtained from the controlled tests bellow are designed to analyze the composite obtained from the production, and to understand the overall properties of the material.

Flexural strength results

Table 3 presents the results of the specimens subjected to the flexural test. The mixture M4 (composed of 50 w% polypropylene and 50 w% brick powder) demonstrated the highest resistance to bending, with the flexural strength values ranging from 11.86 MPa to 12.5 MPa across all samples. The mixture M5 showed slightly lower resistance, with the values between 11.21 MPa and 12.4 MPa. In contrast, the mixture M6 exhibited the lowest resistance to bending, with the flexural strength values ranging from 8.23 MPa to 9.32 MPa.

Table 3 – Flexural strength results

	Flexural strength (MPa)					
Mixtures n°	M_1	M_2	M_3	M_4	M_5	M_6
Sample 1	10.3	11.2	12.11	12.5	12.4	9.32
Sample 2	10.2	11.1	11.98	12.42	12.33	8.22
Sample 3	10.21	10.78	11.89	12.3	12.02	9.12
Sample 4	10.11	10.65	11.73	12.09	11.83	9.05
Sample 5	9.77	10.05	11.45	12	11.58	8.97
Sample 6	8.96	9.75	10.44	11.86	11.21	8.23

Figure 17 illustrates the effect of adding brick powder on the bending resistance of the specimens. The six samples demonstrated consistent behavior in response to the test, indicating a uniform mixture provided by the extruder during production. The results reveal an increase in flexural strength with the addition of brick powder from 20% to 50% by weight. This improvement is attributed to the enhanced bonding performance between the materials. However, a decrease in flexural strength is observed when the brick powder content is increased from 60% to 70% by weight. This decline is likely due to the inferior properties of ceramics under bending stress.
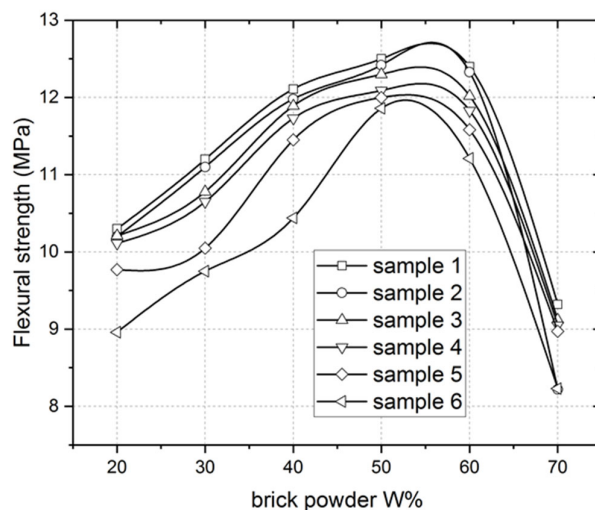
Figure 17 – Influence of brick powder percentage on flexural strength

Compressive strength results

The compressive strength results for various mixtures are presented in Table 4. The data shows the compressive strength values for six different samples of each mixture. The results indicate that the mixture M5 (PP 40w% , brick powder 60w%) exhibits the highest compressive strength, ranges from 23.76 MPa to 24.90 MPa, followed by the mixtures M4 (from 22.30 MPa to 23.44 MPa) and M3 (from 21.36 MPa to 22.50 MPa). The mixture M1 (from 19.18 MPa to 20.32 MPa) shows the lowest compressive strength.

The six samples show good agreement in terms of the observed increases and decreases in compressive strength in Figure 18, which is attributed to the small volume of the 50x50 mm cubes, providing precise results. The graph clearly shows that the mixture M5 (containing 40% polypropylene and 60% brick powder) exhibits the greatest compressive strength, due to the high performance of ceramics under compression. This is followed by the mixture M4 which shows slightly lower compressive strength. The mixtures M1 through M3 display a progressive increase in compressive strength, attributed to the addition of brick powder. The decrease in compressive strength from the mixture M5 to the mixture M6 is explained by the excessive amount of brick powder overwhelming the polymer matrix, leading to poor reinforcement distribution.

Table 4 – Compressive strength results

Mixtures n°	Compressive strength (MPa)					
	M_1	M_2	M_3	M_4	M_5	M_6
Sample 1	20.32	21.83	22.50	23.44	24.90	21.35
Sample 2	19.72	21.15	21.82	22.78	24.22	20.67
Sample 3	19.85	21.30	22.06	22.97	24.43	20.77
Sample 4	19.31	20.82	21.45	22.43	23.89	20.34
Sample 5	20.30	21.01	21.68	22.62	24.08	20.53
Sample 6	19.18	20.69	21.36	22.30	23.76	20.21
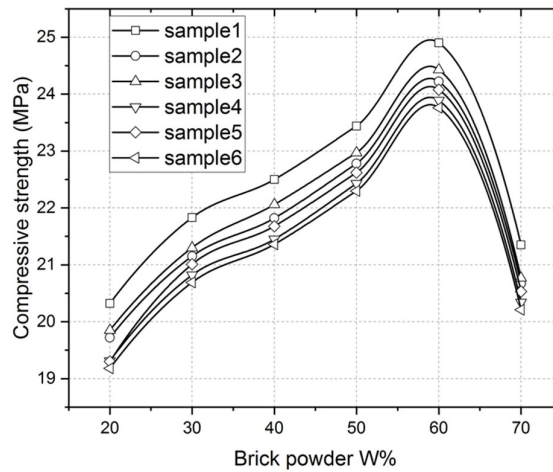
Figure 18 – Influence of brick powder on compressive strength

Charpy test results

Table 5 presents the Charpy test results, showing the impact energy absorbed by various mixtures. The mixture M1 demonstrated the highest impact energy, with the values ranging from 14.9 J to 20.92 J across all samples, indicating superior impact resistance. Conversely, all samples

under the mixture M6 exhibited the lowest impact energy, ranging from 2.62 J to 6.71 J, suggesting poor impact resistance.

Table 5 – Charpy test results

Mixtures n°	Impact energy (J)					
	M_1	M_2	M_3	M_4	M_5	M_6
Sample 1	20.92	16.96	15.73	12.55	8.81	6.71
Sample 2	19.48	16.43	15.21	12.12	8.20	6.28
Sample 3	18.70	15.87	14.64	11.51	7.15	5.80
Sample 4	17.87	15.04	14.08	10.68	6.54	4.58
Sample 5	16.26	14.69	13.51	10.33	5.93	3.97
Sample 6	14.9	13.99	12.99	9.20	5.19	2.62

The graph in Figure 19 illustrates a progressive decline in brick powder content across six samples, ranging from an initial 20 w% to a concluding 70 w%. This reduction is attributed to the unfavorable characteristics of ceramics under mechanical shock. As more powder is incorporated, the polymeric matrix experiences diminished integrity, thereby compromising its ductility typical of polymers while augmenting the inherent fragility characteristic of ceramics.
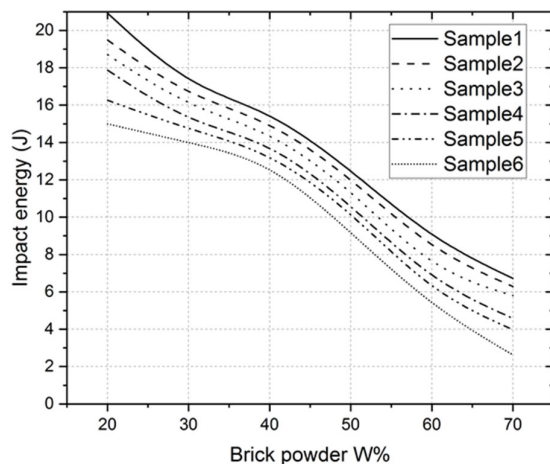
Figure 19 – Influence of brick powder on impact energy

Compressive strength (160mmX320mm) results

Table 6 presents the maximum compressive forces recorded from the cylindrical compression testing. Among the samples tested under the mixture M5, which was selected based on its superior performance in cubic compressive strength from Table 5, sample 3 achieved a peak compressive force of 34 kilonewtons (kN).

Table 6 – Compressive force results

	Max compressive force (KN)
Mixtures n°	M_5
Sample 1	32
Sample 2	32.5
Sample 3	34

Figure 20 presents a compressive force displacement graph.The three samples composed of 40 w% of (PP) and 60w% of brick powder exhibit a progressive rise in compressive force during displacement, until reaching their peak, followed by immediate failure. This pattern mirrors the ceramic material properties and provides a compelling indication that the samples under the mixture M5 adopt a more ceramic-like behavior.
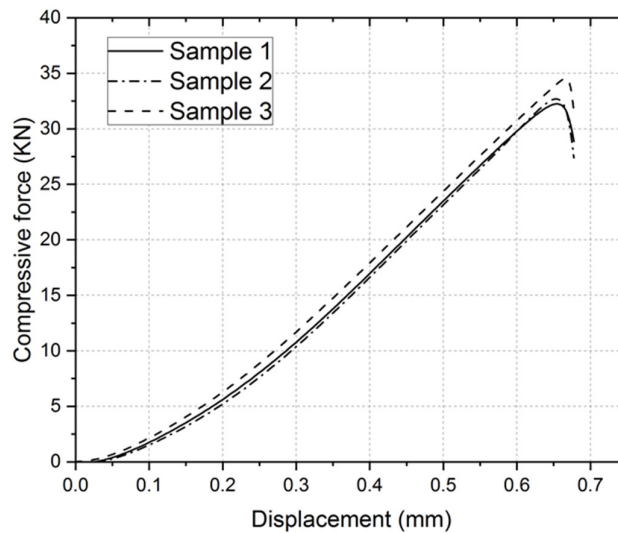
Figure 20 – Force displacement curve for plastic brick

Density test results

Table 7 displays the densities of six samples with varying mixtures. The mixture M1 exhibited the lowest density values, ranging from 1.48 g/cm³ to 1.56 g/cm³, while the mixture M6 demonstrated the highest density values, ranging from 1.68 g/cm³ to 1.77 g/cm³.

Table 7 – Density test results

Mixtures n°	Density (g/cm^3)					
	M_1	M_2	M_3	M_4	M_5	M_6
Sample 1	1.56	1.60	1.64	1.68	1.72	1.77
Sample 2	1.50	1.54	1.58	1.62	1.66	1.70
Sample 3	1.52	1.56	1.6	1.64	1.68	1.72
Sample 4	1.55	1.59	1.63	1.67	1.71	1.75
Sample 5	1.48	1.52	1.56	1.60	1.64	1.68
Sample 6	1.53	1.57	1.61	1.65	1.69	1.73

Figure 21 illustrates the density test results, revealing a trend of increasing density with higher brick powder content in the matrix (from 20 w% to 70 w%). This increase is attributed to the inherently dense properties of ceramics. As shown in Table 2, the density of brick powder is 2.43 g/cm³.
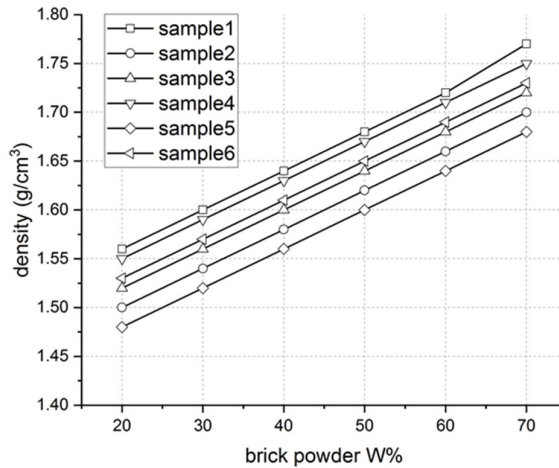
Figure 21 – Influence of brick powder on density

Paver blocks

Figure 22 illustrates the fabrication process of the desired product, which is pavers. The manual extruder enabled the large-scale production of the composite material. The mixture utilized for fabricating pavers is referred to as M5, consisting of 40% polypropylene (PP) and 60% brick powder by weight. This mixture is poured into a pre-oiled mold to facilitate the easy removal of the paver. After allowing the mixture to set for approximately 30 minutes, the paver is removed, resulting in the final product as depicted in the right-hand part of Figure 22.
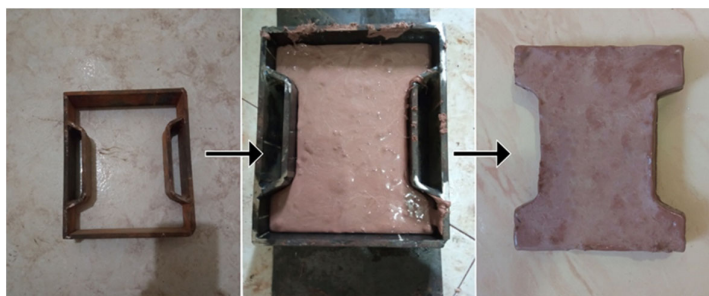
Figure 22 – Plastic brick paver manufacturing

Conclusion

This research successfully developed a cost-effective, manually operated plastic brick extruder for manufacturing composite bricks from recycled polypropylene (PP) and brick powder. The investigation demonstrated that the extrusion of plastic bricks is feasible with careful operation.

The feed mechanism allowed for constant-rate filament drawing, producing uniform mixtures across six samples. However, overloading the hopper led to premature melting and extrusion difficulties. Removal of melted composite from the pipe proved challenging, requiring either remelting or screw removal. Extended operation resulted in heat transfer to the extruder frame, indicating a need for improved thermal management in future designs.

The 60 mm die diameter facilitated easy extrusion, while the single-channel heating system proved sufficient for the melting process. This design successfully melted most polymers, showcasing its versatility.

Through extensive testing, two optimal mixture compositions were identified: a 40:60 PP:brick powder ratio for maximum compressive strength, and a 50:50 ratio for optimal flexural strength. These

compositions effectively balance the ductility of the polymer with the strength of the ceramic component, making them suitable for various construction applications.

This study demonstrates the viability of producing composite bricks using a low-cost, manually operated extruder. The approach offers a promising solution for affordable housing construction while addressing plastic waste management. Future research should focus on optimizing the extrusion process, exploring additional waste materials as potential ingredients, and conducting long-term durability studies of composite bricks under various environmental conditions.

In conclusion, this research contributes significantly to sustainable construction practices and waste management strategies in developing countries. The developed extruder and composite brick formulations have the potential to reduce housing costs and environmental impact, paving the way for more accessible and sustainable building solutions in resource-constrained regions.

References

Abeykoon, C., Kelly, A.L., Brown, E.C. & Coates, P.D. 2016. The effect of materials, process settings and screw geometry on energy consumption and melt temperature in single screw extrusion. *Applied Energy*, 180, pp.880-894. Available at: https://doi.org/10.1016/j.apenergy.2016.07.014.

Ali, D.C., Jassim, A.K. & Al-Sabur, R. 2023. Recycling of Polyethylene and Polypropylene Waste to Produce Plastic Bricks. *Journal of Sustainable Development of Energy, Water and Environment Systems*, 11(4), art.number: 1110462. Available at: https://doi.org/10.13044/j.sdewes.d11.0462.

-ASTM. 2018. ASTM D6110-18: Standard Test Method for Determining the Charpy Impact Resistance of Notched Specimens of Plastics. *ASTM.org,* 09 May. Available at: https://doi.org/10.1520/D6110-18.

-ASTM. 2020. ASTM C109/C109M-20: Standard Test Method for Compressive Strength of Hydraulic Cement Mortars (Using 2-in. or [50-mm] Cube Specimens). *ASTM.org,* 12 March. Available at: https://doi.org/10.1520/C0109_C0109M-20.

-ASTM. 2022. ASTM C78/C78M-22: Standard Test Method for Flexural Strength of Concrete (Using Simple Beam with Third-Point Loading). *ASTM.org,* 30 March. Available at: https://doi.org/10.1520/C0078_C0078M-22.

-ASTM. 2023. ASTM C39/C39M-21: Standard Test Method for Compressive Strength of Cylindrical Concrete Specimens. *ASTM.org,* 15 December. Available at: https://doi.org/10.1520/C0039_C0039M-21.

Hamzah, A.F. & Alkhafaj, R.M. 2022. An investigation of manufacturing technique and characterization of low-density polyethylene waste base bricks. *Materials Today: Proceedings*, 61(Part 3), pp.724-733. Available at: https://doi.org/10.1016/j.matpr.2021.08.318.

Hanifah, U., Taufan, A. & Sholichah, E. 2023. Effect of The Screw-Barrel Clearance and The Cooling Fan on Non-Wheat Noodle Extruder Performance. *BIO Web of Conferences*, 69, art.number:03017. Available at: https://doi.org/10.1051/bioconf/20236903017.

Lamba, P., Kaur, D.P., Raj, S. & Sorout, J. 2022. Recycling/reuse of plastic waste as construction material for sustainable development: a review. *Environmental Science and Pollution Research*, 29, pp.86156-86179. Available at: https://doi.org/10.1007/s11356-021-16980-y.

Moulai Arbi, Y., Mahmoudi, N. & Bentahar, M. 2024. Evaluating the structural performance of masonry walls incorporating recycled plastic bricks under monotonic and cyclic loading. *Vojnotehnički glasnik/Military Technical Courier*, 72(3), pp.1306-1344. Available at: https://doi.org/10.5937/vojtehg72-50560.

Moulai Arbi, Y., Mahmoudi, N. & Djebli, A. 2023. Manufacturing and testing of waste PET reinforced with sand bricks. *Journal of Composite Materials*, 57(16), pp.2513-2526. Available at: https://doi.org/10.1177/00219983231175203.

Patil, G.N., Al Yahmedi, M., Walke, S.M. & Rao, L. 2020. Manufacturing of plastic sand bricks from polypropylene and polyethylene waste plastic. *International Journal of Advanced Science and Technology*, 29(08), pp.2062-2068 [online]. Available at: http://sersc.org/journals/index.php/IJAST/article/view/23320 [Accessed: 29 July 2024].

Qin, W., Li, S., Bai, H. & Jia, S. 2024. Structural design and heat transfer analysis of twin-screw extrusion 3D printer. *The International Journal of Advanced Manufacturing Technology*, 130, pp.5601-5618. Available at: https://doi.org/10.1007/s00170-024-13010-2.

Reichel, H. & Krause, R. 2016. Investigation and Prognosis of Waste Heat Occurrence during the Extrusion Process of Tubular Profiles. *AMM - Applied Mechanics and Materials*, 856, pp.209-216. Available at: https://doi.org/10.4028/www.scientific.net/amm.856.209.

Thatheyus, A.J., Kandasamy, M., Sivarethinamohan, S., Ramakrishan, D. & Suresh, V. 2020. Utilization of plastic waste and polystyrene in making light weight red soil fly ash bricks. *IOP Conference Series: Materials Science and Engineering*, 955, art.number:012055. Available at: https://doi.org/10.1088/1757-899X/955/1/012055.

Abdelkader, D. et al, Design and performance of a manual extruder for recycled plastic-brick composite pavers, pp.1802-1831

Diseño y funcionamiento de una extrusora manual para adoquines compuestos de ladrillo plástico reciclado

Abdelkader Daikh[a]*, Youcef* Moulai Arbi[b], **autor de correspondencia**, *Mohammed* Bentahar[c], *Noureddine* Mahmoudi[c]

[a] Universidad de Mustapha Stambouli, Facultad de Tecnología,
   Departamento de hidráulica,
   Mascara, República Argelina Democrática y Popular

[b] Universidad de Mustapha Stambouli, Laboratorio de Física Cuántica de
   Materia y Modelamiento Matemático (LPQ3M),
   Mascara, República Argelina Democrática y Popular

[c] Universidad de Saida Dr. Moulay Tahar, Facultad de Tecnología,
   Departamento de Ingeniería Civil e Hidráulica,
   Saida, República Argelina Democrática y Popula

CAMPO: ingeniería mecánica, ingeniería civil
TIPO DE ARTÍCULO: artículo científico original

Resumen:

Introducción/objetivo: Este estudio tuvo como objetivo desarrollar una extrusora manual de ladrillos de plástico rentable para fabricar ladrillos compuestos a partir de polipropileno reciclado y polvo de ladrillo. El objetivo era abordar los desafíos de la vivienda en los países en desarrollo y al mismo tiempo promover la gestión sostenible de residuos.

Métodos: Se fabricó una extrusora de un solo tornillo con matriz de 60 mm, con manivela manual, sistema de calentamiento y tolva. Se produjeron especímenes compuestos con diferentes proporciones de polipropileno (30-80 porcentajes en peso) y polvo de ladrillo (20-70 porcentajes en peso). Se realizaron pruebas mecánicas, incluidas mediciones de resistencia a la compresión, resistencia a la flexión, resistencia al impacto y densidad.

Resultados: La mezcla de polvo de ladrillo y polipropileno 40:60 exhibió una resistencia a la compresión óptima, que oscilaba entre 23,76 y 24,90 MPa. La resistencia a la flexión alcanzó su punto máximo en la proporción 50:50 (11,86-12,5 MPa). La resistencia al impacto disminuyó al aumentar el contenido de polvo de ladrillo. La densidad aumentó linealmente con el contenido de polvo de ladrillo, oscilando entre 1,48 y 1,77 g/cm³. La extrusora produjo con éxito muestras compuestas uniformes en todas las mezclas.

Conclusión: El estudio demostró la viabilidad de producir ladrillos compuestos utilizando una extrusora manual de bajo costo. Se identificaron dos composiciones de mezcla óptimas: 40:60 polipropileno:polvo de ladrillo para una máxima resistencia a la compresión y 50:50 para una resistencia óptima a la flexión. Este enfoque ofrece una solución prometedora para la construcción de viviendas asequibles y al mismo tiempo aborda la gestión de residuos plásticos en las regiones en desarrollo. Las investigaciones futuras deberían centrarse en optimizar el proceso de extrusión, explorar

materiales de desecho adicionales y realizar estudios de durabilidad a largo plazo de los ladrillos compuestos.

Palabras claves: extrusora manual, polipropileno, polvo de ladrillo, compuesto, adoquines.

Разработка и производительность ручного экструдера для производства композитной брусчатки из переработанного пластика и кирпичной крошки

Абделкадер Даих[а]*, Юсуф* Мулаи Арби[б], **корреспондент**,
Мухаммед Бентахар[в], *Нуредин* Мамуди[в]

[а] Университет Мустафы Стамбули, технологический факультет,
   кафедра гидравлики,
      г. Маскара, Алжирская Народная Демократическая Республика

[б] Университет Мустафы Стамбули, лаборатория квантовой физики
   материи и математического моделирования (LPQ3M),
      г. Маскара, Алжирская Народная Демократическая Республика

[в] Университет Саиды „Доктор Мулай Тахар", технологический факультет,
   кафедра гражданского строительства и гидравлики,
      г. Саида, Алжирская Народная Демократическая Республика

Резюме:

Введение/цель: Целью данного исследования была разработка экономичного ручного экструдера для производства пластиковых композитных кирпичей из переработанного полипропилена и кирпичной крошки. Целью исследования было решение жилищного строительства в развивающихся странах при одновременном содействии устойчивому управлению отходами.

Методы: Был изготовлен одношнековый экструдер с матрицей диаметром 60 мм, оснащенный ручкой для ручного поворота, системой нагрева и соплом. Также изготовлены образцы композитов с различным соотношением полипропилена (30-80 мас.%) и кирпичной крошки (20-70 мас.%). Проведены механические испытания, в том числе измерения прочности на сжатие, изгиб, ударопрочность и плотность.

Результаты: Смесь полипропилена и кирпичной крошки в соотношении 40:60 продемонстрировала оптимальную прочность на сжатие, составив 23,76-24,90 MPa. Прочность на изгиб достигла своего пика при соотношении 50:50 (11,86-12,5 MPa). Ударопрочность снижалась с увеличением содержания кирпичной крошки. Плотность линейно возрастала с

1829

увеличением содержания кирпичной крошки, составляя от 1,48 до 1,77 г/см3. С помощью экструдера были успешно получены однородные образцы композита из всех смесей.

Вывод: Исследование показало возможность производства композитного кирпича с использованием недорогого экструдера с ручным управлением. Были определены два оптимальных состава смеси: полипропилен и кирпичный порошок в соотношении 40:60 для обеспечения максимальной прочности при сжатии и 50:50 для обеспечения оптимальной прочности при изгибе. Этот подход предлагает многообещающее решение для доступного жилищного строительства и решения проблемы утилизации пластиковых отходов в развивающихся регионах. Будущие исследования должны быть направлены на оптимизацию процесса экструзии, изучение дополнительных отходов и проведение исследований долговечности композитных кирпичей.

Ключевые слова: ручной экструдер, полипропилен, кирпичная крошка, композит, брусчатка.

Пројектовање и перформансе ручног екструдера за композитне цигле за поплочавање од рециклиране пластике и цигленог праха

Абделкадер Деих[а]*, Јусуф* Мулаи Арби[б], **аутор за преписку**,
Мухамад Бентахар[в], *Нуредин* Мамуди[в]

[а] Универзитет „Мустафа Стамбоули", Технолошки факултет,
   Одељење за хидраулику,
   Маскара, Народна Демократска Република Алжир

[б] Универзитет „Мустафа Стамбоули", Лабораторија за квантну физику
   материје и математичко моделирање (LPQ3M),
   Маскара, Народна Демократска Република Алжир

[в] Универзитет у Саиди „Др Мулаи Тахар", Технолошки факултет,
   Департман за грађевинарство и хидраулику,
   Саида, Народна Демократска Република Алжир

ОБЛАСТ: машинство, грађевинарство
КАТЕГОРИЈА (ТИП) ЧЛАНКА: оригинални научни рад

Сажетак:

Увод/циљ: Циљ ове студије био је развој исплативог ручног екструдера пластичних цигли за производњу композитних цигли од рециклираног полипропилена и цигленог праха. Примена овог материјала учинила би за изградњу станова у земљама у развоју економичнијом, уз истовремени допринос одрживом управљању отпадом.

Методе: Израђен је једнопужни екструдер с матрицом од 60 mm, ручком за мануелно окретање, системом за грејање и грлом за

увлачење. Произведени су узорци композита са различитим односима полипропилена (30–80 тежинских процената) и цигленог праха (20–70 тежинских процената). Извршена су механичка испитивања чврстоће на притисак, чврстоће на савијање, отпорности на удар и обављано мерењегустине.

Резултати: Смеша полипропилена и цигленог праха у односу 40:60 показала је оптималну чврстоћу на притисак у распону од 23,76 до24,90 MPa. Чврстоћа на савијање достигла је највећу вредност при односу 50:50 (11,86–12,5 MPa). Отпорност на удар се смањивала с повећањем садржаја цигленог праха. Густина се линеарно повећавала са садржајем цигленог праха у распону од 1,48 до1,77 g/cm³. Екструдер је успешно произвео униформне композитне узорке свих смеша.

Закључак: Студија је показала да је изводљиво произвести композитне цигле користећи јефтин ручни екструдер. Идентификована су два оптимална састава смеша: полипропилен и циглени прах у односу 40 према 60 за максималну чврстоћу на притисак и 50:50 за оптималну чврстоћу на савијање. Овај приступ нуди решење за економичну стамбену изградњу, уз допринос управљању пластичним отпадом у земљама у развоју. Будућа истраживања би требало да се фокусирају на оптимизацију процеса екструзије, истраживања додатних отпадних материјала и на спровођење студија дугорочне издржљивости композитних цигала.

Кључне речи: ручни екструдер, полипропилен, циглени прах, композит, цигле за поплочавање.

Determination of a model of preventive maintenance of special purpose vehicles

Stojko Lj. Biočanin[a], *Milica* S. Timotijević[b],
Željko M. Bulatović[c], *Milan* A. Mišić[d]

[a] Academy of Applied Technical Studies Belgrade, Department of
  Computer and Mechanical Engineering, Belgrade, Republic of Serbia,
  e-mail: sbiocanin@atssb.edu.rs, **corresponding author**,
  ORCID iD: https://orcid.org/0009-0001-6486-5084

[b] College of Applied Studies Aviation Academy,
  Belgrade, Republic of Serbia,
  e-mail: timotijevic.milica93@gmail.com,
  ORCID iD: https://orcid.org/0009-0004-6735-090X

[c] Military Technical Institute, Belgrade, Republic of Serbia,
  e-mail: zetonbulat@gmail.com,
  ORCID iD: https://orcid.org/0009-0009-2339-1933

[d] Kosovo and Metohija Academy od Applied Studies,
  Zvečan, Republic of Serbia,
  e-mail: milan.misic@pr.ac.rs
  ORCID iD: https://orcid.org/0000-0002-9695-7776

Abstract:

Introduction/purpose: The aim of this paper is to obtain quantitative and qualitative indicators of vehicle condition and reliability based on operational data which can be used to determine the optimal periodicity of preventive maintenance for special purpose vehicles, and to more accurately manage the maintenance process and the operational readiness of these vehicles.

Methods: Based on operational failure data and statistical methods, a mathematical model of the reliability of special purpose vehicles was determined. Using this model and operational data, the periodicity of preventive maintenance for the vehicles was determined through multi-criteria optimization, considering both readiness and minimum maintenance costs. The same methodology was applied to determine the optimal preventive maintenance periodicity for 15 components of the mechanical system of special purpose vehicles. A group analysis was conducted using Minitab 15 statistical software, based on the theory of similarity in preventive maintenance periodicity for the 15 components, and a statistical analysis of the conducted research was performed using Minitab 16 statistical software.

Results: Models for preventive maintenance of special purpose vehicles were developed based on the recorded vehicle failures and the failures of

fifteen vital components. A group analysis grouped the fifteen components into optimal maintenance groups, similar in terms of working time between failures. The statistical analysis of the research determined a functional relationship for the optimal periodicity of preventive maintenance for special purpose vehicles.

Conclusion: The maintenance periodicity obtained through multi-criteria analysis is optimal, as it achieves satisfactory vehicle readiness with optimal maintenance costs. The statistical analysis of the research concluded that the maintenance periodicities of the vehicle components are different. In both fleets, the engine and the transmission block have the longest maintenance intervals. The research results can be used to rationalize the existing preventive maintenance concept.

Key words: vehicle, reliability, availability, preventive maintenance, costs, optimal periodicity, multi-criteria analysis.

Introduction

Special purpose vehicles are the most common combat armored vehicles in the Serbian Armed Forces. They are used for general, special, and specific tasks, and are thus exposed to various workloads. Therefore, vehicles, their components, subassemblies, assemblies, and aggregates are exposed to constant environmental influences and disturbances that occur in processes of state changes, resulting in failures of various kinds. Such changes necessitate vehicle maintenance as a system, which should have a required relationship of permissible deviations from its prescribed technical and operational capabilities. The key question in maintaining special purpose vehicles is primarily to avoid the consequences of failures and to return the vehicle to a defined operational state. To achieve this, it is necessary to minimize failures to an acceptable level and, if possible, prevent their occurrence entirely by implementing preventive maintenance procedures at appropriate intervals.

Given all of the above, the aim of this study is to determine, based on vehicle operation data, the quantitative and qualitative indicators of vehicle condition and reliability. These indicators are used to establish the optimal periodicity for preventive maintenance of special purpose vehicles.

Methodology

The subject of this research refers to the vehicles from two technical parks, the A fleet/park and the B fleet/park. Each fleet has 20 special purpose vehicles (referred to as the vehicles in the following text). The vehicles from both fleets were used and stored under different operational and storage conditions. The data on operating times until failure were

collected over a period of two years. During this period, the fleet of the A park had 269 failures, and the fleet of the B park had 279 failures. The mentioned failures, in both fleets of these vehicles, related to 29 vital components.

One of the basic prerequisites for optimizing the vehicle maintenance system and predicting its future behavior is finding a mathematical model that can represent the behavior of vehicles in terms of fault occurrence. If it is possible to determine the reliability distribution law, it is possible to determine all reliability parameters (reliability, unreliability, failure rate, failure density, time to failure). Therefore, based on the recorded failures, a reliability model of vehicles in the two fleets in question was determined.

After grouping failures by intervals of operating times until failure, an assessment was performed of the following reliability indicators: reliability function, unreliability function, failure density distribution function, and failure rate function (Ćatić, 2005, pp.157-232; Biočanin & Pavlović, 2011, pp.106-113; Biočanin & Timotijević, 2020, pp.1-6; Biočanin & Timotijević, 2021, pp.474-480; British Standards Institution, 2024). Based on the obtained data, theoretical distributions that best approximate empirical distributions were selected. The approximation of empirical distributions was done using the theoretical Weibull, exponential, Rayleigh, and normal distributions. The concordance of empirical and theoretical distributions was assessed using Kolmogorov-Smirnov, Pearson, and Romanovsky tests (Ćatić, 2005, pp.157-232; Biočanin & Pavlović, 2011, pp.106-113; Biočanin & Timotijević, 2020, pp.1-6; Biočanin & Timotijević, 2021, pp.474-480; British Standards Institution, 2024; Krstić et al, 2013). Based on the test results, for both vehicle fleets, the Weibull two-parameter distribution was adopted for the reliability model, confirming the universality of the Weibull two-parameter distribution in determining the reliability of complex technical systems.

The optimal maintenance interval for the vehicles was determined based on the criterion of maximum readiness and the criterion of minimum costs. The preventive maintenance interval obtained based on the criterion of maximum readiness, where the highest allowable costs are the constraint, is shorter than the interval obtained based on the criterion of minimum costs, where the minimum level of readiness is the constraint. This means that preventive maintenance according to the maximum readiness model needs to be performed more frequently, leading to higher maintenance costs. Preventive maintenance according to the minimum costs model is performed less frequently, but the vehicle readiness is unsatisfactory. Therefore, the preventive maintenance interval for the vehicles was determined by a compromise solution that considers both

criteria. The maintenance interval obtained in this way is optimal because it achieves satisfactory vehicle availability with optimal maintenance costs.

Following this, the maintenance interval for the vehicle components was determined by a compromise solution, i.e., one of the methods of multi-criteria optimization.

A statistical analysis of the functional relationship of the maintenance periodicity of the vehicle components was performed.

In order to further optimize and manage preventive maintenance processes more precisely based on the determined optimal maintenance intervals for components, a group analysis of the obtained maintenance intervals was performed using Minitab 15 statistical software, which resulted in optimal grouping of local maintenance intervals for multiple components into a single common interval. This yielded another model for preventive maintenance of vehicles.

Results

The periodicity of preventive maintenance for specialized vehicles

According to the established methodology (Ćatić, 2005, pp.158-232; British Standards Institution, 2024; Biočanin & Timotijević, 2021; Biočanin Pavlović, 2011, pp.106-130), based on the systematized data on the vehicle failures from the A fleet and the B fleet, a reliability model of the vehicles from both fleets was determined. Then, the optimal maintenance periodicity for the vehicles was determined based on the criterion of maximum availability (Krstić, 2009, p.488), the criterion of minimum costs (Krstić, 2009, p.488), and a compromise solution (Bass & Kwakernaak, 1977, pp.47-58; Vincke, 1992.; Paul Yoon & Hwang, 1995; Pavličić, 2000, pp.109-122; Vargas, 1990; Biočanin & Timotijević, 2021; Biočanin & Pavlović, 2011, pp.106-130; Biočanin & Timotijević, 2023, pp.1084-1092), which provides satisfactory availability of the vehicles with the optimal maintenance costs.

a) *The reliability model of the vehicles from the A fleet*

In order to determine a theoretical distribution model that could be used to approximate the empirical distribution, an approximation of the empirical distribution was made using the theoretical Weibull, exponential, Rayleigh, and normal distributions. The agreement between the empirical and theoretical distributions was evaluated using the Kolmogorov-Smirnov test, Pearson's test, and the Romanovsky test. Statistical data processing was performed using the Statistics Toolbox for use with MATLAB.

Utilizing non-parametric testing of hypothetical distribution models, the quantitative indicators of deviation of theoretical models from the empirical distribution are obtained. The calculated deviations can be used not only to confirm whether the theoretical model satisfies a certain significance level test, but also to adopt the theoretical model for which all or the majority of deviations are the smallest (Ćatić, 2005, pp.158-232). The reliability function of the vehicles from the A fleet according to (Biočanin & Timotijević, 2021) is as follows:

$$R(t) = e^{-\left(\frac{t}{\eta_{wa}}\right)^{\beta_{wa}}} = e^{-\left(\frac{t}{331.3992}\right)^{2.4993}} \tag{1}$$

where:

- R is the reliability function,
- β_{wa} is the shape parameter for the A fleet,
- η_{wa} is the scale parameter for the A fleet, and
- t is time.

b) The reliability model of the vehicles from the B fleet

According to the same methodology, a reliability model for the vehicles in the B park was determined (Table 1).

Based on the obtained data, the Weibull two-parameter distribution has been adopted as the approximate reliability model with a scale parameter ηwb = 385.7522 and a shape parameter βwb = 2.8800. The reliability function for the special purpose vehicles from the B park is as follows:

$$R(t) = e^{-\left(\frac{t}{\eta_{wb}}\right)^{\beta_{wb}}} = e^{-\left(\frac{t}{385.7522}\right)^{2.8800}} \tag{2}$$

where:

- R is the reliability function,
- β_{wb} is the shape parameter for the B fleet,
- η_{wb} is the scale parameter for the B fleet, and
- t is time.

Table 1 – Distribution models for the B fleet

Distribution	Kolmogorov-Smirnov test			Pearson's test			Romanovsky test			Note
	PA	T	Z/N	PA	T	Z/N	PA	T	Z/N	
Weibull	0.0401	0.0641	Z	0.0103	12.592	Z	1.7291	3	Z	Adopted distribution
Exponential	0.3013	0.0641	N	0.5531	14.067	Z	1.7230	3	Z	
Rayleigh	0.1345	0.0641	N	0.1358	14.067	Z	1.8345	3	Z	
Normal	0.0538	0.0641	Z	0.0146	12.592	Z	1.7278	3	Z	
The reliability function for the vehicles in the B fleet	$R(t) = e^{-\left(\frac{t}{\eta_{wb}}\right)^{\beta_{wb}}} = e^{-\left(\frac{t}{385.9522}\right)^{2.8800}}$									

Determination of the periodicity of preventive maintenance of the vehicles using the maximum avialibility criterion

By varying the periodicity of the time between preventive maintenance, a functional dependence of availability on maintenance periodicity is obtained, based on which the maintenance periodicity that provides maximum readiness can be determined.

The value of operational readiness (Krstić, 2009, p.488) is as follows:

$$G(t) = \frac{t_r + t_{hr}}{t_r + t_{hr} + t_p + \frac{F(t)}{R(t)} t_k} \qquad (3)$$

where:

- *G(t)* is the operational readiness,
- t_r is the operating time,
- t_{hr} is the waiting time for operation availability,
- t_p is the preventive maintenance time,
- *F(t)* is the unreliability function, and
- t_k is the corrective maintenance time.

a) A fleet

The results of determining availability for different maintenance periodicities in the A fleet are given in Table 2.

In Figure 1, a graphical representation of the dependence of readiness on the periodicity of preventive maintenance of the vehicles in the A fleet is given (Krstić et al, 2013).

1837

According to (Biočanin & Timotijević, 2021), based on Figure 5, it can be concluded that the maximum readiness of the vehicles from the A fleet (G_{max}=0.9940) is achieved for a maintenance periodicity of t_r =113 hours of work [h], because for this maintenance periodicity, the function $G(t_r)$ reaches its maximum.

Table 2 – Results of determining the availability for different maintenance periodicities in the A fleet

Maintenance periodicity [h]	50	100	150	200	250	300	350	400	450	500
t_r [h]	50	100	150	200	250	300	350	400	450	500
t_p [h]	10.0	10.0	10.0	10.0	10.0	10.0	10.0	10.0	10.0	10.0
t_k [h]	90.0	90.0	90.0	90.0	90.0	90.0	90.0	90.0	90.0	90.0
$F(t)$	0.0088	0.0488	0.1288	0.2465	0.3900	0.5415	0.6822	0.7982	0.8833	0.9389
$R(t)$	0.9912	0.9512	0.8712	0.7535	0.6100	0.4585	0.3178	0.2018	0.1167	0.0611
t_{hr} [h]	1.150	2.300	3.450	4.600	5.750	6.900	8.050	9.200	10.350	11.500
$G(t)$	0.9910	0.9939	0.9935	0.9918	0.9888	0.9841	0.9763	0.9632	0.93985	0.8959

Figure 1 – Dependency of readiness on the periodicity of preventive maintenance of the special purpose vehicles in the A fleet
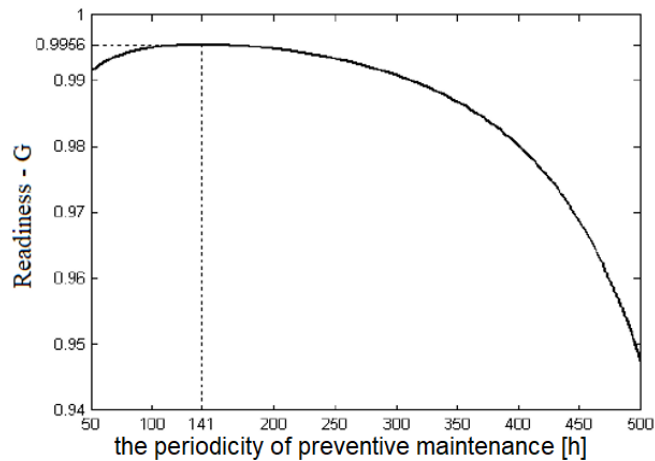
Figure 2 – Dependency of readiness on the periodicity of preventive maintenance of the special purpose vehicles in the B fleet

b) B fleet

Using the same methodology as for the A fleet, the optimal maintenance periodicity for the vehicles in the B fleet has been determined. Table 3 shows the results of the availability determination for different maintenance frequencies in the B fleet.

Table 3 – Results of determining the availability for different maintenance periodicities in the B fleet

Maintenance periodicity [h]	50	100	150	200	250	300	350	400	450	500
t_r [h]	50	100	150	200	250	300	350	400	450	500
t_p [h]	10.0	10.0	10.0	10.0	10.0	10.0	10.0	10.0	10.0	10.0
t_k [h]	90.0	90.0	90.0	90.0	90.0	90.0	90.0	90.0	90.0	90.0
$F(t)$	0.0028	0.0203	0.0637	0.1400	0.2493	0.3842	0.5303	0.6705	0.7895	0.8789
$R(t)$	0.9972	0.9797	0.9363	0.8600	0.7507	0.6158	0.4697	0.3295	0.2105	0.1211
t_{hr} [h]	1.150	2.300	3.450	4.600	5.750	6.900	8.050	9.200	10.350	11.500
$G(t)$	0.9915	0.9950	0.99554	0.9948	0.9934	0.9909	0.9868	0.9802	0.9688	0.9476

Based on Figure 2, it can be concluded that the maximum readiness of the vehicles from the B fleet (G_{max} = 0.9956) is achieved for a maintenance periodicity of t_r = 141 h.

Determination of the periodicity of preventive maintenance of vehicles using the minimum cost criterion

This model determines the optimal interval for the periodic implementation of preventive maintenance procedures for vehicles, which minimizes costs while ensuring the required availability and readiness.

Maintenance costs can be expressed as (Krstić, 2009, p.488; Krstić et al, 2013):

$$C(t) = \frac{C_k - (C_k - C_p) \cdot R(t)}{R(t)dt} \qquad (4)$$

where:

- $C(t)$ is maintenance costs,
- C_k is corrective maintenance costs, and
- C_p is preventive maintenance costs.

a) A fleet

By applying the given expression for maintenance costs, for different periodicities of preventive maintenance of special purpose vehicles, the maintenance cost values for the vehicles in the A fleet were obtained, as shown in Table 4.

Table 4 – Maintenance costs for different maintenance periodicities of the vehicles in the A fleet

Maintenance periodicity [h]	50	100	150	200	250	300	350	400	450	500
C_k [mu]	35000	35000	35000	35000	35000	35000	35000	35000	35000	35000
C_p [mu]	7000	7000	7000	7000	7000	7000	7000	7000	7000	7000
$R(t)$	0.9912	0.9512	0.8712	0.7535	0.6100	0.4585	0.3178	0.2018	0.1167	0.0611
$\int_0^t R(t)dt$	49.87	98.590	144.31	185.07	219.23	245.93	265.26	278.13	285.96	290.30
$C(t)$ [mu]	145.30	84.86	73.49	75.11	81.74	90.11	98.39	105.52	110.,96	114.67

Note: The abbreviation "mu" in Table 4 reffers to a "monetary unit".

The data on preventive maintenance costs (C_p) and corrective maintenance costs (C_k) are taken from the accounting documentation of the authorized maintenance workshop.

Table 2 shows that the minimum maintenance costs for the vehicles in the A fleet are achieved for a preventive maintenance periodicity of 100 to 200 h. By discretizing the maintenance periodicity interval from 50 to 500 with a step of 1, the minimum total specific costs and the maintenance periodicity for minimum total specific costs are calculated.

Figure 3 provides a graphical representation of the dependence of total specific costs on the periodicity of preventive maintenance of vehicles.

According to (Krstić et al, 2013) and Figure 3, the optimal maintenance periodicity is 163 h.
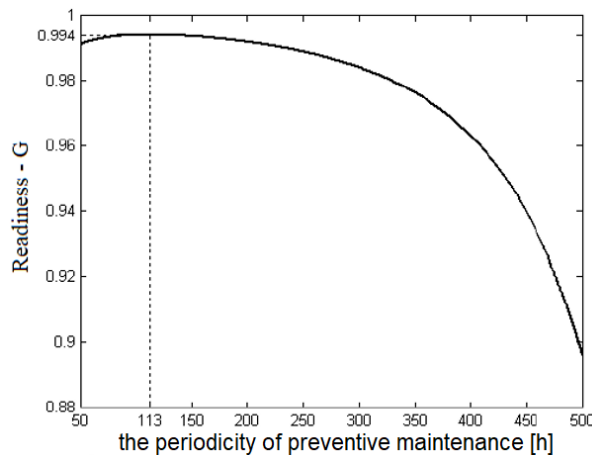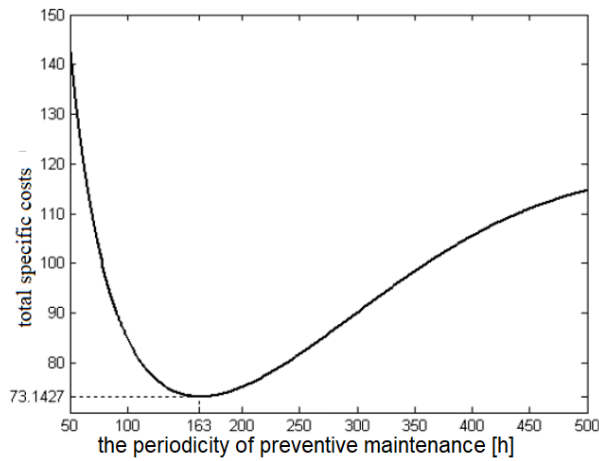

Figure 3 – Dependency of total specific costs on the periodicity of preventive maintenance of the special purpose vehicles in the A fleet
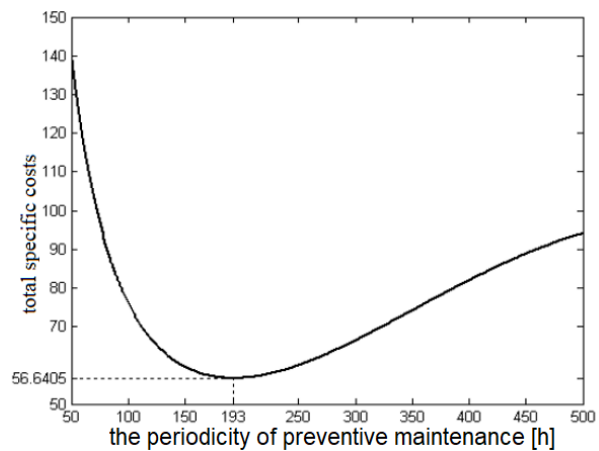
Figure 4 – Dependency of total specific costs on the periodicity of preventive maintenance of the special purpose vehicles in the B fleet

b) B fleet

Using the same methodology as for the A fleet, the maintenance costs (Table 5) and the optimal maintenance periodicity for the vehicles in the B fleet were determined (Figure 4). Based on Figure 4, it can be concluded that the minimum costs (C_{min}=56.6405 [mu]) are achieved for a maintenance periodicity of the vehicles from the B fleet of t_r = 193 h.

Table 5 – Maintenance costs for different maintenance periodicities of the vehicles in the B fleet

Maintenance periodicity [h]	50	100	150	200	250	300	350	400	450	500
C_k [mu]	35000	35000	35000	35000	35000	35000	35000	35000	35000	35000
C_p [mu]	7000	7000	7000	7000	7000	7000	7000	7000	7000	7000
$R(t)$	0.9972	0.9797	0.9363	0.8600	0.7507	0.6158	0.4697	0.3295	0.2105	0.1211
$\int_0^t R(t)dt$	49.964	99.475	147.50	192.55	232.94	267.19	294.34	314.26	327.64	335.80
C_t [mu]	141.658	76.077	59.555	56.709	60.015	66.456	74.230	82.012	88.835	94.126

Determination of the optimal periodicity of preventive maintenance of vehicles using multi-criteria optimization

For solving this task, a multi-criteria optimization method known in the literature as MCDM (Multi Criteria Decision Making) was applied. One of the methods of multi-criteria optimization used in the paper is the Analytic Hierarchy Process (AHP). This method is based on the principle of decision making based on the knowledge and data available at the time of decision making. The creative decision-making process is scientifically based on the concept of analytics, hierarchy, and process, as well as on the benefit and the cost criteria of optimality.

a) A fleet

The optimal periodicity of preventive maintenance has been determined and amounts to 162 h (Biočanin & Timotijević, 2021).

b) B fleet

Using the same methodology, the optimal periodicity of preventive maintenance for the special purpose vehicles in the B fleet was adopted and amounts to 192 h. Figure 6 provides a graphical representation of finding the best alternative.
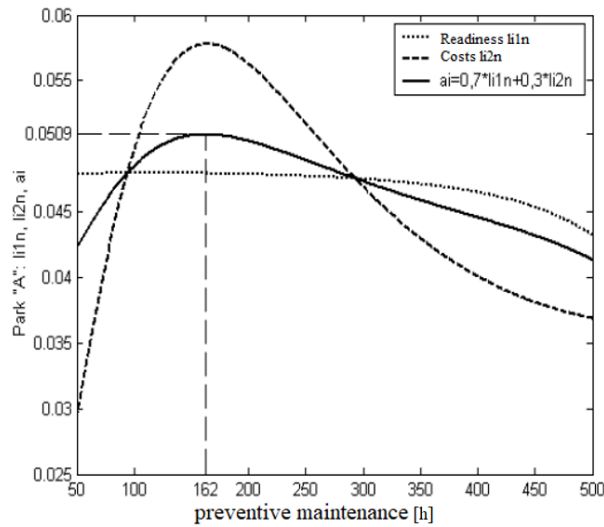
Figure 5 – Graphic representation of finding a compromise solution for the A fleet
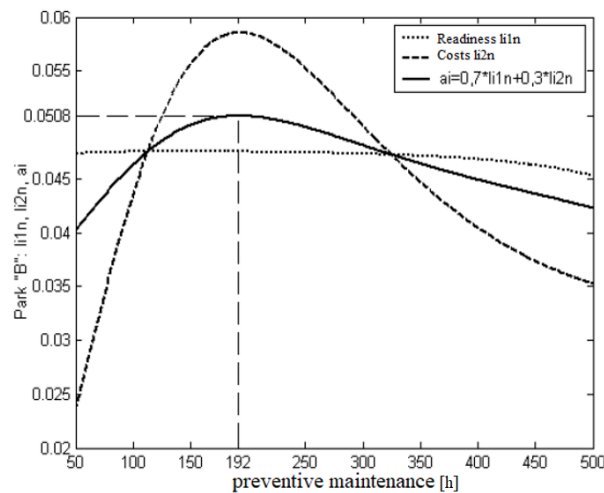
Figure 6 – Graphic representation of alternatives for determining the maintenance periodicity by a compromise solution in the B fleet

The value of the optimal periodicity for conducting preventive maintenance procedures for special purpose vehicles is determined according to the criterion of the maximum vehicle readiness to be 113 h

for the vehicles from the A fleet and 141 h for the vehicles from the B fleet, and according to the criterion of the minimum maintenance costs to be 163 h for the vehicles from the A fleet and 193 h for the vehicles from the B fleet. By compromising, the value of the sought optimal periodicity for conducting preventive maintenance procedures was determined, taking into account both optimization criteria, and it amounts to 162 h for the vehicles from the A fleet and 192 h for the vehicles from the B fleet. A graphical representation of the periodicity of preventive maintenance for special purpose vehicles, determined according to the three mentioned criteria, is given in Figure 7 for the vehicles from the A fleet and in Figure 8 for the vehicles from the B fleet.
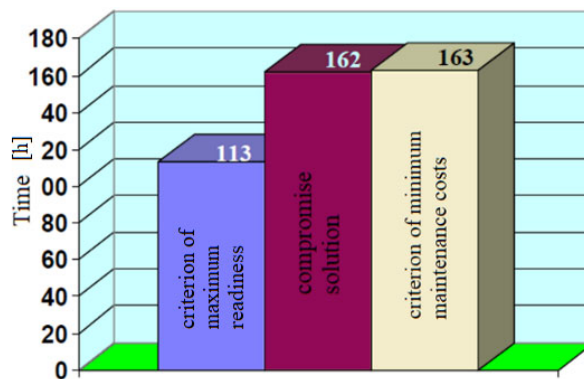
Figure 7 – Graphic representation of the preventive maintenance period for the specialized vehicles in the A park
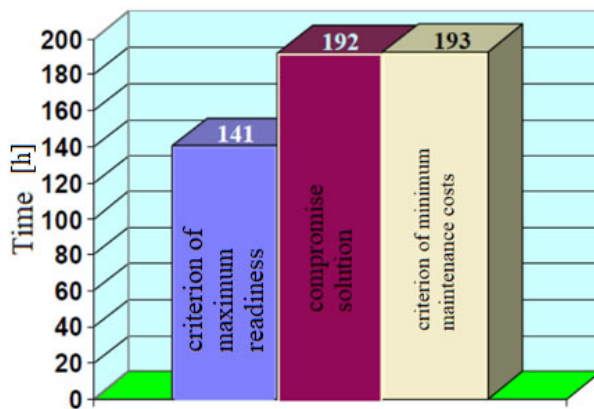
Figure 8 – Graphic representation of the preventive maintenance period for the specialized vehicles in the B park

The calculated periodicities of preventive maintenance for the special purpose vehicles in the A fleet and the B fleet are different. The maintenance periodicity for the vehicles in the B fleet is longer than that for the vehicles in the A fleet.

The vehicles from B fleet were used under harsher operational conditions in a geographic area with notably hilly terrain. The driving crews and maintenance personnel are less trained, and the workshop capacities are inadequate for work, especially during the winter period, with workshop equipment being of an older generation. The storage and preservation conditions for the vehicles are also worse since vehicles in the A fleet are stored under a canopy, while those in the B fleet are stored in an open area.

Determination of the optimal periodicity of preventive maintenance of vehicles by analyzing the maintenance periodicity of vehicle components

Most models optimize preventive maintenance of technical systems at the component level. Therefore, it is a major challenge to optimize the preventive maintenance process of a complex technical system such as a motor vehicle, which consists of several tens of thousands of components, 50-60% of which lose their initial properties during operation, 30-40% have a shorter lifespan than the vehicle, and an average of 200-300 components are critical in terms of reliability and require more frequent preventive inspections and corrective actions. The solution lies in finding an optimization model for preventive maintenance of vehicles based on the combined application of the results of several maintenance mathematical models for vehicle components, and then grouping the preventive maintenance periods for multiple components into a common periodicity. To avoid frequent vehicle downtimes for preventive maintenance, optimal grouping of local periodicities for multiple components into a common periodicity was performed through a group analysis. This approach enables more precise management of vehicle maintenance processes and their operational readiness, which was the goal of this study.

Using the same methodology as in the previous section of this study, a reliability model and optimal periodicity of preventive maintenance were determined for fifteen vital components of the vehicles.

The optimal periodicity of preventive maintenance for the vital components of the vehicles in the A fleet

The results of the research on the optimal periodicity of preventive maintenance for vital components of vehicles according to the three models are presented in the following Table 7.

Table 7 – Optimal maintenance periodicities for the components of the specialized vehicles in the A fleet

No.	Component name	Criterion	Maintenance Periodicity Time (h)
1	*2*	*3*	*4*
1.	Transmission Unit Block (TUB)	Maximum Availability	115
		Minimum Costs	341
		Compromise Solution	332
2.	Hydraulic System for Fan Drive (HCPF)	Maximum Availability	105
		Minimum Costs	183
		Compromise Solution	172
3.	Coolant Heating Device for Engine and Transmission	Maximum Availability	109
		Minimum Costs	169
		Compromise Solution	181
4.	Control Block	Maximum Availability	144
		Minimum Costs	199
		Compromise Solution	162
5.	Side Transmission with Disk Brakes	Maximum Availability	127
		Minimum Costs	161
		Compromise Solution	157
6.	Hand Brake with Command	Maximum Availability	174
		Minimum Costs	113
		Compromise Solution	164
7.	Water Ingress Protection Mechanism for the Engine	Maximum Availability	123
		Minimum Costs	194
		Compromise Solution	181
8.	Engine Throttle Controls	Maximum Availability	117
		Minimum Costs	201
		Compromise Solution	173
9.	Armored Body (connecting parts)	Maximum Availability	139
		Minimum Costs	175
		Compromise Solution	194
10.	Commander's Turret with links to the Armored Body	Maximum Availability	129
		Minimum Costs	187
		Compromise Solution	169

No.	Component name	Criterion	Maintenance Periodicity Time (h)
1	2	3	4
11.	Cooler Louver and Fan Controls	Maximum Availability	117
		Minimum Costs	176
		Compromise Solution	171
12.	Windbreak with Movement Mechanism	Maximum Availability	147
		Minimum Costs	184
		Compromise Solution	173
13.	Fire Prevention Device	Maximum Availability	154
		Minimum Costs	191
		Compromise Solution	181
14.	Barrel Gas Vent Device	Maximum Availability	112
		Minimum Costs	184
		Compromise Solution	163
15.	Engine OM-403	Maximum Availability	142
		Minimum Costs	372
		Compromise Solution	362

The optimal periodicity of preventive maintenance for the vital components of the vehicles in the B fleet

Using the same methodology as for the vital components of the vehicles in the A fleet, the periodicities of preventive maintenance for the components in the B fleet were calculated and provided in Table 8.

Table 8 – Optimal maintenance periodicities for the components of the specialized vehicles in the B fleet

No.	Component name	Criterion	Maintenance Periodicity Time (h)
1	2	3	4
1.	Transmission Unit Block (TUB)	Maximum Availability	140
		Minimum Costs	352
		Compromise Solution	348
2.	Hydraulic System for Fan Drive (HCPF)	Maximum Availability	112
		Minimum Costs	194
		Compromise Solution	186
3.	Coolant Heating Device for Engine and Transmission	Maximum Availability	116
		Minimum Costs	187
		Compromise Solution	182

No.	Component name	Criterion	Maintenance Periodicity Time (h)
1	2	3	4
4.	Control Block	Maximum Availability	152
		Minimum Costs	204
		Compromise Solution	195
5.	Side Transmission with Disk Brakes	Maximum Availability	141
		Minimum Costs	192
		Compromise Solution	184
6.	Hand Brake with Command	Maximum Availability	133
		Minimum Costs	188
		Compromise Solution	186
7.	Water Ingress Protection Mechanism for the Engine	Maximum Availability	136
		Minimum Costs	215
		Compromise Solution	203
8.	Engine Throttle Controls	Maximum Availability	121
		Minimum Costs	204
		Compromise Solution	198
9.	Armored Body (connecting parts)	Maximum Availability	140
		Minimum Costs	202
		Compromise Solution	194
10.	Commander's Turret with links to the Armored Body	Maximum Availability	161
		Minimum Costs	193
		Compromise Solution	183
11.	Cooler Louver and Fan Controls	Maximum Availability	137
		Minimum Costs	199
		Compromise Solution	187
12.	Windbreak with Movement Mechanism	Maximum Availability	162
		Minimum Costs	201
		Compromise Solution	190
13.	Fire Prevention Device	Maximum Availability	157
		Minimum Costs	218
		Compromise Solution	212
14.	Barrel Gas Vent Device	Maximum Availability	141
		Minimum Costs	201
		Compromise Solution	191
15.	Engine OM-403	Maximum Availability	152
		Minimum Costs	369
		Compromise Solution	361

Based on the obtained results, it can be concluded that there are different maintenance periodicities for the components, and that in both fleets, the transmission unit and the OM 403 engine of special purpose vehicles have the longest maintenance periodicity.

Cluster/group analysis

A cluster analysis was performed based on the theory of similarity of the adopted compromise solution for the optimal maintenance periodicity of 15 vehicle components.

The analysis was carried out using Minitab 15statistical software, based on Jaccard similarity coefficients:

$$\text{similarity coefficient} = \frac{A \cap B}{A \cup B} \qquad (5)$$

where:
- A and B are the lengths of the optimal maintenance periodicity for two consecutive components/assemblies compared.

The similarity coefficient matrix for the A fleet is shown in Table 9, and that for the B fleet in Table 10.

Table 11 displays the results of grouping the optimal maintenance periodicities of components into two, three, four, five, and six groups for the A fleet and the B fleet.

Within each group, the components are simultaneously subjected to preventive maintenance with adopted optimal maintenance periodicities.

Depending on the number of optimal maintenance periodicities, a vehicle will enter the workshop many times for the purpose of preventive maintenance.

For the second group, the vehicle will enter the workshop twice, and for the sixth group, six times.

Table 9 – Jaccard similarity coefficients for the A fleet

		ASSEMBLY GROUP/AGGREGATE													
ASSEMBLY GROUP/AGGREGATE	1	2	3	4	5	6	7	8	9	10	11	12	13	14	15
1	1.000	0.518	0.545	0.488	0.473	0.494	0.545	0.521	0.527	0.509	0.515	0.521	0.545	0.491	0.917
2	0.518	1.000	0.951	0.942	0.913	0.953	0.950	0.994	0.983	0.983	0.994	0.994	0.950	0.948	0.475
3	0.545	0.951	1.000	0.895	0.867	0.906	1.000	0.956	0.967	0.340	0.945	0.956	1.000	0.901	0.500
4	0.488	0.942	0.895	1.000	0.969	0.888	0.895	0.936	0.926	0.959	0.947	0.936	0.895	0.994	0.448
5	0.473	0.913	0.867	0.969	1.000	0.957	0.867	0.908	0.897	0.929	0.918	0.908	0.867	0.963	0.434
6	0.494	0.953	0.906	0.888	0.957	1.000	0.906	0.948	0.937	0.970	0.959	0.948	0.906	0.994	0.453
7	0.545	0.950	1.000	0.895	0.867	0.906	1.000	0.956	0.967	0.934	0.945	0.956	1.000	0.901	0.500
8	0.521	0.994	0.956	0.936	0.908	0.948	0.956	1.000	0.989	0.977	0.988	1.000	0.956	0.942	0.478
9	0.527	0.983	0.967	0.926	0.897	0.937	0.967	0.989	1.000	0.956	0.977	0.989	0.967	0.931	0.483
10	0.509	0.983	0.934	0.950	0.924	0.970	0.934	0.977	0.956	1.000	0.988	0.977	0.934	0.964	0.467
11	0.515	0.994	0.945	0.947	0.918	0.959	0.945	0.988	0.977	0.988	1.000	0.988	0.945	0.953	0.472
12	0.521	0.994	0.956	0.936	0.908	0.948	0.956	1.000	0.989	0.977	0.988	1.000	0.956	0.942	0.478
13	0.545	0.950	1.000	0.895	0.867	0.906	1.000	0.956	0.967	0.934	0.945	0.956	1.000	0.901	0.500
14	0.491	0.948	0.901	0.994	0.963	0.994	0.901	0.942	0.931	0.964	0.953	0.942	0.901	1.000	0.450
15	0.917	0.475	0.500	0.448	0.434	0.453	0.500	0.478	0.483	0.467	0.472	0.478	0.500	0.450	1.000

Table 10 – Jaccard similarity coefficients for the B fleet

	ASSEMBLY GROUP/AGGREGATE														
	1	2	3	4	5	6	7	8	9	10	11	12	13	14	15
1	1.000	0.534	0.523	0.560	0.529	0.534	0.583	0.583	0.557	0.053	0.537	0.546	0.609	0.545	0.991
2	0.534	1.000	0.978	0.954	0.989	1.000	0.916	0.939	0.959	0.984	0.995	0.979	0.877	0.974	0.530
3	0.523	0.978	1.000	0.933	0.989	0.978	0.897	0.919	0.938	0.995	0.973	0.958	0.858	0.953	0.519
4	0.560	0.954	0.933	1.000	0.933	0.954	0.961	0.985	0.995	0.938	0.959	0.974	0.920	0.979	0.556
5	0.529	0.989	0.989	0.943	1.000	0.989	0.906	0.929	0.948	0.995	0.984	0.968	0.868	0.963	0.524
6	0.534	1.000	0.978	0.954	0.989	1.000	0.916	0.939	0.959	0.984	0.995	0.979	0.877	0.974	0.530
7	0.583	0.916	0.897	0.961	0.906	0.916	1.000	0.975	0.956	0.901	0.921	0.936	0.958	0.941	0.578
8	0.583	0.939	0.919	0.985	0.929	0.939	0.975	1.000	0.980	0.924	0.944	0.960	0.934	0.965	0.564
9	0.557	0.959	0.938	0.995	0.948	0.959	0.956	0.980	1.000	0.943	0.964	0.979	0.915	0.985	0.553
10	0.053	0.984	0.995	0.938	0.995	0.984	0.901	0.924	0.943	1.000	0.979	0.963	0.863	0.958	0.521
11	0.537	0.995	0.973	0.959	0.984	0.995	0.921	0.944	0.964	0.979	1.000	0.984	0.984	0.995	0.533
12	0.546	0.979	0.958	0.974	0.968	0.979	0.936	0.960	0.979	0.963	0.984	1.000	0.896	0.995	0.541
13	0.609	0.877	0.858	0.920	0.868	0.877	0.958	0.934	0.915	0.863	0.984	0.896	1.000	0.901	0.604
14	0.545	0.974	0.953	0.979	0.963	0.974	0.941	0.965	0.985	0.958	0.995	0.995	0.901	1.000	5.440
15	0.991	0.530	0.519	0.556	0.524	0.530	0.578	0.564	0.553	0.521	0.533	0.541	0.604	5.440	1.000

ASSEMBLY GROUP/AGGREGATE

Table 11 –- Grouping of components/aggregates for simultaneous preventive maintenance

Group	A fleet		B fleet	
	Agregate X_i; i=1,2,3,...,15	Opt. period. Min X_i /hour/	Agregate X_i; i=1,2,3,...,15	Opt. period. Min X_i /hour/
II group	1, 15	332	1, 14,15	191
	2,3,4,5,6,7,8,9,10,11,12,13,14	157	2,3,4,5,6,7,8,9,10,11,12,13	182
III group	1,15	332	1,15	348
	3,7,13	181	4,7,8,13	195
	2, 4, 5, 6, 8, 9,10,11,12,14	157	2,3, 5,6, 9,10,11,12,14	182
IV group	1,15	332	1	348
	2,3,7,8,9,11,12,13	171	2,3,4,5,6,7,8,9,10,11,12,13	182
	4,5,6,14	157	14	191
	10	169	15	351
V group	1,15	332	1	348
	2,8,9,11,12	171	2,3,4,5,6,7,8,9,10,11,12	182
	3,7,13	181	13	212
	4,5,6	157	14	191
	10	169	15	351
VI group	1	332	1	348
	2,8,9,11,12	171	2,3,4,5,6,7,8,9,11,12	182
	3,7,13	181	10	183
	4,5,6,14	157	13	212
	10	169	14	191
	15	362	15	351

An example dendrogram for grouping parts into three groups is shown in Figure 9.

An example dendrogram for grouping parts into five groups is shown in Figure 10.

Based on the obtained results, the following preventive maintenance model for components has been selected:

A fleet: The optimal periodicity for preventive maintenance for the engine and transmission in the specialized vehicle unit block is 332 h, while it is 157 h for all other components. In order to reduce maintenance costs, the engine and transmission in the unit block should undergo preventive maintenance every other time the vehicle enters the workshop.

B fleet: The optimal periodicity for preventive maintenance for the engine and transmission in the specialized vehicle unit block is 348 h, while it is 182 h for all other components.

Figure 9 – Example of software grouping of components/aggregates into three groups
```
Cluster 1:   1  15; Cluster 2:    2   3   4   5   6   7   8   9  11  12
                13  14; Cluster 3:  10
```
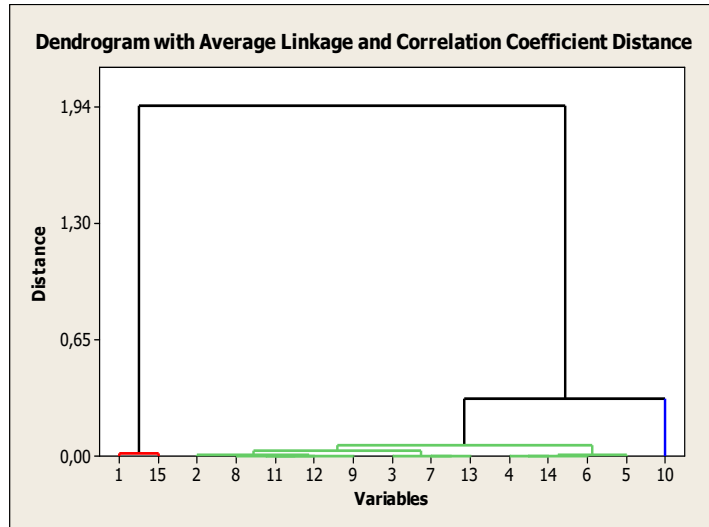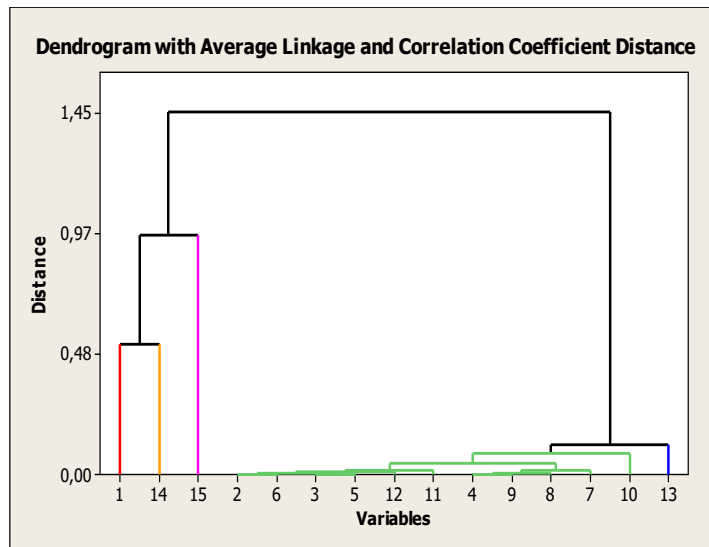

Figure 10 – Example of software grouping of components/aggregates into five groups
```
Cluster 1:   1  15; Cluster 2:    2   8   9  11   12; Cluster 3:   3   7
             13; Cluster 4:   4   5   6   14; Cluster 5:    10
```

Statistical analysis of the research

Based on the analysis of the periodicity of preventive maintenance of vital vehicle components, using the same methodology, it was concluded that the maintenance periodicities of these components are different. In order to investigate the functional relationship of optimal periodicities of preventive maintenance of vehicles, an experiment was conducted in Minitab 16 statistical software based on 5 measurements of time between two failures for the observed 15 groups of components, in the A fleet and the B fleet.

The *General full factorial design* with two factors was applied:

1. Factor A: Relating to the specialized vehicle fleet, with two levels (A fleet and B fleet).

2. Factor B: Relating to the components/aggregates of the specialized vehicles, with 15 levels (components from 1, 2, 3, ..., 14, 15).

The X_0 hypothesis was set, assuming that the mean times between failures in the A fleet and the B fleet are equal, i.e., $\mu_1 = \mu_2$ with an alternative hypothesis X_1: $\mu_1 \neq \mu_2$.

Similarly, for the component groups "system/aggregate groups," the mean times between failures were observed, with X_0 ($\mu_1 = \mu_2$) and X_1($\mu_1 \neq \mu_2$) hypotheses.

After entering the data, certain statistical characteristics of the failure times behavior were obtained depending on the FLEET and the observed COMPONENT.

Multilevel Factorial Design
```
Factors:       2    Replicates:      5
Base runs:    30    Total runs:    150
Base blocks:   1    Total blocks:    1
Number of levels: 2. 15
```

General Linear Model: TIME BETW. FAILURE versus FLEET. SYSTEM GRUPS/AG

```
Factor                   Type   Levels  Values
FLEET                    fixed      2  1. 2
SYSTEM GRUPS/AGREGATES   fixed     15  1. 2. 3. 4. 5. 6. 7. 8. 9.
10. 11. 12.
                                       13. 14. 15

Analysis of Variance for TIME BETW. FAILURE, using Adjusted SS for
Tests
Source                   DF  Seq SS   Adj SS  Adj MS     F
P
FLEET                     1  100259   100259  100259  6,16
0,014
```

```
SYSTEM GRUPS/AGREGATES          14    360803    360803    25772  2,58
0,044
FLEET*SYSTEM GRUPS/AGREGATES    14     72137     72137     5153  0,32
0,991
Error                          120   1954597   1954597    16288
Total                          149   2487795
```

Based on the given analysis of variance and based on the F-statistic and p-value for factor A, it can be concluded that $F_{kr} > F_{tabl.}$ (6.16 > 2.76) and $p < α$ (0.014 < 0.05), which means that the fleet, as a factor of observation, has a different effect on failures, thus rejecting the null hypothesis and accepting the alternative hypothesis.

Based on the given analysis of variance and based on the F-statistic and p-value for factor B, it was concluded that $F_{kr} > F_{tabl.}$ (2.58 > 1.80) and $p < α$ (0.044 < 0.05), which means that the fleet, as a factor of observation, has a different effect on failures, thus rejecting the null hypothesis and accepting the alternative hypothesis.

In addition, the coefficients $R\text{-}C_q$ = 21.43%, $R\text{-}C_{q(adj)}$ = 2.45% indicate that there is no strong correlation between the observed levels of this factor. The regression equation of the time between failures depending on the fleet is:

$$TIME\ BETWEEN\ FAILURES = 227.3 + 51.71\ FLEET \qquad (6)$$

and there is no polynomial relationship.

The functional relationships between the failure times of the vehicles in the A and B fleets is given in Figure 11, and the groups of components are shown in Figures 12 and 13.
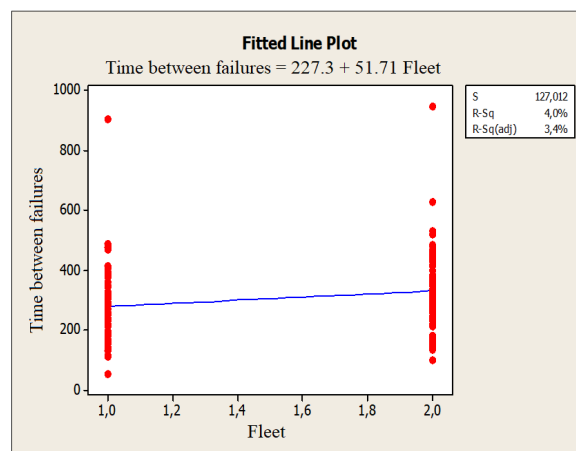
Figure 11 – Functional relationship Time between failure – Park/fleet
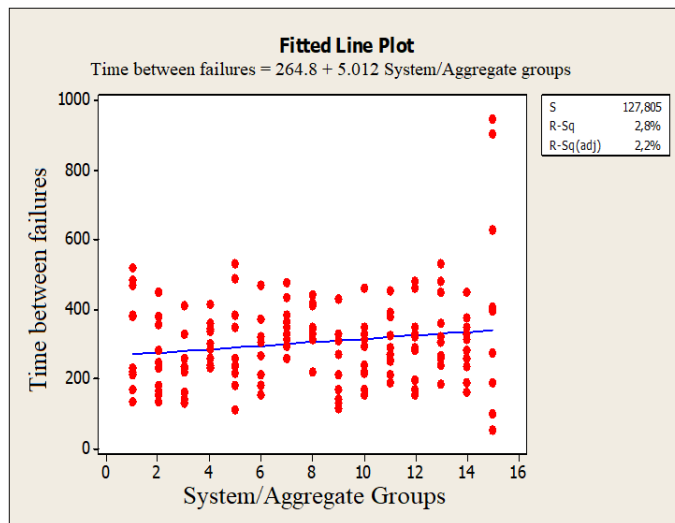
Figure 12 – Functional relationship Time between failure – System/Aggregate groups
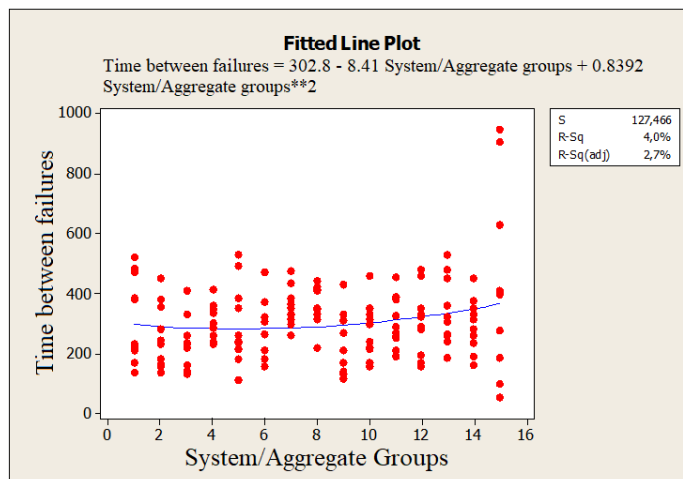
Figure 13 – Functional relationship Time between failure – System/Aggregate groups in the polynomial relationship

A spatial view of the functional relationship of time between failures for fleets and system/aggregate groups is provided in Figure 14, a contour view in Figure 15, and the main effects in relationships and time between failures in Figures 16 and 17.

1856
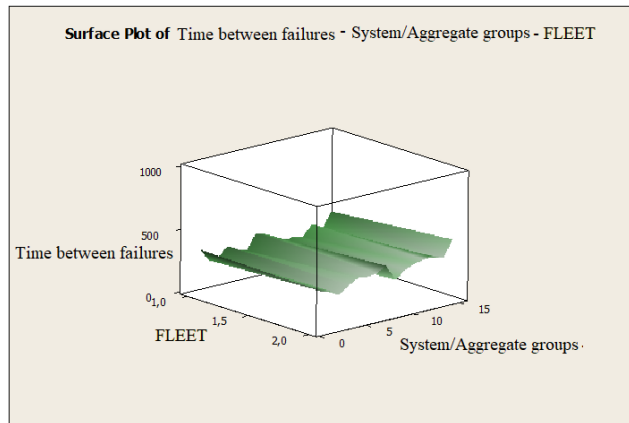
Figure 14 – Spatial view of the functional relationship Time between failure – Fleet - System/Aggregate groups
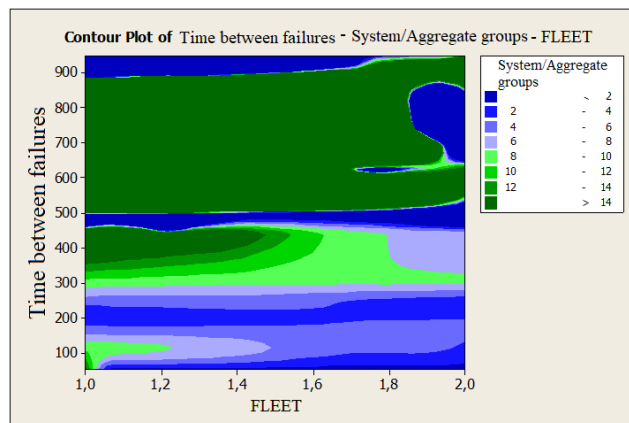
Figure 15 – Contour view of the functional relationship Time between failure – Fleet - System/Aggregate groups

The regression equation for the function of time between failures depending on a system/aggregate group is:

$$TIME\ BETWEEN\ FAILURES\ =\ 264.8\ +\ 5.012\frac{SYSTEM\ OR}{AGGREGATE}\ GROUP \quad (7)$$

and the polynomial relationship is:

$$TIME\ BETWEEN\ FAILURES\ =\ 302.8\ -$$
$$8.41\frac{SYSTEM\ OR}{AGGREGATE}\ GROUP\ +\ 0.8392\frac{SYSTEM\ OR}{AGGREGATE}\ GROUP ** 2 \qquad (8)$$
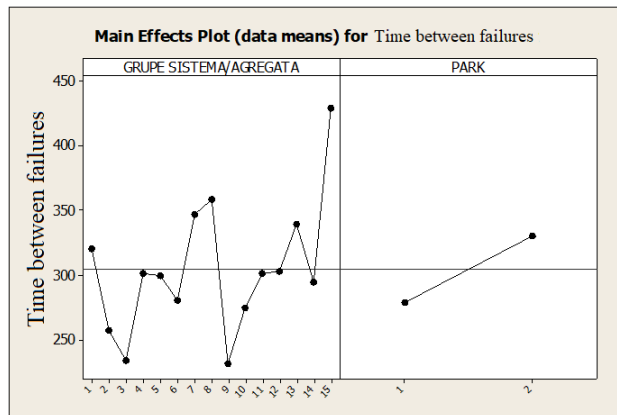
Figure 16 – Main effects in relations Time between failures - Fleet - System/Aggregate groups

Figure 16 clearly shows that there is a polynomial relationship between the maintenance periodicity of fifteen vital components. There is no polynomial relationship between the maintenance periodicity of the vital components in the two specialized vehicle parks.
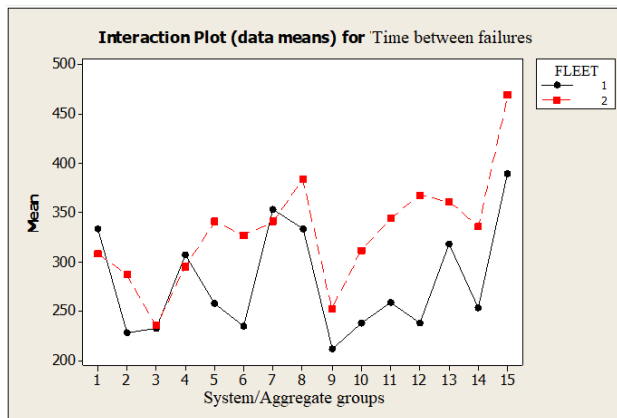
Figure 17 – Main interactions in relations Time between failures - Fleet - System/Aggregate groups

From Figure 17, it can be seen that, by analyzing five times between failures in Minitab 16 statistical software, different maintenance periodicities for vehicles were obtained in fleet 1 (A fleet) and fleet 2 (B

fleet). Approximately the same maintenance periodicity in both fleets is observed for the Coolant Heating Device for the Engine and Transmission (Component 3), the Control Block (Component 4), and the Water Ingress Protection Mechanism for the Engine (Component 7).

Discussion

Stemming from the data from vehicle operation, the quantitative and qualitative indicators of the system condition and reliability of the special purpose vehicles were obtained. Based on it, the optimal maintenance periodicity of these vehicles was determined.

The periodicity of preventive maintenance of the special purpose vehicles was determined by a compromise solution. The maintenance periodicity obtained in this way is optimal because it provides satisfactory vehicle readiness and availability with optimal maintenance costs.

According to the research results, the maintenance periodicity of the vehicles from the B fleet is higher compared to the maintenance periodicity of the vehicles from the A fleet.

Compared to the existing maintenance concept, the calculated periodicity of preventive maintenance for the entire vehicle falls between the first and second technical inspections of the special purpose vehicle. It is concluded that it is unnecessary to implement preventive maintenance with two technical inspections in a relatively short time interval (first and second technical inspection); nevertheless, only one preventive inspection at the calculated time of preventive maintenance is sufficient. This approach would rationalize the existing concept of preventive maintenance, reduce maintenance costs, and increase the availability of special purpose vehicles.

Based on the analysis of the periodicity of preventive maintenance of vital components of special purpose vehicles, it was concluded, using the same methodology, that the maintenance periodicities of these components are different. The analysis and calculations showed that the engine of the vehicle and the transmission, in both fleets, have the highest reliability, which is why their maintenance periodicity is significantly higher than the maintenance periodicity of other components. If preventive maintenance of special purpose vehicles is performed through maintenance of components, in the calculated periods, then the special purpose vehicle would be very often undergoing preventive maintenance, the same operations would be repeated several times (opening documentation, vehicle washing, component construction and installation, testing, etc.), which would increase costs and decrease readiness due to the long time spent on maintenance. In order to avoid this, optimal

grouping of local maintenance periodicities for multiple components into a single common periodicity was achieved through the group analysis. This way, the optimal availability and maintenance costs are achieved. Additionally, the group analysis showed that in the processes of vehicle management and maintenance, operational readiness can be more precisely managed based on the determined optimal periods of preventive maintenance.

Through the statistical analysis in Minitab 15 and Minitab 16 statistical software, it was concluded that there is no polynomial relationship between the time of operation until failure for the A fleet and the B fleet. It was concluded that there is a polynomial relationship between operating time and failure in the analysis of the groups of vital components. By analyzing the five times between two failures in Minitab 16 statistical software, different maintenance periodicities for the vehicles in park 1 (A fleet) and park 2 (B fleet) were obtained. The Coolant System Heating Device (Component 3), the Control Block (Component 4), and the Water Ingress Protection Mechanism for the Engine (Component 7) have approximately the same maintenance periodicity in both fleets. Other components have different maintenance periodicities, indicating that the maintenance periodicity depends on the terrain configuration and other vehicle operation conditions and that if the same vehicle changes its location and maintenance place, optimal maintenance periodicity calculations must be re-performed.

By grouping certain components and assemblies based on similar operating times between two failures, a kind of analysis of the condition of these elements was performed at a qualitative and quantitative level. The group analysis has contributed to more precise management of operational readiness and optimal maintenance costs of vehicles in the processes of vehicle management and maintenance based on the determined optimal periods of preventive maintenance of components. Another preventive maintenance model for vehicles was set up through the group analysis.

The research conducted in the A fleet and the B fleet shows that the condition and the maintenance periodicity of special purpose vehicles depend on the terrain where the vehicle is used, the drivers who operate the vehicle, the crew in the vehicle, and the workshop conditions for maintenance (technical equipment and quality of personnel). The study has proven that the vehicles from the B fleet have longer maintenance intervals, indicating that the operating conditions are different. The conclusion is that if the same vehicle changes its location and maintenance place, then optimal maintenance periodicity calculations

must be re-performed. The analysis also showed that the engine and the transmission in the block have high reliability and are not affected by changes in operating conditions.

Conclusion

Based on the overall results obtained in this study, it can be concluded that the most suitable preventive maintenance concept for special purpose vehicles is maintenance based on time intervals derived from reliability with preventive inspections and preventive replacements according to the periodicities obtained from the calculations in this study, with the application of functional diagnostics and the lean maintenance concept. It is necessary to continuously monitor the behavior of vehicles and the occurrence of failures in operation, which can best be done by introducing a designed information system. By analyzing failure occurrence data, it is possible to predict future reliability, which in turn allows for informed decisions on preventive inspection procedures and the replacement of parts before they fail, ultimately enhancing vehicle reliability and minimizing the impact of potential failures.

The scientific contribution of the conducted research includes:

1. Optimization of Maintenance Periodicity:
-   Quantitative and qualitative indicators of the system condition and vehicle reliability were obtained based on operational data, which led to the determination of the optimal maintenance periodicity for special purpose vehicles.
-   This periodicity, derived as a compromise solution, ensures satisfactory vehicle readiness with optimal maintenance costs.
2. Improvement in Maintenance Strategies:
-   The calculated periodicity for preventive maintenance falls between the first and second technical inspections, suggesting the redundancy of two closely timed technical inspections. Instead, a single preventive inspection at the calculated time would suffice, rationalizing the existing maintenance concept, reducing costs, and enhancing vehicle readiness.
3. Analysis of Vital Assemblies:
-   The analysis revealed different maintenance periodicities for vital assemblies. Engines and transmissions in both parks showed the highest reliability, resulting in significantly longer maintenance intervals compared to other assemblies.
-   Optimal grouping of local periodicities for multiple assemblies into a common periodicity was performed through group analysis, achieving optimal readiness and maintenance costs.

4. Statistical Analysis Findings:
- Statistical analysis using Minitab 15 and 16 concluded that there is no polynomial relationship between operation time until failure for the A and B parks, but such a relationship exists for the group of fifteen vital assemblies.
- Different maintenance periodicities were determined for the vehicles in the A and B parks. Some assemblies, such as the engine cooling system and transmission (assembly 3), the steering block (assembly 4), and the water protection mechanism (assembly 7), had similar maintenance periodicities in both parks.
5. Influence of Operational Conditions:
- The research showed that the condition and the maintenance periodicity of special purpose vehicles depend on the terrain, drivers, crew, and workshop conditions.
- The vehicles in the B park had longer times between maintenance, indicating different operational conditions. If a vehicle changes location and a maintenance site, new calculations for optimal maintenance periodicity must be performed.
6. Development of a New Preventive Maintenance Model:
- Grouping certain assemblies and aggregates based on similar time between failures allowed for a comprehensive analysis of their condition on a qualitative and quantitative level.
- The group analysis contributed to more precise management of vehicle operational readiness with optimal maintenance costs based on determined optimal preventive maintenance periods.
7. Adaptation to Different Operational Conditions:
- The analysis indicated that maintenance periodicity depends on terrain configuration and other operational conditions. If the same vehicle changes the location, optimal maintenance periodicity calculations need to be recalculated.
- The study also found that the engine and the transmission block have high reliability and are not significantly affected by changes in operational conditions.

The results in this paper represent a research contribution to determining the optimal periodicity of preventive maintenance for special purpose vehicles and can serve as a basis for further research. The continuation of the research could proceed in the following directions:
- Using the presented methodology, or a similar one, to investigate the periodicity of preventive maintenance for other assemblies of

special purpose vehicles (such as armaments and communication equipment);

- Conduct research on the optimal periodicity of preventive maintenance for all other fleets of special-purpose equipment using the presented methodology, with the aim of making final and precise conclusions on the optimal periodicity of maintenance for special purpose vehicles;
- Investigate the maintenance periodicity of vehicles in passive operation that are exposed to various degradative factors under such conditions; and
- Explore the possibility of installing an automated diagnostic system for functional diagnostics to ensure objective, highly precise, and continuous monitoring of the vehicle's operation and its vital systems (e.g., oil pressure drop in the engine, insufficient brake fluid level, excessive wear of brake pads, excessive wear of clutch disc linings, clogged fuel filters, failure of missile launch and guidance systems, wear of the drive wheel gear, wear of the support wheel, etc.).

References

Bass, S.M. & Kwakernaak, H. 1977. Rating and ranking of multiple-aspect alternatives using fuzzy sets. *Automatica,* 13(1), pp.47-58. Available at: https://doi.org/10.1016/0005-1098(77)90008-5.

Biočanin, S. & Pavlović, M. 2011. Determining the optimal periodicity of the V46-6 engine preventive maintenance. *Vojnotehnički glasnik/Military Technical,* 59(3), pp.106-130 (in Serbian). Available at: https://doi.org/10.5937/vojtehg1103106B.

Biočanin, S. & Timotijević M. 2020. A reliability analysis of the horizontal milling machine: GVK-1P. *IMK-14 - Istraživanje i razvoj*, 26(1), pp.1-6 (in Serbian). Available at: https://doi.org/10.5937/IMK2001001B.

Biočanin, S. & Timotijević, M. 2021. Određivanje modela pouzdanosti vozila posebne namene. In: *Šesti naučno-stručni skup Politehnika sa međunarodnim učešćem*, Belgrade, Serbia, pp.474-480, December 10 [online]. Available at: https://conference.politehnika.edu.rs/ [Accessed: 15.04.2024].

Biočanin, S. & Timotijević, M. 2023. Analysis of research on optimization models and algorithms for planning preventive maintenance of machine systems. In: *International scientific and professional conference Politehnika 2023*, Belgrade, Serbia, pp.1084-1092, December 15 [online]. Available at: https://conference.politehnika.edu.rs/ [Accessed: 15.04.2024].

-British Standards Institution (BSI). 2024. *Multi-part Document BS 5760 - Reliability of systems, equipment and components*. Available at: https://doi.org/10.3403/BS5760.

Ćatić, D. 2005. *Razvoj i primena metoda teorija pouzdanosti. Monografija*. Kragujevac: University of Kragujevac, Faculty of Mechanical Engineering (in Serbian). ISBN: 86-80581-80-1.

Krstić, B. 2009. Tehnička eksploatacija motornih vozila i motora. Kragujevac, Serbia: University of Kragujevac, Faculty of Engineering (in Serbian). ISBN: 9788690181919.

Krstić, B., Nikolić, R., Biočanin, S., Nikolić, I., Krstić, I. & Krstić, V. 2013. Determination of the Driving Engine Reliability for the Special Purposes Motor vehicle. In: 10-th European Conference of Young Researchers and Scientists, Žilina, Slovak Republic, Section 2, June 24-26.

Pavličić, D. 2000. Normalization of attribute values in MADM violates the conditions of consistent choice IV, DI and α. *Yugoslav Journal of Operations Research*, 10(1), pp.109-122 [online]. Available at: https://scindeks.ceon.rs/article.aspx?artid=0354-02430001109P [Accessed: 10 April 2024].

Paul Yoon, K. & Hwang, C.L. 1995. *Multiple Attribute Decision Making: An Introduction*. Thousand Oaks, CA: Sage Publications. ISBN: 9781452213576.

Vargas, L.G. 1990. An overview of the analytic hierarchy process and its applications. *European Journal of Operational Research*, 48(1), pp.2-8. Available at: https://doi.org/10.1016/0377-2217(90)90056-H.

Vincke, P. 1992. *Multicriteria Decision-Aid.* Wiley. ISBN: 978-0-471-93184-3.

Determinación de un modelo de mantenimiento preventivo de vehículos de propósito especial

Stojko Lj. Biočanin[a], *Milica* S. Timotijević[b], *Željko* M. Bulatović[c], *Milan* A. Mišić[d]

[a] Academia de Estudios Técnicos Aplicados de Belgrado, Departamento de Ingeniería Informática y Mecánica, Belgrado, República de Serbia, **autor de correspondencia**

[b] Academia de Aviación de la Facultad de Estudios Aplicados, Belgrado, República de Serbia

[c] Instituto Técnico Militar, Belgrado, República de Serbia

[d] Academia de Estudios Aplicados de Kosovo y Metohija, Zvečan, República de Serbia

CAMPO: ingeniería mecánica
TIPO DE ARTÍCULO: artículo científico original

Resumen:

Introducción/objetivo: El objetivo de este documento es obtener indicadores cuantitativos y cualitativos del estado y la confiabilidad del vehículo basados en datos operativos que puedan usarse para determinar la periodicidad óptima del mantenimiento preventivo para vehículos de

propósito especial y para gestionar con mayor precisión el proceso de mantenimiento y la disponibilidad operativa de estos vehículos.

Métodos: A partir de datos de fallas operativas y métodos estadísticos, se determinó un modelo matemático de confiabilidad de vehículos para fines especiales. Utilizando este modelo y datos operativos, se determinó la periodicidad del mantenimiento preventivo de los vehículos mediante optimización multicriterio, considerando tanto la disponibilidad como los costos mínimos de mantenimiento. La misma metodología se aplicó para determinar la periodicidad óptima de mantenimiento preventivo de 15 componentes del sistema mecánico de vehículos de propósito especial. Se realizó un análisis grupal mediante el software estadístico Minitab 15, basado en la teoría de la similitud en la periodicidad del mantenimiento preventivo para los 15 componentes, y un análisis estadístico de la investigación realizada mediante el software estadístico Minitab 16.

Resultados: Se desarrollaron modelos para el mantenimiento preventivo de vehículos de propósito especial con base en las fallas registradas de los vehículos y las fallas de quince componentes vitales. Un análisis de grupo reunió los quince componentes en grupos de mantenimiento óptimos, similares en términos de tiempo de trabajo entre fallas. El análisis estadístico de la investigación determinó una relación funcional para la periodicidad óptima del mantenimiento preventivo para vehículos de propósito especial.

Conclusión: La periodicidad de mantenimiento obtenida a través del análisis multicriterio es óptima, ya que logra una disponibilidad satisfactoria del vehículo con costos de mantenimiento óptimos. El análisis estadístico de la investigación concluyó que las periodicidades de mantenimiento de los componentes del vehículo son diferentes. En ambas flotas, el motor y el bloque de transmisión tienen los intervalos de mantenimiento más largos. Los resultados de la investigación pueden utilizarse para racionalizar el concepto de mantenimiento preventivo existente.

Palabras claves: vehículo, confiabilidad, disponibilidad, mantenimiento preventivo, costos, periodicidad óptima, análisis multicriterio.

Определение модели профилактического обслуживания
автомобиля специального назначения

Стойко Л. Биочанин[а], *Милица* С. Тимотиевич[б],
Желько М. Булатович[в], *Милан* А. Мишич[г]

[а] Академия прикладных технических исследований в Белграде,
   факультет компьютерной инженерии и машиностроения,
   г. Белград, Республика Сербия, **корреспондент**

[б] Авиационная академия, г. Белград, Республика Сербия

[в] Военно-технический институт, г. Белград, Республика Сербия

[г] Академия профессиональных исследований Косово и Метохия,
   г. Звечан, Республика Сербия

Резюме:

Введение/цель: Целью данной статьи является получение количественных и качественных показателей состояния и надежности транспортных средств на основании эксплуатационных данных, которые могут быть использованы для определения оптимальной периодичности профилактического обслуживания транспортных средств специального назначения и для более точного управления процессом технического обслуживания и эксплуатационной готовности.

Методы: На основании данных об эксплуатационных отказах и статистических методов была разработана математическая модель надежности транспортных средств специального назначения. Используя эту модель и эксплуатационные данные, путем многокритериальной оптимизации была определена периодичность профилактического обслуживания транспортных средств с учетом как готовности, так и минимальных затрат на техническое обслуживание. Аналогичный метод был применен для определения оптимальной периодичности профилактического обслуживания 15 компонентов механической системы транспортных средств специального назначения. Групповой анализ был проведен с использованием статистического программного обеспечения Minitab 15, основанного на теории подобия периодичности профилактического обслуживания 15 компонентов, а статистический анализ проведенного исследования был выполнен с помощью статистического программного обеспечения Minitab 16.

Результаты: На основании выявленных отказов транспортных средств и их пятнадцати ключевых компонентов были разработаны модели профилактического обслуживания транспортных средств специального назначения. Групповой анализ позволил оптимально сгруппировать пятнадцать компонентов для технического обслуживания, близких по продолжительности эксплуатации между двумя отказами. Благодаря статистическому анализу результатов исследования выявлена функциональную связь оптимальной периодичности профилактического обслуживания транспортных средств специального назначения.

1866

Выводы: Периодичность технического обслуживания, полученная в результате многокритериального анализа, является оптимальной, поскольку обеспечивает удовлетворительную готовность автомобиля при оптимальных затратах на техническое обслуживание. Статистический анализ исследования показал, что периодичность технического обслуживания различных компонентов автомобиля различается. В обоих автопарках наиболее длительной периодичностью технического обслуживания оказалось периодичность обслуживания двигателя и трансмиссии. Результаты исследований могут быть использованы для рационализации существующей концепции профилактического обслуживания.

Ключевые слова: транспортное средство, надежность, готовность, профилактическое обслуживание, затраты, оптимальная периодичность, многокритериальный анализ.

Одређивање модела превентивног одржавања возила посебне намене

Стојко Љ. Биочанин[а], *Милица* С. Тимотијевић[б],
Жељко М. Булатовић[в], *Милан* А. Мишић[г]

[а] Академија техничких струковних студија Београд,
   Катедра за рачунарско и машинско инжењерство,
   Београд, Република Србија, **аутор за преписку**

[б] Висока школа струковних студија Ваздухопловна академија,
   Београд, Република Србија

[в] Војнотехнички институт, Београд, Република Србија

[г] Академија струковних студија косовско метохијска,
   Звечан, Република Србија

ОБЛАСТ: машинство
КАТЕГОРИЈА (ТИП) ЧЛАНКА: оригинални научни рад

Сажетак:

Увод/циљ: Циљ рада јесте да се, на основу података из експлоатације возила, добију квантитативни и квалитативни показатељи стања возила и поузданости, на основу којих се може одредити оптимална периодичност превентивног одржавања возила посебне намене и прецизније управљати токовима процеса одржавања возила и њиховом оперативном готовошћу.

Методе: На основу података о отказима из експлоатације, добијених статистичким методама, одређен је математички модел поузданости возила посебне намене. На основу овог модела и података из експлоатације одређена је периодичност превентивног одржавања возила применом вишекритеријумске оптимизације, уважавајући критеријум готовости и критеријум

минималних трошкова одржавања. По истој методологији одређена је оптимална периодичност превентивног одржавања петнаест склопова моторно-техничког дела возила посебне намене. Извршена је групна анализа, у статистичком софтверу Minitab 15, на основу теорије сличности периодичности превентивног одржавања ових склопова, и статистичка анализа спроведених истраживања у статистичком софтверу Minitab 16.

Резултати: Добијени су модели превентивног одржавања возила посебне намене на основу евидентираних отказа возила и отказа петнаест виталних склопова возила посебне намене. Петнаест склопова је групном анализом груписано у оптималне групе за одржавање, које су сличне по дужини рада између два отказа. Статистичком анализом спроведених истраживања одређена је функционална веза оптималних периодичности превентивног одржавања возила посебне намене.

Закључак: Периодичност одржавања, добијена вишекритеријумском анализом, оптимална је јер се добија задовољавајућа готовост возила уз оптималне трошкове одржавања. Статистичком анализом истраживања дошло се до закључка да су периодичности одржавања склопова возила различите. У обе флоте мотор и трансмисија у блоку имају најдужу периодичност одржавања. Резултати истраживања могу се користити у рационализацији постојећег концепта превентивног одржавања.

Кључне речи: возило, поузданост, готовост, превентивно одржавање, трошкови, оптимална периодичност, вишекритеријумска анализа.

Efficiency assessment of different high-speed tracked vehicle hybrid powertrain conceptions

Luka M. Ponorac[a], *Ivan* A. Blagojević[b]

[a] AMSS-Center for Motor Vehicles Ltd, Belgrade, Republic of Serbia,
  e-mail: luka.ponorac@amss-cmv.co.rs, **corresponding author**,
  ORCID iD: https://orcid.org/0000-0003-2315-8743

[b] University of Belgrade, Faculty of Mechanical Engineering,
  Department of Motor Vehicles, Belgrade, Republic of Serbia,
  e-mail: iblagojevic@mas.bg.ac.rs,
  ORCID iD: https://orcid.org/0000-0002-5776-5990

Abstract:

Introduction/purpose: Increased development of hybrid powertrains during the last decade brought high-speed tracked vehicles into the same spotlight as commercial and passenger hybrid vehicles. There are several hybrid powertrain conceptions for high-speed tracked vehicles that are mainly researched, but there is still no clear conclusion which conception is the most efficient. The main obstacle for more intense research is the increased difficulty to produce a battery storage system which provides both high power density and protection and shock resistance. However, there is a certain number of research studies and prototypes developed from simulation models that show satisfactory performance for both asymmetric and symmetric hybrid powertrain conceptions.

Methods: The developed and verified hybrid simulation model is improved in terms of command signal unit, so that the powertrain and electric motors in the auxiliary drive can easily be operated in the asymmetric hybrid working regime and the symmetric hybrid working regime. The main goal is to simulate specific working regimes where the asymmetric and symmetric hybrid powertrain performance and energy efficiency can be assessed in order to find the most efficient powertrain conception.

Results: The results indicate that the asymmetric hybrid powertrain will have less overall power consumption and a more simple control algorithm, because of controlling just one electric motor. For the same overall power, the asymmetric hybrid powertrain has a smaller turning radius, which is satisfactory. When driven in full power, the symmetric hybrid powertrain will have lower turning radius and better manoeuvrability, but serious increase of power consumption.

Conclusion: The asymmetric drive has clearly better power efficiency, but the symmetric drive has an advantage of maximum performance. Performing a pivot turn (around the vertical axis), and making a turn without reducing the vehicle velocity is of great importance, especially considering the most common special purpose of this vehicle and manoeuvring in challenging terrain conditions.

Key words: high-speed tracked vehicles, hybrid powertrains, turning process analysis, power balance analysis.

Introduction

Research and development of hybrid powertrains brought a new perspective on commercial and passenger transportation, but also on military and special purpose application (Kramer & Parker, 2011; Taira et al, 2017; Ramesh, 2017). High-speed tracked vehicle powertrains were also rapidly brought to attention of researchers and renowned manufacturers, as an almost infinite course for research of powertrain hybridization potential.

Unlike commercial vehicle hybrid powertrains, where basic interest in hybrid powertrain development lies in ecology and fuel consumption reduction, the core value for development of hybrid powertrains for high-speed tracked vehicles is performance enhancement and improving energy efficiency (Dalsjø, 2008; Walker et al, 2015; Salisa et al, 2011). The special purpose and utilization of high-speed tracked vehicles demand robust powertrain systems, due to rough terrain and other conditions which require optimal balance between performance and energy efficiency (Randive et al, 2021; Sabri et al, 2016). This has generated interest in developing powertrain conceptions which provide optimal performance and satisfy demands that stand before these vehicles, by incorporating electric drive machines in the powertrain system, along with ICE. Apart from propulsion, high-speed tracked vehicles have various specialized systems which have moderate to high energy consumption requirements from the ICE. This is also a significant argument to search for an alternative power source solution, with increased potential of storing and producing, as well as managing the required energy.

Even though there are numerous arguments for the implementation of hybrid high-speed tracked vehicle powertrains, only a few prototypes have ever been made. One of the main obstacles is the development of energy source and storage, i.e., batteries, which have the capacity to provide energy required for the expected operation conditions of the vehicle (Bhatia, 2015; Piancastelli et al, 2023; Rizzo, 2014).

This paper presents the continuation of the research into hybrid powertrains for specific high-speed tracked vehicles, with the goal of designing the most efficient hybrid conception and powertrain working regime. The assessment of energy efficiency throughout different hybrid powertrain configurations is a complex challenge, because these systems are influenced by numerous variables such as terrain and atmospheric conditions, driving regimes and specific powertrain configurations.

The assessment of energy efficiency, as well as performance improvement, is conducted on a previously developed and verified simulation model, for the most demanding powertrain working regimes, from the power balance point of view, especially during the turning process (Ponorac & Blagojević, 2023). The hybrid powertrain model is developed so it can work as both an asymmetric and symmetric turning mechanism. Based on these two conceptions, the vehicle is analyzed in different turning scenarios, as well as full electric and hybrid movement scenarios, in order to identify the most efficient working regime of the hybrid powertrain.

Method

Replacing the friction clutches with electric motors in the auxiliary drive of the subject vehicle powertrain, as shown in Figure 1, has led to essential improvement because the hybrid powertrain can work in various working regimes, depending on the user's demand. The mentioned upgrade allows the powertrain system, which incorporates the turning mechanism, to operate both as an asymmetric and a symmetric vehicle turning mechanism, depending on the electric motor engagement scheme and the direction of electric motor shaft rotation.

By engaging the electric motor on the inner track, the powertrain output shaft, i.e., the inner track drive shaft angular velocity is reduced. The vehicle center of mass velocity is also reduced, while the outer track maintains the rectilinear movement velocity. The described working regime represents a classic case of an asymmetric vehicle turning mechanism.

If both electric motors are engaged, with the angular velocity of the same intensity, but different directions, the outer track velocity is increased proportionally to the inner track velocity decrease while the vehicle center of mass velocity is maintained. The described working regime represents a classic case of a symmetric vehicle turning mechanism (Muždeka & Perić, 2012).
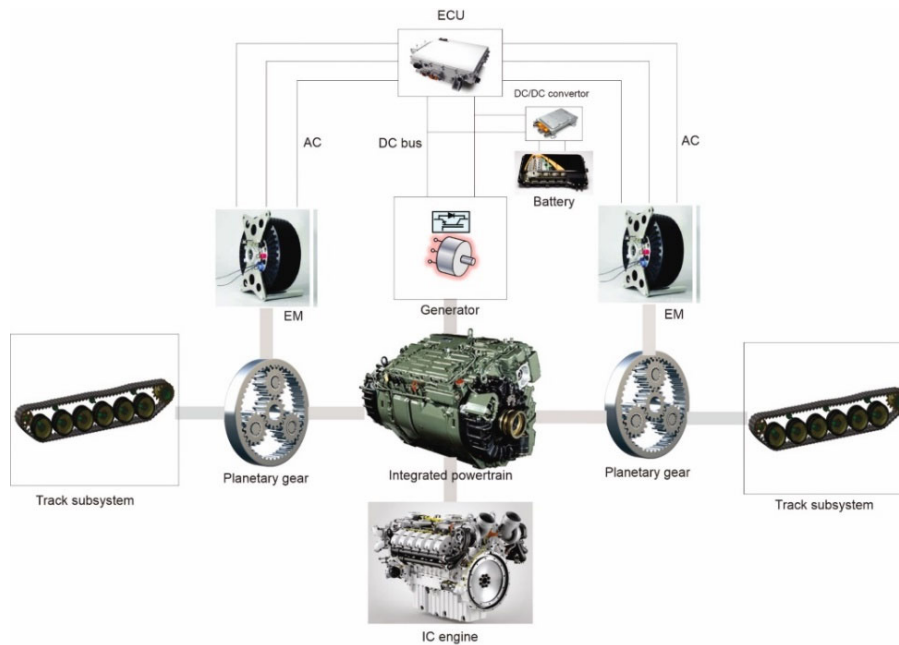
Figure 1 – Hybrid powertrain conception scheme

In a general case, the overall power required to achieve the turning manoeuver must be sufficient to overcome moving resistance, internal powertrain resistance and resistance in the turning mechanism (Muždeka, 2012)

that is:

$$P_{mz} = P_o + P_{tr} + P_{sz} \qquad (1)$$

where:

- P_o is the power required to overcome moving resistance,
- P_{tr} is the power required to overcome internal powertrain resistance, and
- P_{sz} is the power lost in the turning mechanism elements.

The power lost in the turning mechanism is not taken into consideration because, in the specific case, this power is not delivered from the ICE, but from the electric motors. Also, since there are friction clutches, there are no slipping losses, so the power lost in the turning mechanism is assessed by the electric motor efficiency. Since the electric

motors are used in the most efficient working regimes, the overall power lost in the turning mechanism is insignificant.

The power required to overcome the internal resistance in the powertrain is taken into account through the efficiency of the powertrain components.

The power required to overcome moving resistance depends on the turning mechanism conception.

In the case of the asymmetric turning mechanism, the power required to overcome moving resistance is:

$$P_o = F_2 v_0 - F_1 v_0 \frac{R - \frac{B}{2}}{R + \frac{B}{2}} = \frac{F_2\left(R + \frac{B}{2}\right) - F_1\left(R - \frac{B}{2}\right)}{\left(R + \frac{B}{2}\right)} v_0 \qquad (2)$$

In order to make a symmetric turn, the ICE and electric motors need to supply greater power than the asymmetric turning mechanism, because the vehicle keeps the center of mass velocity by increasing the velocity of the outer track and decreasing the velocity of the inner track. This can be concluded from (3):

$$P_o = F_2 v_0 \frac{R + \frac{B}{2}}{R} - F_1 v_0 \frac{R - \frac{B}{2}}{R} = \frac{F_2\left(R + \frac{B}{2}\right) - F_1\left(R - \frac{B}{2}\right)}{R} v_0 \qquad (3)$$

where:

- F2, F1 are the forces on the outer and inner track, respectively,
- v_0 is the vehicle center of mass velocity during rectilinear movement,
- R is the vehicle turning radius, and
- B is the track width.

Efficiency assessment

Energy efficiency

In order to asses and compare the energy efficiency of the symmetric and asymmetric hybrid powertrains, the simulation has to be set up in such a manner that the same turning conditions are provided, i.e., the same turning radius and resistance. The developed hybrid simulation model is verified in the previous research papers, by comparing the simulation results with the real vehicle simulation model and the experimental testing results (Ponorac et al, 2022).

The simulation starts from a steady state for both hybrid powertrain conceptions, where the main vehicle brakes K1 and K2 are engaged. The simulation conditions are controlled from the corresponding input signal block, as shown in Figure 2 and Figure 3. By disengaging the brakes and

applying throttle, the vehicle starts rectilinear movement. In both symmetric and asymmetric turning scenarios, the vehicle turning process starts at t≈4s.
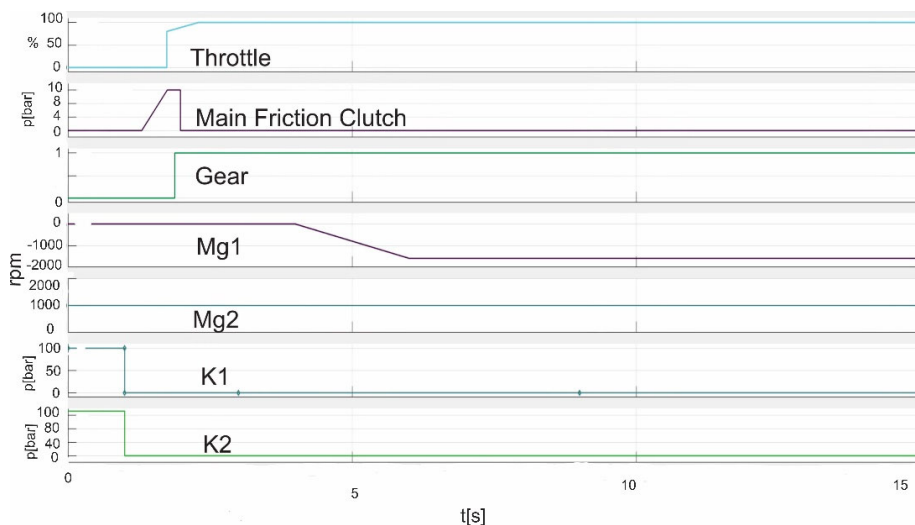

Figure 2 – Asymmetric hybrid powertrain model input signals
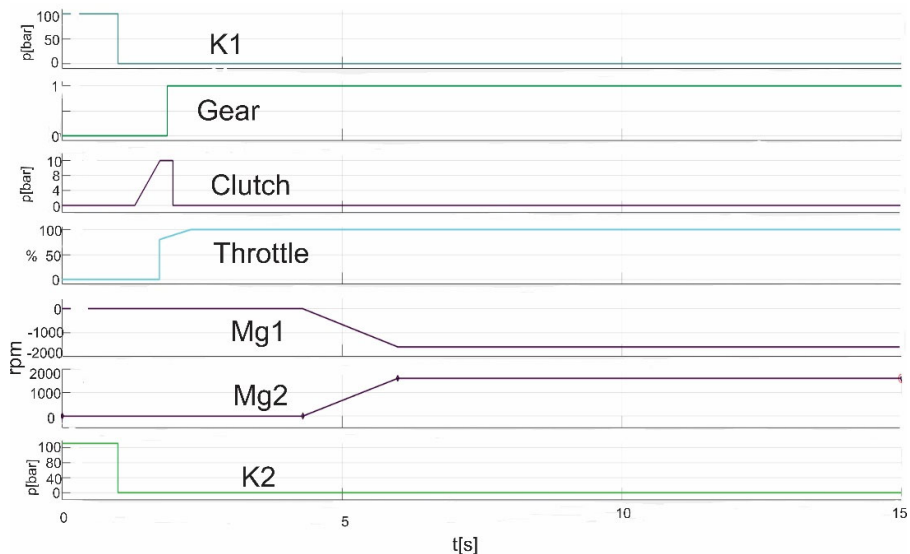

Figure 3 – Symmetric hybrid powertrain model input signals

1874

The vehicle with the asymmetric turning mechanism starts the turning process by engaging the electric motor Mg1 on the inner track, as shown in Figure 2. The electric motor is engaged with n=1600 rpm.

The vehicle with the symmetric turning mechanism starts the turning process at the same moment, but in order to achieve the same turning radius, the electric motor on the inner track, labeled Mg1, is engaged with n=1100 rpm, while the electric motor on the outer track, Mg2, is engaged with the same rpm value but in the opposite direction, as shown in Figure 3.

Performance review

In order to assess the vehicle performance benefits for both developed conceptions, it is needed to provide equal energy consumption conditions. Different working principles of symmetric and asymmetric hybrid turning mechanisms make this a complicated task, so it will be divided in two scenarios.

The first scenario is assessing the turning process performance while the overall power consumption for both symmetric and asymmetric hybrid powertrains is equivalent. This means that the power provided by the ICE and the inner track electric motor in the asymmetric hybrid powertrain is equivalent to power provided by the ICE and the inner and outer track electric motors in the symmetric hybrid powertrain.

The second scenario includes assessing the turning process performance while the power delivered on the inner track is equivalent for both symmetric and asymmetric hybrid powertrains.

Results

Assessing the energy efficiency of symmetric and asymmetric hybrid powertrains of a high speed tracked vehicle requires equal turning conditions, i.e., the equivalent turning radius. Figure 4 shows the turning radius during the symmetric and asymmetric turning process.

Both symmetric and asymmetric hybrid powertrain vehicles achieve the requested turning radius R=3 m at t=6s.

In order to achieve the equal turning radius as the asymmetric hybrid powertrain, the symmetric hybrid powertrain engages the inner track electric motor with lower rpm, n=1100 rpm, but the same rpm is required on the outer track, as shown in Figure 5. In other words, the vehicle center of mass maintains its former velocity, while the inner and outer track velocities are decreased/increased. On the other hand, it is obvious that the outer track of the asymmetric hybrid powertrain maintains the

rectilinear movement velocity, the center of mass and inner track velocities are decreased.
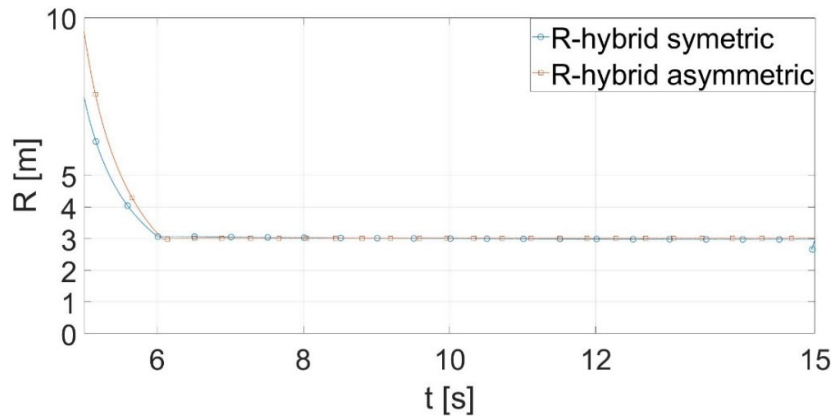
Figure 4 – Vehicle turning radius comparison- asymmetric vs symmetric
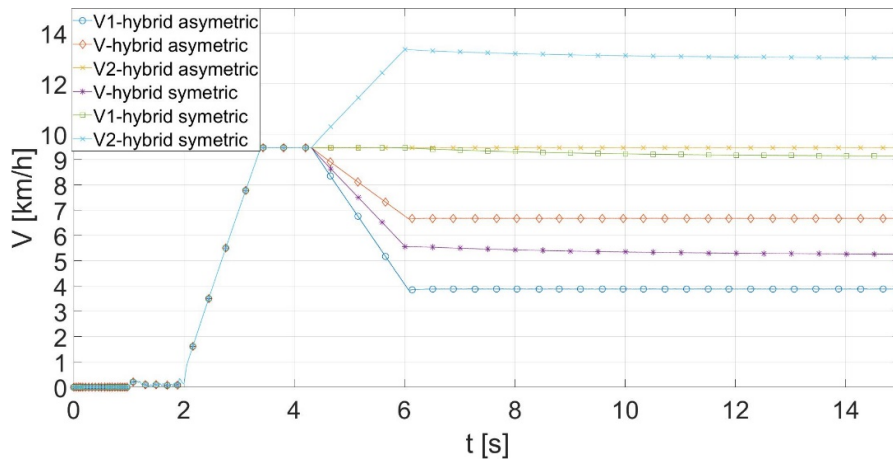
Figure 5 – Asymmetric vs symmetric hybrid vehicle velocities-equal turning radius

The power balance curve for the considered scenarios is shown in Figure 6. The overall power needed to achieve the required turning radius for asymmetric turning mechanism is Pasymmetric=84 kW. This power is supplied by the ICE Pice-hybrid asymmetric=41 kW, and the electric motor on the inner track PMG1-asymmetric=42 kW.

Figure 6 – Asymmetric vs symmetric hybrid powertrain power consumption-equal turning radius
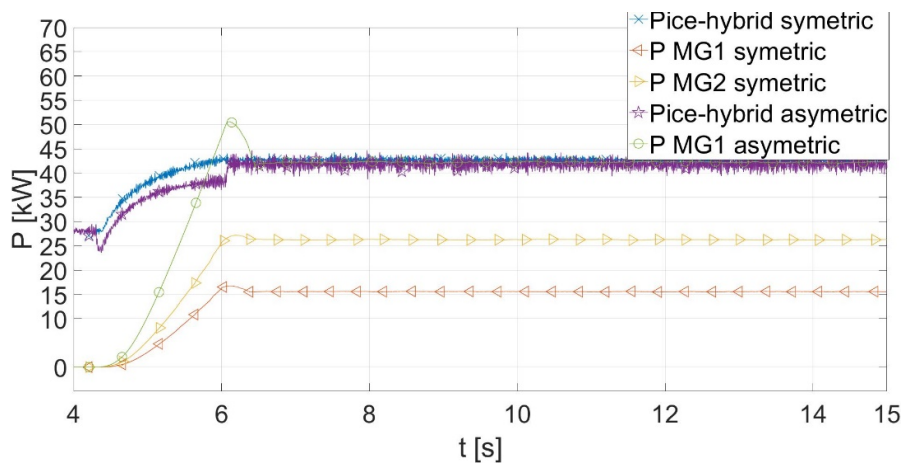
Figure 7 – Asymmetric vs symmetric hybrid powertrain power consumption-equal overall power

The symmetric hybrid powertrain requires less power on the inner track electric motor, PMG1-symmetric=30kW, but in order to maintain the vehicle velocity in turn, the power delivered from the outer track electric motor is PMG2-symmetric=48 kW. The ICE supplies the same power in both scenarios, 41 kW, so the overall power required for the requested turning radius is P-symmetric=118 kW. This means that the symmetric

hybrid powertrain requires more overall power than the asymmetric hybrid powertrain for the same turning radius; therefore, in this turning scenario, the asymmetric powertrain consumes less energy.

When the overall power required for the turning process of both symmetric and asymmetric hybrid powertrains is equal, the power is distributed as shown in Figure 7.

As in the previous cases, the ICE power for both hybrid powertrain conceptions is equal, Pice asymmetric=Pice symmetric=41 kW. In order to achieve the requested overall power required for the turning process Pasymmetric=84 kW, the inner track electric motor of the asymmetric hybrid powertrain delivers the remaining P MG1 asymmetric=43 kW.

Since the overall power requested for the symmetric hybrid powertrain is also Psymmetric=84 kW, the remaining 43 kW are delivered from both electric motors, where PMG1 symmetric=15 kW and PMG2=26 kW. Even though the track velocities are symmetrically increased/decreased, the power consumption of the electric motors is not equal. This is because the turning resistance is not equal on both tracks.

When the overall power for both hybrid powertrains is equal, the turning radius for both hybrid powertrains change as shown in Figure 7. The asymmetric hybrid powertrain turns with a turning radius of R=3m, which is the same turning radius as the calculated turning radius of the real vehicle. However, the symmetric hybrid powertrain turns with a larger turning radius of Rsymmetric=5 m.
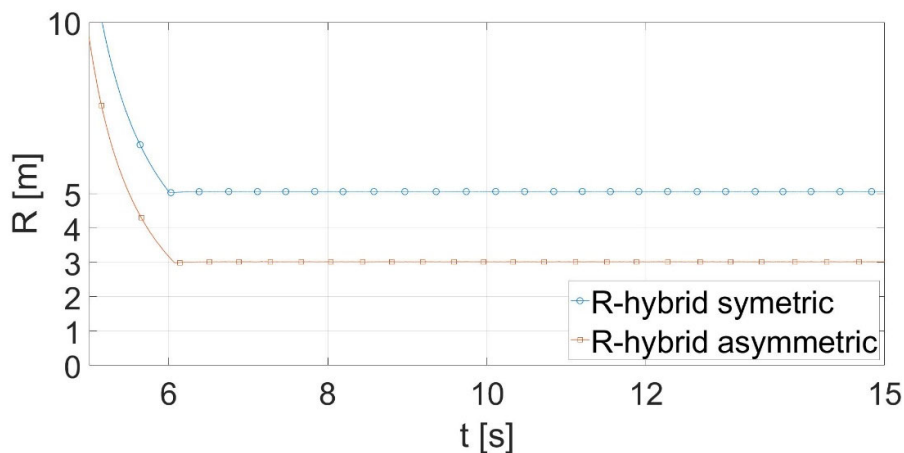
Figure 8 – Asymmetric vs symmetric hybrid powertrain turning radius-equal overall power

The track velocities, shown in Figure 9, confirm the obtained results and conclusions. With the same overall power consumption, the inner track velocity of the symmetric hybrid powertrain is significantly larger than in the asymmetric hybrid powertrain. The inner and outer tracks are driven by electric motors at n≈700 rpm. The vehicle center of mass maintains the rectilinear movement velocity, while the asymmetric hybrid vehicle center of mass velocity is near the velocity value of the symmetric hybrid inner track. In other words, the asymmetric hybrid vehicle turns with almost equal velocity as the symmetric hybrid vehicle inner track; thus the turn radius of the asymmetric hybrid powertrain vehicle is significantly lower.
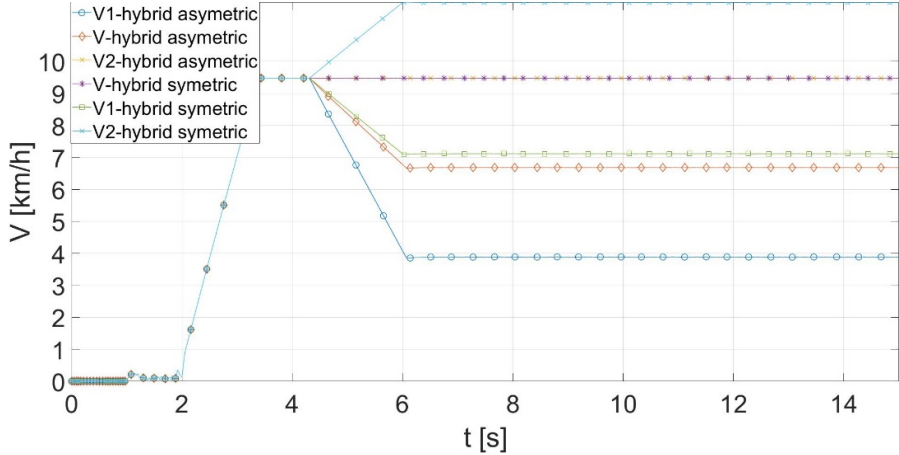
Figure 9 – Asymmetric vs symmetric hybrid powertrain vehicle velocities-equal overall power

When delivering equal power on the inner track of both hybrid powertrains, the inner track of both hybrid conceptions will have equal velocities, which is needed to assess the turning performance of the symmetric hybrid powertrain. The power balance curves are shown in Figure 10.

The asymmetric powertrain has the same power distribution as in the previous cases. The ICE delivers 41 kW and the inner track electric motor delivers 43 kW, making the overall power requested for the turning process P asymmetric =84 kW.

If the tracks of the symmetric hybrid powertrain are driven with at n=1600 rpm, which is equal to the rotational speed of the asymmetric hybrid inner track electric motor, the power delivered to the inner track of both hybrid conceptions will be equal, i.e., PMG1 symmetric=43 kW.

Meanwhile, the power on the outer track is significantly higher and is PMG2 symmetric=65 kW, which makes the overall power requirement for symmetric turn Psymmetric≈149 kW.
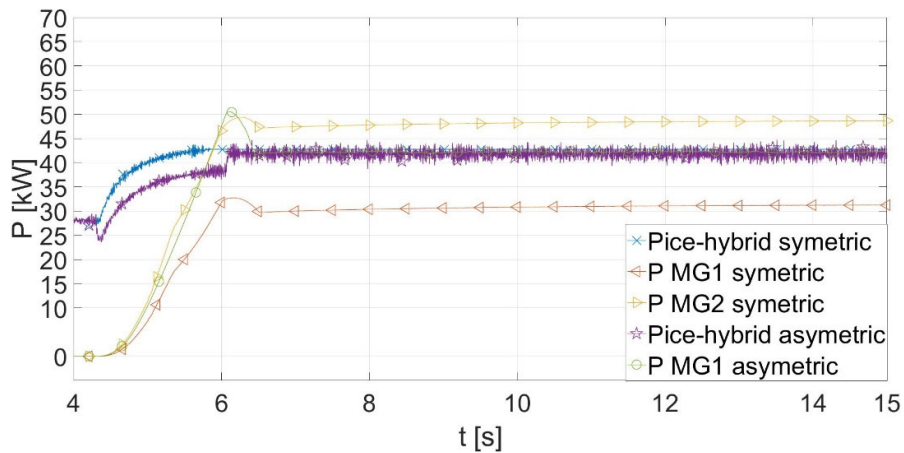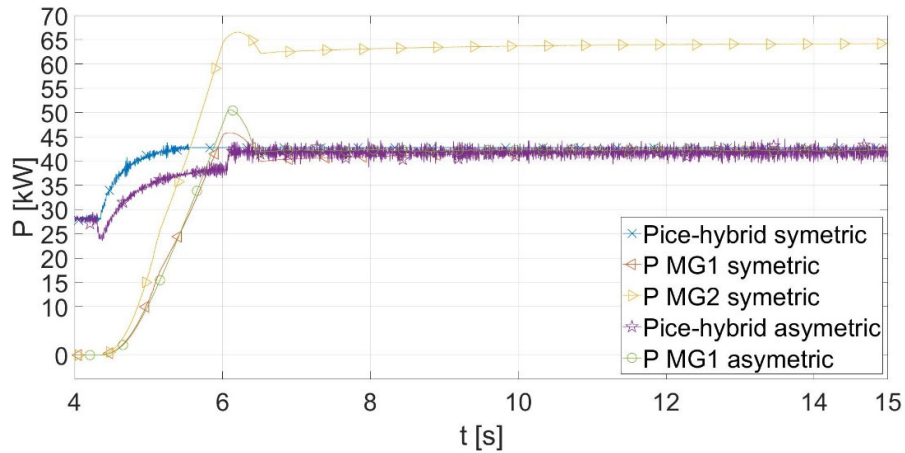

Figure 10 – Asymmetric vs symmetric hybrid powertrain power consumption- equal power on the inner track
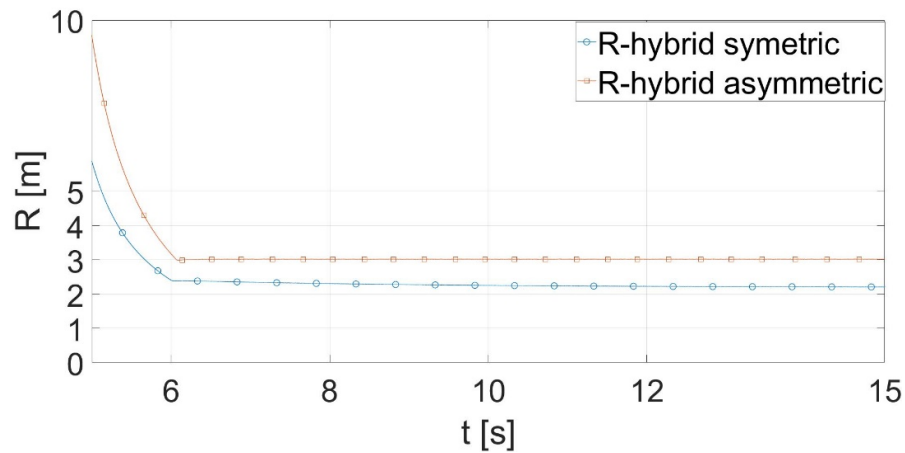
Figure 11 – Asymmetric vs symmetric hybrid powertrain turning radius- equal power on the inner track

The turning radius for the described scenario is shown in Figure 11. When the inner track velocities are equal, i.e., is when the inner track electric motor delivers equal power in both symmetric and asymmetric

hybrid powertrains, the vehicle with the symmetric hybrid powertrain has a lower turning radius Rsymmetric≈2 m, while Rasymmetric=3 m. The velocities follow the turning radius behavior, as shown in Figure 12.
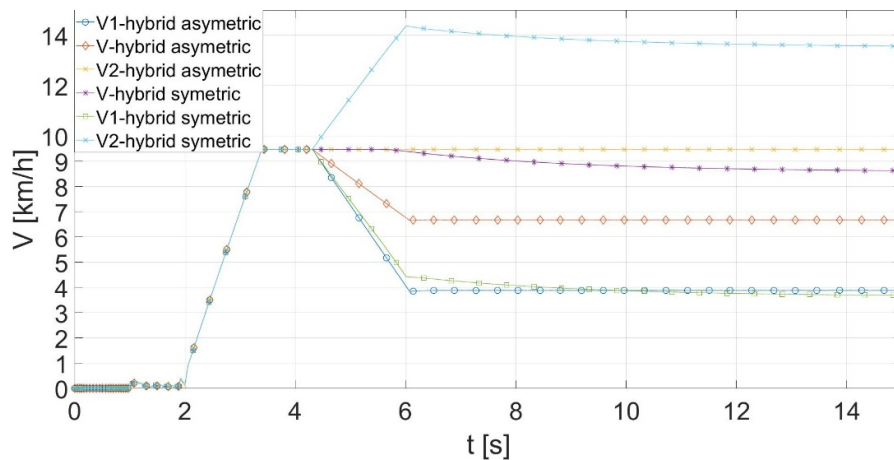
Figure 12 – Asymmetric vs symmetric hybrid powertrain vehicle velocities- equal power on the inner track

Discussion

The obtained results indicate that hybrid powertrains for high speed tracked vehicles, in most of cases, provide either increased power balance and efficiency or increased vehicle performances, compared to classic mechanical powertrains. The explanation for this lies in the fact that, in hybrid powertrains, the power required for the turning process is not provided by the ICE. The second reason is that the hybrid powertrain does not use friction clutches in the turning mechanism, so there are no slip losses.

Asymmetric hybrid powertrain vehicles will achieve the required turning radius with 40% lower overall power demands than the symmetric one, i.e., with the lowest electrical energy consumption. To achieve this, the vehicle velocity reduces. The symmetric hybrid powertrain has greater power consumption, but maintains vehicle velocity, which can be crucial in certain conditions.

For the same overall power demands, the asymmetric hybrid powertrain has a 40% lower turning radius in the analyzed working regime, which results in a lower manoeuvring area compared to the symmetric

hybrid powertrain. In certain conditions, such as small manoeuvring space, or in urban conditions, a lower turning radius is more desirable.

When the inner track is loaded with the same turning resistance for both symmetric and asymmetric hybrid powertrains, the symmetric hybrid powertrain turns with a 33% lower turning radius than the asymmetric powertrain, but the overall power demand is 77% greater.

It would seem that, in almost all cases, the asymmetric powertrain is more efficient. However, the symmetric hybrid powertrain has two major advantages. First, the vehicle center of mass maintains the same velocity when the vehicle starts the turning process, which is very important given the nature of the vehicle utilization. The asymmetric hybrid powertrain vehicle reduces its velocity in every turning scenario.

The second significant advantage of the symmetric hybrid powertrain is the capability of making a pivot turn, around the central axis of the vehicle. During the years of high-speed tracked vehicle utilization, this advantage has shown to be extremely valuable, especially when the vehicle is utilized in urban conditions.

Conclusion

Improving the classic mechanical high-speed tracked vehicle powertrain into a hybrid powertrain improves the vehicle potential power efficiency and performance. The need to overcome the mechanical powertrain concept comes from the fact that mechanical powertrains lose significant amount of power due to losses in the friction elements due to slip, which has impact on the turning radius, manoeuvrability, stability and other vehicle performances.

Even though most of performance and power efficiency parameters go in favor of asymmetric hybrid powertrains where the same turning parameters are achieved with 40% less power, most of the world known manufacturers opted for symmetric hybrid powertrains. The symmetric hybrid powertrain has a great advantage - turning with a 33% lower turning radius than the asymmetric powertrain, and also the lowest theoretical turning radius, which is turning around the vertical axis of the vehicle, referred to as the pivot turn. Turning around the vertical axis allows the vehicle to turn in urban conditions and other areas that provide low manoeuvrability, which is one of the greatest advantages and parameters of a high-speed tracked vehicle. By utilizing electric motors as drive machines for the turning mechanisms, the turning algorithm can be fully controlled, making the turn with asymmetric increase/decrease of outer/inner track velocity. The suggested hybrid powertrain has the

potential to be programmed in such a way that it provides the function of both asymmetric and symmetric turning mechanism, depending on the driver's demands.

Considering multiple improvements and virtues of the analyzed hybrid powertrain solutions, one obstacle stands before these powertrain solutions, and that is the power source which provides enough energy for the required working regimes. The capacity and power of the power sources have to be analyzed in detail, especially in the case of fully electric working regime of the powertrain and other conceptions including using electric motors for purposes other than trajectory correction. Opposite to the vehicle turning regime where electric motors are briefly used, rectilinear movement would demand significantly more electric energy from batteries which are charged by the ICE. Analyzing the ICE power needed for battery charging is obligatory in the mentioned working regimes.

References

Bhatia, V. 2015. Hybrid Tracked Combat Vehicle. In: *2015 IEEE International Transportation Electrification Conference (ITEC)*, Chennai, India, pp.1-23, August 27-29. Available at: https://doi.org/10.1109/ITEC-India.2015.7386862.

Dalsjø, P. 2008. *Hybrid electric propulsion for military vehicles - overview and status of the technology*. Kjeller, Norway: Norweigan Defence Research Establishment [online]. Available at: https://www.ffi.no/en/publications-archive/hybrid-electric-propulsion-for-military-vehicles-overview-and-status-of-the-technology [Accessed: 15 September 2024]. ISBN: 978-82-464-1394-5.

Kramer, D.M. & Parker, G.G. 2011. Current state of military hybrid vehicle development. *International Journal of Electric and Hybrid Vehicles (IJEHV)*, (4), pp.369-387. Available at: https://doi.org/10.1504/IJEHV.2011.044373.

Muždeka, S. 2012. *Osnovi konstrukcije borbenih vozila*. Belgrade, Serbia: Medija Centar Odbrana (in Serbian). ISBN: 9788633503761.

Muždeka, S. & Perić, S. 2012. *Osnovi borbenih vozila, praktikuum za vežbe*. Belgrade, Serbia: Medija Centar Odbrana (in Serbian). ISBN: 9788633503693.

Piancastelli, L., Toccaceli, M., Sali, M., Leon-Cardenas, C. & Pezzuti, E. 2023. Electric Hybrid Powertrain for Armored Vehicles. *Energies*, 16(6), art.number:2605. Available at: https://doi.org/10.3390/en16062605.

Ponorac, L. & Blagojević, I. 2023. Experimental Validation of a High-speed Tracked Vehicle Powertrain Simulation Model. *Measurement Science Review*, 23(5), pp.192-201. Available at: https://doi.org/10.2478/msr-2023-0025.

Ponorac, L., Blagojević, I. & Grkić, A. 2022. Analysis of powertrains's workload during the turning process of a high-speed tracked vehicle. *IOP Conference Series: Materials Science and Engineering*, 1271, art.number:012003. Available at: https://doi.org/10.1088/1757-899X/1271/1/012003.

Ramesh, S. 2017. Armoured Fighting Vehicle - Future Perspective. *Defence Science Journal*, 67(4), pp.341-342. Available at: https://doi.org/10.14429/dsj.67.11544.

Randive, V., Subramanian, S.C. & Thondiyath, A. 2021. Design and analysis of a hybrid electric powertrain for military tracked. *Energy*, 229, art.number:120768. Available at: https://doi.org/10.1016/j.energy.2021.120768.

Rizzo, D.M. 2014. *Military Vehicle Optimization and Control*. PhD thesis. Michigan Technological University. Available at: https://doi.org/10.37099/mtu.dc.etds/863.

Sabri, M.F.M., Danapalasingam, K.A. & Rahmat, M.F. 2016. A review on hybrid electric vehicles architecture and energy management strategies. *Renewable and Sustainable Energy Reviews*, 53, pp.1433-1442. Available at: https://doi.org/10.1016/j.rser.2015.09.036.

Salisa, A.R., Zhang, N. & Zhu, J. 2011. A Comparative Analysis of Fuel Economy and Emissions Between a Conventional HEV and the UTS PHEV. *IEEE Transactions on Vehicular Technology*, 60(1), pp.44-54. Available at: https://doi.org/10.1109/TVT.2010.2091156.

Taira, H., Yoshikawa, T. & Jumonji, K. 2017. Development of Tracked Combat Hybrid-Electric Vehicle. *DST.defence.gov.au* [online]. Available at: https://www.dst.defence.gov.au/sites/default/files/basic_pages/documents/ICSIL P18Thu1430_Taira_et_al-Tracked_Hybrid-Electric_Combat_vehicle.pdf [Accessed: 15 September 2024].

Walker, P.D., Roser, H., Zhang, N. & Fang, Y. 2015. Comparison of Powertrain System Configurations for Electric Passenger Vehicles. In: *18th Asia Pacific Automotive Engineering Conference*. SAE Technical Paper 2015-01-00520. Available at: https://doi.org/10.4271/2015-01-0052.

Evaluación de la eficiencia de diferentes concepciones de sistemas de propulsión híbridos para vehículos de orugas de alta velocidad

Luka M. Ponorac[a], *Ivan* A. Blagojević[b]

[a] AMSS- Centro de vehículos motorizados, Belgrado, República de Serbia,
   autor de correspondencia

[b] Universidad de Belgrado, Facultad de Ingeniería Mecánica,
   Departamento de Vehículos Motorizados, Belgrado, República de Serbia

Resumen:

Introducción/objetivo: El aumento en el desarrollo de sistemas de propulsión híbridos durante la última década puso a los vehículos de orugas de alta velocidad en el mismo centro de atención que los vehículos híbridos comerciales y de pasajeros. Hay varias concepciones de sistemas de propulsión híbridos para vehículos de orugas de alta velocidad que se

están investigando principalmente, pero todavía no hay una conclusión clara sobre cuál es la más eficiente. El principal obstáculo para una investigación más intensa es la creciente dificultad para producir un sistema de almacenamiento de batería que proporcione una potencia de alta densidad y protección y resistencia a los golpes. Sin embargo, existe un cierto número de estudios de investigación y prototipos desarrollados a partir de modelos de simulación que muestran un rendimiento satisfactorio para concepciones de sistemas de propulsión híbridos tanto asimétricos como simétricos.

Métodos: El modelo de simulación híbrido desarrollado y verificado se mejora en términos de unidad de señal de comando, de modo que el sistema de propulsión y los motores eléctricos en el accionamiento auxiliar puedan operarse fácilmente en el régimen de trabajo híbrido asimétrico y en el régimen de trabajo híbrido simétrico. El objetivo principal es simular regímenes de trabajo específicos en los que se puedan evaluar el rendimiento y la eficiencia energética del sistema de propulsión híbrido simétrico y asimétrico para encontrar el concepto de sistema de propulsión más eficiente.

Resultados: Los resultados indican que el sistema de propulsión híbrido asimétrico tendrá menos consumo de energía general y un algoritmo de control más simple, debido a que controla un solo motor eléctrico. Para la misma potencia total, el sistema de propulsión híbrido asimétrico tiene un radio de giro menor, lo cual es satisfactorio. Cuando se conduce a máxima potencia, el sistema de propulsión híbrido simétrico tendrá un radio de giro más bajo y una mejor maniobrabilidad, pero aumentará considerablemente el consumo de energía.

Conclusión: El accionamiento asimétrico tiene una eficiencia energética claramente mejor, pero el accionamiento simétrico tiene la ventaja de un rendimiento máximo. Realizar un giro de pivote (alrededor del eje vertical) y realizar un giro sin reducir la velocidad del vehículo es de gran importancia, especialmente considerando el propósito especial más común de este vehículo y las maniobras en condiciones de terreno difíciles.

Palabras claves: vehículos de orugas de alta velocidad, sistemas de propulsión híbridos, análisis del proceso de giro, análisis del equilibrio de potencia.

Оценка эффективности различных концепций гибридных систем передачи мощности высокоскоростных гусеничных машин

Лука М. Понорац[а], *Иван* А. Благоевич[б]

[а] ООО "АМСС-Центр автомобильных транспортных средств",
 г. Белград, Республика Сербия, **корреспондент**

[б] Белградский университет, факультет машиностроения,
 кафедра транспортных средств, г. Белград, Республика Сербия

Резюме:

Введение/цель: Прогрессирующее развитие гибридных силовых установок в течение последнего десятилетия привлекло внимание к высокоскоростным гусеничным транспортным средствам. Существует несколько устойчивых концепций гибридных систем передачи мощности для высокоскоростных гусеничных машин, которые были тщательно исследованы и доведены до стадии прототипа, однако конкретного анализа и заключения о наиболее эффективной концепции нет. Основным препятствием для более глубоких исследований является проблема создания системы хранения аккумуляторных батарей, т.е. аккумулятора достаточной емкости и удельной мощности, устойчивому к ударам и нагрузкам, возникающим при использовании вышеупомянутых транспортных средств. Однако существует определенное количество научных исследований и прототипов, разработанных на основе имитационных моделей, которые демонстрируют удовлетворительную производительность как для асимметричных, так и для симметричных гибридных силовых установок.

Методы: Разработанная и проверенная гибридная имитационная модель усовершенствована с точки зрения блока командных сигналов, так что управление силовой установкой и электродвигателями вспомогательного привода максимально упрощено как в асимметричном, так и симметричном гибридном рабочем режиме. Основная цель состоит в моделировании конкретных режимов работы, при которых можно оценить производительность и энергоэффективность асимметричных и симметричных гибридных силовых установок для того, чтобы найти наиболее эффективную концепцию силового агрегата.

Результаты: Результаты показывают, что у асимметричной гибридной силовой установки будет меньшее

энергопотребление и более простой алгоритм управления благодаря управлению всего одним электродвигателем. При той же общей мощности у асимметричной гибридной силовой установки радиус поворота будет меньше, что является удовлетворительным показателем. При работе на полной мощности симметричный гибридный силовой агрегат будет иметь меньший радиус поворота и лучшую маневренность, но значительно увеличит энергопотребление.

Вывод: Асимметричный привод явно обладает большей энергоэффективностью, но преимущество симметричного привода заключается в максимальной производительности. Выполнение разворота (вокруг вертикальной оси) и выполнение разворота без снижения скорости транспортного средства имеет большое значение, особенно учитывая наиболее распространенное специальное назначение этого транспортного средства и маневрирование в сложных условиях местности.

Ключевые слова: высокоскоростные гусеничные машины, гибридные силовые установки, анализ процесса разворота, анализ баланса мощности.

Оцена ефикасности различитих концепција хибридних система за пренос снаге брзоходних гусеничних возила

Лука М. Понорац[а], *Иван* А. Благојевић[б]

[а] АМСС – Центар за моторна возила д.о.о, Београд, Република Србија,
   аутор за преписку

[б] Универзитет у Београду, Машински факултет,
   Катедра за моторна возила, Београд, Република Србија

ОБЛАСТ: машинство
КАТЕГОРИЈА (ТИП) ЧЛАНКА: оригинални научни рад

Сажетак:

Увод/циљ: Захваљујући убрзаном развоју хибридних система за пренос снаге у последњој деценији, у центру пажње нашли су се и системи за пренос снаге брзоходних гусеничних возила. Постоји неколико устаљених концепција хибридних система за пренос снаге ових возила која су у великој мери истражена и доведена до фазе прототипа, али нема конкретних анализа и закључка о најефикаснијој концепцији. Главну препреку за интензивнија истраживања представља проблем производње складишта електричне енергије, односно батерија довољног капацитета и густине снаге, која би била отпорна на ударе и оптерећења која настају услед употребе наведених возила. Ипак, постоји одређени број истраживања и произведених прототипа, развијених из

1887

симулационих модела, који показују задовољавајуће перформансе и карактеристике и за симетрични и за несиметрични хибридни систем за пренос снаге брзоходних гусеничних возила.

Методе: Развијени и верификовани симулациони модел хибридне трансмисије специфичног брзоходног гусеничног возила унапређен је новом управљачком јединицом која омогућава олакшано управљање електромоторима у помоћном погону ради управљања несиметричним и симетричним заокретом возила. Главни циљ је симулирање специфичних режима рада помоћу којих се може извршити оцена перформанси и енергетске ефикасности несиметричних и симетричних хибридних система за пренос снаге брзоходних гусеничних возила, како би се установила најефикаснија концепција.

Резултати: Резултати указују да несиметрични хибридни систем за пренос снаге захтева мање укупне снаге за извршење заокрета и има знатно једноставнији алгоритам управљања, имајући у виду да се управљање врши само једним електромотором. За исту уложену снагу, несиметрични хибридни систем за пренос снаге имаће мањи полупречник заокрета, што је задовољавајуће. У режиму максималне ангажоване снаге, симетрични систем за заокрет имаће мањи полупречник заокрета и бољу управљивост, али и знатно повећање утрошка снаге у односу на несиметрични систем.

Закључак: Несиметрични систем за пренос снаге има, очигледно, бољу енергетску ефикасност. Међутим, предност симетричног система за пренос снаге је у максималним перформансама. Извођење пивот заокрета (заокрет око вертикалне осе возила) и заокрет без смањења брзине тежишта возила од великог су значаја, посебно имајући у виду специјалну намену ових возила и кретање у захтевним теренским условима.

Кључне речи: брзоходно гусенично возило, хибридни систем за пренос снаге, анализа заокрета возила, анализа биланса снаге.

Effect of near-fault vertical seismic excitation on the response of long-span continuous deck truss bridges

Khaled Benmahdi[a], *Noureddine* Lahbari[b], *Nacer* Rahal[c], *Abdellah* Demdoum[d], *Mohamed* Sadoun[e], *Houda* Beghdad[f]

[a] University of Batna 2, Department of Civil Engineering, Laboratory for the Study of Structures and Mechanics of Materials, Batna, People's Democratic Republic of Algeria, e-mail: k.benmahdi@univ-mascara.dz, **corresponding author,** ORCID iD: https://orcid.org/0000-0002-8244-5817

[b] University of Batna 2, Department of Civil Engineering, Laboratory of Research in Applied Hydraulics (LRHYA), Batna, People's Democratic Republic of Algeria, e-mail: n.lahbari@univ-batna2.dz, ORCID iD: https://orcid.org/0000-0001-9468-0673

[c] Mustapha Stambouli University, Department of Civil Engineering, Mascara, People's Democratic Republic of Algeria; Laboratory of Mechanical Structure and Construction Stability, Oran, People's Democratic Republic of Algeria, e-mail: n.rahal@univ-mascara.dz, ORCID iD: https://orcid.org/0009-0002-0400-8360

[d] Mustapha Stambouli University, Department of Civil Engineering, Mascara, People's Democratic Republic of Algeria, e-mail: abdellah.demdoum@univ-mascara.dz, ORCID iD: https://orcid.org/0000-0001-5214-8160

[e] Mustapha Stambouli University, Department of Civil Engineering, Laboratory for the Study of Structures and Mechanics of Materials, Mascara, People's Democratic Republic of Algeria, e-mail: m.sadoun@univ-mascara.dz, ORCID iD: https://orcid.org/0009-0008-2314-9402

[f] Mustapha Stambouli University, Department of Civil Engineering, Mascara, People's Democratic Republic of Algeria, e-mail: houda.beghdad@univ-mascara.dz, ORCID iD: https://orcid.org/0009-0001-3548-5138

Abstract:

Introduction/purpose: This study investigates the seismic response of long-span continuous deck truss bridges under the effect of near-fault vertical ground motions. The primary objective is to assess how near-fault vertical seismic excitation affects the structural safety and performance of these bridges.

By exploring the nuanced dynamics induced by near-fault vertical motions, the research aims to improve the understanding of the vulnerabilities and challenges faced by long-span continuous deck truss bridges during seismic events.

Methods: To achieve this objective, the truss bridge was subjected to a series of ground motions, representing natural seismic events. The seismic response of the bridge was investigated by applying the linear time history method to the 3D finite element model. This analysis focused specifically on the evaluation of base shear and displacement. The analysis was extended to include the seismic performance of truss structures. The comparison between the bridge responses with and without consideration of the vertical component of ground motion was made to clarify the effect of vertical excitation.

Results: The results show that there is a significant contribution of vertical excitation, particularly concerning the internal force in the truss elements, where it exceeded 60 % during a severe earthquake, and consequently increased the demand-to-capacity ratio in most elements of the truss bridge structure.

Conclusion: For structural engineers and designers, the results of this research suggest that neglecting to include the vertical ground motion component in the analytical assessments of this type of bridges can lead to a greater degree of uncertainty and risk, particularly in near-fault regions.

Key words: deck-truss bridge, vertical displacement, seismic performance, axial force, V/H ratio, D/C ratio.

Introduction

Truss bridges are ubiquitous in modern infrastructure, owing to their efficient use of materials and structural stability. However, the seismic response of long-span truss bridges to near-fault vertical ground motions poses an important research gap, as it can profoundly impact bridge safety and serviceability after seismic events. It is known that the vertical component of ground motion weakens faster than its horizontal counterparts, especially for bridges located in moderate to high seismic zones and in close proximity to active faults (less than 25 km). The vertical component of ground motion is often more significant and can cause damage alongside the horizontal components, by amplifying the demand on some of the bridge's structural elements, which could damage the entire bridge. The vertical acceleration depends on the earthquake magnitude, soil conditions, and the site-epicenter distance (Bhanu et al, 2018; Nouri et al, 2020). The incorporation of vertical excitation in seismic bridge design has been extensively studied. Research has shown that vertical

earthquake loads impose excessive axial demands on reinforced concrete bridge columns (Saadeghvaziri & Foutch, 1988; Papazoglou & Elnashai, 1996; Elnashai & Papazoglou, 1997; Collier & Elnashai, 2001; Kunnath et al, 2008; Pollino & Bruneau, 2010; Kim et al, 2011a, 2011b; Di Sarno et al, 2011; Matsuzaki et al, 2012; Wilson et al, 2015; Li et al, 2017; Guo et al, 2023). Other works found that vertical excitation amplifies bending in bridge components, potentially causing structural failure. Veletzos et al. (2006) examined bridge segment joints subjected to concurrent vertical and horizontal seismic motions. The authors observed that vertical excitation amplified positive bending rotations by 400% and negative rotations by 90%. Recent numerical studies indicated that increased vertical acceleration heightens damage across bridge components (Li & Yao, 2020; Aryan & Ghassemieh, 2020). Predicting vertical earthquake intensity using the vertical-to-horizontal (V/H) acceleration ratio has been studied extensively. Though a V/H ratio of 2/3 was initially proposed, values exceeding 1.0 have been recorded in several major earthquakes (Newmark et al, 1973; Newmark & Hall, 1982). High V/H ratios above 1.5 have also occurred in near-fault zones (Bozorgnia et al, 1995; Papazoglou & Elnashai, 1996; Ambraseys & Douglas, 2003; Campbell, 2004).

As span length increases, truss bridges become more flexible and prone to vertical vibrations. Such vibrations can adversely affect stability and strength, consequently altering a seismic response (Saadeghvaziri & Foutch, 1988). Although prior research has focused predominantly on the effects of vertical excitation on bridge piers, such excitation may also detrimentally impact bridge decks, especially those incorporating truss girders. Further research is needed on the complex interplay between vertical excitations and the nonlinear response of long-span truss bridges.

To address this gap, the current study utilizes analytical simulation to examine the seismic response of long-span truss bridges subjected to near-fault vertical ground motions, considering the influence of vertical-to-horizontal (V/H) acceleration ratios.

Using SAP 2000 software, spatial finite element models were generated for a 165-meter truss bridge. Time history analyses were conducted to evaluate the bridge behavior under vertical earthquake loads. A seismic response was assessed via bridge displacements, base shear, and axial forces. Additionally, the effects of varying V/H ratios on seismic performance were investigated through demand/capacity (D/C) ratios. Findings may hold important implications for seismic design modifications and retrofitting to enhance the earthquake resilience of long-span truss bridges.

Materials and methods

Description of the bridge

The bridge under consideration in this study features a continuous 165 m long x 9.75 m wide steel truss deck with an upper slab that includes a center 90 m span flanked by two 37.5 m and 17.5 m side spans (Figure 1). Two longitudinal truss girders support the 200 mm thick reinforced concrete deck, with HEB300 sections serving as intermediate stiffeners and HE450B sections serving as outer girders. Transverse floor beams are joined to longitudinal deck beams at 3.75 m intervals by two 150 x 100 x 12 mm angle sections and bear on 120 x 80 x 12 mm angle seats.
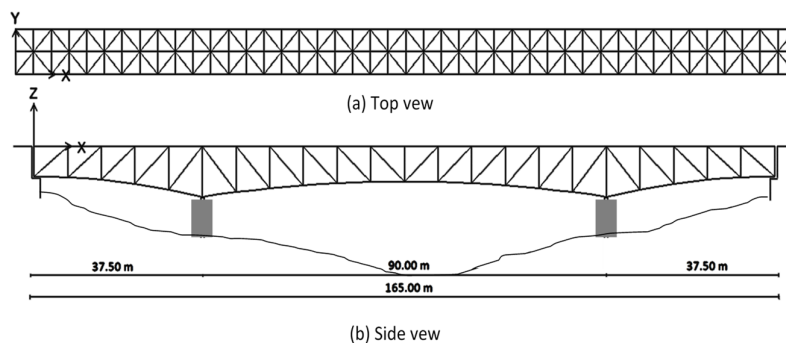
Figure 1 – Truss bridge geometry: (a) Top view; (b) Side view

Analytical model of the truss bridge

To undertake a seismic study of the 165-meter-long truss bridge, a three-dimensional finite element model was created using Sap 2000. To effectively reflect structural behavior, the three-span deck truss was modeled utilizing truss components with hinged joints. Bridge bearings were modeled as one fixed and three moveable transversely fixed supports (Figure 2). There were 1670 nodes and 2180 elements in the finite element model. For all seismic events investigated, the accelerograms from earthquake recordings were input at the base in both horizontal directions, with the vertical component also added in the second phase. The model utilized the measured material properties for the bridge components (Table 1). This advanced numerical simulation enables an in-depth evaluation of the seismic response of long-span truss bridges to multi-axial earthquake excitations.
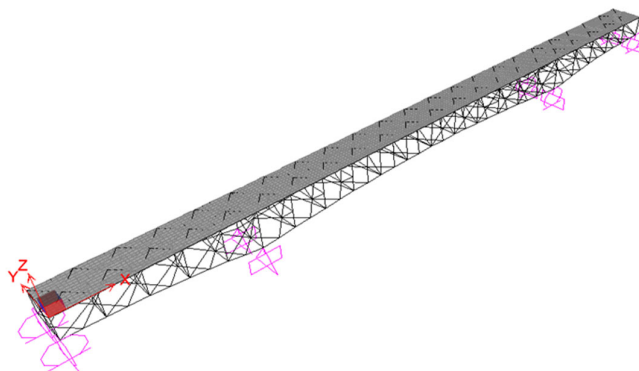
Figure 2 – Finite element model of the truss bridge

Table 1 – Mechanical properties of the materials

Material	Concrete	Steel
Young's modulus/MPa	34500	210000
Poisson ratio	0.2	0.3
Yielding strength/MPa	/	345
Compression strength/MPa	28	/

Parameters and options considered in the seismic analysis

Input ground motions

Five significant near-fault earthquake records with magnitudes ranging from 6.8 to 7.3 were used to assess the effects of vertical stimulation on the bridge seismic response. The accelerations were measured in three directions (horizontal, transverse, and vertical). The records were chosen based on the comparable horizontal peak ground acceleration (PGA) values (Table 2), although the vertical PGA ranged from 0.24g to 1.34g. The vertical-to-horizontal (V/H) acceleration ratios ranged from 0.39 to 1.89 as a result. All data were obtained within 2 to15 kilometers of a fault.

Figure 3 shows the three-component accelerograms for the earthquake in Gazli, Uzbekistan. This collection of the near-fault movements allowed for the systematic evaluation of vertical shaking effects at different but realistic V/H ratios.

Table 2 – Earthquakes used in the time history analysis (PEER ground motion database, 2024)

No	Seismic event	Mw	Station	PGA-Long (g)	PGA-Tran (g)	PGA-Ver (g)	V/H
1	Gazli, Uzbekistan (1976)	6.8	Karakyr	0.71	0.63	1.34	1.89
2	Loma-Prieta, USA (1989)	6.9	LGPC	0.56	0.61	0.89	1.47
3	Landers, USA (1992)	7.3	Lucerne valley	0.72	0.79	0.82	1.04
4	Kobe, Japan (1995)	6.9	Nishi-Akashi	0.51	0.50	0.37	0.73
5	Kobe, Japan (1995)	6.9	JR Takatori	0.61	0.61	0.24	0.39
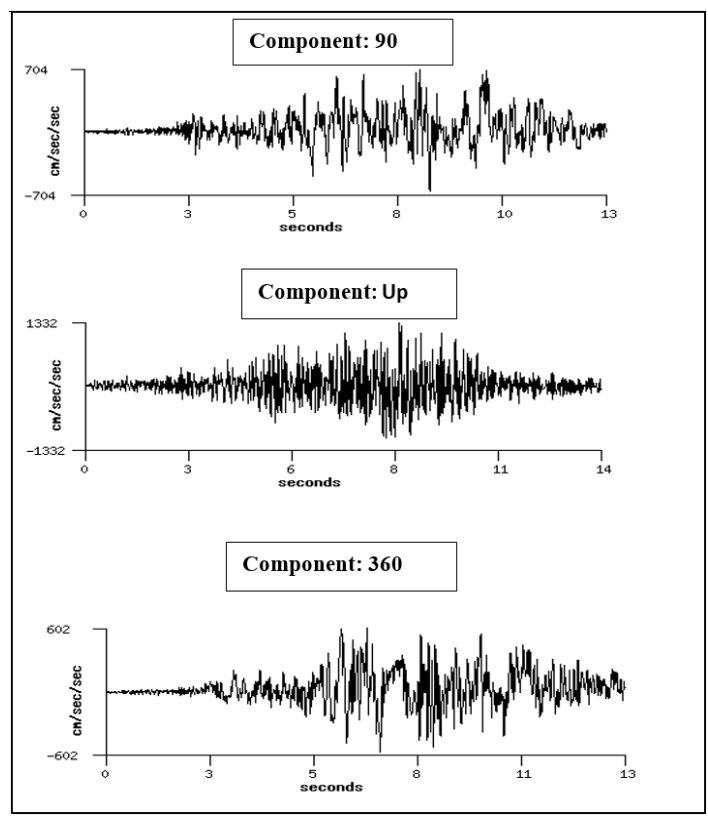
Figure 3 – Ground time-histories of the Gazli (Uzbekistan) earthquake in three directions

Modal analysis

A modal analysis was conducted to determine the dynamic properties of the bridge, which depend on structural mass and stiffness. The results can be utilized to calibrate the finite element model and evaluate structural damage. In this study, a modal analysis of the truss bridge was performed prior to a time history analysis to obtain fundamental vibration modes and frequencies. These dynamic characteristics provide insights into the bridge's seismic response and validate the numerical model's ability to realistically simulate dynamic behavior. The first six modal shapes and periods obtained from the analysis are presented. The comparison of the analytical and experimental modal properties enables model calibration and confirmation that the model accurately represents the inertia and flexibility of the actual bridge. This modal analysis provides the basis for the in-depth time history seismic evaluations described in the subsequent sections.

Time history analysis by direct integration

Time-history analysis is a common technique for evaluating bridge seismic performance, as implemented in several prior studies, e.g. (Behnamfar & Velni, 2019, An & Lee, 2022). So, a linear time-history analysis can provide useful insights into fragility across damage levels and near-source seismic response (De Luca & Lombardi, 2017). In the current study, three-component earthquake ground motions obtained from the PEER database were input in the (x, y, and z) directions to the structural model (Figure 1). The seismic response history was computed using direct integration with Rayleigh proportional viscous damping, assigning the structure 5% critical damping ratio for the first two vibration modes. The average acceleration Newmark method was utilized for the dynamic time integration. The details of the time history analysis factors and settings are provided in Table 3. This rigorous numerical simulation method enables an in-depth evaluation of the truss bridge response under multidirectional seismic excitations.

Table 3 – Parameters input in the time-history analysis

Mass Coeff	Stiff Coeff	Frequency	Damping1	Frequency	Damping2	γ	β
1/Sec	Sec	Cyc/sec	Unitless	Cyc/sec	Unitless	Unitless	Unitless
1.122	0.0022	3.25	0.05	3.68	0.05	0.5	0.25

Analysis and discussion of the results

Natural vibration results

A modal analysis was first conducted to characterize the bridge's dynamic properties which are critical in determining a structural vibration response (Li et al, 2014; Fouché et al, 2017; Xin et al, 2019). The eigenvector method identified the natural frequencies and mode shapes.

Four primary mode types were observed (Figure 4): longitudinal, transverse, vertical bending, and torsional. The fundamental frequency was a longitudinal oscillation at 0.32 sec. The second mode was transverse at 0.24 sec, and the first vertical bending mode occurred at 0.22 sec. The torsional response did not appear until the fourth mode at 0.20 sec.

Nineteen natural modes were computed, accounting for over 90% mass participation in the longitudinal, transverse, and vertical directions. This meets recommended design code requirements, e.g. (Ministère des Travaux Publics Algérie, 2008; European Standard, 2011; AASHTO, 2017). The modal analysis provided essential insights into the bridge's dynamic characteristics governing its seismic response.

(a) Longitudinal : f= 3.25 Hz   (b) Tranverse : f= 3.68 Hz

(c) Vertical : f= 4.21 Hz   (d) Torsional : f= 4.63 Hz

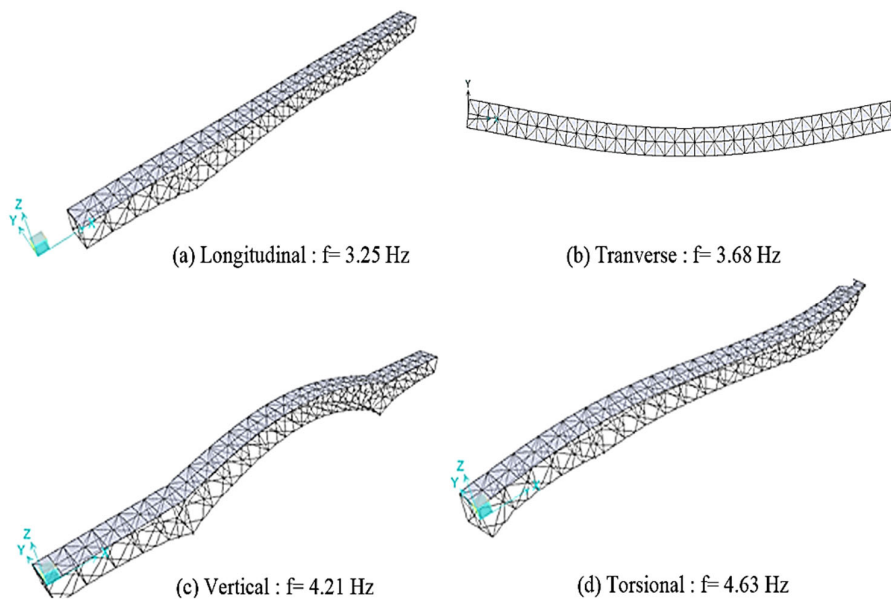*Figure 4 – The four first analytical mode shapes: (a) Longitudinal: f= 3.25 Hz, (b) Tranverse: f = 3.68 Hz, (c) Vertical: f = 4.21 Hz, (d) Torsional: f = 4.63 Hz.*

Time history results

The two horizontal components of the earthquake were the primary focus of this study's first phase, and the vertical component which is integrated with the two horizontal components was considered in the second phase. Equation (1) was utilized to determine the proposed earthquake amplification ratio (RHV) which was used to assess the contribution of the vertical component of ground motion to the bridge reaction. By incrementally introducing the vertical acceleration in the time history analysis, its specific impact on bridge seismic demands could be isolated and quantified through RHV (1).

$$RHV = \frac{RSP(DL + H + V)}{RSP(DL + H)} \qquad (1)$$

RHV: The ratio of the bridge response due to combined dead load and earthquake loading with and without the vertical ground motion components.

RSP(DL+H): Response resulting from the two horizontal ground motion components and dead loads.

RSP (DL + H + V): The response resulting from the three components of ground motion and dead loads.

Effect of vertical seismic excitation

A linear time-history analysis was performed on the truss bridge model using five near-fault earthquake records with three-directional components to evaluate the influence of vertical ground motion. The key response parameters examined were:

Vertical displacement

The peak vertical displacement at numerous nodes along the deck truss top chord was examined to quantify the role of vertical excitation to bridge deformation. There were three load situations studied: dead load only (DL), dead load plus horizontal motions (DL+H), and dead load plus horizontal and vertical motions (DL+H+V). Figure 5 depicts the peak drift profile along the top chord for the three load situations during the Karakyr earthquake. In all cases, the deck displayed a symmetric parabolic displacement form, with the greatest displacement at the midspan. Figure 6 depicts the temporal history of the Nishi-Akashi event's midspan displacement, demonstrating amplification after integrating vertical acceleration.
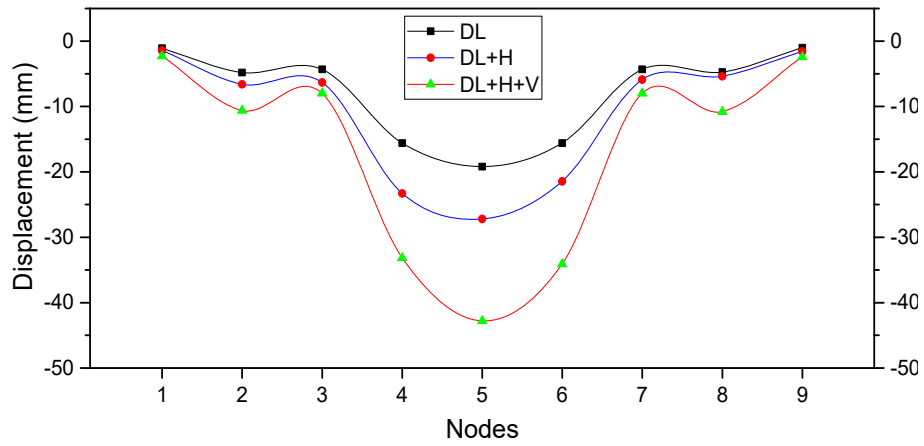
Figure 5 – Vertical deck truss deformations due to the Karakyr seismic event and the dead load
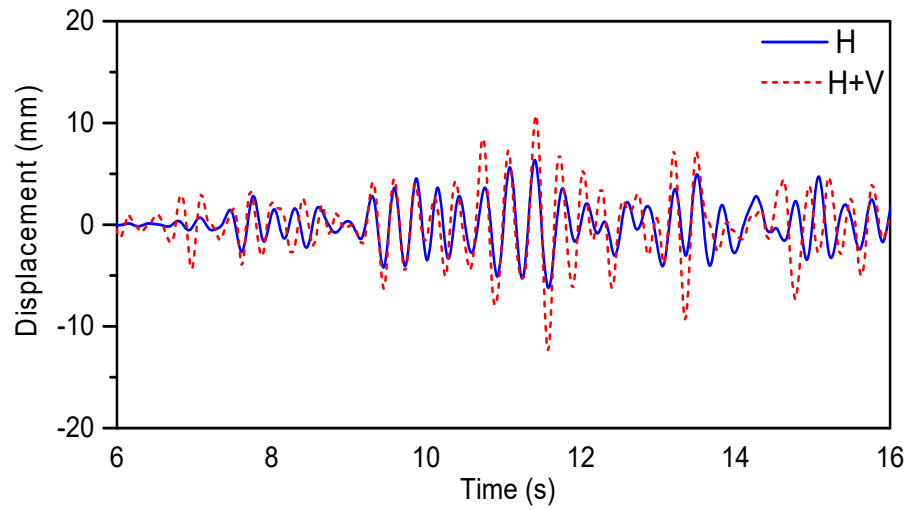
Figure 6 – Mid-span deck vertical displacement history for the Nishi-Akashi ground motion

Figure 7 compares the midspan vertical displacement for the Gazli and J-R Takatori events.

Table 4 summarizes the peak midspan displacements across the five earthquakes for each load case. With only dead load (DL), the displacement was 19 mm. Adding horizontal excitation (DL+H) increased this moderately to 23-29 mm. Incorporating vertical acceleration (DL+H+V) substantially amplified displacements by 57-66%.

Table 4 – Peak displacement at the middle point of the main span of the deck truss under tow load cases

Seismic events	Load cases	U1 (mm)	U2 (mm)	U3 (mm)
Karakyr	DL+H	13.35	21.33	27.22
	DL+H+V	11.54	21.33	42.80
	RHV	0.86	1.00	1.57
LGPC	DL+H	15.03	14.85	29.10
	DL+H+V	15.97	14.84	34.26
	RHV	1.06	1.00	1.18
Lucerne valley	DL+H	7.02	21.31	23.23
	DL+H+V	9.22	21.30	38.49
	RHV	1.31	1.00	**1.66**
Nishi-Akashi	DL+H	12.18	8.65	25.40
	DL+H+V	13.37	8.64	31.56
	RHV	1.10	1.00	1.24
J R Takatori	DL+H	13.88	25.31	27.84
	DL+H+V	13.67	25.32	29.86
	RHV	0.98	1.00	1.07

The vertical motion caused the highest displacement amplification for the Karakyr event (RHV = 1.57). The lowest amplification occurred for the J-R Takatori (RHV = 1.07). In most cases, RHV increased proportionally with the V/H ratio (Figure 8).

(a) Gazli seismic events

(b) J R Takatori seismic events
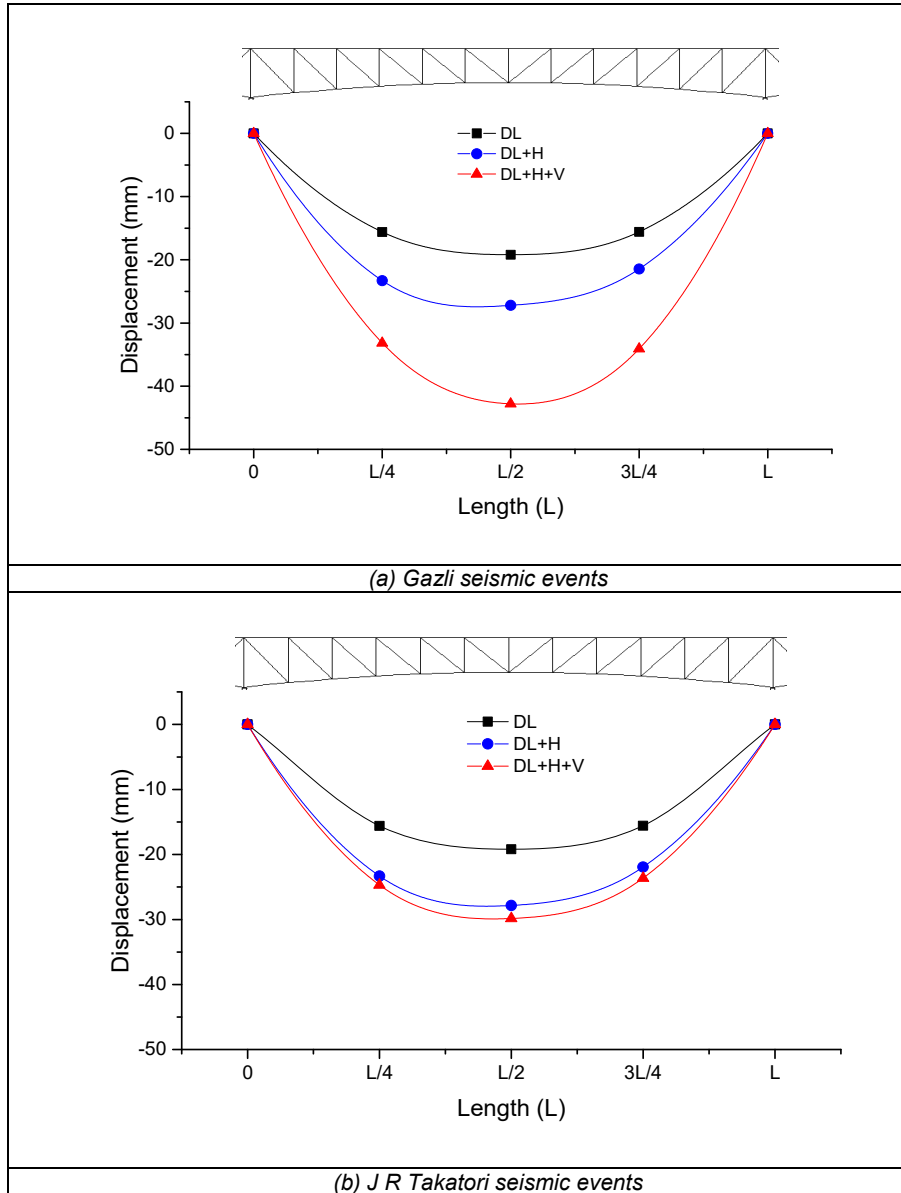
Figure 7 – Peak vertical displacement of the main span for seismic and dead load: (a) Gazli seismic events; (b) J R Takatori seismic events

1900
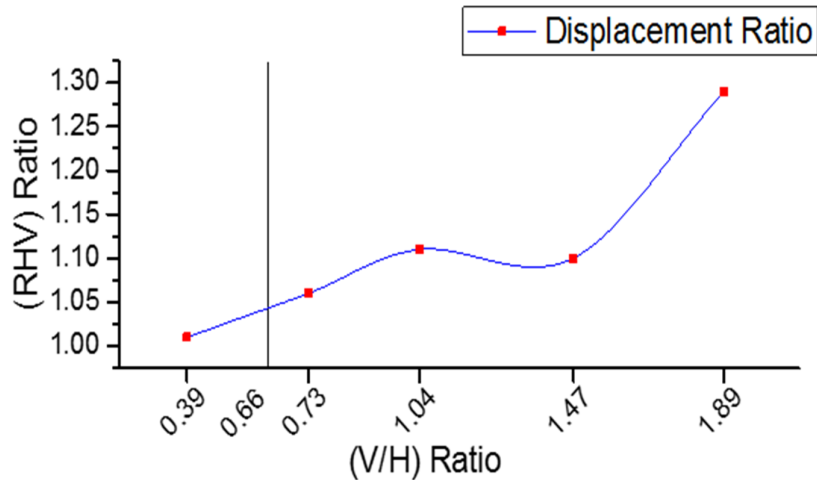
Figure 8 – Variation in the RHV ratio at the midpoint of the main span with the increase in the V/H ratio

Horizontal displacement

Table 4 shows that the DL condition did not result in any displacement in the horizontal direction. In contrast, Case 2, which involved the introduction of both horizontal components, showed an increase in displacements in the longitudinal direction that were almost identical in magnitude. Nevertheless, the longitudinal displacement estimates for each of the five earthquakes changed dramatically when the vertical component of ground motion was included, where it also somewhat decreased for certain ground motions, like in the case of the Karakyr ground motion, but it grew greatly for some other ground motions (e.g. the Lucerne valley).

This demonstrates that the vertical component can substantially influence the bridge response in the longitudinal direction. However, its effect on transverse displacement was negligible. Compared to dead load alone, horizontal excitation notably increased vertical displacement by up to 53%, likely due to the large span and light weight of this truss bridge type. Overall, the analyses highlighted the potential for vertical ground motion to alter longitudinal seismic demands on long-span truss bridges.

The time-history analysis results demonstrate the vertical ground motion component considerably influences vertical deformation of the bridge deck at the mid-span. However, horizontal deck displacement was less susceptible to vertical excitation, aligning with the past findings by Shrestha (Shrestha, 2015) for a long-span cable-stayed bridge.

Notably, the contribution of vertical motion to vertical displacement does not necessarily correlate directly with the peak ground acceleration ratio (V/H). This contribution can also depend on soil conditions, ground motion characteristics (Tonyali et al, 2019), the closest distance to the fault (Button et al, 2002), and earthquake duration.

(a) longitudinal direction

(b) transverse direction

Figure 9 – Base shear force history during the JR Takatori seismic events

(a) longitudinal direction

(b) transverse direction

Figure 10 – Base shear force history during the Karakyr seismic events.
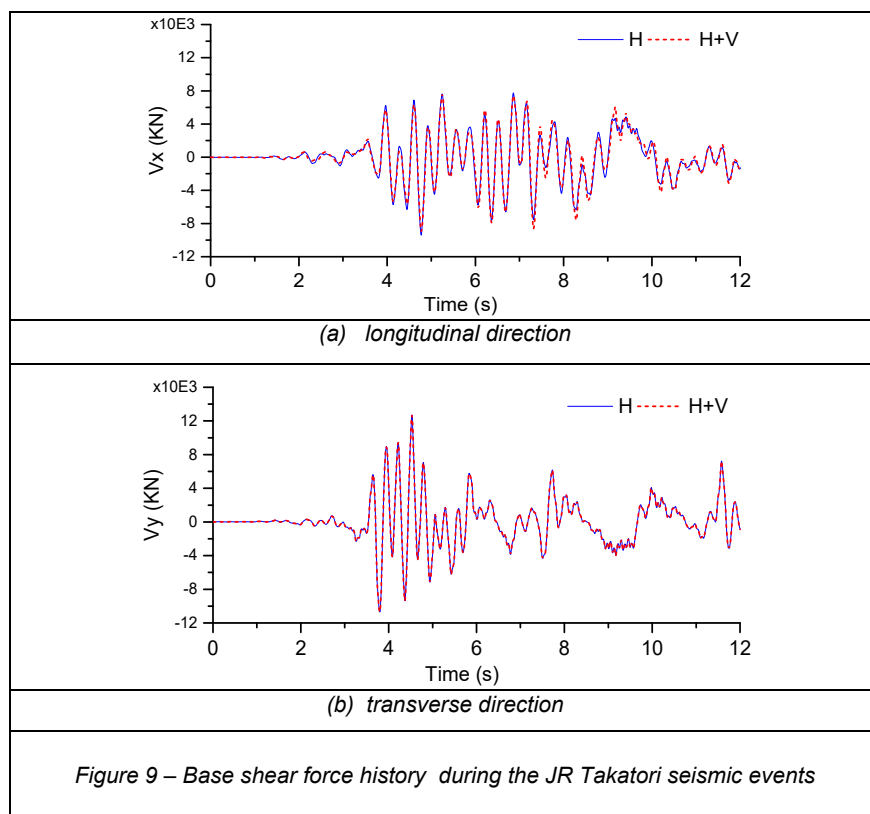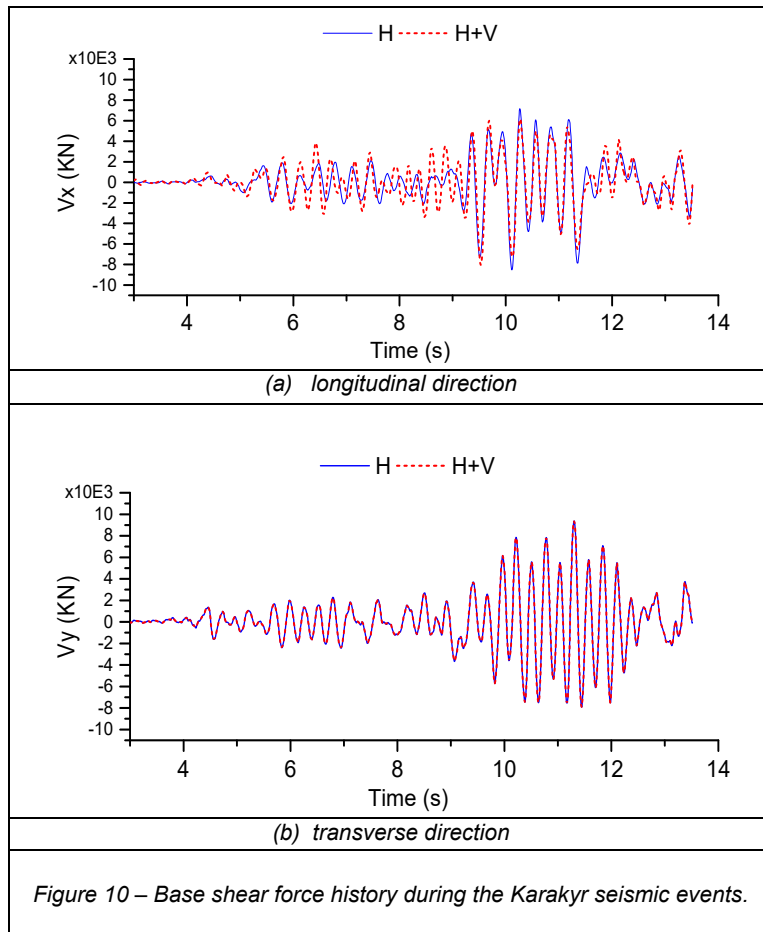
Base shear

Figures 9 and 10 present the examples of the base shear force time histories with and without vertical motion for the JR Takatori and Karakyr events, in longitudinal (V_x) and transverse (V_y) directions. The deck response appears identical for both load cases over the vibration duration. Table 5 compares the base shear amplification ratios (RHV) and the amplification percent (Amp %) with and without vertical excitation for the five earthquakes. The results show the vertical component has a negligible effect, increasing base shear by no more than 2% and 0% in some cases.

This demonstrates the vertical ground motion does not meaningfully contribute to base shear force in the deck truss bridge.

Table 5 – Amplification ratio with and without the vertical ground motion of the base shear force

| Ground motion | V/H | Base shear | | | |
| | | Vx | | Vy | |
		RHV	Amp %	RHV	Amp %
Karakyr	1.89	1.00	0%	1.01	1%
LGPC	1.47	1.00	0%	1.00	0%
Lucerne valley	1.04	1.00	0%	1.00	0%
Nishi-Akashi	0.73	1.02	2%	1.02	2%
J R Takatori	0.39	1.00	0%	1.00	0%

Structure performance

Axial frame force

Figures 11-14 compare the axial force time histories with and without vertical motion for four critical members on the intermediate pier under the Lander seismic events. Including vertical acceleration dramatically increased axial forces, exceeding 64% in diagonal members. Table 6 summarizes the axial force amplification from the vertical component for the members on the intermediate support across the five earthquakes. The signs (-) and (+) represent the compression and tension in an element, respectively. The results show that the effect was independent of the V/H ratio and most significant in vertical and diagonal members versus top and bottom chords. The table indicates that the effect of the vertical ground motion component was independent of the V/H ratio.

Table 6 – Amplification ratio (RHV) for internal axial force of the members situated on the intermediate support

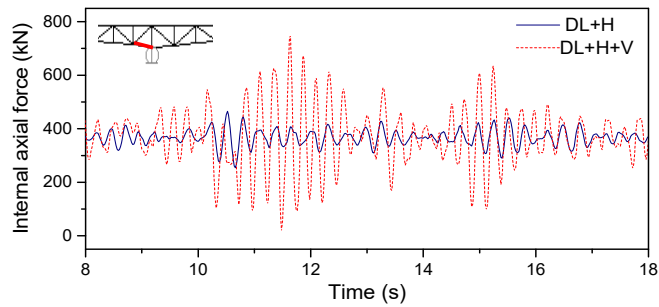| Element | | Column (-) | | Brace (+) | | Bottom chord (-) | | Top chord (+) | |
Ground motion	V/H	RHV	Amp %	RHV	Amp %	RHV	Amp %	RHV	Amp %
Karakyr	1.89	1.33	33%	1.44	44%	1.61	61%	0.94	-6%
LGPC	1.47	1.10	10%	1.20	20%	1.31	31%	1.05	5%
Lucerne valley	1.04	1.18	18%	1.64	64%	1.64	64%	1.01	1%
Nishi-Akashi	0.73	1.09	9%	1.19	19%	1.17	17%	1.08	8%
J R Takatori	0.39	1.03	3%	1.10	10%	1.12	12%	1.02	2%

Figure 11 – Axial frame force history under the Landers seismic events combined with the dead load for the bottom chord
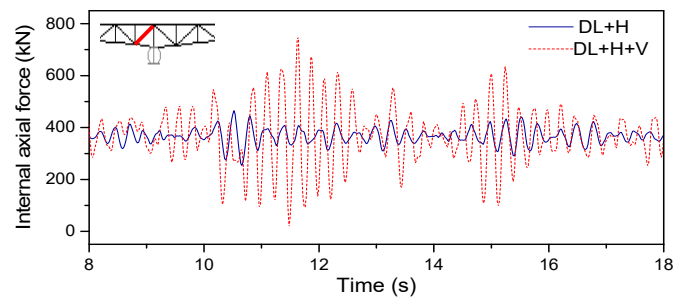

Figure 12 – Axial frame force history under the Landers seismic events combined with the dead load for the brace
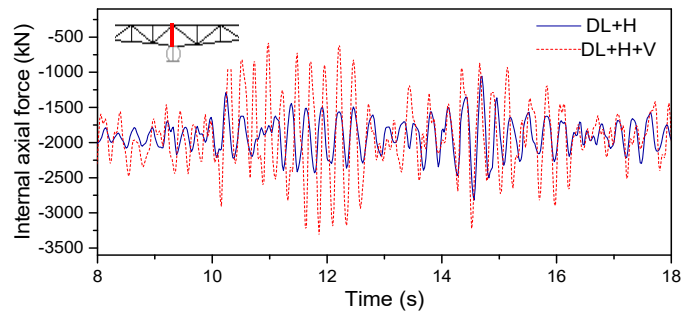
Figure 13 – Axial frame force history under the Landers seismic events combined with the dead load for the column
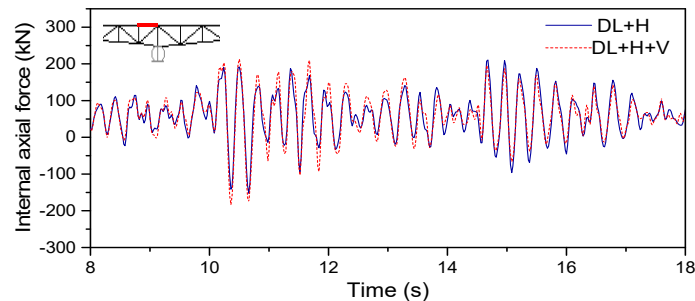
Figure 14 – Axial frame force history under the Landers seismic events combined with the dead load for the top chord

The time history analysis performed on the truss bridge using five natural recordings of earthquakes with different V/H ratios revealed that the vertical component contributed significantly to the internal axial force; however, its effect was greatest in the vertical and diagonal brace members and least in the upper and lower chord members. It should be noted that the contribution of the vertical ground motion component to vertical displacement does not necessarily change proportionally to the change in the ratio of the PGA value (V/H), which is due to variations in seismic and soil characteristics and could be the closest distance to the fault.

Demand to capacity ratio

Seismic evaluation in terms of the demand-to-capacity (D/C) ratio is a standard approach used in structural engineering to analyze a building's or structure's seismic performance. The (D/C) ratio is computed by dividing an element's capacity to withstand seismic forces by the demand for seismic forces predicted during an earthquake. The (D/C) ratio is a valuable measure of a structure's capacity to withstand seismic force.

A (D/C) ratio more than once has shown that the element's ability to resist seismic pressures is greater than the demand it is anticipated to face during an earthquake, which is a desired outcome. A (D/C) ratio less than one indicates that the structure's capacity may be insufficient to resist the expected seismic forces, and further strengthening may be necessary.

Table 7 – Amplification ratio (RHV) for the maximal demand of the members situated on the intermediate support

Element	Ground motion	Karakyr	LGPC	Lucerne valley	Nishi-Akashi	J R Takatori
	V/H	1.89	1.47	1.04	0.73	0.39
Column	Ratio	1.29	1.09	1.24	1.09	1.02
	Amp %	29%	9%	24%	9%	2%
Brace	Ratio	1.48	1.27	1.61	1.22	1.07
	Amp %	48%	27%	61%	22%	7%
Bottom chord	Ratio	1.42	1.2	1.4	1.14	1.08
	Amp %	42%	20%	40%	14%	8%
Top chord	Ratio	1.27	1.22	1.41	1.19	1.05
	Amp %	27%	22%	41%	19%	5%

The seismic performance was evaluated through the demand-to-capacity (D/C) ratios by comparing the member seismic demand to capacity. Table 7 presents the D/C ratio amplification (RHV) for the four most affected members on the intermediate support. The D/C ratios differed substantially between the load cases with and without vertical excitation. For example, the D/C ratio for the vertical member at Pier C increased from 0.78 (DL+H) to 0.89 (DL+H+V) under the Lucern event, an amplification of 24%. For the Karakaty, it increased from 0.77 to 0.99, with an amplification of 29%.

In summary, the vertical component significantly impacted the truss member seismic performance, especially for the members near the supports. This highlights the importance of incorporating vertical excitation in analysis models to accurately evaluate seismic responses.

Conclusions

The effects of vertical ground motion on the seismic response of a long-span truss bridge under near-fault excitations were evaluated using numerical simulation in this study. The time history analysis revealed the following major trends in the dynamic response:

- Vertical acceleration primarily affects vertical deck displacement, with a lesser but still significant impact on

longitudinal deformation. However, the lateral response is minimally influenced.

- Inclusion of the vertical component does not alter base shear forces.
- Axial forces in truss members, especially near supports, are substantially amplified by the vertical motion.
- Vertical excitation heightens member demand beyond capacity limits in some cases.
- Applying the vertical component markedly increases vertical deformation and demand-to-capacity ratios compared to horizontal excitation alone.
- The three-directional analysis provides a greater insight into seismic behavior than the one with one or two components.
- Maximum vertical acceleration does not necessarily govern response amplification.
- Vertical effects are more pronounced for V/H ratios exceeding 1.0 versus the 2/3 ratio in codes.

The results demonstrate that vertical excitation significantly impacts deck trusses, not just bridge piers. Considering all three ground motion components is critical for accurate seismic evaluation of near-fault truss bridges. These findings can guide engineers toward improved design and assessment of truss bridges in seismic regions.

Additional research on different truss arrangements could lead to more thorough findings about their seismic performance under vertical excitation.

References

-AASHTO. 2017. *AASHTO LRFD Bridge Design Specifications, 8th Edition.* Washington, USA: American Association of State Highway and Transportation Officials [online]. Available at: https://store.transportation.org/Common/DownloadContentFiles?id=1648 [Accessed: 10 February 2024].

Ambraseys, N.N. & Douglas, J. 2003. Near-field horizontal and vertical earthquake ground motions. *Soil Dynamics and Earthquake Engineering*, 23(1), pp.1-18. Available at: https://doi.org/10.1016/S0267-7261(02)00153-7.

An, H. & Lee, J.-H. 2022. Deep neural network for prediction of time-history seismic response of bridges. *Structural Engineering and Mechanics*, 83(3), pp.401-413. Available at: https://doi.org/10.12989/sem.2022.83.3.401.

Aryan, H. & Ghassemieh, M. 2020. Numerical assessment of vertical ground motion effects on highway bridges. *Canadian Journal of Civil Engineering*, 47(7), pp.790-800. Available at: https://doi.org/10.1139/cjce-2019-0096.

Behnamfar, F. & Velni, M.T. 2019. A rapid screening method for selection and modification of ground motions for time history analysis. *Earthquakes and Structures*, 16(1), pp.29-39. Available at: https://doi.org/10.12989/EAS.2019.16.1.029.

Bhanu, V., Ozcebe, A.G. & Smerzini, C. 2018. A study on vertical component of earthquake ground motion and its effects on a bridge. In: *16th European conference on earthquake engineering*, Thessaloniki, Greece, June 18-21.

Bozorgnia, Y., Niazi, M. & Campbell, K.W. 1995. Characteristics of Free-Field Vertical Ground Motion during the Northridge Earthquake. *Earthquake Spectra*, 11(4), pp.515-525. Available at: https://doi.org/10.1193/1.1585825.

Button, M.R., Cronin, C.J. & Mayes, R.L. 2002. Effect of Vertical Motions on Seismic Response of Highway Bridges. *Journal of Structural Engineering*, 128(12), pp.1551-1564. Available at: https://doi.org/10.1061/(ASCE)0733-9445(2002)128:12(1551).

Campbell, K.W. 2004. Updated Near-Source Ground-Motion (Attenuation) Relations for the Horizontal and Vertical Components of Peak Ground Acceleration and Acceleration Response Spectra. *Bulletin of the Seismological Society of America*, 94(6), pp.2417-2417. Available at: https://doi.org/10.1785/0120040147.

Collier, C. & Elnashai, A.S. 2001. A procedure for combining vertical and horizontal seismic action effects. *Journal of Earthquake Engineering*, 5(4), pp.521-539. Available at: https://doi.org/10.1142/S136324690100056X.

De Luca, F.D. & Lombardi, L. 2017. EC8 design through linear time history analysis versus response spectrum analysis – is it an enhancement for PBEE? In: *16th World Conference on Earthquake (16WCEE)*, Santiago, Chile, Paper No. 1155, January 9-13 [online]. Available at: https://www.wcee.nicee.org/wcee/article/16WCEE/WCEE2017-1155.pdf [Accessed: 10 February 2024].

Di Sarno, L., Elnashai, A.S. & Manfredi, G. 2011. Assessment of RC columns subjected to horizontal and vertical ground motions recorded during the 2009 L'Aquila (Italy) earthquake. *Engineering Structures*, 33(5), pp.1514-1535. Available at: https://doi.org/10.1016/j.engstruct.2011.01.023.

Elnashai, A. & Papazoglou, A. 1997. Procedure and spectra for analysis of RC structures subjected to strong vertical earthquake loads. *Journal of Earthquake Engineering*, 01(01), pp.121-155. Available at: https://doi.org/10.1142/S1363246997000076.

-European Standard. 2011. *EN 1998-2:2005+A2 - Eurocode 8: Design of structures for earthquake resistance - Part 2: Bridges* [online]. Available at: https://www.phd.eng.br/wp-content/uploads/2014/12/en.1998.2.2005.pdf [Accessed: 10 February 2024].

Fouché, P., Bruneau, M. & Chiarito, V. 2017. Dual-Hazard Blast and Seismic Behavior of Concrete-Filled Double-Skin Steel Tubes Bridge Pier. *Journal of Structural Engineering*, 143(12), art.number:04017155. Available at: https://doi.org/10.1061/(ASCE)ST.1943-541X.0001883.

Guo, W., Yang, S., Jiang, L., Yu, Z., Zeng, C., Wang, Y., Huang, R., Wu, S. & Ren, S. 2023. Effect of near-fault vertical seismic excitation on running safety of trains on high-speed railway bridges. *Engineering Structures*, 296, art.number:116880. Available at: https://doi.org/10.1016/j.engstruct.2023.116880.

Kim, S.J., Holub, C.J. & Elnashai, A.S. 2011a. Analytical Assessment of the Effect of Vertical Earthquake Motion on RC Bridge Piers. *Journal of Structural Engineering*, 137(2), pp.252-260. Available at: https://doi.org/10.1061/(ASCE)ST.1943-541X.0000306.

Kim, S.J., Holub, C.J. & Elnashai, A.S. 2011b. Experimental investigation of the behavior of RC bridge piers subjected to horizontal and vertical earthquake motion. *Engineering Structures*, 33(7), pp.2221-2235. Available at: https://doi.org/10.1016/j.engstruct.2011.03.013.

Kunnath, S.K., Erduran, E., Chai, Y.H. & Yashinsky, M. 2008. Effect of near-fault vertical ground motions on seismic response of highway overcrossings. *Journal of Bridge Engineering*, 13(3), pp.282-290. Available at: https://doi.org/10.1061/(ASCE)1084-0702(2008)13:3(282).

Li, H., Gao, X., Liu, Y. & Luo, Y. 2017. Seismic performance of new-type box steel bridge piers with embedded energy-dissipating shell plates under tri-directional seismic coupling action. *International Journal of Steel Structures*, 17(1), pp.105-125. Available at: https://doi.org/10.1007/s13296-015-0192-z.

Li, R. & Yao, C. 2020. Effects of Vertical Earthquake Ground Motions on Seismic Response of Steel-Concrete Plate Composite Beam Bridges. In: *2020 International Conference on Intelligent Transportation, Big Data & Smart City (ICITBS),* Vientiane, Laos, pp.114-117, January 11-12. Available at: https://doi.org/10.1109/ICITBS49701.2020.00032.

Li, X., Zhang, D.-Y., Yan, W.-M., Xie, W.-C. & Pandey, M.D. 2014. Effects of model updating on the estimation of stochastic seismic response of a concrete-filled steel tubular arch bridge. *Structure and Infrastructure Engineering*, 10(12), pp.1620-1637. Available at: https://doi.org/10.1080/15732479.2013.837079.

Matsuzaki, H., Kumagai, Y. & Kawashima, K. 2012. Effect of Strong Vertical Excitation on the Seismic Performance of RC Bridge Columns. In: *15th World Conference in Earthquake Engineering,* Lisbon, Portugal, September 24-28 [online]. Available at: https://www.iitk.ac.in/nicee/wcee/article/WCEE2012_2696.pdf [Accessed: 10 February 2024].

-Ministère des Travaux Publics Algérie. 2008. *Regles parasismiques applicables au domaine des ouvrages d'art RPOA 2008 - Document technique reglementaire DTR*. Algérie: Ministère des Travaux Publics Algérie.

Newmark, N.M., Blume, J.A. & Kapur, K.K. 1973. Seismic Design Spectra for Nuclear Power Plants. *Journal of the Power Division*, 99(2), pp.287-303. Available at: https://doi.org/10.1061/JPWEAM.0000753.

Newmark, N.M. & Hall, W.J. 1982. *Earthquake spectra and design, First Edition*. Oakland, CA, USA: Earthquake Engineering Research Institute. ISBN: 978-0943198224.

Nouri, G., Shahrouzi, M. & Farhadi, E. 2020. Seismic performance of bridges to a spatially varying horizontal and vertical earthquake ground motion. *AUT Journal of Civil Engineering*, 4(1), pp.27-36. Available at: https://doi.org/10.22060/ajce.2019.15333.5536.

Papazoglou, A.J. & Elnashai, A.S. 1996. Analytical and field evidence of the damaging effect of vertical earthquake ground motion. *Earthquake Engineering & Structural Dynamics*, 25(10), pp.1109-1137. Available at: https://doi.org/10.1002/(SICI)1096-9845(199610)25:10<1109::AID-EQE604>3.0.CO;2-0.

-PEER ground motion database. 2024. PEER Ground Motion Database - Pacific Earthquake Engineering Research Center. *Ngawest2.berkeley.edu* [online]. Available at: https://ngawest2.berkeley.edu/ [Accessed: 10 February 2024].

Pollino, M. & Bruneau, M. 2010. Seismic Testing of a Bridge Steel Truss Pier Designed for Controlled Rocking. *Journal of Structural Engineering*, 136(12), pp.1523-1532. Available at: https://doi.org/10.1061/(ASCE)ST.1943-541X.0000261.

Saadeghvaziri, M.A. & Foutch, D.A. 1988. *Inelastic response of R/C bridges under horizontal and vertical earthquake motions*. Urbana, Illinois, USA: Department of Civil Engineering, University of Illinois at Urbana-Champaign [online]. Available at: https://www.ideals.illinois.edu/items/14178 [Accessed: 10 February 2024].

Shrestha, B. 2015. Seismic response of long span cable-stayed bridge to near-fault vertical ground motions. *KSCE Journal of Civil Engineering*, 19(1), pp.180-187. Available at: https://doi.org/10.1007/s12205-014-0214-y.

Tonyali, Z., Ates, S. & Adanur, S. 2019. Spatially variable effects on seismic response of the cable-stayed bridges considering local soil site conditions. *Structural Engineering and Mechanics,* 70(2), pp.143-152 Available at: https://doi.org/10.12989/sem.2019.70.2.143.

Veletzos, M.J., Restrepo, J.I. & Seible, F. 2006. *Seismic response of precast segmental bridge superstructures.* California. Department of Transportation [online]. Available at: https://rosap.ntl.bts.gov/view/dot/27611 [Accessed: 10 February 2024].

Wilson, T., Chen, S. & Mahmoud, H. 2015. Analytical case study on the seismic performance of a curved and skewed reinforced concrete bridge under vertical ground motion. *Engineering Structures*, 100, pp.128-136. Available at: https://doi.org/10.1016/j.engstruct.2015.06.017.

Xin, L., Li, X., Zhang, Z. & Zhao, L. 2019. Seismic behavior of long-span concrete-filled steel tubular arch bridge subjected to near-fault fling-step motions. *Engineering Structures*, 180, pp.148-159. Available at: https://doi.org/10.1016/j.engstruct.2018.11.006.

Efecto de la excitación sísmica vertical cercana a la falla en la respuesta de puentes de celosía de tablero continuo de largo alcance

Khaled Benmahdi[ac], **autor de correspondencia**, *Noureddine* Lahbari[ad], *Nacer* Rahal[be]*, Abdellah* Demdoum[b]*, Mohamed* Sadoun[bf]*, Houda* Beghdad[b]

[a] Universidad de Batna 2, Departamento de Ingeniería Civil, Batna, República Argelina Democrática y Popular

[b] Universidad Mustapha Stambouli, Departamento de Ingeniería Civil, Mascara, República Argelina Democrática y Popular

[c] Laboratorio para el Estudio de Estructuras y Mecánica de Materiales

[d] Laboratorio de Investigación en Hidráulica Aplicada

[e] Laboratorio de Estructuras Mecánicas y Estabilidad, Orán, República Argelina Democrática y Popular

[f] Laboratorio para el Estudio de Estructuras y Mecánica de Materiales

CAMPO: materiales, ingeniería civil
TIPO DE ARTÍCULO: artículo científico original

Resumen:

Introducción/objetivo: Este estudio investiga la respuesta sísmica de puentes de celosía de cubierta continua de largo alcances bajo el efecto de movimientos verticales del terreno cercanos a la falla. El objetivo principal es evaluar cómo la excitación sísmica vertical cercana a la falla afecta la seguridad estructural y el desempeño de estos puentes. Al explorar la dinámica matizada inducida por los movimientos verticales cercanos a la falla, la investigación tiene como objetivo mejorar la comprensión de las vulnerabilidades y los desafíos que enfrentan los puentes de celosía de cubierta continua de largo alcance durante eventos sísmicos.

Métodos: Para lograr este objetivo, el puente de celosía fue sometido a una serie de movimientos del suelo, que representan eventos sísmicos naturales. La respuesta sísmica del puente se investigó aplicando el método de historia del tiempo lineal al modelo de elementos finitos 3D. Este análisis se centró específicamente en la evaluación del corte y desplazamiento de la base. El análisis se amplió para incluir el comportamiento sísmico de las estructuras de celosía. La comparación entre las respuestas del puente con y sin consideración del componente vertical del movimiento del suelo se realizó para aclarar el efecto de la excitación vertical.

Resultados: Los resultados muestran que existe una contribución significativa de la excitación vertical, particularmente en lo que respecta a la fuerza interna en los elementos de la armadura, donde superó el 60 % durante un terremoto severo, y en consecuencia aumentó la relación demanda-capacidad en la mayoría de los elementos de la estructura del puente de celosía.

Conclusión: Para los ingenieros y diseñadores estructurales, los resultados de esta investigación sugieren que no incluir el componente de movimiento

vertical del suelo en las evaluaciones analíticas de este tipo de puentes puede generar un mayor grado de incertidumbre y riesgo, particularmente en regiones cercanas a la falla.

Palabras claves: puente tablero-armazón, desplazamiento vertical, comportamiento sísmico, fuerza axil, relación V/H, relación D/C.

Влияние вертикального сейсмического возбуждения вблизи разлома на отклик большепролетных неразрезных ферменных мостов

Халед Бенмахди[ав], **корреспондент**, *Нуредин* Лабари[аг],
Насер Рахал[бд], *Абдела* Демдум[б], *Мухамад* Садун[бе], *Хауда* Бегдад[б]

[а] Университет Батны 2, строительный факультет,
  г. Батна, Народная Демократическая Республика Алжир

[б] Университет „Мустафа Стамбули", строительный факультет,
  г. Маскара, Народная Демократическая Республика Алжир

[в] Лаборатория испытаний конструкций и механики материалов

[г] Лаборатория прикладной гидравлики

[д] Лаборатория машиностроительных конструкций и прочности,
  г. Оран, Народная Демократическая Республика Алжир

[е] Лаборатория испытаний конструкций и механики материалов

Резюме:

Введение/цель: В данном исследовании изучается сейсмическая реакция большепролетных неразрезных ферменных мостов на воздействие вертикальных подвижек грунта вблизи разлома. Основная цель статьи заключается в оценке того, как вертикальное сейсмическое возбуждение вблизи разлома влияет на безопасность конструкции и эксплуатационные характеристики этих мостов. Исследуя тонкую динамику, вызванную вертикальными смещениями вблизи разлома, появляется лучшее понимание уязвимостей большепролетных неразрезных ферменных мостов во время сейсмических событий.

Методы: Для достижения этой цели ферменный мост подвергался серии колебаний грунта, представляющих естественные сейсмические явления. Сейсмическая реакция моста была исследована с помощью метода линейного течения времени с использованием трехмерной конечно-элементной модели. Этот анализ был сосредоточен, в частности, на оценке сдвига и смещения основания. Анализ был расширен, учитывая сейсмические характеристики ферменных конструкций. Сравнение откликов моста с учетом и без учета вертикальной

составляющей движения грунта было проведено в целях выяснения влияния вертикального возбуждения.

Результаты: Результаты исследования показали значительное влияние вертикального возбуждения, особенно в отношении внутреннего усилия в элементах фермы, где оно превышало 60% во время сильного землетрясения и, следовательно, увеличило соотношение нагрузки и пропускной способности в большинстве элементов конструкции моста.

Вывод: На основании результатов данного исследования инженеры-строители и проектировщики должны убедиться в том, что игнорирование вертикального движения грунта при аналитических оценках мостов подобного типа может привести к большей степени неопределенности и риска, особенно вблизи разломов.

Ключевые слова: палубно-ферменный мост, вертикальное смещение, сейсмические характеристики, осевое усилие, соотношение вертикального и горизонтального ускорений, соотношение требований и возможностей.

Утицај вертикалног сеизмичког кретања у близини раседа на одговор гредних континуалних мостова решеткасте конструкције и већег распона

Халед Бенмахди[ав], **аутор за преписку**, *Нуредин* Лабари[аг], *Насер* Рахал[бд], *Абдела* Демдум[б], *Мухамад* Садун[бе], *Хауда* Бегдад[б]

[а] Универзитет у Батни 2, Департман за грађевинарство, Батна, Народна Демократска Република Алжир

[б] Универзитет „Мустафа Стамболи", Одсек за грађевинарство, Маскара, Народна Демократска Република Алжир

[в] Лабораторија за проучавање конструкција и механике материјала

[г] Лабораторија за истраживање примењене хидраулике

[д] Лабораторија за машинске конструкције и стабилност, Оран, Народна Демократска Република Алжир

[е] Лабораторија за проучавање конструкција и механике материјала

ОБЛАСТ: материјали, грађевинарство
КАТЕГОРИЈА (ТИП) ЧЛАНКА: оригинални научни рад
Сажетак:

Увод/циљ: У овој студији испитује се сеизмички одговор гредних континуалних мостова решеткасте конструкције и већег распона на вертикална померања тла у близини раседа. Основни циљ јесте да се процени како вертикално померање тла услед земљотреса у близини раседа утиче на сигурност конструкције и перформансе ових мостова.

Истраживање танане динамике проузроковане вертикалним померањем тла у близини раседа има за циљ да прошири сазнања о слабостима гредних континуалних мостова решеткасте конструкције и великог распона и указује на изазове којима су изложени током сеизмичких догађаја.

Методе: У ту сврху, решеткасти мост подвргнут је серији померања тла, што је представљало природне сеизмичке догађаје. Сеизмички одговор моста испитиван је применом методе линеарног протока времена на тродимензионални модел коначних елемената. Ова анализа се фокусира нарочито на смицање и померање базе, али је и проширена како би укључила сеизмичке перформансе решеткастих конструкција мостова. Одговор моста са узимањем у обзир вертикалне компоненте померања тла упоређен је са одговором без узимања у обзир дате компоненте како би се разјаснио утицај вертикалне екситације.

Резултати: Резултати показују да постоји значајан допринос вертикалне екситације, нарочито када је реч о унутрашњој сили у решеткастим елементима, где она прелази 60% током јаких земљотреса и има за последицу повећање односа захтева и капацитета у већини елемената решеткасте конструкције моста.

Закључак: Резултати овог истраживања показују да занемаривање укључивања компоненте вертикалног померања тла у аналитичке процене ове врсте моста може да доведе до већег степена неизвесности и ризика, нарочито у подручјима са раседима.

Кључне речи: гредни мост решеткасте конструкције, вертикално померање, сеизмичке перформансе, аксијална сила, однос вертикалног и хоризонталног убрзања, однос захтева и капацитета.

Influence of confinement by transverse reinforcement on the nonlinear behaviour of reinforced concrete structures

Adnane Ourabah[a], *Youcef* Bouafia[b],
Abdelkader Iddir[c], *Mohand Said* Kachi[d]

University Mouloud Mammeri,
Civil Engineering Department, L2MSGC Laboratory,
Tizi Ouzou, People's Democratic Republic of Algeria

[a] e-mail: adnane.ourabah@ummto.dz, **corresponding author,**
    ORCID iD: https://orcid.org/0009-0003-2094-8990

[b] e-mail: youcef.bouafia2012@yahoo.com,
    ORCID iD: https://orcid.org/0000-0002-4222-2176

[c] e-mail: abdelkader.iddir@ummto.dz,
    ORCID iD: https://orcid.org/0009-0006-7693-5197

[d] e-mail: kachi_ms@yahoo.fr,
    ORCID iD: https://orcid.org/0000-0001-7357-0424

Abstract:

Introduction/purpose: Structural design and calculation are based on the behavior of concrete and steel separately, without taking into account the contribution of stirrups in concrete confinement. The influence of confinement in structural modeling can be used to better approximate real behavior. The purpose of this study is to develop and validate a non-linear model for the behavior of reinforced concrete structures, taking into account concrete confinement.

Methods: A 3D finite element model is used to analyze framed structures. This model takes into account shear deformations. The cross-section of the beam is discretized into trapezoidal layers, while each layer is assumed to be uniaxially stressed. Non-linear constitutive laws are applied to the materials. For concrete confinement, the material's ductility is considered using the relationships proposed by Bouafia et al. These models are implemented in a computer program. The software monitors the behavior of column-beam structures under variable loads until reaching their load-bearing capacity.

Results: The results are compared with experiment results, focusing on maximum strength and deformability. The comparison shows very satisfactory results. In addition, the use of transverse reinforcement for

concrete confinement significantly impacts the global behavior of reinforced concrete structures by influencing the contribution of ductility.

Conclusion: The consideration of confinement in structures provides the best possible approach to the real behavior of structures. In contrast to existing calculation codes, concrete behavior laws do not take into account the contribution of confinement by transverse reinforcement.

Keywords: reinforcement, confinement, modelling, simulation, ductility, stirrups.

Introduction

In the field of engineering, particularly in construction of civil and industrial structures, design and modeling are mainly based on the finite element method (FEM). This method has developed considerably (Zienkiewicz & Taylor, 2005), initially employing a linear approach for discretizing beam elements before evolution towards non-linear methodologies (Bathe, 2006). Successive research has continued to refine and develop these approaches (Bratina et al, 2004; Rozman & Fajfar, 2009; Eltoft & Lande, 2015).

Recent models have introduced various approaches to taking non-linearity into account in the analysis of reinforced concrete structures, including concentrated non-linearities at end nodes, based on the concept of plastic hinges (Spacone et al, 1996) or distributed along the element (Spacone et al, 1992). These models aim to provide a more accurate representation of actual structural behavior, particularly in the case of complex or elongated structures subjected to high loads (Scott et al, 1982; Mander et al, 1988). Analysis of these structures requires consideration of the actual behavior of the materials used - concrete and steel - with recent studies proposing various behavioral relationships for these materials (Popovics, 1973; Bentz & Collins, 2000; Elwood & Moehle, 2003).

The main objective is to simulate the actual behavior of structures up to failure. This requires the consideration of mechanical non-linearities between stress and strain and the effects of transverse reinforcements, which not only absorb shear forces but also improve the compressive strength of concrete through a confinement effect. Recent experimental and theoretical studies have focused on the strength and ductility of ordinary concrete elements reinforced with transverse reinforcement, illustrating the significant impact of confinement on the behavior of concrete sections, whether circular or rectangular (Blume et al, 1961; Roy & Sozen, 1965; Soliman & Yu, 1967).

Several recent experimental and theoretical studies have analyzed the strength and ductility of ordinary concrete elements reinforced with transverse steel. This research has highlighted the critical role of confinement in the behavior of concrete sections, whether circular or rectangular. Recent research by Lu et al. (2019) and Paultre & Légeron (2008) has expanded on previous findings, exploring the effects of confinement in both rectangular and circular sections. Further experimental analyses on small-scale specimens have been advanced by researchers such as Canbolat et al. (2005) and Li et al. (2023), providing further insight into material behaviors under various loading conditions. These studies continue to highlight the critical influence of steel reinforcement on the mechanical properties of concrete.

For confined concrete, Kent & Park (1971) proposed a model based on previous experimental studies. Park et al. (1982), Saatcioglu & Razvi (1992), Sheikh & Uzumeri (1982), Ahmad & Shah (1982), Mander et al. (1988), Tang et al. (2021) and Chung et al. (2002) have proposed stress-strain relationships based on the results of tests they carried out. Mander et al. (1988) propose a single mathematical relationship that describes the entire application domain. Yalcin & Saatcioglu (2000) and Hoshikuma et al. (1997) propose two behavior branches.

Each of the authors proposes stress-strain relationships that take confinement into account. Each model is more or less limited; the percentages of longitudinal ρ_l and transverse ρ_t steel are more or less restricted. The proposed relationships are applied for confinement percentages (which depend on the density of longitudinal and transversal steels) of between 20 and 25 ‰ only. When applying these models, there is a considerable discrepancy between experimental results and calculation, especially in the post-peak branch, for confinement percentages below 20 ‰. It can be noted that the ascending part is more or less representative of all these models, but the descending part after the deformation peak differs significantly from the experimental results. Another approach, carried out by Bouafia et al (Bouafia et al, 2014; Iddir, 2016) consists of the proposal of three relations to better approximate the post-peak behavior. The correlation of the stress-strain curves with the experimental results is satisfying for confinement percentages between 10 and 25 ‰.

The present work then asks how to estimate this contribution regarding the structures' ductility, particularly by considering confinement at the nodal zones at the connection of the reinforced concrete columns-beams. This study aims to model structures in reinforced concrete under monotonic increasing loads until rupture by the finite element method. The

1918

modeling is performed considering the six degrees of freedom; it is a three-dimensional analysis.

This modeling considers the material non-linearity; the behavior relationships of concrete and steel are those derived from actual behavior until rupture. This modeling considers the geometric non-linearity and the evolution of the shear stresses due to the variation of the shear force outside the linear domain. The last parameter is considered by estimating the degradation of the shear modulus of concrete. The most interesting methods for predicting total displacements were developed from the 1980s onwards. Studies by Vecchio & Collins in 1986 (Vecchio & Collins, 1986; Kachi, 2006; Kachi et al, 2006; Houde, 2007) led to the modified compression field theory, which allows shear force to be taken into account in reinforced concrete beams. This model uses the method of strips and ties, representing a beam section by a succession of diagonal cracks crossed by transverse reinforcement.

Based on the modified compression field theory, a theoretical model presented by (Kachi, 2006) analyzes the failure behavior of reinforced and prestressed concrete beams subjected to the combined effect of plane bending and shear force in non-linear elasticity. It can be used to estimate the shear stiffness of beams with various cross-sectional shapes and reinforcement details.

The compressive strength of the concrete is limited by the strength of the concrete at the struts, which decreases as a function of the principal tensile strains perpendicular to the cracking. Cracks affect the transfer of shear forces, increasing the compressive forces to maintain equilibrium, which reduces the principal compressive stress in the concrete parallel to the cracks.

The third method used in the present study to account for the effect of shear stress is that proposed by Adjrad, which adjusts the shear modulus as a function of distortion evolution (Adjrad, 2015).

The present study is organized as follows: first, the behavior of concrete and steel used is presented, followed by the effect of transverse steel in concrete confinement. Finally, the numerical results, given by applying the software developed for this study, are compared and validated with the results of experimental tests published in the literature.

Material behavior

Concrete in compression and tension

The non-linear behavior until failure in compression of concrete, without taking into account confinement, is given by Sargin's relation

(Sargin, 1971). The advantage of this relationship is that the ascending and descending branches can be adjusted by the coefficients Kb and K'b, respectively, to the results of tests carried out on specimens of standard dimensions (Ø = 16 cm, h = 32 cm). The graphical representation of this relationship is given in Figure 1 and its mathematical expression is given by Eq.1.
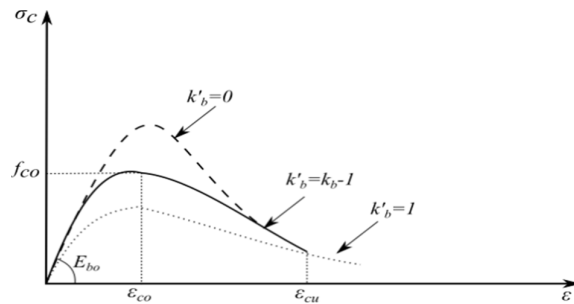
Figure 1 – Stress-strain diagram of unconfined concrete, the Sargin model

The behavior of concrete in tension is described by the relations proposed by (Grelat, 1978) and shown in Figure 2.
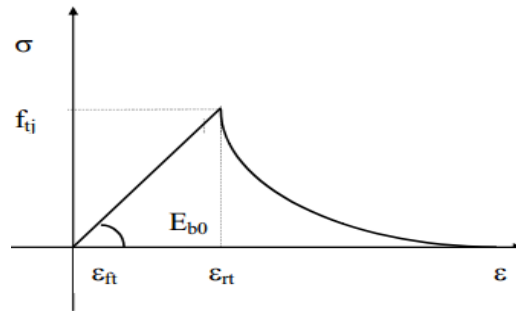
Figure 2 – Stress-strain diagram of unconfined concrete, the Grelat model

$$\sigma = f_{cj} \frac{k_b \bar{\varepsilon} - \left(k_b' - 1\right)\bar{\varepsilon}^2}{1 + \left(k_b - 1\right)\bar{\varepsilon} - k_b' \bar{\varepsilon}^2}$$

(1)

with

$$\bar{\varepsilon} = \frac{\varepsilon}{\varepsilon_0}, k_b = \frac{E_{b0}\varepsilon_0}{f_{cj}}$$

f_{cj} is the compressive strength of concrete,

1920

ε_0 is the peak deformation corresponding to f_{cj}, and

E_{b0} is the elastic modulus of concrete at the origin.

The stress-strain relationships, for the tension behavior of concrete, are given by Eq (2).

$$\sigma_{bt} = E_{b0}\varepsilon_{bt} \qquad\qquad ; |\varepsilon_{bt}| \le \varepsilon_{ft}$$

$$\sigma_{bt} = -f_{ft}\frac{(\varepsilon - \varepsilon_{rt})^2}{(\varepsilon_{rt} - \varepsilon_{ft})^2} \qquad ; \varepsilon_{ft} < |\varepsilon_{bt}| \le \varepsilon_{rt}$$

$$\sigma_{bt} = 0 \qquad\qquad ; |\varepsilon_{bt}| > \varepsilon_{rt} \tag{2}$$

f_{tj}: is the tensile strength of concrete,

ε_{ft} is the peak deformation corresponding to f_{cj}, and

ε_{rt} is the deformation corresponding to the plasticization of the tensest steel.

Confined concrete by transverse reinforcement

The behavior of concrete confined by transverse reinforcement is described by the relations proposed by Bouafia et al. (2014). These relations define three behavior segments:
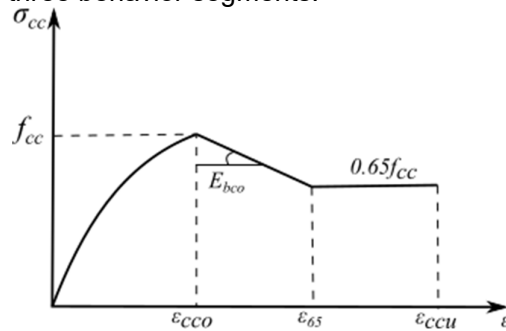
Figure 3 – Stress-strain diagram of confined concrete, model by Bouafia et al. (2014)

The first part of the curve is ascending and non-linear; the authors have proposed a modification of Sargin's relation (Sargin, 1971) to account for the confinement (see Equations 3 to 8).

For $0 \le \varepsilon_c \le \varepsilon_{cc0}$

$$\sigma_{cc} = f_{cc}\frac{k_c\bar{\varepsilon}_c - (k_c'-1)\bar{\varepsilon}_c^2}{1+(k_c-2)\bar{\varepsilon}_c - k_c'\bar{\varepsilon}_c^2} \tag{3}$$

with:

$$\overline{\varepsilon}_c = \frac{\varepsilon_c}{\varepsilon_{cc0}} \tag{4}$$

$$\varepsilon_{cc0} = \varepsilon_{c0}\left[1 + 5\left(\frac{f_{cc}}{f_{c0}} - 1\right)\right] \tag{5}$$

$$k_c = \frac{E_{b0}\varepsilon_{cc0}}{f_{cc}} \tag{6}$$

$$E_{b0} = 11000\sqrt[3]{f_{cc}} \tag{7}$$

$$k_c' = k_c - 1 \tag{8}$$

where:

f_{cc} is the compressive strength of confined concrete,
f_{c0} is the compressive strength of unconfined concrete,
ε_{cc0} is the peak deformation corresponding to f_{cc},
ε_{c0} is the peak deformation corresponding to f_{c0}, and
K_c is the adjustment coefficient.

After reaching the maximum stress, i.e., after the peak stress, the behavior tends to decrease along a linear descending branch (this is the post-peak zone). The behavior is described by equation (9). When the longitudinal strain reaches the value given by equation (11), the stress decreases to the value given by equation (12). This stress remains constant and a ductility phase is observed, in which the deformation reaches values close to ε_{ccu} (see Equation 13).

For $\varepsilon_{cc0} \leq \varepsilon_c \leq \varepsilon_{65}$

$$\sigma_{cc} = f_{cc} - E_s\left(\varepsilon_c - \varepsilon_{cc0}\right) \tag{9}$$

with:

$$E_s = \frac{6f_{c0}^2}{k_e \rho_s f_{yh}} \tag{10}$$

$$\varepsilon_{65} = \frac{0.35 f_{cc}}{E_s} + \varepsilon_{cc} \tag{11}$$

$$\sigma_{cc} = 0.65 f_{cc} \tag{12}$$

$$\varepsilon_{ccu} = 0.0035 + 0.4\frac{f_l}{f_{c0}} \tag{13}$$

k_e is the effective confinement coefficient,
f_{yh} is the yield stress of transverse steels, and
ε_{ccu} is the ultimate strain.

1922

Behavior of steels

The behavior of steels under monotonic loads is quasi-identical in tension and compression; the steels used are natural and hardened. For natural steels, the perfect elastoplastic law is adopted (Eyrolles, 2000).

$$\sigma = E_s \varepsilon_s \qquad ; \varepsilon_s \leq \varepsilon_e$$
$$\sigma = f_e \qquad ; \varepsilon_e < \varepsilon_s < \varepsilon_u$$
$$\sigma = 0 \qquad ; \varepsilon_s > \varepsilon_u \tag{14}$$

The behavior law of work-hardened steels is defined as follows (Eyrolles, 2000):

$$\sigma_s = E_s \varepsilon_s \qquad ; \sigma_s \leq 0.7\sigma_e$$
$$\sigma_s = \frac{\sigma_e}{E_s} + 0.823\left(\frac{\sigma_s}{\sigma_e} - 0.7\right)^5 \qquad ; 0.7\sigma_e < \sigma_s < 1.1\sigma_e$$
$$\sigma_s = 1.1\sigma_e \qquad ; 1\% < \varepsilon_s < \varepsilon_u \tag{15}$$

where:
E_s is the longitudinal modulus of steel,
ε_e: is the elastic limit strain of steel,
σ_e is the elastic limit stress of steel, and
ε_u is the ultimate deformation of steel.

Degradation of the shear modulus of concrete

To more accurately predict the deformation evolution of structures subjected to increasing external forces, it is essential to take into account deformations attributed to shear in the non-linear domain. Traditional studies, such as (Kwon & Spacone, 2002; Buyukozturk, 1977), have often neglected these non-linear deformations induced by shear stress. Although shear strength can generally be estimated using simple formulas, these do not take into account the effects of bending in composite materials. In addition, the appearance of shear cracks can result in considerable shear displacement, complicating the overall response of the structure. Recent research (Lee et al, 2015; Chen et al, 2013) has addressed these complexities by incorporating shear deformations into their analysis, providing a more complete understanding of structural behavior under such conditions.

The truss analogy model, consisting of connecting diagonal concrete struts inclined at an angle θ (see Figure 4) and transverse steel ties, is

used to calculate the tensile forces in the reinforcement and the compressive forces in the concrete connecting struts subjected to longitudinal sliding forces (Bouafia, 1991).
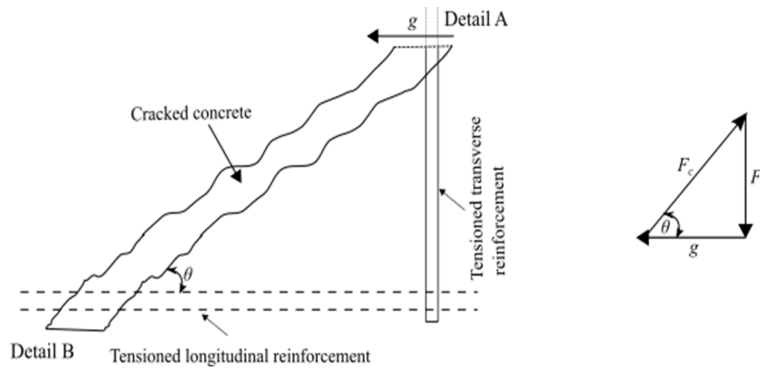
Figure 4 – Truss analogy model

The tension in the reinforcement ranges from maximum to mid-distance from the cracks (see Figure 5. A), while the strut of concrete is subjected to compression parallel to the cracks and tension in the direction of the reinforcement (see Figure 5. B). The average elongation of the reinforcement is related to the maximum stress. Modeling must take into account the compression of the concrete in the direction where the reinforcement stress is tension (Bouafia, 1991; Kachi et al, 2006).

Figure 5 – Local behavior of reinforced concrete in the transverse direction (A) and the longitudinal direction (B)

In an alternative method, the degradation of the shear modulus is taken into account by applying the model proposed by (Adjrad, 2015). The authors propose expressions for estimating the value of the shear modulus as a function of the characteristics of the cross-section and the steels (see Eqs. 16, 18, 19). These expressions are given according to the three behavior zones defined in Figure 6 which allow following the degradation of this shear modulus according to the evolution of the cracking of the concrete.
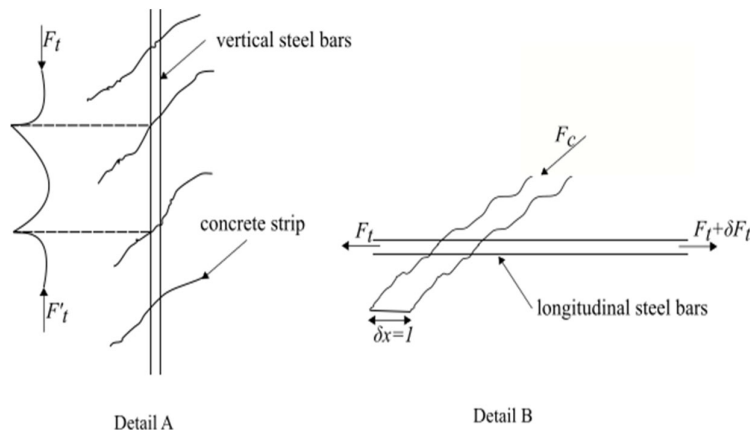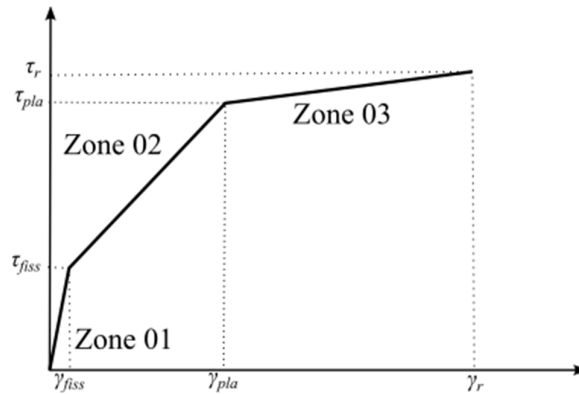

Figure 6 – Shear stress evolution versus distortion for a cross-section of reinforced concrete (Adjrad, 2015)

The model proposed by the authors is based on a theoretical and also statistical study that exploits more than 17 test results carried out on reinforced concrete beam and wall elements. These three zones are defined as follows:

Zone 01: before the concrete cracks, the variation of shear stress as a function of distortion is linear; the transverse deformation modulus G is given by the formula derived from the theory of linear elasticity (see Eq. 16).

$$G = \frac{E_c}{2(1-\mu)} \qquad \text{for } 0 \leq \gamma \leq \gamma_{fiss} = 0.0003$$

(16)

Zone 02: this is the post-cracking phase of the concrete and extends to the beginning of the softening of the steel. This zone is represented by a straight line whose slope is given by Eq.(17).

$$G = 604 \frac{\rho_t f_{et} \rho_l f_{el}}{f_{cj}} \qquad \text{for } \gamma_{fiss} \leq \gamma \leq \gamma_{plas} = 0.0025$$

(17)

Zone 03: this phase is characterized by the development of softening of the steels, and the shear modulus is given by Eq.(18).

$$G = 327 \frac{\rho_t f_{et} \rho_l f_{el}}{f_{cj}} \qquad for \ \gamma_{fiss} \leq \gamma \leq \gamma_r = 0.006$$

(18)

where:

ρ_t is the percentage of transverse reinforcement,

ρ_l is the percentage of longitudinal reinforcement,

fe_t is the yield strength of transverse reinforcement,

fe_l is the yield strength of longitudinal reinforcement,

fc_j is the characteristic compressive strength of concrete,

γ_{fiss} is the shear strain at concrete cracking,

γ_{pla} is the shear deformation due to steel plasticization,

γ_r is the shear strain at fracture, and

μ is Poisson's ratio.

The behavior of confined concrete

The compression forces applied to a reinforced concrete section produce lateral forces on the concrete inside the transverse reinforcement. The transverse steels are then solicited and thus provide concrete confinement. This (internal) confinement, generated by an adequate disposition of the steels, increases the load-bearing capacity and ductility of the structure. The compressive strength of confined concrete is given by Eq.(03) (Ngo & Scordelis, 1967; Soliman & Yu, 1967; Nait-Rabah, 1990; Spacone et al, 1992, 1996).

Circular section

The circular section, Figure 7, can be idealized by an effectively confined concrete which is inside the spiral steel, and an unconfined concrete which represents the cover.

Horizontal section   *Vertical section*
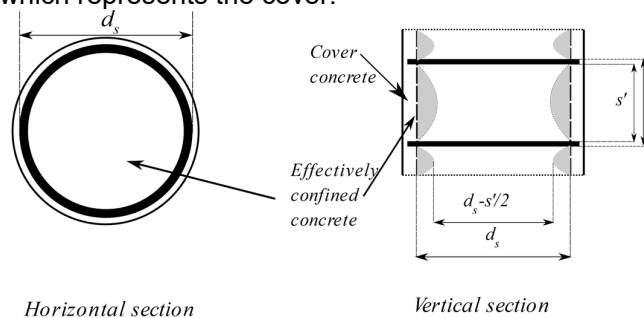
Figure 7 – Confined concrete in a circular section

The confinement coefficient is defined by (Mander et al, 1988):

$$k_e = \frac{A_e}{A_{cc}} = \frac{\left(1 - \dfrac{s'}{2d_c}\right)}{1 - \rho_{cc}}$$

(19)

The equilibrium of forces in the section can be written as follows:

$$2f_{yh}.A_{sp} = f_{yh}.s.d$$

(20)

The lateral confinement stress is given by:

$$f_l' = \frac{1}{2}\rho_s k_e f_{yh}$$

(21)

Rectangular section

For a rectangular section, the effective confined section is the area obtained after subtracting all the unconfined parabolas, see Figure 8. The effective confinement coefficient is given by:
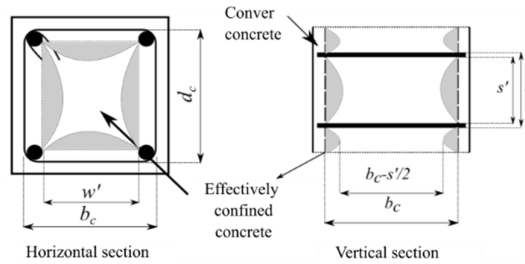

Figure 8 – Confined concrete in a rectangular section

The effective confinement coefficient is given by:

$$k_e = \frac{A_e}{A_{cc}} = \frac{\left(1 - \displaystyle\sum_{i=1}^{n} \dfrac{w_i'^2}{6b_c d_c}\right)\cdot\left(1 - \dfrac{s'}{2b_c}\right)\cdot\left(1 - \dfrac{s'}{2d_c}\right)}{\left(1 - \rho_{cc}\right)}$$

(22)

1927

The longitudinal and transverse steel proportions, respectively, can be expressed by the following relationships:

$$f_{lx} = \frac{A_{sx}}{s.d_c} f_{yh} = \rho_x f_{yh}$$

(23)

$$f_{ly} = \frac{A_{sy}}{s.b_c} f_{yh} = \rho_y f_{yh}$$

(24)

The result will be:

$$f'_{lx} = k_e \rho_x f_{yh}$$

(25)

$$f'_{ly} = k_e \rho_y f_{yh}$$

(26)

The distribution of the lateral confining stress is at an angle of 45°, and the value is given by:

$$f'_l = \frac{f'_{lx} + f'_{ly}}{2}$$

(27)

Model validation

A finite element analysis software for three-dimensional reinforced concrete structures, based on the displacement method, taking into account the confinement of the concrete by the transverse reinforcements, is developed in the present study and written in Fortran language. This program is then applied to isostatic, continuous beams and column-beam structures. The comparison with the experimental results is given below and is rather satisfactory.

Confinement is taken into account using the compressive strength of the concrete, the diameter and percentage of longitudinal and transverse reinforcement, and the geometry of the concrete cross-section. A comparison is made with a series of experimental tests carried out by Mander (10 tests for circular sections and 13 tests for rectangular sections). Figures 9 and 10 present a comparison of the results between the experimental and the model of Bouafia et al, for a rectangular and circular section, respectively. (Mander et al, 1988; Bouafia et al, 2014; Iddir, 2016)

1928
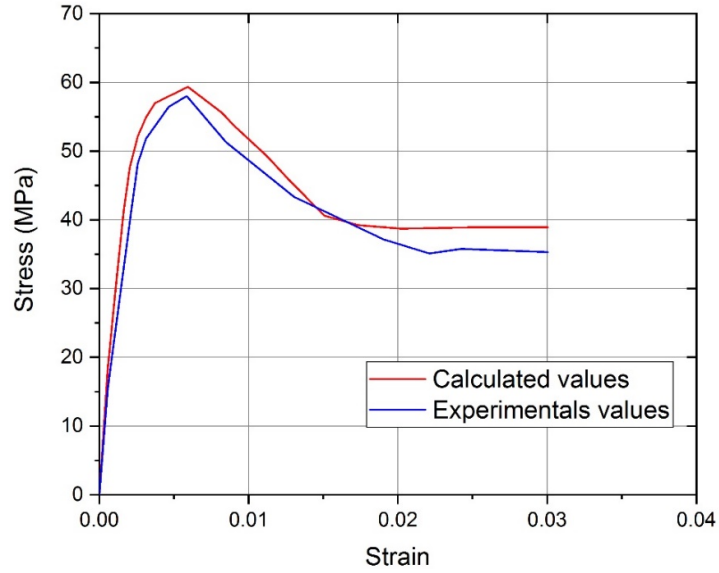
Figure 9 – Comparison of the experimental and theoretical stress-strain curves for a rectangular shape
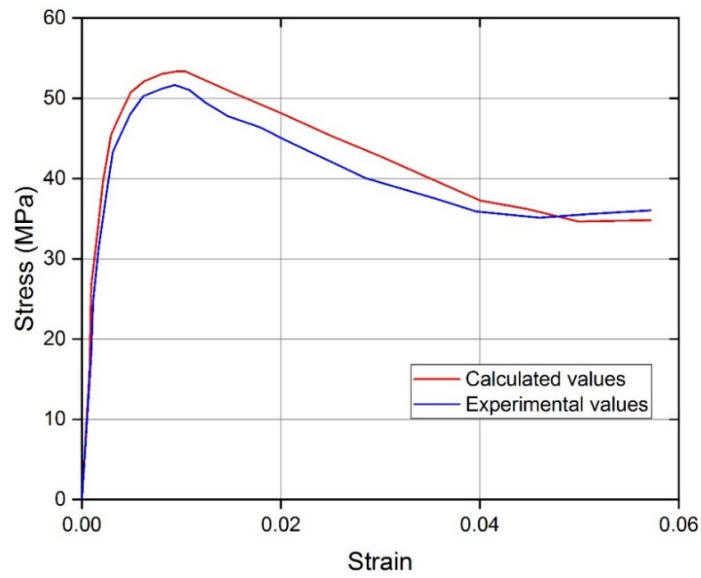
Figure 10 – Comparison of the experimental and theoretical stress-strain curves for circular shape

1929

The influence of taking into account the transverse reinforcement (percentage, spacing, and diameter) was demonstrated in the proposed model.

There is a clear contribution in terms of strength and ductility due to the confinement of the section. Thus, the approach adopted (proposal of three branches) provides certain flexibility to the model and therefore provides a better approach to the behavior of the material. Its application for confinement percentages from 10 to 25 ‰ is reasonably satisfactory. This model is used in the present study.

Isostatic beam: Toronto test

This experiment was done at the University of Toronto by (Vecchio & Shim, 2004). It is a program that regroups a series of tests on 12 reinforced concrete beams. In our study, we were interested in two representative beams from the geometric and reinforcement aspects: B2 and C2. The geometric characteristics are shown in Figure 11.
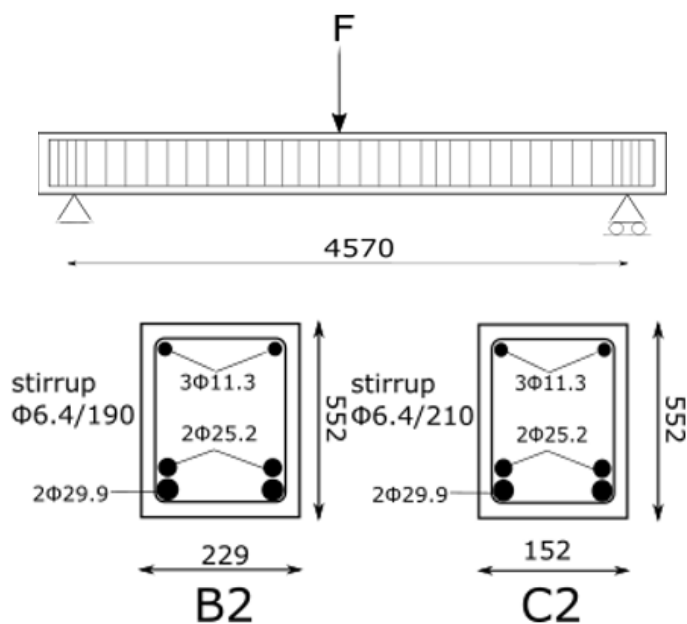
Figure 11 – Detail of the Toronto beam B2 and C2

The test consists of applying a load to the mid-span of the beam using a hydraulic jack. The load increments are 40 KN until the beam fails. The mechanical characteristics of the concrete and the longitudinal and transverse reinforcement are given in Table 1.

Table 1 – Mechanical characteristics of materials. Toronto Beam B2 and C2

Concrete	f_c' (MPa)	f_t' (MPa)	E_c (MPa)	ε_0
Beam B2	23.2	3.76	32900	0.0021
Beam C2	23.8	3.93	32900	0.0021
Steels	Diameter (mm)	Area (mm²)	f_y (MPa)	E_s (GPa)
M25	25.2	500	440	210
M30	29.9	700	436	200
Stirrup	6.4	32.2	600	200

Figures 12 and 13 show the evolution of the deflection as a function of the loading at the point of application of the incremental force. It can be seen that the simulation of our study approaches the experimental curve with good results. The concrete confinement is of course taken into account according to the real spacing of the transverse steels.

These figures show a comparison of the results with the confined concrete model used in the EN 1992-1-1 code. It can be seen that the two behavior laws for confined concrete (Bouafia et al, 2014; Eyrolles, 2000) satisfactorily approximate the actual behavior of the experimental tests on the beams B2 and C2. The experimental behavior is better approximated in the present study.

Figure 12 – Load deflection curves - Toronto Beam B2
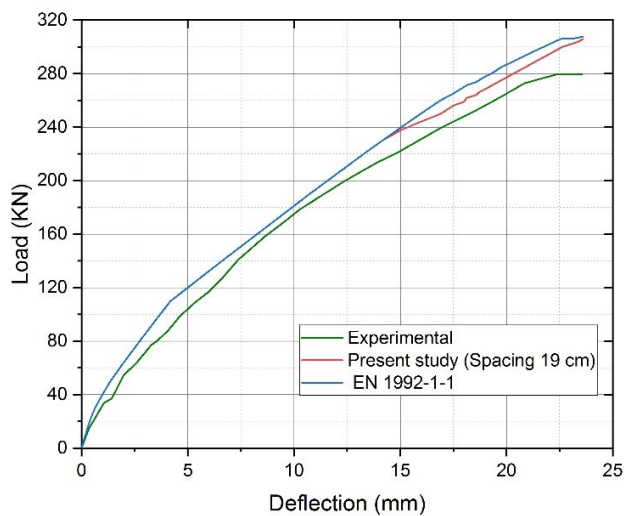
Figure 13 – Load deflection curves - Toronto Beam C2

Figure 14 shows the influence of transverse steel spacing on concrete confinement.

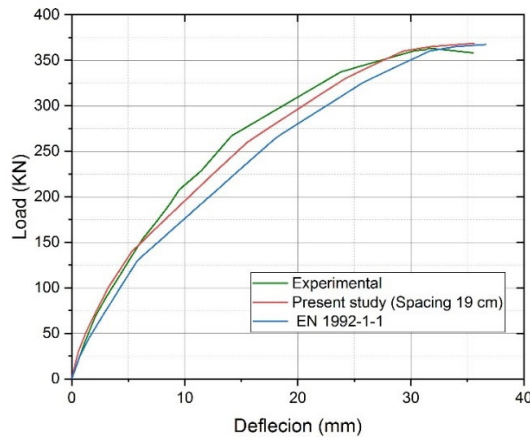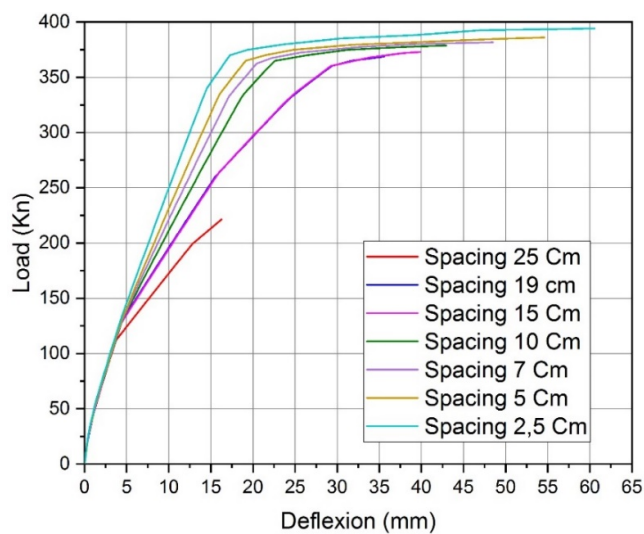

Figure 14 – Load deflection curves for different spacings – Toronto beam B2

1932

Thus, the evolution of ductility in terms of displacement, as well as a potential energy of the beam as a function of the ratio of transverse reinforcement can be observed as shown in Table 2.

Table 2 – Potential energy versus stirrup spacing. Toronto Beam B2

Spacing (cm)	Potential energy (Joules)	The gain in comparison to the experimental (%)
2.5	20479.4	124.56
5	17613.4	93.14
7	14997.1	64.45
10	14997.1	38.51
15	10680.4	17.11
25	8496.83	-83.17

Hyperstatic beam: Mattock tests

The example is taken from a series of tests carried out by Mattock (1965) on continuous hyperstatic reinforced concrete beams. The beam to be studied has two equal spans and a load point applied in the middle of the first span (see Figure 15). The cross-section beam is rectangular and the percentage of reinforcement is summarised in Table (3).

Table 3 – Mechanical characteristics of materials. Mattock beam

Concrete	f'_c (MPa)	f'_t (MPa)	E_c (MPa)	ε_0
Beam 03	24.99	2.1	32160	0.0024
Steels	Diameter (mm)	Area (mm²)	f_y (MPa)	E_s (GPa)
Top layer	6.35	31.67	400	200
Bottom layer	6.35	31.67	400	200
Stirrup spacing 15.24 cm	6.35	31.67	400	200
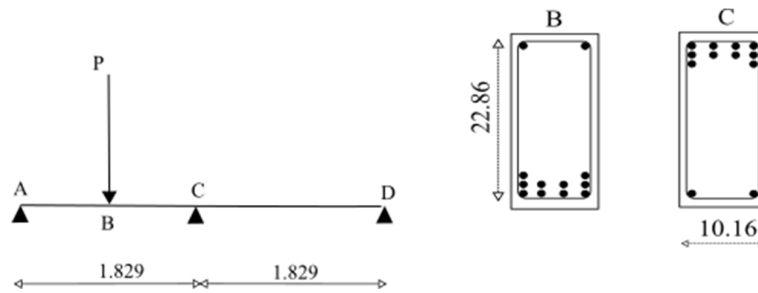
Figure 15 – Details of the Mattock beam - B3 Beam

1933

According to Figure 16, there is a good correlation between the simulation and the experiment. The ratio between the calculated and experimental rupture load is close to 1 (see Table 4). For displacement, the relative error does not exceed 6%.
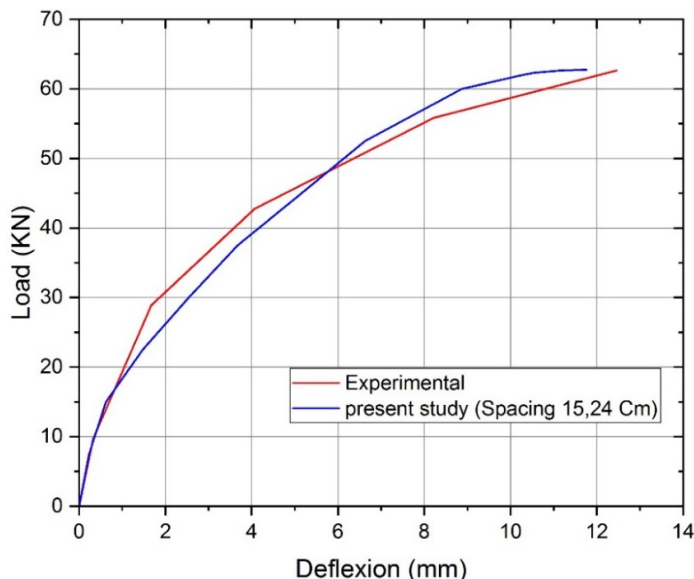
Figure 16 – Load deflection curves - Mattock beam

Table 4 – Load and displacement at the rupture. Mattock beam

	Displacement (mm)	Rupture load (KN)
Simulation	11.75	62.75
Experimental	12.45	62.63
Relative error (%)	5.62	0.19

To assess the influence of the concrete confinement, the spacing of the transverse reinforcement was increased from 2.5 to 20 cm.

The results, in terms of potential energy, gain compared to the experimental, are given in Table 5 and the behavior curves in Figure 17.

The contribution in terms of gain in potential energy and also in ductility of the beam is clearly shown.

Table 5 – Potential energy versus stirrup spacing. Mattock beam

Spacing (cm)	Potential energy (Joules)	The gain in comparison to the experimental (%)
2.5	1165.13	104.77
5	976.78	71.66
7	942.30	65.60
11	685.56	20.48
20	354.43	-37.71
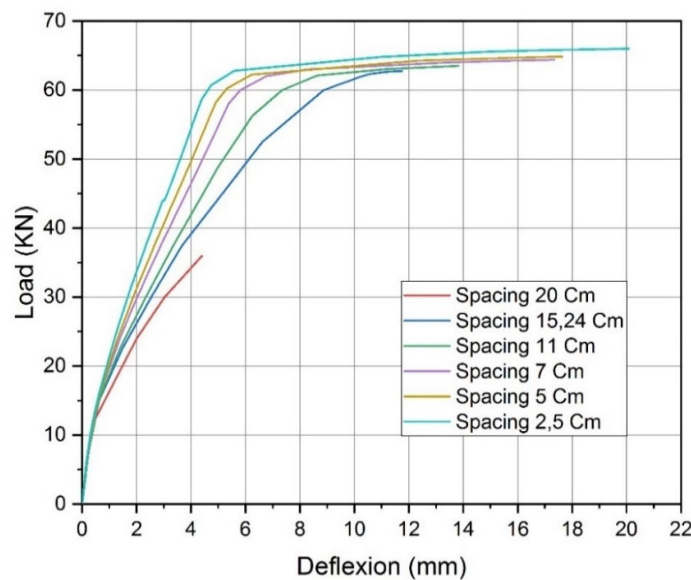
Figure 17 – Load deflection curves for different spacings – Mattock beam

Portal Frames: Cranston P7 - P9

The portals we are proposing for study are part of an experimental program initiated by Cranston (Grelat, 1978; Espion, 1986; Nait-Rabah, 1990; Robert, 1999).

The study concerns eight portal frames of the same dimensions, hinged at the base (Figure 18).
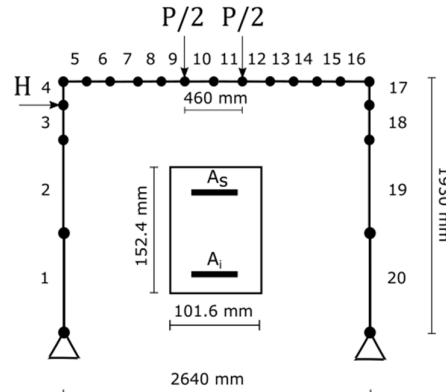
Figure 18 – Cranston portal frame

These portals are loaded at the top of the column by a force H which equals one-tenth of the force P applied at two points on the beam.
The mechanical characteristics of the portal frame are given in Table 6.

Table 6 – Mechanical characteristics of materials. Cranston portal frame

Concrete	f'_c (MPa)		f'_t (MPa)	E_c (MPa)	ε_0
Portal frame P7	33.2		2.59	32000	0.0020
Element	As ϕ 9,5	Ai ϕ 9,5	f_y (MPa)		E_s (GPa)
1, 20	2	2	278		200
2, 6, 15, 19	2	2	278		200
3, 4, 5, 16, 17, 18	2	2	278		200
7, 14	4	2	278		200
8, 13	4	2	278		200
9, 10, 11, 12	6	2	278		200

The vertical deflection at the middle section of the beam (at the junction of elements 10 and 11, see Figure 18) versus the vertical load P is shown in Figure 20.

The simulation results conform with the experimental results, especially in the linear domain and in the region of the rupture. The disparities observed in the post-cracking domain may be due to the incertitude of the mechanical properties of the steels; these are not provided by the author but are given by Grelat (1978). The difference (relative error) observed between the rupture loads (calculation/test) is 0.39% and in terms of displacement, this difference is 1.79%. (see Table 7).
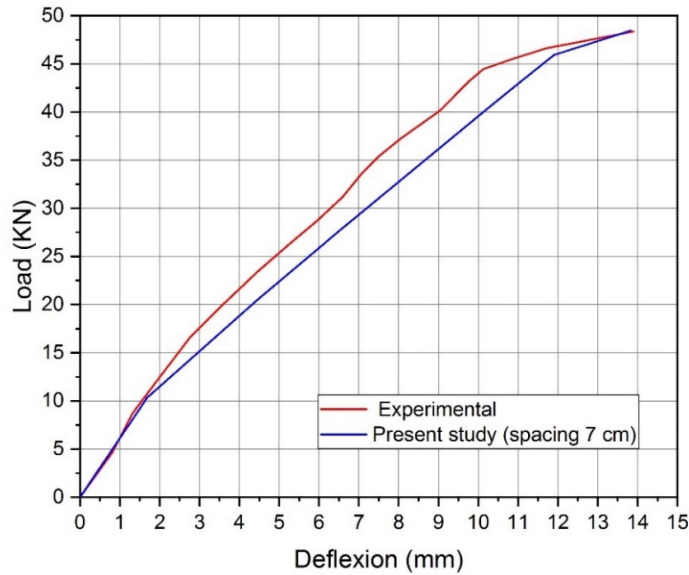
Figure - 19 Load deflection curves – Cranston portal frame

Table 7 – Load and displacement at the rupture. Cranston Portal frame

	Displacement (mm)	Rupture load (KN)
Simulation	13.64	48.16
Experimental	13.89	48.35
Relative error (%)	1.79	0.39

Closer stirrups provide a gain in potential energy. This gain is also estimated and compared to the portal frame configuration with the actual stirrup spacing (Table 8). The ductility contribution is shown in Figure 20.

Table 8 – Potential energy versus stirrup spacing. Cranston portal frame

Spacing (cm)	Potential energy (Joules)	The gain in comparison to the experimental (%)
2.5	487.28	14.26
5	439.86	3.15
15	256.31	-39.90

1937
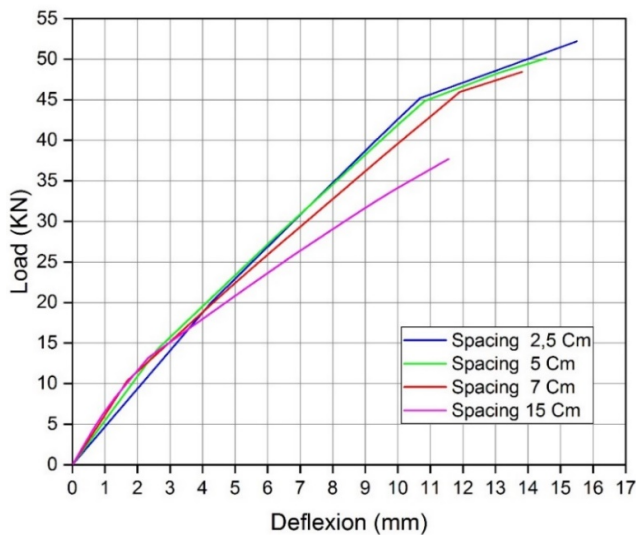
Figure 20 – Load deflection curves for different spacings – Cranston portal frame

For the behavior of the portal frame under the effect of the horizontal load, Figure 21 shows the evolution of the horizontal displacement of the top of the portals as a function of the lateral load H.
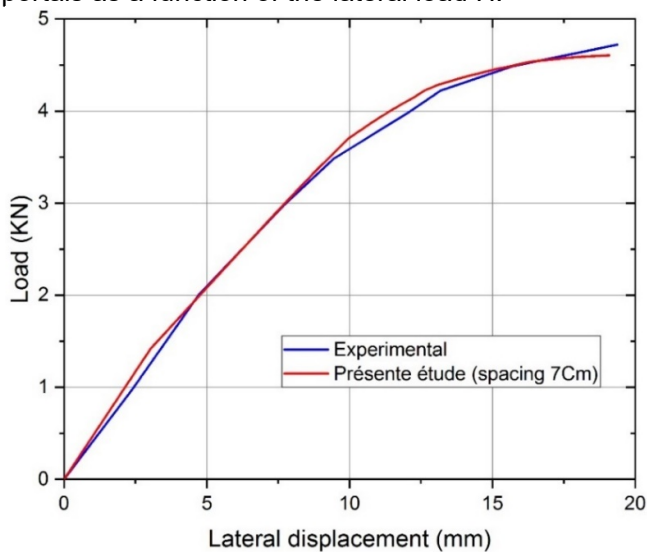
Figure 21 – Lateral displacement versus the horizontal load H – Cranston portal frame P7

1938

The results of the calculation/test comparison are satisfactory; the behavior is well described by the numerical simulation (see Table 9).

Table 9 – Lateral load and displacement at the rupture. Cranston portal frame

	Displacement (mm)	Rupture load (KN)
Simulation	19.09	4.60
Experimental	19.37	4.63
Relative error (%)	1.46	0.60

The closer spacing of the transverse reinforcement allows better confinement of the concrete; this increases ductility (Figure 22). This gain is also reflected in an increase in potential energy, which is estimated as a function of the spacing of the transverse steels and by comparison with the experimental configuration (Table 10).

Table 10 – Potential energy versus stirrup spacing. Cranston portal frame

Spacing (cm)	Potential energy (Joules)	The gain in comparison to the experimental (%)
2.5	1036.49	72.84
5	860.73	43.53
15	336.47	-43.89
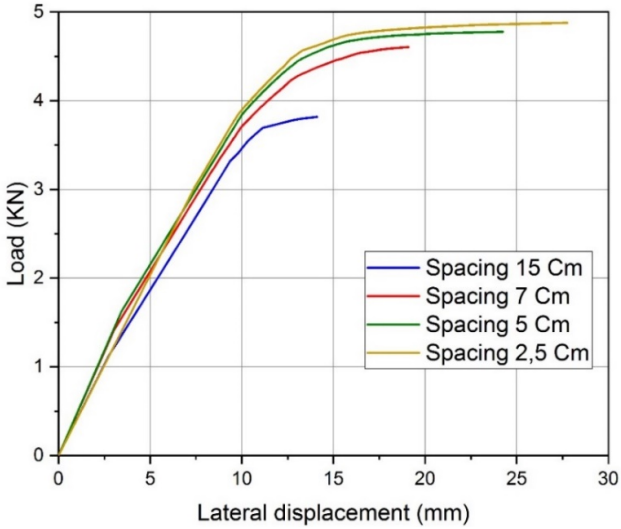
Figure 22 – Lateral displacement versus load for different spacings - Cranston portal frame

Conclusion

Taking into account the confinement of concrete permits us to appreciate the contribution in terms of ductility and the gain in potential energy. It also allows the increase in the ultimate load of reinforced concrete structures to be appreciated. The selected model is implemented in a computer program written in the Fortran language. This program allows following the behavior of column-beam structures subjected to variable loading until the structure's capacity is exhausted. The calculation results are compared with the experimental test results on reinforced concrete beams and frames obtained by other authors.

The comparison results, in terms of maximum load and deformability, are very satisfactory. The difference between the calculated values and those obtained experimentally does not exceed 2% in terms of maximum load. The contribution in terms of deformability represents 10 % to 70 %.

The ultimate value of the rupture load is greater the smaller the spacing of the stirrups. Finally, the influence of taking into account the confinement of concrete by transverse reinforcements on the nonlinear behavior of column-beam structures and their ductility was demonstrated.

References

Adjrad, A. 2015. *Modelisation non lineaire des structures triangulees composites*. PhD Thesis. Tizi Ouzou, People's Democratic Republic of Algeria: University Mouloud Mammeri [online]. Available at: https://dspace.ummto.dz/handle/ummto/1242 [Accessed: 28 May 2024].

Ahmad, S.H. & Shah, S.P. 1982. Complete Triaxial Stress-Strain Curves for Concrete. *Journal of the Structural Division*, 108(4), pp.728-742. Available at: https://doi.org/10.1061/JSDEAG.0005921.

Bathe, K-J. 2006. *Finite Element Procedures*. New Jersey: Prentice-Hall. ISBN: 978-0-9790049-0-2.

Bentz, E.C. & Collins, M.P. 2000. *Response-2000: Load-Deformation Response of Reinforced Concrete Sections* [online]. Available at: https://ingenieriasismica.utpl.edu.ec/sites/default/files/publicaciones/UCG-ES-00012.pdf [Accessed: 28 May 2024].

Blume, J.A., Newmark, N.M. & Corning, L.H. 1961. *Design of multistory reinforced concrete buildings for earthquake motions.* Portland Cement Association.

Bouafia, Y. 1991. *Résistance à l'effort tranchant des poutres en béton à precontrainte exterieure : étude experimentale et calcul à la rupture.* PhD Thesis. Châtenay-Malabry, Ecole centrale de Paris [online]. Available at: http://www.theses.fr/1991ECAP0198 [Accessed: 28 May 2024].

Bouafia, Y., Iddir, A., Kachi, M.S. & Dumontet, H. 2014. Stress-Strain relationship for the confined concrete. In: *11th World Congress on Computational Mechanics (WCCM XI)*, Barcelona, Spain, July 20 - 25 [online]. Available at: https://congress.cimne.com/iacm-eccomas2014/admin/files/fileabstract/a1410.pdf [Accessed: 28 May 2024].

Bratina, S., Saje, M. & Planinc, I. 2004. On materially and geometrically non-linear analysis of reinforced concrete planar frames. *International Journal of Solids and Structures*, 41(24-25), pp.7181-7207. Available at: https://doi.org/10.1016/j.ijsolstr.2004.06.004.

Buyukozturk, O. 1977. Nonlinear analysis of reinforced concrete structures. *Computers & Structures*, 7(1), pp.149-156. Available at: https://doi.org/10.1016/0045-7949(77)90069-4.

Canbolat, B.A., Parra-Montesinos, G.J. & Wight, J.K. 2005. Experimental Study on Seismic Behavior of High-Performance Fiber-Reinforced Cement Composite Coupling Beams. *ACI Structural Journal*, 102(1), pp.159-166. Available at: https://doi.org/10.14359/13541.

Chen, G., Teng, J.G. & Chen, J.-F. 2013. Shear Strength Model for FRP-Strengthened RC Beams with Adverse FRP-Steel Interaction. *Journal of Composites for Construction*, 17(1), pp.50-66. Available at: https://doi.org/10.1061/(ASCE)CC.1943-5614.0000313.

Chung, H.-S., Yang, K.-H., Lee, Y.-H. & Eun, H.-C. 2002. Stress–strain curve of laterally confined concrete. *Engineering structures*, 24(9), pp.1153-1163. Available at: https://doi.org/10.1016/S0141-0296(02)00049-4.

Eltoft, T. & Lande, T. 2015. *Nonlinear Analyses of RC Frames under Vertical and Horizontal Loading*. Master's Thesis. Trondheim, Torgarden, Norway: Norwegian University of Science and Technology - NTNU [online]. Available at: https://hdl.handle.net/11250/2351358 [Accessed: 28 May 2024].

Elwood, K.J. & Moehle, J.P. 2003. *Shake Table Tests and Analytical Studies on the Gravity Load Collapse of Reinforced Concrete Frames*. Pacific Earthquake Engineering Research Center, College of Engineering, University of California, Berkeley [online]. Available at: https://peer.berkeley.edu/sites/default/files/0301_k._elwood_j._moehle.pdf [Accessed: 28 May 2024].

Espion, B. 1986. *Contribution à l'analyse non linéaire des ossatures planes. Application aux structures en béton armé*. PhD Thesis. Bruxelles: Université libre de Bruxelles, Faculté des sciences [online]. Available at: https://difusion.ulb.ac.be/vufind/Record/ULB-DIPOT:oai:dipot.ulb.ac.be:2013/213542/Details [Accessed: 28 May 2024].

-Eyrolles. 2000. *Regles Bael 91 Modifiees 99. 3eme Edition: Règles techniques de conception et de calcul des ouvrages et constructions en béton armé suivant la méthode des états-limites*. Eyrolles. ISBN: 978-2212100235.

Grelat, A. 1978. *Calcul non linéaire des ossatures en béton armé*. PhD Thesis. Paris 6: Pierre and Marie Curie University - UPMC.

Hoshikuma, J., Kawashima, K., Nagaya, K. & Taylor, A.W. 1997. Stress-Strain Model for Confined Reinforced Concrete in Bridge Piers. *Journal of*

Structural Engineering, 123(5), pp.624-633. Available at: https://doi.org/10.1061/(ASCE)0733-9445(1997)123:5(624).

Houde, M.-J. 2007. *Modélisation de poutres en béton armé endommagées par chargements cycliques: comportement en flexion et en cisaillement*. PhD Thesis. Québec, Canada: Université Laval, Faculty of Civil Science and Engineering, Department of Engineering [online]. Available at: https://library-archives.canada.ca/eng/services/services-libraries/theses/Pages/item.aspx?idNumber=1276807867 [Accessed: 28 May 2024].

Iddir, A. 2016. *Modélisation des éléments de structure de section circulaire en béton armé confiné (Analyse de la fissuration)*. PhD Thesis. Tizi-Ouzou, Algeria: University Mouloud Mammeri, Faculty of Engineering and Construction, Department of Civil Engineering [online]. Available at: https://dspace.ummto.dz/server/api/core/bitstreams/0b664013-a868-4a03-9a0b-d50ad7b5b523/content [Accessed: 28 May 2024].

Kachi, M.S. 2006. *Modélisation du comportement jusqu'à rupture des poutres à précontrainte extérieure*. PhD Thesis. Tizi-Ouzou, Algeria: University Mouloud Mammeri, Faculty of Engineering and Construction, Department of Civil Engineering.

Kachi, M.S., Fouré, B., Bouafia, Y. & Muller, P. 2006. L'effort tranchant dans la modélisation du comportement jusqu'à rupture des poutres en béton armé et précontraint. *Revue Européenne de Génie Civil*, 10(10), pp.1235-1264. Available at: https://doi.org/10.1080/17747120.2006.9692914.

Kent, D.C. & Park, R. 1971. Flexural Members with Confined Concrete. *Journal of the Structural Division*, 97(7), pp.1969-1990. Available at: https://doi.org/10.1061/JSDEAG.0002957.

Kwon, M. & Spacone, E. 2002. Three-dimensional finite element analyses of reinforced concrete columns. *Computers & Structures*, 80(2), pp.199-212. Available at: https://doi.org/10.1016/S0045-7949(01)00155-9.

Lee, J.-Y., Lee, D.H., Lee, J.-E. & Choi, S.-H. 2015. Shear Behavior and Diagonal Crack Width for Reinforced Concrete Beams with High-Strength Shear Reinforcement. *ACI Structural Journal*, 112(3), pp.323-334. Available at: https://doi.org/10.14359/51687422.

Li, H., Li, X., Fu, J., Zhu, N., Chen, D., Wang, Y. & Ding, S. 2023. Experimental study on compressive behavior and failure characteristics of imitation steel fiber concrete under uniaxial load. *Construction and Building Materials*, 399, art.number:132599. Available at: https://doi.org/10.1016/j.conbuildmat.2023.132599.

Lu, Y., Liu, Z., Li, S. & Zhao, X. 2019. Effect of the Outer Diameter on the Behavior of Square RC Columns Strengthened with Self-Compacting Concrete Filled Circular Steel Tube. *International Journal of Steel Structures*, 19, pp.1042-1054.

Mander, J.B., Priestley, M.J.N. & Park, R. 1988. Theoretical Stress-Strain Model for Confined Concrete. *Journal of Structural Engineering*, 114(8), pp.1804-1826. Available at: https://doi.org/10.1061/(ASCE)0733-9445(1988)114:8(1804).

Mattock, A.H. 1965. Rotational Capacity of Hinging Regions in Reinforced Concrete Beams, Flexural Mechanics of Reinforced Concrete. In: *Proceedings of the ASCE-ACI Internatl. Symposium,* Miami, Fl, USA, 12, pp.143-181, November 10-12 [online]. Available at: https://www.concrete.org/publications/internationalconcreteabstractsportal.aspx?m=details&id=16716 [Accessed: 28 May 2024].

Nait-Rabah, O. 1990. *Simulation numérique du comportement non-linéaire des ossatures spatiales*. PhD Thesis. Châtenay-Malabry, Ecole centrale de Paris [online]. Available at: https://theses.fr/1990ECAP0151 [Accessed: 28 May 2024].

Ngo, D. & Scordelis, A.C. 1967. Finite Element Analysis of Reinforced Concrete Beams. *ACI Journal Proceedings*, 64(3), pp.152-163. Available at: https://doi.org/10.14359/7551.

Park, R., Priestley, M.J.N. & Gill, W.D. 1982. Ductility of Square-Confined Concrete Columns. *Journal of the Structural Division*, 108(4), pp.929-950. Available at: https://doi.org/10.1061/JSDEAG.0005933.

Paultre, P. & Legeron, F. 2008. Confinement Reinforcement Design for Reinforced Concrete Columns. *Journal of Structural Engineering*, 134(5). Available at: https://doi.org/10.1061/(ASCE)0733-9445(2008)134:5(738).

Popovics, S. 1973. A numerical approach to the complete stress-strain curve of concrete. *Cement and concrete research*, 3(5), pp.583-599. Available at: https://doi.org/10.1016/0008-8846(73)90096-3.

Robert, F. 1999. *Contribution à l'analyse non linéaire géométrique et matérielle des ossatures spatiales en Génie Civil : application aux ouvrages d'art*. PhD thesis. Lyon, France: INSA - National Institute of Applied Sciences [online]. Available at: https://theses.fr/1999ISAL0032 [Accessed: 28 May 2024].

Roy, H.E.H. & Sozen, M.A. 1965. Ductility of Concrete. *ACI Symposium Publication*, 12, pp.213-235 [online]. Available at: https://www.concrete.org/publications/internationalconcreteabstractsportal/m/details/id/16718 [Accessed: 28 May 2024].

Rozman, M. & Fajfar, P. 2009. Seismic response of a RC frame building designed according to old and modern practices. *Bulletin of Earthquake Engineering,* 7(3), pp.779-799. Available at: https://doi.org/10.1007/s10518-009-9119-4.

Saatcioglu, M. & Razvi, S.R. 1992. Strength and Ductility of Confined Concrete. *Journal of Structural engineering*, 118(6), pp.1590-1607. Available at: https://doi.org/10.1061/(ASCE)0733-9445(1992)118:6(1590).

Sargin, M. 1971. *Stress-strain Relationships for Concrete and the Analysis of Structural Concrete Sections*. Waterloo, Ont: University of Waterloo, Solid Mechanics Division.

Scott, B.D., Park, R. & Priestley, M.J.N. 1982. Stress-Strain Behavior of Concrete Confined by Overlapping Hoops at Low and High Strain Rates. *ACI Journal Proceedings*, 79(1), pp.13-27. Available at: https://doi.org/10.14359/10875.

Sheikh, S.A. & Uzumeri, S.M. 1982. Analytical Model for Concrete Confinement in Tied Columns. *Journal of the Structural Division*, 108(12), pp.2703-2722. Available at: https://doi.org/10.1061/JSDEAG.0006100.

Soliman, M.T.M. & Yu, C.W. 1967. The flexural stress-strain relationship of concrete confined by rectangular transverse reinforcement. *Magazine of Concrete Research*, 19(61), pp.223-238. Available at: https://doi.org/10.1680/macr.1967.19.61.223.

Spacone, E., Ciampi, V. & Filippou, F.C. 1992. *Beam Element for Seismic Damage Analysis*. Berkeley: University of California, College of Engineering, Earthquake Engineering Research Center, Report No. UCB/EERC-92/07 [online]. Available at: https://nehrpsearch.nist.gov/article/PB95-192126/XAB [Accessed: 28 May 2024].

Spacone, E., Filippou, F.C. & Taucer, F.F. 1996. Fibre beam–column model for non-linear analysis of R/C frames: Part I. Formulation. *Earthquake Engineering & Structural Dynamics*, 25(7), pp.711-725. Available at: https://doi.org/10.1002/(SICI)1096-9845(199607)25:7<711::AID-EQE576>3.0.CO;2-9.

Tang, H., Liu, R., Zhao, X., Guo, R. & Jia, Y. 2021. Axial compression behavior of CFRP-confined rectangular concrete-filled stainless steel tube stub column. *Frontiers of Structural and Civil Engineering*, 15, pp.1144-1159. Available at: https://doi.org/10.1007/s11709-021-0762-4.

Vecchio, F.J. & Collins, M.P. 1986. The Modified Compression-Field Theory for Reinforced Concrete Elements Subjected to Shear. *ACI Journal Proceedings*, 83(2), pp.219-231. Available at: https://doi.org/10.14359/10416.

Vecchio, F.J. & Shim, W. 2004. Experimental and Analytical Reexamination of Classic Concrete Beam Tests. *Journal of Structural Engineering*, 130(3), pp.460-469. Available at: https://doi.org/10.1061/(ASCE)0733-9445(2004)130:3(460).

Yalcin, C. & Saatcioglu, M. 2000. Inelastic analysis of reinforced concrete columns. *Computers & Structures*, 77(5), pp.539-555. Available at: https://doi.org/10.1016/S0045-7949(99)00228-X.

Zienkiewicz, O.C. & Taylor, R.L. 2005. *The Finite Element Method for Solid and Structural Mechanics, 6th Edition*. Butterworth-Heinemann. ISBN: 9780750663212.

Influencia del confinamiento por refuerzo transversal sobre el comportamiento no lineal de estructuras de hormigón armado

Adnane Ourabah, **autor de correspondencia**, *Youcef* Bouafia, *Abdelkader* Iddir, *Mohand Said* Kachi

Universidad Mouloud Mammeri, Departamento de Ingeniería Civil, Laboratorio L2MSGC,
Tizi Ouzou, República Argelina Democrática y Popular

CAMPO: ingeniería mecánica, ingeniería civil
TIPO DE ARTÍCULO: artículo científico original

Resumen:

Introducción/objetivo: El diseño y cálculo estructural se basan en el comportamiento del hormigón y del acero por separado, sin tener en cuenta el aporte de los estribos en el confinamiento del hormigón. La influencia del confinamiento en el modelado estructural se puede utilizar para aproximarse mejor al comportamiento real. El propósito de este estudio es desarrollar y validar un modelo no lineal para el comportamiento de estructuras de hormigón armado, teniendo en cuenta el confinamiento del hormigón.

Métodos: Se utiliza un modelo de elementos finitos 3D para analizar estructuras enmarcadas. Este modelo tiene en cuenta las deformaciones por corte. La sección transversal de la viga se discretiza en capas trapezoidales, mientras que se supone que cada capa está estresada uniaxialmente. A los materiales se les aplican leyes constitutivas no lineales. Para el confinamiento del hormigón, la ductilidad del material se considera utilizando las relaciones propuestas por Bouafia et al. Estos modelos se implementan en un programa informático. El software monitorea el comportamiento de estructuras columna-viga bajo cargas variables hasta alcanzar su capacidad portante.

Resultados: Los resultados se comparan con los resultados del experimento, centrándose en la máxima resistencia y deformabilidad. La comparación muestra resultados muy satisfactorios. Además, el uso de refuerzo transversal para el confinamiento del hormigón impacta significativamente el comportamiento global de las estructuras de hormigón armado al influir en la contribución de la ductilidad.

Conclusión: La consideración del confinamiento en estructuras proporciona la mejor aproximación posible al comportamiento real de las estructuras. A diferencia de los códigos de cálculo existentes, las leyes de comportamiento del hormigón no tienen en cuenta la contribución del confinamiento mediante el refuerzo transversal.

Palabras claves: refuerzo, confinamiento, modelado, simulación, ductilidad, estribos.

Влияние давления поперечной арматуры на нелинейные характеристики железобетонных конструкций

Аднан Ораба, **корреспондент**, *Jусуф* Буафиа,
Абделкадер Иддир*, Муханд Саид* Качи

Университет Мулауд Маммери,
Факультет гражданского строительства, лаборатория L2MSGC,
г. Тизи-Узу, Алжирская Народная Демократическая Республика

Резюме:

Введение/цель: Проектирование и расчет конструкций основаны на поведении бетона и стали, рассматриваемых отдельно, без учета влияния хомутов в предварительно напряженном бетоне. Эффект давления при структурном моделировании можно использовать для лучшего приближения к реальному поведению. Целью данного исследования является разработка и испытание нелинейной модели поведения железобетонных конструкций с учетом сжатия бетона.

Методы: Для расчета железобетонных конструкций используется трехмерная модель конечных элементов, учитывающая сдвиговые деформации. Поперечное сечение балки разделено на трапециевидные слои, при этом предполагается, что каждый слой имеет одноосное напряжение. К материалам применяются нелинейные определяющие законы. Для определения прочности бетона учитывается пластичность материала с использованием соотношений, предложенных Буафией и соавторами. Эти модели реализованы в компьютерной программе. Программное обеспечение отслеживает поведение колонно-балочных конструкций при переменных нагрузках до достижения их несущей способности.

Результаты: Полученные результаты сравнивались с результатами экспериментов с акцентом на максимальную прочность и деформируемость. Сравнительный анализ показал весьма удовлетворительные результаты. Помимо того, использование поперечного армирования для прочности бетона существенно влияет на общие характеристики железобетонных конструкций, в том числе и на его пластичность.

Вывод: Учет сжатия в конструкциях обеспечивает наилучший подход к реальному поведению конструкций. В отличие от существующих правил расчета, законы поведения бетона не учитывают влияние сжатия за счет поперечного армирования.

Ключевые слова: армирование, сжатие, моделирование, симуляция, пластичность, хомуты.

Утицај притискања попречном арматуром на нелинеарно понашање армиранобетонских конструкција

Аднан Ораба, **аутор за преписку**, *Јусуф* Буафиа, *Абделкадер* Идир, *Муханд Саид* Качи

Универзитет „Мулуд Мамери",
Одељење за грађевинарство, Лабораторија L2MSGC,
Тизи Узу, Народна Демократска Република Алжир

Сажетак:

Увод/циљ: Пројектовање и прорачун конструкција заснивају се на понашању бетона и челика посматраних одвојено, без узимања у обзир утицаја узенгија у притиснутом бетону. Утицај притискања у моделовању конструкције може се искористити за бољу апроксимацију стварног понашања. У студији је развијен и тестиран нелинеарни модел за понашање армиранобетонских конструкција, узимајући у обзир притискање бетона.

Методе: За анализу армираних конструкција користи се модел коначних елемената 3Д који узима у обзир деформације смицања. Попречни пресек греде је дискретизован у слојеве облика трапеза где се за сваки слој узима де је у једноосном стању напрезања. Примењују се нелинеарни конститутивни закони материјала. За притискање бетона разматра се дуктилност материјала коришћењем релација предложених у Буафиа и др. Ти модели су имплементирани у компјутерски програм. Софтвер прати понашање конструкција стуб-греда под различитим оптерећењима до достизања њихове пуне носивости.

Резултати: Резултати који су поређени са експерименталним резултатима, нарочито када је реч о максималној чврстоћи и деформабилности, показали су се као веома задовољавајући. Поред тога, коришћење попречног ојачања за притискање бетона утиче на понашање армиранобетонских конструкција у целини путем доприноса дуктилности.

Закључак: Разматрање притиснутости у конструкцијама обезбеђује најбољи могући приступ понашању конструкција у реалности. За разлику од постојећих прорачунских израза, закони понашања бетона не узимају у обзир допринос притискања помоћу попречне арматуре.

Кључне речи: армирање, притискање, моделовање, симулација, дуктилност, узенгије.

Guidelines for technology selection in intralogistics: a scientific approach

Mladen S. Božić[a], *Dragan* B. Đurđević[b],
Svetlana A. Dabić-Miletić[c]

University of Belgrade, Faculty of Transport and Traffic Engineering,
Belgrade, Republic of Serbia

[a] email:mladen.bozic@sf.bg.ac.rs, **corresponding author**,
 ORCID iD: https://orcid.org/0000-0002-2313-2343

[b] email:d.djurdjevic@sf.bg.ac.rs,
 ORCID iD: https://orcid.org/0000-0001-5918-1625

[c] email: cecad@sf.bg.ac.rs,
 ORCID iD: https://orcid.org/0000-0002-9316-0817

Abstract:

Introduction/purpose: Intralogistics involves the organization, control, realization, and optimization of material and information flows within a technologically integrated system. The selection and application of appropriate material handling equipment (MHE) play a crucial role in shaping intralogistics systems. This paper aims to define guidelines for selecting MHE based on scientific research. The methodology implemented to achieve this goal comprises several fundamental steps.

Methods: The initial step involves analyzing three typical groups of tasks in (intra)logistics systems: transshipment, internal transport, and production activities. The analysis focuses on identifying and describing key task parameters, such as the type of unit load, quantity, flow intensity, and the location and timing of task initiation and completion. Next, there is a step devoted to the analysis of relevant scientific research. The literature is searched according to specific criteria, such as publication year, keywords, and citation count, to form a database of relevant papers. The analysis focuses on identifying and linking the parameters of practical tasks with those described in the literature and on the characteristics of the MHE used to facilitate the selection of appropriate MHE for these tasks.

Results: Following this, in the third step, the observed task is classified according to standard task types found in the literature.

Conclusion: Finally, in the last/fourth step, regression analysis is applied to define the guidelines for MHE selection based on the frequency of use of specific MHE groups for certain task groups as described in the literature.

Key words: intralogistics, MHE selection, transshipment, internal transport, production.

Introduction

The term "intralogistics" was officially adopted at the CeMAT trade fair in 2008 in Hanover. It refers to a set of operations management activities ("*logistics*") within ("*intra*") a technologically integrated unit, such as a storage, a production system, a distribution center, etc. (Fottner et al, 2021). The task of intralogistics is the optimization and planning of material and information flows within the observed system, from the moment the material enters the system until it is packed and delivered further (Tompkins et al, 2010; Fottner et al, 2021). The primary tasks of intralogistics, stemming from the stochastic demands of the market, include efficient inventory management, rapid and accurate order preparation, and adaptability to changes in demand concerning assortment and order quantity. In fulfilling these requirements, the selection and application of appropriate material handling technology (MHE) play a crucial role in shaping intralogistics systems (Tompkins et al, 2010; Zajac & Rozic, 2022).

The task of selecting MHE under specific conditions is highly complex, as it is influenced by a multitude of factors. On the one hand, these include task parameters such as the type of goods, their appearance, quantity, spatial and temporal coordinates, system requirements and constraints, safety and legal regulations, and many other conditions. On the other hand, there is a plethora of potentially applicable MHE, ranging from manual to mechanized and fully automated and robotic technologies, such as carts, forklifts, cranes, conveyor systems, AGVs, AS/RS, and others (Zrnić et al, 2021; Zajac & Rozic, 2022). Material handling stands out due to its share in overall logistics costs, approximately 40% (Tompkins et al, 2010; Zajac & Rozic, 2022). Engaging appropriate MHE can enhance intralogistics systems by efficiently utilizing manpower, increasing flexibility and productivity (Zajac & Rozic, 2022). Generally, the selection of MHE (Material Handling Equipment) in the process of designing intralogistic systems goes through different levels—decision-making phases, characterized by varying degrees of detail, from choosing the type of MHE to specifying the MHE performance, manufacturer, supplier, etc. In the project practice, this complex task has been approached in several ways: relying on equipment manufacturers' recommendations, expert opinions, and stakeholder input; applying ready-made solutions; and utilizing scientific research results to support decision-making. Therefore, the aim of this paper is to establish guidelines for MHE selection based on scientific research. The intention is to frame the selection problem in a practical context and solve it in the manner illustrated in Figure 1.
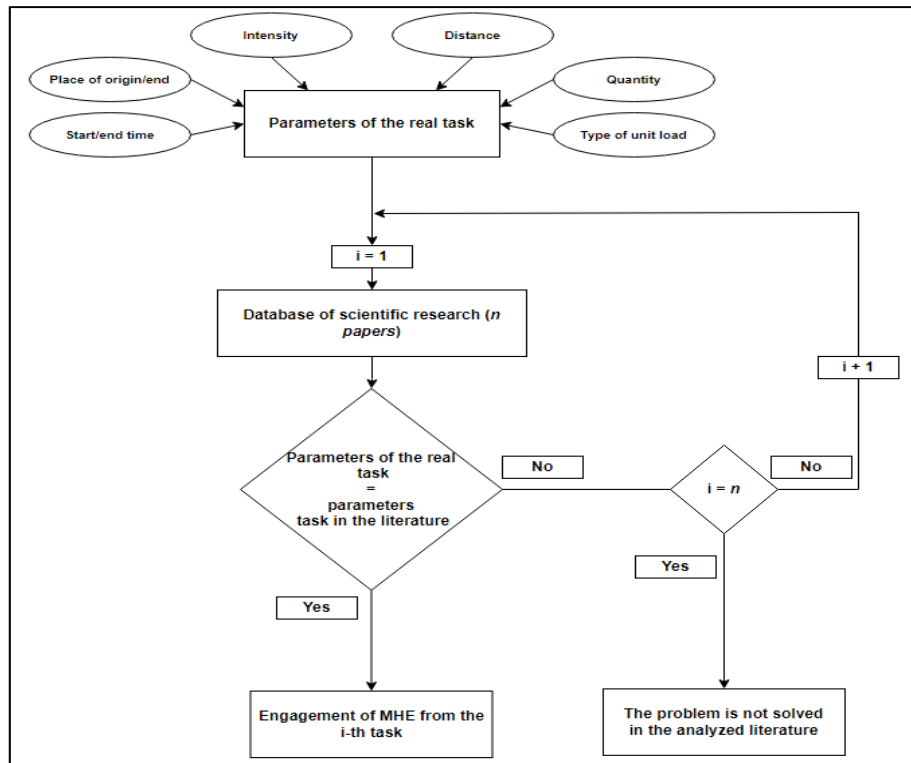
Figure 1 – Methodology for defining guidelines for MHE selection

The methodology for defining guidelines for MHE selection consists of several steps. Initially, it is necessary to identify and describe the key parameters of the analyzed task. These parameters include, but are not limited to (Vukićević, 1995; Sretenović, 1996):

- Task start/end time: outlining when the task starts and ends, important for planning and coordination. It can have stochastic/deterministic, stationary/non-stationary, and continuous/discontinuous features.

- Task origin/end place: the characteristics of the location where tasks begin and end, critical for routing and scheduling. It may have stochastic/deterministic features.

- Distance: the total distance that needs to be covered during the task, affecting travel time and resource allocation. It can have small, medium, or large features.

- Flow intensity: the amount of material over time, influencing the required capacity and speed of the MHE. It can have small, medium, or large features.
- Quantity: the volume or number of unit loads handled.
- Type of unit load: the nature of the items being transported (e.g., pallets, bags, individual items), which determines the appropriate handling and MHE.

Next, an analysis of relevant scientific research is conducted, focusing on the parameters of the task and the types of the MHE engaged. Following this, the observed task is classified according to standard task types found in the literature. If the parameters of the observed task match those of the resolved task in the literature, the guidelines for MHE selection for the observed task type are derived as a conclusion. This approach allows for systematic analysis and identification of MHE, ensuring that all relevant parameters are considered and that the guidelines are based on established solutions from the literature. The goal of this methodology is to provide concrete, applicable guidelines that will support decision making for MHE selection in future situations.

The paper is organized into seven chapters. Following the introduction, the second chapter discusses the concept and scope of the term intralogistics. The third chapter analyzes typical tasks in intralogistics and the MHE used for their realization. The fourth chapter focuses on the analysis of approaches to MHE selection. The fifth chapter presents and comments on the results of the analysis of relevant studies. The sixth chapter examines the validity of the obtained results through regression analysis and defines the guidelines for MHE selection based on this. In the conclusion, the research is summarized, encompassing the key information obtained from the literature analysis, and potential directions for future research are highlighted.

The role and importance of intralogistics processes

Intralogistics, as a term defining the field of logistics, first emerged in the period immediately following World War II. It referred to material handling activities within a factory, carried out using basic equipment and technologies such as hand carts and overhead cranes. A significant milestone in the development of intralogistics was the advent and implementation of the pallet system. Further development of intralogistics has paralleled the growth of the industry, evolving in step with the third and fourth industrial revolutions. The concept of Industry 4.0 has had a

substantial impact on the advancement of intralogistics, introducing the use of smart sensors, information and communication technologies, and cloud-based software support (Zrnić et al, 2021). According to the Intralogistics Forum of VDMA (Verband Deutscher Maschinen und Anlagenbau), intralogistics is defined as the organization, control, realization, and optimization of material and information flow within a technologically integrated unit, as well as the materials handling activities in industry, distribution, and public facilities (Kartnig et al, 2012; Yousefifar et al, 2015). In line with modern business trends, which include circular supply chains, this definition can be expanded to encompass this aspect. Intralogistics represents the complex interaction of various logistics functions aimed at controlling the flow of materials throughout the entire supply chain. It describes the internal flow of materials within different logistics hubs, from material flows in manufacturing, distribution centers, airports, and seaports, along with all accompanying flows (information, financial, and others) (Zrnić et al, 2021).

The connection between the spatial dislocation of production and consumption is achieved through the realization of material flows between them. Transforming these flows (spatially, temporally, quantitatively, and by aligning assortments) generates a large number of intralogistic activities. These activities depend significantly on which (sub)systems are connected, e.g., transshipment-storage, transshipment-production, production-storage, etc. (Overmeyer et al, 2009; Telek, 2016; Jusufbašić, 2023). Within intralogistics processes, activities can be grouped according to different criteria to identify classes of activities with similar characteristics and features. This enables more efficient management and synergy of intralogistics activities. One possible way to categorize them is as follows (Yousefifar et al, 2015; Taş, 2023):

1. Activities related to material flow realization: These involve materials handling and their flow within a technologically integrated unit (e.g., a production facility).
2. Activities related to information and inventory flow management: These activities focus on ensuring and updating inventory information at all levels.
3. Warehouse management operations: This encompasses all logistical operations conducted within a warehouse.

Within (intra)logistics systems, various flows are present, including raw materials, semi-finished products, finished goods, spare parts, maintenance consumables, waste materials, fuels, lubricants, and similar items. The realization of these flows involves fulfilling a multitude of

activities and requirements. It is crucial to accurately identify the characteristics and features of tasks to appropriately select suitable MHE for their realization (Overmeyer et al, 2009; Yousefifar et al, 2015; Telek, 2016). The technological requirements' characteristics and features provide detailed information describing the type of units and the quantity of materials; the origin and destination of the requirements; the timing, duration, and completion time of the requirements; tolerance intervals; and limiting factors present during task execution (Sretenović, 1996). Typical tasks encountered in intralogistics systems include transshipment (loading, unloading, storage, retrieval); internal transport (transportation, picking, positioning); production activities (packaging, protection, inspection, sorting); and many others. This research focuses on the previously defined groups of tasks rather than individual activities within them. Additionally, it analyzes the characteristics of the MHE engaged to execute these tasks.

Material handling technologies in intralogistics activities

In the process of technological design for new or enhanced existing (intra)logistics systems, a crucial step is selecting the appropriate MHE that will realize the specified task (Telek, 2016). During the MHE selection process, properly defining the intralogistics task is of great importance. A clear understanding of the task guides decision makers toward the category and type of MHE needed. Conversely, misunderstanding the task can lead to selecting the wrong MHE, resulting in reduced system productivity, increased costs, and similar issues. This chapter is dedicated to analyzing tasks within intralogistics systems and the MHE used to execute them.

Materials handling - task analysis

The analysis of tasks in intralogistics involves identifying and describing technological requirements. Describing technological requirements entails understanding their characteristics and features. This is a crucial step in defining a set of potentially applicable MHE for the realization of specific tasks. Below is a description of the characteristics and features of the previously identified tasks observed in the analyzed papers.

Transshipment represents a part of the intralogistics process where the transfer of goods occurs between transport vehicles and/or storage systems. Transshipment involves activities such as picking up,

transporting over short distances, and depositing material at various heights and locations. The transshipment task can be characterized as follows: the unit load type is typically a pallet in the analyzed papers; the intensity is generally high; the origin and destination are stochastic; and the timing of initiation, duration, and completion is discontinuous and stationary over longer periods. **Internal transport** encompasses the movement of materials within storage spaces or manufacturing facilities, emphasizing the transportation function. It involves activities such as picking up, transporting, delaying, and positioning materials at various heights and locations. The characteristics of internal transport tasks include the type of unit load—typically individual pieces, boxes, or pallets in the analyzed papers—moderate intensity; stochastic origin and destination; and the timing of initiation, duration, and completion, which can be continuous, discontinuous, or stationary. **Production tasks** involve assembly, packaging, or other operations that alter the appearance and chemical or physical characteristics of materials. These tasks include activities such as picking up, delaying, packaging, sorting, and similar operations. The characteristics of production tasks include the unit load type, typically individual pieces in analyzed papers, very high intensity, deterministic origin and destination, and the timing of initiation, duration, and completion being continuous and stationary.

Understanding the task characteristics plays a significant role in selecting MHE, as it enables the alignment of task requirements with the capabilities of MHE. Further in the paper, the characteristics of the typical MHE engaged in the realization of fundamental types of intralogistics tasks are analyzed.

Characteristics of material handling equipment

In intralogistics, there is a wide range of MHE used for various processes and activities. In recent years, with the development of Industry 4.0, MHE has been continuously evolving and innovating. Each type of MHE has techno-operational characteristics that recommend or limit its engagement for specific tasks to some extent. The primary classification is based on the action of the working organ, distinguishing between equipment with cyclic and continuous actions. Typical representatives of the MHE with cyclic operation include forklifts, tow trucks, AGVs, cranes, and carts, while the MHE with continuous operation includes chutes, belt conveyors, roller conveyors, elevators, and others. Various classifications of MHE are found in the literature based on task type (transport, positioning, unit formation, storage), drive type (motorized, manual, gravitational), degree of automation (semi-automated, automated), and

many others, which can be found in the reference literature: (Apple, 1977; Kulweic, 1991; Sretenović, 1996; Vukićević, 1995; Tompkins et al, 2010). This paper highlights and analyzes the MHE applied to typical intralogistics tasks, presented in Table 1.

Table 1 – Typical intralogistics tasks with the corresponding MHE

Task type	MHE
Transshipment	forklifts, cranes, conveyors, AGVs, robotic systems
Internal transport	forklifts, cranes, conveyors, AGVs, robotic systems
Oreder picking	forklifts, conveyors, robotic systems
Storage/retrieval	forklifts, cranes, AGVs, robotic systems
Production activities	cranes, conveyors, robotic systems
Positioning	forklifts, cranes

Forklifts as material handling and manipulation technology in intralogistics processes are represented by various types, most commonly counterbalance, side loader, reach truck, and others. Forklifts are used when overcoming height differences is necessary; they can grasp and deposit units of load (usually pallets), lift and lower them to different positions. They are flexible in terms of path, and are adaptable to various forms and operating modes. Counterbalance forklifts have universal use and can be used at docks, in storage, for positioning tasks, and for similar activities. Side loader forklifts are used for handling longer materials during loading, storage, and unloading tasks. Reach trucks are employed in warehouses for tasks requiring higher lifting heights or narrower aisle operations (Kulweic, 1991; Vukićević, 1995; Sretenović, 1996).

Technology based on conveyors includes belt conveyors, roller conveyors, gravity conveyors, and other types. They are used for loading, transporting, and order picking, as well as in production activities (depending on the configuration of production lines). They are engaged when continuous processes, high demand intensity, and deterministic origins and destinations are required. Belt conveyors, with specific characteristics (such as the type of material the belt is made of, width, and shape), are used for handling small granular and piece goods. They can also be used for horizontal and inclined transport within certain incline limits suitable for the characteristics of the materials and the conveyor. Roller conveyors are used for transporting larger pieces of material, typically at gentle inclines. There are versions of roller conveyors with and without drives. Gravity conveyors are used for both bulk and piece goods

when it is necessary to overcome height differences in limited spaces (Kulweic, 1991; Vukićević, 1995; Sretenović, 1996).

The category of cranes includes various types, such as overhead and jib cranes. They are engaged in loading, unloading, internal transport, and production activities. They are involved in labor-intensive processes for handling large quantities of material. Overhead cranes are most commonly used in manufacturing facilities, while jib cranes are designed for handling materials at individual workstations (Kulweic, 1991; Vukićević, 1995; Sretenović, 1996).

AGV technology encompasses MHE such as AGV carts, AGV forklifts, AGV towing vehicles, and similar equipment. They are commonly used for internal transport and loading and unloading in systems requiring a certain level of automation. AGV carts are used for horizontal material transport as they cannot lift materials. AGV forklifts are similar to conventional forklifts but differ in their restricted path of movement compared to AGV vehicles. Robotic systems have wide applications in highly automated systems, from loading and unloading to production activities. Robotic systems include autonomous mobile robots (AMRs) for internal cargo transport, collaborative robots, and robotic arms used in manufacturing environments unsuitable for humans (Kulweic, 1991; Vukićević, 1995; Sretenović, 1996).

Approaches for selecting material handling equipment

The engagement of appropriate MHE can significantly enhance system productivity, activity realization quality, workplace safety, and ergonomic conditions. Therefore, the selection of MHE depends on the specific task that needs to be realized. It is necessary to thoroughly analyze the task parameters to understand their specificity. Additionally, understanding the MHE itself and the context in which it will be engaged is crucial. The selection of MHE in the process of technological design can be realized in the following situations (Saputro et al, 2015):

1. Designing a new system, and
2. Reconstructing an existing system.

The process of selecting MHE involves a series of steps in which the planner makes decisions to select the appropriate MHE that will best meet the specified task (Tompkins et al, 2010; Telek & Cservenák, 2020). The selection of MHE can be done in several ways, depending on the level of detail in the analysis. Depending on the level of decision making, in some situations, it is not enough to simply conclude that the task requires the

use of a conveyor; it is also necessary to determine its type and techno-exploitation characteristics. Accordingly, the selection of MHE can be classified at different levels (Saputro et al, 2015):

1. Level I: This level focuses on finding the appropriate category of MHE. It includes the analysis of conveyors, cranes, industrial trucks, positioning equipment, etc.
2. Level II: This level focuses on finding the appropriate type of MHE within the category. The selection is directed towards selecting the best variant from the category of conveyors, such as belt conveyors, roller conveyors, or similar.
3. Level III: This level focuses on finding the appropriate model of MHE within the selected type. For example, selecting the best alternative among types of hand pallet trucks in terms of dimensions and technological and operational characteristics.

There are numerous tools that facilitate the decision-making process in the evaluation and selection of appropriate MHE. One of the pioneers in solving the problem of MHE selection, Apple (1977), in his book "Plant Layout and Material Handling," proposes the Material Handling Equation to aid decision making in selecting MHE. The essence of this equation consists of six main questions related to the following aspects of material handling: WHY (the reason for selecting MHE), WHAT (the materials being handled), WHERE and WHEN (the timing and location of handling), HOW (the method of handling materials), and WHO (the person responsible for handling materials). All six questions are crucial and must be satisfactorily answered. The outcome of the equation, or the solution, should represent a list of the characteristics that the potential MHE must fulfill to be engaged in the given task. Modern research employs analytical methods, multi-criteria decision-making (MCDM) methods, mathematical programming, simulation models, tools based on artificial intelligence, and more. In practice, designers rely most often on the following sources (Fonseca et al, 2004; Sharp et al, 2021):

1. Manufacturer catalogs and MHE manuals;
2. Designers' own experience;
3. Consulting with experts from the same/similar fields;
4. Engaging experts;
5. Including the opinions of workers involved in MHE operations in the decision-making process; and
6. Results from scientific research studies.

The mentioned approaches have their advantages, but they also carry certain risks. Planers who rely on personal experience tend to select the MHE they are most familiar with, which in some cases may not be suitable for the task at hand. MHE sellers have an interest in selling their equipment, so their recommendations can sometimes be biased. On the other hand, consultants often charge significant fees for their recommendations. Therefore, these options do not always guarantee a cost-effective solution.

The results of scientific research can indeed be utilized as ready-made solutions in specific situations. When research successfully models, analyzes, and solves a particular problem, the findings become valuable references for practical application. Such ready-made solutions have the potential to be adapted and applied to similar or identical problems encountered in practice. The main contribution of this paper lies in facilitating the use of scientific research results as ready-made solutions, thereby simplifying and expediting the decision-making process regarding the selection of MHE in specific scenarios. It is important to note that while research results often serve as ready-made solutions in certain situations, they are not universal and have their limitations. Their applicability requires careful identification of the specific conditions and characteristics of each task. Planers (decision makers) should consider all changes in the environment to ensure that the applied solutions remain relevant and provide long-term efficiency.

This paper aims to establish the guidelines for selecting MHE within the framework of the first level of selection. In this regard, a literature analysis has been conducted focusing on the selection of MHE for specific types of tasks. This approach enables the development of a specific decision-making system (such as algorithms, decision trees, etc.) for selecting MHE. Therefore, the next section of the paper is dedicated to analyzing these research studies.

Analysis of research in the field of MHE selection

In shaping intralogistics systems, a central issue is the selection and engagement of MHE. The task of selecting MHE is widely represented in logistics subsystems, including production, transshipment, storage, and others. The process of selecting MHE involves a series of steps and decisions made by decision makers to select the appropriate MHE that will efficiently meet the specified task requirements (Tompkins et al, 2010; Zubair et al, 2019). This paper focuses on defining the guidelines for selecting MHE based on the findings from scientific research. For the

purposes of this paper, the literature base was formed by searching Google Scholar using the keywords such as MHE, MHE selection, and MHE intralogistics. A detailed analysis included 20 relevant studies selected according to the following criteria: published between 2018 and 2023, higher citation levels, and available for online reading. Compared to the existing review papers in this field (Saputro et al, 2015; Telek & Cservenák, 2020), this study connects the task types with the MHE characteristics to provide the guidelines for MHE selection. This approach enables a comprehensive examination of current trends and innovations in the field of MHE selection. By using the criteria such as publication date, citation impact, and accessibility, this analysis ensures that relevant and influential research is included. By linking the task types with the specific MHE characteristics, this study provides practical guidelines that can help optimize intralogistics processes through the selection of appropriate technology. This contributes to improving operational efficiency and effectiveness, reducing costs, and enhancing system performance.

Review of relevant research

In the available literature, there are review articles on the selection of MHE. These papers provide an overview of the current state of the issue for a specific period. Telek and Cservenák (2020) analyzed research dealing with the selection of MHE using the database of the Science Direct publishing house. They considered which MHE is used for certain segments of MHE system planning. Under planning segments, they included MHE engagement in operational tasks and MHE engagement in automation processes. Also, they presented the tools and methods that were used in the analyzed research about the considered MHE. Unlike their research (Telek & Cservenák, 2020), this paper includes research from various publishing houses (Science Direct, MDPI, Springer, and others), and the engagement of MHE is considered for specific types of tasks. Saputro et al. (2015) analyzed 42 studies from the period 1971-2014. They analyzed the research from the aspect of the problem solved, the level of decision-making, and the applied methodology/tools. In relation to the research of Saputro et al. (2015), this paper includes the papers in the period from 2018-2023; in addition, it provides a broader picture of the solved problem and provides an insight into which MHE was considered for which type of task. Based on their paper (Saputro et al, 2015), it can be stated that 20 papers (as many as analyzed in this paper) represent an adequate database for the analysis of this issue. In the analyzed research, a large number of papers are about palletized goods (over 80% of the research). Accordingly, the obtained guidelines for the selection of MHE

should be considered as application recommendations for the given task parameters. Table 2 shows the analyzed research from the aspect of the solved task type, the considered MHE, and the applied methods for solving the select problem.

Table 2 – Overview of the analyzed papers

Author	Type of the solved task	Considered MHE	Applied method
Agarwal & Bharti (2022)	internal transport	AGVs	Fuzzy AHP, Fuzzy TOPSIS, Fuzzy DEMETAL
Voćkić et al. (2018)	transshipment, internal transport	forklifts	Rough SWARA, ARAS
Mathew & Sahu (2018)	internal transport	AGVs, conveyors	CODAS, EDAS, MOORA, WASPAS
Zavadskas et al. (2018)	internal transport	AGVs	R-ROV, WASPAS, Rough SAW, Rough MABAC, FUCOM
Průša et al. (2018)	transshipment, internal transport	forklifts	TOPSIS
Zubair et al. (2019)	transshipment, internal transport, production activities	conveyors, AGVs, cranes	AHP
Kučera (2020)	transshipment, internal transport	forklifts, AGVs	AHP, WSA
Goswami et al. (2021)	internal transport, production activities	forklifts, conveyors, robots	TOPSIS, ARAS, COPRAS, CRITIC
Horňáková et al. (2021)	transshipment, internal transport	forklifts, robots	AHP
Soufi et al. (2021)	transshipment, production activities	conveyors	AHP
Chakraborty & Saha (2024)	transshipment, internal transport	forklifts	FUCOM, MOORA

Author	Type of the solved task	Considered MHE	Applied method
Shchemeleva (2022)	transshipment, internal transport	conveyors	Optimization model
Simic et al. (2023)	transshipment, internal transport	AGVs, robots	T2NN-LOPCOW-ARAS
Tadić et al. (2023)	transshipment, internal transport	conveyors, AGVs, robots	Fuzzy AHP, Fuzzy COBRA
Yazid et al. (2023)	transshipment, internal transport, production activities	conveyors, AGVs, robots	CRITIC, TOPSIS
Huskanović et al. (2023)	internal transport	forklifts	SWARA, CRITIC, MARKOS
Chatterjee & Chakraborty (2023)	internal transport, production activities	conveyors, cranes, AGVs	R method
Ulutaş et al. (2023)	transshipment, internal transport	forklifts, cranes	Fuzzy BWM, Fuzzy MCRAT

In the analyzed research, typical factors (criteria) considered during the selection of MHE include productivity, flexibility, automation, safety, material handling capability, spatial constraints, and similar aspects. With increasing the awareness of sustainability and the goal of enhancing it, the following criteria are also included in the MHE selection process: energy consumption, CO_2 emissions, financial indicators (return on investment, profitability, and similar), ecological parameters, and similar factors.

Discussion of the analyzed research

This paper aims to analyze the reference research based on Apple's equation. Specifically, the testing of Apple's equation was conducted, which provides a proposed material handling solution for the defined task parameters (type of unit load, quantity, distance, lifting height, etc.). This approach represents a form of Decision Support System (DSS) for selecting MHE. Chan et al. (2001) present an example of the application of Apple's equation. An analysis of the type unit of load and the characteristics of materials may indicate the need to handle pallets.

Further analysis might show that lifting the material to a height of 6 meters is necessary, the transport distance is 50 meters, and certain maneuvering is required during material transport. This suggests that a forklift would be the appropriate MHE in this case. Even further analysis of methods can provide more information about the specific characteristics of the forklift.

In the analyzed papers, it was concluded that forklifts are most commonly used for carrying out transshipment tasks, as shown in Figure 2. The transshipment tasks in the analyzed papers are characterized by the following: the type of unit load– pallet; large quantity of materials (more than 50 pallets) in a unit of time; origin – transshipment dock; destination – storage locations; distance – on average more than 20 meters; occurrence time – stochastic; and lifting height – up to 10 meters required. Accordingly, forklifts are MHE that efficiently handles palletized materials, ensures high process intensity, is flexible regarding movement paths, and provides intermittent operation. Additionally, it is important to highlight the multifunctionality of forklifts, which allows for the realization of multiple types of tasks simultaneously (transshipment and internal transport), a requirement often seen in practice. The least applied technology for the realization of transshipment tasks is cranes, which are considered atypical when it comes to handling palletized materials. Factors such as limited working space, the complexity of grasping loads from the vehicle's cargo area, reduced employee safety (since the load being manipulated is above the working area), and lower productivity compared to forklifts for handling lighter unit loads indicate the incompatibility of cranes for transshipment tasks.

When it comes to internal transport tasks, the conclusion drawn from the analyzed papers addressing this issue is as follows. In the majority of cases (over 50% of the papers), the MHE considered for the realization of internal transport activities are AGVs (Figure 3). Internal transport tasks in the analyzed papers are characterized by the following: the type of unit load – pallets and packages; large quantity in a unit of time; origin and destination – storage locations or workstations; distance – on average more than 50 meters; and occurrence time – stochastic. Based on the task description, AGVs provide the necessary flexibility in handling various types of unit loads, as well as the intermittent operation characteristic that is common in the majority of tasks analyzed. The use of AGVs for internal transport tasks is supported by the automation of intralogistics activities in line with the development of Industry 4.0 solutions. In contrast, cranes are used in the least number of cases due to their limitations in path flexibility and access to storage locations, workstations, and similar areas.

MHE based on conveyors (roller, belt, slide) is most considered in production activities (Figure 4). Production activities require high process intensity, continuity, and determinism, which conveyor technology facilitates. Production is also characterized by: the type of load unit – individual pieces; large quantity in a unit of time; origin and destination – workstations; and occurrence time – deterministic. Additionally, the configuration of production and assembly lines favors the use of conveyors. Forklifts are least used for production activities because the production process is continuous and involves handling individual product units.
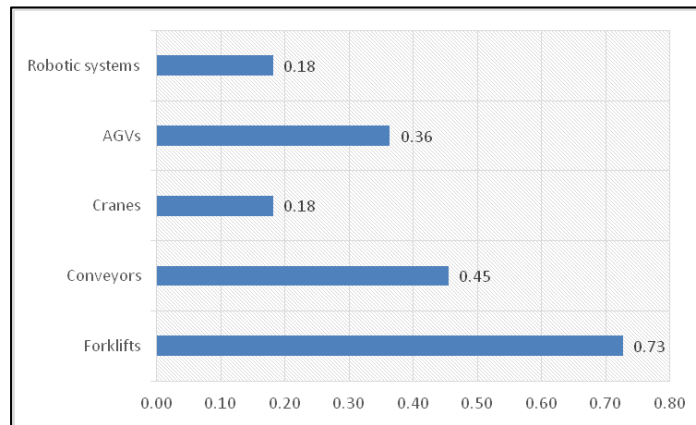
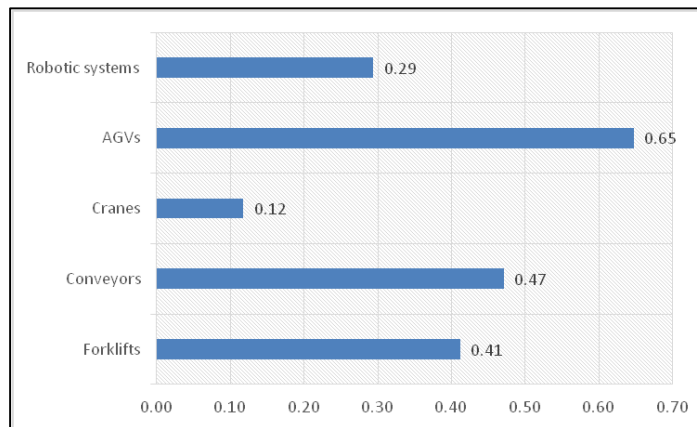*Figure 2 – MHE used for the realization of transshipment tasks*

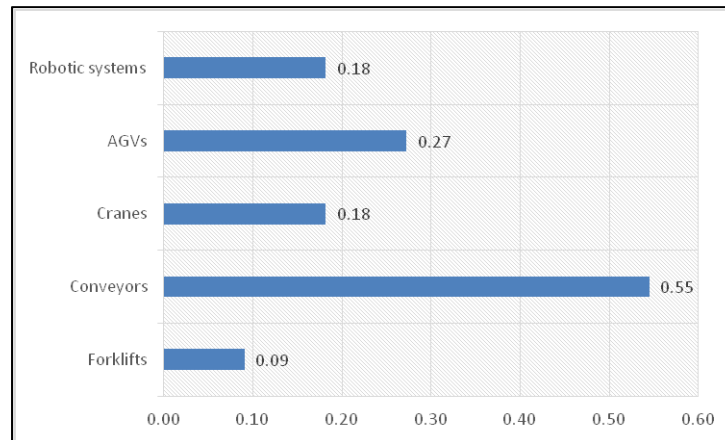*Figure 3 – MHE used for the realization of internal transport tasks*

Figure 4 – MHE used in production activities

Analysis of the results and the generation of the guidelines for MHE selection

The results of the analyzed research indicate which MHE is most commonly considered for specific types of tasks. However, the data on the frequency of MHE engagement in the literature is not sufficient to make informed decisions regarding the appropriate selection of MHE. With this in mind, it is necessary to establish the relationship between task parameters on the one hand and the characteristics of the applied MHE on the other. Therefore, this paper applied regression analysis to define this relationship. Based on the obtained relationship, it is possible to establish the guidelines for selecting MHE based on task parameters.

Regression analysis

Regression is a statistical method used to investigate and model relationships between two or more variables. Its primary purpose is to determine how changes in one or more independent variables affect a dependent variable (Uyanık & Güler, 2013). In the context of this paper, regression analysis is employed to define the relationship between the task parameters (independent variables) and the applied MHE (dependent variable), enabling informed decision making for MHE selection. There are several types of regression, with linear regression and logistic regression being the most commonly used. For this paper, linear regression has been used.

The process of applying regression analysis involved several steps. Data were collected from relevant research containing information on task parameters (type of unit load, quantity, intensity, distance, origin/destination time). These task parameters were categorized into two groups based on their physical and temporal characteristics, respectively: Parameter-1 (type of unit load, quantity, distance, origin/destination) and Parameter-2 (intensity and origin/destination time). The values of these parameters were quantified on a scale from 1 to 9. Larger dimensions and types of units of load received higher values, as did larger quantities, intensity, and distance. Origin/destination and time received higher values if they leaned towards determinism and lower values in cases of stochasticity.

Linear regression was chosen as an appropriate model for analyzing the relationship between the task parameters and the MHE characteristics. The equation of the linear regression model is (Uyanık & Güler, 2013):

$$Y = \beta_0 + \beta_1 X_1 + \beta_2 X_2 + \cdots + \beta_n X_n + \epsilon, \tag{1}$$

where:
Y is the dependent variable (MHE),
$X_1, X_2, X_3 \ldots$ are the independent variables (task parameters),
$\beta_0, \beta_1, \ldots, \beta_n$ are the regression coefficients, and
ϵ is the random error.

In Figure 5, the task parameters addressed in the literature are represented by points, with the tasks employing forklifts highlighted in red (Figure 2). The characteristics of forklifts in addressing these tasks are depicted by the regression line. It can be seen that for most of the tasks for which the forklift is considered, it is suitable. Additionally, other tasks that do not deviate significantly from the regression line can also be successfully executed using forklifts. This highlights the flexibility and versatility of forklifts across various task parameters.

In Figure 6,the task parameters for internal transport addressed in the literature are represented by points, with the task engagement AGVs highlighted in red (Figure 3). The characteristics of AGVs in addressing these tasks are depicted by the regression line. It can be seen that for most of the tasks for which AGVs are considered, they are suitable. Additionally, other tasks that do not deviate significantly from the regression line can also be successfully realized using AGVs. This highlights the trend towards automation in intralogistics systems.

In Figure 7, the task parameters for production activities analyzed and addressed in the literature are represented by points, with the tasks employing conveyors highlighted in red (Figure 4). The characteristics of conveyors in addressing these tasks are depicted by the regression line. It can be seen that for most of the tasks for which the conveyor is considered, it is suitable. Additionally, other tasks that do not deviate significantly from the regression line can also be successfully realized using conveyors. This is supported by the configuration of production and assembly lines.
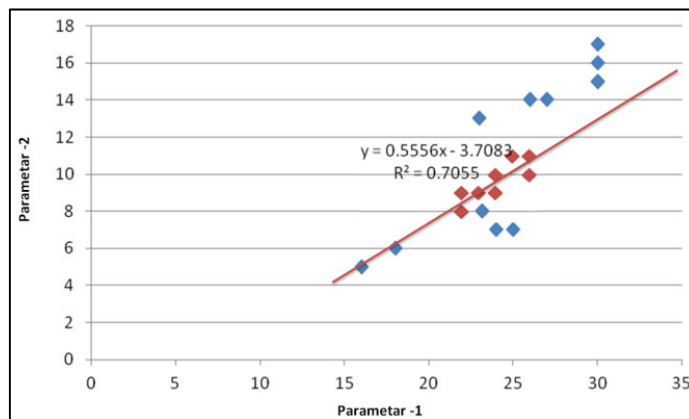

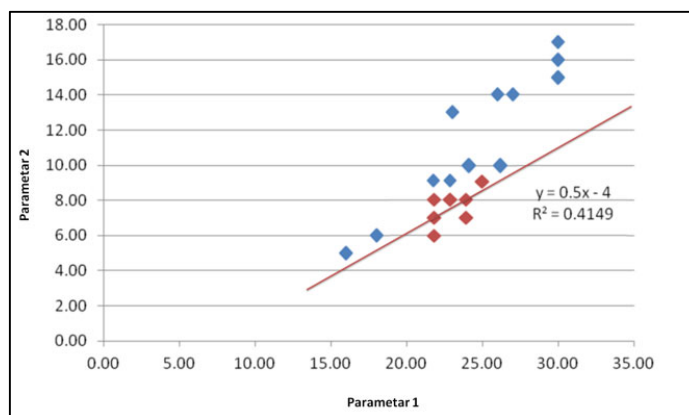*Figure 5 – Regression analysis of the transshipment task*

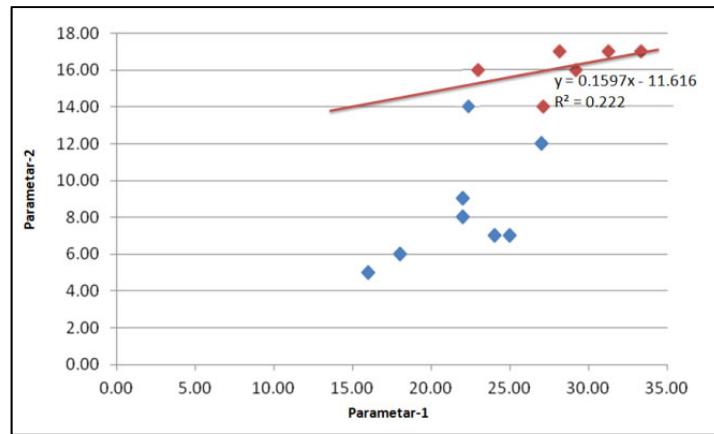*Figure 6 – Regression analysis of the internal transport task*

Figure 7 – Regression analysis of production activities

Guidelines for selecting MHE

The conclusion of the research analysis is that different types of MHE are used for various tasks according to task characteristics and technology. Based on the results obtained from the analyzing relevant studies, regression analysis was conducted to validate the applied solutions/MHE. The conclusion of the regression analysis indicates the justification for using MHE most frequently cited in the literature for specific types of tasks. Consequently, the guidelines for selecting MHE derived from this analysis are presented in Figure 8.

In the analyzed studies of intralogistics activities, the tasks were viewed as integrated units. Accordingly, MHE was considered in the context of realizing multiple tasks simultaneously (transshipment and internal transport, internal transport and positioning, transshipment and production activities, etc.). The grouping of MHE according to the types of tasks, i.e., summing up the requirements, contributes to the reduction of costs and the number of required MHE.

It also increases efficiency, optimizes resource utilization, reduces errors in activities, and minimizes damage to goods. In contrast, if the execution of intralogistics activities were considered separately, the outcome would likely be different. Certainly, this area represents a direction for future research.
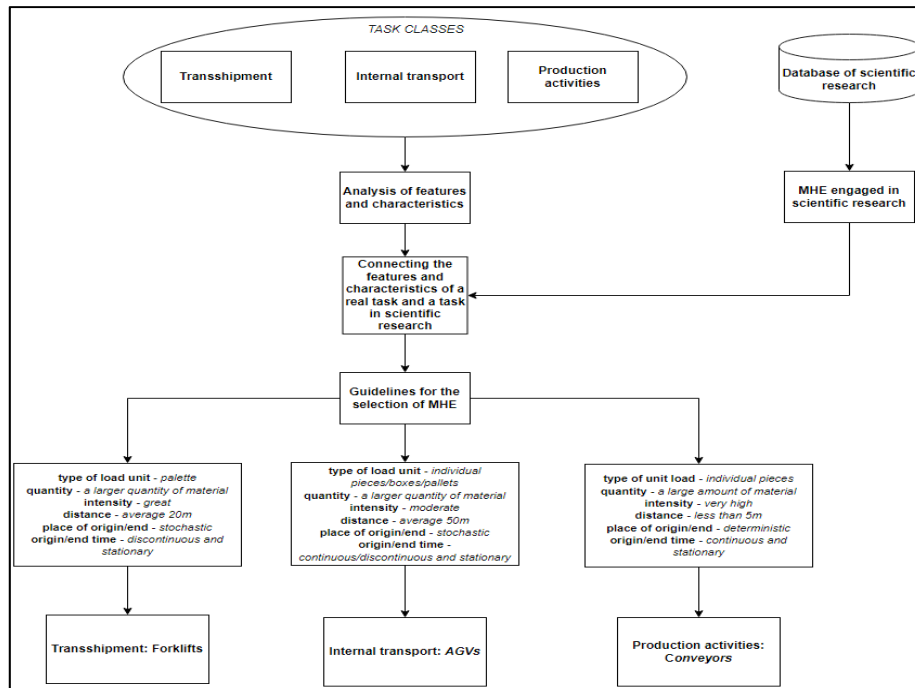
Figure 8 – Guidelines for MHE selection based on scientific research

When deciding the selection of MHE in the analyzed research, MCDM methods dominate. Numerous methods and their combinations are used. Through analysis, it has been determined that the Analytic Hierarchy Process (AHP) method is most commonly used for determining criterion weights, while the Technique for Order of Preference by Similarity to Ideal Solution (TOPSIS) method is frequently applied for ranking alternatives. The AHP method relies on pairwise comparisons of criterion importance to establish weights, whereas the TOPSIS method calculates the distances of alternatives from ideal and anti-ideal solutions to determine rankings. In the literature, there are attempts to apply artificial intelligence and machine learning to solve MHE selection problems. However, results so far are not as stable and reliable as those from MCDM methods, but progress in this field is expected with advancements in computational algorithms. Another limitation identified in the analyzed research is the inadequate task description for which MHE selection is needed. When tasks are described comprehensively with all relevant characteristics, the process of matching tasks to MHE becomes significantly more straightforward.

Conclusion

When generating intralogistics solutions, the central issue is the selection and engagement of adequate MHE. The process of MHE selection occurs in two scenarios: during the design of new systems and during the reconstruction of the existing ones. Selecting MHE involves aligning task characteristics and requirements with the appropriate type of MHE. Given the existence of a wide range of MHE, which carries with it certain limitations, the task of selection represents a multi-vector quantity. This paper is devoted to the analysis of the reference papers in the field of MHE selection in intralogistics systems. For this research, the Google Academic database was searched for keywords such as MHE, MHE selection, and MHE intralogistics. A more detailed analysis included 20 relevant papers/research studies, which were selected according to the following criteria: period of publication—the period from 2018 to 2023 was taken; number of citations; and online availability. Intralogistics represents a complex interaction of various logistics functions aimed at controlling internal flows of materials, information, money, and others within production, storage, distribution, and other systems. Accordingly, a wide set of intralogistic tasks occurs in these systems. For this research, three types of tasks were analyzed: internal transport, transshipment, and production activities. Numerous MHE types are used for the realization of intralogistics tasks. The paper analyzed the engagement of typical MHE, such as forklifts, cranes, conveyors, AGVs, and robotic systems. Each of these categories includes different types and models (counterbalance forklift, overhead crane, AGV forklift), which are not analyzed in detail in this paper. After the analysis of the research according to the mentioned aspects, the section on data sets on solved types of tasks and the applied MHE was made in the paper. When it comes to transshipment, forklifts are most often engaged. Factors that indicate this are the type of unit load (pallet), the ability to overcome the height difference, adaptability to different intensities, and the ability to realize several different intralogistics tasks. MHE based on AGVs is most often used to realize internal transport tasks, which indicates the trend of automation and improvement of intralogistics systems with the development of Industry 4.0. MHE based on conveyors is the most represented in production activities as a consequence of the configuration of production and assembly lines. In the paper, regression analysis was applied to examine the reliability of these data, that is, the relationship between the task parameters and the applied MHE. Regression analysis showed that in most cases, it is justified to use the proposed MHE from the literature.

By analyzing the papers dedicated to the selection of MHE, certain aspects of the research were identified that were not adequately covered, such as clearly defining the parameters of the task and detailed analysis of MHE according to their characteristics. Also, the existing research often lacks a holistic approach that would include a wider range of criteria. Therefore, the main contribution of this paper is the generation of guidelines for the selection of MHE in intralogistics, taking into account specific parameters of the task such as type of unit, intensity, time of origin/end, and place of origin/end of the task. With this approach, the MHE selection process becomes structured and based on relevant data, which enables consistent and accurate decision making. Future research should be focused on improving the following segments:

Additional types of unit load and materials: It is necessary to pay attention to different types of materials, such as rods, bulk, irregular, and others encountered in practice.

Industrial specifics: The problem of MHE selection should be viewed in the context of different industries, which have specific types of tasks with stricter restrictions on their implementation.

Atypical MHE: Consideration of certain atypical MHE (monorail cranes, air cushion vehicles) in the realization of intralogistics tasks.

New MCDM methods: Implementation of new MCDM methods and their combinations, application of fuzzy logic, efficiency assessment model (DEA), and operational research model.

Artificial intelligence and machine learning: Direct research towards the development of MHE selection algorithms based on machine learning is in accordance with the development of artificial intelligence and computer technology.

These directions of research would contribute to the further improvement of the MHE selection process, enabling even more efficient, economical, and sustainable intralogistics systems.

References

Agarwal, D. & Bharti, P.S. 2022. A case study on AGV's alternatives selection problem. *International Journal of Information Technology*, 14, pp.1011-1023. Available at: https://doi.org/10.1007/s41870-018-0223-z.

Apple, J.M. 1977. *Plant Layout and Material Handling*. John Wiley & Sons. ISBN: 9780826005014.

Chakraborty, S. & Saha, A. K. 2024. Selection of Forklift unit for transport handling using integrated MCDM under neutrosophic environment. *Facta Universitatis, Series: Mechanical Engineering*, 22(2), pp.235-256. Available at: https://doi.org/10.22190/FUME220620039C.

Chan, F.T.S., Ip, R.W.L. & Lau, H. 2001. Integration of expert system with analytic hierarchy process for the design of material handling equipment selection system. *Journal of Materials Processing Technology*, 116(2-3), pp.137-145. Available at: https://doi.org/10.1016/S0924-0136(01)01038-X.

Chatterjee, S. & Chakraborty, S. 2023. Application of the R method in solving material handling equipment selection problems. *Decision Making: Applications in Management and Engineering*, 6(2), pp.74-94. Available at: https://doi.org/10.31181/dmame622023391.

Fonseca, D.J., Uppal, G. & Greene, T.J. 2004. A knowledge-based system for conveyor equipment selection. *Expert Systems with Applications*, 26(4), pp.615-623. Available at: https://doi.org/10.1016/j.eswa.2003.12.011.

Fottner, J., Clauer, D., Hormes, F., Freitag, M., Beinke, T., Overmeyer, L., Gottwald, S.N., Elbert, R., Sarnow, T., Schmidt, T., Reith, K.B., Zadek. H. & Thomas, F. 2021. Autonomous Systems in Intralogistics – State of the Art and Future Research Challenges. *Journal LOGISTICS RESEARCH*, 14(2), pp.1-41. Available at: https://doi.org/10.23773/2021_2.

Goswami, S.S., Behera, D.K., Afzal, A., Razak Kaladgi, A., Khan, S.A., Rajendran, P., Subbiah, R. & Asif, M. 2021. Analysis of a Robot Selection Problem Using Two Newly Developed Hybrid MCDM Models of TOPSIS-ARAS and COPRAS-ARAS. *Symmetry*, 13(8), art.number:1331. Available at: https://doi.org/10.3390/sym13081331.

Horňáková, N., Jurík, L., Hrablik Chovanová, H., Cagáňová, D. & Babčanová, D. 2021. AHP method application in selection of appropriate material handling equipment in selected industrial enterprise. *Wireless Networks*, 27(3), pp.1683-1691. Available at: https://doi.org/10.1007/s11276-019-02050-2.

Huskanović, E., Stević, Ž. & Simić, S. 2023. Objective-Subjective CRITIC-MARCOS Model for Selection Forklift in Internal Transport Technology Processes. *Mechatronics and Intelligent Transportation Systems*, 2(1), pp.20-31. Available at: https://doi.org/10.56578/mits020103.

Jusufbašić, A. 2023. MCDM Methods for Selection of Handling Equipment in Logistics: A Brief Review. *Spectrum of Engineering and Management Sciences*, 1(1), pp.13-24. Available at: https://doi.org/10.31181/sems1120232j.

Kartnig, G., Grösel, B. & Zrnic, N. 2012. Past, state-of-the-art and future of intralogistics in relation to megatrends. *FME Transactions*, 40(4), pp.193-200 [online]. Available at: https://www.mas.bg.ac.rs/_media/istrazivanje/fme/vol40/4/7_gkartnig.pdf [Accessed: 15 July 2024].

Kučera, T. 2020. Selection of Handling Equipment in Warehouse Using Multi-Criteria Decision-Making. In: *Proceedings of 24th International Scientific Conference Transport Means,* Online Conference - Kaunas, Lithuania*, pp.114-118, September 30 – October 02 [online]. Available at: https://transportmeans.ktu.edu/wp-content/uploads/sites/307/2018/02/Transport-means-A4-I-dalis.pdf [Accessed: 15 July 2024].

Kulweic, R.A. 1991. *Materials Handling Handbook, 2nd Edition*, John Wiley & Sons. ISBN: 978-0-471-09782-2.

Mathew, M. & Sahu, S. 2018. Comparison of new multi-criteria-decision-making methods for material handling equipment selection. *Management Science Letters*, 8(3), pp.139-150. Available at: https://doi.org/10.5267/j.msl.2018.1.004.

Overmeyer, L., Ventz, K., Falkenberg, S. & Krühn, T. 2009. Interfaced multidirectional small-scaled modules for intralogistics operations. *Logistics Journal*, 01 [online]. Available at: https://www.logistics-journal.de/archive/archive/2009/2094 [Accessed: 15 July 2024].

Průša, P., Jovčić, S., Němec, V. & Mrázek, P. 2018. Forklift truck selection using TOPSIS method. *International Journal for Traffic and Transport Engineering*, 8(3) pp.390-398. Available at: https://doi.org/10.7708/ijtte.2018.8(3).10.

Saputro, T.E., Masudin, I. & Daneshvar Rouyendegh, B. 2015. A literature review on MHE selection problem: levels, contexts, and approaches. *International Journal of Production Research*, 53(17), pp.5139-5152. Available at: https://doi.org/10.1080/00207543.2015.1005254.

Sharp, G., Wan, Y.-T., McGinnis, L.F., Goetschalckx, M., Bodner, D., Govindaraj, T., Ram, B. & Everette, J. 2021. A Structured Approach to Material Handling System Selection and Specification for Manufacturing. *Academia.edu* [online]. Available at: https://www.academia.edu/18955739/A_Structured_Approach_to_Material_Handling_System_Selection_and_Specification_for_Manufacturing [Accessed: 15 July 2024].

Shchemeleva, Y.B. 2022. Selection of Conveyor Equipment as a Multicriteria Task. In: Radionov, A.A. & Gasiyarov, V.R. (Eds.) *Proceedings of the 7th International Conference on Industrial Engineering (ICIE 2021). Lecture Notes in Mechanical Engineering,* pp.496-503. Cham: Springer. Available at: https://doi.org/10.1007/978-3-030-85230-6_58.

Simic, V., Dabic-Miletic, S., Tirkolaee, E.B., Stević, Ž., Ala, A. & Amirteimoori, A. 2023. Neutrosophic LOPCOW-ARAS model for prioritizing industry 4.0-based material handling technologies in smart and sustainable warehouse management systems. *Applied Soft Computing*, 143, art.number:110400. Available at: https://doi.org/10.1016/j.asoc.2023.110400.

Soufi, Z., David, P. & Yahouni, Z. 2021. A methodology for the selection of Material Handling Equipment in manufacturing systems. *IFAC-PapersOnLine*, 54(1), pp.122-127. Available at: https://doi.org/10.1016/j.ifacol.2021.08.193.

Sretenović, M. 1996. *Mehanizacija pretovara: pretovarne mašine i projektovanje pretovarnih procesa*. Belgrade, Serbia: University of Belgrade (in Serbian).

Tadić, S., Krstić, M., Dabić-Miletić, S. & Božić, M. 2023. Smart Material Handling Solutions for City Logistics Systems. *Sustainability*, 15(8), art.number:6693. Available at: https://doi.org/10.3390/su15086693.

Taş, Ü. 2023. Case Study of Intralogistics in the Framework of Logistics 4.0. *International Journal of Automotive Science and Technology*, 7(1), pp.18-24. Available at: https://doi.org/10.30939/ijastech..1215381.

Telek, P. 2016. Material flow relations in the design process of materials handling. *Advanced Logistic Systems - Theory and Practice*, 10(1), pp.53-64.

Telek, P. & Cservenák, Á. 2020. Planning of material handling–literature review. *Advanced Logistic Systems - Theory and Practice*, 13(2), pp.29-44. Available at: https://doi.org/10.32971/als.2020.003.

Tompkins, J.A., White, J.A., Bozer, Y.A. & Tanchoco, J.M.A. 2010. *Facilities planning, 4th Edition*. Wiley. ISBN: 978-0470444047.

Ulutaş, A., Topal, A., Karabasevic, D. & Balo, F. 2023. Selection of a Forklift for a Cargo Company with Fuzzy BWM and Fuzzy MCRAT Methods. *Axioms*, 12(5), art.number:467. Available at: https://doi.org/10.3390/axioms12050467.

Uyanık, G.K. & Güler, N. 2013. A Study on Multiple Linear Regression Analysis. *Procedia - Social and Behavioral Sciences*, 106, pp.234-240. Available at: https://doi.org/10.1016/j.sbspro.2013.12.027.

Voćkić, M., Stojić, G. & Stević, B. 2018. Integrated rough SWARA-ARAS model for selection of electric forklift. In: *ICMNEE 2018 The 2nd International Conference on Management, Engineering and Environment*, Belgrade, Serbia, pp.216-227, October 11-12.

Vukićević, S.1995. *Skladišta*. Belgrade, Serbia: Preving (in Serbian).

Yazid, N.A., Sabtu, N.I., Azmiral, N.U.S. & Mahad, N.F. 2023. The application of critic-topsis method in solving the material handling equipment selection problem. *Malaysian Journal of Computing*, 8(1), pp.1311-1330 [online]. Available at: https://mjoc.uitm.edu.my/main/index.php/journal/29-volume-7-2-2022/176-vol-8-1-1311 [Accessed: 15 July 2024].

Yousefifar, R., Popp, J., Beyer, T. & Wehking, K.-H. 2015. Adaptive Intra-Logistics. In: Kersten, W., Blecker, T. & Ringle, C.M. (Eds.) Innovations and Strategies for Logistics and Supply Chains: Technologies, Business Models and Risk Management. Proceedings of the Hamburg International Conference of Logistics (HICL), 20, pp.285-304. Hamburg University of Technology (TUHH), Institute of Business Logistics and General Management. Available at: https://doi.org/10.15480/882.1264.

Zajac, P. & Rozic, T. 2022. Energy consumption of forklift versus standards, effects of their use and expectations. *Energy*, 239(Part D), art.number:122187. Available at: https://doi.org/10.1016/j.energy.2021.122187.

Zavadskas, E.K., Nunić, Z., Stjepanović, Ž. & Prentkovskis, O. 2018. A Novel Rough Range of Value Method (R-ROV) for Selecting Automatically Guided Vehicles (AGVs). *Studies in informatics and Control*, 27(4), pp.385-394. Available at: https://doi.org/10.24846/v27i4y201802.

Zrnić, N.Đ., Popović, T.M., Milojević, G.Z. & Kosanić, N.Ž. 2021. A Survey of Research on Industry 4.0 in Intralogistics. In: *Proceedings of X Triennial International Conference Heavy Machinery HM 2021,* Vrnjačka Banja, Serbia, pp.B.1-B.8, June 23-25 [online]. Available at: http://www.hm.kg.ac.rs/documents/HM2021-Proceedings.pdf [Accessed: 15 July 2024].

Zubair, M., Maqsood, S., Omair, M. & Noor, I. 2019. Optimization of material handling system through material handling equipment selection. *International*

Božič, M. et al, Guidelines for technology selection in intralogistics: a scientific approach, pp.1948-1976

Directrices para la selección de tecnología en intralogística: un enfoque científico

Mladen S. Božić, **autor de correspondencia**,
Dragan B. Đurđević, *Svetlana* A. Dabić-Miletić

Universidad de Belgrado, Facultad de Ingeniería de Transporte y Tráfico, Belgrado, República de Serbia

CAMPO: ingeniería mecánica, logística
TIPO DE ARTÍCULO: artículo científico original

Resumen:

Introducción/objetivo: La intralogística implica la organización, control, realización y optimización de flujos de materiales e información dentro de un sistema tecnológicamente integrado. La selección y aplicación de equipos de manipulación de materiales (MHE) adecuados desempeñan un papel crucial en la configuración de los sistemas intralogísticos. Este artículo tiene como objetivo definir pautas para la selección de MHE con base en investigaciones científicas. La metodología implementada para lograr este objetivo comprende varios pasos fundamentales.

Métodos: El paso inicial implica analizar tres grupos típicos de tareas en los sistemas (intra)logísticos: transbordo, transporte interno y actividades de producción. El análisis se centra en identificar y describir parámetros clave de la tarea, como el tipo de carga unitaria, la cantidad, la intensidad del flujo y la ubicación y el momento de inicio y finalización de la tarea. A continuación, hay un paso dedicado al análisis de investigaciones científicas relevantes. Se busca en la bibliografia según criterios específicos, como año de publicación, palabras clave y recuento de citas, para formar una base de datos de artículos relevantes. El análisis se centra en identificar y vincular los parámetros de las tareas prácticas con los descritos en la bibliografia y en las características del MHE utilizado para facilitar la selección del MHE apropiado para estas tareas.

Resultados: Continuando, en el tercer paso, la tarea observada se clasifica según los tipos de tareas estándar que se encuentran en la bibliografia.

Conclusión: Finalmente, en el último/cuarto paso, se aplica el análisis de regresión para definir las pautas para la selección de MHE en función de la frecuencia de uso de grupos MHE específicos para ciertos grupos de tareas como se describe en la bibliografia.

Palabras claves: intralogística, selección de MHE, transbordo, transporte interno, producción.

1974

Рекомендации по выбору технологии в интралогистике, основанные на научных исследованиях

Младен С. Божич, **корреспондент**,
Драган Б. Джурджевич, *Светлана* А. Дабич-Милетич
Белградский университет, факультет транспорта и организации дорожного движения, г. Белград, Республика Сербия

Резюме:

Введение/цель: Интралогистика включает в себя организацию, контроль, реализацию и оптимизацию материальных и информационных потоков в рамках технологически интегрированной системы. Выбор и применение соответствующего погрузочно-разгрузочного оборудования (МНЕ) играют решающую роль в формировании интралогистических систем. Цель данной статьи – определить главные принципы отбора, основанные на научных исследованиях. Метод, применяемый для достижения этой цели, включает в себя несколько основных этапов.

Методы: Начальный этап включал в себя анализ трех типичных групп задач в (внутри) логистических системах: перевалка, внутренние перевозки и производственная деятельность. Анализ сосредоточен на выявлении и описании ключевых параметров задачи, таких как: способ погрузки товара, количество, интенсивность товарного потока, а также местоположение и время начала и завершения задачи. Далее следует этап, посвященный анализу соответствующих научных исследований. Для формирования базы данных соответствующих статей исследование литературы осуществлялось в соответствии с определенными критериями, такими как: год публикации, ключевые слова и количество цитирований.

Результаты: Анализ сосредоточен на выявлении и увязке параметров практических задач с параметрами, описанными в литературе, а также на характеристиках МНЕ, используемых для облегчения выбора подходящего МНЕ для этих задач.

Вывод: После этого, на третьем этапе, наблюдаемая задача была классифицирована в соответствии со стандартными типами задач, описанными в литературе.

Ключевые слова: интралогистика, выбор МНЕ, перевалка, внутренний транспорт, производство.

Смернице за избор технологије у интралогистици, засноване на научним истраживањима

Младен С. Божић, **аутор за преписку**,
Драган Б. Ђурђевић, *Светлана* А. Дабић Милетић

Универзитет у Београду, Саобраћајни факултет,
Београд, Република Србија

ОБЛАСТ: машинство, логистика
КАТЕГОРИЈА (ТИП) ЧЛАНКА: оригинални научни рад

Сажетак:

Увод/циљ: Интралогистика обухвата организацију, контролу, реализацију и оптимизацију токова материјала и информација унутар технолошке заокружене целине. Кључну улогу у обликовању интралогистичких система има избор и примена одговарајуће технологије руковања материјалима (MXE). Циљ овог рада јесте дефинисање смерница за избор MXE, ослањањем на научна истраживања. За његову реализацију примењена је методологија која се састоји од неколико основних корака.

Методе: Почетни корак обухвата анализу три типичне групе задатака у (интра)логистичким системима: претовару, унутрашњем транспорту и активностима у производњи. Анализа је посвећена идентификацији и опису кључних параметара задатка, као што су: појавни облик робе, количина, интензитет робног тока, место и време настанка и завршетак задатка. Затим, следи корак посвећен анализи релевантних научних истраживања. Литература је претраживана према одређеним критеријумима, као што су године објављивања, кључне речи и број цитата, на основу којих је формирана база релевантних радова.

Резултати: Фокус анализе био је на идентификацији и повезивању параметара практичних задатака са задацима описаним у литератури, као и на карактеристикама коришћених MXE, како би се омогућио избор одговарајућих MXE за те задатке.

Закључак: У трећем кораку посматрани задатак се класификује према стандардним типовима задатака из литературе.

Кључне речи: интралогистика, избор MXE, претовар, унутрашњи транспорт, производња.

Modification of synthetic polyisoprene by combination with high-density polyethylene

*Serge*y V. Chernyshov[a], *Lyudmila* R. Lyusova[b],
Manizha B. Zharylganova[c], *Dmitry* Y. Nebratenko[d]

[a] MIREA-Russian Technological University, Institute of Fine Chemical
Technologies named after M.V. Lomonosov,
Department of Chemistry and Technology of Elastomer Processing,
Moscow, Russian Federation,
e-mail: chernyshov.9898@mail.ru,
ORCID iD: https://orcid.org/0000-0002-4659-468X

[b] MIREA-Russian Technological University, Institute of Fine Chemical
Technologies named after M.V. Lomonosov,
Department of Chemistry and Technology of Elastomer Processing,
Moscow, Russian Federation,
e-mail: luslr@mail.ru,
ORCID iD: https://orcid.org/0000-0001-9515-6347

[c] MIREA-Russian Technological University, Institute of Fine Chemical
Technologies named after M.V. Lomonosov,
Department of Chemistry and Technology of Elastomer Processing,
Moscow, Russian Federation,
e-mail: zharylganovamb@gmail.com,
ORCID iD: https://orcid.org/0009-0007-3293-9572

[d] Russian University of Transport, Institute of Roads, Construction and
Structures, Department of Highways, Airfields, Base and Foundations,
Moscow, Russian Federation,
e-mail: nebratenko@mail.ru, **corresponding author**,
ORCID iD: https://orcid.org/0000-0002-3607-8876

Abstract:

Introduction/purpose: The development of elastomeric materials based on synthetic polyisoprene (IR) with high green strength is a rather urgent task, because it allows to replace, completely or partially, the main ingredient - natural rubber in responsible rubber products. The aim of the work was an additional increase in the green strength values of IR and rubber mixtures based on it by its modification with high-density polyethylene of PND 277-73.

Methods: The main methods of the research of the technological, physical-mechanical and operational properties were used. All tests conformed to ASTM or ISO standards. Rubber compounds were made in the Haake PolyLab rubber mixer. In parallel with the effects of modification, the

influence of the mixing temperature on the main properties of IR and NR based elastomeric materials was investigated.

Results: It is shown that the increase in the mixing temperature of NR and IR for 20ºC leads to significant changes in the technological properties of rubber compounds (primarily green strength), as well as the physical-mechanical and operational properties of cured rubber. It has been established that a significant increase in the green strength of the rubber compound is achieved by combining IR with 7 mass. % HDPE.

Conclusion: The developed polymer composition based on IR and HDPE has a level of green strength of the rubber compound 2 times higher than that of natural rubber, while maintaining the physical-mechanical and operational characteristics of cured rubbers at the level of natural rubber.The polymer composition IR/HDPE 93/7 can be recommended for use in the manufacture of products whose manufacturing technology requires increased green strength of rubber compounds, including large-sized and all-metal tires.

Key words: synthetic polyisoprene, natural rubber, green strength, polymer mixtures, high-density polyethylene.

Introduction

The range of industrially synthesized rubber is quite limited, and the industry of synthetic rubber is unable to satisfy the ever-increasing needs of the rubber industry. The use of polymer mixtures in fact expands the range of elastomeric materials without requiring complex special equipment, which ultimately makes it possible to produce technical products with the required properties. Therefore, interest and attention to extraordinary mixtures of rubber with rubber or thermoplastics are constantly increasing. Previous experience and modern practice show that the use of polymer mixtures of different classes allows to improve the technological properties of rubber mixtures, the physical-mechanical properties of cured rubbers and the operational properties of finished products (Schwartz & Dinzburg, 1972; Kerber et al, 2024; Alekseenko et al, 2024).

Natural rubber is an indispensable elastomer for the manufacture of a wide range of rubber products, including tires, rubber and defense products. Now, one of the most popular materials in the tire industry is imported natural rubber (NR). This is especially true for all-metal, aviation and large-scale civil and defense tires, which are made of more than 85% NR. The only synthetic analogue for NR is synthetic isoprene rubber of the SKI-3 (IR) brand, which is inferior to natural rubber in several important indicators. Thus, one of the main disadvantages of IR compared to NR is

the low green strength of rubber compounds based on IR, which is important in the prefabrication and assembly operations. Green strength is the most important technological characteristic of rubber compounds and is responsible for the confection adhesion and stable frame of the product elements until their complete assembly and vulcanization (Zolotarev et al, 2021; Zuev et al, 2024; Nasyrov et al, 2020; Lyusova & Chernyshov, 2022).

There are two ways to improve the green strength of IR: chemical modification (Aksenov, 2021; Akhmetov et al, 2023) and physical modification of rubber (Cruz-Morales et al, 2023; Chernyshov et al, 2023a, 2023b). Over the past more than 50 years, a lot of research work has been done on the first path, i.e. chemical modification of synthetic isoprene rubber (Aksenov, 2021). Many ways of chemical modification of IR gave an opportunity to increase cohesive strength, but did not receive further development for various reasons: carcinogenicity, toxicity or unsatisfactory processability. Physical modification, i.e. combining IR with other polymers, is the most promising way to increase green strength in the production of rubber products, as it does not require additional technological operations and is environmentally friendly.

As early as in the 1960s and 1970s, the possibility of increasing the green strength of rubber mixtures made of synthetic polyisoprene by introducing crystallizing polyolefins, including polyethylene, was considered (Schwartz & Dinzburg, 1972; Priklonskaya et al, 1969). Then high-density polyethylene (HDPE) was the most effective due to its high crystallinity. Presumably, the reinforcing effect of HDPE could be due to the presence of crystalline particles contributing to the orientation effect of the macromolecules of highly elastic polymer, accelerating the crystallization of rubber during deformation (Priklonskaya et al, 1969; Yanez Flores et al, 1997). But the number of the published works in this direction with specific test results is quite small, and those that exist are incomplete and the data in them are ambiguous. For example, there is no information on the used brands of polyethylene and on the process for producing a rubber compound containing polyethylene. There are no vulcanization characteristics and viscosity values for Mooney rubber compounds, no data on fatigue characteristics of vulcanizations, and no direct comparison with rubber mixtures and rubbers based on NR (Guseva et al, 2002). It should also be noted that since then the brand assortment of polyethylene has changed significantly, and there have been notable changes in the synthesis of SKI-3.

Materials and methods

The objects of the research in this work were elastomeric materials based on synthetic isoprene rubber (IR) brand SKI-3 (Mooney viscosity – 74 units) produced by LLC «Tolyattikauchuk». High-density polyethylene (HDPE) of LLC «Stavrolen» brand PND 277-73 was used to increase the green strength of the material. Based on the previous obtained data (Chernyshov et al, 2023a), the content of HPDE was 7 mass. %. The elastomeric material based on natural rubber brand RSS-1 was chosen as a standard.

The combination of the tested polymers and the production of the rubber compounds based on them were carried out in the Haake PolyLab rubber mixer (within 9 minutes) with the subsequent introduction of sulfur on rollers at a temperature of $50℃$ for 1.5 minutes. The mixing mode is given in Table 1. The initial mixing temperature in the rubber mixer was 120-140°C for IR and NR based rubber compounds. For a mixture containing HDPE (melting point – 134°C), the initial mixing temperature was 140°C.

The formulations of the rubber compounds are presented in Table 2.

Table 1 – Mixing mode of the rubber compounds

Compound	Duration, min	General time, min.
1st stage		
Rubber (IR and/or NR)	1	1
HDPE (PND 277–73)	2	3
Stearic acid	6.0	9.0
Zinc oxide	6.0	9.0
Accelerator CBS	6.0	9.0
Carbon black N330	5.0	9.0
2nd stage		
Sulfur	1.5	10.5

The green strength of the rubber compounds and the physical-mechanical characteristics of cured rubber were determined on the Gotech AI-3000-U tensile testing machine according to ASTM D 6747-15 and ASTM D 412, respectively, and the vulcanization characteristics were determined on the MonTech MDR 3000 Professional rheometer according to ASTM D 5289. Using the MonTech MV 3000 Basic viscometer, the

Mooney viscosity was measured according to ASTM D 1646. The fatigue endurance at repeated elongation (ε = 125% at 3 Hz) and fatigue endurance under repeated bending with puncture (3 Hz) was determined on the MonTech FT 3000 CH according to ISO 6943 and ASTM D 813, respectively. Hardness and rebound resilience were determined according to ASTM D 2240 and ISO 4662.

Thus, the above methods and materials were used in the study of the influence of the mixing temperature on the technological properties of the rubber compounds based on NR and IR, and the physical-mechanical and operational properties of cured rubber based on them Their properties were also compared with the indicators of the polymer composition containing HDPE.

Table 2 – Formulations of the rubber compounds

Compound	Contents, parts per hundred rubber		
	NR	IR	IR/HDPE 93/7
NR (RSS-1)	100.0	-	-
IR (SKI-3)	-	100.0	93.0
HDPE (PND 277–73)	-	-	7.0
Stearic acid	1.0	2.0	2.0
Zinc oxide	5.0	5.0	5.0
Accelerator CBS	1.5	1.5	1.5
Carbon black N330	35.0	35.0	35.0
Sulfur	2.5	2.0	2.0

Results and discussion

As it is known, tire rubber mixtures are manufactured at temperatures above 120℃, so in the first stage of the work, the influence of the mixing temperature in the range of 130±10℃ on the main complex of the properties of elastomer materials was investigated.

As it can be seen in Figure 1, an increase in the mixing temperature leads to a decrease in the green strength of both NR and IR-based rubber compounds, and for natural rubber the decrease in green strength is much greater. It can be assumed that the mixing temperature increases, the rate of thermal-oxidative degradation increases, which leads to a decrease in the molecular weight of polymers. This assumption is supported by the Mooney viscosity data given in Table 3.
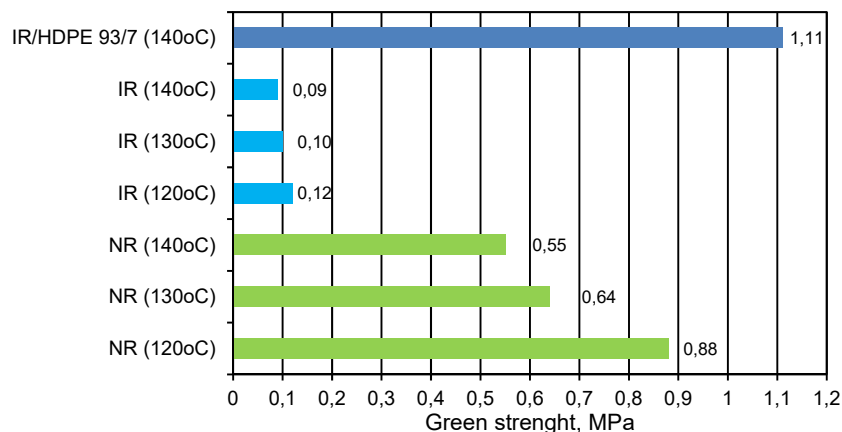
Figure 1 – Green strength of the rubber compounds

Table 3 – Technological properties of the rubber compounds and the physical and mechanical properties of the vulcanizates

Index	Polymer base						
	NR 120°C	NR 130°C	NR 140°C	IR 120°C	IR 130°C	IR 140°C	IR/HDPE 93/7 140°C
Technological properties of the rubber compounds							
Mooney Viscosity, units Mooney viscosity	40	39	37	46	39	39	49
ε_{CM}, %	725	612	550	887	1137	1350	762
Physical-mechanical properties of the vulcanizates							
f_{100}, MPa	3.2	2.7	2.4	2.5	1.7	1.5	2.9
f_{300}, MPa	18.6	14.3	14.6	14.7	10.2	9.4	14.2
f_p, MPa	30.7	27.7	26.9	31.4	27.4	25.3	27.5
ε_p, %	422	473	443	465	520	503	461
θ, %	32	23	21	31	20	22	36
P_r, kN/m	103.1	108.9	96	94	95.8	85.6	100.4

Note: ε_{CM} – elongation of a rubber compound in tension, f_{100}, f_{300} – stresses at an elongation of 100 and 300 %, f_p – tensile strength, ε_p –elongation at break, θ – residual elongation, and P_r –tear resistance.

1982

As shown in Figure 1 and Table 3, the introduction of HDPE in the amount of 7 mass. % (IR/HDPE 93/7) can significantly increase the green strength of the rubber compound and increase the Mooney viscosity to some extent. When comparing rubber mixtures (Figure 1), it is shown that during mixing at 140℃, the green strength of the mixture is 2 times higher than that of NR and 12 times higher than that of IR.

The analysis of the curing curves (Figure 2) showed that an increase in the mixing temperature of the rubber compounds leads to a significant decrease in the torque increment (ΔM), as well as to a slight decrease in the induction period and an increase in the rate of the vulcanization process. The decrease in ΔM is probably due to thermo-oxidative destruction of rubber macromolecules during the mixing process. At the same time, the introduction of HDPE has practically no effect on the vulcanization process.
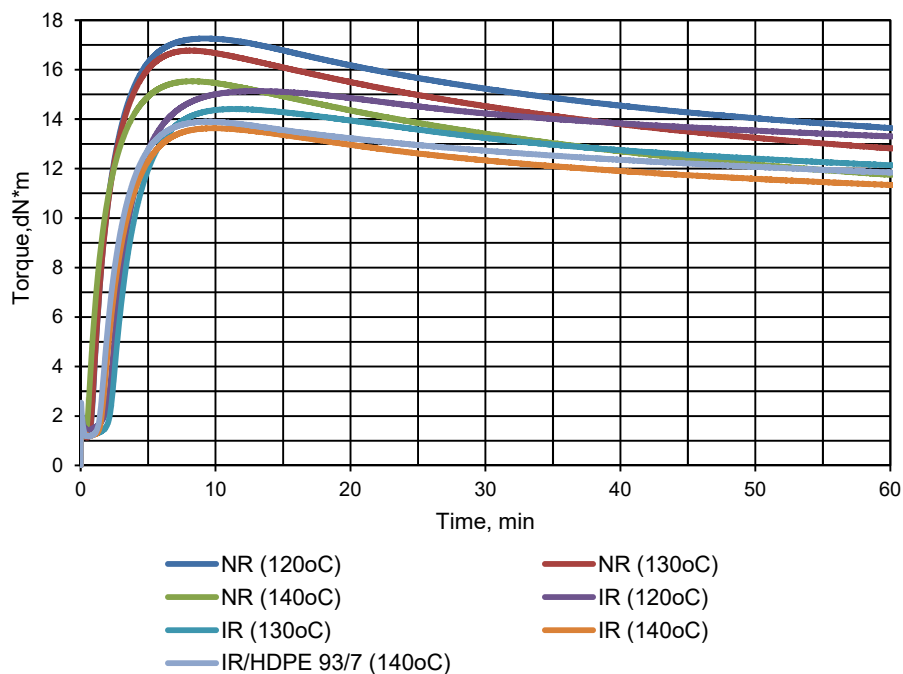
Figure 2 – Curing curves for the rubber compounds

The increase in the mixing temperature, which leads to an increase in the rate of thermo-oxidative destruction of rubber leads to a decrease in the physical-mechanical properties of rubber. Table 3 shows that there is a decrease in the tensile strength, the stresses at an elongation of 100 and 300%, and the tear resistance. The introduction of HDPE into the rubber composition leads, in comparison with IR based rubber, to a 93% increase in the stresses at an elongation of 100% and an increase in the tear resistance by 17%. As a result, the parameters of the vulcanizate are almost the same as for the NR-based rubber. The increase in these parameters is probably due to the same mechanism as the increase in green strength.

Table 4 shows that, as the temperature of mixing increases, there is a slight increase in rebound resilience and a decrease in hardness in rubbers regardless of the rubber base. The decrease in hardness is probably due to a decrease in the molecular weight of rubber macromolecule during destruction.

Table 4 – Hardness and rebound elasticity of the vulcanizates

Index	Polymer base						
	NR 120ºC	NR 130ºC	NR 140ºC	IR 120ºC	IR 130ºC	IR 140ºC	IR/HDPE 93/7 140ºC
Hardness (Shore A), units.	59	58	57	55	55	54	60
Rebound resilience, %	60	61	61	56	56	58	51

As shown in Table 4, the introduction of HDPE into rubber results in an increase in its hardness, since polyethylene is in a solid state at normal condition and its influence on this parameter is like that of fillers. When combining IR with polyethylene, there is a significant reduction in rebound resilience. This is probably due to the small number of physical and/or chemical bonds of the rubber matrix with polyethylene and the existence of the interface that prevents the distribution of fluctuations throughout the volume of the material.

One of the main operational properties of rubber and rubber products exposed to dynamic loads is fatigue, which characterizes the durability of the product. The fatigue characteristics for the tested compositions are shown in Figure 3.
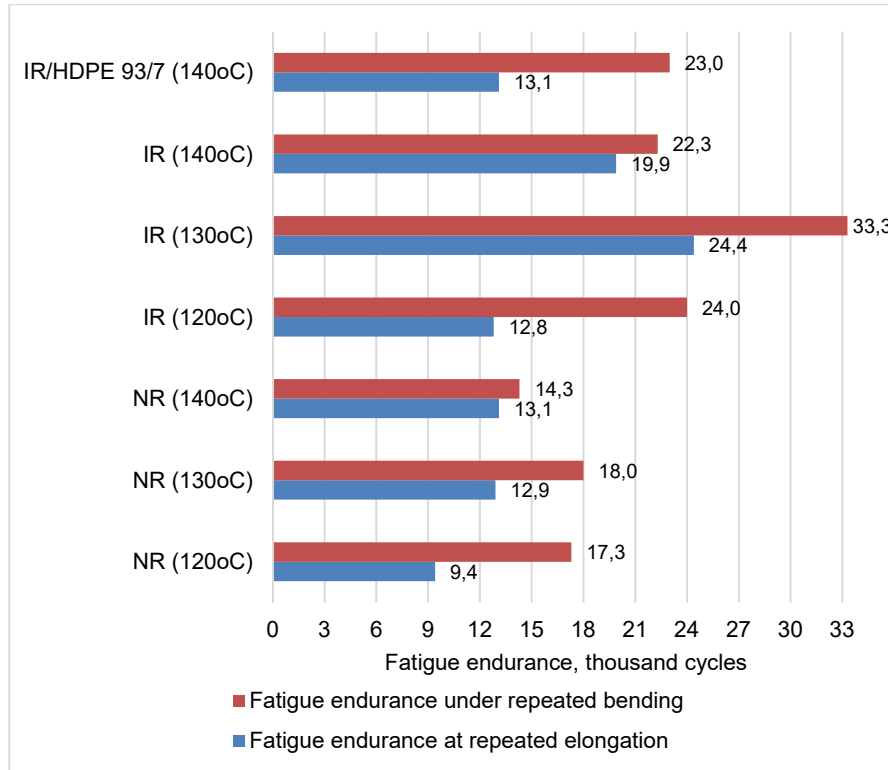
Figure 3 – Fatigue characteristics

It has been found that the increase in the mixing temperature of the rubber compounds has different effects on the fatigue endurance of NR and IR-based rubbers. As the mixing temperature rises, fatigue endurance increases in NR-based rubber and in IR-based rubber passes through the optimum with a maximum at 130ºC. At the same time, fatigue endurance under repeated bending changes similarly for both rubbers (passes through the optimum at a maximum temperature of $130℃$). The increase in fatigue is due to the reduction of the rubber modules due to thermo-oxidative destruction.

The fatigue characteristics of the rubber presented in Figure 3 showed that the introduction of HDPE into IR-based rubber had little or no effect on fatigue endurance at repeated elongation and repeated bending when comparing equal modulus rubber. However, IR/HDPE's fatigue endurance at repeated elongation is like NR-based cured rubber, and fatigue endurance under repeated bending is 28% higher.

Conclusions

Thus, it is shown that the increase in the mixing temperature of the rubber compounds based on NR and IR from 120℃ to 140℃ leads to significant changes in both the technological properties of the rubber compounds and the physical-mechanical properties of cured rubber and the operational properties of their vulcanizates. At the same time, it is worth noting separately that the increase in the temperature of the mixture negatively affects the green strength of the rubber compounds, especially based on natural rubber.

The work shows that combining IR with 7 mass. % HDPE leads to a significant increase in the green strength of the rubber compound. Moreover, at similar mixing temperatures, it exceeds the level of the green strength of a rubber compound based on natural rubber by 2 times.

The rubber based on the proposed polymer composition IR/HDPE 93/7 has the physical-mechanical and operational characteristics close to the NR-based rubber. The inventive polymer mixture is characterized in that it exceeds the NR-based rubber for fatigue endurance under repeated bending by 28%.

References

Akhmetov, I.G., Vasiliev, V.A., Nasyrov, I.Sh. & Agzamov, R.Z. 2023. Chemical modification of isoprene rubber. *Kauchuk I Rezina*, 82(3), pp.130-139 [online]. Available at: https://www.elibrary.ru/item.asp?id=54098477 (in Russian) [Accessed: 08 July 2024].

Aksenov, V.I. 2021. Some ways of making the properties of synthetic rubbers close to that of natural ones. *Kauchuk I Rezina*, 80(2), pp.86-97 (in Russian). Available at: https://doi.org/10.47664/0022-9466-2021-80-2-86-97.

Alekseenko, V., Verkhoturova, E., Zhitov, R. & Nebratenko, D. 2024. Rheology properties of bitumen binders with various fillers. *Vojnotehnički glasnik/Military Technical Courier*, 72(2), pp.695-707. Available at: https://doi.org/10.5937/vojtehg72-48380.

Chernyshov, S.V., Lyusova, L.R., Maxmudova, S.R., Zharylgapova, M.B. & Konyaeva, I.A. 2023a. The effect of high-density polyethylene on the properties of elastomeric materials made of synthetic polyisoprene. *Kauchuk I Rezina*, 82(5), pp.242-247 [online]. Available at: https://www.elibrary.ru/item.asp?id=54707582 (in Russian) [Accessed: 08 July 2024].

Chernyshov, S.V., Lyusova, L.R., Maxmudova, S.R. & Zolotarev, V.L. 2023b. The effect of 1,2-polybutadiene on the properties of elastomeric materials made of synthetic polyisoprene. *Kauchuk I Rezina*, 82(2), pp.66-70 [online]. Available at: https://www.elibrary.ru/item.asp?id=50767659 (in Russian) [Accessed: 08 July 2024].

Cruz-Morales, J.A., Gutiérrez-Flores, C., Zárate-Saldaña, D., Burelo, M., García-Ortega, H., & Gutiérrez, S. 2023. Synthetic Polyisoprene Rubber as a Mimic of Natural Rubber: Recent Advances on Synthesis, Nanocomposites, and Applications. *Polymers*, 15(20), art.number:4074. Available at: https://doi.org/10.3390/polym15204074.

Guseva, S.G., Strygin, V.D., Lyakin, Yu.I., Ushakova, O.B. & Potapov E.E. 2002. Investigation of modification of SKI-3 with a nitron-polyethylene concentrate. *Kauchuk I Rezina*, 1, pp.16-18 (in Russian).

Kerber, M.L., Bukanov, A.M., Wolfson, S.I., Gorbunova, I.Yu., Kandyrin, L.B., Sirota, A.G. & Sheryshev M.A. 2024. *Tehnologija pererabotki polimerov. Fizicheskie i himicheskie processy, 2-e izd., ispr. i dop.* Moscow: Izdatel'stvo Jurajt [online]. Available at: https://urait.ru/bcode/539476 (in Russian) [Accessed: 08 July 2024]. ISBN: 978-5-534-04915-2. (In the original: Кербер, М.Л., Буканов, А.М., Вольфсон, С.И., Горбунова, И.Ю., Кандырин, Л.Б., Сирота, А.Г. и Шерышев М.А. 2024. *Технология переработки полимеров. Физические и химические процессы, 2-е изд., испр. и доп.* Москва: Издательство Юрайт [онлайн]. Доступно на: https://urait.ru/bcode/539476 [Дата обращения: 08 июля 2024 г.]. ISBN: 978-5-534-04915-2.)

Lyusova, L.R. & Chernyshov, S.V. 2022. Study of the possibility of modifying synthetic polyisopreneby combining it with a highly cohesive polymer. *Prom. Proizvod. Ispol'z. Elastomerov*, 1, pp.40-44 (in Russian). Available at: https://doi.org/10.24412/2071-8268-2022-1-40-44.

Nasyrov, I.Sh., Faizova, V.Yu., Zhavoronkov, D.A., Shurupov, O.K. & Vasiliev, V.A. 2020. Natural rubber and synthetic cis-polyisoprene. Part 1. Current state and prospects of production development. *Prom. Proizvod. Ispol'z. Elastomerov*, 2, pp.34-47 [online]. Available at: https://cyberleninka.ru/article/n/naturalnyy-i-sinteticheskiy-tsis-poliizopreny-chast-1-sovremennoe-sostoyanie-i-perspektivy-razvitiya-proizvodstva (in Russian) [Accessed: 08 July 2024].

Priklonskaya, N.M., Timofeeva, M.V. & Poyarkova, A.D. 1969. Svojstva karkasnyx rezin dlya shin R. *Kauchuk I Rezina*, 2, pp.7-10 (in Russian). (In the original: Приклонская, Н.М., Тимофеева, М.В. и Пояркова, А.Д. 1969. Свойства каркасных резин для шин Р. *Каучук и резина*, 2, с.7-10.)

Schwartz, A.G. & Dinzburg, B.N. 1972. *Sovmeshhenie kauchukov s plastikami i sinteticheskimi smolami*. Moscow: Himija (in Russian). (In the original: Шварц, А.Г. и Динзбург, Б.Н. 1972. *Совмещение каучуков с пластиками и синтетическими смолами*. Москва: Химия.)

Yanez Flores, I.G., Ramos-DeValle, L.F., Rodriguez-Fernandez, O.S. & Sanchez-Valdes, S. 1997. Blends of Polyethylene-Polyisoprene Rubbers: Study of the Flow Properties. *Journal of Polymer Engineering*, 17(4), pp.295-310. Available at: https://doi.org/10.1515/POLYENG.1997.17.4.295.

Zolotarev, V.L., Levenberg, I.P., Zuev, A.A., Kovaleva, L.A., Lyusova, L.R. & Lipatova, A.A. 2021. Once again about cis-1.4-polyisoprene rubber. *Prom. Proizvod. Ispol'z. Elastomerov*, 2, pp.3-9 [online]. Available at:

https://cyberleninka.ru/article/n/esche-raz-o-1-4-tsis-poliizoprenah/viewer (in Russian) [Accessed: 08 July 2024].

Zuev, A.A., Zolotarev, V.L., Levenberg, I.P., Kovaleva, L.A. & Nasyrov, I.Sh. 2024. Natural and synthetic isoprene rubbers obtained using Ziegler–Natta catalysts. *Fine Chemical Technologies*, 19(2), pp.139-148 Available at: https://doi.org/10.32362/2410-6593-2024-19-2-139-148.

Modificación del poliisopreno sintético mediante combinación con polietileno de alta densidad

Sergey V. Chernyshov[a], *Lyudmila* R. Lyusova[a],
Manizha B. Zharylganova[a], *Dmitry* Y. Nebratenko[b]

[a] MIREA-Universidad Tecnológica Rusa, Instituto de Química Fina
   Tecnologías que llevan el nombre de M.V. Lomonósov,
   Departamento de Química y Tecnología de Procesamiento de Elastómeros,
   Moscú, Federación de Rusia

[b] Universidad Rusa de Transporte, Instituto de Carreteras, Construcción y
   Estructuras, Departamento de Carreteras, Aeródromos, Base y
   Cimentaciones, Moscú, Federación de Rusia, **autor de correspondencia**

CAMPO: tecnología química, materiales
TIPO DE ARTÍCULO: artículo científico original

Resumen:

Introducción/objetivo: El desarrollo de materiales elastoméricos basados en poliisopreno (IR) sintético con alta resistencia en verde es una tarea bastante urgente, porque permite reemplazar, total o parcialmente, el ingrediente principal, el caucho natural, en productos de caucho responsable. El objetivo del trabajo era aumentar adicionalmente los valores de resistencia en verde del IR y de las mezclas de caucho basadas en él mediante su modificación con polietileno de alta densidad de PND 277-73.

Métodos: Se utilizaron los principales métodos de investigación de las propiedades tecnológicas, físico-mecánicas y operativas. Todas las pruebas se ajustaron a las normas ASTM o ISO. Los compuestos de caucho se fabricaron en el mezclador de caucho Haake PolyLab. Paralelamente a los efectos de la modificación, se investigó la influencia de la temperatura de mezcla sobre las principales propiedades de los materiales elastoméricos basados en IR y NR.

Resultados: Se demuestra que el aumento de la temperatura de mezcla de NR e IR por 20ºC conduce a cambios significativos en las propiedades tecnológicas de los compuestos de caucho (principalmente resistencia en verde), así como en las propiedades físico-mecánicas y operativas del caucho curado. Se ha establecido que se logra un aumento significativo en

la resistencia en crudo del compuesto de caucho combinando IR con 7 masa. %PEAD.

Conclusión: La composición polimérica desarrollada a base de IR y HDPE tiene un nivel de resistencia en verde del compuesto de caucho 2 veces mayor que el del caucho natural, manteniendo las características físico-mecánicas y operativas de los cauchos curados al nivel del caucho natural. La composición polimérica IR/HDPE 93/7 se puede recomendar para su uso en la fabricación de productos cuya tecnología de fabricación requiere una mayor resistencia en verde de los compuestos de caucho, incluidos neumáticos de gran tamaño y totalmente metálicos.

Palabras claves: poliisopreno sintético, caucho natural, resistencia en verde, mezclas de polímeros, polietileno de alta densidad.

Модификация синтетического полиизопрена путем совмещения с полиэтиленом высокой плотности

Сергей В. Чернышов[а], *Людмила* Р. Люсова[а],
Манижа Б. Жарылганова[а], *Дмитрий* Ю. Небратенко[б]

[а] МИРЭА – Российский технологический университет, Институт тонких химических технологий им. М.В. Ломоносова, кафедра химии и технологии переработки эластомеров, г. Москва, Российская Федерация

[б] Российский университет транспорта, Институт пути, строительства и сооружений, кафедра «Автомобильные дороги, аэродромы, основания и фундаменты», г. Москва, Российская Федерация, **корреспондент**

Резюме:

Введение/цель: Разработка эластомерных материалов на основе синтетического полиизопрена (IR), обладающего повышенной когезионной прочностью, является достаточно актуальной задачей, так как это позволяет полностью или частично заменить в ответственных резиновых изделиях основной ингредиент – натуральный каучук. Целью работы являлось дополнительное повышение значений когезионной прочности IR и резиновых смесей на его основе путем его модификации полиэтиленом высокой плотности марки ПНД 277–73.

Методы: Использованы основные методы исследования технологических, физико-механических и эксплуатационных свойств. Все испытания соответствовали стандартам ASTM или ISO. Резиновые смеси изготавливали в резиносмесителе

Haake PolyLab. Параллельно с эффектами от модификации, в работе было исследовано влияние температуры смешения на основные свойства эластомерных материалов на основе IR и NR.

Результаты: Показано, что увеличение температуры смешения резиновых смесей на основе NR и IR на 20ºC приводит к существенным изменениям технологических свойств резиновых смесей (прежде всего когезионной прочности), а также физико-механических и эксплуатационных свойств резин на их основе. Установлено, что существенное увеличение когезионной прочности резиновой смеси достигается при совмещении IR с 7 мас. % HDPE.

Выводы: Разработанная полимерная композиция на основе IR и HDPE имеет уровень когезионной прочности резиновой смеси в 2 раза выше, чем у натурального каучука, при сохранении физико-механических и эксплуатационных характеристик вулканизатов на уровне резин на основе натурального каучука.

Ключевые слова: синтетический полиизопрен, натуральный каучук, когезионная прочность, смеси полимеров, полиэтилен высокой плотности.

Модификација синтетичког полиизопрена комбиновањем са полиетиленом високе густине

Сергеј В. Чернишов[а], *Људмила* Р. Љусова[а],
Манижа Б. Жарилганова[а], *Дмитриј* Ј. Небратенко[б]

[а] МИРЕА – Руски технолошки универзитет, Институт финих хемијских технологија „М.В. Ломоносов", Катедра хемије и технологије прераде еластомера, Москва, Руска Федерација

[б] Руски саобраћајни универзитет, Институт за путеве, грађевинарство и постројења, Катедра „Саобраћајнице, аеродроми, базе и темељи», Москва, Руска Федерација, **аутор за преписку**

ОБЛАСТ: хемијске технологије, материјали
КАТЕГОРИЈА (ТИП) ЧЛАНКА: оригинални научни рад

Сажетак:

Увод/циљ: Развој еластомерних материјала на бази синтетичког полиизопрена (IR) високе кохезионе чврстоће прилично је хитан задатак због потребе да се потпуно или делимично замени главни састојак критичних производа од гуме – природна гума. Циљ рада јесте да се додатно повећају вредности кохезионе чврстоће IR и гумених мешавина заснованих на њему путем његове модификације полиетиленом велике густине PND 277-73.

Методе: Коришћене су основне методе истраживања технолошких, физичко-механичких и експлоатационих својстава.

1990

Сва испитивања била су у складу са стандардима ACTM и ИСО. Мешавине гуме биле су припремљене у мешалици за гуме Haake PolyLab. Истовремено са ефектима модификације испитиван је утицај температуре мешања на главна својства еластомерних материјала на бази полиизопрена и каучука.

Резултати: Показано је да повећање температуре мешања полиизопрена и каучука за 20°C доводи до значајних промена у технолошким својствима гумених смеша (пре свега кохезионе чврстоће), као и физичко-механичких и експлоатационих карактеристика вулканизата. Утврђено је да се постиже знатно повећање кохезионе чврстоће смеше гуме комбиновањем полиизопрена са 7 тежинских % HDPE.

Закључак: Изведено је полимерно једињење на бази IR и HDPE с нивоом кохезионе чврстоће гумене смеше два пута веће од природне гуме, а притом су задржане физичко-механичке и експлоатационе карактеристике вулканизата на нивоу природне гуме.

Кључне речи: синтетички полиизопрен, природна гума, кохезиона чврстоћа, полимерне мешавине, полиетилен велике густине.

Mechanical behaviour of austenitic stainless steel loaded in the aqueous solution of H$_2$SO$_4$ during tensile testing

Amar Abboub[a], *Ahmed* Aboura[b],
Khaled Benmahdi[c], *Mohamed* Sadoun[d],
Mokhtar Belkacem[e], *Djameleddine* Semsoum[f]

[a] Mustapha Stambouli University, Faculty of Sciences and Technology,
Department of Mechanical Engineering,
Mascara, People's Democratic Republic of Algeria,
e-mail: abboub.amar@yahoo.com, **corresponding author**,
ORCID iD: https://orcid.org/0009-0004-0158-5837

[b] Ahmed Zabana University, Faculty of Sciences and Technology,
Department of Mechanical Engineering,
Relizane, People's Democratic Republic of Algeria,
e-mail: ahmed.aboura @univ-relizane.dz,
ORCID iD: https://orcid.org/0009-0005-3509-2026

[c] Mustapha Stambouli University, Faculty of Sciences and Technology,
Department of Civil Engineering,
Laboratory for the Study of Structures and Mechanics of Materials,
Mascara, People's Democratic Republic of Algeria,
e-mail: k.benmahdi@univ-mascara.dz,
ORCID iD: https://orcid.org/0000-0002-8244-5817

[d] Mustapha Stambouli University, Faculty of Sciences and Technology,
Department of Civil Engineering,
Laboratory for the Study of Structures and Mechanics of Materials,
Mascara, People's Democratic Republic of Algeria,
e-mail: m.sadoun@univ-mascara.dz,
ORCID iD: https://orcid.org/0009-0008-2314-9402

[e] Mustapha Stambouli University, Faculty of Sciences and Technology,
Department of Mechanical Engineering,
Mascara, People's Democratic Republic of Algeria,
e-mail: mokhtar.belkacem@univ-mascara.dz,
ORCID iD: https://orcid.org/0009-0004-2533-9622

[f] Mustapha Stambouli University, Faculty of Sciences and Technology,
Department of Mechanical Engineering,
Mascara, People's Democratic Republic of Algeria,
e-mail: djameleddinesemsoum@gmail.com,
ORCID iD: https://orcid.org/0009-0009-8304-9072

Abstract:

Introduction/purpose: Stainless steels have excellent corrosion resistance and adequate mechanical properties. However, their use in aggressively hydrogenated environments in the energy industry causes a loss of ductility. This work studied the effect of hydrogen on the mechanical behavior of the DINX15CrNiSi25.21/AISI310 austenitic stainless steel loaded in an aqueous solution of purely sulfuric acid H_2SO_4 at 1N at room temperature during tensile testing.

Methods: Experimental characterization techniques are applied to standardised machining-manufactured tensile specimens which underwent a series of heat treatments ranging from quenching at 1050°C for 35 minutes to tempering at 680°C for 30 minutes. This is accompanied by a succession of immersions of these samples by cryogenic quenching cycles at -196°C for a duration of 1 hour. The hydrogen was electrolytically loaded in a Pyrex glass cell for various loading times, ranging from 1h00 to 15h00, with a step of 2h00.

Results: The results showed a reduction in mechanical properties and plasticity. The electrochemical method confirmed the material's sensitivity to hydrogen embrittlement, calculating the embrittlement criterion EI (%). This method indicates a rapid increase in values depending on hydrogen loading times, with a maximum value of 41.60%.

Conclusion: The study highlights the negative impact of hydrogen on the mechanical properties of AISI310 stainless steel, emphasising the need for reduced hydrogen exposure in steel applications.

Key words: austenitic stainless steel, heat treatments, hydrogen pre-loaded, mechanical properties, hydrogen embrittlement (HE), faces.

Introduction

The ORSIM Oued Rhiou production unit employs the AISI310 series of austenitic stainless steel. These materials are refractory and are well-known for their categories of ferritic-austenitic steel. They contain 25% chromium and 21% nickel as additional elements. Chemical industry, petrochemicals, and energy sectors, including offshore wind turbines, highly recommend these alloys for their superior corrosion resistance due to their crystalline structure and high tensile strength, surpassing 950 MPa (Chauveau & Aubry, 2008). Working conditions in aggressive environments may require high percentages of chromium, nickel, and molybdenum to improve corrosion resistance. Several authors have

conducted laboratory tests to study the electrochemical corrosion of this alloy (Chauveau & Aubry, 2008; Brass et al, 2000).

Other authors (Bach, 2018; Chêne, 2009; Brass et al, 2000) have studied the mechanical behaviour of these steels in relation to pitting corrosion, temperatures, and hydrogen embrittlement (the phenomenon of the absorption of the hydrogen molecule inside the crystal lattice) during exposure to different media, including gases, liquids, and high temperatures. Recently, several in-depth studies (Sales, 2015; Bach, 2018; Grimault et al, 2012; Lo et al, 2009; Iacoviello, 1995; Matsui et al, 1979) have been published on the mechanism of hydrogen embrittlement (H.E). These studies examine how the methods and protocols used in industrial cathodic loading conditions lead to a reduction in ductility. The studies aim to determine the appropriate medium, concentration, and pre-charging time in hours while fixing the current intensity (Hamissi et al, 2016).

This experiment aims to fully penetrate the hydrogen molecule (H_2), similar to the work of other authors (Laureys et al, 2020; Cauwels et al, 2020; Robertson et al, 2015; Kittel et al, 2013; Lynch, 2012; Depover et al, 2014), in order to make a comparison using the experimental curves obtained in tensile tests (Grimault et al, 2012; He et al, 1999; Smanio et al, 2008) at slow strain rates in the interest of looking at and analysing the performance of mechanical characteristics and ductility from the point of view of their service conditions, application, and operation.

Experimental work

Materials

Chemical composition

The chemical composition of the stainless steel duplex, type X15CrNiSi25.21/AISI310, is represented in mass percentage in Table 1.

Table 1 – Weight (%) of the AISI310 chemical composition

Fe%	C%	Cr%	Ni%	Si%	Mn%
52,201	0.057	25,23	21.08	1,712	1.013
P%	S%	NB%	Mo%	Al%	Co%
<0.0003	0.052	0.035	0.204	0.041	0.103
B%	V%	Ti%	Cu%	W%	Pb%
0.005	0.124	0.035	0.176	0.011	0.052

Tensile test specimens

The tensile specimens used in this experimental part are cylindrical (Figure 1) and obtained by machining according to DIN50125 Standard using a semi-automatic (TSA) lathe of the reference: Oerlikon—Bührle.SA, Switzerland Type: DEOa.
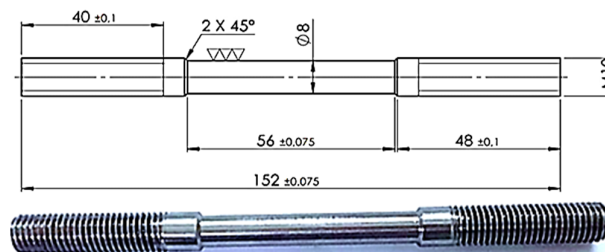

Figure 1 – Geometric shape and dimensions of the used tensile specimens

Mechanical characteristics

A mechanical tensile fracture test was carried out on a standardized reference test specimen in order to obtain the desired initial mechanical characteristics in the raw state without heat treatment (see Table 2).

– The method used for this test is mechanical fracture by traction using a Frank Karl GMBH traction machine, with a constant applied load of P_{max}= 400 kN and a slow deformation speed of (ε =2.7x10^{-6} S^{-1}),

– The elongation (A) is measured as percentage (%), according to the equation:

A (%) = (A-A$_0$)/A$_0$ x100 (%).

– The aim is to obtain the mechanical properties in the initial state (raw and without thermal treatment).

Table 2 – Initial mechanical characteristics of the AISI310 austenitic stainless steel studied

Initial mechanical characteristics				
Material	σm (Air) (MPa)	σe (Air) (MPa)	σr (Air) (MPa)	Z (Air) (%)	A (Air) (%)
AISI310 Reference (Air)	750.0	720.0	542.0	68.60%	24.10%

Heat treatments (quenching, tempering)

After the manufacture of the tensile specimens, they undergo an austenization heat treatment cycle, see (Figure 2), which first consists of heating the specimens for 35 minutes at 1050°C followed by rapid quenching in water. This treatment can be followed by tempering at a temperature of 680°C for 30 minutes, then cooling in the open air (Poupeau, 1981; Sassoulas, 1997; Kenfack, 2015). Tempering makes it possible to eliminate the surface tensions developed during quenching. After these heat treatments, the material is perfectly homogeneous with a stable austenite and a relaxation of internal residual stresses, which leads to an increase in the yield strength (σe) (Grimault et al, 2012; Barralis et al, 1999).
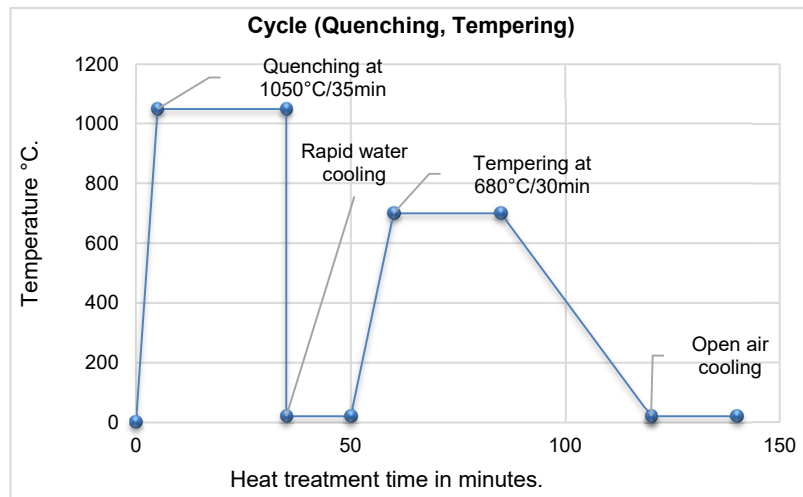
Figure 2 – Cycle of the heat treatment applied

Cryogenic heat treatment at -196°C

The next step consists of heat treating all the test specimens by cryogenic quenching at -196°C by immersion in a liquid nitrogen (N_2) bath for a holding time of 1 hour prior to heating in the open air for 40 minutes (see Figure 3).

The number of cycles is repeated in succession up to fifteen cycles (Aurélie Laureys et al, 2020; Cauwels et al, 2020; Robertson et al, 2015; Kenfack, 2015).
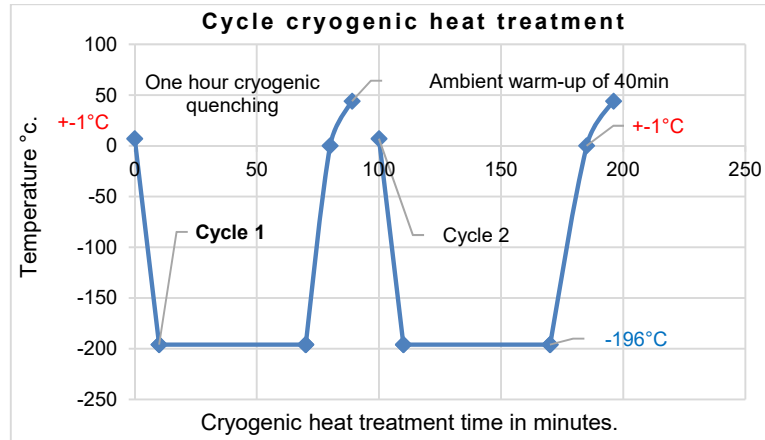
Figure 3 – Cycles of the applied cryogenic heat treatment at -196°C

Cathodic loading conditions of the test specimens

At room temperature ±20°C, the test specimens underwent cathodic loading by the aqueous solution of purely sulfuric acid H_2SO_4 at 1N (Laureys et al, 2020; Cauwels et al, 2020; Robertson et al, 2015) using a Pyrex glass enclosure (see Figure 4). Galvanostatique charge by two electrodes (cathode and anode) was carried out under the conditions adopted:

- The applied cathodic current density is fixed at 100(mA/cm^2).
- With an amperage of 1.5A, the hydrogen charging times are varied from 1 hour to 15 hours with a step of 2 hours.
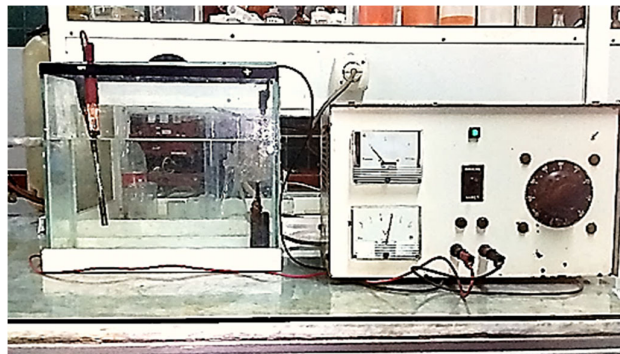
Figure 4 – Pyrex cell of cathodic loading in the aqueous solution of sulfuric acid H_2SO_4 at 1N

Mechanical fracture tensile test

After the electrolytic loading protocol (hydrogenated), all the specimens of the steel studied underwent a machine test by fracture using a reference tensile machine: Frank Karl GMBH, type: 83431 - Work Nr: 10650 (Figure 5 (a) and (b)). The fracture tests are carried out according to industrial conditions: the displacement nominal speed is ε: $2.7 \times 10^{-6} S^{-1}$ (Cauwels et al, 2020) which corresponded to a constant applied load of 400kN. The mechanical results are recorded for analysis and construction of experimental curves (see Figures 6, 7 and 8).

(a)   (b)
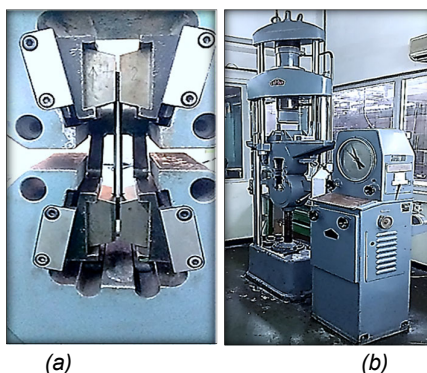
Figure 5 – (a), (b) Tensile machine Karl frank GMBH used

Table 3 shows the results of the mechanical properties following the fracture testing of all specimens before (specimen Reference) (Air) and after (specimen's hydrogenated) electrolytic pre-loading with hydrogen at room temperature ±20°C.

Table 3 – Mechanical properties of the AISI310 austenitic stainless steel after cathodic loading

Mechanical properties after hydrogenated						
N° specimen	Hydrogen Loaded in hours	$\sigma m_{(H)}$ (MPa)	$\sigma e_{(H)}$ (MPa)	$\sigma r_{(H)}$ (MPa)	$Z_{(H)}$ (%)	$A_{(H)}$ (%)
N°1	1hour	552	252	465	53%	21%
N°2	3hours	538	227	375	52%	20%
N°3	5hours	526	224	355	52%	19%
N°4	7hours	523	240	375	51%	18%
N°5	9hours	535	235	372	51%	17%
N°6	11hours	526	226	354	50%	16%
N°7	13hours	516	215	340	51%	15%
N°8	15hours	508	212	374	51%	14%

Embrittlement index EI (%)

The embrittlement index (EI) is calculated in the result part and discussion by relationship (1), which compares the lengths of an uncharged reference sample (A_0) and those of the other samples that are pre-charged (A_H) electrolytically by hydrogen. The weakening index leads to a loss of plasticity which translates into a reduction in the elongation A (%).

$$EI=(A_{0(Air)}-A_{(H)}) /(A_{0(Air)}) \times 100(\%). \qquad (1)$$

where

- A_0 is the elongations specimen with no charge (air),
- A_H is the elongation specimen charged in hydrogen.

Results and discussion

The results of the mechanical properties obtained are represented by experimental charts in Figures 6, 7 and 8. These charts show tensile strength, yield strength and failure strength.

The resistance of the steel results in a slight decrease in tensile strength, with a reduction of 26.40% observed at the shortest hydrogen loading time. As the loading time is extended, the tensile strength decreases further, reaching 26.67% at the longest loading time.

It was also observed that the failure strength of this type of material increased by 14.20 % during short loading times, reaching a value of 31.18 % following the hydrogen loading time until 15 hours (see Figure 6 and Table 3).
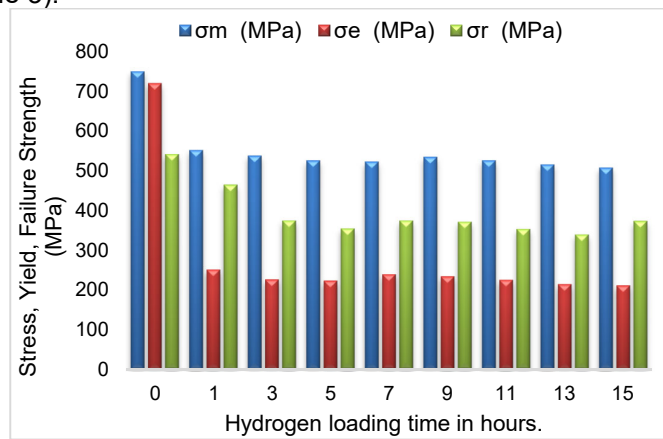
Figure 6 – Effect of the hydrogen loading time on the stress, the failure, and the yield strength in MPa of the AISI310 austenitic stainless steel

Variation of plasticity A, Z (%)

Figure 7 represents the variation of the plasticity characteristics of the X15CrNiSi25.21/AISI310 steel influenced by hydrogen loading, which causes slight reductions in these Z (%) restrictions compared to the reference from $Z_{(Air)}$: 68.60 % to $Z_{(H)}$: 53.0 % to reach a stable value of $Z_{(H)}$: 51.0 % throughout the level of hydrogen pre-charging times in hours (Table 3).

Losses of its plasticity are explained by a progressive decrease in elongations A (%) in percentage compared to the reference, from $A_{(Air)}$: 24.10 (%) to $A_{(H)}$: 21.0 (%) until reaching a minimum value of its plasticity of $A_{(H)}$: 14.0 % (see Table 3). These results are similar to the work by (Hamissi et al, 2016) which shows losses of plasticity translating into a gradual reduction at the lengths A %, under the industrial conditions adopted (simulated medium, loading time in hours, high concentration)
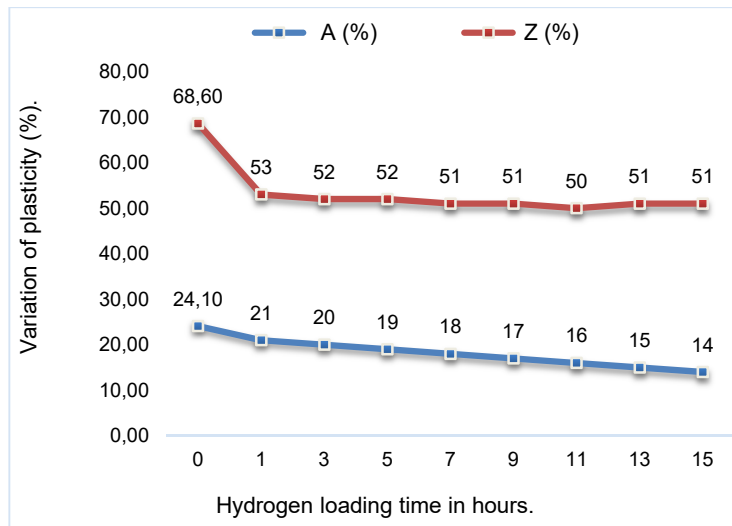
Figure 7 – Effect of the hydrogen loading time on the variation of plasticity in (%) of the AISI310austenitic stainless steel

Yield strength σe (MPa)

Figure 8 shows a progressive reduction in the yield strength (σe) of the material studied compared to the reference under the usual atmosphere of $σe_{(Air)}$: 720.0 (MPa), to that under a high concentration of hydrogen $σe_{(H)}$: 252.0 (MPa). The yield strength passes through a

minimum value after the loading level of 15hours, $\sigma e_{(H)}$: 212.0 (MPa), due to high solubility of bound hydrogen to industrial conditions: high current density, charging time in hours and significant mechanical stress. It allows the absorption of a significant quantity of hydrogen, which causes the embrittlement of the material. The phenomenon of hydrogen embrittlement (H.E) was studied by several authors (Brass et al, 2000). In the same direction, one can note a plastic deformation of the useful part of the specimen exerted by the applied tensile stress (Lo et al, 2009), which leads to the conclusion that this type of steel has a fragile behavior with a reduction in ductility and its yield strength by producing an internal cracking structure, see Figure 10 (a) and (b).
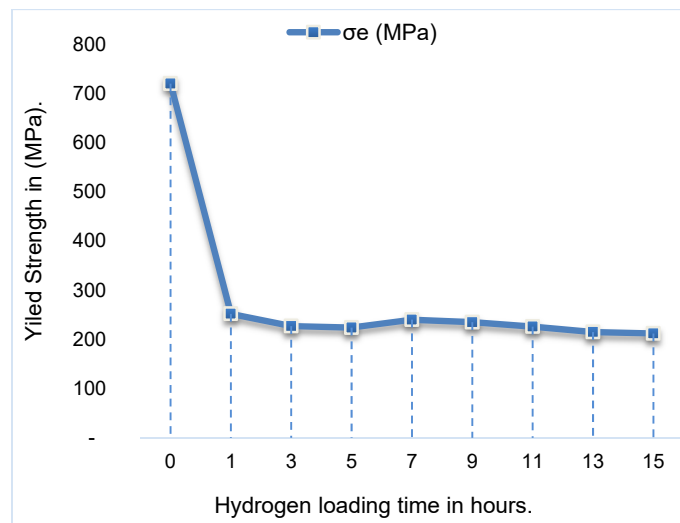
Figure 8 – Effect of the hydrogen loading time on the yield strength (σe) in (MPa) of the AISI310 austenitic stainless steel

Hardness HRV (N/mm²)

Table 4 presents the results of the evolution hardness which changes the level of loading time in hours. It was noticed that the reference specimen presents the greatest value in $HRV_{(Air)}$ of the order 246.0 (N/mm²) in relation to the other test specimens which are pre-loaded during ifferent hydrogen cathodic charging times of the order $HRV_{(H)}$ of 175.0 (N/mm²), where the hardness HRV passing through a minimum HRV hardness is of the order $HRV_{(H)}$: 140.0 (N/mm²).

Table 4 – Evolution hardness HRV of the AISI310 austenitic stainless steel after cathodic loading

Hydrogen loading in hours	Values of hardness HRV(30) (N/mm^2)
Reference0 (Air)	246.00
1 hour	175.00
3 hours	170.00
5 hours	160.00
7 hours	160.00
9 hours	170.00
11 hours	150.00
13 hours	165.00
15 hours	140.00

Embrittlement index EI (%)

Table 5 shows the results of the embrittlement index (EI, in %) of this specimen, obtained by the cathodic method. This index corresponds to the loss of mechanical properties, in particular plasticity, and is deduced from the measured elongations.

The samples preloaded with hydrogen, $A_{(H)}$, were compared with a non-hydrogenated reference specimen, $A_{0(Air)}$. No additional loading was carried out after the mechanical tensile tests. The values of the embrittlement index are calculated according to formula (1) (Lo et al, 2009; Brass et al, 2000).

From formula (1), it was concluded that the hydrogen embrittlement index (EI, in %) values are irreversible (see Table 5).

The results show a significant increase in EI, from 0.0% for the $A_{0(Air)}$ reference to 12.50% for the $A_{(H)}$ samples after a hydrogen loading time of up to 15hours. This rapid increase continues, reaching an embrittlement index EI(H) of 41.60%, validated by the work of M. Cauwels (Cauwels et al, 2020)

Table 5 – Embrittlement Index EI (%) of the AISI310 austenitic stainless steel

Hydrogen loading in hours	Values of the Embrittlement Index EI (%)
Reference0 (Air)	0.00%
1 hour	12.50%
3 hours	16.60%
5 hours	20.80%
7 hours	25.10%
9 hours	29.10%
11 hours	33.30%
13 hours	37.50%
15 hours	41.60%

Specimen states faces

Other experimental work by the authors (Smanio et al, 2008; Laureys et al, 2020; Kittel et al, 2013) was based on observations. The cracking of the test specimen types of the useful part subjected to fracture by tensile testing was observed in order to distinguish and validate the type of cracking which is linked to the zones of localized fractures (1) and (2). For further details, please refer to Figures 9 and 10.

The experimental study enables a comparison of the two examples of faces of the reference test specimens (Reference 0) of the useful part in the raw state and before the heat treatment. In Figure 9, face 1 (a) and face 2 (b) illustrate the aspects of specimen N°8 which underwent all the heat treatment applied, being electrolytically charged for 15 hours. A mechanical fracture tensile test was then carried out on the specimen at slow nominal speed, as illustrated in Figure 10, face 1 (a) and face 2 (b).

Face 1 (a)   Face 2 (b)
Figure 9 – Faces of the specimen raw states (a): raw state Face 1; (b): raw state Face 2 of the AISI310 austenitic stainless steel

Figures 10 (a) and 10 (b) show the evolution of two brittle fracture surfaces of a specimen loaded with hydrogen for 15 hours. These figures easily identify cracks after the mechanical tensile test, which generally results in a reduction in ductility and the capacity to support cyclic loads. This reduction is associated with the cleavage of the weakened (α) ferrite (Philibert et al, 2013) and the ductile fracture of austenite (γ).

Internal cracks are typically observed at both ends of this tensile test specimen; these are continuous cracks propagating over the entire fractured zone within the grain boundaries (Laureys et al, 2020; Lo et al, 2009) of the ferrite phase (inter-granular cracking) (Brass et al, 2000). The crack is broken at an angle of 90° with the axis of the applied stress load (Kittel et al, 2013; Smanio et al, 2008).

Hydrogen promotes trans-granular cracking of the ferrite phase, including the indices of micro-cracks in the austenitic phase, which is validated by a previous study (Lo et al, 2009).
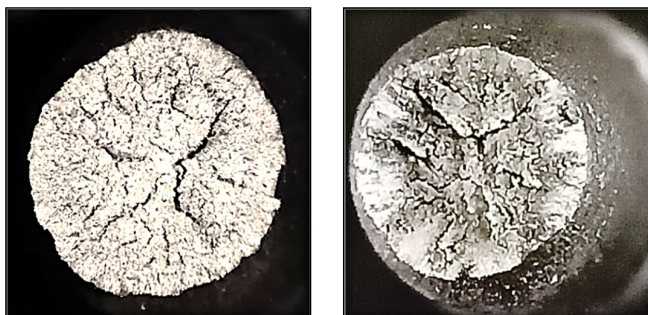
Face 1 (a)   Face 2 (b)

Figure 10 – Specimen faces (a): face1, (b): face 2 - fractured specimen (propagation of cracking after hydrogenation at 15hours of sulfuric acid H_2SO_4 at 1N of the AISI310 austenitic stainless steel

Conclusion

The objective of this study was to characterise experimentally the influence of electrolytic hydrogen on the mechanical characteristics of AISI310 austenitic stainless steel. The remarks that can be made from this study are given as follows:

- The variation in tensile strength, yield strength, and failure strength of austenitic stainless steel decreases significantly with the increase in the duration of hydrogen loading, with reductions of 32.26%, 70.55%, and 30.99%, respectively. This can be

explained by the fact that hydrogen diffusing into the steel's atomic lattice in the form of (H^+) weakens the metallic bond, reducing resistance until the material breaks.

- The structure of steel plays a very important role in the diffusion of hydrogen. The variation in mechanical resistance between the initial, untreated material and the hydrogen-charged material demonstrates this. This variation in resistance is pronounced by the variation in the hydrogen charging time as well as the temperature.

- The phenomenon of hydrogen embrittlement is more pronounced under high concentrations of hydrogen produced by industrial polarization conditions (charging time in hours, high current density, high acid concentration); this is because the martensitic pseudo-transformation makes the material harder and therefore more fragile.

- The mechanical tensile tests, which are related to the damage index EI (%), show that the absorbed hydrogen causes the elongation to decrease at break and creates a difference in elongation between the specimens that are loaded and those that are not loaded. High loading times produce a maximum value of the embrittlement index equal to EI=41.60(%).

- AISI310 stainless steel experiences strength reduction and embrittlement with increased hydrogen exposure, requiring minimized exposure, alternative material selection, and design considerations for hydrogen environments. Engineers should make informed decisions for safety and longevity of structures when using AISI310 stainless steel.

Symbols and abbreviations

σm: tensile strength (MPa)

σe: yield strength in (MPa).

σr: failure strength in (MPa).

A: elongations in (%).

Z: restriction in (%).

HRV (30): Vickers hardness in (N/mm^2).

ε: Nominal speed in (S^{-1}).

γ: Austenitic.

α: Ferritic.

EI: Embrittlement indice in (%).

A_0: Elongations specimen not charged, (Reference not charged (air).

A_H: Elongations specimen charged in hydrogen. (Specimen charged).

References

Bach, A.-C. 2018. *Etude du piégeage de l'hydrogène dans un acier inoxydable austénitique dans le cadre de la corrosion sous contrainte assistée par l'irradiation*. PhD thesis. Paris: Université PSL (Paris Sciences & Lettres) [online]. Available at: https://theses.fr/2018PSLEM044 [Accessed: 20 March 2024].

Barralis, J., Castex, L. & Maeder, G. 1999. Précontraintes et traitements superficiels. *Techniques de L'Ingénieur - Traitements des métaux*, art.ref:M1180v2, December 10. Available at: https://doi.org/10.51257/a-v2-m1180.

Brass, A.-M., Chêne, J. & Coudreuse, L. 2000. Fragilisation des aciers par l'hydrogène : étude et prévention. *Techniques de L'Ingénieur - Corrosion Vieillissement,* art.ref:M175v2, June 10. Available at: https://doi.org/10.51257/a-v2-m175.

Cauwels, M., Claeys, L., Depover, T. & Verbeken, K. 2020. The hydrogen embrittlement sensitivity of duplex stainless steel with different phase fractions evaluated by in-situ mechanical testing. *Frattura ed Integrità Strutturale*, 14(51), pp.449-458. Available at: https://doi.org/10.3221/IGF-ESIS.51.33.

Chauveau, E. & Aubry, D. 2008. Les aciers inoxydables austéno-ferritiques en fils et barres et leur utilisation dans l'industrie de l'eau. *Techniques Sciences Méthodes*, 6, pp.65-72. Available at: https://doi.org/10.1051/tsm/200806065.

Chêne, J. 2009. L'hydrogène dans les matériaux métalliques en relation avec les interactions plasticité-environnement. In: Viguier, B. (Ed.) *PlastOx 2007 - Mécanismes et Mécanique des Interactions Plasticité - Environnement*, Argelès-sur-Mer, France, pp.131-145, May 19-25. Available at: https://doi.org/10.1051/ptox/2009010.

Depover, T., Pérez Escobar, D., Wallaert, E., Zermout, Z. & Verbeken, K. 2014. Effect of hydrogen charging on the mechanical properties of advanced high strength steels. *International Journal of Hydrogen Energy*, 39(9), pp.4647-4656. Available at: https://doi.org/10.1016/j.ijhydene.2013.12.190.

Grimault, B., Chauveau, E., Gaillet, L., Drissi-Habti, M., Chaussadent, T. & Mantel, M. 2012. Comportement d'aciers inoxydables à hautes caractéristiques mécaniques vis-à-vis de la corrosion par piqûre et de la fragilisation par hydrogène. *Matériaux & Techniques*, 100(2), pp.113-125. Available at: https://doi.org/10.1051/mattech/2012008.

Hamissi, C., Lakhdari, A.A., Aboura, A. & Seddak, M. 2016. Hydrogénation Des Vis En Acier 35b2 Lors Du Décapage Acide. *Revue des matériaux et énergies renouvelables*, 1(1), pp.1-7. Available at: https://www.asjp.cerist.dz/en/article/67672 [Accessed: 10 July 2024].

He, J., Han, G., Fukuyama, S. & Yokogawa, K. 1999. Tensile behaviour of duplex stainless steel at low temperatures. *Materials Science and Technology*, 15(8), pp.909-920. Available at: https://doi.org/10.1179/026708399101506715.

Iacoviello, F. 1995. V - Fragilisation par l'hydrogène de l'acier inoxydable duplex Z2CND2205 chargé en hydrogène à 200°C. *Matériaux & Techniques*, 83, pp.48-50. Available at: https://doi.org/10.1051/mattech/199583120048s.

Kenfack, C. 2015. Guide hors production operateur traitement thermique. *Academia* [online]. Available at: https://www.academia.edu/33201915/Guide_hors_production_operateur_traitement_thermique [Accessed: 10 July 2024].

Kittel, J., Ropital, F., Grosjean, F., Sutter, E.M.M. & Tribollet, B. 2013. Corrosion mechanisms in aqueous solutions containing dissolved H2S. Part 1: Characterisation of H2S reduction on a 316L rotating disc electrode. *Corrosion Science*, 66, pp.324-329. Available at: https://doi.org/10.1016/j.corsci.2012.09.036.

Laureys, A., Pinson, M., Claeys, L., Deseranno, T., Depover, T. & Verbeken, K. 2020. Initiation of hydrogen induced cracks at secondary phase particles. *Frattura ed Integrità Strutturale*, 14(52), pp.113-127. Available at: https://doi.org/10.3221/IGF-ESIS.52.10.

Lo, K.H., Shek, C.H. & Lai, J.K.L. 2009. Recent developments in stainless steels. *Materials Science and Engineering: R: Reports*, 65(4–6), pp.39-104. Available at: https://doi.org/10.1016/j.mser.2009.03.001.

Lynch, S. 2012. Hydrogen embrittlement phenomena and mechanisms. *Corrosion Reviews*, 30(3-4), pp.105-123. Available at: https://doi.org/10.1515/corrrev-2012-0502.

Matsui, H., Kimura, H. & Moriya, S. 1979. The effect of hydrogen on the mechanical properties of high purity iron I. Softening and hardening of high purity iron by hydrogen charging during tensile deformation. *Materials Science and Engineering*, 40(2), pp.207-216. Available at: https://doi.org/10.1016/0025-5416(79)90191-5.

Philibert, J., Vignes, A., Bréchet, Y. & Combrade, P. 2013. *Métallurgie. Du minerai au matériau*, *2e édition*. Paris: Dunod [online]. Available at: https://www.dunod.com/sites/default/files/atoms/files/9782100597543/Feuilletage.pdf. ISBN: 978-2-10-059754-3.

Poupeau, P. 1981. Traitements thermiques des métaux et alliages. *Techniques de L'Ingénieur - Traitements des métaux*, art.ref:M1105v1, January 10. Available at: https://doi.org/10.51257/a-v1-m1105.

Robertson, I.M., Sofronis, P., Nagao, A., Martin, M.L., Wang, S., Gross, D.W. & Nygren, K.E. 2015. Hydrogen Embrittlement Understood. *Metallurgical and Materials Transactions A*, 46(6), pp.2323-2341. Available at: https://doi.org/10.1007/s11661-015-2836-1.

Sales, D.G. 2015. *Etude des mécanismes d'endommagement d'aciers martensitiques associés au SSC (Sulphide Stress Cracking)*. PhD thesis. University of Rochelle [online]. Available at: https://theses.fr/2015LAROS041 [Accessed: 20 March 2024].

Sassoulas, H. 1997. Traitements thermiques des aciers inoxydables. *Techniques de L'Ingénieur - Traitements des métaux*, art.ref:M1155v2, March 10. Available at: https://doi.org/10.51257/a-v2-m1155.

Smanio, V., Fregonese, M., Kittel, J., Cassagne, T., Ropital, F. & Normand, B. 2008. Wet Hydrogen Sulfide Cracking Monitoring by Acoustic Emission. In: *Eurocorr 2008*, Edinburgh, UK, September [online]. Available at: https://ifp.hal.science/hal-02475510 [Accessed: 20 March 2024].

Comportamiento mecánico del acero inoxidable austenítico cargado en la solución acuosa de H_2SO_4 durante ensayos de tracción

Amar Abboub[ac], **autor de correspondencia**, *Ahmed* Aboura[b],
Khaled Benmahdi[ad], *Mohamed* Sadoun[ad],
Mokhtar Belkacem[ac], *Djameleddine* Semsoum[ac]

[a] Universidad Mustapha Stambouli, Facultad de Ciencias y Tecnología,
  Departamento de Ingeniería Mecánica,
  Mascara, República Argelina Democrática y Popular

[b] Universidad Ahmed Zabana, Facultad de Ciencias y Tecnología,
  Departamento de Ingeniería Mecánica,
  Relizane, República Argelina Democrática y Popular

[c] Departamento de Ingeniería Mecánica

[d] Departamento de Ingeniería Civil
 Laboratorio para el Estudio de Estructuras y Mecánica de Materiales

CAMPO: materiales
TIPO DE ARTÍCULO: artículo científico original

Resumen:

Introducción/objetivo: Los aceros inoxidables tienen una excelente resistencia a la corrosión y adecuadas propiedades mecánicas. Sin embargo, su uso en ambientes agresivamente hidrogenados en la industria energética provoca una pérdida de ductilidad. Este trabajo estudió el efecto del hidrógeno sobre el comportamiento mecánico del acero inoxidable austenítico DINX15CrNiSi25.21/AISI310 cargado en una solución acuosa de ácido puramente sulfúrico H_2SO_4 a 1N a temperatura ambiente durante ensayos de tracción.

Métodos: Se aplican técnicas de caracterización experimental a probetas de tracción fabricadas mediante mecanizado estandarizado que se sometieron a una serie de tratamientos térmicos que van desde templado a 1050°C durante 35 minutos hasta revenido a 680°C durante 30 minutos. Esto va acompañado de una sucesión de inmersiones de estas muestras mediante ciclos de enfriamiento criogénico a -196°C durante una duración de 1 hora. El hidrógeno se cargó electrolíticamente en una celda de vidrio Pyrex durante varios tiempos de carga, que oscilaron entre 1h00 y 15h00, con un paso de 2h00.

Resultados: Los resultados mostraron una reducción en las propiedades mecánicas y la plasticidad. El método electroquímico confirmó la sensibilidad del material a la fragilización por hidrógeno, calculando el

criterio de fragilización EI (%). Este método indica un rápido aumento de los valores en función de los tiempos de carga de hidrógeno, con un valor máximo del 41,60%.

Conclusión: El estudio destaca el impacto negativo del hidrógeno en las propiedades mecánicas del acero inoxidable AISI310, enfatizando la necesidad de reducir la exposición al hidrógeno en las aplicaciones de acero.

Palabras claves: acero inoxidable austenítico, tratamientos térmicos, precarga de hidrógeno, propiedades mecánicas, fragilización por hidrógeno (HE), caras.

Механическое поведение аустенитной нержавеющей стали, погруженной в водный раствор H_2SO_4, при испытании на растяжение

Амар Аббоуб[ав]*,* **корреспондент***, Ахмед* Абаура[б]*,*
Халед Бенмахди[аг]*, Мухаммед* Садун[аг]*,*
Мохтар Белкацем[ав]*, Джамелиддин* Семсум[ав]

[а] Университет Мустафы Стамбули, факультет науки и технологии,
   г. Маскара, Алжирская Народная Демократическая Республика

[б] Университет Ахмеда Забаны, факультет науки и технологии,
   кафедра машиностроения,
   Релизан, Алжирская Народная Демократическая Республика

[в] кафедра машиностроения

[г] отделение гражданского строительства,
   Лаборатория исследований структур и механики материалов

Резюме:

Введение/цель: Нержавеющие стали обладают превосходной коррозионной стойкостью и соответствующими механическими свойствами. Однако их использование в агрессивно гидрированных средах в энергетической промышленности приводит к потере пластичности. В данной статье изучалось влияние водорода на механические свойства аустенитной нержавеющей стали DINX15CrNiSi25.21/AISI310, погруженной в водный раствор чистой серной кислоты H_2SO_4 при 1N при комнатной температуре во время испытания на растяжение.

Методы: Экспериментальные методы определения характеристик применялись на стандартных образцах в испытании на растяжение. Образцы, изготовленные механической обработкой, подвергались ряду термообработок, начиная от закалки при температуре 1050°C в течение 35 минут и заканчивая отпуском при температуре 680°C в течение 30

минут. Испытание сопровождалось последовательным погружением образцов по циклам в криогенной закалки при температуре -196°C продолжительностью 60 минут. Получение водорода производилось электролизом в емкости из термостойкого стекла в течение различного времени загрузки, варьирующегося от одного до пятнадцати часов с двухчасовым интервалом.

Результаты: Результаты показали снижение механических свойств и пластичности. Электрохимический метод подтвердил чувствительность материала к водородному охрупчиванию, рассчитав критерий охрупчивания EI (%). Данный метод показывает быстрый рост значений в зависимости от времени загрузки водорода с максимальным значением 41,60%.

Вывод: В исследовании выявлено негативное влияние водорода на механические свойства нержавеющей стали AISI310, что подчеркивает необходимость снижения воздействия водорода при производстве стали.

Ключевые слова: аустенитная нержавеющая сталь, термообработка, предварительная загрузка водорода, механические свойства, водородное охрупчивание (HE), поперечные сечения в месте повреждения.

Механичко понашање аустенитног нерђајућег челика изложеног воденом раствору H_2SO_4 при испитивању затезањем

Амар Абаб[ав], **аутор за преписку**, *Ахмед* Абаура[б],
Халед Бенмахди[аг], *Мухамад* Садун[аг],
Моктар Белкацем[ав], *Џамелидин* Семсум[ав]

[а] Универзитет „Мустафа Стамболи", Факултет науке и технологије,
 Маскара, Народна Демократска Република Алжир

[б] Универзитет „Ахмед Забана", Факултет науке и технологије,
 Одсек за машинство,
 Релизан, Народна Демократска Република Алжир

[в] Одсек за машинство

[г] Одсек за грађевинарство,
 Лабораторија за проучавање конструкција и механике материјала

Сажетак:

Увод/циљ: Нерђајући челици имају одличну отпорност на корозију и одговарајућа механичка својства. Међутим, њихова употреба у агресивним хидрогенизованим срединама у индустрији енергетике доводи до губитка дуктилности. У овом раду проучава се ефекат

водоника на механичко понашање аустенитног нерђајућег челика DINX15CrNiSi25.21/AISI310, оптерећеног у воденом раствору чисте сумпорне киселине (H_2SO_4) при 1N на собној температури током испитивања на затезање.

Методе: Експерименталне технике карактеризације примењене су на стандардизоване затезне епрувете добијене машинском обрадом и подвргнуте серији термичких обрада – од каљења на 1050°C током 35 минута до отпуштања на 680°C током 30 минута. То је праћено низом потапања епрувета током циклуса криогеног каљења на -196°C у трајању од 60 минута. Водоник је оптерећен електролитички у стакленој посуди од пирекса за различита времена оптерећења, од једног сата до 15 сати, с кораком од 2 сата.

Резултати: Резултати су показали редукована механичка својства и пластичност. Електрохемијски метод је потврдио осетљивост материјала на водоничну кртост, израчунавањем критеријума кртости EI (%). Овај метод указује на брзи раст вредности зависно од времена оптерећења водоником, при чему је максимална вредност 41,60%.

Закључак: У раду се наглашава негативан утицај водоника на механичка својства нерђајућег челика AISI310, при чему се истиче да је при употреби челика потребно смањити његову изложеност водонику.

Кључне речи: аустенитни нерђајући челик, термичка обрада, претходно оптерећење водоником, механичка својства, водонична кртост (HE), попречни пресеци на месту лома.

Corrosion of Zn-Ni coated reinforcing steel in simulated concrete pore solutions

Mihael M. Bučko[a], *Ljubica* M. Radović[b], *Marko* N. Dimitrijević[c], *Radovan* M. Karkalić[d], *Jelena* B. Bajat[e]

[a] University of Defence in Belgrade, Military Academy, Department for Military Chemical Engineering, Belgrade, Republic of Serbia, e-mail: mihael.bucko@va.mod.gov.rs, **corresponding author**, ORCID ID: https://orcid.org/0000-0001-6992-8841

[b] Military Technical Institute, Belgrade, Republic of Serbia, e-mail: ljubica.radovic@mod.gov.rs, ORCID ID: https://orcid.org/0000-0002-5204-983X

[c] University of Defence in Belgrade, Military Academy, Department for Military Chemical Engineering, Belgrade, Republic of Serbia, e-mail: markodimitrijevic2402@gmail.com, ORCID ID: https://orcid.org/0009-0009-2517-6532

[d] University of Defence in Belgrade, Military Academy, Department for Military Chemical Engineering, Belgrade, Republic of Serbia, e-mail: rkarkalic@yahoo.com, ORCID ID: https://orcid.org/0000-0002-8074-7264

[e] University of Belgrade, Faculty of Technology and Metallurgy, Belgrade Republic of Serbia, e-mail: jela@tmf.bg.ac.rs, ORCID ID: https://orcid.org/0000-0003-0742-8176

FIELD: materials
ARTICLE TYPE: original scientific paper

Abstract:

Introduction/purpose: The anticorrosion protection of steel reinforcement bars in concrete is a critical concern in civil engineering, particularly for the construction of concrete structures intended for military applications. Currently, the most important methods for achieving this protection include the application of coatings on steel rebar (such as epoxy or hot-dip galvanized zinc), the use of stainless-steel rebar, composite rebars, or high-performance concrete that incorporates corrosion inhibitors, surface sealers, silica fume, or fly ash admixtures.

Methods: This study aims to determine whether an electroplated Zn-Ni coating of sufficient thickness can offer better long-term corrosion resistance to reinforcing steel in concrete compared to the traditional pure Zn coating typically used for this purpose. The Zn-Ni coatings produced were 40 μm thick and contained approximately 13 mass.% Ni. Scanning electron microscopy revealed a smooth and homogeneous surface morphology, although microcracks extending through the entire coating depth were observed. The protective effectiveness of the coatings was evaluated using electrochemical impedance spectroscopy, with samples immersed in various electrolytes that simulate the chemical environments present in different types of concrete.

Results: The measurements indicated a significantly slower dissolution rate of the corrosion product formed on the Zn-Ni coating in chloride-rich environments, compared to pure Zn.

Conclusion: It can be concluded that Zn-Ni alloy presents a viable alternative to pure Zn for protecting steel in concrete structures where high chloride penetration is anticipated.

Key words: steel rebar corrosion, Zn-Ni coating, concrete pore solution, electroplating.

Introduction

Corrosion of steel reinforcement in concrete structures remains a significant challenge, particularly in military applications where durability and long-term structural integrity are critical. The harsh environments to which these structures are often exposed - such as marine, coastal, or chemically aggressive conditions - accelerate corrosion processes, necessitating the development of more effective protective measures. Recent advances in corrosion prevention of steel rebar in concrete include enhancing the compactness of concrete, application of protective coatings to concrete surface, using epoxy and zinc-based coatings on steel, along with cathodic protection systems, and novel admixtures like corrosion inhibitors and nanomaterials which are mixed into concrete (Qiao et al, 2024). The steel corrosion in concrete is typically attributed to either the presence of chloride salts, which can depassivate steel in an alkaline environment, or carbonation, which lowers the alkalinity of concrete. Zinc coatings produced through the batch hot-dip galvanizing process are frequently employed as a preventative measure in reinforced concrete structures exposed to carbonation or mild chloride contamination, as Zn forms a sufficiently thick passive film (Short et al, 1996). However, the protective mechanism of Zn evolves through several stages. In fresh concrete, where $Ca(OH)_2$ is present, the slightly soluble compound

$Ca[Zn(OH)_3]_2 \cdot 2H_2O$ (calcium hydroxyzincate) forms, which is primarily responsible for Zn passivation (Tan & Hansson, 2008). Studies conducted in solutions simulating carbonated concrete show that galvanized steel remains passive even after carbonation, although the reaction of calcium hydroxyzincate with CO_2 leads to the formation of $CaCO_3$ and $Zn_5(CO_3)_2(OH)_6$ (hydrozincite), which exhibits reduced protective properties (Roventi et al, 2013). Ultimately, prolonged exposure to a chloride-rich environment following concrete carbonation results in the rapid corrosion of galvanized steel, producing $Zn_5(OH)_8Cl_2 \cdot H_2O$ (zinc hydroxychloride) once the threshold concentration of chloride ions is exceeded (Roventi et al, 2014).

Nickel alloying is a widely-used technique to enhance the protective properties and hardness of zinc, and the demand for corrosion-resistant Zn–Ni coatings is substantial, primarily encompassing applications in the automotive and electronics industries (Mosavat et al, 2012). As a result, most corrosion tests on this alloy have been conducted in environments with approximately neutral solution pH. The superior corrosion resistance of Zn–Ni compared to pure Zn in neutral conditions has been attributed to several factors. One of these is the formation of complex corrosion products on the Zn-Ni alloy, which act as a barrier against the diffusion of corrosive agents. Additionally, it has been suggested that the fine cracked structure of Zn–Ni coatings distributes anodic reactions across a larger surface area, thereby reducing the likelihood of localized corrosion (Tian et al, 2009). Some researchers also propose that nickel may slow down the dehydration of $Zn(OH)_2$, a corrosion product, into ZnO, which, in turn, delays the oxygen reduction process on the corroding surface (Wilcox & Gabe, 1993). Lastly, there is considerable evidence that the dezincification of the alloy surface results in a Ni-enriched layer, providing an improved barrier against anodic dissolution (Short et al, 1996).

Building on this background, the present study aims to investigate whether a sufficiently thick electroplated Zn-Ni coating can offer superior long-term corrosion resistance compared to pure Zn, when both are exposed to carbonation and chloride ions in an alkaline environment—conditions that closely mimic those found in concrete pores. Over the past 20 years, this possibility has been the subject of extensive research, yielding varied results depending on the experimental setup. Early studies conducted in alkaline and chloride-rich solutions concluded that Zn-Ni coatings did not demonstrate improved corrosion resistance compared to pure Zn (Short et al, 1996), though the impact of concrete carbonation was not accounted for, as the pH of the test solutions was 12.00 or higher. In contrast, more recent literature suggests that in alkaline solutions, Ni

enhances Zn passivation, reduces its dissolution rate, and as a result, Zn-Ni alloys have found widespread application in alkaline batteries (Hosseini et al, 2012; El-Sayed et al, 2015).

There is no single electrolyte that can be used in laboratory settings to universally replicate the conditions found in concrete, as many factors, such as pH levels and the concentration of corrosive agents, change over time in real concrete. However, extensive studies have been conducted to compare results obtained from concrete and simulated solutions. Based on these studies (Farina & Duffo, 2007; Moreno et al, 2004), this work employs three different electrolytes to predict and compare the behavior of Zn and Zn-Ni in three distinct environments: fresh concrete, concrete exposed to CO_2, and concrete containing Cl^- ions. For the corrosion testing, electrochemical impedance spectroscopy (EIS) and scanning electron microscopy (SEM) were utilized.

Experimental section

Coating samples

To compare the corrosion performance of Zn-Ni alloy-coated steel with that of galvanized steel, pure zinc was selected as a reference material for the Zn-coated steel. This choice allowed for a consistent point of comparison in all tests, eliminating the influence of various parameters that may affect the quality of the zinc coating obtained through hot-dip galvanizing.

The zinc specimens were cut from a pure Zn (99.99%) sheet with a thickness of 2 mm. The Zn-Ni alloy coatings were produced via electrochemical deposition on mild steel plates with an active surface area of 2x2 cm², using a chloride acidic bath containing 15 g/dm³ ZnO, 60 g/dm³ $NiCl_2·6H_2O$, 250 g/dm³ NH_4Cl, and 20 g/dm³ H_3BO_3 (Bajat et al, 2001). Direct current was supplied using a PAR M173 potentiostat/galvanostat in galvanostatic mode, with a zinc plate serving as the counter electrode. Prior to the deposition of the Zn-Ni alloy, the steel substrate underwent several preparatory treatments: abrasion with emery papers of grades 600, 1000, and 1200, degreasing in a saturated NaOH solution in ethanol, pickling with 2 mol/dm³ HCl for 30 seconds, and finally rinsing with distilled water.

The plating process was conducted at 40 °C without stirring, with deposition times adjusted to achieve coating thicknesses of up to 40 µm, as verified by a DUALSCOPE MPOR coating thickness measuring instrument.

Characterization techniques

The morphology and composition of the freshly prepared Zn-Ni coatings were analyzed using a scanning electron microscope (SEM), a Tescan VEGA TS 5130 MM, equipped with an energy-dispersive spectroscopy (EDS) system (INCAPenta-FETex3, Oxford Instruments). For the SEM images of the cross-section, the samples were embedded in epoxy resin, then cut and mechanically polished using various grades of emery paper.

To compare the corrosion behavior of the samples, pure Zn and Zn–Ni alloy-coated steel were sequentially exposed to three different solutions that simulated fresh, carbonated, and chloride-rich concrete environments, as described in (Farina & Duffo, 2007; Moreno et al, 2004), i.e., the same samples were exposed over a total period of 21 days, divided into three cycles of 7 days each. The solutions were prepared using analytical grade reagents and double-distilled water, with their compositions outlined in Table 1.

Table 1 – Composition of the simulated concrete pore solutions

Composition	Exposure time	Corrosion media simulating
Saturated $Ca(OH)_2$	7 days	Fresh concrete
0.015 mol dm^{-3} $NaHCO_3$ + 0.005 mol dm^{-3} Na_2CO_3, pH 9.50	7 days	Carbonated concrete
0.015 mol dm^{-3} $NaHCO_3$ + 0.005 mol dm^{-3} Na_2CO_3 + 0.5 mol dm^{-3} NaCl	7 days	Carbonated concrete with chloride penetration

The corrosion processes in the solutions outlined in Table 1 were monitored using electrochemical impedance spectroscopy (EIS). All measurements were conducted at room temperature in a Pyrex glass three-electrode cell, which included a platinum mesh counter electrode and a saturated calomel reference electrode, with electrode potential measured through a Luggin capillary. The EIS studies involved applying a sinusoidal voltage of 10 mV amplitude at the open circuit potential of the working electrode, utilizing a ZRA Reference 600 potentiostat from Gamry Instruments. The frequency ranged from 100 kHz to 10 mHz. The working electrode consisted of a coated sample placed in a Teflon holder, with an exposed area of 1 cm². Data fitting for the impedance was performed using Gamry Instruments Echem Analyst software. The impedance spectrum was recorded at 24-hour intervals over a total immersion period of 21 days.

Results and discussion

The electrodeposition of Zn-Ni coating of a sufficient thickness

The first part of the results focuses on two key requirements for producing a coating capable of withstanding the conditions in concrete: the optimal chemical composition and a sufficient thickness of the electroplated Zn–Ni coating. The Zn–Ni coatings were electrodeposited using a constant current density of 20 mA/cm², a parameter based on our previous research (Bajat & Mišković-Stanković, 2004), to ensure the production of non-dendritic deposits with a nickel content of 12–15 wt.%. SEM images (both normal and cross-sectional views) of Zn–Ni coatings with two different thicknesses are shown in Figure 1, along with their elemental compositions. The images reveal that the surface morphology was smooth and uniform for both specimens, characterized by hemispherical clusters. In the thinner sample, a fine-grained, smoother morphology was observed, with clusters less than 1 µm in size (Figure 1a). In contrast, the thicker coating exhibited larger clusters, approximately 10 µm in size, with a more pronounced cauliflower-like morphology (Figure 1b). This type of surface appearance has been previously reported for Zn–Ni electrodeposits containing a single γ–Zn–Ni phase (Mosavat et al, 2012).

The cross-sectional SEM analysis confirms that the coatings exhibit uniform thickness and homogeneity throughout their depth (Figures 1c, d). However, both samples contained through-thickness microcracks. Defects such as cracks and through-thickness pores are common in electroplated Zn–Ni coatings with a nickel content exceeding 8–10 wt.% (Kwon et al, 2016). These cracks are attributed to the inherent lattice strain associated with the formation of the γ–Zn–Ni phase, making it challenging to achieve a continuous coating layer (Kwon et al, 2016, Sriraman et al, 2013). Despite this, studies have shown that cracked Zn–Ni coatings still offer superior sacrificial corrosion protection compared to Zn and Cd coatings, particularly in NaCl environments (Sriraman et al, 2013). Therefore, in this work, the corrosion performance of 40 µm thick Zn–Ni alloy coatings was further compared with that of pure Zn coatings. The semiquantitative EDS analysis (Figure 1e) confirms that the Zn–Ni coatings contain an average of ~13 wt.% Ni throughout their depth.
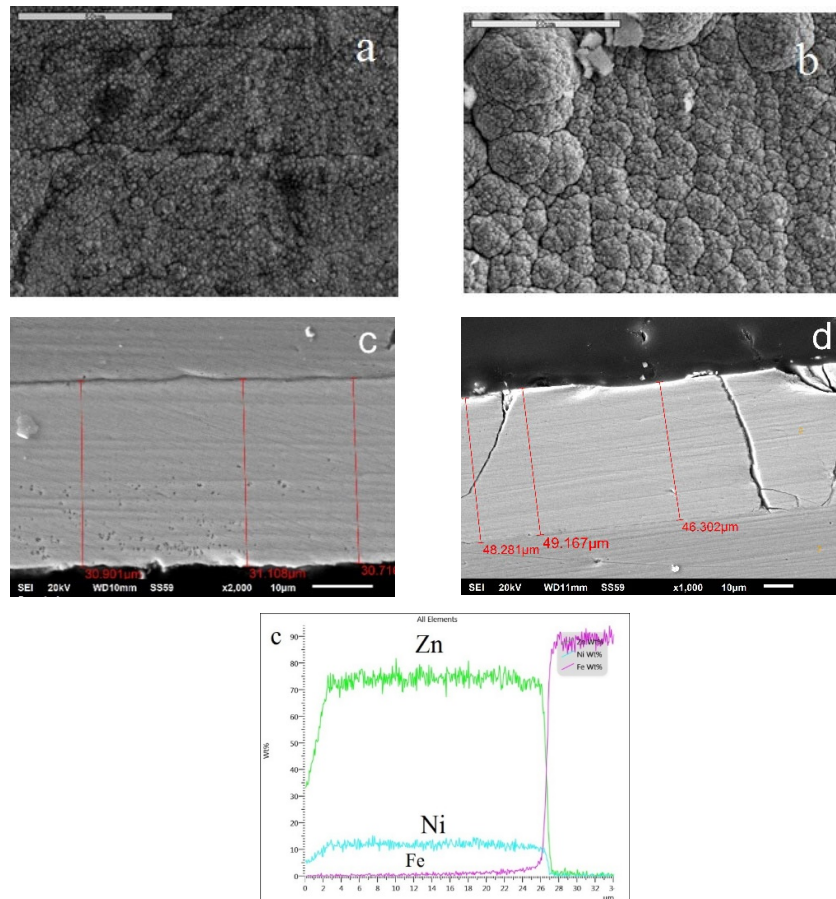
Figure 1 – SEM/EDS analysis of Zn–Ni coatings: a), b) surface morphology (scale bar length is 50 μm), (c, d) cross section, e) EDS line analysis through a coating cross section. Coating thickness of 30 μm (a, c) and 40 μm (b,d)

The hot-dip galvanizing process, a standard method for coating reinforcing steel, typically results in a Zn–Ni alloy containing a maximum of 0.5 wt.% Ni, as higher nickel levels have been associated with disadvantages such as a rough surface and insufficient coating thickness (Emel'yanov et al, 2009). However, much of the literature on the corrosion resistance of Zn–Ni alloy coatings in neutral and alkaline media suggests that the best performance is achieved with a nickel content in the range of 11–15 wt.%, where the coating consists predominantly of the γ–$Zn_{21}Ni_5$ phase (Mosavat et al, 2012; Short et al, 1996; Bajat et al, 2001).

Electrodeposition has been found to successfully achieve this optimal composition, which is why it was selected as the coating method for reinforcing steel in this study.

Most scientific studies on Zn–Ni electrodeposition have focused on achieving a maximum coating thickness of around 30 μm. Furthermore, standard specifications for atmospheric corrosion protection of steel typically require Zn–Ni electroplated coatings to be only 10 μm thick (ASTM, 2019). In contrast, ASTM A767, the Standard Specification for Zinc-Coated (Galvanized) Steel Bars for Concrete Reinforcement, mandates a minimum zinc coating thickness of 85 μm (equivalent to 6.1 g/m² by mass) for concrete applications. Therefore, this study aimed to investigate whether it is possible to produce an adherent and homogeneous Zn–Ni coating of greater thickness (>30 μm) through electrodeposition, comparable to the commercial zinc layers used in concrete reinforcement. Notably, "thick" Zn–Ni electrodeposits have been reported in the past, with thicknesses of 40 μm (Ravindran & Muralidharan, 2006) and 100 μm (El-Sayed et al, 2015). In both cases, smooth, semi-bright, and homogeneous coatings were achieved by using additives such as sodium lauryl sulfate (El-Sayed et al, 2015) or substituted aldehydes (Ravindran & Muralidharan, 2006).

Electrochemical impedance spectroscopy results

The EIS studies were conducted on a daily basis for both the Zn bulk plate and the Zn–Ni coated samples, with each being successively exposed to three different corrosion media simulating fresh concrete, carbonated concrete, and carbonated concrete containing chloride salts. The EIS Nyquist spectra for the Zn plate and the Zn–Ni coated samples, recorded in these three different solutions, are presented in Figures 2, 3, and 4, respectively.
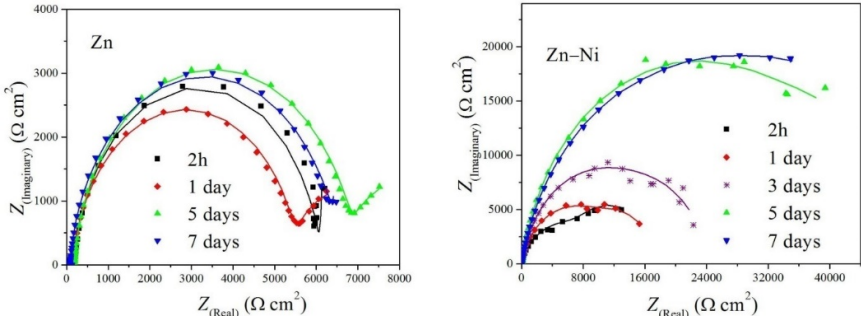

Figure 2 – Nyquist plots for the Zn plate and the Zn–Ni coated reinforcing steel in saturated $Ca(OH)_2$ during the first 7-day cycle of immersion
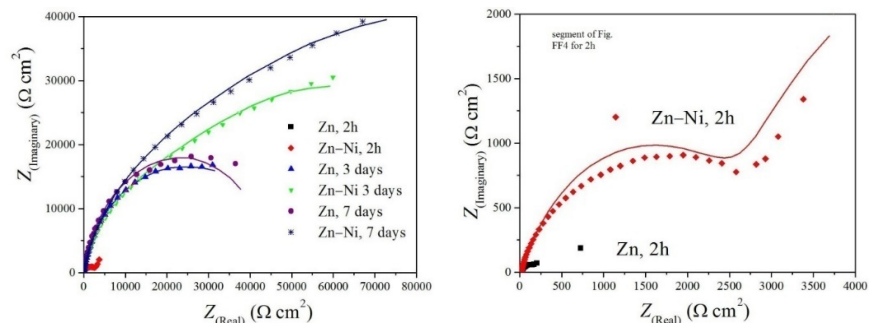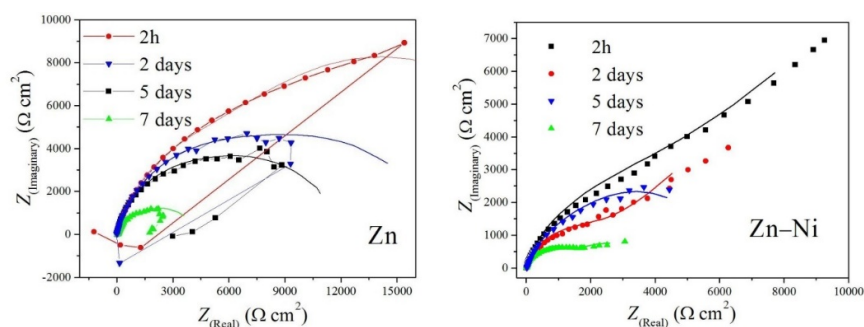
Figure 3 – Nyquist plots for the Zn plate and the Zn–Ni coated reinforcing steel in 0.015 mol dm^{-3} NaHCO$_3$ + 0.005 mol dm^{-3} Na$_2$CO$_3$ during the second 7-day cycle of immersion

Figure 4 – Nyquist plots for the Zn plate and the Zn–Ni coated reinforcing steel in 0.015 mol dm^{-3} NaHCO$_3$ + 0.005 mol dm^{-3} Na$_2$CO$_3$ + 0.5 mol dm^{-3} NaCl during the 3rd 7-day cycle of immersion. For Zn, the recorded data are presented as dot+line, so that the inductive behaviour is clearly visible

Throughout the 21-day immersion in the three different solutions, the EIS response for all the samples exhibited two distinct patterns: either a depressed semicircular arc followed by a second arc or an ill-defined tail, or a single depressed arc resulting from the superposition of two semicircles. Based on equivalent circuit (EC) studies for corrosion processes of metal coatings covered by protective corrosion products (Hamlaoui et al, 2008), this system can be modeled using the equivalent circuit shown in Figure 5. This circuit effectively accounts for the two time constants observed in the impedance plots, whether they are well-separated or merged. The first time constant, observed at high frequencies, corresponds to the properties of the corrosion product layer,

while the second time constant at low frequencies characterizes the corrosion process occurring at the interface between the corrosion product and the metal.

In this model, R_s represents the electrolyte resistance between the sample and the Luggin capillary. The R_1/Q_1 pair represents the electrolytic resistance and capacitance within defects of the corrosion product layer, while the R_2/Q_2 pair refers to the charge transfer resistance and the double-layer capacitance associated with the metal corrosion process in the cavities of the protective layer (Hamlaoui et al, 2008). To account for the non-ideal capacitive behavior at the interface between the sample and the solution, which is responsible for the appearance of depressed Nyquist semicircles, a constant phase element (CPE) was applied to replace pure capacitance for fitting the spectra (Hsu & Mansfeld, 2001).

The model shown in Figure 5 assumes that the corrosion product film does not completely cover the metal and should be considered a defective layer rather than a homogeneous one. The fitting results of the experimental data using this EC model are represented by the solid lines in Figures 2, 3, and 4, which show a good agreement with the experimental data. The calculated resistance parameters for the simulated diagrams are presented in Table 2. Additionally, the overall corrosion resistance of the samples was evaluated by calculating the total polarization resistance as the sum of R_1 and R_2 (Cao et al, 2017; Wu et al, 2017), with the calculated values depicted in Figure 6.
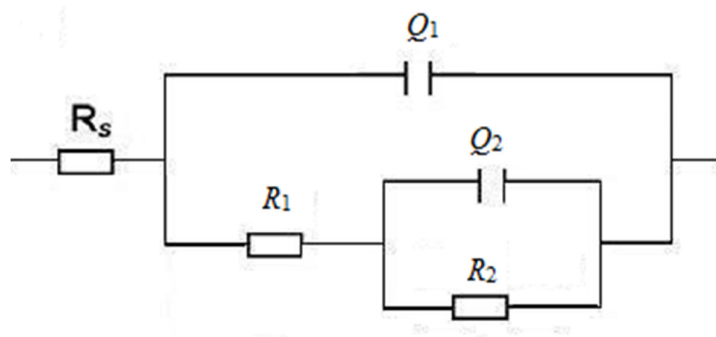

Figure 5 – Equivalent electrical circuit of the corroding Zn–Ni coated steel orthe pure Zn plate in different electrolytes simulating concrete media

Table 2 – The values of the resistance parameters R1 and R2 for different corroding samples in three different media

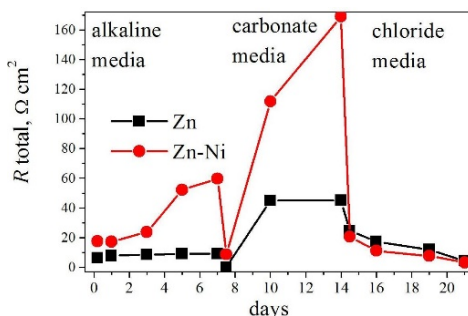| Immersion period	Pure Zn sample		Zn–Ni coating, 40 μm thick	
Saturated Ca(OH)$_2$	R_1 / kΩ cm^2	R_2 / kΩ cm^2	R_1 / kΩ cm^2	R_2 / kΩ cm^2
2h	5.201	1.037	10.16	7.416
1 day	5.409	2.447	12.72	4.557
3 days	-	-	19.80	3.933
5 days	6.770	2.332	43.74	8.511
7 days	6.413	2.667	40.47	19.26
0.015 mol dm^{-3} NaHCO$_3$ + 0.005 mol dm^{-3} Na$_2$CO$_3$				
2h	0.21	0.009	3.322	5.441
3 days	32.78	12.19	32.28	79.49
7 days	39.38	5.757	37.26	131.8
0.015 mol dm^{-3} NaHCO$_3$ + 0.005 mol dm^{-3} Na$_2$CO$_3$ + 0.5 mol dm^{-3} NaCl				
2h	12.07	12.53	4.10	16.57
2 days	9.628	7.745	5.17	5.986
5 days	7.111	4.802	4.003	3.654
7 days	2.355	1.974	2.213	1.010

Figure 6 – The change of the total resistance with immersion time, for the pure Zn plate and the Zn–Ni corroding samples

The fitted resistance values for both the Zn plate and the Zn–Ni coated steel during the first seven days of testing exhibit high values, in the order of several kΩ cm², which progressively increase over time. These elevated R values indicate the formation of a protective film on both the pure Zn and the Zn–Ni alloy surfaces in saturated Ca(OH)$_2$. This observation aligns

with the findings of Farina & Duffo (2007) who demonstrated that a stable passive film can form on zinc in a fresh concrete environment within just 40 minutes. Similarly, earlier studies have confirmed the formation of a passive layer on Zn–Ni alloys in alkaline corrosion media (El-Sayed et al, 2011). For pure Zn, the relatively stable resistance values suggest that the characteristics of the passive layer remain largely unchanged throughout the seven-day testing period. In contrast, the Zn–Ni coating shows a marked increase in the diameter of the impedance semicircles over time, indicating that the porosity of the protective layer decreases and its thickness increases with prolonged exposure to $Ca(OH)_2$. The results obtained from our measurements may be compared with those reported by Wang et al. (2019), where the corrosion behavior of Zn-Al, Zn-Mg, and Zn-Mg-Al coatings was monitored in an alkaline electrolyte designed to simulate concrete pore conditions. In their study, after a 7-day immersion period, the most favorable corrosion performance was observed for the Zn-0.5Mg and Zn-0.5Mg-0.2Al alloys which exhibited a corrosion current density of approximately 50 µA cm^{-2}, correlating to a polarization resistance of around 500 Ω cm². This comparison highlights that the Zn-Ni coating employed in our investigation provides superior protective characteristics in alkaline solutions.

Following the initial 7-day exposure in an alkaline medium, the samples were transferred to a carbonate-rich electrolyte without any cleaning procedures, ensuring that the corrosion products formed in the alkaline environment remained on the surface. This step aimed to investigate how concrete carbonation influences the modification of the protective layer on Zn and Zn–Ni alloy coatings, previously formed in a solution simulating fresh concrete. Figure 3 illustrates the Nyquist plot of both Zn and Zn–Ni coatings, revealing a similar corrosion behavior in carbonated media. The spectra recorded 2 hours after the immersion show very low initial impedance values, likely due to rapid chemical changes in the passive film formed earlier in the alkaline solution. This behavior persists for up to 8 hours. However, after 8 hours, the corrosion resistance of both coatings increases progressively with time, reaching a total impedance of 140 kΩ for Zn–Ni and 70 kΩ for Zn after 7 days. The shape of the impedance curves corroborates previous findings on Zn corrosion in carbonated media where independent studies have demonstrated rapid metal passivation. Nevertheless, the composition of the passive layer varies depending on experimental conditions such as temperature, carbonate/bicarbonate content, and pH, ranging from a thin ZnO film (Kaesche, 1964) to hydrozincite which is specific to concrete pores (Roventi et al, 2013).

Following the second exposure cycle, the experiment proceeded into the final 7-day cycle where the samples were immersed in a solution simulating chloride penetration into carbonated concrete. It is important to note that, similarly to the second cycle, the impedance response was not from the bare metal, but from the metal coated with the corrosion products formed in the alkaline phase and later modified in the carbonate electrolyte. The visual appearance of the two specimens differed at the start of immersion in the chloride solution: the Zn surface appeared white and smooth, while the Zn–Ni surface was flat and black. Over the 7-day exposure period to the chloride-rich electrolyte, Zn–Ni retained its black appearance, while the white product on Zn continued to grow in volume and began peeling off the sample. It is likely that the white product was zinc hydroxychloride, as it is known to occupy approximately 3.6 times the volume of the original zinc (Sistonen et al, 2008).

Figure 4 presents the Nyquist plots recorded for the samples exposed to the simultaneous action of carbonation and chloride ions (i.e., the 3rd immersion cycle) at four different immersion times. As immersion time increases, the total impedance decreases in both diagrams, indicating the degradation of the corrosion product layer on the coatings. Chloride ions, known as strong anodic activators, create pores in the corrosion product layer, allowing them to penetrate through and attack the underlying metal (Padilla & Alfantazi, 2014). The Nyquist diagrams in Figures 4a and b feature two irregularly shaped, overlapping semicircles. A key distinction between the diagrams for the Zn and Zn–Ni specimens is the presence of a low-frequency inductive loop observed throughout the immersion period in the spectra related to Zn. This low-frequency inductive behavior has been attributed to surface coverage changes by the adsorbed species involved in the Zn dissolution process and is typical when bare Zn or Zn under a poorly protective film is corroding (Padilla & Alfantazi, 2014). Unfortunately, we were unable to identify an appropriate electrical equivalent circuit to fit the low-frequency portion of the EIS spectra for Zn in Figure 4. Therefore, the resistance data were obtained by fitting only the high- and mid-frequency sections of the EIS spectra in this case.

It can be concluded from the diagrams in Figure 4 that the passive layer formed on both Zn and Zn–Ni alloy in fresh concrete does not provide adequate protection to the coatings when exposed to concrete containing 0.5 mol dm^{-3} chloride ions. However, the corrosion patterns differ significantly between Zn and Zn–Ni alloy. The voluminous corrosion product on Zn poses a significant issue, as it leads to swelling of the Zn coating, disrupts the bond between the metal and concrete, and causes concrete cracking due to product expansion (Dong et al, 2012).

2024

Additionally, the inductive behavior observed in Figure 4 indicates that, despite its thickness, the corrosion product on Zn is discontinuous, allowing for continual corrosion of the underlying metal. These findings align with the research conducted by Roventi et al. (2014) regarding concrete exposed to Cl⁻ ions. In contrast, the corrosion layer formed on the Zn–Ni alloy in both fresh and carbonated concrete is thin, smooth, and black, maintaining its appearance over the 7-day exposure in chloride media. Although the protective properties of this layer diminish over time, as evidenced by the Nyquist plots, it can be asserted that significant dissolution of the Zn–Ni coating is not observed in a chloride-contaminated environment.

Conclusion

The corrosion of steel reinforcement in concrete is very important issue in military applications, where highly durable concrete structures are often required. Hot-dip galvanization with Zn is a common method used to prevent corrosion, but it has its limitations. In this study, we propose using a thick Zn-Ni alloy coating instead, as this alloy has already proven successful as protective coating for steel bodies in the automotive industry. The Zn-Ni alloy coating with a thicknesses of 30 and 40 µm was applied to steel through electrochemical deposition. The SEM images revealed that the coatings had a uniform, smooth surface with micro-cracks characteristic of the Zn-Ni alloy.

The main goal of this research was to compare the behavior of pure Zn and the Zn-Ni alloy in an environment simulating fresh concrete. For this purpose, three types of electrolytes were used, and the samples were sequentially exposed to each one. The first electrolyte simulated the alkaline conditions present in fresh concrete, the second simulated the penetration of CO_2 into the concrete, and the third represented the entry of chloride ions into the concrete. After 21 days of testing, it was observed that in the chloride-rich electrolyte, the corrosion resistance, as measured by electrochemical impedance spectroscopy, was nearly identical for both pure Zn and the Zn-Ni alloy. However, the corrosion product on pure Zn was a bulky zinc oxide layer that tended to flake off, while on the Zn-Ni alloy, the corrosion product was a thin, smooth black layer that retained its protective properties for a longer time.

Therefore, the Zn-Ni alloy coating could be an excellent alternative for protecting steel reinforcement from corrosion in concrete structures.

References

-ASTM. 2019. *ASTM B841-18: Standard Specification for Electrodeposited Coatings of Zinc Nickel Alloy Deposits,* 12 March. Available at: https://doi.org/10.1520/B0841-18.

Bajat, J.B., Maksimović, M.D., Mišković-Stanković, V.B. & Zec, S. 2001. Electrodeposition and characterization of Zn-Ni alloys as sublayers for epoxy coating deposition. *Journal of Applied Electrochemistry*, 31, pp.355-361. Available at: https://doi.org/10.1023/A:1017580019551.

Bajat, J.B. & Mišković-Stanković, V.B. 2004. Protective properties of epoxy coatings electrodeposited on steel electrochemically modified by Zn–Ni alloys. *Progress in Organic Coatings*, 49(3), pp.183-196. Available at: https://doi.org/10.1016/j.porgcoat.2003.09.019.

Cao, Z., Kong, G., Che, C. & Wang, Y. 2017. Influence of Nd addition on the corrosion behavior of Zn-5%Al alloy in 3.5 wt.% NaCl solution. *Applied Surface Science*, 426, pp.67-76. Available at: https://doi.org/10.1016/j.apsusc.2017.07.109.

Dong, S., Zhao, B., Lin, C., Du, R., Hu, R. & Zhang, G.X. 2012. Corrosion behavior of epoxy/zinc duplex coated rebar embedded in concrete in ocean environment. *Construction and Building Materials*, 28(1), pp.72-78. Available at: https://doi.org/10.1016/j.conbuildmat.2011.08.026.

El-Sayed, A.R., Abd El-Lateef, H.M. & Mohran, H.S. 2015. Effect of nickel content on the anodic dissolution and passivation of zinc–nickel alloys in alkaline solutions by potentiodynamic and potentiostatic techniques. *Bulletin of Materials Science*, 38, pp.379-391. Available at: https://doi.org/10.1007/s12034-014-0814-7.

El-Sayed, A.R., Mohran, H.S. & Abd El-Lateef, H.M. 2011. Inhibitive action of ferricyanide complex anion on both corrosion and passivation of zinc and zinc–nickel alloy in the alkaline solution. *Journal of Power Sources*, 196(15), pp.6573-6582. Available at: https://doi.org/10.1016/j.jpowsour.2011.03.057.

Emel'yanov, A.V., Sapunov, S.Yu. & Kudryakov, O.V. 2009. Principles of controlling crystallization kinetics for a multicomponent coating on steel. *Metallurgist*, 53, pp.648-654. Available at: https://doi.org/10.1007/s11015-010-9228-y.

Farina, S.B. & Duffo, G.S. 2007. Corrosion of zinc in simulated carbonated concrete pore solutions. *Electrochimica Acta*, 52(16), pp.5131-5139. Available at: https://doi.org/10.1016/j.electacta.2007.01.014.

Hamlaoui, Y., Pedraza, F. & Tifouti, L. 2008. Corrosion monitoring of galvanised coatings through electrochemical impedance spectroscopy. *Corrosion Science*, 50(6), pp.1558-1566. Available at: https://doi.org/10.1016/j.corsci.2008.02.010.

Hosseini, M.G., Abdolmaleki, M. & Ashrafpoor, S. 2012. Preparation, characterization, and application of alkaline leached Ni/Zn–Ni binary coatings for electro-oxidation of methanol in alkaline solution. *Journal of Applied*

Electrochemistry, 42, pp.153-162. Available at: https://doi.org/10.1007/s10800-012-0382-8.

Hsu, C.H. & Mansfeld, F. 2001. Concerning the conversion of the constant phase element parameter Y_0 into a capacitance. *Corrosion*, 57(9), pp.747-748. Available at: https://doi.org/10.5006/1.3280607.

Kaesche, H. 1964. The passivity of zinc in aqueous solutions of sodium carbonate and sodium bicarbonate. *Electrochimica Acta*, 9(4), pp.383-394. Available at: https://doi.org/10.1016/0013-4686(64)80044-X.

Kwon, M., Jo, D., Cho, S., Kim, H., Park, J.T. & Park, J.M. 2016. Characterization of the influence of Ni content on the corrosion resistance of electrodeposited Zn–Ni alloy coatings. *Surface and Coatings Technology*, 288, pp.163-170. Available at: https://doi.org/10.1016/j.surfcoat.2016.01.027.

Moreno, M., Morris, W., Alvarez, M. G. & Duffo, G. S. 2004. Corrosion of reinforcing steel in simulated concrete pore solutions. Effect of carbonation and chloride content. *Corrosion Science*, 46(11), pp.2681-2699. Available at: https://doi.org/10.1016/j.corsci.2004.03.013.

Mosavat, S.H., Shariat, M.H. & Bahrololoom, M.E. 2012. Study of corrosion performance of electrodeposited nanocrystalline Zn–Ni alloy coatings. *Corrosion Science*, 59, pp.81-87. Available at: https://doi.org/10.1016/j.corsci.2012.02.012.

Padilla, V. & Alfantazi, A. 2014. Corrosion film breakdown of galvanized steel in sulphate–chloride solutions. *Construction and Building Materials*, 66, pp.447-457. Available at: https://doi.org/10.1016/j.conbuildmat.2014.05.053.

Qiao, X., Guan, H., Zhou, Z., Song, D. 2024. Research Progress in Corrosion Behavior and Anti-Corrosion Methods of Steel Rebar in Concrete. *Metals*, 14(8), art.number:862. Available at: https://doi.org/10.3390/met14080862.

Ravindran, V. & Muralidharan, V.S. 2006. Characterization of zinc–nickel alloy electrodeposits obtained from sulphamate bath containing substituted aldehydes. *Bulletin of Materials Science*, 29, pp.293-301. Available at: https://doi.org/10.1007/BF02706499.

Roventi, G., Bellezze, T., Barbaresi, E. & Fratesi, R. 2013. Effect of carbonation process on the passivating products of zinc in $Ca(OH)_2$ saturated solution. *Materials Corrosion*, 64(11), pp.1007-1014. Available at: https://doi.org/10.1002/maco.201206868.

Roventi, G., Bellezze, T., Giuliani, G. & Conti, C. 2014. Corrosion resistance of galvanized steel reinforcements in carbonated concrete: effect of wet–dry cycles in tap water and in chloride solution on the passivating layer. *Cement and Concrete Research*, 65, pp.76-84. Available at: https://doi.org/10.1016/j.cemconres.2014.07.014.

Short, N.R., Zhou, S. & Dennis, J.K. 1996. Electrochemical studies on the corrosion of a range of zinc alloy coated steel in alkaline solutions. *Surface and Coatings Technology*, 79(1-3), pp.218-224. Available at: https://doi.org/10.1016/0257-8972(95)02428-X.

Sistonen, E., Cwirzen, A. & Puttonen, J. 2008. Corrosion mechanism of hot-dip galvanised reinforcement bar in cracked concrete. *Corrosion Science*, 50(12), pp.3416-3428. Available at: https://doi.org/10.1016/j.corsci.2008.08.050.

Sriraman, K., Brahimi, S., Szpunar, J., Osborne, J. & Yue, S. 2013. Characterization of corrosion resistance of electrodeposited Zn–Ni Zn and Cd coatings. *Electrochimica Acta*, 105, pp.314-323. Available at: https://doi.org/10.1016/j.electacta.2013.05.010.

Tan, Z.Q. & Hansson, C.M. 2008. Effect of surface condition on the initial corrosion of galvanized reinforcing steel embedded in concrete. *Corrosion Science*, 50(9), pp.2512-2522. Available at: https://doi.org/10.1016/j.corsci.2008.06.035.

Tian, W., Xie, F.Q., Wu, X.Q. & Yang, Z.Z. 2009. Study on corrosion resistance of electroplating zinc–nickel alloy coatings. *Surface and Interface Analysis*, 41(3), pp.251-254. Available at: https://doi.org/10.1002/sia.3017.

Wang, Y.-q., Kong, G., Che, C.-s. 2019. Corrosion Behavior of Zn-Al, Zn-Mg, and Zn-Mg-Al coatings in simulated concrete pore solution. *Corrosion*, 75(2), pp.203-209. Available at: https://doi.org/10.5006/3029.

Wilcox, G.D. & Gabe, D.R. 1993. Electrodeposited zinc alloy coatings. *Corrosion Science*, 35(5-8), pp.1251-1258. Available at: https://doi.org/10.1016/0010-938X(93)90345-H.

Wu, P.-p., Zhang, Z.-z., Xu, F.-j., Deng, K., Nie, K.-b. & Gao, R. 2017. Effect of duty cycle on preparation and corrosion behavior of electrodeposited calcium phosphate coatings on AZ91. *Applied Surface Science*, 426, pp.418-426. Available at: https://doi.org/10.1016/j.apsusc.2017.07.111.

Corrosión del acero de refuerzo recubierto de Zn-Ni en soluciones de poros de concreto simuladas

Mihael M. Bučko[a], **autor de correspondencia**, *Ljubica* M. Radović[b], *Marko* N. Dimitrijević[a], *Radovan* M. Karkalić[a], *Jelena* B. Bajat[c]

[a] Universidad de Defensa de Belgrado, Academia Militar, Departamento de Ingeniería Química Militar, Belgrado, República de Serbia

[b] Instituto Técnico Militar, Belgrado, República de Serbia

[c] Universidad de Belgrado, Facultad de Tecnología y Metalurgia, Belgrado República de Serbia,

CAMPO: materiales
TIPO DE ARTÍCULO: artículo científico original

Resumen:

Introducción/objetivo: La protección anticorrosión de barras de refuerzo de acero en concreto es una preocupación crítica en ingeniería civil, particularmente para la construcción de estructuras de concreto destinadas a aplicaciones militares. Actualmente, los métodos más importantes para lograr esta protección incluyen la aplicación de recubrimientos sobre barras de refuerzo de acero (como epoxi o zinc galvanizado en caliente), el uso de barras de refuerzo de acero inoxidable, barras de refuerzo compuestas o concreto de alto rendimiento que incorpore inhibidores de corrosión, selladores de superficies, humo de sílice o aditivos de cenizas volantes.

Métodos: Este estudio tiene como objetivo determinar si un recubrimiento galvanizado de Zn-Ni de suficiente espesor puede ofrecer una mejor resistencia a la corrosión a largo plazo al acero de refuerzo en concreto en comparación con el recubrimiento tradicional de Zn puro que se usa típicamente para este propósito. Los recubrimientos de Zn-Ni producidos tenían un espesor de 40 μm y contenían aproximadamente un 13% en masa de Ni. La microscopía electrónica de barrido reveló una morfología superficial suave y homogénea, aunque se observaron microfisuras que se extendían por toda la profundidad del recubrimiento. La efectividad protectora de los recubrimientos se evaluó mediante espectroscopía de impedancia electroquímica, con muestras sumergidas en diversos electrolitos que simulan los ambientes químicos presentes en diferentes tipos de concreto.

Resultados: Las mediciones indicaron una velocidad de disolución significativamente más lenta del producto de corrosión formado en el recubrimiento de Zn-Ni en ambientes ricos en cloruro, en comparación con el Zn puro.

Conclusión: Se puede concluir que la aleación Zn-Ni presenta una alternativa viable al Zn puro para proteger el acero en estructuras de concreto donde se prevé una alta penetración de cloruro.

Palabras claves: corrosión de barras de acero, recubrimiento de Zn-Ni, solución de poros de hormigón, galvanoplastia.

Коррозия арматурной стали, защищенной покрытием из сплава Zn-Ni, в электролитах, имитирующих поры в бетоне

Михаел М. Бучко[а] , **корреспондент**, *Любица* М. Радович[б],
Марко Н. Димитриевич[а], *Радован* М. Каркалич[а], *Елена Б*. Баят[в]

[а] Университет обороны в г. Белград, Военная академия, департамент военного химического инжиниринга, г. Белград, Республика Сербия

[б] Военно-технический институт, г. Белград, Республика Сербия

[в] Белградский университет, факультет технологии и металлургии, г. Белград, Республика Сербия

Резюме:

Введение/цель: Антикоррозийная защита стальных арматурных стержней в бетоне является важнейшей задачей в гражданском строительстве, особенно при строительстве бетонных конструкций, предназначенных для военного применения. В настоящее время наиболее важными методами обеспечения такой защиты являются нанесение покрытий на стальную арматуру (например, эпоксидных покрытий или покрытий

методом горячего цинкования), использование арматуры из нержавеющей стали, композитной арматуры или высококачественного бетона, в состав которого входят ингибиторы коррозии, поверхностные герметики, диоксид кремния или летучая зола.

Методы: Цель данного исследования − определить, может ли гальваническое покрытие Zn-Ni достаточной толщины обеспечить лучшую и более долгосрочную коррозионную стойкость арматурной стали в бетоне по сравнению с традиционным покрытием из чистого Zn, которое чаще используется в этой цели. Толщина покрытия Zn-Ni составляла 40 µm и содержала приблизительно 13 мас.%Ni.

Результаты: С помощью метода сканирующей электронной микроскопии выявлена гладкая и однородная морфология поверхности, несмотря на микротрещины, проходящие по всей глубине покрытия. Защитная эффективность покрытий оценивалась с помощью электрохимической импедансной спектроскопии. При этом образцы погружались в различные электролиты, имитирующие химическую среду, присутствующую в различных типах бетона.

Вывод: На основании результатов исследования можно сделать вывод, что сплав Zn-Ni представляет собой устойчивую альтернативу чистому Zn для защиты стали в бетонных конструкциях с высокой степенью проникновения хлоридов.

Ключевые слова: коррозия стальной арматуры, Zn-Ni покрытие, поровый раствор в бетоне, гальванопокрытие.

Корозија арматурног челика заштићеног превлаком легуре Zn-Ni у електролитима који симулирају поре у бетону

Михаел М. Бучко[а], **аутор за преписку**, *Љубица* М. Радовић[б],
Марко Н. Димитријевић[а], *Радован* М. Каркалић[а], *Јелена* Б. Бајат[в]

[а] Универзитет одбране у Београду, Војна академија,
  Катедра војнохемијског инжењерства, Београд, Република Србија

[б] Војнотехнички институт, Београд, Република Србија

[в] Универзитет у Београду, Технолошко-металуршки факултет,
  Београд, Република Србија

Сажетак:

Увод/циљ: Антикорозивна заштита челичне арматуре у бетону представља кључни изазов у грађевинарству, нарочито у изградњи бетонских конструкција намењених за војне сврхе. Тренутно,

2030

Bučko, M. et al, Corrosion of Zn-Ni coated reinforcing steel in simulated concrete pore solutions, pp.2012-2031

најважније методе за постизање ове заштите укључују примену епоксидних или топлоцинкованих превлака, употребу арматуре од нерђајућег челика или композитних материјала, или бетона који садржи инхибиторе корозије, површинске заптиваче, силицијумску прашину или додатак летећег пепела.

Методе: Ова студија има за циљ да утврди да ли превлака од легуре Zn-Ni одговарајуће дебљине, нанета електрохемијским таложењем, може дати бољу и дуготрајнију отпорност на корозију арматурног челика у бетону, у поређењу са традиционалном превлаком Zn која се обично примењује у ту сврху. Нанете превлаке Zn-Ni биле су дебљине 40 μm и садржале су око 13 mas. % Ni.

Резултати: Снимање електронским микроскопом открило је да су превлаке имале глатку и хомогену морфологију, иако су показивале микропукотине које су се протезале кроз целу њихову дубину. Заштитна ефикасност превлаке оцењена је електрохемијском импеданцијском спектроскопијом, при чему су узорци били потопљени у различите електролите који симулирају хемијске услове присутне у различитим врстама бетона. Мерења су показала знатно мању брзину растварања продукта корозије формираног на превлаци Zn-Ni у електролиту богатом хлоридима, у поређењу са чистим Zn.

Закључак: Може се закључити да легура Zn-Ni представља одрживу алтернативу чистом Zn, за заштиту челика у бетонским конструкцијама где се очекује висока пенетрација хлорида.

Кључне речи: корозија челичне арматуре, превлака Zn-Ni, електролит у порама бетона, електрохемијско таложење.

EDITORIAL NOTE: The first author of this article, Mihael Bučko, is a current member of the Editorial Board of the *Military Technical Courier*. Therefore, the Editorial Team has ensured that the double blind reviewing process was even more transparent and more rigorous. The Team made additional effort to maintain the integrity of the review and to minimize any bias by having another associate editor handle the review procedure independently of the editor – author in a completely transparent process. The Editorial Team has taken special care that the referee did not recognize the author's identity, thus avoiding the conflict of interest.

Paper received on: 14.02.2024.
Manuscript corrections submitted on: 16.11.2024.
Paper accepted for publishing on: 18.11.2024.

© 2024 The Authors. Published by Vojnotehnički glasnik / Military Technical Courier (www.vtg.mod.gov.rs, втг.мо.упр.срб). This article is an open access article distributed under the terms and conditions of the Creative Commons Attribution license (http://creativecommons.org/licenses/by/3.0/rs/).

САВРЕМЕНО НАОРУЖАЊЕ И ВОЈНА ОПРЕМА

СОВРЕМЕННОЕ ВООРУЖЕНИЕ И ВОЕННОЕ ОБОРУДОВАНИЕ

MODERN WEAPONS AND MILITARY EQUIPMENT

Руска нова балистичка ракета *Iskander-1000* угрожава украјинске *F-16* и пола Европе[1]

Руски председник Владимир Путин изјавио је, 28. јуна 2024, да би Русија могла да започне производњу и распоређивање ракета средњег и краћег домета као одговор на слична распоређивања САД ван њихове територије. Ове ракете би потенцијално могле да укључују *Iskander-1000*, који је први пут представљен јавности у мају 2024. у видео-снимку поводом 78. годишњице тестирања ракете *Kapustin Yar*. Према руским изворима, ове ракете би могле да буду распоређене у Калињинграду или Смоленској области, што би Русији омогућило да потенцијално угрози скоро половину европских земаља, као и поморске објекте у Балтичком мору.

Балистичка ракета средњег домета Iskander-1000, која се тренутно развија у Руском конструкционом бироу за машиноградњу (Коломна). (Извор фотографије: руске друштвене мреже)

Изјава руског председника уследила је након изјаве главнокомандујућег стратешких ракетних снага, 17. децембра 2023. године, у којој се указује да би руски војноиндустријски комплекс могао брзо да започне производњу и снабдевање овим ракетним системима ако буде

---

[1] Defense News Army 2024 1 August

потребно. Руско Министарство спољних послова потврдило је да ће производња започети 6. маја 2024. године.

Једна од ових ракета могла би бити, како се незванично сазнаје, балистичка ракета средњег домета *Iskander-1000,* која је тренутно у развоју у Руском конструкционом бироу за машиноградњу (Коломна). Заснована је на балистичком ракетном систему *9K720 Iskander-M*, који има домет до 1.000 километара, двоструко већи од тренутног домета ракете *Iskander-M*. Ова нова ракета први пут је представљена јавности у мају 2024. у видео-снимку поводом 78. годишњице полигона за ракете *Kapustin Yar*.

Развој ракете *Iskander-1000* прате извештаји који сугеришу побољшања ракета *Iskander* и *Kinzhal* која се односе на већи домет, снажније бојеве главе и побољшане могућности за пробијање противавионске одбране. Овај развој догађаја представља одговор Русије на поступање САД и њених савезника, посебно након што су Американци објавили планове, у јулу 2024, да ће распоредити ракете дугог домета у Немачку. Председник Путин је наговестио да ће Русија, на основу акција САД и њихових савезника, предузети реципрочне мере. Потенцијално распоређивање ракета *Iskander-1000* у регионима попут Смоленска такође би могло да представља значајну претњу за новопристигле украјинске борбене авионе *F-16*

Извештаји сугеришу да ће Iskander-1000 задржати класични распоред ракета 9M723-1/K5, али са повећањем запремине пуњења чврстим горивом од 10 до 15%, као и модернизованим мотором, побољшаним системом контроле и ревидираном бојевом главом. (Извор фотографије: руски друштвени медији)

Ова нова руска балистичка ракета вероватно ће имати аутономни инерцијални систем за навођење, могуће са корекцијом сателитске навигације и можда радарским навођењем на основу мапе терена циљног подручја током завршне фазе лета. Процењује се да је одступање пројектила од циља унутар 5 метара.

Како би се олакшало распоређивање ракете *Iskander-1000*, очекује се да ће бити лансирана помоћу стандардних лансера *Iskander*, који деле

структурне сличности са балистичком ракетом 9М723 из тактичког ракетног система *Iskander*. Предвиђа се да ће погонски систем бити ракетни мотор на чврсто гориво, сличан ракети 9М723, али потенцијално јачи. Могао би да користи нови тип ракетног горива већег импулса, вероватно на бази октогена, са специфичним импулсом до 480 јединица.

Према доступним информацијама, ово ново гориво може да покрене ракету до брзина од 2.700 до 3.100 м/с, испоручујући високоексплозивне парчадне (HE-Frag) или касетне бојеве главе масе до 350 кг на удаљеностима од 900 до 1.000 км или мање бојеве главе до 1.250,или 1.300 км. Ракета ће имати гаснодинамичко управљање и аеродинамичка кормила за маневрисање, капацитета оптерећења до 25, односно 30 јединица. Такође, укључиваће INS и модул за корекцију Comet-P8 GLONASS/GPS или систем за електронско ратовање у опсегу X/J/Ka.

Предност нове модификације ракете Iskander у односу на друге системе, као што је MiG-31K који носи балистичке ракете Kh-47M2 Kinzhal, јесте њена способност да знатно смањи време детекције и одзива. (Фотографија преузета из МО Русије)

Развој ракете *Iskander-1000* има потенцијалне импликације за НАТО и украјинске снаге. Предност ове нове модификације у односу на друге системе, као што је MiG-31K који носи ваздухопловне балистичке ракете Kh-47M2 *Kinzhal*, јесте њена способност да знатно смањи време детекције и одзива. Систем MiG-31K скоро одмах по полетању детектују радари ПВО и оптичко-електронски извиђачки сателити, који могу да прате летелицу и дању и ноћу. Ово рано откривање даје особљу у стратешки важним објектима у Украјини упозорење од 15 до 20 мин пре удара.

Насупрот томе, ракетни мотори ракете *Iskander-1000* на чврсто гориво генеришу топлотноконтрастне бакље које су видљиве само током активних фаза лета, што значи краће време упозорења од само 2 до 7 мин, у зависности од удаљености мете, што компликује напоре противваздухопловне одбране у пресретању система као што су *Patriot, SAMP-T* и *Iris-T SLM.*

Владимир Путин је недавно изјавио да би Русија могла да започне са распоређивањем ракета средњег домета као одговор на слична распоређивања америчких ракета у Немачкој. Стога руски војни експерти верују да би неколико региона могло да стационира ове ракете средњег домета. Тако би Смоленска област, заједно са Вороњешком и Московском регијом, могла да понуди стратешку дубину а да није близу граница, а Калињинградска област би могла имати стратешку предност, јер би потенцијално време лета од Калињинградске области до америчких ракетних база у Немачкој могло бити мање од 8 мин.

Очекује се да ће ракета Iskander-1000 бити лансирана помоћу стандардних лансера Iskander, који имају структурне сличности са балистичком ракетом 9M723 из тактичког ракетног система Iskander. (Извор фотографије: Виталиј Кузмин)

Ако Русија распореди балистичку ракету домета 1.000 км у Калињинграду или Смоленској области, неколико земаља би се нашло у њеном домету због своје близине. Из Калињинграда, који се налази на Балтичком мору и граничи се са Пољском на југу и Литванијом на северу и

истоку, ракета домета 1.000 км могла би да досегне до значајног дела Европе, укључујући Пољску, Литванију, Летонију, Естонију, Немачку, Данску, Шведску , Чешку, Словачку и Белорусију. Ова област, такође, потенцијално укључује делове Финске, Украјине и Норвешке, у зависности од тачних локација које су циљане унутар ових земаља.

Из региона Смоленска, који се налази источније унутар Русије и ближе западној граници земље, ракета домета 1.000 км могла би да угрози Белорусију, Украјину, Пољску, Литванију, Летонију, Естонију, Молдавију и делове Румуније. Ово распоређивање би, такође, обухватило делове Балтичког мора, што би потенцијално могло утицати на поморске руте и поморске операције у региону.

Стратешке локације Калињинграда и Смоленска омогућавају Русији да потенцијално циља бројне земље чланице НАТО-а и ЕУ, што изазива велику безбедносну забринутост у региону. Распоређивање ракета *Искандер-1000* у овим областима повећало би способност Русије да угрози критична средства Европе, али и подстакло даље одбрамбене мере Украјине, што би могло додатно ограничити употребу њених новопристиглих *F-16*.

Недавни долазак борбених авиона *F-16* у Украјину из арсенала НАТО савезника, укључујући шест авиона из Холандије, означава значајан корак у јачању одбрамбених способности Украјине.Фотографија коју је објавила украјинска публикација „Думскаиа", 31. јула 2024, приказује авион *F-16* који лети изнад Украјине, што је била потврда да је испоручен. Овај развој догађаја део је текућих напора Украјине да се супротстави руским ваздушним претњама.

Међутим, ови млазњаци представљају и потенцијалне мете за *Iskander-1000*. Руски председник Владимир Путин упозорио је да ће се свака западна ваздухопловна база у којој се налазе авиони *F-16* намењени Украјини сматрати легитимном метом руских снага, укључујући аеродроме у земљама НАТО-а, као што су Пољска и Румунија. Способност ракете *Искандер-1000* да погоди циљеве са високом прецизношћу и минималним временом упозорења повећава рањивост ових ваздухопловних база и склоништа.

Украјина се припрема за долазак *F-16* тако што обучава своје пилоте у иностранству и унапређује системе противваздухопловне одбране. Упркос овим напорима, потенцијално распоређивање ракета *Iskander-1000* у регионима попут Смоленска могло би да представља значајну претњу оперативној ефикасности *F-16*. Проширени домет ракете и способност да избегне пресретање чине је новим руским оружјем за гађање кључних украјинских ваздушних база и склоништа, што потенцијално утиче на распоређивање и ефикасност нових украјинских борбених авиона.

Иначе, ракетни систем *Iskander* није адекватно коришћен на почетку Специјалне војне операције у Украјини. Наиме, систем одлучивања био је врло централизован, могло би се рећи бирократизован. Снимци свих руских расположивих сензора прослеђивани су у надлежну команду која је

2036

одлучивала о коришћењу ракетног система. Тек након њихове одлуке долазило би до употребе ракете *Iskander* на циљ. Време доношења одлуке након прегледа стационарних и покретних циљева било је и дуже од 24 часа, што је украјинским снагама омогућавало доста времена да промене локације покретних циљева. Уназад неколико месеци до годину дана дошло је до значајне промене употребе система *Iskander* који сада ради у пару са осматрачким беспосадним летелицама и одмах, неколико минута након лоцирања циља, бива употребљен врло успешно. Руска војска је до сада имала великих проблема са америчким мобилним ракетним системима типа HIMARS којима је требало неколико минута да се релоцирају након испаљивања борбеног комплета. Након промене тактике употребе система *Iskander* циљеви се врло успешно уништавају.

Украјинска војска, као ни стручњаци НАТО-а, још увек нису пронашли ефикасан начин на који би се уништавале ракете типа *Iskander*.

Драган М. Вучковић (*Dragan* M. Vučković),
e-mail: draganvuckovic64@gmail.com,
ORCID iD: https://orcid.org/0000-0003-1620-5601

Компанија *Lockheed Martin* представља крстарећу ракету великог домета *JASSM XR*[2]

Шеснаестог септембра 2024. године, током Ваздушне, свемирске и сајбер конференције Удружења ваздушних и свемирских снага, компанија „Lockheed Martin" је представила најновију верзију своје крстареће ракете AGM-158B JASSM, познату као JASSM XR (eXtreme Range). Она је пројектована тако да одржи могућности прикривености и прецизности удара, а њен домет супериорнији је од постојеће ракете JASSM-ER.

До сада су постојале три верзије: *AGM-158A: JASSM* основна верзија ваздух-земља; *AGM-158B JASSM-ER*, верзија ваздух-копно проширеног домета и *AGM-158C LRASM* (противбродска ракета дугог домета), противбродска варијанта која се може употребити у операцијама ваздух-море или море-море преко вертикалних лансирних ћелија *Mk 41 VLS*.

Крстарећа ракета *AGM-158 XR* има за циљ да још више помери границе домета. Иако технички детаљи остају ограничени, Michael Rothstein, потпредседник за стратегију и потребе у компанији „Lockheed Martin Missiles and Fire Control", изјавио је да је домет знатно другачији. Подсећања ради, америчко ратно ваздухопловство објавило је да JACCM-ER има домет већи од 500 наутичких миља, односно више од 926 км.

---

[2] Defense News Army 2024 17 Sep, 2024

Ракета JASSM XR задржава исту бојеву главу од 1.000 фунти (453,6 кг), као и ракета JASSM-ER, а структурне промене су направљене на основу модела JASSM-ER и LRASM. (Извор фотографије: Lockheed Martin)

Jon Hill, потпредседник и генерални директор ресора ваздушне доминације и ударног оружја у компанији „Lockheed Martin Missiles and Fire Control", објаснио је да је JASSM XR пројектован да буде следећа итерација ракетама JASSM-D и LRASM-C3, које су тренутно уговорене са америчким ратним ваздухопловством и морнарицом. Хил је нагласио да XR користи постојеће производне линије и процесе, односно да представља ракету екстремног домета и да проширује постојећу породицу JASSM и LRASM како би се омогућило складиштење више горива, што би омогућило већи домет.

Ракета JASSM XR задржава исту бојеву главу од 1.000 фунти (453,6 кг) као JASSM-ER. Структурне промене су извршене на основу модела JASSM-ER и LRASM. Ракета је дужа, што јој омогућава да носи више горива, чиме се повећава њен домет. Остала потенцијална побољшања могу укључивати употребу лакших легура, побољшану аеродинамику, редизајнирану структуру, модификована пераја и ефикаснији погонски систем. Физичке модификације биле су неопходне да би се побољшао домет, укључујући продужење структуре како би ракета примила више горива. Упркос овим променама, циљ је био да се поново искористи што више технологије и компоненти из тренутне производње ракета.

Упркос овим модификацијама, пројектил задржава своје карактеристике прикривености и прецизности. Проширени домет омогућава лансирним посадама да распореде *JASSM XR* са веће удаљености, омогућавајући ударе по дубљим циљевима док остају ван домашаја непријатељских система противваздухопловне одбране.

Међутим, повећање укупне тежине пројектила спречава одређене борбене авионе, као што је *F-16 Fighting Falcon*, да их носе. Насупрот томе, *F/A-18,* вероватно у верзији *F/A-18E/F Super Hornet*, већ је компатибилан. Такође, очекује се да ће *F-35 Lightning II* бити компатибилан у блиској будућности, заједно са ловцем-бомбардером *F-15 Eagle*. Иако нема конкретних информација о стратешким бомбардерима, видео-презентација компаније *Lockheed Martin* често приказује бомбардер *B-1B Lancer*.

Поред тога, велики капацитет носивости бомбардера *B-52H Stratofortress* не би требало да представља проблем, а ракета JASSM XR ће вероватно бити интегрисана у одељак за муницију бомбардера *B-2A Spirit и B-21 Raider* стелт бомбардера америчког ратног ваздухопловства.

Компанија „Lockheed Martin" је, такође, настојала да оптимизује трошкове развоја коришћењем постојећих производних линија и дизајна ракета *JASSM* и *LRASM*. Модуларна природа пројектила наговештава могућност противбродске употребе. Док *LRASM* може бити лансиран из ћелија бродског лансирног система Mk 41 VLS на разарачима и крстарицама америчке морнарице, остаје да се види да ли ће *JASSM XR* такође бити интегрисан у ове системе.

Питање је какве су потенцијалне способности лансирања са транспортних авиона. Ракете *JASSM* и *JASSM-ER* могу се утоварити на стандардну структуру палета познату као *Rapid Dragon*. Када се отвори летелица, палета се избацује помоћу падобрана, а ракете покрећу своје моторе током слободног пада. Тежа и већа ракета може захтевати прилагођавање овом систему или развој XR верзије *Rapid Dragon*.

Ракета *JASSM XR* још није у употреби, а први лет прототипа планиран је за 2025. или 2026. годину. Америчко ратно ваздухопловство или морнарица нису наручили овај ракетни систем, а цео развој финансира компанија „Lockheed Martin". Без обзира на то, а с обзиром на своје способности, ова нова ракета могла би да има значајну улогу у сузбијању „anti-access" и „area-denial" systems (система против приступа и ускраћивања области), посебно оних које је Кина поставила у Јужном кинеском мору.

Током #AFA2024 конференције, Џон Хил је објаснио да се *AGM-158 XR* развија проактивно како би испунио будуће захтеве САД, наследивши ракете *AGM-158D JASSM-ER* и *AGM-158C LRASM*. Детаљи остају непознати, осим потврде о издуженом трупу. Чињеница да Ф-16 не може да носи*JASSM XR* због његове тежине од 4.500 фунти која премашује капацитет унутрашње станице овелетелице, говори о повећаној маси пројектила.

Чини се да су спроведене неке инжењерске промене, које су укључивале мање, али паметне унутрашње структурне модификације како би се постигло издужење пројектила.

Иначе, ове врсте ракета нису још испробане на украјинском ратишту, бар не до сада и не званично, али јесу европске верзије, британско-француске крстареће ракете *Storm Shadow* и *Scalp* које дефинитивно нису „невидљиве" за руске радаре и ракетне системе. Остаје да се види како ће се показати нова верзија америчке крстареће ракета ако буде усвојена у наоружање.

Драган М. Вучковић (*Dragan* М. Vučković),
e-mail: draganvuckovic64@gmail.com,
ORCID iD: https://orcid.org/0000-0003-1620-5601

Нови кинески јуришни хеликоптер *Z-10МЕ* представљен на међународном тржишту на ААД 2024[3]

На сајму наоружања Africa Aerospace and Defence (AAD) 2024 у Јужној Африци, кинеска компанија *Aviation Industry Corporation of China (AVIC)* представила је јуришни хеликоптер *Z-10МЕ*. Овај модел је извозно побољшана верзија оригиналног *Z-10* и пројектован је као вишенаменски средњи јуришни хеликоптер од 6 т за све временске услове. У хеликоптер *Z-10МЕ* уведено је неколико побољшања ради оптимизације његових борбених способности и укупних перформанси, одражавајући сталне напоре Кине да ојача своје присуство на глобалном тржишту одбране. Први купац овог модела је наводно Пакистан.

Развој Z-10МЕ је први пут приказан на 11. сајму авиона у Џухају у новембру 2016. године. Од тада је приказиван и на другим великим одбрамбеним догађајима, укључујући *Dubai Air Show 2017*. и 12. *Zhuhai Air Show* у новембру 2018, где је званично представљена коначна верзија хеликоптера. Летелица има аеродинамичан труп, један ротор са репним ротором, тандем-кокпит и задњи распоред стајног трапа у три тачке, што је чини погодном за различите оперативне сценарије.

Једно од кључних побољшања овог хеликоптера јесте његов унапређени мотор –*WZ-9G* који замењује претходни *WZ-9* и који повећава излазну снагу са 1.250 КС на 1.500 КС. Ово повећање снаге је допуњено редизајнираним усисником мотора са центрифугалним сепарационим пешчаним филтером, побољшавајући перформансе хеликоптера у песковитим и ветровитим срединама. Поред тога, издувни отвор је премештен нагоре како би се смањио инфрацрвени одраз хеликоптера. Наиме, коришћењем протока ваздуха надоле потенцијално би се повећала способност преживљавања услед инфрацрвених претњи.

---

[3] Defense News Aerospace 2024, 19 Sep, 2024

Хеликоптер Z-10ME сада користи WZ-9G мотор, замењујући ранији WZ-9 који повећава излазну снагу са 1.250 КС на 1.500 КС. (Извор фотографије: Army Recognition)

Хеликоптер *Z-10ME* такође поседује додатни оклоп око трупа и кокпита, пружајући побољшану заштиту од ватре из малокалибарског оружја. Опремљен је системима противмера, укључујући инфрацрвене/ултраљубичасте аларме и ласерске противмере, као и активни инфрацрвени систем за ометање и опрему за упозорење на приближавање пројектила на својим кратким крилима. Ове карактеристике побољшавају авионику и системе контроле ватре оригиналног *Z-10,* омогућавајући посади да боље прати ситуацију и одбрамбене способности. Поред тога, *Z-10ME* је дизајниран да носи уређаје за ометање у оквиру мисија електронског ратовања.

Што се тиче наоружања, *Z-10ME* има топ калибра 23 мм и четири спољна упоришта, са носивошћу до три тоне. Ова разноврсна опрема му омогућава да носи широку лепезу оружја, укључујући ракете ваздух-земља и противоклопне ракете, ракете ваздух-ваздух, подвесне топове, вођене бомбе и мале дронове. Такође, може да понесе до 16 противтенковских вођених пројектила, четири подвесна контејнера са невођеним ракетама са по 7 цеви или два лансера невођених ракета са по 32 цеви. Поред тога, компатибилан је са муницијом као што су вођене бомбе *GB-25/50* и невођене ракете ваздух-земља калибра 57 мм, а може да лансира и дронове *SW-6* и бомбе *CM-501XA*, додатно проширујући своје оперативне могућности.

Хеликоптер Z-10ME је приказан на изложби наоружања AAD 2024 са различитим врстама наоружања које је обезбедила кинеска компанија CATIC. (Извор фотографије: ArmyRecognition)

Хеликоптер *Z-10ME* је опремљен радарским системом милиметарских таласа постављеним изнад главног ротора, пројектованим тако да побољша његове могућности нишањења. Овај систем му омогућава да ефикасније води противтенковске ракете великог домета и другу муницију, пружајући значајну тактичку предност у борбеним ситуацијама.

Главни конструктор *Wu Ximing* упоређује *Z-10ME* са другим хеликоптерима у својој класи, као што су руски *Ka-52* и *Mi-28,* амерички *Apache* и европски *Tiger*. Према конструктору, *Z-10ME* се такмичи у погледу маневрисања, борбеног радијуса и способности обављања више задатака. Анализа сугерише да се *Z-10ME* може похвалити оперативним дометом од 800 км, надмашујући пријављени домет од 480 км америчког хеликоптера *Apache,* док се такође узима у обзир однос снаге и тежине и агилност.

Поред ових карактеристика, Z-10ME је приказан на сајму наоружања AAD 2024 са лепезом наоружања које је обезбедила кинеска компанија CATIC. Међу овим наоружањем су:

– муниција 23 мм: високоексплозивна запаљива муниција 23-2А која достиже брзину од 720±10 м/с и укључује временски упаљач од 4 до 14 с, обезбеђујући контролисану детонацију и пробојно-запаљива муниција 23-2 *(Armor-Piercing Incendiary Tracer Ammunition)* способна да пробије челичну плочу дебљине 10 мм под углом од 30° на 200 м, што доприноси свестраности ватрене моћи хеликоптера;

AAD 2024 © Army Recognition

Наоружање Z-10ME чине топ калибра 23 мм и четири спољне подвесне тачке, са носивошћу до три тоне. (Извор фотографије: ArmyRecognition)

– вођена ракета *GR5*: има ефективни домет од 2 до 6 км и прецизност са радијусом погађања од ≤2м. Опремљена је експлозивном бојевом главом, а радијус уништења износи 18 м. Способност продирања фрагмената бојеве главе омогућава пробијање челичне плоче дебљине 6 мм на 8 м, побољшавајући офанзивне опције хеликоптера;

– ракета ваздух-ваздух *TY-90:* дизајнирана је за гађање ваздушних циљева. Има домет од 500 до 6000 м, тешка је 20 кг и дугачка 1862 мм. Погодна је за хеликоптере, беспилотне летелице и разне летелице, пружајући хеликоптеру Z-10ME значајне ваздушне борбене способности;

– *CM-502KG* ракета ваздух-земља: пројектована је за гађање циљева на земљи, са максималним дометом од 25 км и чврстим ракетним мотором. Има експлозивно-фрагментациону или оклопну бојеву главу масе12 кг. Систем навођења комбинује *MEMS INS* са *GNSS* нудећи терминалне опције навођења преко ТВ-а, инфрацрвених или ласерских трагача;

– невођена ракета *FS70B*: опремљена је распрскавајућом бојевом главом. Калибар ракете је 70 мм, има домет од 5,5 км када се испаљује под углом од 13,5°, а радијус уништења је 21 м, што је чини моћним додатком арсеналу хеликоптера.

Презентација овог наоружања, као и самог *Z-10ME* на сајму наоружања *AAD 2024,* наглашава свестраност овог хеликоптера и његов

потенцијал за обављање низа мисија – од блиске ваздушне подршке до борбе ваздух-ваздух.

Представљање *Z-10ME* на сајму наоружања *AAD 2024* одражава фокус компаније *AVIC* на проширење свог тржишног удела у глобалној одбрамбеној индустрији. Напредне карактеристике овог хеликоптера, у комбинацији са његовим свестраним борбеним способностима и широким опцијама наоружања, позиционирају га као конкурентну понуду за земље које траже ефикасан и флексибилан хеликоптер за напад. Уз континуиране напоре Кине за унапређење својих одбрамбених технологија, *Z-10ME* је спреман за потенцијални продор на међународно тржиште.

Драган М. Вучковић (*Dragan* M. Vučković),
e-mail: draganvuckovic64@gmail.com,
ORCID iD: https://orcid.org/0000-0003-1620-5601

ПОЗИВ И УПУТСТВО АУТОРИМА О НАЧИНУ ПРИПРЕМЕ ЧЛАНКА

Упутство ауторима о начину припреме чланка за објављивање у *Војнотехничком гласнику* урађено је на основу Правилника о категоризацији и рангирању научних часописа Министарства просвете, науке и технолошког развоја Републике Србије ("Службени гласник РС", број 159/20). Примена овог Правилника првенствено служи унапређењу квалитета домаћих часописа и њиховог потпунијег укључивања у међународни систем размене научних информација.

Војнотехнички гласник / Vojnotehnički glasnik / Military Technical Courier (втг.мо.упр.срб, www.vtg.mod.gov.rs, ISSN 0042-8469 – штампано издање, e-ISSN 2217-4753 – online, UDC 623+355/359, DOI: 10.5937/VojnotehnickiGlasnik; https://doi.org/10.5937/VojnotehnickiGlasnik), јесте рецензирани научни часопис.

Власници часописа су Министарство одбране Републике Србије и Војска Србије. Издавач и финансијер часописа је Универзитет одбране у Београду (Војна академија).

Програмска оријентација часописа заснива се на годишњој категоризацији часописа, коју врши надлежно државно министарство у одређеним областима, као и на његовом индексирању у међународним индексним базама.

Часопис обухвата научне, односно стручне области у оквиру образовно-научног поља **природно-математичких наука**, као и у оквиру образовно-научног поља **техничко-технолошких наука**, а нарочито области **одбрамбених наука и технологија**. Објављује теоријска и практична достигнућа која доприносе усавршавању свих припадника српске, регионалне и међународне академске заједнице, а посебно припадника војски и министарстава одбране. Публикује радове са уравнотеженим извештавањем о аналитичким, експерименталним и примењеним истраживањима, као и нумеричким симулацијама, обухватајући различите дисциплине. Објављени материјали су високог квалитета и релевантности, написани на начин који их чини доступним широкој читалачкој публици. Сви радови који извештавају о оригиналним теоријским и/или практично оријентисаним истраживањима или проширеним верзијама већ објављених радова са конференција су добродошли. Радови за објављивање одабиру се двоструко слепим поступком рецензије како би се осигурала оригиналност, релевантност и читљивост. Притом циљ није само да се квалитет објављених радова одржи високим већ и да се обезбеди правовремени, темељни и уравнотежени поступак рецензије.

Уређивачка политика *Војнотехничког гласника* заснива се на препорукама Одбора за етичност у издаваштву (COPE Core Practices) и заједничким принципима транспарентности и најбоље праксе у издаваштву COPE, DOAJ, OASPA и WAME, као и на најбољим прихваћеним праксама у научном издаваштву. *Војнотехнички гласник* је члан COPE (Committee on Publication Ethics) од 2. маја 2018. године и члан OASPA (Open Access Scholarly Publishers Association) од од 27. новембра 2015. године.

Министарство науке, технолошког развоја и иновација Републике Србије утврдило је дана 27. 12. 2023. године категоризацију *Војнотехничког гласника*, за 2023. годину:

– **на листи часописа за рачунарске науке:**
категорија врхунски часопис националног значаја **(М51)**,

– **на листи часописа за електронику, телекомуникације и информационе технологије:**
категорија врхунски часопис националног значаја **(М51)**,

– **на листи часописа за машинство:**
категорија национални часопис међународног значаја **(М24)**,

– **на листи часописа за материјале и хемијске технологије:**
категорија национални часопис међународног значаја **(М24)**.

Усвојене листе домаћих часописа за 2023. годину могу се видети на сајту *Војнотехничког гласника*, страница *Категоризација часописа*.

Детаљније информације могу се пронаћи и на сајту Министарства просвете, науке и технолошког развоја Републике Србије.

Подаци о категоризацији могу се пратити и на сајту КОБСОН-а (Конзорцијум библиотека Србије за обједињену набавку).

Категоризација часописа извршена је према Правилнику о категоризацији и рангирању научних часописа Министарства просвете, науке и технолошког развоја Републике Србије ("Службени гласник РС", број 159/20).

Часопис се прати у контексту Српског цитатног индекса – СЦиндекс (база података домаћих научних часописа), Научно-информационог система Redalyc и Руског индекса научног цитирања (РИНЦ). Подвргнут је сталном вредновању (мониторингу) у зависности од утицајности (импакта) у самим базама. Детаљи о индексирању могу се видети на сајту *Војнотехничког гласника*, страница *Индексирање часописа*.

Војнотехнички гласник, у погледу свог садржаја, пружа могућност отвореног приступа (DIAMOND OPEN ACCESS) и примењује Creative Commons (CC BY) одредбе о ауторским правима. Детаљи о ауторским правима могу се видети на сајту часописа, страница *Ауторска права и политика самоархивирања*.

Радови се предају путем онлајн система за електронско уређивање АСИСТЕНТ, који је развио Центар за евалуацију у образовању и науци (ЦЕОН).

Приступ и регистрација за сервис врше се на сајту www.vtg.mod.gov.rs, преко странице *АСИСТЕНТ* или *СЦИНДЕКС*, односно директно на линку aseestant.ceon.rs/index.php/vtg.

Детаљно упутство о регистрацији и пријави за сервис налази се на сајту www.vtg.mod.gov.rs, страница *Упутство за АСИСТЕНТ*.

Потребно је да се сви аутори који подносе рукопис за објављивање у *Војнотехничком гласнику* региструју у регистар ORCID (Open Researcher and Contributor ID), према упутству на страници сајта *Регистрација за добијање ORCID идентификационе шифре*.

Војнотехнички гласник објављује чланке на енглеском језику (arial, величина слова 11 pt, проред Single).

Поступак припреме, писања и уређивања чланка треба да буде у сагласности са *Изјавом о етичком поступању* (http://www.vtg.mod.gov.rs/izjava-o-etickom-postupanju.html).

Чланак треба да садржи сажетак са кључним речима, увод (мотивацију за рад), разраду (адекватан преглед репрезентативности рада у његовој области, јасну изјаву о новини у представљеном истраживању, одговарајућу теоријску

2046

позадину, један или више примера за демонстрирање и дискусију о представљеним идејама), закључак и литературу (без нумерације наслова и поднаслова). Обим чланка треба да буде до једног ауторског табака (16 страница формата А4 са проредом Single), а највише 24 странице.

Чланак треба да буде написан на обрасцу за писање чланка, који се у електронској форми може преузети са сајта на страници *Образац за писање чланка*.

Наслов

Наслов треба да одражава тему чланка. У интересу је часописа и аутора да се користе речи прикладне за индексирање и претраживање. Ако таквих речи нема у наслову, пожељно је да се придода и поднаслов.

Текући наслов

Текући наслов се исписује са стране сваке странице чланка ради лакше идентификације, посебно копија чланака у електронском облику. Садржи презиме и иницијал имена аутора (ако аутора има више, преостали се означавају са „et al." или „и др."), наслове рада и часописа и колацију (година, волумен, свеска, почетна и завршна страница). Наслови часописа и чланка могу се дати у скраћеном облику.

Име аутора

Наводи се пуно име и презиме (свих) аутора. Веома је пожељно да се наведу и средња слова аутора. Имена и презимена домаћих аутора увек се исписују у оригиналном облику (са српским дијакритичким знаковима), независно од језика на којем је написан рад.

Назив установе аутора (афилијација)

Наводи се пун (званични) назив и седиште установе у којој је аутор запослен, а евентуално и назив установе у којој је аутор обавио истраживање. У сложеним организацијама наводи се укупна хијерархија (нпр. Универзитет одбране у Београду, Војна академија, Катедра природно-математичких наука). Бар једна организација у хијерархији мора бити правно лице. Ако аутора има више, а неки потичу из исте установе, мора се, посебним ознакама или на други начин, назначити из које од наведених установа потиче сваки од наведених аутора. Афилијација се исписује непосредно након имена аутора. Функција и звање аутора се не наводе.

Контакт подаци

Адреса или е-адреса свих аутора даје се поред имена и презимена аутора.

Категорија (тип) чланка

Категоризација чланака обавеза је уредништва и од посебне је важности. Категорију чланка могу предлагати рецензенти и чланови уредништва, односно уредници рубрика, али одговорност за категоризацију сноси искључиво главни уредник.

Војнотехнички гласник објављује научне чланке.

Научни чланак је:

– оригиналан научни рад (рад у којем се износе претходно необјављени резултати сопствених истраживања научним методом);

– прегледни рад (рад који садржи оригиналан, детаљан и критички приказ истраживачког проблема или подручја у којем је аутор остварио одређени допринос, видљив на основу аутоцитата);

– кратко или претходно саопштење (оригинални научни рад пуног формата, али мањег обима или прелиминарног карактера);

– научна критика, односно полемика (расправа на одређену научну тему, заснована искључиво на научној аргументацији) и осврти.

Изузетно, у неким областима, научни рад у часопису може имати облик монографске студије, као и критичког издања научне грађе (историјско-архивске, лексикографске, библиографске, прегледа података и сл.), дотад непознате или недовољно приступачне за научна истраживања.

Радови класификовани као научни морају имати бар две позитивне рецензије.

Ако се у часопису објављују и прилози ваннаучног карактера, научни чланци треба да буду груписани и јасно издвојени у првом делу свеске.

Пожељно је да обим кратких саопштења буде 4 до 7 страница, научних чланака и студија случаја 10 до 14 страница, док прегледни радови могу бити и дужи. Број страница није строго ограничен и, уз одговарајуће образложење, пријављени чланци такође могу бити дужи или краћи.

Ако су радови који су претходно објављени на конференцији проширени, уредници ће проверити да ли је додато довољно новог материјала који испуњава стандарде часописа и квалификује поднесак за поступак рецензије. Додати материјал не сме бити претходно објављен. Нови резултати нису нужно потребни, али су пожељни. Међутим, поднесак треба да садржи проширене кључне идеје, примере, разраде, итд., који су претходно били садржани у поднеску са конференције.

Језик рада

Језик рада треба да буде енглески.

Текст мора бити језички и стилски дотеран, систематизован, без скраћеница (осим стандардних). Све физичке величине морају бити изражене у Међународном систему мерних јединица – SI. Редослед образаца (формула) означава се редним бројевима, са десне стране у округлим заградама.

Сажетак

Сажетак јесте кратак информативан приказ садржаја чланка који читаоцу омогућава да брзо и тачно оцени његову релевантност. У интересу је уредништва и аутора да сажетак садржи термине који се често користе за индексирање и претрагу чланака. Саставни делови сажетка су увод/циљ истраживања, методи, резултати и закључак. Сажетак треба да има од 100 до 250 речи и треба да се налази између заглавља (наслов, имена аутора и др.) и кључних речи, након којих следи текст чланка.

Кључне речи

Кључне речи су термини или фразе које адекватно представљају садржај чланка за потребе индексирања и претраживања. Треба их додељивати ослањајући се на неки међународни извор (попис, речник или тезаурус) који је најшире прихваћен или унутар дате научне области. За нпр. науку уопште, то је листа кључних речи Web of Science. Број кључних речи не може бити већи од 10, а у интересу је уредништва и аутора да учесталост њихове употребе буде што већа. У чланку се пишу непосредно након сажетка.

Систем АСИСТЕНТ у ту сврху користи специјалну алатку KWASS: аутоматско екстраховање кључних речи из дисциплинарних тезауруса/речника по избору и рутине за њихов одабир, тј. прихватање односно одбацивање од стране аутора и/или уредника.

Датум прихватања чланка

Датум када је уредништво примило чланак, датум када је уредништво коначно прихватило чланак за објављивање, као и датуми када су у међувремену достављене евентуалне исправке рукописа наводе се хронолошким редоследом, на сталном месту, по правилу на крају чланка.

Захвалница

Назив и број пројекта, односно назив програма у оквиру којег је чланак настао, као и назив институције која је финансирала пројекат или програм, наводи се у посебној напомени на сталном месту, по правилу при дну прве стране чланка.

Претходне верзије рада

Ако је чланак у претходној верзији био изложен на скупу у виду усменог саопштења (под истим или сличним насловом), податак о томе треба да буде наведен у посебној напомени, по правилу при дну прве стране чланка. Рад који је већ објављен у неком часопису не може се објавити у *Војнотехничком гласнику* (прештампати), ни под сличним насловом и измењеном облику.

Табеларни и графички прикази

Пожељно је да наслови свих приказа, а по могућству и текстуални садржај, буду дати двојезично, на језику рада и на енглеском језику.

Табеле се пишу на исти начин као и текст, а означавају се редним бројевима са горње стране. Фотографије и цртежи треба да буду јасни, прегледни и погодни за репродукцију. Цртеже треба радити у програму word или corel. Фотографије и цртеже треба поставити на жељено место у тексту.

За слике и графиконе не сме се користити снимак са екрана рачунара програма за прикупљање података. У самом тексту чланка препоручује се употреба слика и графикона непосредно из програма за анализу података (као што су Excel, Matlab, Origin, SigmaPlot и други).

Навођење (цитирање) у тексту

Начин позивања на изворе у оквиру чланка мора бити једнообразан.

Војнотехнички гласник за референцирање (цитирање и навођење литературе) примењује Харвардски систем референци, односно Харвардски приручник за стил (Harvard Referencing System, Harvard Style Manual). У самом тексту, у обичним заградама, на месту на којем се врши позивање, односно цитирање литературе набројане на крају чланка, обавезно у обичној загради написати презиме цитираног аутора, годину издања публикације из које цитирате и, евентуално, број страница. Нпр. (Petrović, 2012, pp.10–12).

Детаљно упутство о начину цитирања, са примерима, дато је на страници сајта *Упутство за Харвардски приручник за стил*. Потребно је да се позивање на литературу у тексту уради у складу са поменутим упутством.

Систем АСИСТЕНТ у сврху контроле навођења (цитирања) у тексту користи специјалну алатку CiteMatcher: откривање изостављених цитата у тексту рада и у попису референци.

Напомене (фусноте)

Напомене се дају при дну стране на којој се налази текст на који се односе. Могу садржати мање важне детаље, допунска објашњења, назнаке о коришћеним

изворима (на пример, научној грађи, приручницима), али не могу бити замена за цитирану литературу.

Листа референци (литература)

Цитирана литература обухвата, по правилу, библиографске изворе (чланке, монографије и сл.) и даје се искључиво у засебном одељку чланка, у виду листе референци. Референце се не преводе на језик рада и набрајају се у посебном одељку на крају чланка.

Војнотехнички гласник, као начин исписа литературе, примењује Харвардски систем референци, односно Харвардски приручник за стил (Harvard Referencing System, Harvard Style Manual).

Литература се обавезно пише на латиничном писму и набраја по абецедном редоследу, наводећи најпре презимена аутора, без нумерације.

Детаљно упутство о начину пописа референци, са примерима, дато је на страници сајта *Упутство за Харвардски приручник за стил*. Потребно је да се попис литературе на крају чланка уради у складу са поменутим упутством.

Нестандардно, непотпуно или недоследно навођење литературе у системима вредновања часописа сматра се довољним разлогом за оспоравање научног статуса часописа.

Систем АСИСТЕНТ у сврху контроле правилног исписа листе референци користи специјалну алатку RefFormatter: контрола обликовања референци у складу са Харвардским приручником за стил.

Изјава о ауторству

Поред чланка доставља се *Изјава о ауторству* у којој аутори наводе свој појединачни допринос у изради чланка. Такође, у тој изјави потврђују да су чланак урадили у складу са *Позивом и упутством ауторима* и *Изјавом о етичком поступању часописа*.

Сви радови подлежу стручној рецензији.

Списак рецензената *Војнотехничког гласника* може се видети на страници сајта *Списак рецензената*. Процес рецензирања објашњен је на страници сајта *Рецензентски поступак*.

Уредништво

Адреса редакције:
Војнотехнички гласник
Веља Лукића Курјака 33
11042 Београд
e-mail: vojnotehnicki.glasnik@mod.gov.rs.
тел: војни 40-260 (011/3603-260), 066/8700-123

2050

ПРИГЛАШЕНИЕ И ИНСТРУКЦИЯ ДЛЯ АВТОРОВ О ПОРЯДКЕ ПОДГОТОВКИ СТАТЬИ

Инструкция для авторов о порядке подготовки статьи к опубликованию в журнале *«Военно-технический вестник»* разработана согласно Регламенту о категоризации и ранжировании научных журналов Министерства образования, науки и технологического развития Республики Сербия («Служебни гласник РС», № 159/20). Применение этого Регламента способствует повышению качества отечественных журналов и их более полному вовлечению в международную систему обмена научной информацией.

Военно-технический вестник (**Vojnotehnički glasnik / Military Technical Courier**), втг.мо.упр.срб, www.vtg.mod.gov.rs/index-ru.html, ISSN 0042-8469 – печатное издание, e-ISSN 2217-4753 – online, UDK 623+355/359, DOI: 10.5937/VojnotehnickiGlasnik; https://doi.org/10.5937/VojnotehnickiGlasnik, является рецензируемым научным журналом.

Собственники журнала: Министерство обороны и Вооруженые силы Республики Србия.

Издатель журнала: Университет обороны в г. Белград (Военная академия).

Программная ориентация журнала основана на ежегодной категоризации журнала, которая производится соответствующим отраслевым министерством, в зависимости от области исследований, а также на его индексировании в международных наукометрических базах данных.

Журнал охватывает научные и профессиональные сферы в рамках учебно-научной области **естественно-математических наук**, а также в рамках учебно-научной области **технико-технологических наук**, особенно в области **оборонных наук и технологии**. В журнале публикуются теоретические и практические достижения, которые способствуют повышению квалификации представителей сербского, регионального и международного академического сообщества, особенно служащих Министерств Обороны и Вооружённых сил. В журнале публикуются статьи со соответствующими обзорами об аналитических, экспериментальных и прикладных исследованиях, а также о численном моделировании, охватывая различные дисциплины. Публикуемые материалы отличаются высоким качеством и актуальностью. Они написаны научным, но понятным и доступным для широкого круга читателей языком. Приветствуются все статьи, сообщающие об оригинальных теоретических и/или практических исследованиях и/или расширенные версии ранее опубликованных статей, представленных на конференциях. Статьи для публикации отбираются путем двойного слепого рецензирования, которое гарантирует оригинальность, актуальность и удобочитаемость. Цель состоит не только в поддержании высокого качества публикуемых статей, но и в обеспечении своевременного, тщательного и соответствующего процесса рецензирования.

Редакционная политика журнала *«Военно-технический вестник»* основана на рекомендациях Комитета по этике научных публикаций (COPE Core Practices), общих принципах прозрачности и лучшей практике издательской деятельности COPE, DOAJ, OASPA и WAME, а также на лучшей практике научно-издательской деятельности. Журнал *«Военно-технический вестник»* является членом COPE (Комитет по этике научных публикаций) со 2 мая 2018 года и членом OASPA (Ассоциация научных издателей открытого доступа) с 27 ноября 2015 года.

Министерством науки, технологического развития и инноваций Республики Сербия утверждена 27 декабря 2023 г. категоризация журнала *«Военно-технический вестник»* за 2023 год:

- **Область компьютерные науки:**
ведущий журнал государственного значения **(М51)**,
- **Область электроники, телекоммуникаций и информационных технологий:**
ведущий журнал государственного значения **(М51)**,
- **Область машиностроения:**
национальный журнал международного значения **(М24)**,
- **Область материалов и химической технологии:**
национальный журнал международного значения **(М24)**.

С информацией относительно категоризации за 2023 год можно ознакомиться на странице сайта *«Военно-технического вестника» Категоризация Вестника*.

Более подробную информацию можно найти на сайте Министерства образования, науки и технологического развития Республики Сербия.

С информацией о категоризации можно ознакомиться и на сайте КОБСОН (Консорциум библиотек Республики Сербия по вопросам объединения закупок).

Категоризация Вестника проведена согласно Регламенту о категоризации и ранжировании научных журналов Министерства образования, науки и технологического развития Республики Сербия («Службени гласник РС», № 159/20)

Журнал соответствует стандартам Сербского индекса научного цитирования (СЦИндекс/SCIndeks) - наукометрической базы данных научных журналов Республики Сербия, Научно-информационного система Redalyc, а также Российского индекса научного цитирования (РИНЦ). Журнал постоянно подвергается мониторингу и оценивается количественными наукометрическими показателями отражающими его научную ценность.

С информацией об индексировании можно ознакомиться на странице сайта журнала *Индексирование Вестника*.

«Военно-технический вестник» относительно своего содержания предоставляет пользователям возможность открытого доступа (DIAMOND OPEN ACCESS) и положениями об авторских правах, утвержденными Creative Commons (CC BY). С инструкцией об авторских правах можно ознакомиться на странице сайта журнала *Авторские права и политика самоархивирования*.

Рукописи статей направляются в редакцию журнала с использованием online системы ASSISTANT, запущенной Центром поддержи развития образования и науки (ЦПРОН). Регистрация в системе и оформление прав доступа выполняется по адресу http://www.vtg.mod.gov.rs/index-ru.html, через страницу *ASSISTANT* или *СЦИНДЕКС* (aseestant.ceon.rs/index.php/vtg). С инструкцией по регистрации и правам доступа можно ознакомиться по адресу http://www.vtg.mod.gov.rs/index-ru.html, на странице *Инструкция по ASSISTANT*.

Все авторы, предоставляющие свои рукописи для публикации в редакцию журнала *«Военно-технический вестник»* должны пройти предварительную регистрацию в реестре ORCID (Open Researcher and Contributor ID). Эта процедура осуществляется в соответствии с инструкцией, размещенной на странице сайта *Регистрация в реестре ORCID для присвоения идентификационного кода*.

«Военно-технический вестник» публикует статьи на английском языке (Arial, шрифт 11 pt, пробел Single). Процесс подготовки, написания и редактирования статьи

должен осуществляться в соответствии с принципами *Этического кодекса* (http://www.vtg.mod.gov.rs/etichyeskiy-kodyeks.html). Статья должна содержать резюме с ключевыми словами, введение (цель исследования), основную часть (соответствующий обзор представительного исследования в данной области, четкое изложение научной новизны в представленном исследовании, соответствующую теоретическую основу, один или несколько примеров для демонстрирования и обсуждения представленных тезисов), заключение и список литературы (без нумерации заголовков и подзаголовков). Объем статьи не должен превышать один авторский лист (16 страниц формата А4 с одинарным интервалом, максимум до 24 страниц, включая ссылки и приложения). Статья должна быть набрана на компьютере с использованием специально подготовленного редакцией макета, который можно скачать на странице сайта *Правила и образец составления статьи*.

Заголовок

Заголовок должен отражать тему статьи. В интересах журнала и автора необходимо использовать слова и словосочетания, удобные для индексации и поиска. Если такие слова не содержатся в заголовке, то желательно их добавить в подзаголовок.

Текущий заголовок

Текущий заголовок пишется в титуле каждой страницы статьи с целью упрощения процесса идентификации, в первую очередь копий статьей в электронном виде. Заголовок содержит в себе фамилию и инициал имени автора (в случае если авторов несколько, остальные обозначаются с «et al.» или «и др.»), название работы и журнала (год, том, выпуск, начальная и заключительная страница). Заголовок статьи и название журнала могут быть приведены в сокращенном виде.

ФИО автора

Приводятся полная фамилия и полное имя (всех) авторов. Желательно, чтобы были указаны инициалы отчеств авторов. Фамилия и имя авторов из Республики Сербия всегда пишутся в оригинальном виде (с сербскими диакритическими знаками), независимо от языка, на котором написана работа.

Наименование учреждения автора (аффилиация)

Приводится полное (официальное) наименование и местонахождение учреждения, в котором работает автор, а также наименование учреждения, в котором автор провёл исследование. В случае организаций со сложной структурой приводится их иерархическая соподчинённость (напр. Военная академия, кафедра военных электронных систем, г. Белград). По крайней мере, одна из организаций в иерархии должна иметь статус юридического лица. В случае если указано несколько авторов, и если некоторые из них работают в одном учреждении, нужно отдельными обозначениями или каким-либо другим способом указать в каком из приведённых учреждений работает каждый из авторов. Аффилиация пишется непосредственно после ФИО автора. Должность и специальность по диплому не указываются.

Контактные данные

Электронный адрес автора указываются рядом с его именем на первой страницы статьи.

Категория (тип) статьи

Категоризация статьей является обязанностью редакции и имеет особое значение. Категорию статьи могут предлагать рецензенты и члены редакции, т.е.

редакторы рубрик, но ответственность за категоризацию несет исключительно главный редактор.

Журнал «*Военно-технический вестник*» публикует научные статьи.

Научные статьи:

– оригинальная научная статья (работа, в которой приводятся ранее неопубликованные результаты собственных исследований, полученных научным методом);

– обзорная статья (работа, содержащая оригинальный, детальный и критический обзор исследуемой проблемы или области, в который автор внёс определённый вклад, видимый на основе автоцитат);

– краткое сообщение (оригинальная научная работа полного формата, но меньшего объёма или имеющая предварительный характер);

– научная критическая статья (дискуссия-полемика на определённую научную тему, основанная исключительно на научной аргументации) и научный комментарий.

Однако, в некоторых областях знаний научная работа в журнале может иметь форму монографического исследования, а также критического обсуждения научного материала (историко-архивного, лексикографического, библиографического, обзора данных и т.п.) – до сих пор неизвестного или недостаточно доступного для научных исследований. Работы, классифицированные в качестве научных, должны иметь, по меньшей мере, две положительные рецензии. В случае если в журнале объявляются и приложения, не имеющие научный характер, научные статьи должны быть сгруппированы и четко выделены в первой части номера.

Объем кратких сообщений составляет 4-7 страниц, исследовательские статьи и тематические исследования с проблемно-ситуационным анализом – 10-14 страниц, однако объем обзорных статей может быть больше. Ограничения по количеству страниц не являются строгими, следовательно при соответствующем обосновании предоставленные работы могут быть длиннее или короче. В случае подачи расширенных версий ранее опубликованных докладов, представленных на конференции, редакция проверит было ли добавлено достаточно новых материалов для того, чтобы статья соответствовала стандартам журнала и условиям рецензирования. Добавленный материал должен быть новым, неопубликованным ранее. Новые результаты приветствуются, но не являются обязательным условием; однако ключевые тезисы, примеры, разработки и пр. должны быть более подробно представлены в статье по сравнению с первичным докладом на конфереции.

Язык работы

Статья должна быть написана на английском языке. Текст должен быть в лингвистическом и стилистическом смысле упорядочен, систематизирован, без сокращений (за исключением стандартных). Все физические величины должны соответствовать Международной системе единиц измерения – СИ. Очередность формул обозначается порядковыми номерами, проставляемыми с правой стороны в круглых скобках.

Резюме

Резюме является кратким информативным обзором содержания статьи, обеспечивающим читателю быстроту и точность оценки её релевантности. В интересах редакции и авторов, чтобы резюме содержало термины, часто используемые для индексирования и поиска статей. Составными частями резюме

являются введение/цель исследования, методы, результаты и выводы. В резюме должно быть от 100 до 250 слов, и оно должно находится между титулами (заголовок, ФИО авторов и др.) и ключевыми словами, за которыми следует текст статьи.

Ключевые слова

Ключевыми словами являются термины или фразы, адекватно представляющие содержание статьи, необходимые для индексирования и поиска. Ключевые слова необходимо выбирать, опираясь при этом на какой-либо международный источник (регистр, словарь, тезаурус), наиболее используемый внутри данной научной области. Число ключевых слов не может превышать 10. В интересах редакции и авторов, чтобы частота их встречи в статье была как можно большей. В статье они пишутся непосредственно после резюме.

Программа ASSISTANT предоставляет возможность использования сервиса KWASS, автоматически фиксирующего ключевые слова из источников/словарей по выбору автора/редактора.

Дата получения статьи

Дата, когда редакция получила статью; дата, когда редакция окончательно приняла статью к публикации; а также дата, когда были предоставлены необходимые исправления рукописи, приводятся в хронологическом порядке, как правило, в конце статьи.

Выражение благодарности

Наименование и номер проекта, т.е. название программы благодаря которой статья возникла, совместно с наименованием учреждения, которое финансировало проект или программу, приводятся в отдельном примечании, как правило, внизу первой страницы статьи.

Предыдущие версии работы

В случае если статья в предыдущей версии была изложена устно (под одинаковым или похожим названием, например, в виде доклада на научной конференции), сведения об этом должны быть указаны в отдельном примечании, как правило, внизу первой страницы статьи. Работа, которая уже была опубликована в каком-либо из журналов, не может быть напечатана в *«Военно-техническом вестнике»* ни под похожим названием, ни в изменённом виде.

Нумерация и название таблиц и графиков

Желательно, чтобы нумерация и название таблиц и графиков были исполнены на двух языках (на языке оригинала и на английском). Таблицы подписываются таким же способом как и текст и обозначаются порядковым номером с верхней стороны. Фотографии и рисунки должны быть понятны, наглядны и удобны для репродукции. Рисунки необходимо делать в программах Word или Corel. Фотографии и рисунки надо поставить на желаемое место в тексте. Для создания изображений и графиков использование функции снимка с экрана (скриншота) не допускается. В самом тексте статьи рекомендуется применение изображений и графиков, обработанных такими компьютерными программами, как: Excel, Matlab, Origin, SigmaPlot и др.

Ссылки (цитирование) в тексте

Оформление ссылок на источники в рамках статьи должно быть однообразным. *«Военно-технический вестник»* для оформления ссылок, цитат и списка использованной литературы применяет Гарвардскую систему (Harvard Referencing System, Harvard Style Manual). В тексте в скобках приводится фамилия цитируемого автора (или фамилия первого автора, если авторов несколько), год издания и по

необходимости номер страницы. Например: (Petrović, 2010, pp.10-20). Рекомендации о способе цитирования размещены на странице сайта *Инструкция по использованию Гарвардского стиля*. При оформлении ссылок, цитат и списка использованной литературы необходимо придерживаться установленных норм. Программа ASSISTANT предоставляет при цитировании возможность использования сервиса CiteMatcher, фиксирующего пропущенные цитаты в работе и в списке литературы.

Примечания (сноски)

Примечания (сноски) к тексту указываются внизу страницы, к которой они относятся. Примечания могут содержать менее важные детали, дополнительные объяснения, указания об использованных источниках (напр. научном материале, справочниках), но не могут быть заменой процедуры цитирования литературы.

Литература (референции)

Цитированной литературой охватываются, как правило, такие библиографические источники как статьи, монографии и т.п. Вся используемая литература в виде референций размещается в отдельном разделе статьи. Названия литературных источников не переводятся на язык работы. *«Военно-технический вестник»* для оформления списка использованной литературы применяет Гарвардскую систему (Harvard Style Manual). В списке литературы источники указываются в алфавитном порядке фамилий авторов или редакторов. Рекомендации о способе цитирования размещены на странице сайта *Инструкция по использованию Гарвардского стиля*. При оформлении списка использованной литературы необходимо придерживаться установленных норм. При оформлении списка литературы программа ASSISTANT предоставляет возможность использования сервиса RefFormatter, осуществляющего контроль оформления списка литературы в соответствии со стандартами Гарвардского стиля. Нестандартное, неполное и непоследовательное приведение литературы в системах оценки журнала считается достаточной причиной для оспаривания научного статуса журнала.

Авторское заявление

Авторское заявление предоставляется вместе со статьей, в нем авторы заявляют о своем личном вкладе в написание статьи. В заявлении авторы подтверждают, что статья написана в соответствии с *Приглашением и инструкциями для авторов*, а также с *Кодексом профессиональной этики журнала*.

Все рукописи статей подлежат профессиональному рецензированию.

Список рецензентов журнала *«Военно-технический вестник»* размещён на странице сайта *Список рецензентов*. Процесс рецензирования описан в разделе *Правила рецензирования*.

Редакция

Почтовый адрес редакции:
«Војнотехнички гласник»
ул. Велька Лукича Куряка 33, 11042 Белград, Республика Сербия
e-mail: vojnotehnicki.glasnik@mod.gov.rs,
тел: +381 11 3603 260, +381 66 8700 123

CALL FOR PAPERS AND ARTICLE FORMATTING INSTRUCTIONS

The instructions to authors about the article preparation for publication in the *Military Technical Courier* are based on the Regulations on categorization and ranking of scientific journals of the Ministry of Education, Science and Technological Development of the Republic of Serbia (Official Gazette of the Republic of Serbia, No 159/20). This Regulations aims at improving the quality of national journals and raising the level of their compliance with the international system of scientific information exchange.

The Military Technical Courier / Vojnotehnički glasnik (www.vtg.mod.gov.rs/index-e.html, втг.мо.упр.срб, ISSN 0042-8469 – print issue, e-ISSN 2217-4753 – online, UDC 623+355/359, DOI: 10.5937/VojnotehnickiGlasnik; https://doi.org/10.5937/VojnotehnickiGlasnik), is an peer-reviewed scientific journal.

The owners of the journal are the Ministry of Defence of the Republic of Serbia and the Serbian Armed Forces. The publisher and financier of the *Military Technical Courier* is the University of Defence in Belgrade (Military Academy).

The program of the journal is based on the annual classification of journals performed by a relevant Ministry as well as on its indexing in international indexing databases.

The journal covers scientific and professional fields within the educational-scientific field of **Natural-Mathematical Sciences**, as well as within the educational-scientific field of **Technical-Technological Sciences**, and especially the field of **defense sciences and technologies**. It publishes theoretical and practical achievements leading to professional development of all members of Serbian, regional and international academic communities as well as members of the military and ministries of defence in particular. It publishes papers with balanced coverage of analytical, experimental, and applied research as well as numerical simulations from various disciplines. The material published is of high quality and relevance, written in a manner that makes it accessible to a wider readership. The journal welcomes papers reporting original theoretical and/or practice-oriented research as well as extended versions of already published conference papers. Manuscripts for publication are selected through a double-blind peer-review process to validate their originality, relevance, and readability. This being so, the objective is not only to keep the quality of published papers high but also to provide a timely, thorough, and balanced review process.

The editorial policy of the *Military Technical Courier* is based on the COPE Core Practices, common COPE, DOAJ, OASPA and WAME Principles of Transparency and Best Practice in Scholarly Publishing as well as on the best accepted practices in scientific publishing. The Military Technical Courier has been a COPE (Committee on Publication Ethics) member since 2nd May 2018 and a member of OASPA (Open Access Scholarly Publishers Association) since 27th November 2015.

The Ministry of Science, Technological Development and Innovation of the Republic of Serbia classified the *Military Technical Courier* for the year 2023, on December 27, 2023

  – on the list of periodicals for computer sciences,
  category: reputed national journal **(M51)**,

  – on the list of periodicals for electronics, telecommunications and IT,
  category: reputed national journal **(M51)**,

  – on the list of periodicals for mechanical engineering,
  category: national journal of international importance **(M24)**,

  – on the list of periodicals for materials and chemical technology,
  category: national journal of international importance **(M24)**.

The approved lists of national periodicals for the year 2023 can be viewed on the website of the *Military Technical Courier*, page *Journal categorization*.

More detailed information can be found on the website of the Ministry of Education, Science and Technological Development of the Republic of Serbia.

The information on the categorization can be also found on the website of KOBSON (Consortium of Libraries of Serbia for Unified Acquisition).

The periodical is categorized in compliance with the Regulations on categorization and ranking of scientific journals of the Ministry of Education, Science and Technological Development of the Republic of Serbia (Official Gazette of the Republic of Serbia, No 159/20). More detailed information can be found on the website of the Ministry of Education, Science and Technological Development.

The journal is in the Serbian Citation Index – SCIndex (data base of national scientific journals), in the Scientific Information System Redalyc, and in the Russian Index of Science Citation/Российский индекс научного цитирования (RINC/РИНЦ) and is constantly monitored depending on the impact within the bases themselves. More detailed information can be viewed on the website of the *Military Technical Courier*, page *Journal indexing*.

The *Military Technical Courier*, in terms of its content, offers the possibility of open access (DIAMOND OPEN ACCESS) and applies the Creative Commons Attribution (CC BY) licence on copyright. The copyright details can be found on the *Copyright notice and Self-archiving policy* page of the journal's website.

Manuscripts are submitted online, through the electronic editing system ASSISTANT, developed by the Center for Evaluation in Education and Science – CEON.

The access and the registration are through the *Military Technical Courier* site http://www.vtg.mod.gov.rs/index-e.html, on the page *ASSISTANT* or the page *SCINDEKS* or directly through the link (aseestant.ceon.rs/index.php/vtg).

The detailed instructions about the registration for the service are on the website http://www.vtg.mod.gov.rs/index-e.html, on the page *Instructions for ASSISTANT*.

All authors submitting a manuscript for publishing in the *Military Technical Courier* should register for an ORCID ID following the instructions on the web page *Registration for an ORCID identifier*.

The *Military Technical Courier* publishes articles in English, using Arial and a font size of 11pt with Single Spacing.

The procedures of article preparation, writing and editing should be in accordance with the *Publication ethics statement* (http://www.vtg.mod.gov.rs/publication-ethics-statement.html).

The article should contain an abstract with keywords, introduction (motivation for the work), body (adequate overview of the representative work in the field, a clear statement of the novelty in the presented research, suitable theoretical background, one or more examples to demonstrate and discuss the presented ideas), conclusion, and references (without heading and subheading enumeration). The article length should not normally exceed 16 pages of the A4 paper format with single spacing, up to a maximum of 24 pages with references and supplementary material included.

The article should be formatted following the instructions in the Article Form which can be downloaded from website page *Article form*.

Title

The title should be informative. It is in both Journal's and author's best interest to use terms suitable for indexing and word search. If there are no such terms in the title, the author is strongly advised to add a subtitle.

Letterhead title

The letterhead title is given at a top of each page for easier identification of article copies in an electronic form in particular. It contains the author's surname and first name initial (for multiple authors add "et al"), article title, journal title and collation (year, volume, issue, first and last page). The journal and article titles can be given in a shortened form.

Author's name

Full name(s) of author(s) should be used. It is advisable to give the middle initial. Names are given in their original form (with diacritic signs if in Serbian).

Author's affiliation

The full official name and seat of the author's affiliation is given, possibly with the name of the institution where the research was carried out. For organizations with complex structures, give the whole hierarchy (for example, University of Defence in Belgrade, Military Academy, Department for Military Electronic Systems). At least one organization in the hierarchy must be a legal entity. When some of multiple authors have the same affiliation, it must be clearly stated, by special signs or in other way, which department exactly they are affiliated with. The affiliation follows the author's name. The function and title are not given.

Contact details

The postal addresses or the e-mail addresses of the authors are given in the first page.

Type of articles

Classification of articles is a duty of the editorial staff and is of special importance. Referees and the members of the editorial staff, or section editors, can propose a category, but the editor-in-chief has the sole responsibility for their classification.

The *Military Technical Courier* publishes scientific articles.

Scientific articles:

– Original scientific papers (giving the previously unpublished results of the author's own research based on scientific methods);

– Review papers (giving an original, detailed and critical view of a research problem or an area to which the author has made a contribution demonstrated by self-citation);

– Short communications or Preliminary communications (original scientific full papers but shorter or of a preliminary character);

– Scientific commentaries or discussions (discussions on a particular scientific topic, based exclusively on scientific argumentation) and opinion pieces.

Exceptionally, in particular areas, a scientific paper in the Journal can be in a form of a monograph or a critical edition of scientific data (historical, archival, lexicographic, bibliographic, data survey, etc.) which were unknown or hardly accessible for scientific research.

Papers classified as scientific must have at least two positive reviews.

If the journal contains non-scientific contributions as well, the section with scientific papers should be clearly denoted in the first part of the Journal.

Short communications are usually 4-7 pages long, research articles and case studies 10-14 pages, while reviews can be longer. Page number limits are not strict and, with

appropriate reasoning, submitted manuscripts can also be longer or shorter. If extended versions of previously published conference papers are submitted, Editors will check if sufficient new material has been added to meet the journal standards and to qualify such manuscripts for the review process. The added material must not have been previously published. New results are desired but not necessarily required; however, submissions should contain expansions of key ideas, examples, elaborations, etc. of conference papers.

Language

The language of the article should be in English. The grammar and style of the article should be of good quality. The systematized text should be without abbreviations (except standard ones). All measurements must be in SI units. The sequence of formulae is denoted in Arabic numerals in parentheses on the right-hand side.

Abstract and summary

An abstract is a concise informative presentation of the article content for fast and accurate evaluation of its relevance. It contains the terms often used for indexing and article search. A 100- to 250-word abstract has the following parts: introduction/purpose of the research, methods, results and conclusion.

Keywords

Keywords are terms or phrases showing adequately the article content for indexing and search purposes. They should be allocated heaving in mind widely accepted international sources (index, dictionary or thesaurus), such as the Web of Science keyword list for science in general. The higher their usage frequency is, the better. Up to 10 keywords immediately follow the abstract and the summary, in respective languages. For this purpose, the ASSISTANT system uses a special tool KWASS for the automatic extraction of key words from disciplinary thesauruses/dictionaries by choice and the routine for their selection, i.e. acceptance or rejection by author and/or editor.

Article acceptance date

The date of the reception of the article, the dates of submitted corrections in the manuscript (optional) and the date when the Editorial Board accepted the article for publication are all given in a chronological order at the end of the article.

Acknowledgements

The name and the number of the project or programme within which the article was realised is given in a separate note at the bottom of the first page together with the name of the institution which financially supported the project or programme.

Article preliminary version

If an article preliminary version has appeared previously at a meeting in a form of an oral presentation (under the same or similar title), this should be stated in a separate note at the bottom of the first page. An article published previously cannot be published in the *Military Technical Courier* even under a similar title or in a changed form.

Tables and illustrations

All the captions should be in the original language as well as in English, together with the texts in illustrations if possible. Tables are typed in the same style as the text and are denoted by Arabic numerals at the top. Photographs and drawings, placed appropriately in the text, should be clear, precise and suitable for reproduction. Drawings should be created in Word or Corel.

For figures and graphs, proper data plot is recommended i.e. using a data analysis program such as Excel, Matlab, Origin, SigmaPlot, etc. It is not recommended to use a screen capture of a data acquisition program as a figure or a graph.

Citation in the text

Citation in the text must be uniform. The *Military Technical Courier* applies the Harvard Referencing System given in the Harvard Style Manual. When citing sources within your paper, i.e. for in-text references of the works listed at the end of the paper, place the year of publication of the work in parentheses and optionally the number of the page(s) after the author's name, e.g. (Petrovic, 2012, pp.10-12). A detailed guide on citing, with examples, can be found on *Military Technical Courier* website on the page *Instructions for Harvard Style Manual*. In-text citations should follow its guidelines. For checking in-text citations, the ASSISTANT system uses a special tool CiteMatcher to find out quotes left out within papers and in reference lists.

Footnotes

Footnotes are given at the bottom of the page with the text they refer to. They can contain less relevant details, additional explanations or used sources (e.g. scientific material, manuals). They cannot replace the cited literature.

Reference list (Literature)

The cited literature encompasses bibliographic sources such as articles and monographs and is given in a separate section in a form of a reference list. References are not translated to the language of the article.

In compiling the reference list and bibliography, the *Military Technical Courier* applies the Harvard System – Harvard Style Manual. All bibliography items should be listed alphabetically by author's name, without numeration. A detailed guide for listing references, with examples, can be found on *Military Technical Courier* website on the page *Instructions for Harvard Style Manual*. Reference lists at the end of papers should follow its guidelines. In journal evaluation systems, non-standard, insufficient or inconsequent citation is considered to be a sufficient cause for denying the scientific status to a journal.

Authorship Statement

The Authorship statement, submitted together with the paper, states authors' individual contributions to the creation of the paper. In this statement, the authors also confirm that they followed the guidelines given in *the Call for papers* and the *Publication ethics and malpractice statement of the journal*.

All articles are peer reviewed.

The list of referees of the *Military Technical Courier* can be viewed at website page *List of referees*. The article review process is described on the *Peer Review Process* page of the website.

Editorial Team

Address of the Editorial Office:
Vojnotehnički glasnik / Military Technical Courier
Veljka Lukića Kurjaka 33
11042 Belgrade, Republic of Serbia
e-mail: vojnotehnicki.glasnik@mod.gov.rs, tel.: +381 11 3603 260, +381 66 8700 123

ОД 1953.

72

ВТГ

ГОДИНА

OD 1953.

72

ВТГ

GODINA

С 1953 г.

72

ВТГ

ЛЕТ

SINCE 1953

72

ВТГ

YEARS